Progress in Soil Science

Alfred E. Hartemink
Budiman Minasny *Editors*

Digital Soil Morphometrics

Springer

Digital Soil Morphometrics

Progress in Soil Science

Aims and Scope

Progress in Soil Science series aims to publish books that contain novel approaches in soil science in its broadest sense – books should focus on true progress in a particular area of the soil science discipline. The scope of the series is to publish books that enhance the understanding of the functioning and diversity of soils in all parts of the globe. The series includes multidisciplinary approaches to soil studies and welcomes contributions of all soil science subdisciplines such as: soil genesis, geography and classification, soil chemistry, soil physics, soil biology, soil mineralogy, soil fertility and plant nutrition, soil and water conservation, pedometrics, digital soil mapping, proximal soil sensing, digital soil morphometrics, soils and land use change, global soil change, natural resources and the environment.

More information about this series at http://www.springer.com/series/8746

Alfred E. Hartemink · Budiman Minasny
Editors

Digital Soil Morphometrics

Editors
Alfred E. Hartemink
Department of Soil Science, FD Hole Soils Lab
University of Wisconsin—Madison
Madison, WI
USA

Budiman Minasny
Faculty of Agriculture and Environment
The University of Sydney
Sydney
Australia

ISSN 2352-4774 ISSN 2352-4782 (electronic)
Progress in Soil Science
ISBN 978-3-319-28294-7 ISBN 978-3-319-28295-4 (eBook)
DOI 10.1007/978-3-319-28295-4

Library of Congress Control Number: 2016930178

Printed on acid-free paper

This Springer imprint is published by SpringerNature
The registered company is Springer International Publishing AG Switzerland

Foreword

Digital Soil Morphometrics: needed now because just seeing is not enough anymore!

The visionary discovery by our pioneers in the late nineteenth century that soils were more than dirt obscuring rocks has been the remarkable start of the development of soil science as a separate and vital discipline. As the importance of soils contributing to ecosystem services and sustainable development goals becomes increasingly evident at this point in time, soil scientists should not only cherish their existing knowledge and expertise but should also be alert as to new developments that can increase the significance of their input into interdisciplinary programs aimed at sustainable development.

Seeing, feeling, smelling, and tasting represented basic activities in the early phases of soil science and they still are highly relevant. The "seeing" deserves special attention, because our pioneers noticed elements that had apparently been overlooked by earlier observers as they were restricted in their views by their particular paradigms and hang-ups. I recall lectures at Wageningen University where a vertisol expert mentioned many early profile descriptions of vertisols where slickensides were not noticed. Once they were recognized, they became operational morphological features, quite significant to illustrate swelling processes and soil behavior and for soil classification. The lesson is to always keep an open eye when "seeing" morphological features in soil: Allow yourself to be surprised.

Be that as it may, there still is a high variability among observations by different observers. Standardization of description schemes has helped, and an excellent, early, example are the Munsell color charts of 1938. This book on Digital Soil Morphometrics represents a major step forward in "seeing" in at least two ways. First, several innovative techniques are discussed that allow in situ characterization of soil morphological features which is comparable, in principle, to use of the Munsell charts. These techniques provide quantitative, reproducible data that are crucial for modern applications. Second, data will be part of a digital environment allowing statistical and spatial variability analyses and modern forms of visualization.

The analogy with soil survey is striking. In essence, empirical survey procedures of the past have been strengthened by geostatistical spatial analyses and by the introduction of innovative field techniques and digital landscape modeling. In a comparable manner, Digital Soil Morphometrics closes an obvious gap in the pedological toolkit because so far profile descriptions were just that: descriptions. Of course, quantitative analyses have been a successful part of micromorphological analyses over the years, but preparation of thin sections is costly and time-consuming, and even though micromorphology has made major contributions to soil genesis studies, it has never become a standard tool in soil survey interpretations. Direct measurement of morphological features in soil profiles presents therefore an approach with a much higher operational potential when facing modern soil survey interpretations.

Finally, this is an age where scientists have to continually earn their "societal license to research" and their particular "niche," facing a critical population and policy arena. Soil science has major contributions to make to research on food, water and energy security, climate change, and biodiversity loss. What could be a "niche" for Digital Soil Morphometrics? Chemical soil analyses of mixed samples indicate what is there on average. Soil morphology explains why chemical reactions are different when the compounds occur as, e.g., small or large concretions or as cutans. Physical flow models still implicitly assume that soils are isotropic and homogeneous. Soil morphology defines heterogeneous pore systems that are also important for root functioning, etc.

Digital Soil Morphometrics will earn its place in the pedological toolkit when it demonstrates that moving away from approaches based on "averages" or "simplifications" provides new enlightening insights into the incredibly complicated but highly fascinating ways of the living soil.

Johan Bouma
Em. Prof. Soil Science
Wageningen University
The Netherlands

Preface

After years of diminishing investment and intellectual efforts, pedology is thriving again. The reasons hereto are several fold, but increased interest and appreciation in soils as well as a range of new instruments and techniques brightened soil research across the globe. Although soils can be studied without digging a pit or taking a soil core, the soil profile is at the heart of many soil studies. Rightfully so, much of our understanding has come from careful and precise measurement and observations along a soil profile wall. However, the observational and interpretative techniques have not changed much in the past decades despite the technical revolution that is taken place in many soil science subdisciplines. We have proposed the use of *digital soil morphometrics* to expand and compliment the pedologists's fieldkit to observe soil profiles. Digital soil morphometrics is defined as the application of instruments and techniques for measuring, mapping, and quantifying soil profile properties and deriving depth functions of soil properties. The pedon is at the heart of digital soil morphometrics.

In 2014, the *International Union of Soil Sciences* (IUSS) recognized the need for a Working Group on Digital Soil Morphometrics. The *IUSS Inaugural Global Workshop on Digital Soil Morphometrics* was held in June 2015 in Madison, USA, and consisted of three days of presentations and discussions, preceded by a one-day fieldtrip. There were 70 participants from over 15 countries. This book contains selected papers from the *IUSS Inaugural Global Workshop on Digital Soil Morphometrics*. The conference presentations (and this book) were structured along four research topics: (i) soil profile properties, (ii) soil profile imaging, (iii) soil depth functions, and (iv) use and applications of digital soil morphometrics. We have selected 26 papers that focus on novel and exciting aspects of soil morphometrics and included a few review papers and summary chapter.

We are greatly indebted to all conference participants and authors that helped shape the conference and made excellent contributions to discussions and papers in this book. We acknowledge the financial support from the University of Wisconsin —Madison, College of Agriculture and Life Science (CALS), and the Department of Soil Science. Special thanks to Bill Bland, Birl Lowery, and Carol Duffy, and to

Leah leighty of CALS Conference Services for their kind assistance. It is our hope that the ideas and results in this book will help to shape critical thinking about how we look at soil profiles for we need to move forward and deepen our understanding.

Alfred E. Hartemink
Budiman Minasny

Contents

Contributors

Kabindra Adhikari Department of Soil Science, FD Hole Soils Lab, University of Wisconsin-Madison, Madison, WI, USA

Matt Aitkenhead The James Hutton Institute, Scotland, UK

Lucia Helena Cunha dos Anjos Soils Department—Agronomy, Federal Rural University of Rio de Janeiro, Seropédica, RJ, Brazil

Francisco J. Arriaga Department of Soil Science, University of Wisconsin-Madison, Madison, WI, USA

Dylan Beaudette USDA-Natural Resource Conservation Service, Sonora, CA, USA

D.E. Beaudette USDA-Natural Resource Conservation Service, Sonora, CA, USA

Bedrich Benes Department of Computer Graphics Technology, Purdue University, West Lafayette, IN, USA

Benito R. Bonfatti Universidade Federal do Rio Grande do Sul, UFRGS—Faculdade de Agronomia, Porto Alegre, RS, Brazil; Department of Soil Science, FD Hole Soils Lab, University of Wisconsin—Madison, Madison, WI, USA; CAPES Grand Holder—Process BEX 3095/14-2, CAPES Foundation, Ministry of Education of Brazil, Brasília, DF, Brazil

Glenn Borchardt Soil Tectonics, Berkeley, CA, USA

Waldir de Carvalho Jr. Embrapa Solos, Jardim Botânico, RJ, Brazil

Cesar da Silva Chagas Embrapa Solos, Jardim Botânico, RJ, Brazil

Zueng-Sang Chen Department of Agricultural Chemistry, National Taiwan University, Taipei, Taiwan

Malcolm Coull The James Hutton Institute, Scotland, UK

Adam Csorba Department of Soil Science and Agricultural Chemistry, Szent István University, Gödöllő, Hungary

Ricardo Simão Diniz Dalmolin Soil Department, Federal University of Santa Maria, Santa Maria, RS, Brazil

José A.M. Demattê Department of Soil Science, Luiz de Queiroz College of Agriculture, University of São Paulo, Piracicaba, SP, Brazil

David Donnelly The James Hutton Institute, Scotland, UK

Minerva J. Dorantes Agronomy Department, Purdue University, West Lafayette, IN, USA

André Carnieletto Dotto Federal University of Santa Maria, Santa Maria, RS, Brazil

Kim Drager Department of Animal Biology, University of Illinois, Urbana, IL, USA

Dennis V. Eck Bennett and Schulte Oil Company, Russell, KS, USA

Marta Fuchs Department of Soil Science and Agricultural Chemistry, Szent István University, Gödöllő, Hungary

Gilles Gagné Centre de Référence en Agriculture et Agroalimentaire du Québec (CRAAQ), Québec, QC, Canada

Elvio Giasson Universidade Federal do Rio Grande do Sul, UFRGS—Faculdade de Agronomia, Porto Alegre, RS, Brazil; Federal University of Rio Grande do Sul, Porto Alegre, RS, Brazil

Daniel Giménez Department of Environmental Sciences, Rutgers University, New Brunswick, NJ, USA

Jenna R. Grauer-Gray Department of Soil Science, F.D. Hole Laboratory, University of Wisconsin—Madison, Madison, WI, USA

Richard Gwatkin The James Hutton Institute, Scotland, UK

Alfred E. Hartemink Department of Soil Science, FD Hole Soils Lab, University of Wisconsin—Madison, Madison, WI, USA

Carolyn Hedley Landcare Research, Palmerston North, New Zealand

Jon Hempel USDA-NRCS, National Soil Survey Center, Lincoln, NE, USA

Daniel R. Hirmas Department of Geography and Atmospheric Science, University of Kansas, Lawrence, KS, USA

David Hoover USDA-NRCS, National Soil Survey Center, Lincoln, NE, USA

Zeng-Yei Hseu Department of Agricultural Chemistry, National Taiwan University, Taipei, Taiwan

Ho Jun Jang Department of Environmental Sciences, Faculty of Agriculture and Environment, The University of Sydney, New South Wales, Australia

Shih-Hao Jien Department of Soil and Water Conservation, National Pingtung University of Science and Technology, Pingtung, Taiwan

Edward J. Jones Department of Environmental Sciences, Faculty of Agriculture and Environment, The University of Sydney, Sydney, NSW, Australia

Laura Kenny Rutgers, The State University of New Jersey, New Brunswick, NJ, USA

Hansoo Kim Department of Computer Graphics Technology, Purdue University, West Lafayette, IN, USA

Vince Lang Department of Soil Science and Agricultural Chemistry, Szent István University, Gödöllő, Hungary

Vincent Lang Department of Soil Science and Agricultural Chemistry, Szent István University, Gödöllő, Hungary

Michaël A. Leblanc Department of Soils and Agri-Food Engineering, Université Laval, Québec, QC, Canada

Zamir Libohova USDA-NRCS, Lincoln, NE, USA

Robert Long USDA-NRCS, St. Johnsbury Soil Survey Office, St. Johnsbury, VT, USA

Birl Lowery Department of Soil Science, University of Wisconsin-Madison, Madison, WI, USA

Y. Lucas PROTEE, Université de Toulon, La Garde, Provance, France

Andrew Manderson Landcare Research, Palmerston North, New Zealand

Alex McBratney Department of Environmental Sciences, Faculty of Agriculture and Environment, The University of Sydney, Sydney, NSW, Australia

Alex B. McBratney Department of Environmental Sciences, Faculty of Agriculture and Environment, The University of Sydney, Sydney, NSW, Australia

Kevin McSweeney Department of Natural Resources and Environmental Sciences, University of Illinois, Urbana, IL, USA

A.J. Melfi IEE, ESALQ, Universidade de São Paulo, São Paulo, Brazil

Erika Micheli Department of Soil Science and Agricultural Chemistry, Szent István University, Gödöllő, Hungary

Budiman Minasny Department of Environmental Sciences, Faculty of Agriculture and Environment, The University of Sydney, Sydney, NSW, Australia

Edison A. Mome Filho Department of Soil Science, University of São Paulo, Piracicaba, SP, Brazil

C.R. Montes CENA, NUPEGEL, Universidade de São Paulo, Piracicaba, São Paulo, Brazil

Edwin Muñiz United States Department of Agriculture, Natural Resources Conservation Service, Somerset, NJ, USA

Judit Nagy Department of Soil Science and Agricultural Chemistry, Szent István University, Gödöllő, Hungary

Phillip R. Owens Lilly Hall of Life Sciences, Purdue University—Agronomy Department, West Lafayette, IN, USA

Léon E. Parent Department of Soils and Agri-Food Engineering, Université Laval, Québec, QC, Canada

Matthew Patterson Department of Environmental Sciences, Rutgers University, New Brunswick, NJ, USA

O.J.R. Pereira CENA, NUPEGEL, Universidade de São Paulo, Piracicaba, São Paulo, Brazil

Helena Saraiva Koenow Pinheiro Soils Department—Agronomy, Federal Rural University of Rio de Janeiro, Seropédica, RJ, Brazil

Brian F. Platt Department of Geology and Geological Engineering, University of Mississippi, University, MS, USA

Dalvan J. Reinert Department of Soil, University Federal de Santa Maria, Rio Grande do Sul, Brazil

Stephen Roecker USDA-Natural Resource Conservation Service, Indianapolis, IN, USA

Pierre Roudier Landcare Research, Lincoln, Palmerston North, New Zealand

Philip Schoeneberger USDA-NRCS, Lincoln, NE, USA

Darrell G. Schulze Agronomy Department, Purdue University, West Lafayette, IN, USA

Cathy Seybold USDA-NRCS, Lincoln, NE, USA

Richard K. Shaw United States Department of Agriculture, Natural Resources Conservation Service, Somerset, NJ, USA

Elisângela Benedet Silva Epagri—Agricultural Research and Rural Extension Corporation of Santa Catarina, Federal University of Rio Grande do Sul, Porto Alegre, RS, Brazil

Walquiria Chaves Silva Federal University of Santa Catarina Campus Curitibanos, Curitibanos, SC, Brazil

Jay Skovlin USDA-Natural Resource Conservation Service, Missoula, MT, USA

Uta Stockmann Department of Environmental Sciences, Faculty of Agriculture and Environment, The University of Sydney, New South Wales, Australia

Chen-Chi Tsai Department of Forestry and Natural Resources, National Ilan University, I-Lan, Taiwan

Candiss Williams USDA-NRCS, Lincoln, NE, USA

Carey A. Williams Rutgers, The State University of New Jersey, New Brunswick, NJ, USA

Skye Wills USDA-Natural Resource Conservation Service, Lincoln, NE, USA

Doug Wysocki USDA-NRCS, Lincoln, NE, USA

Alexandre ten Caten Biology and Veterinary Science Department, Federal University of Santa Catarina Campus Curitibanos, Curitibanos, SC, Brazil

Chapter 1
What Is Digital Soil Morphometrics and Where Might It Be Going?

Edward J. Jones and Alex B. McBratney

Abstract A large number of devices exist that are able to provide quantitative and objective representation of soil properties. Many of these devices are able to elucidate properties unattainable to the human eye and may cause us to redefine what we term "field observable" properties. We discuss possible meanings for, and approaches to, digital soil morphometrics (DSMorph). Digital soil morphometrics' relationship to other domains of research and practice such as proximal soil sensing and conventional field soil description is explored, with the suggestion that DSMorph has greatest potential as a special case of proximal soil sensing. The application areas of DSMorph outside of routine soil description are canvassed, and the technological gaps are discussed.

Keywords Pedology · Soil description · Proximal soil sensing

1.1 Introduction

The development of morphometrics in the biological sciences enabled the quantitative analysis of form and revolutionised the description and statistical analysis of specimens. To bring a similar revolution to soil description and to unite diverse tools and techniques that are able to provide more objective and quantitative description of soil attributes, the subdiscipline of digital soil morphometrics (DSMorph) has been proposed (Hartemink and Minasny 2014). In general terms, DSMorph has been defined as the "*application of tools and techniques for measuring, mapping and quantifying soil profile attributes and deriving continuous depth functions*" (Hartemink and Minasny 2014). DSMorph is thus at the forefront of technology and innovation in soil science and promises to provide a much

E.J. Jones · A.B. McBratney (✉)
Department of Environmental Sciences, Faculty of Agriculture and Environment, The University of Sydney, Sydney, NSW 2006, Australia
e-mail: alex.mcbratney@sydney.edu.au

A.E. Hartemink and B. Minasny (eds.), *Digital Soil Morphometrics*, Progress in Soil Science, DOI 10.1007/978-3-319-28295-4_1

needed scientific and technological overhaul to field soil description, a discipline which has been relatively technology stable, possibly averse, for decades. DSMorph tools and techniques have untold pedological, edaphic and environmental applications.

While mathematical approaches and the computing power to perform morphometric analyses have greatly advanced in recent years, there remain two fundamental issues encumbering the supply of relevant input data: first, labour intensity, as examining and recording appropriate attributes can be a time-consuming task (Blackith and Reyment 1971, p. 286); second, subjectivity, as there is always elements to the observation of natural forms that may be considered more of an art than a science (Blackith and Reyment 1971, p. 1). These issues underlie the development of DSMorph and highlight the value of any technique that may provide less labour-intensive data collection and increased objectivism of soil observations. The marriage of digital data collection with morphometric approaches is crucial to the success of this new subdiscipline. However, key in recognising DSMorph as a subdiscipline is the identification of which particular attributes or contributions it may deliver that other subdisciplines cannot deliver independently. DSMorph approaches can better represent variation within observed soil objects, facilitate the quantification of uncertainties and will change the way we observe and describe soils. Nonetheless, the offered definition is quite broad, and its boundaries need to be better delineated so that we may clearly define what DSMorph is, what it is not and where it might be going. To better understand DSMorph, we deconstruct its component topics of digital data acquisition, soil form and morphometric approaches, and investigate the unique contribution of each. As innovation in the application of DSMorph tools and techniques as they pertain to routine soil description has recently been reviewed (Hartemink and Minasny 2014), the second half of this chapter is focused on highlighting a selection of novel and potential applications of DSMorph techniques outside of routine soil description. Technological and information gaps are identified and ways forward discussed.

1.2 Conventional Field Soil Description

Before we investigate DSMorph further, we must understand the need for its development. Most people would agree that field soil description has largely stagnated following rapid initial development. This development includes the formalisation of procedures for observing and classifying soils (Clarke 1936; Soil Survey Staff 1937), as well as the codification of morphological classification of soil structure (Nikiforoff 1941). This was a significant step towards the standardised observation and reporting of soil attributes mandated by widespread soil survey programmes beginning from the turn of the twentieth century. Pedology has historically been a hands-on, technology limited discipline. During this period of standardisation, it was noted that the most important tool for the soil observer was

the humble spade (Soil Survey Staff 1937, p. 28). In fact, excluding a small number of qualitative analyses involving HCl or H_2O_2, and basic tests for soil reaction, there were "*few reliable field tests of soils that serve a useful purpose in the soil survey*" (Soil Survey Staff 1937, pp. 30–32). Fast-forward eight decades and little has changed. The field of soil description has remained largely technologically stable since the 1950s, and to this day, the main modus operandi in soil description remains trained human observation. Stagnation in itself is not a cause for action; in fact, it may signify the successful maturation of a field. However, the reliance on human observation brings into question sources of error, as although professional observers may be trained and calibrated to one another, this training cannot completely eliminate inter- or intra-observer variation.

If we focus on soil colour, one of the most significant soil attributes, we can see just how much variation in assessment can be introduced. In addition to differences in light under which colour measurements are being made, it is also well established that physiological differences in the eye mean that not everyone perceives colour in the same manner, and that colour perception also drifts with ageing due to the gradual yellowing of the eye's lens (Billmeyer and Saltzman 1981, p. 174). The use of reference charts is meant to eliminate the effects of these differences and standardise the reporting of soil colour. The Munsell chart is not free from variation. Sánchez-Marañón et al. (2005) investigated these ubiquitous colour books and found that manufacturer production differences and non-uniform fading characteristics can significantly affect colour determination. The authors found that visual judgement of soil colour between individuals using the same Munsell chart under heavily controlled conditions was variable. Similar results were obtained by Shields et al. (1966), leading them to suggest the use of spectrophotometry to standardise colour observation and eliminate observer variability; a reasonable suggestion that was never implemented. In fact, the use of a spectrophotometer system to eliminate observer variation had been suggested another 35 years prior (Carter 1931). Decades have passed since brewing industries dropped reference charts in favour of spectrophotometric colour standards (ASBC 1949). It is absurd to imagine modern medical studies and analytical assays using reference charts for quantitative analysis. So why is soil science so slow to change? When observing soils we should strive to eliminate, or at least account for, the sources of variability. Thus, approaches, such as DSMorph, that can give more objectivity are a useful way forward.

1.3 Deconstructing DSMorph

In the appropriation of terms from other scientific disciplines, one must be sure to clearly define how they translate to their new environment. To avoid confusion, we need to deconstruct the component topics of this new subdiscipline to clarify meanings for, and approaches to, DSMorph.

1.3.1 Digital Data Acquisition

The digital component refers not to the devices themselves, but rather to the quantitative data that they can deliver. Data obtained using DSMorph tools are more objective and at times able to measure attributes that are unattainable using traditional methods. To investigate the benefits of these approaches, we will look at the progress made by observing some soil structural attributes using digital techniques. The procurement of digital data is not new, with those who might be considered pioneering digital soil morphometricians looking for new methods to quantify treatment effects on soil surface condition. Currence (1969), for example, quantified soil surface roughness under different tillage treatments using a profilometer system. The automated system was able to record relief information recorded on punchcards at a height resolution of 0.01 inch. Meanwhile, O'Callaghan and Loveday (1973) were able to use digitised images to quantify the effect of gypsum application on the length and width of crack skeletons (Fig. 1.1). In both of these studies, digital quantification allowed investigation of attributes on a scale that was not feasible using manual techniques, and in doing so discerned treatment effects.

Digital data acquisition of structural properties then extended vertically into the soil profile with a focus on micromorphology. Although not analysed directly in the field, thin sections were taken and image analysers were used to study pore distributions and how they work (Bouma et al. 1977; Murphy et al. 1977). Then, CT scanning was used to investigate undisturbed soil material (Petrovic et al. 1982; Hainsworth and Aylmore 1983). Mesomophological analysis was introduced to bridge the gap between these micromorphological approaches and field description, which was largely qualitative and macromorphological (Koppi and McBratney 1991). This meant that instead of measuring discrete points, a continuous description of properties such as pore size and porosity could be presented (Fig. 1.2a). This allowed interpretation of the relationship between structural properties and others such as redoximorphic features (Fig. 1.2c). When representing

Fig. 1.1 Section of original photograph showing a cracked soil surface (*left*), digitised crack "skeleton" (*middle*) and "ballooned" discrete peds (*right*), adapted from (O'Callaghan and Loveday 1973)

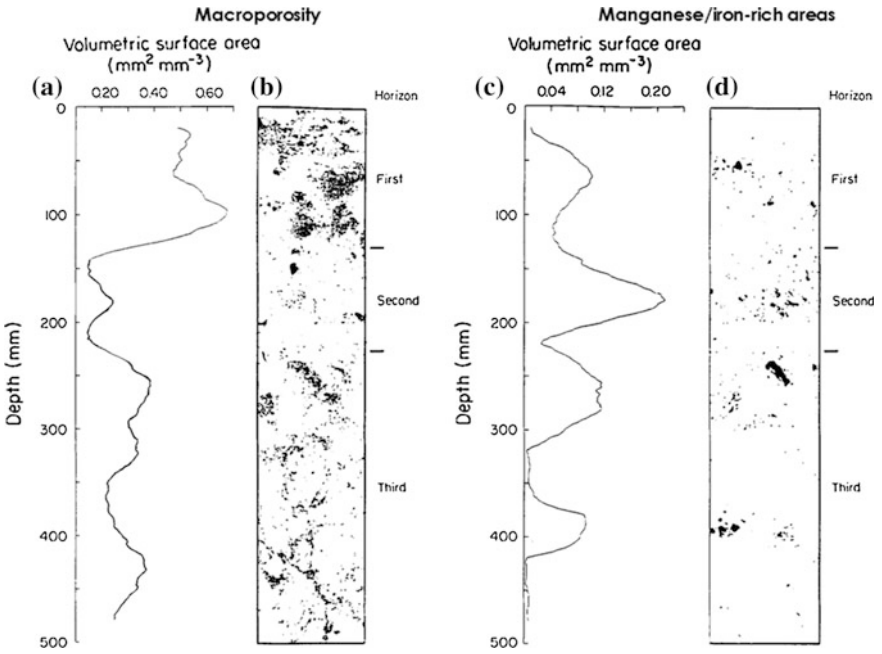

Fig. 1.2 Mesomorphological analysis of a Paleustalfs (Koppi and McBratney 1991): **a** smoothed volumetric surface area of macropores; **b** image of macropores (*black*) and soil solids (*white*) with horizon designations; **c** smoothed volumetric surface area of manganese-/iron-rich areas; **d** image of manganese-/iron-rich areas (*black*) and other soil solids and pores (*white*) with horizon designations. Images represent a 100 × 500 mm section of the soil profile with a resolution of approximately 0.2 mm. Smoothed lines were produced using a 20 mm moving averages

soils in this continuous manner, we can see that soil properties are not uniform within soil horizons. This may lead us to question the conventional horizon-based representation of soil attributes and to ask whether the tools used to analyse soils are updated and does this mean that the way in which we describe soils also needs to be readdressed?

1.3.2 Soil Form

"*The essential problem in morphometrics is to measure the degree of similarity of two forms*" (Blackith and Reyment 1971, p. 9). However, what does form mean when applied to the soil profile? When assessing profile attributes, the concept of form extends beyond its original biological definition concerning the size and shape of a specimen. For our purposes, form encompasses two aspects: geometric, or the disposition of attributes in a 2-3-4D space, and multivariate, or the various attributes of interest within the space.

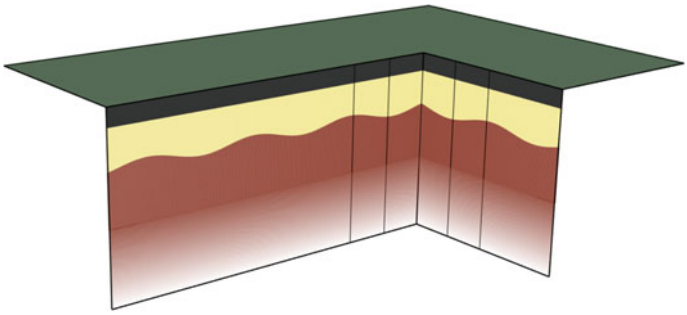

Fig. 1.3 A potential standard soil volumetric object. Three transects are analysed on one wall and others on adjacent wall orthogonal to the first

So how do we describe the geometric aspect of form? As suggested above, currently we do not describe it very well. When samples are taken to the laboratory, dried, ground and then analysed, we are only reporting an average value of the sample and have lost the information on spatial variability. Some DSMorph devices, such as hyperspectral cameras (Steffens and Buddenbaum 2013) and laser scanners (Eck et al. 2013), are able to scan in two dimensions and capture some of this vertical and lateral variation. Do we capture this variation using point-based devices such as portable NIR and XRF spectroscopy? To do so, we must rethink how we spatially describe a soil. An expedient solution would be to include multiple vertical transects to allow the characterisation of variability within the observed object. For standardisation of variation over a fixed distance, the vertical transects need to be a set distance apart and cover a fixed area, or if you take samples at right angles within a fixed volume (Fig. 1.3). Given the mean and the range of values calculated with depth, you can recognise that there is variation within that observed object (Fig. 1.4). The richness of information obtained if soil properties are described in this way can then be manipulated in a model such as a depth function or other laterally isotropic, vertically non-stationary random functions (McBratney and Moran 1990).

1.3.3 Morphometric Analyses

After soil properties have been captured digitally, we can perform multivariate statistics. Hole and Hironaka (1960) were able to represent soil profiles in a multidimensional space and quantify the degree of similarity between two profiles. Around this time, numerically based taxonomic systems were developing in diverse fields, the key advantages of these being repeatability and objectivity (Sneath and Sokal 1962). Such systems attempt to remove subjectivity from decision-making processes and should allow different scientists to arrive at the same conclusions, while increasing the accuracy and precision of the results (Bidwell and Hole 1964).

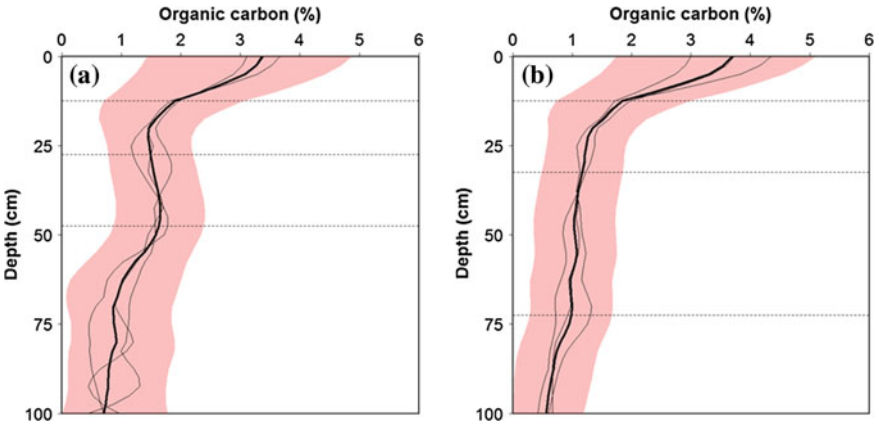

Fig. 1.4 Predicted organic carbon (%) of **a** Eutrudepts and **b** Udipsamments produced from NIR readings of pit walls sampled with three vertical transects at 25-mm intervals to a depth of 100 cm. Thin *black lines* represent predicted values for the three vertical transect; *thick black lines* indicate the mean predicted value with depth; *pink halos* indicate the mean 95 % confidence interval; and *dashed horizontal lines* indicate horizon designations

These benefits translate to numeric soil classification systems, and such analyses may also play an important role in the development of a universal classification system (Brevik et al. 2015). However, morphometric analyses extend beyond classificatory attempts. As they are able to connect both geometric and morphometric attributes, morphometric analyses may also provide evidence for pedogenetic theories. Stockmann et al. (2016), for example, used variation of pXRF-derived geochemical indices with depth to identify if a profile is polygenetic or derived from uniform parent material. Morphometric analysis may also shed light on soil-forming processes, connect properties and processes, and facilitate identification of relationships between properties.

1.4 Delineating Digital Soil Morphometrics

One of the mantras of the subdiscipline seems to be to digitally enrich the toolkit of the field pedologist. However, Hartemink and Minasny (2014) also list many laboratory-based techniques, e.g. scanning electron microscopy and X-ray computed tomography, as potential DSMorph tools. While these devices can provide valuable information about soil profile attributes, they will probably not enrich the toolkit of the field pedologist anytime soon. Their inclusion also blurs the definition of what DSMorph is to such an extent that it encompasses laboratory analysis. We believe the power of DSMorph comes with the capacity to objectively quantify soil attributes in the field using methods that have the capacity to increase sampling intervals and more readily quantify spatial variation compared to traditional

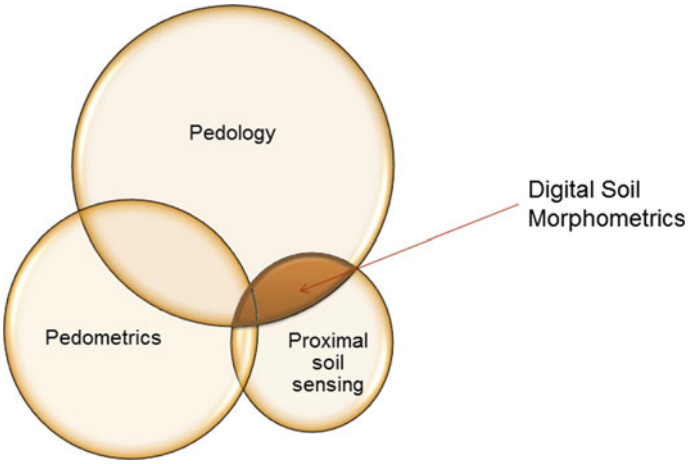

Fig. 1.5 Suggested relationship of digital soil morphometrics to pedology, pedometrics and proximal soil sensing

methods. We put DSMorph at the confluence of pedology, pedometrics and proximal soil sensing (Fig. 1.5). Subsequently, we will focus on techniques that have been performed, or have the potential to be performed, in the field.

1.5 Novel and Potential Applications

When incorporating new tools and techniques into the field of soil science, we must also ask ourselves, are we simply trying to update the technology of field soil description, or are we seeking to pose and answer new scientific questions? A review of the applications of DSMorph techniques as they apply to the prediction of attributes commonly used in soil description is given by Hartemink and Minasny (2014). Therefore, we will highlight some of the peripheral, novel and developing fields that are progressing with potential to benefit from DSMorph techniques. These include continuous depth functions, spectrally derived soil horizons, soil inference systems, adaptive sampling procedures and monitoring soil change.

1.5.1 Horizons or Depth Functions?

A unique question for DSMorph is to what extent is the distribution of soil properties better described by horizons or depth functions and to which properties do these pertain? Most of pedology as it relates to soil description identifies properties based on horizons. This involves describing horizons and identifying the average

properties of these horizons, resulting in the representation of discrete property distributions with depth (Fig. 1.6a). For some soil properties, it may be a reasonable representation, but for many it is not. For example, Russell and Moore (1968) showed that the decrease in OC with depth in a soil profile is better represented by smooth exponential decay functions. Therefore, mass-preserving splines have been fitted to obtained horizon data (Fig. 1.6b, c), signifying a movement from using discrete horizon values to describing soil depth functions. The superiority of such functions compared to average horizon values at describing the vertical non-stationarity of profiles has been established (Bishop et al. 1999). However, when converting horizon-based data to splines some, assumptions need to be made to create this additional data, which may decrease accuracy. For example, splines invariably dampen actual minima and maxima values, resulting in a smoother predicted distribution (Ponce-Henandez et al. 1986). What can this loss of information mean in terms of process or pedological understanding? If we to assess soil

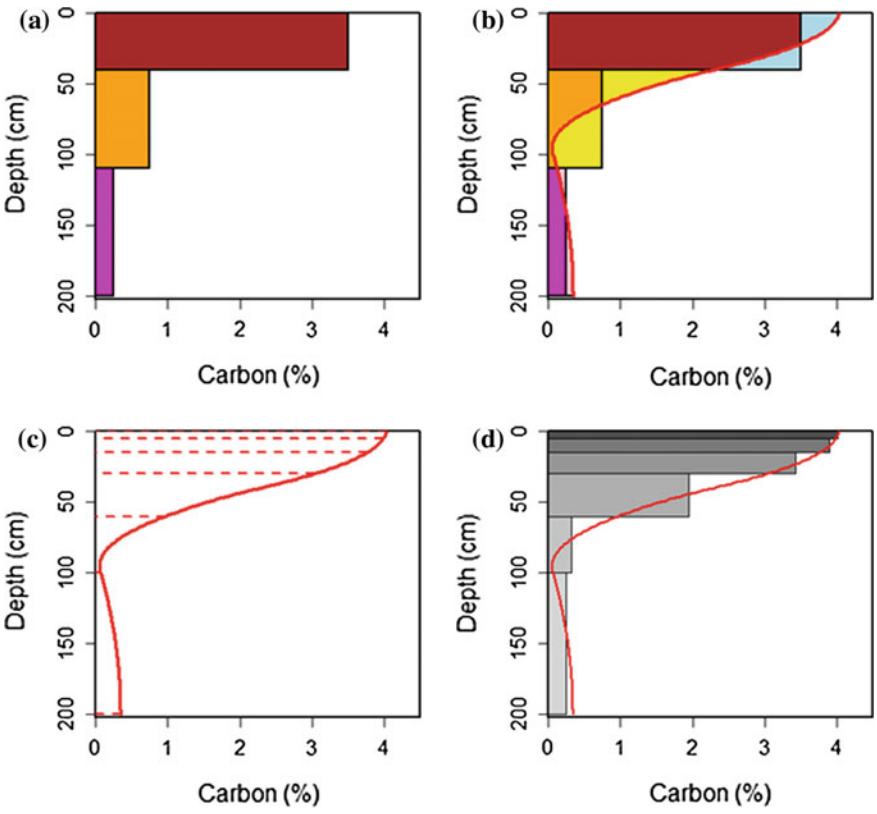

Fig. 1.6 Comparison of current techniques used to represent soil profile data: **a** conventional quantitative profile/pedon description; **b** fitting mass-preserving spline to horizon data (lambda = 0.01); **c** fitted spline, *horizontal lines* indicate GlobalSoilMap depth intervals; **d** average spline predicted carbon % fitted to GlobalSoilMap depth intervals

permeability models, how would they benefit from continuous measurement of properties such as clay, OC, pore size and connectivity, compared to models based on average horizon values? While the concept of horizons must be conserved as they are a unique feature of soil, it does not mean that they are the only unique feature of soils. Going forward, we must determine whether we want to continue collecting horizon-based data and convert it to continuous depth data. Alternatively, we could take advantage of the finer sampling resolution enabled using DSMorph techniques to capture more spatial variation (such as the example in Fig. 1.4) and create more accurate depth functions directly.

1.5.2 Spectrally Derived Horizons

Nikiforoff (1931) lamented that "*soil horizons and their nomenclature is probably the most confused point in the technic of the description of the soil*". Nikiforoff's frustration was that the term "B" horizon was so broad that it did not convey any real pedogenic meaning other than filling its place in the A-B-C horizon succession. At the time, it was known that there was great diversity in the horizons from different soil types, but the nomenclature was too simple to account for this richness of interpretation. It was not until much later with the implementation of suffix notation that succinctly distinguish differences (Soil Survey Staff 1951). Is this nomenclature now sufficient to adequately describe the diversity of soil horizons? Any horizon is a mixture of materials. Using current soil description, it is difficult to capture this heterogeneity. With DSMorph techniques, we may advance the boundaries of horizon identification and classification, and include measures to describe profiles in a more continuous manner. One suggested method involves identifying spectrally homogeneous zones from Vis–NIR-derived fuzzy cluster memberships (Fajardo et al. 2015). This method eliminates observer bias and allows direct investigation of class membership within and between profiles (Fig. 1.7). Could spectrally derived horizons become the new nomenclature to better characterise soils, and interclass memberships the new descriptors? Objective horizon recognition is also being explored using XRF (Weindorf et al. 2012; Minasny et al. 2016; Adhikari et al. this book) and hyperspectral cameras (Steffens and Buddenbaum 2013).

1.5.3 Adaptive Sampling

DSMorph techniques have the potential to derive data in the field, but how can we use this information to perform more meaningful operations in the field? A proposed strategy for assessing soil contamination suggests taking advantage by adapting sampling and analysis in real time (Horta et al. 2015). Calculations were made to find the conditional probability density function of the contaminant and the

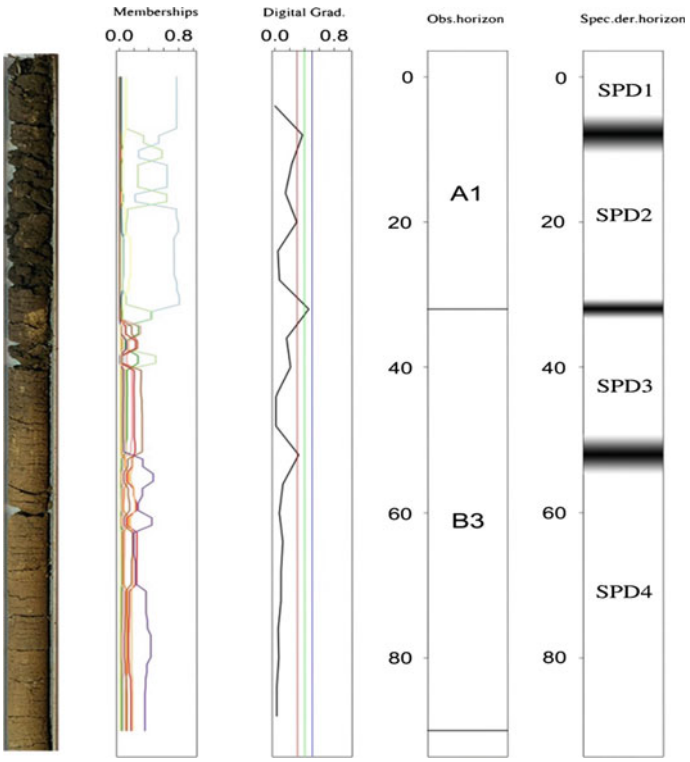

Fig. 1.7 *Left to right* Photograph of soil core; fuzzy membership classes; digital gradient; horizons observed using conventional techniques; spectrally derived horizons. Taken from (Fajardo et al. 2015)

loss function. From this information, an optimal remediation plan can be made taking into account both sampling and remediation costs. The method facilitates honing in on contaminated areas, prioritisation of areas of high uncertainty for subsequent focussed sampling and continuous updating of the map until an overall quality criterion is achieved. A similar approach can be envisaged for soil mapping units, but how to do it? A methodology is required to couple imaging or other techniques with point-based sampling devices to identify the next most valuable point of a soil profile to investigate, and determine when sufficient information has been gained for effective characterisation.

1.5.4 Monitoring Soil Change

The soil environment is not static, though it is sometimes represented as such. Increasing global recognition of issues, such as C sequestration (Lal 2004),

provision of ecosystem services (Kreuter et al. 2001) or soil security (McBratney et al. 2014), has generated a corresponding need for increased knowledge on the variability of soil attributes in space and time. Monitoring soil condition indicators, as well as elements of soil degradation such as contamination, loss of organic matter, compaction, acidification and salinisation, is important. The monitoring of soil requires the use of reliable, inexpensive and, at times, non-destructive techniques. These issues have proved troublesome for soil monitoring programs, especially when considering costs of sampling and analysis. As most DSMorph techniques are quantitative and generate a wealth of data, more subtle changes can be detected. We should identify how the application of DSMorph tools and techniques can improve the efficiency and viability of soil monitoring programs.

1.6 Missing Technology

The future of DSMorph is tied to progress in pedology but in particular to proximal soil sensing techniques. Current techniques need to be tested and utilised, new technologies need to be adapted as they arise, and overlooked technologies resurrected. Large sections of the electromagnetic spectrum are being used, as well as ultrasonics, electrical resistivity and physical measurements but others, such as magnetic susceptibility, appear to be underexploited (Mullins 1977). We must continue investigating what other technologies might be useful. Current techniques are predominately intrusive. Ideally, we would be able to predict all soil attributes from the surface using non-invasive techniques. Ground-penetrating radar and electromagnetic induction are two such existing techniques, but they can predict only a few properties of interest. While invasive techniques may fill the gap in the near term as expedient intermediaries, the holy grail of soil observation would be the development of a non-invasive sensor that could quantify all attributes of interest from the soil surface.

In reality, such a device is a long way off, and currently no single sensor or technique has the capacity to accurately predict all attributes of interest. The great power in the near future will come from putting the information gained from multiple sensors together. It is this data fusion combined with soil inference systems that will provide the most useful information. When combining data from multiple sensors, a number of approaches have been utilised. For example, input data may be analysed individually and then results were combined using a model-averaging procedure (Malone et al. 2014). Spectral data have also first been combined using concatenation and then analysed concurrently (Viscarra Rossel et al. 2006; Wang et al. 2015). Other techniques focus on exploiting the strengths of individual devices. Jones and McBratney (2016) suggest combining NIR's ability to provide information on bonding environments with the elemental concentrations reported from an XRF device to predict soil mineralogy using an integrated chemometric

and mass balance approach. The potential data fusion methodologies are myriad, but more focus needs to be given to the quantification of uncertainties. This will offer more valuable input data for soil inference systems that may connect predictions with the wealth of existing soil knowledge and amplify the number of predicted attributes (McBratney et al. 2006).

1.7 Conclusions

- DSMorph can provide more precise soil properties data with quantified spatial uncertainty than conventional soil description. There are untold pedological, edaphic and environmental applications to be gained from applying DSMorph tools and techniques.
- If DSMorph is going to digitally enrich the toolkit of the field pedologist, then DSMorph is probably best considered as a special case of proximal soil sensing.
- DSMorph can represent soil profiles in two different ways—depth functions or horizons—but as yet we are not clear of the best approach for the various properties.
- DSMorph can be used to make field inferences to optimise and adapt sampling in real time.
- DSMorph can enable quantification of change in soil condition and prove useful in soil monitoring programs.

References

ASBC American Society of Brewing Chemists (1949) Beer 10-A spectrophotometric color method. ASBC Methods of Analysis

Bidwell O, Hole F (1964) Numerical taxonomy and soil classification. Soil Sci 97(1):58–62

Billmeyer FW, Saltzman M (1981) Principles of color technology. Wiley, New York, NY

Bishop T, McBratney A, Laslett G (1999) Modelling soil attribute depth functions with equal-area quadratic smoothing splines. Geoderma 91(1):27–45

Blackith RE, Reyment RA (1971) Multivariate morphometrics. Academic Press, London

Bouma J, Jongerius A, Boersma O, Jager A, Schoonderbeek D (1977) The function of different types of macropores during saturated flow through four swelling soil horizons. Soil Sci Soc Am J 41(5):945–950

Brevik EC, Calzolari C, Miller BA, Pereira P, Kabala C, Baumgarten A, Jordán A (2015) Soil mapping, classification, and pedologic modeling: history and future directions. Geoderma

Carter W (1931) Color analysis of soils with spectrophotometer. Am Soil Surv Assoc Bull 12:169–170

Clarke GR (1936) The study of the soil in the field. Oxford University Press, London

Currence HD (1969) Development of a method for measuring and describing soil surface roughness. Retrospective theses and dissertations, Paper 3568, Iowa State University

Eck DV, Hirmas DR, Giménez D (2013) Quantifying soil structure from field excavation walls using multistripe laser triangulation scanning. Soil Sci Soc Am J 77(4):1319–1328

Fajardo M, McBratney A, Whelan B (2015) Fuzzy clustering of Vis–NIR spectra for the objective recognition of soil morphological horizons in soil profiles. Geoderma. doi:10.1016/j.geoderma.2015.05.010 (Advance online publication)
Hainsworth J, Aylmore L (1983) The use of computer assisted tomography to determine spatial distribution of soil water content. Soil Res 21(4):435–443
Hartemink AE, Minasny B (2014) Towards digital soil morphometrics. Geoderma 230:305–317
Hole FD, Hironaka M (1960) An experiment in ordination of some soil profiles. Soil Sci Soc Am J 24(4):309–312
Horta A, Malone B, Stockmann U, Minasny B, Bishop T, McBratney A, Pallasser R, Pozza L (2015) Potential of integrated field spectroscopy and spatial analysis for enhanced assessment of soil contamination: a prospective review. Geoderma 241:180–209
Jones EJ, McBratney AB (2016) In-situ analysis of soil mineralogy through conjoint use of visible, near-infrared and X-ray fluorescence spectroscopy. In: Hartemink AE, Minasny B (eds) Digital soil morphometrics. Springer, Dordrecht
Koppi A, McBratney A (1991) A basis for soil mesomorphological analysis. J Soil Sci 42(1):139–146
Kreuter UP, Harris HG, Matlock MD, Lacey RE (2001) Change in ecosystem service values in the San Antonio area, Texas. Ecol Econ 39(3):333–346
Lal R (2004) Soil carbon sequestration to mitigate climate change. Geoderma 123(1):1–22
Malone BP, Minasny B, Odgers NP, McBratney AB (2014) Using model averaging to combine soil property rasters from legacy soil maps and from point data. Geoderma 232–234:34–44
McBratney AB, Moran C (1990) A rapid method of analysis for soil macropore structure: II. Stereological model, statistical analysis, and interpretation. Soil Sci Soc Am J 54:509–515
McBratney AB, Minasny B, Viscarra-Rossel RA (2006) Spectral soil analysis and inference systems: a powerful combination for solving the soil data crisis. Geoderma 136(1):272–278
McBratney A, Field DJ, Koch A (2014) The dimensions of soil security. Geoderma 213:203–213
Minasny B, Stockmann U, Hartemink AE, McBratney AB (2016) Measuring and modelling soil depth functions. In: Hartemink AE, Minasny B (eds) Digital soil morphometrics. Springer, Dordrecht
Mullins C (1977) Magnetic susceptibility of the soil and its significance in soil science—a review. J Soil Sci 28(2):223–246
Murphy CP, Bullock P, Turner RH (1977) The measurement and characterisation of voids in soil thin sections by image analysis. Part I. Principles and techniques. J Soil Sci 28(3):498–508
Nikiforoff C (1931) The history of A, B, C. Am Soil Surv Assoc Bull 12:67–70
Nikiforoff C (1941) Morphological classification of soil structure. Soil Sci 52(3):193–212
O'Callaghan JF, Loveday J (1973) Quantitative measurement of soil cracking patterns. Pattern Recogn 5(2):83–98
Petrovic A, Siebert J, Rieke P (1982) Soil bulk density analysis in three dimensions by computed tomographic scanning. Soil Sci Soc Am J 46(3):445–450
Ponce-Henandez R, Marriott F, Beckett P (1986) An improved method for reconstructing a soil profile from analyses of a small number of samples. J Soil Sci 37(3):455–467
Russell JS, Moore AW (1968) Comparison of different depth weightings in the numerical analysis of anisotropic soil profile data. Trans Int Congr Soil Sci 4:205–213
Sánchez-Marañón M, Huertas R, Melgosa M (2005) Colour variation in standard soil-colour charts. Soil Res 43(7):827–837
Shields J, St. Arnaud R, Paul E, Clayton J (1966) Measurement of soil color. Can J Soil Sci 46 (1):83–90
Sneath PH, Sokal RR (1962) Numerical taxonomy. Nature 193(4818):855–860
Soil Survey Staff (1937) Soil survey manual. USDA, Washington DC
Soil Survey Staff (1951) Soil survey manual. USDA, Washington DC
Steffens M, Buddenbaum H (2013) Laboratory imaging spectroscopy of a stagnic Luvisol profile—high resolution soil characterisation, classification and mapping of elemental concentrations. Geoderma 195:122–132

Stockmann U, Cattle SR, Minasny B, McBratney AB (2016) Utilizing portable X-ray fluorescence spectrometry for in-field investigation of pedogenisis. Catena 139:220–231

Viscarra-Rossel RA, Walvoort DJJ, McBratney AB, Janik LJ, Skjemstad JO (2006) Visible, near infrared, mid infrared or combined diffuse reflectance spectroscopy for simultaneous assessment of various soil properties. Geoderma 131(1–2):59–75

Wang D, Chakraborty S, Weindorf DC, Li B, Sharma A, Paul S, Ali MN (2015) Synthesized use of VisNIR DRS and PXRF for soil characterization: total carbon and total nitrogen. Geoderma 243–244:157–167

Weindorf DC, Zhu Y, Haggard B, Lofton J, Chakraborty S, Bakr N, Zhang W, Weindorf WC, Legoria M (2012) Enhanced pedon horizonation using portable X-ray fluorescence spectrometry. Soil Sci Soc Am J 76(2):522–531

Part I
Soil Profile Properties

Chapter 2
Quantifying Soil Structure and Porosity Using Three-Dimensional Laser Scanning

Daniel R. Hirmas, Daniel Giménez, Edison A. Mome Filho, Matthew Patterson, Kim Drager, Brian F. Platt and Dennis V. Eck

Abstract Advancements in three-dimensional (3D) digital surface scanning have opened up the possibility of capturing soil morphological information from irregular objects in high resolution. One of these advancements has been the development of a multistripe laser triangulation (MLT) technique that sweeps a series of laser stripes across a surface, while a camera offset from the laser source monitors the deformation and intensity of the reflected laser stripes. MLT scanning can be used to describe soil architecture (i.e., soil structure and porosity) from soil surfaces and soil specimens. The technique allows for the geometry of both small (<1 cm) and large (several meters) objects to be digitally captured in fine detail. In this paper, we provide examples of how MLT scanning has been applied to 3D soil specimens including the determination of bulk density from clods, the quantification of ped geometries, and the development of morphometrics from casted biopores. Examples of soil surface application of MLT scanning include the quantification of soil structure and interpedal pores from the field (excavation walls) and quantification of volume changes and crack formation in the laboratory

D.R. Hirmas (✉)
Department of Geography and Atmospheric Science, University of Kansas, Lawrence, KS, USA
e-mail: hirmas@ku.edu

D. Giménez · M. Patterson
Department of Environmental Sciences, Rutgers University, New Brunswick, NJ, USA

E.A. Mome Filho
Department of Soil Science, University of São Paulo, Piracicaba, SP, Brazil

K. Drager
Department of Animal Biology, University of Illinois, Urbana-Champaign, Urbana, IL, USA

B.F. Platt
Department of Geology and Geological Engineering, University of Mississippi, University, MS, USA

D.V. Eck
Bennett and Schulte Oil Company, Russell, KS, USA

A.E. Hartemink and B. Minasny (eds.), *Digital Soil Morphometrics*, Progress in Soil Science, DOI 10.1007/978-3-319-28295-4_2

(soil cores). When combined with other digital morphometric tools such as computed tomography, 3D laser scanning has the potential to quantify the architecture of soils across scales ranging from submicrometers to meters.

Keywords Soil structure · Quantitative pedology · Multistripe laser triangulation scanning · Soil macroporosity · Digital soil morphometrics

2.1 Introduction

Noncontact optical methods utilizing lasers to map the topography of fine-scale surfaces of soils have been developed and used in the study of soil roughness and surface deformation since the 1980s (e.g., Harral and Cove 1982; Huang and Bradford 1990; Eltz and Norton 1997; Darboux and Huang 2003; Zielinski et al. 2014). Most of these methods illuminate a spot on the soil surface that is detected by an optical sensor offset from the laser source, the distance from which is determined utilizing the geometry of the setup and the position of the spot on the detection array of the sensor (Thwaite and Bendeli 1980; Huang et al. 1988).

Laser scanners utilizing laser stripe triangulation techniques have recently been used in the investigation of soils, rocks, and sediments because of the ease of use, accuracy, portability, and low cost (e.g., Aguilar et al. 2009; Platt et al. 2010). These scanners project and sweep one or more laser stripes onto the surface of a target and generate a high-resolution three-dimensional (3D) surface based on the intensity of the laser stripes deformed on the surface of the object as observed from an image sensing array offset from the light source (Knighton et al. 2005; Usamentiaga et al. 2014). A 3D object is digitized when scans taken from multiple angles are aligned and merged into a continuous surface (Rossi et al. 2008).

Three-dimensional laser scanning opens up the possibility to digitize and, therefore, nondestructively measure both soil surfaces and 3D soil specimens (e.g., individual peds). These techniques are well suited to quantify soil structure and the distribution of pores (i.e., soil architecture) of the soil profile. This is needed given the paucity of techniques available to quantify macroscale soil architecture despite its importance in pedological, hydrological, biological, physical, and chemical soil processes (Eck et al. 2013; Hartemink and Minasny 2014).

The objectives of this paper are to: (i) provide a relevant overview of the expanding literature on the application of 3D laser scanning techniques to quantify soil architecture; (ii) provide several examples of how this technology is being used; and (iii) guide future applications aimed at enhancing our understanding of soil morphology. Although other laser scanning methods have been employed in geosciences over the past three decades, we focus on multistripe laser triangulation (MLT) because of its high resolution and applicability of quantifying in situ interpedal macropores compared to noncontact spot methods.

2.2 Three-Dimensional MLT Scanning of Soils

2.2.1 Bulk Density

Bulk density is used in part to convert measurements of soil properties on a mass basis such as water content, soil organic carbon, NO_3^-–N, or calcium carbonate equivalent into a volumetric basis. Bulk density can be used in combination with soil texture as a predictor of soil hydraulic properties such as water retention and hydraulic conductivity (e.g., Schaap et al. 2001). Bulk density is used to calculate void ratio (i.e., ratio of pore volume to volume of the solids) and total porosity (i.e., a measure of the total volume fraction of pores in a soil). Total porosity is used as a measure of saturated volumetric water content and necessary to calculate degree of saturation in water retention measurements.

One of the first 3D applications of MLT scanning to soils was the accurate determination of bulk density from clods (Rossi et al. 2008). The clod method is the standard used by the USDA-NRCS when determining bulk density (Burt 2004) and is useful when the excavation of cores is impossible or impractical. For instance, in order to calculate the fine-earth bulk density of stony soils, the coarse fraction (>2 mm) has to be removed, weighed, and used to correct the total mass of the clod. Because the clod method is typically immersed in liquid saran or molten paraffin to make it water tight for volume determination by displacement using Archimedes' principle, separation of the coarse fraction can be problematic because the coating agent often binds the coarse and fine-earth fractions together (Hirmas and Furquim 2006). Thus, the determination of fine-earth bulk density from the clod method greatly benefits from a noninvasive procedure for obtaining clod volume.

The accurate determination of bulk density on very small (e.g., a few millimeters in diameter) and irregularly shaped samples such as soil aggregates is limited by the accuracy of the volume determination (Subroy et al. 2012). Several methods have been developed to measure these small samples, but they require sealing the aggregates by filling up the pores with an organic liquid and submerging the saturated aggregate in either the same liquid used to saturate the aggregate or in a liquid that is immiscible with it (Subroy et al. 2012).

Rossi et al. (2008) showed that the volumes obtained from the clod method (Blake and Hartge 1986) were not significantly different from those obtained by MLT scanning. Hirmas et al. (2013) compared aggregate volume measurements obtained with a displacement technique (Subroy et al. 2012) against those obtained by MLT scanning. They found no significant difference between the regression parameters. When data from those two studies are combined on the same plot, the measurements align close to the 1:1 line (Fig. 2.1), with a nearly perfect coefficient of determination ($r^2 = 0.999$). The axes in this figure are on a log scale to illustrate the 3-orders of magnitude in volumes provided by the combination of the traditional clod method and the aggregate displacement method, which indicates that MLT scanning can extend the range of volumes that a single method can measure. In theory, there is no upper limit for the scanner, provided there is enough storage and computational

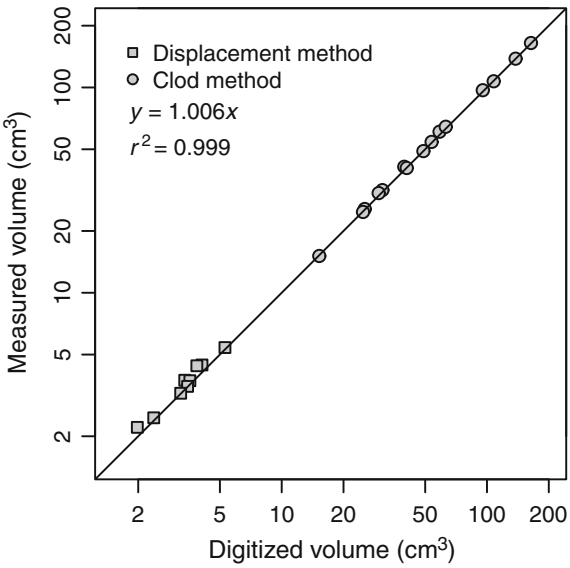

Fig. 2.1 Measured volume of aggregates and clods determined from a displacement technique (Subroy et al. 2012) and the clod method (Blake and Hartge 1986) against calculated volumes from MLT-derived digital scans. Data from Rossi et al. (2008) and Hirmas et al. (2013). The slope of the regression for a model where the *y*-intercept was set to zero and the coefficient of the determination are shown in the plot. *Solid line* represents a 1:1 relationship for reference

memory to process the resulting data. The lower limit is a function of the resolution of the scanner, which, for this study, was 120 μm (Desktop 3D Scanner Model 2020i, NextEngine, Inc., Santa Monica, CA) at its highest setting (macro).

Other methods for measuring bulk density such as the core method or excavation method (Blake and Hartge 1986) may also benefit from the incorporation of MLT scanning. The latter method is preferred where the loose consistence of a soil or the abundance of coarse fragments precludes the use of core or clod methods. In the excavation method, bulk density is obtained by excavating and weighing a dry quantity of soil and measuring the excavation volume (Blake and Hartge 1986). Variants of the excavation method primarily differ on the technique used to determine the volume of the cavity. Thus, there are two possible ways that this method could benefit from MLT scanning. First, the irregular surface of a cavity could be digitized in 3D by scanning the excavation surface before and after excavation of the material. This would allow for irregularities in the original surface of the excavation to be accounted for as opposed to current methods, which assume a previously leveled and smooth surface (Blake and Hartge 1986). Second, a modification of the excavation method proposes that casts of the cavity be made in dental plaster and volumes determined in the laboratory either by displacement or by MLT scanning (Frisbie et al. 2014). Drager (2014) used this plaster cast-MLT scanning modification of the excavation method to assess the effects of ant turbation on bulk density within a centimeter of excavated galleries in a fine-textured soil.

The determination of bulk density by MLT scanning is also applicable when bulk density is determined from core samples with an uneven soil surface, caused by, for example, gravel, roots, or soil shrinkage (see also Sect. 2.3.3). Accurate volume assessment is difficult in those situations due to the lack of a Euclidean shape.

Multistripe laser triangulation scanning has the potential to enhance analyses of soil architecture by allowing repeated bulk density measurements (i.e., at each soil water potential) on the same clod on which water retention is determined. This may be important in the volumetric determination of water content for water retention in swell and shrink soils (e.g., Vertisols).

2.2.2 *Quantification of Ped Geometries*

Rossi et al. (2008) showed that individual 3D peds could be digitized at high resolution and volumes measured accurately. New measurements of ped geometries and ped surface area can now be obtained from 3D laser scanning. Ped surface area, in particular, may prove useful in the quantification of ped type and grade or for assessing tortuosity of interpedal macropores. In addition, surface roughness may be quantified using an approach proposed by Platt et al. (2010) for characterizing irregular 3D target objects opening up possibilities to investigate the interface between inter- and intrapedal pores.

Figure 2.2a illustrates an individual prism specimen extracted from the soil and scanned using MLT. The ped is sliced in three orthogonal planes (Fig. 2.2b–d) to reveal cross sections and cutaways of the ped. These cross sections can be quantified from 2D measurements of size, shape, and orientation using standard image analysis software such as ImageJ (Research Services Branch, National Institute of Health, Bethesda, MD). Measurements of size include net, filled, and convex areas, equivalent area circular diameter, minimum circumscribed and maximum inscribed circle diameters, equivalent area ellipse major and minor axes lengths, caliper dimensions (i.e., Feret diameters; Fig. 2.2d), and perimeter (Russ 2011). Orientation measurements include the angle of the moment axis, longest caliper dimension, and major ellipse axis (Russ 2011). Common shape descriptors include form factor or circularity, roundness, aspect ratio, elongation, curl, convexity, solidity, compactness, modification ratio, and extent (Russ 2011). The possibility of quantifying ped shape is promising, as it is currently only characterized with subjective and categorical type classes (Schoeneberger et al. 2012). Quantifying shape can also be important when comparing ped or aggregate sizes from samples with different shapes (e.g., Hirmas et al. 2013).

2.2.3 *Biopore Morphometrics*

Biopores created from the movement of soil fauna and growth of soil flora have been digitized by MLT scanning and have allowed the quantification of biological

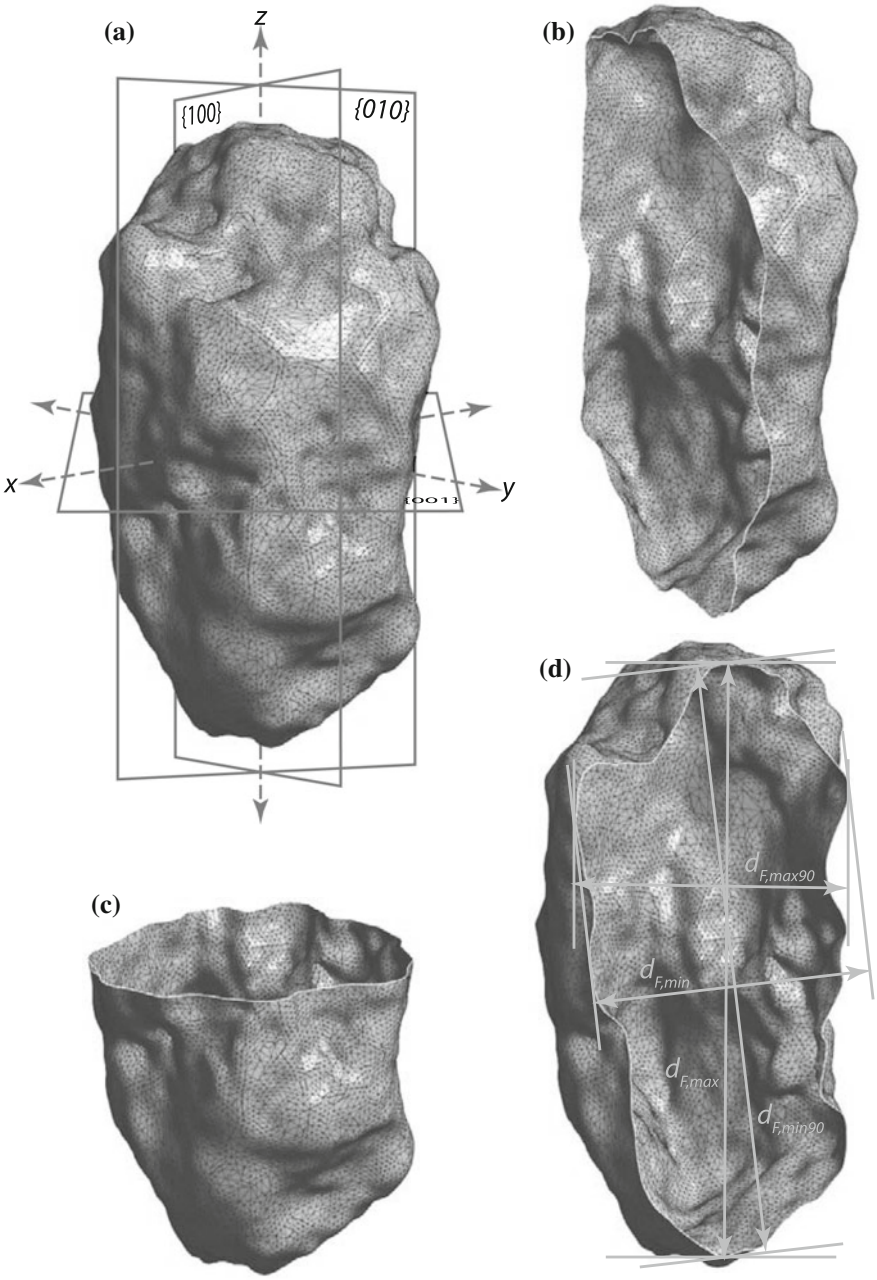

Fig. 2.2 **a** Scanned prismatic ped showing cross sections through the approximate middle of the aggregate and parallel to the **b** {100}-plane, **c** {010}-plane, and **d** {001}-plane. *Numbers between braces* represent Miller index notation. Feret diameter calculations are shown in (**d**). Length of the ped along the z-axis in (**a**) is approximately 4.5 cm

macropore networks and identification of trace makers in paleosols for reconstruction of paleo-environments (Platt et al. 2010). These pores often represent complex and tortuous 3D geometries (Fig. 2.3a) and are typically casted with fiberglass, epoxy, plaster, wax, concrete or molten metal (Hasiotis and Bourke 2006; Tschinkel 2010); the casts are subsequently allowed to harden, excavated, and cleaned. The application of MLT scanning to these casted biopores will increase the accuracy of metrics such as lengths, diameters, and angles (Fig. 2.3); this is because pore measurements can be taken in the exact center of the digitized biopores avoiding errors with lengths measured on the outside of casted pores (Platt et al. 2010). Surface area of casted biopores can also be measured from MLT scans. The current method proposes to wrap the cast with a single layer of foil and record the foil weight. Surface area is then calculated from the known ratio of foil weight to surface area (Atkinson and Nash 1990).

Accurate determination of surface area from MLT scanning allows for the calculation of surface roughness over a range of scales (subcentimeter to meter). Platt et al. (2010) termed this measure surface area index and defined it as the ratio of the total surface area to the projected surface area of a biopore. The projected surface area is calculated as the surface area of a biopore after it has been smoothed;

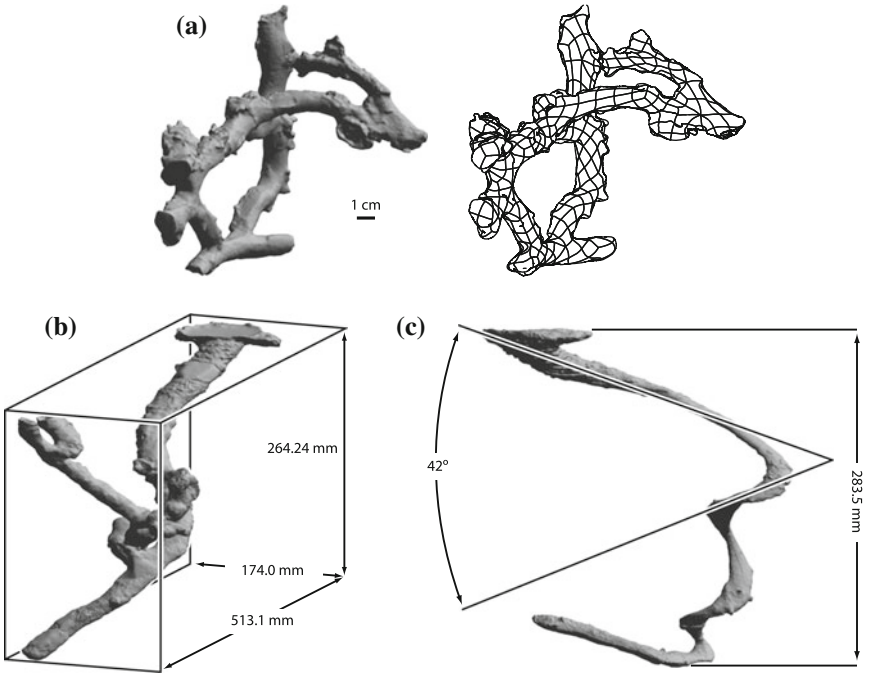

Fig. 2.3 Scanned resin casts of **a** an *Amphisbaena camurea* burrow alongside a smoothed mesh rendering of the cast, **b** desert skink (*Egernia inornata*) burrow with bounding box, and **c** a brown scorpion (*Urodacus* sp.) burrow showing depth and ramp angle of the uppermost spiral. Modified from Platt et al. (2010)

smoothing is attained by coarsening the resolution of the digital mesh, which effectively averages over the fine-scale variability. The resolution chosen to smooth the surface of the biopore represents the scale over which the surface roughness is calculated (Fig. 2.3a). Platt et al. (2010) plotted surface area index against mesh resolution for a variety of biopores and used the inflection point of the relationship to compare surface roughness of the casts. Results show that surface area index can be used to identify the trace makers of ichnological specimens.

Other metrics developed as a result of the MLT scanning of biopores include volume exploited (Fig. 2.3b)—defined as the ratio of volume of the biopore to volume of a bounding box fit around the biopore expressed as a percentage—and relative compactness—defined as the ratio of volume/surface area of the casted biopore to the volume/surface area of a sphere that has the same volume as the biopore (Platt et al. 2010). The relative compactness can be considered a measure of sphericity. The volume limitation of the scanner reached by Platt et al. (2010) that still preserved sufficient detail on the cast for ichnological interpretation was approximately 0.8 cm^3.

2.2.4 Aggregate Mass–Volume Relationships

Soils commonly exhibit a hierarchical organization in the arrangement of primary particles where larger soil aggregates are formed from smaller and denser aggregates (Rieu and Sposito 1991; Hirmas et al. 2013). The inverse relationship in aggregate density and size stems from the "pore-exclusion principle," which postulates that smaller aggregates selectively exclude larger interaggregate pores which increases their density compared to larger aggregates. This relationship can be described using a power-law relationship (Giménez et al. 2002):

$$M(d) = k_{\mathrm{m}} d^{D_m} \tag{2.1}$$

where $M(d)$ is the aggregate mass, d is the diameter of the aggregate, k_{m} is the mass of an aggregate with unit diameter, and D_{m} is the slope of the relationship between $M(d)$ and d on a log–log plot also known as the fractal dimension of mass.

Previous attempts at examining the hierarchical organization in soils through the fractal dimension of mass have been restricted to relatively small aggregate sizes—often less than approximately 10 cm^3. This is because it is difficult to measure the volume of larger aggregates or clods with the conventional methods (displacement techniques and/or clod method). Furthermore, as these methods either saturate the aggregates with an organic liquid or coat their outer surfaces, it has not been possible to investigate mass–volume relationships by sequentially breaking down large soil volumes into smaller aggregates while measuring volumes of the resulting fragments.

The ability for MLT scanning to nondestructively digitize aggregates down to approximately 1 cm^3 allows for the assessment of volumes over several orders of

magnitude using aggregates that were originally part of the same sample volume. For example, in a comparative study on the effects of tillage and erosion on the mass–volume relationship, Hirmas et al. (2013) investigated surface and subsurface horizons in two adjacent soils in northeastern Kansas. One of the soils was sampled in an unplowed native tallgrass prairie and the other in a restored field where erosion had exhumed the subsoil and a new shallow A horizon was forming in the previous Btss horizon. Six large ($\sim$1000 cm^3) clods were taken from each horizon investigated, weighed, scanned to measure volumes, and broken down into smaller aggregates that were weighed and scanned (Fig. 2.4a). This procedure was followed until MLT scanning was no longer practical and a displacement technique described by Subroy et al. (2012) was used for aggregates down to approximately 1 mm in diameter. As the shapes of the aggregates varied considerably, nine independent cross sections were digitally created for each aggregate and the roundness shape parameter was calculated, averaged, and used to normalize the diameter of each aggregate. The distribution of roots and organic carbon as controlled by the soil morphology had a considerable effect on the fractal distribution of mass in different aggregate size domains (Hirmas et al. 2013). The break point between aggregate size domains with different fractal dimensions of mass was controlled by the quantity of fines (silt + clay) and organic carbon in the soil. In addition, large within-horizon variability was observed in the k_m and D_m parameters from samples taken only centimeters to decimeters apart.

The study illustrated the usefulness of MLT scanning to investigate soil architecture at the horizon scale. Future MLT scanning should incorporate spatially explicit designs in the sampling of horizon-scale clods and aggregates to quantify the variability observed. In addition, the mass–volume approach would be enhanced if soil constituents were assessed on each aggregate from which size was determined. One possible way to achieve this is to couple MLT scanning with proximal

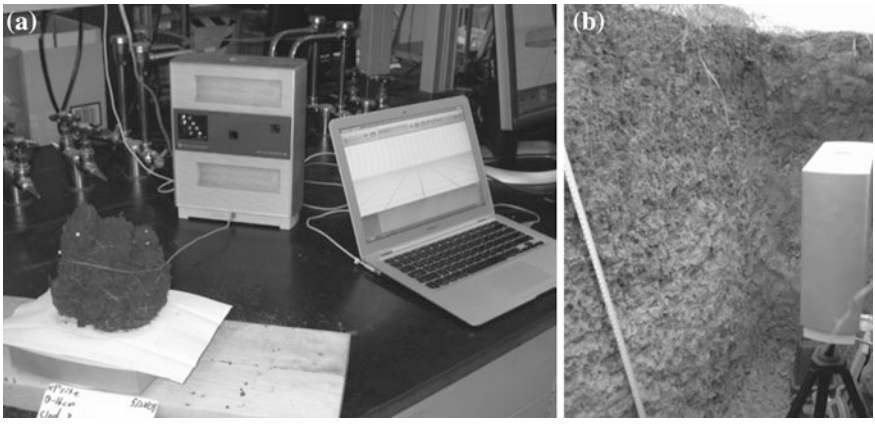

Fig. 2.4 Multistripe laser triangulation (MLT) scanner in use in the **a** laboratory scanning a large clod and **b** in the field scanning a prepared soil pit wall

sensing (e.g., hyperspectral scanning; Steffens and Buddenbaum 2013) to map binding agents such as organic matter or Fe-oxides on the surface of the aggregates.

2.3 Application of MLT Scanning for Digitizing Soil Surfaces

2.3.1 Quantification of Soil Structure and Interpedal Pores from Excavation Walls

An issue of MLT scanning is the formation of areas of missing data in the resulting digital mesh. These data gaps result from the offset between the laser source and the image sensing array in the triangulation arrangement. Sections of the laser stripes projected and swept on the surface disappear from the field of view of the camera as they are hidden in the recess of cracks.

Eck et al. (2013) took advantage of these data gaps to quantify interpedal macropores from an in situ soil excavation wall by projecting them onto a 2D surface and subsequently determining morphometrics using ImageJ (Fig. 2.4b). Several challenges were overcome in the process of surface scanning of the soil profile wall. First, the surface was prepared using a freeze and peel method following Hirmas (2013) to remove artifacts. Second, the surface was allowed to dry for several days in order to maximize the exposure of interpedal pores on the excavation wall. Third, scans were done at night to eliminate the effect of ambient light, minimize differences in surface color between horizons, and keep the scanner within its operational temperature range. Figure 2.5 illustrates a portion of a carefully prepared monolith surface that was saturated, allowed to dry, and scanned using MLT at various times during the drying process. The cracks became progressively more pronounced with time especially after 25 h of drying. The outlining of soil structural units such as angular blocks and prisms also became more striking as the soil surface dried (Fig. 2.5).

Size, shape, orientation, and abundance metrics were determined from the projected map of the surface scan gaps and included area, perimeter, bounding box width and height, ellipse axis lengths and angles, Feret diameters, circularity, roundness, pore density, pore fraction, and relative surface area (Eck et al. 2013). Probability distribution functions of these measurements within a depth zone can be assessed and used to create continuous depth functions of macropore interpedal geometries and quantify the uncertainty of these properties. Several of these metrics correlated well to traditional descriptions of the grade, size, and type of soil structure following Schoeneberger et al. (2012). The pore width obtained from MLT scanning in combination with coefficient of linear extensibility measurements can be used to predict the effective saturated hydraulic conductivity of the soil (Eck et al. 2016).

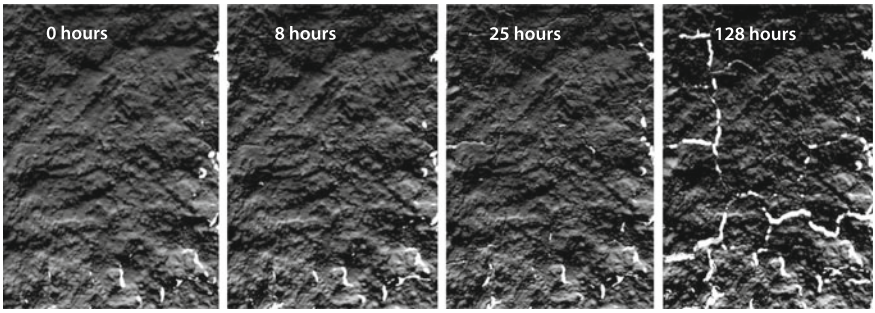

Fig. 2.5 Scanned monolith at 0, 8, 25, and 128 h after prolonged visible saturation of the profile surface. Depths are from 38 to 61 cm below the soil surface. *White areas* in the sections are data not returned during the MLT scan and represent pores outlining structural units in the digital mesh

The ability to quantify interpedal macropore geometries and soil structure in the field from a soil profile represents a step forward in understanding the genesis of soil architecture and its interactions with hydrological and transport processes. As with quantifying aggregate mass–volume relationships, quantifying and mapping the spatial arrangement of macropores and soil structure would be enhanced if coupled to high-resolution proximal sensing techniques. Here, the movement of soil constituents such as clay and organic matter and the presence of redoximorphic features could be consistently and quantitatively assessed in relation to soil structure and proximity to macropores. This ability would aid the hydrological interpretation of a site and likely enhance and standardize the assessment of soil quality.

2.3.2 *Geostatistical and Multifractal Analyses of Soil Surfaces*

Surface roughness is the result of the structural organization of the soil at the surface and is influenced by both extrinsic (e.g., tillage and topography) and intrinsic (e.g., texture and aggregate size distribution) factors. Surface information from MLT makes it possible to generate high-resolution (≤1 mm) digital elevation models (DEMs; Fig. 2.6) suited to investigate intrinsic factors defining microtopography, such as the mapping of clods on freshly tilled surfaces (Chimi-Chiadjeu et al. 2014).

Surface roughness is characterized by the statistical distribution of elevations either considering or disregarding their spatial location. The semivariogram (Dalla Rosa et al. 2012) and related fractal techniques (Huang and Bradford 1992; Vidal Vázquez et al. 2005) are examples of considering spatial location. Multifractal studies of soil surface elevations have been conducted, however, disregarding the spatial location of the elevation points (García Moreno et al. 2008; San José Martínez et al. 2009). Multifractal models consider the distribution of elevations as

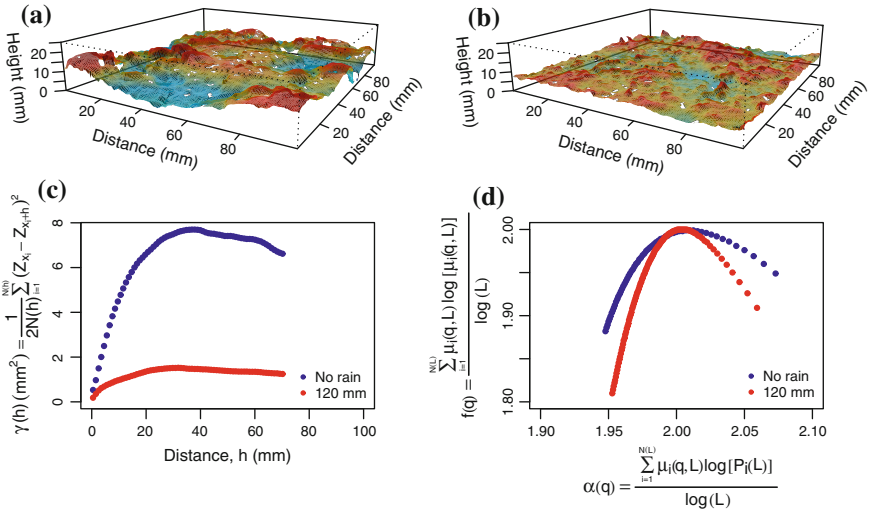

Fig. 2.6 Surface digital elevation models (DEMs) with a resolution of 500 μm^2 obtained in the laboratory from the center (10 × 10 cm^2) of soil blocks collected **a** immediately after tillage (heavy disk + leveling harrow), and **b** after the application of 120 mm of simulated rainfall during a 1-h period, and the corresponding **c** semivariograms and **d** multifractal spectra estimated from the distribution of elevations. The experiment was located at the campus of the Luiz de Queiroz College of Agriculture of the University of São Paulo in Piracicaba, Brazil. The soils are classified as Rhodic Kandiudalfs. *White areas* are data gaps in the MLT mesh

probabilities, P_i, and use it to calculate the partition function μ_i (q, L) (Chhabra and Jensen 1989):

$$\mu_i(q, L) = \frac{P_i(L)^q}{\sum_{i=1}^{N(L)} P_i^q} \tag{2.2}$$

where L defines the scale and q the moments of the measure. The main expression of a multifractal system is its $f(\alpha)$ spectrum, which represents the relationship between the exponent α that characterizes the local behavior of $P_i(L)$ and its fractal dimension $f(\alpha)$, both calculated using the partition function (Fig. 2.6).

Figure 2.6 shows DEMs of soil blocks (10 × 10 cm) sampled from a freshly tilled soil and after 120 mm of rainfall. Multifractal spectra were calculated according to Posadas et al. (2003) with the software Multifractal Analysis System 3.0 (http://inrm.cip.cgiar.org/home/downmod.htm, accessed on June 27, 2015) after rasterizing the MLT data. Semivariograms were calculated using the geoR package (Ribeiro and Diggle 2015). Both the semivariogram and multifractal spectra were sensitive to changes in the surface properties induced by rainfall. Rainfall reduced the variation of elevation values as reflected by a decrease in the sill of the semivariograms and by a narrower range of α values in the multifractal spectra. The disadvantage of the MLT method to generate surface elevations is the presence of

data gaps (Fig. 2.6) that could compromise the multifractal analysis. This problem can be avoided by using techniques that do not define L by averaging increasingly larger surfaces, but rather by considering L as the separation between elevation points (Davis et al. 1994).

2.3.3 Soil Shrinkage and Volume Determination

In the investigation of soil surface deformation from shrinkage, laser triangulation scanning has been useful in accurately assessing processes such as curling (e.g., Zielinski et al. 2014) and crack formation dynamics (e.g., Sanchez et al. 2013). In these investigations, it is important that the surface be prepared to maintain the features under consideration. Figure 2.7 illustrates a surface that was prepared with the freeze and peel method (Hirmas 2013) leaving behind an irregular micro-topography. Using the edge of the core as a reference, the surface of the core was digitized by MLT and the missing volume determined to be 16.2 cm^3 which was 6.4 % of the core volume.

Soil shrinkage during desiccation has been studied using MLT (Sanchez et al. 2013). Volume changes were quantified as well as the dynamics of crack formation at the surfaces of packed cores along with soil water content (estimated by recording the loss of mass of the cores). By combining the morphological characterization of the surface with soil water content, this approach allows the development of mechanistic models of the evaporation process. Figure 2.8a shows results of a similar experiment using a soil core sampled from the argillic (2Bt3)

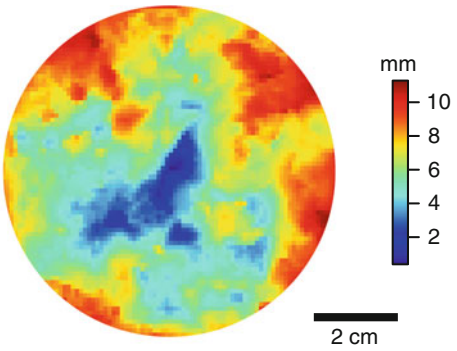

Fig. 2.7 A MLT-derived digital elevation model (DEM) of the surface of an approximately 250 cm^3 core (8 cm diameter × 5 cm length) sampled from the National Ecological Observatory Network (NEON) Konza Prairie Biological Station Relocatable site for bulk density, hydraulic conductivity, and water retention determination. The exposed surface of the core was prepared using a freeze and peel following Hirmas (2013) leaving behind a smear-free but irregular surface. The volume between the end of the core ring and the irregular surface was calculated as 16.2 cm^3 representing 6.4 % of the total volume of the core

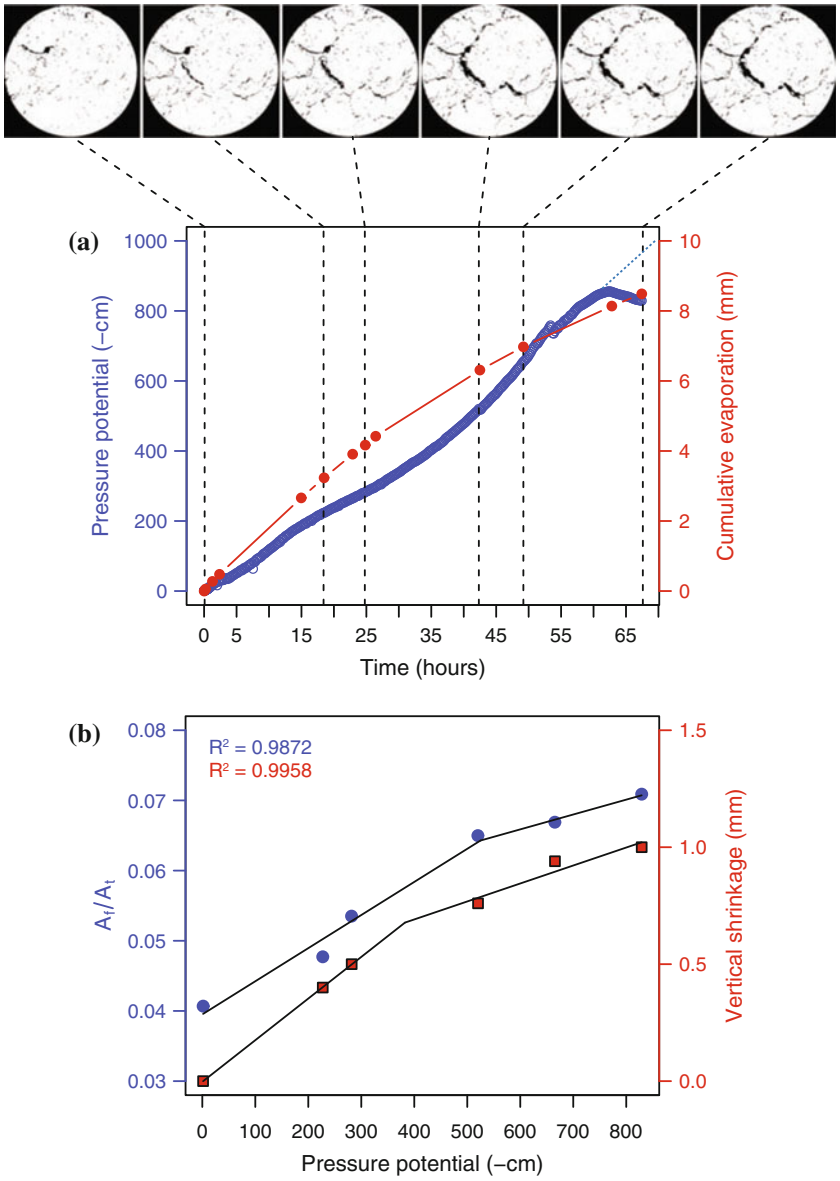

Fig. 2.8 **a** Pressure potential and cumulative evaporation measurements as a function of time from an evaporation experiment. Pressure potential was measured using a tensiometer located at 3.75 cm depth in a cylindrical 8 cm diameter × 5 cm height core. The tensiometer failed at approximately −800 cm. *Blue dotted line* is the projected pressure potential. Binary images (*top*) are taken from MLT scans performed at times indicated by the *black dashed lines*. **b** Lateral and vertical shrinkage trends. The lines are piecewise regression fits between soil pressure potential and fracture areas from image analysis, A_f, normalized by the total surface area of soil, A_t (*blue*), and between pressure potential and mean vertical shrinkage (*red*)

horizon of a fine, smectitic, mesic Pachic Argiudoll (Rosendale series). The core was water-saturated and allowed to dry by evaporation. Water loss was measured by frequently weighing the core, and pressure potential was recorded throughout the duration of the experiment with a tensiometer placed 3.75 cm below the surface. Similar to Eck et al. (2013), the area covered by the cracks was mapped with MLT six times and the results quantified with ImageJ. The nonlinear nature of the evaporation process can be seen at pressure potentials between −400 and −500 cm where the rate of drying determined with the tensiometer increased, while the evaporation rate declined. The evaporation rate decreased despite the increase in evaporating surface area created by the continuous formation of cracks until the end of the experiment (Fig. 2.8a). The MLT data allowed for comparison between the rates of crack formation (lateral shrinkage) and vertical shrinkage, estimated as the average reduction in sample height within the core (see Fig. 2.7). For this sample, a similar rate was observed in both directions (Fig. 2.8b), suggesting an isotropic process. High-resolution MLT scanning can be used to increase our understanding of evaporation processes in soils using both the elevation data returned from the scanner as well as the gaps in the digital mesh that can be used to map and quantify the patterns and abundance of cracks.

2.4 Conclusions and Future Directions

Digital morphometrics is defined by Hartemink and Minasny (2014) as the, "… application of tools and techniques for measuring and quantifying soil profile attributes and deriving continuous depth functions." To the growing list of tools and techniques, we add laser stripe scanning technology as a means of quantifying soil architecture, which has proven to be one of the most elusive soil profile attributes for which to quantify and derive continuous depth functions. In particular, MLT scanning can be used to quantify the spatial arrangement of soil particles and pores at scales ranging from centimeters to meters (i.e., horizon to pedon scales). As MLT is a surface scanning technique with no depth penetration and because constituent information is not obtained about the surface being scanned, a coupled approach using this scanning in combination with proximal sensing such as hyperspectral scanning and fine-scale geophysical imaging with X-ray CT holds potential to advance our understanding of soil morphology.

Other 3D digitizing methods such as time-of-flight scanning, structured-light scanning, photogrammetry, and silhouette techniques have been used to digitize and measure a variety of soil properties. We expect that most of the concepts discussed in this paper will be equally applicable to these techniques in the investigation of soil architecture.

References

Aguilar MA, Aguilar FJ, Negreiros J (2009) Off-the-shelf laser scanning and close-range digital photogrammetry for measuring agricultural soils microrelief. Biosyst Eng 103:504–517

Atkinson RJA, Nash RDM (1990) Some preliminary observations on the burrows of *Callianassa subterranea* (Montagu) (Decapoda: Thalassinidea) from the west coast of Scotland. J Nat Hist 24:403–413

Blake GR, Hartge KH (1986) Bulk density. In: Klute A (ed) Methods of soil analysis, Part 1, 2nd edn. Agron. Monogr. 9. ASA and SSSA, Madison, WI, pp 363–375

Burt R (ed) (2004) Soil survey laboratory methods manual, Ver. 4.0, Soil Survey Investigations Report No. 42. Natural Resources Conservation Service, Washington, DC

Chhabra AB, Jensen RV (1989) Direct determination of the f (alpha) singularity spectrum. Phys Rev Lett 62–12:1327–1330

Chimi-Chiadjeu O, Hégarat-Mascle S, Vannier E, Taconet O, Dusséaux R (2014) Automatic clod detection and boundary estimation from Digital Elevation Model images using different approaches. Catena 118:73–83

Dalla Rosa J, Cooper M, Darboux F, Medeiros JC (2012) Soil roughness evolution in different tillage systems under simulated rainfall using a semivariogram-based index. Soil Tillage Res 124:226–232

Darboux F, Huang C (2003) An instantaneous-profile laser scanner to measure soil surface microtopography. Soil Sci Soc Am J 67:92–99

Davis A, Marshak A, Wiscombe W, Cahalan R (1994) Multifractal characterizations of nonstationarity and intermittency in geophysical fields—Observed, retrieved, or simulated. J Geophys Res Atmos 99:8055–8072

Drager K (2014) Alterations of fine and coarse-textured soil material caused by the ant *Formica subsericea*. MS thesis. University of Kansas, Lawrence, KS

Eck DV, Hirmas DR, Giménez D (2013) Quantifying soil structure from field excavation walls using multistripe laser triangulation scanning. Soil Sci Soc Am J 77:1319–1328

Eck DV, Qin M, Hirmas DR, Giménez D, Brunsell N (2016) Relating quantitative soil structure metrics to saturated hydraulic conductivity. Vadose Zone J doi: 10.2136/vzj2015.05.0083

Eltz FLF, Norton LD (1997) Surface roughness changes as affected by rainfall erosivity, tillage, and canopy cover. Soil Sci Soc Am J 61:1746–1755

Frisbie JA, Graham RC, Lee BD (2014) A plaster cast method for determining soil bulk density. Soil Sci 179:103–106

García Moreno R, Díaz Álvarez M, Saa Requejo CA, Tarquis AM (2008) Multifractal analysis of soil surface roughness. Vadose Zone J 7-2:512–520

Giménez D, Karmon JL, Posadas A, Shaw RK (2002) Fractal dimensions of mass estimated from intact and eroded soil aggregates. Soil Tillage Res 64:165–172

Harral BB, Cove CA (1982) Development of an optical displacement transducer for the measurement of soil surface profiles. J Soil Agric Eng Res 27:412–429

Hartemink AE, Minasny B (2014) Towards digital soil morphometrics. Geoderma 230–231:305–317

Hasiotis ST, Bourke MC (2006) Continental trace fossils and museum exhibits: displaying organism behavior frozen in time. Geol Curator 8:211–226

Hirmas DR (2013) A simple method for removing artifacts from moist fine-textured soil faces 77:591–593

Hirmas DR, Furquim SAC (2006) Simple modification of the clod method for determining bulk density of very gravelly soils. Commun Soil Sci Plant Anal 37:899–906

Hirmas DR, Giménez D, Subroy V, Platt BF (2013) Fractal distribution of mass from the millimeter- to decimeter-scale in two soils under native and restored tallgrass prairie. Geoderma 207–208:121–130

Huang C, Bradford JM (1990) Portable laser scanner for measuring soil surface roughness. Soil Sci Soc Am J 54:1402–1406

Huang C, Bradford JM (1992) Applications of a laser scanner to quantify soil microtopography. Soil Sci Soc Am J 56:14–21

Huang C, White I, Thwaite EG, Bendeli A (1988) A noncontact laser system for measuring soil surface topography. Soil Sci Soc Am J 52:350–355

Knighton MS, Agabra DS, McKinley WD, Zheng JZ, Drobnis DD, Logan JD, Bahhour BF, Haynie JE, Vuong KH, Tandon A, Sidney KE, Diaconescu PL (2005) Three dimensional digitizer using multiple methods. US Patent 6,980,302 B2. Filed 17 Sept 2003, issued 27 Dec 2005

Platt BF, Hasiotis ST, Hirmas DR (2010) Use of low-cost multistipe laser triangulation (MLT) scanning technology for three-dimensional, quantitative paleoichnological and neoichnological studies. J Sedim Res 80:590–610

Posadas A, Giménez D, Quiroz R, Protz R (2003) Multifractal characterization of soil pore systems. Soil Sci Soc Am J 67:1361–1369

Ribeiro Jr PJ, Diggle PJ (2015) geoR: analysis of geostatistical data. R package version 1.7-5.1. http://CRAN.R-project.org/package=geoR

Rieu M, Sposito G (1991) Fractal fragmentation, soil porosity, and soil-water properties. I. Theory. Soil Sci Soc Am J 55:1231–1238

Rossi AM, Hirmas DR, Graham RC, Sternberg PD (2008) Bulk density determination by automated three-dimensional laser scanning. Soil Sci Soc Am J 72:1591–1593

Russ JC (2011) The image processing handbook, 6th edn. CRC Press, Boca Raton

Sanchez M, Atique A, Kim S, Romero E, Zielinski M (2013) Exploring desiccation cracks in soils using a 2D profile laser device. Acta Geotech 8:583–596

San José Martínez F, Caniego J, Guber A, Pachepsky Y, Reyes M (2009) Multifractal modeling of soil microtopography with multiple transects data. Ecol Complexity 6:240–245

Schaap MG, Leij FJ, van Genuchten MTh (2001) ROSETTA: a computer program for estimating soil hydraulic parameters with hierarchical pedotransfer functions. J Hydrol 251:163–176

Schoeneberger PJ, Wysocki DA, Benham EC, Soil Survey Staff (2012) Field book for describing and sampling soils, ver. 3.0. Natural Resources Conservation Service, National Soil Survey Center, Lincoln, NE

Steffens M, Buddenbaum H (2013) Laboratory imaging spectroscopy of a stagnic Luvisol profile —High resolution soil characterisation, classification and mapping of elemental concentrations. Geoderma 195–196:122–132

Subroy V, Giménez D, Hirmas DR, Takhistov P (2012) On determining soil aggregate bulk density by displacement in two immiscible liquids. Soil Sci Soc Am J 76:1212–1216

Thwaite EG, Bendeli A (1980) A noncontact profile recording instrument. In: Proceedings of the international conference on manufacturing engineering, Melbourne, Australia, 25–27 Aug 1980. Institution of Engineers in Canberra, ACT, Australia, pp 393–396

Tschinkel WR (2010) Methods for casting subterranean ant nests. J Insect Sci 10:88

Usamentiaga R, Molleda J, Garcia DF, Bulnes FG (2014) Removing vibrations in 3D reconstruction using multiple laser stripes. Opt Lasers Eng 53:51–59

Vidal Vázquez E, Vivas-Miranda JG, Paz Gónzalez A (2005) Characterizing anisotropy and heterogeneity of soil surface microtopography using fractal models. Ecol Model 182:337–353

Zielinski M, Sánchez M, Romero E, Atique A (2014) Precise observation of soil surface curling. Geoderma 226–227:85–93

Chapter 3
Portable X-Ray Fluorescence (pXRF) for Determining Cr and Ni Contents of Serpentine Soils in the Field

Zeng-Yei Hseu, Zueng-Sang Chen, Chen-Chi Tsai and Shih-Hao Jien

Abstract Serpentine-derived soils have high concentrations of Cr and Ni from the parent materials and pose a risk to human health and environmental quality. The use of pXRF is a viable and effective technique for digital soil morphometrics. Soil digestion by aqua regia (AR) is a common method for screening heavy metals in contaminated soils. To provide *in situ* measurements, pXRF was performed for quantifying Cr and Ni in 49 soil horizons from 11 pedons at 3 serpentine areas in eastern Taiwan. Cr and Ni were also determined by the AR method for the samples. The correlation between pXRF and AR methods was linear and significant ($r = 0.90$ and 0.99, respectively, $P < 0.001$). The metal contents by pXRF were, however, higher than by AR. The difference is much larger for Cr than for Ni, because Cr was mainly fixed in the chromite minerals which were resistant to the AR reagent, but Ni was easily released from weatherable serpentine silicates. When additional 192 surface soil samples were used, the correlation was significant for Cr and Ni ($r = 0.89$ and 0.98, respectively, $P < 0.001$, $n = 241$). It was concluded that the pXRF was valid to rapidly screen Cr and Ni levels in serpentine soils in the field.

Keywords Aqua regia · Chromium · Digital soil morphometrics · Nickel · Portable X-ray fluorescence · Serpentine soil

Z.-Y. Hseu (✉) · Z.-S. Chen
Agricultural Chemistry, National Taiwan University, Taipei 10617, Taiwan
e-mail: zyhseu@ntu.edu.tw

C.-C. Tsai
Department of Forestry and Natural Resources, National I-Lan University, I-Lan 26047, Taiwan

S.-H. Jien
Department of Soil and Water Conservation, National Pingtung University of Science and Technology, Pingtung 91201, Taiwan

A.E. Hartemink and B. Minasny (eds.), *Digital Soil Morphometrics*,
Progress in Soil Science, DOI 10.1007/978-3-319-28295-4_3

3.1 Introduction

Hartemink and Minasny (2014) defined the term digital soil morphometrics as the application of tools and techniques for measuring, mapping, and quantifying soil profile attributes. They indicated the potential for in situ digital morphometrics for all attributes of a soil profile to give continuous depth functions of soil properties, when small depth increments were sampled and analyzed. Among the digital morphometric techniques, X-ray fluorescence (XRF) spectrometry is a rapid, proximal scanning technology which allows for total metal quantification in soils within approximate two minutes. The operational theory concerning XRF uses high-energy X-ray photons to forcibly eject an inner sphere (K or L orbital) electron from the atom. This ejection causes electron shell instability whereby outer shell electrons cascade down to fill the inner shell electron void. In doing so, a secondary energy emission is produced, termed X-ray fluorescence (Jenkins 1999). The energy emitted as fluorescence is element specific, allowing for nondestructive elemental identification and quantification. For decades, XRF has been used in traditional laboratory-based soil analysis. Recent advances in the technology have made it field portable and useful in many soil science applications from pedology to environmental quality assessment (Weindorf et al. 2012a, b, c).

Soil metal content can be detected by analytical techniques such as electrochemical methods, chromatographic separation, and spectroscopic techniques (Radu and Diamond 2009). Analysis involves soil sample collection, subsequent sample treatments such as extraction or digestion, and quantification using a flame atomic absorption spectroscopy (FAAS), inductively coupled plasma atomic emission spectrometry (ICP-AES), ICP-mass spectrometry, or atomic fluorescence spectroscopy (Zhu and Weindorf 2009). However, XRF provides a multi-element analytical method for the routine nondestructive analysis of soils with minimal sample preparation (Kalnicky and Singhvi 2001; Herpin et al. 2002). The most attractive feature of XRF is its wide dynamic range, from parts per million (or milligrams per kilogram) to 100 %, for many elements in a given sample (Hettipathirana 2004). Portable XRF (pXRF) technology can be implemented in soil geochemical analysis for faster and more efficient testing of metals in soil profiles. As pXRF can be applied directly in the field, sample treatments such as extraction, digestion, or long mechanical stages of separation are no longer necessary. Determination directly from soil samples provides a better representation of the matrix in which metals naturally exist.

To date, pXRF has been used in soil science. Kalnicky and Singhvi (2001) demonstrated the benefits of pXRF for rapid assessment of soil contamination. Several official methods such as Environmental Protection Agency (EPA) Method 6200 in USA (USEPA 2007) and National Institute of Environmental Analysis Method S322.60C in Taiwan (2006) include the use of pXRF technology for on-site analysis of metal contaminants in soil and sediments to guide evaluation and remediation programs. Radu and Diamond (2009) used pXRF for evaluating 17 soil samples from abandoned mining sites in Ireland. They found excellent correlations

with traditional FAAS results for As, Cu, and Zn in soils. For pedolocial and archaeological use, Arnoldussen and van Os (2015) demonstrated the suitability of pXRF analysis to extract paleo-geochemical information from lacquer-peel soil sections that have been taken to document pedological information at archaeological sites. The values for Si, K, Al, Fe, Ti, Sr, Zr, and Rb in the lacquer peels reflected lithogenic and pedological processes, and the contents of S, Ca, and P were used as a proxy for anthropogenic influence. The lacquer peels provided consistent and reliable geochemical readings with the pXRF. Most previous applications of pXRF in soil science were focused on the determination of heavy metal concentrations for environmental assessment, screening, monitoring, and mitigation (Palmer et al. 2009; Radu and Diamond 2009; Stallard et al. 1995; Weindorf et al. 2012b). Few studies have attempted to infer the enrichment of Cr and Ni in serpentine soils by using pXRF (Panagopoulos et al. 2015).

Serpentine soils are often not only derived from ultramafics but also from hydrothermal alternation of ultramafic minerals and a presence of serpentine minerals (Alexander et al. 2007). Most serpentine soils pose ecological or environmental risk because of high levels of potentially toxic metals such as Cr and Ni (Oze et al. 2004; Hseu 2006; Kierczak et al. 2007; Cheng et al. 2009, 2011; Bonifacio et al. 2010; Becquer et al. 2010; Hseu and Iizuka 2013). The high amounts of Cr and Ni in serpentine soils are harmful in crop production or result in unique natural vegetation (Yang et al. 1985; Brooks 1987). Serpentine soils are abundant in the ophiolite belts and are typically found within regions of the Circum-Pacific margin and Mediterranean Sea (Oze et al. 2004). Mafic and ultramafic rocks-derived soils are richer in Cr and Ni and up to 3400 mg/kg of Cr along with 3600 mg/kg of Ni. The average concentrations of Cr and Ni in soils of the world are about 84 and 34 mg/kg, respectively (McGrath 1995). Lithogenic heavy metals are considered less mobile than those of anthropogenic origin in soils, but their potential risk to the environment occurs through the increase of bioavailability of Cr and Ni (Becquer et al. 2003; Chardot et al. 2007). Fernandez et al. (1999) found that sugar beet, cabbage, and pasture on the serpentine soils in northwestern Spain accumulated significant quantities of Cr and Ni, despite low to moderate EDTA-extractable amounts in these soils. Miranda et al. (2009) evaluated Cr and Ni accumulation in cattle raised in a serpentine area. Samples of liver, kidney, and muscle of the 41 animals aged 8–12 months were collected. Accumulation of Cr in the animal tissues was generally low and within the normal range, but 20 % of the animals had toxic levels of Ni in their kidneys.

Serpentine landscapes are intensively found in eastern Taiwan, adjacent to the convergent boundary of Eurasia Plate and Pacific Plate. The influence of pedological conditions on Cr and Ni concentration is an essential consideration when analyzing the ecological functions of serpentine soils. The behavior of Cr and Ni and their origin and vertical distribution in serpentine soils on different landscapes need to be studied (Hseu 2006; Hseu et al. 2007; Hseu and Iizuka 2013). The FAAS/ICP-AES measurement with aqua regia digestion is an official standard to determine soil contamination with heavy metals in Taiwan. The pXRF technology for on-site analysis of the metals is used as a rapidly screening approach for

contaminated sites. The objectives of this study were to: (1) evaluate the effectiveness of using pXRF for quantifying Cr and Ni concentrations through serpentine soil profiles, (2) validate the results obtained from the pXRF using the aqua regia method, and (3) verify the pXRF measurement of Cr and Ni for surface soils at serpentine sites.

3.2 Materials and Methods

3.2.1 Description of Study Sites

The Huadong longitudinal valley (HLV) in eastern Taiwan was selected as the study area. The HLV is a long and narrow rift stretching for about 180 km and ranging from 2 to 7 km in width, flanked by the central ridge to the west and the coastal range to the east. Three rural sites were selected in the northern part of HLV (Fig. 3.1), which soil parent materials, serpentines, are exotic blocks of ophiolite from the Philippine Sea Plate that developed during the Late Pliocene epoch (Ho 1988). They are Kuang-Shan (23° 02′ 18″N, 121° 11′ 24″E), Ruei-Shui (23° 30′ 27″

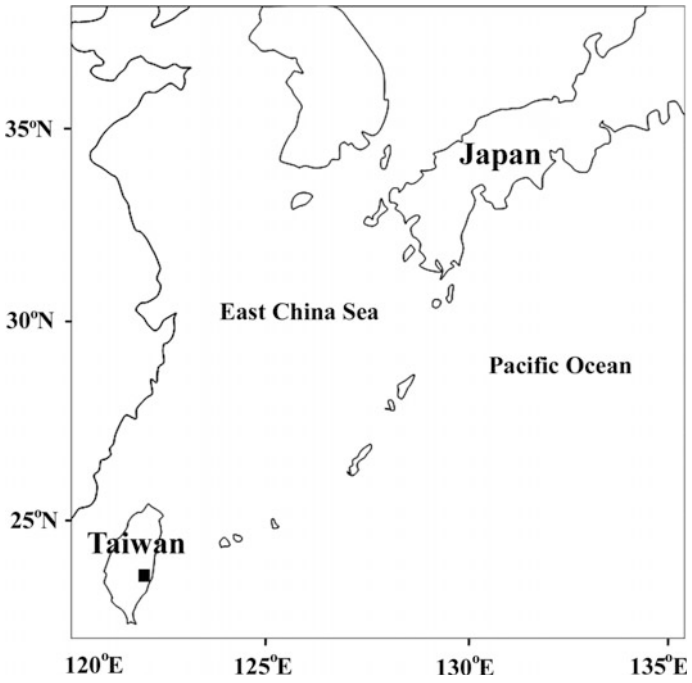

Fig. 3.1 Location of the study sites in Taiwan

N, 121° 22′ 25″E), and Wang-Long (23° 42′ 54″N, 121° 24′ 41″E), which are corresponding to 109, 427, and 127 ha in area for selecting reference soil profiles and additional surface soils.

3.2.2 Sample Collection and Analysis

A total of 11 pedons were selected, and they were identified using the prefixes KS, RS, and WL for the soils from the HLV at the sites of Kuang-Shan, Ruei-Shui, and Wang-Long, respectively. For each pedon, morphological characteristics were described according to Soil Survey Staff (1993). Cr and Ni were determined by a pXRF directly in the soil profile. The pXRF instrument (X-50) was an Olympus Innov-X (MA, USA) and used to scan the surfaces of the soil *in situ*. The X-50 pXRF was conducted with a Ta/Au X-ray tube operated at 50 keV and a current of 200 μA with quantification via ultra-high-resolution (<190 eV) silicon pin diode detector. Prior to its use, various concentration ranges of the National Institute of Standards and Technology (NIST) standard reference material (NIST 2702) were scanned to assure the analytical quality of pXRF. The X-ray fluorescence signal was collected for 30 s. To verify the effectiveness of pXRF for the studied soils, an additional 192 surface soils at 3 serpentine sites were scanned.

Soil sample was also collected and air-dried, homogenized, and screened for standard soil analyses and Cr and Ni. Soil particle size distribution was determined with the pipette method (Gee and Bauder 1986). The soil pH was measured in a mixture of soil and deionized water (1:1, w/v) using a glass electrode (McLean 1982). Total organic carbon (OC) content was determined using the Walkley-Black wet oxidation method (Nelson and Sommers 1982). Cr and Ni were determined by the digestion of soil with concentrated HNO_3 and HCl (1:3, v/v) (aqua regia) for all horizons and additional surface soil samples. The filtered suspension was measured with an ICP-AES (Optimal DV 2100; Perkin-Elmer, USA), following the procedure recommended by Taiwan EPA (Taiwan EPA 2015).

3.3 Results and Discussion

3.3.1 Soil Characteristics

All pedons are dark or gray colored and display no clear rubification. The particle size distribution for the soils varied between pedons. Clay content ranged from 8 % in the C2 horizon of Pedon RS04 to 78 % in the A1 horizon of Pedon KS01 (Table 3.1). The elemental composition of serpentine soils is not affected by pedogenic processes and by the differences in ophiolite origin (Cheng et al. 2009); thus, soil pH differs between pedons. Pedons at Wang-Long site had higher pH

Table 3.1 Characteristics of the pedons

Pedon	Horizon	Depth (cm)	Color	Sand (%)	Silt (%)	Clay (%)	pH	OC[a] (%)
KS01	A1	0–10	7.5YR 3/2	15	13	78	5.8	4.10
	A2	10–23	7.5YR 3/2	17	12	71	5.8	2.55
	AB	23–40	7.5YR 4/3	13	13	74	5.7	1.98
	Bss1	40–60	7.5YR 4/4	15	10	75	5.7	1.88
	Bss2	60–80	7.5YR 4/6	18	13	69	5.9	1.96
	Bss3	80–100	7.5YR 4/6	20	13	64	5.9	1.28
	C	>100	7.5YR 5/6	25	16	59	5.9	1.34
KS03	A	0–15	5YR 2.5/2	25	14	61	6.1	3.78
	AB	25–30	5YR 2.5/2	37	14	49	6.2	2.60
	Bss1	30–50	5YR 3/4	25	18	57	6.1	2.03
	Bss2	50–70	5YR 4/4	33	11	56	6.1	1.50
	Bss3	70–90	5YR 4/6	35	20	45	6.1	1.19
	BSS4	90–110	5YR 4/6	33	16	51	6.1	1.38
	C	110–130	7.5YR 4/6	40	16	44	6.2	1.09
RS01	A	0–18	2.5Y 3/2	72	14	14	5.4	1.53
	C	18–28	2.5Y 4/2	79	11	10	5.4	0.92
	2C1	28–42	2.5Y 4/4	66	24	10	4.7	1.71
	2C2	42–62	10YR 3/2	62	23	15	4.8	1.92
RS02	Ap	0–15	2.5Y 4/2	59	24	17	5.1	2.14
	C	15–35	2.5Y 3/4	60	28	12	5.9	1.50
RS03	Ap	0–12	10YR 3/3	56	26	18	5.0	1.95
	C	12–32	10YR 4/3	61	22	17	5.1	1.52
RS04	Ap1	0–17	2.5Y 4/2	63	23	14	5.1	2.05
	Ap2	17–32	2.5Y 4/1	67	23	10	5.1	1.23
	Bw1	32–42	2.5Y 3/3	67	15	18	5.5	1.32
	Bw2	42–60	2.5Y 5/2	71	15	14	5.8	1.71
	Bw3	60–76	2.5Y 5/2	70	14	16	6.1	0.85
	C1	76–100	2.5Y 5/1	77	10	13	6.3	1.15
	C2	100–120	2.5Y 5/1	80	12	8	5.5	0.62
RS05	Ap1	0–15	2.5Y 3/3	80	6	14	5.6	2.52
	Ap2	15–30	5Y 4/3	73	10	17	6.0	1.04
	Bw1	30–50	5Y 5/2	62	24	14	6.2	0.61
	Bw2	50–70	5Y 5/2	61	22	17	6.3	1.28
	Bw3	70–90	5Y 5/3	42	41	17	6.1	1.48
	Bw4	90–115	5Y 5/1	55	32	17	6.5	0.57
	Bw5	115–130	5Y 5/1	60	26	14	6.4	1.08
	C1	130–170	2.5Y 5/1	74	12	14	6.4	0.49
	C2	170–190	2.5Y 5/1	75	11	14	6.4	1.31
WL01	A	0–10	2.5Y 3/1	70	10	20	7.2	2.65
	C	>10	2.5Y 5/3	69	8	23	7.5	1.11
WL02	Ap1	0–10	5Y 3/2	42	30	28	7.4	2.78
	Ap2	10–20	5Y 4/1	26	59	15	7.6	0.77
	Bw	20–35	5Y 3/1	38	44	18	7.8	1.98
	C1	35–55	5Y 2.5/1	45	44	11	7.8	0.86
	C2	>55	5Y 2.5/1	45	45	10	7.7	1.80
WL03	Ap	0–13	5Y 3/1	51	36	13	7.5	1.97
	C	13–33	5Y 4/1	51	39	10	7.5	2.11
WL04	Ap	0–10	5Y 3/1	30	51	19	7.5	1.79
	C	10–20	5Y 4/2	37	46	17	7.8	1.04

[a]Organic carbon

values than those at the other sites. Organic C (OC) contents were generally highest in the surface horizon and decreased with depth. The OC content was below 5.0 %. According to *Soil Taxonomy*, these pedons are Typic Hapluderts (KS01 and KS03), Typic Udorthents (RS01), Lithic Udorthents (RS02, RS03, WL01, Wl03, and WL04), and Typic Eutrudepts (RS04, RS05, WL02) (Soil Survey Staff 2014).

3.3.2 Comparison Between pXRF and the Aqua Regia Methods

Concentrations of Cr and Ni in soil horizons were determined by the pXRF in situ, and the results indicated very high Cr and Ni levels (Table 3.2). The highest concentration of Cr was 2329 mg/kg and the lowest was 168 mg/kg. The mean concentration of Cr (772 mg/kg) was much higher than the average Cr in worldwide soils (McGrath 1995). The Cr concentration varied among horizons and pedons (Fig. 3.2). The aqua regia soluble Cr was lower than Cr determined by pXRF, and this difference increased with soil development from the Entisols to the Vertisols. The difference in Cr between pXRF and aqua regia methods was high in the topsoils. The pXRF analysis showed that the mean concentration of Ni was similar to Cr, but the difference of Ni between pXRF and aqua regia methods was lower than that of Cr (Table 3.2). The difference of Ni between the pXRF and aqua regia methods appeared to be consistent in all soils (Fig. 3.3). On the other hand, the soil with more Cr-spinels caused a larger difference of Cr determined between the pXRF and aqua regia methods, like the Vertisols rather than the Entisols.

The Cr and Ni concentrations reflected the ultramafic characteristics of serpentine soils. According to the soil control standards of heavy metals in Taiwan by using the aqua regia method, 250 and 200 mg/kg of Cr and Ni would label the soil as a potentially contaminated (Taiwan EPA 2001). The metal source was geogenic in serpentine soils, but they posed the potential risk to human health and the environment.

Table 3.2 Descriptive statistical parameters of Cr and Ni concentrations (mg/kg) in all horizons (n = 49) of pedons determined by pXRF and aqua regia methods

	Cr		Ni	
	pXRF	Aqua regia	pXRF	Aqua regia
Maximum	2329	1260	3338	3300
Minimum	168	88.4	60.0	62.6
Mean	772	435	748	676
Medium	528	309	372	187
Standard derivation	579	301	784	872
Skewness	1.39	1.20	1.72	1.63
Kurtosis	0.83	045	2.49	1.86

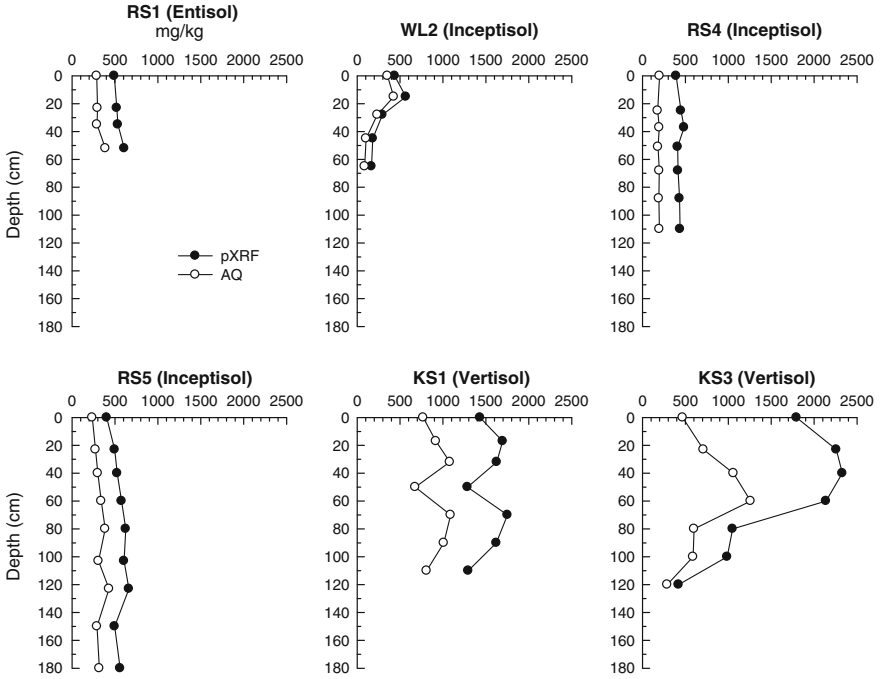

Fig. 3.2 Profile distribution of Cr with aqua regia method (*white circle*) and pXRF (*black circle*) in selected pedons

Bonifacio et al. (2010) found that Ni showed a more homogeneous distribution than Cr with a smaller range in 66 soil horizons of 19 poorly developed serpentine soils of the Alps in northwestern Italy. In their study, Cr appeared to increase with Ni and both metals had similar ranges, even if the differences in mineral sources between Cr and Ni have been identified (Oze et al. 2004; Kierczak et al. 2007; Cheng et al. 2011). Chromium (III) and Ni can substitute for Mg or Fe in the octahedral sheet in olivine and pyroxene in peridotites, but chromium is substituted into serpentine minerals in very low amounts (Oze et al. 2004). However, Cr is mostly found in spinel minerals such as Cr-magnetite, chromite, and other mixed-composition spinels containing Al, Cr, Mg, and Fe (Cheng et al. 2011; Hseu and Iizuka 2013). These Cr-spinels are recalcitrant (Oze et al. 2004) and hardly dissolved by the aqua regia reagent (Morrison et al. 2009). Hseu and Iizuka (2013) found that Cr has localized high concentrations in serpentine soils because of discrete bodies of chromite with strong resistance to weathering. Silicates were reported as important Ni-bearing minerals in serpentine soils, and the Ni concentration of serpentine minerals ranges from 0.2 to 0.4 % (Kierczak et al. 2007). Chlorite and serpentine are the most common minerals in serpentine soils of eastern Taiwan (Hseu et al. 2007), and thus, they influence the total metal contents. These diverse mineral sources of Cr and Ni may justify the discrepancies in the differences

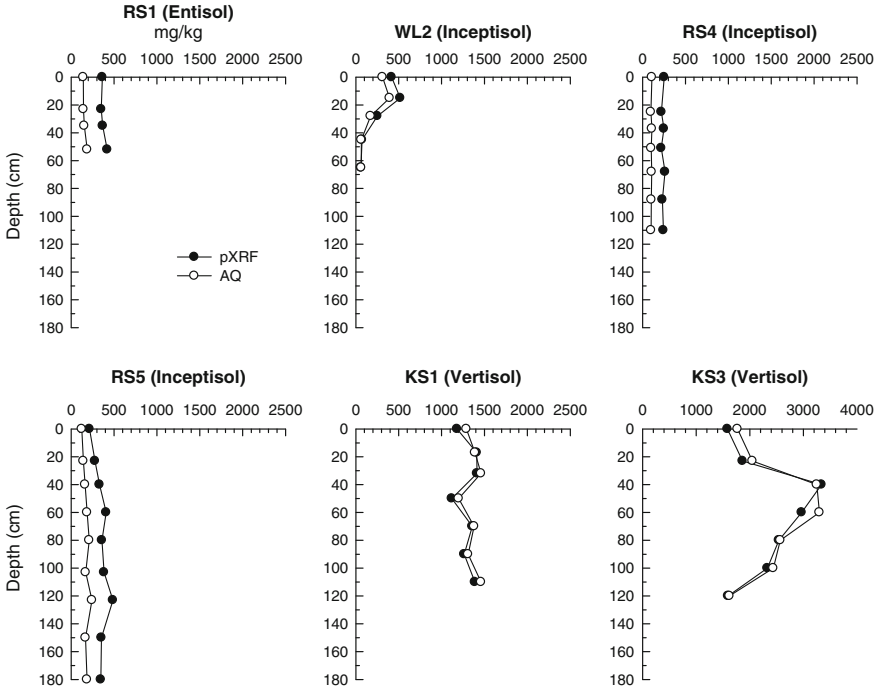

Fig. 3.3 Profile distribution of Ni with aqua regia method (*white circle*) and pXRF (*black circle*) in selected pedons

of total contents in this study by using the pXRF and aqua regia methods (Table 3.2). Kierczak et al. (2007) found, however, a weak and positive correlation between Cr and Ni ($r^2 = 0.47$, $n = 22$) for well-drained serpentine soils from Poland, France, and Italy.

3.3.3 Validation of pXRF

For serpentine soil analysis, the aqua regia reagent can dissolve all metal fractions outside silicate structures, but only partially Ni from silicates and Cr from silicates and Cr-spinels such as chromite and magnetite (Cheng et al. 2011) The XRF methodology obtained the total contents of metals in the soils. This is why the Cr and Ni concentrations by the aqua regia method were lower than those by pXRF (Table 3.2). Regarding the mean value of metal concentration, the aqua regia soluble Cr and Ni was approximately 56 and 90 % of Cr and Ni determined by the pXRF. However, Fig. 3.4 shows the correlation between the aqua regia and pXRF measurements of Cr and Ni concentrations for all horizons. For both methods, good correlation of the two techniques was found. The r values were 0.90 and 0.99,

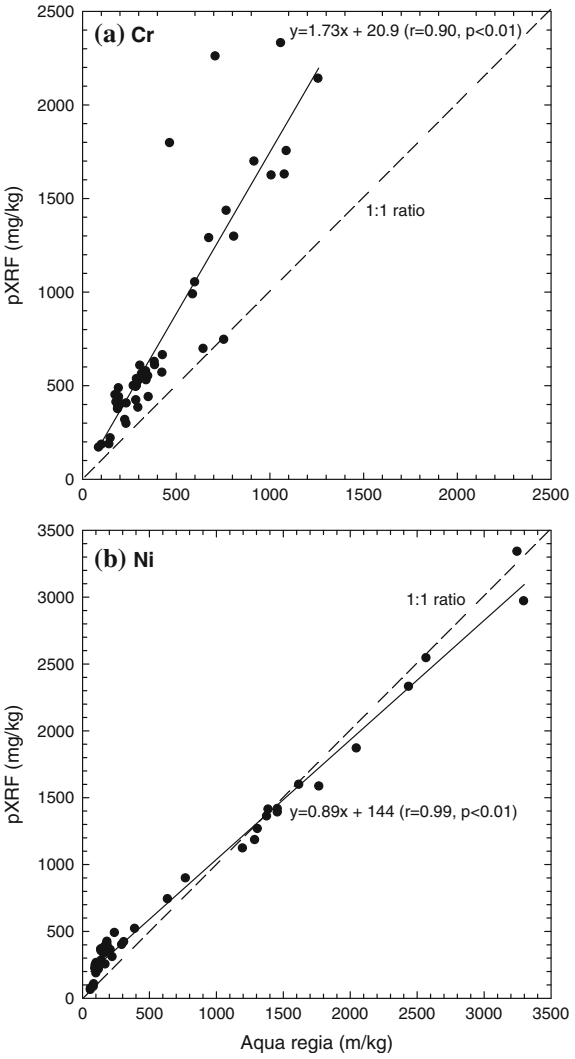

Fig. 3.4 Chromium (**a**) and nickel (**b**) determined by aqua regia compared to those as determined by pXRF for soil horizon samples (n = 49) in all pedons

respectively. This confirmed an excellent performance over a range of concentration. The data of Cr concentration from the two methods followed a linear model: $y = 1.73x + 20.9$, indicating a bias from the line of 1:1 ratio particularly when Cr levels were high (Fig. 3.4a). The data of Ni from the two methods followed the linear model: $y = 0.89x + 144$, but the bias was smaller than for Cr (Fig. 3.4a), because the aqua regia reagent could dissolve the relatively weak frameworks of silicate containing (i.e., Fe-chlorite and antigorite) predominant Ni compared to Cr-spinels.

When an additional 192 surface soils at all sites were used for the comparison between the two methods, the correlation was significant for Cr and Ni (r = 0.89

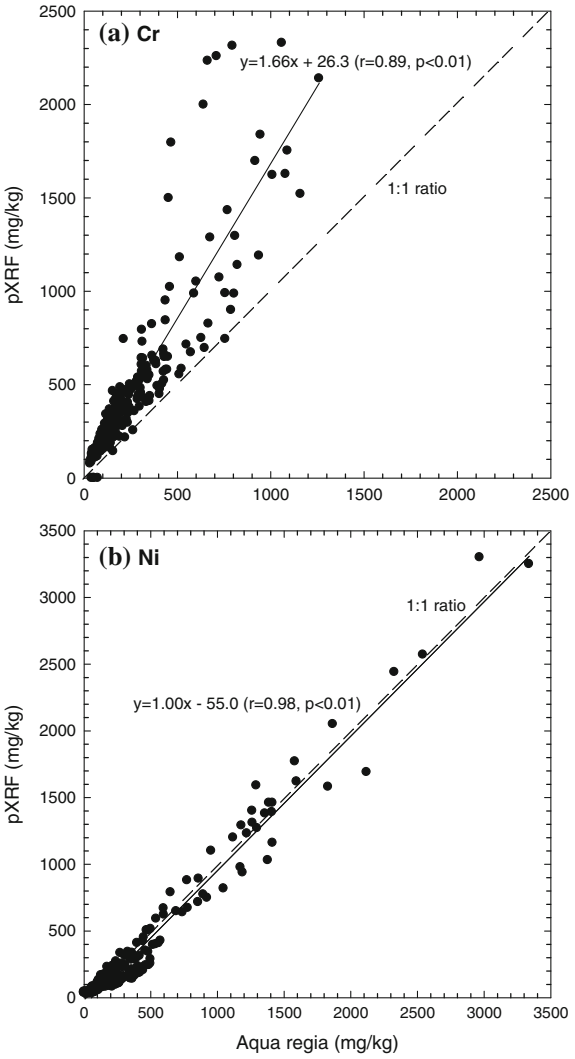

Fig. 3.5 Chromium (**a**) and nickel (**b**) determined by aqua regia compared to those as determined by pXRF for soil horizon samples (n = 49) in all pedons and additional 192 surface soil samples

and 0.98, respectively, $P < 0.001$, n = 241) (Fig. 3.5). For the 241 samples from pedons and addition surface soils, the linear model was $y = 1.66x + 26.3$ for Cr and $y = 1.00x - 55.0$ for Ni. These correlations established a reference for the pXRF measurement for Cr and Ni in serpentine soils. The major concern of pXRF performance is the non-homogeneity of efficiency for different elements (Kalnicky and Singhvi 2001; Weindorf et al. 2012b). Although the studied soils varied in texture, pH, and OC content, the pXRF offers quantitative results regarding Cr and Ni of serpentine soils, as reported by Panagopoulos et al. (2015).

3.4 Summary and Conclusions

The aqua regia soluble Cr was lower than Cr determined by pXRF, and this difference increased along with soil development from Entisol to Vertisols. Regardless of soil development, the difference of Ni between the pXRF and the aqua regia methods appeared to be consistent. The mean concentration of Ni was similar to Cr, but the difference of Ni between pXRF and aqua regia methods was lower than that of Cr. The correlations between the two methods established an adjustment reference of the pXRF measurement for Cr and Ni in serpentine soils. Although the studied soils varied, the pXRF is able to offer acceptable quantitative results regarding Cr and Ni of serpentine soils. The pedology community has accepted pXRF methodology as viable and effective technique for analyzing soil samples. It is a nondestructive technique, and the analyses can be performed with the same samples. Detailed site investigation requires extensive sampling and subsequent laboratory analysis. The main purpose for using pXRF is to guide on-site decision making for identifying the enrichment of Cr and Ni in serpentine soils. The application of pXRF to perform analyses in situ has the potential to decrease costs and analysis time over formal laboratory methods of extraction and instrumental measurement such as the aqua regia method.

Acknowledgments The authors would like to thank the Ministry of Science and Technology of the Republic of China, Taiwan, for financially supporting this research under Contract No. MOST 102-2313-B-020-009-MY3.

References

Alexander EB, Coleman RG, Keeler-Wolf T, Harrison S (2007) Serpentine soil distributions and environmental influences. In: Alexander EB, Coleman RG, Keeler-Wolf T, Harrison S (eds) Serepntine geoecology of Western North America. Oxford University Press, New York, pp 55–78

Arnoldussen S, van Os BJH (2015) The potential of lacquer-peel soil profiles for palaeo-geochemical analysis using XRF analysis. Catena 128:16–30

Becquer T, Quantin C, Sicot M, Boudot JP (2003) Chromium availability in ultramafic soils from New Caledonia. Sci Total Environ 301:251–261

Becquer T, Quantin C, Boudot JP (2010) Toxic levels of metals in Ferralsols under natural vegetation and crops in New Caledonia. Eur J Soil Sci 61:994–1004

Bonifacio E, Falsone G, Piazza S (2010) Linking Ni and Cr concentrations to soil mineralogy: does it help to asses metal contamination when the natural background is high? J Soils Sediments 10:1475–1486

Brooks RR (1987) Serpentine and its vegetation: a multidisciplinary approach. Croom Helm, London

Chardot V, Echevarria G, Gury M, Massoura S, Morel JL (2007) Nickel bioavailability in an ultramafic toposequence in the Vosges Mountains (France). Plant Soil 293:7–21

Cheng CH, Jien SH, Tsai H, Chang YH, Chen YC, Hseu ZY (2009) Geochemical element differentiation in serpentine soils from the ophiolite complexes, eastern Taiwan. Soil Sci 174:283–291

Cheng CH, Jien SH, Iizuka Y, Tsai H, Chang YS, Hseu ZY (2011) Pedogenic chromium and nickel partitioning in serpentine soils along a toposequence. Soil Sci Soc Am J 75:659–668

Fernandez S, Seoane S, Merino A (1999) Plant heavy metal concentrations and soil biological properties in agricultural serpentine soils. Commun Soil Sci Plant Anal 30:1867–1884

Gee GW, Bauder JW (1986) Particle-size analysis. In: Klute A (ed) Methods of soil analysis, Part 1, 2nd edn. Agronomy Monograph No 9. American Society of Agronomy and Soil Science Society of America, Madison, WI, pp. 383–411

Ho CS (1988) An introduction to the geology of Taiwan: explanatory text of the geologic map of Taiwan, 2nd edn. Central Geology Survey, Taipei, Taiwan

Hartemink AF, Minasny B (2014) Towards digital soil morphometrics. Geoderma 203–231:305–317

Herpin U, Cerri CC, Carvalho MCS, Markert B, Enzweiler J, Friese K, Breulmanne G (2002) Biogeochemical dynamics following land use change from forest to pasture in a humid tropical area (Rondonia, Brazil): a multi-element approach by means of XRF-spectroscopy. Sci Total Environ 286:97–109

Hettipathirana TD (2004) Simultaneous determination of parts-per-million level Cr, As, Cd and Pb, and major elements in low level contaminated soils using borate fusion and energy dispersive X-ray fluorescence spectrometry with polarized excitation. Spectrochim Acta, Part B 59:223–229

Hseu ZY (2006) Concentration and distribution of chromium and nickel fractions along a serpentinitic toposequence. Soil Sci 171:341–353

Hseu ZY, Iizuka Y (2013) Pedogeochemical characteristics of chromite in a paddy soil derived from serpentinites. Geoderma 202–203:126–133

Hseu ZY, Tsai H, Hsi HC, Chen YC (2007) Weathering sequences of clay minerals in soils along a serpentinitic toposequence. Clays Clay miner 55:389–401

Jenkins R (1999) X-ray fluorescence spectrometry. In: Winefordner JD (ed). Wiley, New York

Kalnicky DJ, Singhvi R (2001) Field portable XRF analysis of environmental samples. J Hazard Mater 83:93–122

Kierczak J, Neel C, Bril H, Puziewicz J (2007) Effect of mineralogy and pedoclimatic variations on Ni and Cr distribution in serpentine soils under temperate climate. Geoderma 142:165–177

McGrath SP (1995) Chromium and nickel. In: Alloway BJ (ed) Heavy metals in soils, 2nd edn. Blackie Academic and Professional, London, pp 152–178

McLean EO (1982) Soil pH and lime requirement. In: Page AL, Miller RH, Keeney DR (eds) Methods of soil analysis, Part 2, Chemical and microbiological properties, 2nd edn. Agronomy Monograph No 9. American Society of Agronomy and Soil Science Society of America, Madison, WI, pp 199–224

Miranda M, Benedito J, Blanco-Penedo I, López-Lamas C (2009) Metal accumulation in cattle raised in a serpentine-soil area: relationship between metal concentrations in soil, forage and animal tissues. J Trace Elem Med Biol 23:231–238

Morrison JM, Goldhaber MB, Lee L, Holloway JM, Wanty RB, Wolf RE, Ranville JF (2009) A regional-scale study of chromium and nickel in soils of northern California, USA. Appl Geochem 24:1500–1511

Nelson DW, Sommers LE (1982) Total carbon, OC, and organic matter. In: Page AL, Miller RH, Keeney DR (eds) Methods of soil analysis, Part 2, Chemical and microbiological properties, 2nd edn. Agronomy Monograph No 9. American Society of Agronomy and Soil Science Society of America, Madison, WI, pp 539–557

Oze C, Fendorf S, Bird DK, Coleman RG (2004) Chromium geochemistry in serpentinized ultramafic rocks and serpentine soils from the Franciscan complex of California. Am J Sci 304:67–101

Palmer PT, Jacobs R, Baker PE, Ferguson K, Webber S (2009) Use of field-portable XRF analyzers for rapid screening of toxic elements in FDA-regulated products. J Agric Food Chem 57:2605–2613

Panagopoulos I, Karayannis A, Kollias K, Xenidis A, Papassiopi N (2015) Investigation of potential soil contamination with Cr and Ni in four metal finishing facilities at Asopos industrial area. J Hazard Mater 281:20–25

Radu T, Diamond D (2009) Comparision of soil pollution concentrations determined using AAS and portable XRF techniques. J Hazard Mater 171:1168–1171

Soil Survey Staff (1993) Soil survey manual. Agricultural Handbook No. 18. US Governmental Printing Office, Washington, DC

Soil Survey Staff (2014) Keys to soil taxonomy, 12th edn. NRCS, USDA, Washington, DC

Stallard MO, Apitz SE, Dooley CA (1995) X-ray fluorescence spectrometry for field analysis of metals in marine sediments. Mar Pollut Bull 31:297–305

Taiwan EPA (2001) Soil and Groundwater Pollution Remediation Act. http://sgw.epa.gov.tw/public/En/index.htm. Verified 1 May 2015

Taiwan EPA (2006) NIEA Method S322.60C: field portable X-ray fluorescence spectrometry for rapidly screening elemental concentrations in soil and sediment. Available at http://www.niea.gov.tw/niea/SOIL/S32260C.htm. Verified 1 May 2015 (in Chinese)

Taiwan EPA (2015) NIEA Method S321.64B: heavy metal analysis for soil-aqua regia digestion. Available at http://www.niea.gov.tw/analysis/method/methodfile.asp?mt_niea=S321.64B. Verified 1 May 2015 (in Chinese)

USEPA (2007) Method 6200: field portable X-ray fluorescence spectrometry for the determination of elemental concentrations in soil and sediment (Online). www.epa.gov2007. Verified 1 May 2015

Weindorf DC, Zhu Y, McDaniel P, Valerio M, Lynn L, Michaelson G, Clark M, Ping CL (2012a) Characterizing soils via portable X-ray fluorescence spectrometer: 2. Spodic and Albic horizons. Geoderma 189–190:268–277

Weindorf DC, Zhu Y, Chakraborty S, Bakr N, Huang B (2012b) Use of portable X-ray fluorescence spectrometry for environmental quality assessment of peri-urban agriculture. Environ Monit Assess 184:217–227

Weindorf DC, Zhu Y, Haggard B, Lofton J, Chakraborty S, Bakr N, Zhang W, Weindorf WC, Legoria M(2012c) Enhanced pedon horizonation using portable x-ray fluorescence spectrometry. Soil Sci Soc Am J 76:522–531

Yang XH, Brooks RR, Jaffre T, Lee J (1985) Elemental levels and relationships in the Flacourtiaceae of New Caledonia and their significance for the evaluation of the 'serpentine problem'. Plant Soil 87:281–291

Zhu Y, Weindorf DC (2009) Determination of soil calcium using field portable X-ray fluorescence. Soil Sci 174:151–155

Chapter 4
In Situ Analysis of Soil Mineral Composition Through Conjoint Use of Visible, Near-Infrared and X-Ray Fluorescence Spectroscopy

Edward J. Jones and Alex B. McBratney

Abstract Soil mineral composition impacts soil behaviour but field estimation of the soil mineralogy has been difficult. Preliminary results of a model to rapidly quantify soil mineral composition are presented. To investigate the efficacy of predicting soil mineral composition in situ two soils under agriculture from New South Wales, Australia, was scanned with visible–near-infrared (Vis–NIR) and portable X-ray fluorescence (pXRF) spectrometers to a depth of 1 m at 2.5 cm sampling increments. The Vis–NIR spectra were preprocessed and the presence of individual minerals was assessed using pattern matching with mineral end-member libraries. Rule-based iterative partitioning was then applied on the recorded pXRF elemental compositions based on known stoichiometric ranges of the identified minerals. This gave a mineral abundance prediction and distinguished between mineral groupings not clearly differentiated by Vis–NIR spectra alone, i.e. kaolinite, illite and smectite. Predicted mineral composition compared favourably to existing mineralogical interpretation of horizon-based random powder and orientated clay samples analysed using laboratory X-ray diffraction. This fine-scale mapping of the distribution of soil minerals in situ has potential to enhance soil morphological description, support site-specific pedogenetic theories and may be further used to moderate properties predicted directly from the Vis–NIR and pXRF spectra.

Keywords X-ray fluorescence · Near-infrared spectroscopy · Proximal soil sensing · Data fusion · Elemental mass balance

E.J. Jones (✉) · A.B. McBratney
Department of Agriculture and Environmental Sciences,
The University of Sydney, New South Wales 2006, Australia
e-mail: edward.jones@sydney.edu.au

A.E. Hartemink and B. Minasny (eds.), *Digital Soil Morphometrics*,
Progress in Soil Science, DOI 10.1007/978-3-319-28295-4_4

4.1 Introduction

Soil mineral composition directly or indirectly affects nearly all soil properties. As such, soil mineral composition has a large impact on soil behaviour and to gain insight into soil function, we must capture and explore its spatial variability. Routine soil mineral analysis involves laboratory-based X-ray diffraction (XRD). To provide more objective interpretations and enhance current field soil description techniques, there has been a growing push to digitally capture and quantify soil properties in the field (Hartemink and Minasny 2014).

In addition being confined to the laboratory, XRD analysis of random powder samples and basally oriented clays with appropriate pretreatment (e.g. Mg/K saturation, ethylene glycol, heating to 550 °C) is a time-consuming task. Although some spectral interpretation software is available, expert interpretation is still required and mineral estimation remains semi-quantitative. Field portable XRD devices exist and have been used for lithological investigation both on Earth and on Mars (Downs 2015). However, they require samples to be relatively dry and also ground before analysis (Sarrazin et al. 2005). These devices can take several hours to analyse complex materials (a complex material is an apt, basic definition of soil). Non-destructive, in situ XRD devices are available although they commonly have a reduced range and are limited to angles greater than 20° 2θ (Gianoncelli et al. 2008). This is problematic as most phyllosilicates have primary peaks at lower angles (<10° 2θ), and thus, these devices are less equipped to estimate these important soil constituents. Subsequently, portable XRD devices have been mostly limited to archaeological and lithological investigations (e.g. Nakai and Abe 2012; Uda 2004; Cannon et al. 2015).

Recently, there has been growing interest in using proximal soil sensors to obtain information on soil systems. Two devices, visible–near-infrared (Vis–NIR) and portable X-ray fluorescence (pXRF) spectrometers, have shown potential as field diagnostic devices as they can provide a wealth of information in a timely manner. Vis–NIR has been used to predict a diverse range of soil attributes (Viscarra Rossel et al. 2011). As many soil minerals have characteristic absorption features in the Vis–NIR range (Clark et al. 1990), studies have been able successfully to predict a range of minerals including montmorillonite, kaolinite, dioctahedral mica and calcite (e.g. Brown et al. 2006; Mulder et al. 2013). Although these analyses were performed on dried and ground samples, it has been shown that analyses are also possible under field conditions (Viscarra Rossel et al. 2009; Malone et al. 2014). Applications of pXRF to pedology and soil science are increasing (Weindorf et al. 2014). While no studies could be found that attempted to quantify soil mineral composition using pXRF, Zhu et al. (2011) demonstrated pXRF's ability to predict soil textural attributes, which is of interest as texture is related to mineral composition (McKenzie et al. 2004).

The benefit of combining the two devices is that Vis–NIR gives information on sample colour as well as molecular overtones and combination vibrations (Burns

and Ciurczak 2007), whereas pXRF can give an estimate of the concentration of elements with atomic number ≥12 and is also relatively more stable under varying moisture conditions (Stockmann et al. 2016). Thus, by using the data from both the systems, we have access to information on the elemental constitution of a sample via pXRF, as well as an idea of how some of these elements are bonded via Vis–NIR. This study aims to investigate the potential of combining Vis–NIR and pXRF data through model-averaging procedures and an elemental mass balance to characterise soil mineral composition in situ.

4.2 Methods

4.2.1 Site Selection

Two sites were chosen with known pedogenetic variation. A Natrustalfs was identified on a site near Spring Ridge and a Eutrudepts near Pokolbin in New South Wales, Australia (Table 4.1). The Natrustalfs has a polygenetic profile comprised of sandstone-derived alluvium and colluvium overlying previously deposited, mudstone-derived alluvial and colluvial materials (Stockmann et al. 2016). The Eutrudepts has formed from the weathering of the underlying marl.

Existing horizon-based XRD analysis of the two sites was performed using monochromatic CuKα radiation at 30 kV and 28.5 mA using a GBC MMA diffractometer. Basally oriented clay samples were also analysed after various pretreatments for the identification of phyllosilicate species, as described by Brown and Brindley (1980). Expert interpretation identified a large variation in mineral composition between the two profiles:

Natrustalfs mineral composition

> X-ray diffraction patterns of basally oriented clays show the presence of kaolinite, illite and traces of an interstratified mineral. Illite content in the clay fraction increases slightly with depth. In addition to the phyllosilicates, the random powder diffraction patterns also identify quartz (increases with depth), anatase and goethite in the clay fractions (University of Sydney 2010).

Eutrudepts mineral composition

> Smectite and kaolinite throughout the soil profile. Small amount of illite are present in the top two horizons. Smectite content increases with depth and the clay fraction of the C horizon is composed of predominately smectite with small amount of kaolinite. Random powder analysis showed the presence of calcite in the lower two horizons (University of Sydney 2010) (Fig. 4.1).

Table 4.1 Properties of bulk soil samples (<2 mm) used in this study

Natrustalfs	Organic carbon (mg g^{-1})	Inorganic carbon (mg g^{-1})	pH (1:5 H_2O)	CEC ($mmol_c$ kg^{-1})	Exchangeable cations ($mmol_c$ kg^{-1})				PSA[a]		
					Ca	Mg	K	Na	Clay (<2 μm)	Silt (2–50 μm)	Sand (>50 μm)
A	45	–	5.80	34	16	4	11	0.7	7.6	18.7	73.7
E	7	–	5.71	21	16	3	3	0.4	9.2	9.4	81.4
Btqn	6	–	5.65	114	26	78	11	18	59.4	6.3	34.3
Btn1	4	–	5.70	130	24	91	13	22	71.2	2.0	26.8
Btn2	2	–	5.86	119	12	82	13	24	61.3	5.9	32.8
Eutrudepts											
A	44	8	8.72	389	370	9.1	9.7	0.6	46.1	39.9	14.0
AB	31	26	8.78	373	360	8.2	3.7	0.7	38.7	44.0	17.3
B	14	59	8.96	288	280	6.0	1.2	0.7	39.5	47.9	12.6
C	1	71	9.43	310	300	8.0	0.9	1.3	35.2	53.4	11.4

[a]Estimated from Australian particle sizes: clay (<2 μm); silt (2–20 μm); fine sand (20–200 μm); and coarse sand (200–2000 μm)

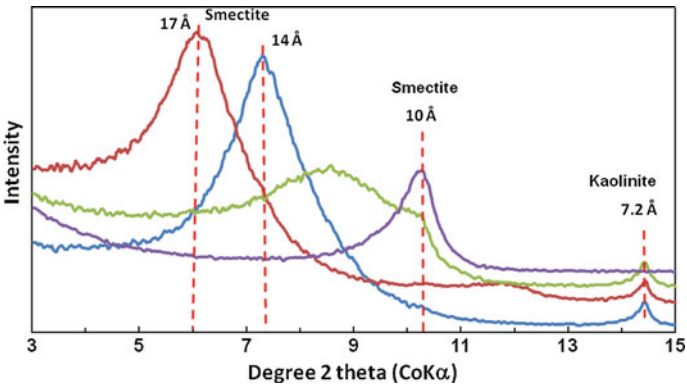

Fig. 4.1 Oriented clay X-ray diffraction patterns of the C horizon of the Eutrudepts after various pre-treatments: Mg saturated and air-dried (*blue curve*), Mg saturated and ethylene glycolated (*Red curve*), K saturated and air-dried (*green curve*) and K saturated and heated at 550 °C (*violet curve*)

4.2.2 Sampling

Vis–NIR and pXRF were used to scan three vertical transects at each site, starting at the soil surface and then at 2.5 cm intervals to a depth of 1 m. This gave 41 scans per transect and 123 scans per site. The three transects were taken at 50 cm spacing to give 1 m lateral coverage. Gravimetric moisture content ranged from 0.00 to 0.23 g g^{-1}. An Agrispec portable spectrophotometer with a contact probe attachment was used to take Vis–NIR spectroscopic measurements (Analytical Spectral Devices, Boulder, Colorado). This particular instrument has a spectral range between 350 and 2500 nm. The device was calibrated with a spectral on white tile after every 15 scans. The pXRF used was an Olympus Delta Premium handheld portable X-ray fluorescence analyser (Olympus InnovX-Systems, USA, 2010). NIST soil standards were scanned before and after each vertical transect to test the performance of the device. Samples were scanned in GEOCHEM mode, which consisted of two 30 s beams, at 50 and 10 kV, respectively. The internal calibration model returned estimated elemental mass values in mg kg^{-1}.

4.2.3 Data Fusion

Mineralogical prediction was based on a data-fusion approach, utilising both the model-averaging procedures and an elemental mass balance (Fig. 4.2). All statistical analyses were performed in R Core Team (2014). First, the elemental ratios of Si:Al:K:Ca:Fe:Ti were calculated from the received pXRF data. These seven selected elements made a mean of 99.88 (s.d = 0.24) of the mass of total identifiable elements. Prediction of phyllosilicates, kaolinite, smectite and illite, as well as Fe

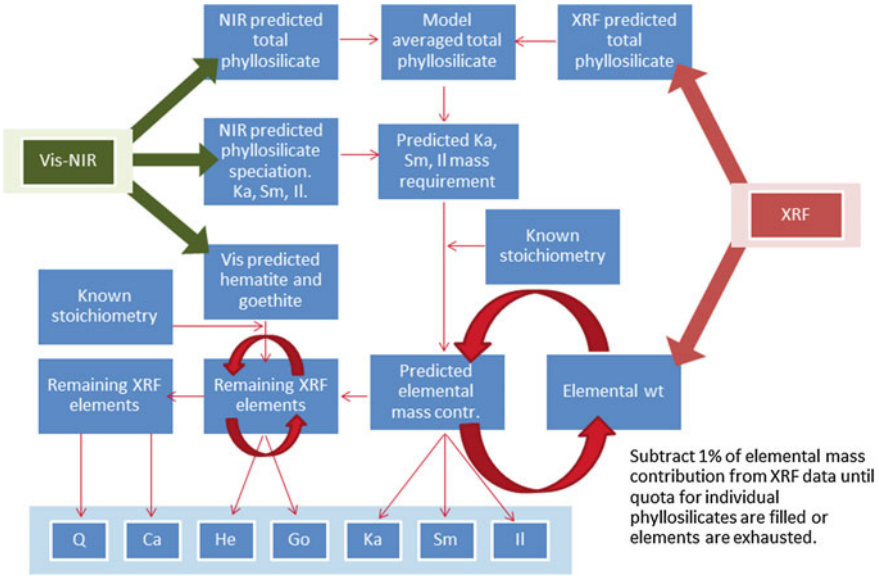

Fig. 4.2 The data-fusion approach. Vis–NIR and pXRF data are input into the model and the mass contributions of individual species to total mineral mass is returned. *Ka* kaolinite; *Sm* smectite; *Il* illite; *He* haematite; *Go* goethite; *Ca* $CaCO_3$; and *Q* quartz

oxides (haematite and goethite), was performed using a shape-fitting algorithm across diagnostic wavelength ranges to quantify deviation from convex hull-corrected reference mineral spectra. This method is defined by Malone et al. (2014) and previously utilised in the Tetracorder decision-making framework by the US Geological Survey (Clark et al. 2003). A prediction of total phyllosilicate was also gained using a simple linear relationship with Rb concentration reported by pXRF. Rb is readily adsorbed onto the surface of clay minerals and is higher in clayey soils (Kabata-Pendias 2010). The Vis–NIR and pXRF total phyllosilicate predictions were combined using an equal-weight model average. This model average total phyllosilicate prediction was then used to scale phyllosilicate speciation ratios to give quantitative predictions of each phyllosilicate species. Known stoichiometry (Table 4.2) of these elements was applied to the predicted values to give their respective elemental mass requirement. These values were then tested against the reported elemental ratios by iteratively subtracting 1 % of the predicted elemental requirement from the available elements until individual quotas are filled or until a constituent element is exhausted in which case the partitioning of further elements to that species is halted, but the remaining species may continue to draw elements to fill their quota. For example, illite requires contributions from Si, Al

Table 4.2 Mass-based mineral stoichiometry used in the elemental mass balance

Mineral	Element contribution to total soil mass						
	LE[a]	Si	Al	K	Ca	Fe	Ti
Quartz	53.3	46.7	0.0	0.0	0.0	0.0	0.0
Kaolinite	57.6	21.2	20.1	0.1	0.0	0.5	0.7
Smectite	58.8	27.9	9.8	0.3	1.1	2.1	0.1
Illite	54.5	24.3	11.8	6.3	0.3	2.6	0.4
Haematite	30.1	0.0	0.0	0.0	0.0	69.9	0.0
Goethite	37.1	0.0	0.0	0.0	0.0	62.9	0.0
$CaCO_3$	60.0	0.0	0.0	0.0	40.0	0.0	0.0

[a]Light elements (LE) are those with atomic number ≤12, which are unidentifiable by pXRF
Stoichiometric relationships were calculated from compositional analyses accompanying the US Geological Survey digital spectral library (Clark et al. 2007) and other sources (Brigatti et al. 2006)

and K. In the event that K runs out before the illite quota is filled, and Si and Al are still available, the partitioning of elements to illite is halted but kaolinite may continue to fill its quota as it only requires the presence of Si and Al. Once all quotas have been filled or constituent elements exhausted, the moderated values are recorded and the remaining elements are passed for Fe oxide prediction in a similar fashion. The assumption made is that all remaining Ca is in the form of $CaCO_3$ and that all remaining Si is involved in siloxane bonds, simplified in the model to quartz. The predicted identifiable element mass contributions are converted to mineral mass contributions by including light elements based on known stoichiometry (Table 4.2) to give the final mass contribution to mineral fraction.

4.2.4 *$CaCO_3$ Prediction*

The $CaCO_3$ values predicted using the above approach were modified for comparison with horizon-based values that were obtained by gravimetric loss of carbon dioxide (Allison and Moodie 1965). The $CaCO_3$ contribution to the mineral soil fraction had to be converted to the $CaCO_3$ contribution to total soil mass. This was achieved by incorporating the mass of OM content using the following equation:

$$[CaCO_3]_{soil} = [CaCO_3]_{mineral} * (100 - OC * 1.72)/100$$

Predicted soil contributions for each sample (123 totally) were then plotted by horizon and the mean values obtained by horizon compared to laboratory results.

4.3 Results and Discussion

4.3.1 Predicted Mineral Contributions

Predicted minerals varied greatly between soils and also with depth, with notable changes across most horizon boundaries (Fig. 4.3). In the Natrustalfs, phyllosilicate speciation was dominated by kaolinite with contributions from smectite in the A horizon and illite in the B horizons (Fig. 4.3a). Quartz was the dominant mineral in the A and E horizons, making up a mean of 92 % of the mineral mass of the E horizon. The expression of Fe oxides increases with depth and was strongest in the mottled Btqn1 and Btqn2 horizons. Meanwhile, $CaCO_3$ was noticeable absent in the entire Natrustalfs profile.

By comparison, the Eutrudepts profile phyllosilicate speciation was dominated by smectite (Fig. 4.3b). Significant amounts of kaolinite and illite were identified but their relative contribution decreased with depth as smectite became increasingly dominant. $CaCO_3$ was found throughout the profile, increasing at horizon boundaries, with the highest concentrations found in the marly C horizon. The proportion of quartz was relatively low and decreased gradually with depth, as did Fe oxides.

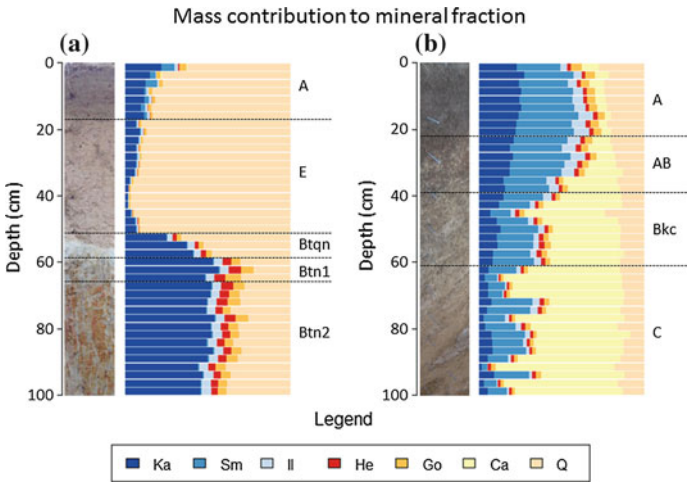

Fig. 4.3 Predicted soil mineral contribution to total mineral mass for **a** Natrustalfs and **b** Eutrudepts. *Ka* kaolinite; *Sm* smectite; *Il* illite; *He* haematite; *Go* goethite; *Ca* $CaCO_3$; and *Q* quartz. Predictions cover a depth of 1 m at 2.5 cm intervals including a sample taken at the soil surface. The average of three vertical transects is presented. Horizon designations are indicated

4.3.2 Comparison to XRD Interpretation

The predicted mineral composition agreed well with the XRD interpretation presented in the Methods section. All major trends were represented and all minerals were identified correctly with the exception of anatase which is not included in the model. Phyllosilicate speciation was correlated with the documented XRD interpretations. As the soils do not contain muscovite or biotite and given the fact that the clay fraction in these soils consists mainly of secondary minerals (McKenzie et al. 2004), we can assume that all phyllosilicates are found in the clay fraction and this allows direct comparison with the basally oriented clay XRD analysis. Our predictions agree with nearly all XRD phyllosilicate observations. For example, we identify the dominance of kaolinite in the Natrustalfs and the increase in illite with depth in this soil. In the Eutrudepts, we identified that there are large amounts of smectite throughout the profile and that the relative proportion of smectite to kaolinite and illite increases with depth. Further, we also identified the increased proportion of illite in the A and AB horizons as described from the XRD analysis. The one phyllosilicate XRD observation that our prediction did not match was the presence of smectite in the A horizon of the Natrustalfs. This may have been misinterpreted as the identified interstratified mineral. Previous investigations at the same site identified the presence of smectite in the A horizon of the Natrustalfs, with the hypothesis that it has been eroded from nearby Vertisol profiles and deposited in the topsoil (Quilty 2007), suggesting that the mineral may have a high spatial variation.

4.3.3 Comparison to Soil Properties

Some relationship can be seen between the predicted mineral composition and the soil properties. The noticeable lack of $CaCO_3$ in the Natrustalfs coincided with its low pH (Table 4.1). The opposite was noted in the Eutrudepts where both predicted $CaCO_3$ and pH increased with soil depth. The lowest observed CEC of 21 $mmol_c$ kg^{-1} was found in the E horizon of the Natrustalfs which coincided with the high quartz content. The CEC observations in the Natrustalfs increased in the B horizons where concentrations of kaolinite and illite significantly increased. However, the highest CEC values occured in the Eutrudepts coinciding with the dominance of smectite. Although these observations remain qualitative, they provided support to the predicted values. If we are able to parametise these relationships, then the data-fusion approach may provide a valuable means to validate or moderate predictions made directly using Vis–NIR or pXRF.

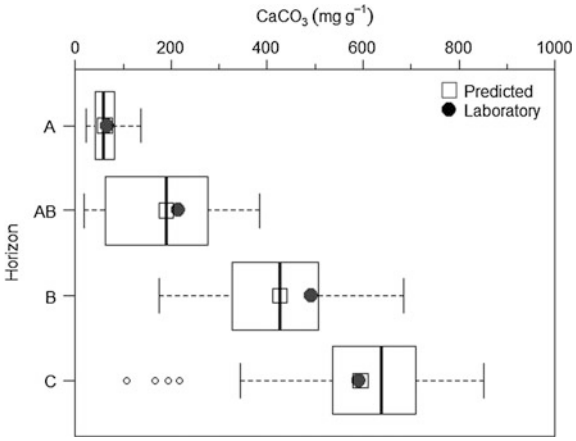

Fig. 4.4 Boxplots of $CaCO_3$ (mg g^{-1}) predicted by horizon from three vertical transects for the Eutrudepts. *Hollow squares* indicate mean predicted $CaCO_3$ by horizon; meanwhile, *filled circles* indicate laboratory-derived values by gravimetric loss of carbon dioxide (Allison and Moodie 1965). Predicted $CaCO_3$ values are modified from those shown in Fig. 4.3b by correcting for OM content (OM content was calculated as 1.72 * OC from Table 4.1)

4.3.4 $CaCO_3$ Prediction Versus Laboratory Analysis

$CaCO_3$ was chosen for further investigation as it can be readily quantified using laboratory techniques (Allison and Moodie 1965). Our mean $CaCO_3$ predictions for the Eutrudepts with depth had a strong correlation with laboratory results (Fig. 4.4) but the predicted values showed a large amount of spatial variation. The variation increased with depth, with the A horizon displaying a relatively low observed range, is possible due to increased bioturbation. In the saprolitic, marly C horizon, the predicted values range from 108 to 851 (mg g^{-1}). This exemplifies the strength of our approach in capturing the spatial variation, which is lost when samples are ground for homogeneity and mean values are reported. The benefits of fine-scale soil profile mapping are unexplored and also demand further investigation.

4.3.5 Further Development

Although the model has achieved promising preliminary results, there is much to improve on. Future work needs to be directed to incorporate more minerals into the model, including feldspars, gibbsite, gypsum, anatase and rutile. The inability to discriminate between feldspars and quartz is a limitation of the model. As neither quartz nor feldspars has strong absorption features in the 350–2500 nm Vis–NIR range, we need to investigate the pXRF data for a potential solution. An OC

prediction could also be implemented and combined with the mineral prediction and known CEC values to deterministically estimate soil CEC. A comparison of the prediction using Vis–NIR or pXRF individually compared to the data-fusion approach is crucial to quantify the benefits of the approach.

4.4 Conclusion

A new method for rapid, in situ quantification of soil mineral composition based on Vis–NIR and pXRF spectroscopy was investigated. Preliminary results show a good ability to differentiate between phyllosilicate species, as well as predicting levels of inorganic C and quartz, although prediction of Fe oxides is less convincing. Further study is needed to increase the range of predicted minerals and to test the method on different soils.

References

Allison L, Moodie C (1965) Carbonate. In: Black CA (ed) Methods of soil analysis Part 2. Chemical and Microbiological Properties. American Society of Agronomy and Soil Science Society of America, Madison, pp. 1379–1396

Brigatti MF, Galan E, Theng BKG (2006) Structures and mineralogy of clay minerals. In: Bergaya F, Theng BKG, Lagaly G (eds) Developments in clay science. Elsevier, Amsterdam

Brown DJ, Shepherd KD, Walsh MG, Mays MD, Reinsch TG (2006) Global soil characterization with VNIR diffuse reflectance spectroscopy. Geoderma 132(3):273–290

Brown G, Brindley G (1980) X-ray diffraction procedures for clay mineral identification. In: Brindley GW, Brown G (eds) Crystal structures of clay minerals and their X-ray identification. Mineralogical Society, London

Burns DA, Ciurczak EW (2007) Handbook of near-infrared analysis. CRC Press, Boca Raton

Cannon KM, Mustard JF, Salvatore MR (2015) Alteration of immature sedimentary rocks on Earth and Mars: recording aqueous and surface–atmosphere processes. Earth Planet Sci Lett 417:78–86

Clark RN, King TV, Klejwa M, Swayze GA, Vergo N (1990) High spectral resolution reflectance spectroscopy of minerals. J Geophys Res Solid Earth 95(B8):12653–12680

Clark RN, Swayze GA, Livo KE, Kokaly RF, Sutley SJ, Dalton JB, McDougal RR, Gent CA (2003) Imaging spectroscopy: earth and planetary remote sensing with the USGS Tetracorder and expert systems. J Geophys Res Planet 108(E12)

Clark RN, Swayze GA, Wise R, Livo KE, Hoefen TM, Kokaly RF, Sutley SJ (2007) USGS digital spectral library splib06a. U.S. Geological Survey, Data Series, 231

Downs RT (2015) Determining mineralogy on mars with the CheMin X-ray diffractometer. Elements 11(1):45–50

Gianoncelli A, Castaing J, Ortega L, Dooryhee E, Salomon J, Walter P, Hodeau JL, Bordet P (2008) A portable instrument for in situ determination of the chemical and phase compositions of cultural heritage objects. X-Ray Spectrom 37(4):418–423

Hartemink AE, Minasny B (2014) Towards digital soil morphometrics. Geoderma 230:305–317

Kabata-Pendias A (2010) Trace elements in soils and plants. CRC Press, Boca Raton

Malone BP, Hughes P, McBratney AB, Minasny B (2014) A model for the identification of terrons in the Lower Hunter Valley, Australia. Geoderma Reg 1:31–47

McKenzie N, Jacquier D, Isbell R, Brown K (2004) Australian soils and landscapes: an illustrated compendium. CSIRO Publishing, Melbourne

Mulder V, Plötze M, de Bruin S, Schaepman ME, Mavris C, Kokaly RF, Egli M (2013) Quantifying mineral abundances of complex mixtures by coupling spectral deconvolution of SWIR spectra (2.1–2.4 μm) and regression tree analysis. Geoderma 207:279–290

Nakai I, Abe Y (2012) Portable X-ray powder diffractometer for the analysis of art and archaeological materials. Appl Phys A 106(2):279–293

Quilty JR (2007) A pedological investigation of the evolution of the soil types on "Nowley": defining the boundaries of soil landscapes. Unpublished Honours thesis, The University of Sydney, Australia

R Core Team (2014) R: a language and environment for statistical computing. R Foundation for Statistical Computing, Vienna, Austria. URL:http://www.R-project.org/

Rossel RV, Adamchuk V, Sudduth K, McKenzie N, Lobsey C (2011) Proximal soil sensing: an effective approach for soil measurements in space and time. Adv Agron 113:243–291

Sarrazin P, Blake D, Feldman S, Chipera S, Vaniman D, Bish D (2005) Field deployment of a portable X-ray diffraction/X-ray flourescence instrument on Mars analog terrain. Powder Diffr 20(02):128–133

Stockmann U, Cattle SR, Minasny B, McBratney AB (2016) Utilizing portable X-ray fluorescence spectrometry for in-field investigation of pedogenisis. Catena 139:220–231

Stockmann U, Jang HJ, Minasny B (2016) The effect of soil moisture and texture on Fe concentration using portable X-ray fluorescence spectrometers. In: Hartemink AE, Minasny B (eds) Digital soil morphometrics. Springer, Dordrecht

Uda M (2004) In situ characterization of ancient plaster and pigments on tomb walls in Egypt using energy dispersive X-ray diffraction and fluorescence. Nucl Instrum Methods Phys Res, Sect B 226(1–2):75–82

University of Sydney (2010) Handbook for the agricultural heartlands tour. In: 19th World Conference of Soil Science (Unpublished)

Viscarra Rossel RA, Cattle SR, Ortega A, Fouad Y (2009) In situ measurements of soil colour, mineral composition and clay content by vis–NIR spectroscopy. Geoderma 150(3–4):253–266

Weindorf DC, Bakr N, Zhu Y (2014) Advances in portable X-ray fluorescence (PXRF) for environmental, pedological, and agronomic applications. Adv Agron 128:1–45

Zhu Y, Weindorf DC, Zhang W (2011) Characterizing soils using a portable X-ray fluorescence spectrometer: 1. Soil texture. Geoderma 167–168:167–177

Chapter 5
The Effect of Soil Moisture and Texture on Fe Concentration Using Portable X-Ray Fluorescence Spectrometers

Uta Stockmann, Ho Jun Jang, Budiman Minasny and Alex B. McBratney

Abstract Portable XRF (pXRF) instruments can be used in the field for measurement of soil elemental concentrations. The pXRF measurements in the field, however, are affected by several factors including soil texture, moisture and sample heterogeneity. In this chapter, we investigated the effect of moisture on the Fe concentration of pXRF laboratory and field measurements. In the laboratory study, soil samples were analysed that were wetted to different moisture contents. In the field study, pXRF measurements were made from topsoil samples and the data were compared to samples that were air-dried and ground to pass a 2-mm sieve. Soil moisture mainly dampens the X-ray intensity resulting in lower Fe concentrations, and this effect is more pronounced for clayey soils (higher Fe content) as compared to sandy soils (lower Fe content). In addition, the field moisture content is highly related to clay and Fe content. Thus, the response of XRF intensity to soil moisture content depends on soil texture and mineralogy. We could not find a general correction factor for soil moisture and X-ray intensity but the relationship between air-dried and field-moist Fe concentration is highly linear which allows to correct for moisture content by establishing an empirical correction function.

Keywords In situ XRF analysis · Soil moisture · Soil iron content · Proximal soil sensing

U. Stockmann (✉) · H.J. Jang · B. Minasny · A.B. McBratney
Department of Environmental Sciences, Faculty of Agriculture and Environment, The University of Sydney, New South Wales 2006, Australia
e-mail: uta.stockmann@sydney.edu.au

A.E. Hartemink and B. Minasny (eds.), *Digital Soil Morphometrics*, Progress in Soil Science, DOI 10.1007/978-3-319-28295-4_5

5.1 Introduction

Handheld portable X-ray fluorescence (pXRF) devices offer great opportunity to enrich the *in situ* description of soil profiles by rapidly measuring the elemental concentration of unprocessed soil materials and are therefore a highly valuable tool in digital soil morphometrics and pedology studies (Hartemink and Minasny 2014).

XRF devices operate on the principle of energy dispersive spectrometry whereby the amount of emitted fluorescence photons is directly measured by an X-ray detector that simultaneously analyses their energy levels. The number of element-specific characteristic X-rays produced (or intensity) determines the quantity of a given element. Measurements by portable XRF measurements, however, can be affected by soil particle size, moisture, the presence of coarse organic residues, soil structure, smearing, stoniness, mottles and redoximorphic features. For example, a soil sample ground to finer particle sizes can show higher elemental concentrations when compared to the same soil sample unground or of coarser particle sizes (Markowicz 2008). This effect is more pronounced for elements with small atomic numbers such as K, V, Cr, Mn and Ca (Laiho and Perämäki 2005). There are two factors that affect the measurement of pXRF in the field, i.e. sample heterogeneity and soil moisture (Ge et al. 2005; Horta et al. 2015).

In the laboratory, soil samples are usually ground to pass certain size fractions (<2 mm) to homogenise the sample and eliminate coarse fragments. When the soil particle size decreases, the XRF intensity is increased because of smaller incident angles (Maruyama et al. 2008). Generally, sieving the soil to <2 mm is recommended because it results in less variation (Laiho and Perämäki 2005). In the field, the soil particle sizes can be variable, and pXRF measurements from the field can be different from laboratory measurements.

Soil moisture affects XRF measurements in two ways (Ge et al. 2005). First, the presence of water particles enhances the absorption of X-rays which reduces the intensity of the X-ray signal. Secondly, the presence of water particles can cause primary X-rays to scatter which results in the increase of the X-ray intensity. Therefore, the elemental concentration in wet soil is generally lower than in dry soil, and this can lead to a lower precision, poor detection limit and overall lower accuracy. Kalnicky and Singhvi (2001) and Laiho and Perämäki (2005) recommended scanning soil samples with gravimetric moisture content less than 20 %. Most of these studies used samples from a single source with limited variability (e.g. Parsons et al. 2013 and Bastos et al. 2012). They have not considered different soil textures and soil water potentials. The 20 % moisture is rather arbitrarily defined, as 20 % gravimetric water content in a clayey and a sandy soil is different in terms of its water potential.

The aim of this study was to investigate the influence of soil moisture on the pXRF spectrum, in particular Fe concentration and to explore the potential for quantifying and removing this effect and to increase the accuracy of field pXRF measurements.

5.2 Materials and Methods

We conducted two studies to investigate the effect of soil moisture on the measurement of elemental concentrations, particularly Fe. The XRF spectra were collected in SOILMODE using an Olympus Delta Premium Handheld pXRF Analyzer which operates at three beam configurations of 50, 40 and 15 kV, respectively (Olympus InnovX-Systems, USA, 2010).

5.2.1 Laboratory-Based Study

Eleven soil samples with texture contents ranging from loam to medium clay were collected from the Hunter Valley, NSW, Australia. The samples were air-dried and ground to pass a 2-mm sieve. The air-dried samples were evenly wetted until they reached a sticky consistency (~30 % wetness), and subsequently scanned with a pXRF at different moisture conditions after air-drying the samples for 1 day in a controlled laboratory environment. Wetness (%) was determined gravimetrically by measuring the amount of water in the soil by drying in the oven at 105 °C for 24 h. Maximum peak heights as well as the total peak area around 6.2 and 6.6 keV for Fe were used to investigate the response of the XRF spectrum to different moisture conditions.

5.2.2 Field Study

This study used 120 topsoil samples (0–7.5 cm depth) from Nowley Farm in the Liverpool Plains, NSW, Australia. The samples were collected using a stratified random sampling design. The samples were scanned with pXRF under field-moist conditions. The samples were then dried in the oven at 40 °C for 24 h, ground to pass a 2-mm sieve and rescanned under these air-dried conditions. All scans were replicated thrice.

5.3 Results and Discussion

5.3.1 Laboratory Study

Figure 5.1 shows the intensity of the Fe peak at 6.40 keV at different moisture contents for a sample from the Bt horizon of a Dermosol. The intensity decreases with increasing moisture content. Ge et al. (2005) proposed a model for the correction of soil moisture on XRF measurement based on the principle that the

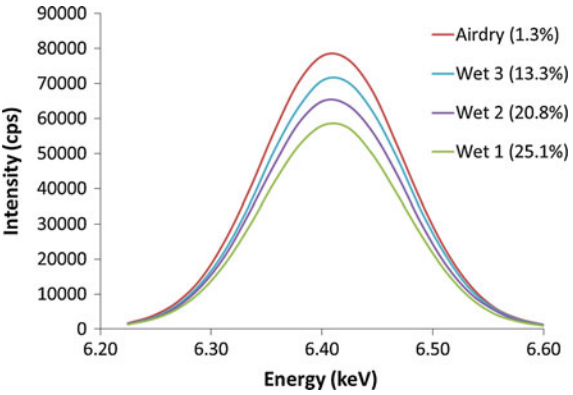

Fig. 5.1 Intensity of the Fe peak at four different water contents for the Bt horizon of a clay-rich soil (Dermosol)

reduction in X-ray intensity is proportional to the increment of water content of the sample:

$$dI_x = -\mu_w I_x dw$$

where dI_x is the reduction in the X-ray intensity, I_x is the X-ray intensity, dw is the increment of gravimetric water content in the sample, and μ_w is the attenuation coefficient of moisture. Integrating this equation from $w = 0$, gives:

$$I_0 = I_x \exp(\mu_w w)$$

where I_0 is the intensity at $w = 0$. This implies that based on Beer–Lambert's law, the intensity will attenuate exponentially with increasing moisture content. Ge et al. (2005) estimated w from the intensity of scattered radiation.

The laboratory study using different soils showed that the response of the intensity (or Fe-peak height) decreases with moisture content but that the decrease is not uniform (Fig. 5.2). Although the three soil samples can all be classified as clay-rich Bt horizons (35–55 % clay content), and belong to the same soil order (Dermosol), and also show the existence of an exponential relationship between wetness and intensity, the attenuation factor is different for the three soil samples. The correction factor as proposed by Ge et al. (2005) can therefore not be uniformly applied.

5.3.2 *Field Study*

In the field study, we collected a range of topsoil samples with soil textures ranging from sand to clay. Figure 5.3 shows the relationship between Fe-peak height for soil samples collected under field and air-dried conditions. The Fe content (as estimated by the maximum Fe-peak height) was underestimated for field-moist soil as

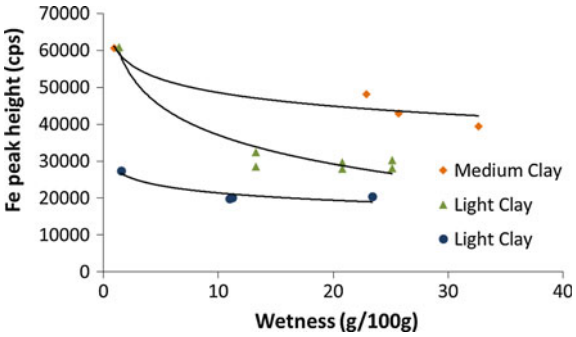

Fig. 5.2 The response of X-ray peak height to moisture content for three soil samples of the Bt horizon of three Dermosols. Here, a light clay equates to about 35 % clay content, whereas a medium clay equates to about 45 % clay content

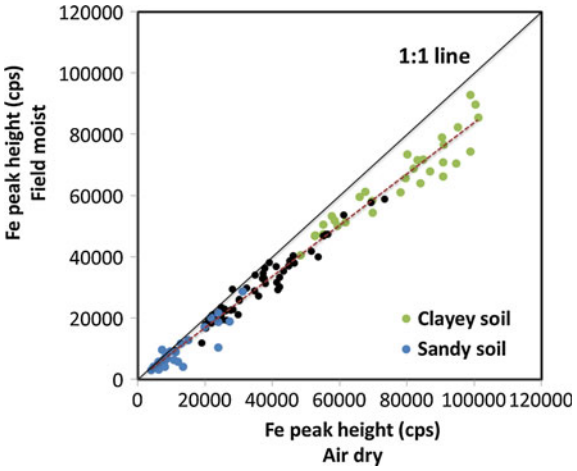

Fig. 5.3 The Fe concentration between air-dry soil and field-moist soil. Here, a clayey soil refers to a clay content of >40 %. Loamy, intermediate textures are shown in *black*

compared to air-dry soils. The relationship of Fe content between air-dried and field-moist conditions is linear. Some field-moist samples showed higher Fe concentrations compared to air-dry samples possibly due to the scattering effects. Hürkamp et al. (2009) also found a solid linear relationship for Pb content between field measurement and laboratory measurement (air-dried and ground to pass a 2-mm sieve). Tjallingii et al. (2007) who worked on marine sediments found that heavier elements (such as K, Ca, Ti and Fe) are relatively unaffected by soil moisture, but that lighter elements (such as Al and Si) are more sensitive to moisture changes. In this study, we have not included any comparisons for heavy or light elements yet.

Clay-rich soils (>40 % clay) showed higher concentrations of Fe compared to sandy soils (>60 % sand). There is a tendency for the relative difference of the max Fe peaks (or Fe content) to be larger (between the field-moist and air-dry soil

samples) in Fe-rich soils (Fig. 5.4). The general relationship proposed by Ge et al. (2005) $w \sim \mu_w \log(I_0/I_w)$ is not observed which suggests that the attenuation coefficient is soil-dependent.

As we measured three replicates for each soil sample, the standard deviation and coefficient of variation of measurements can be calculated. Table 5.1 shows the mean and standard deviation of measurements along with the average standard deviation and coefficient of variation (CV) of the measurements. The concentration of Fe is lower under field conditions as compared to air-dry conditions (Fig. 5.3). However, the standard deviation and CV of the measurements are relatively similar between field-moist and air-dry soil samples. This suggests that measuring the soil under field conditions does not introduce much more variation when compared to a more uniform dried and sieved sample. This differs from the findings of Laiho and Perämäki (2005). We hypothesised that our samples are more variable, and thus, the field variation is larger than the variation in measurement.

We mapped the Fe concentration using the 240 observations collected for the study area (2083 ha) of Nowley Farm using ordinary kriging. As shown in Fig. 5.5, the spatial pattern of Fe content between field-moist and air-dried conditions is

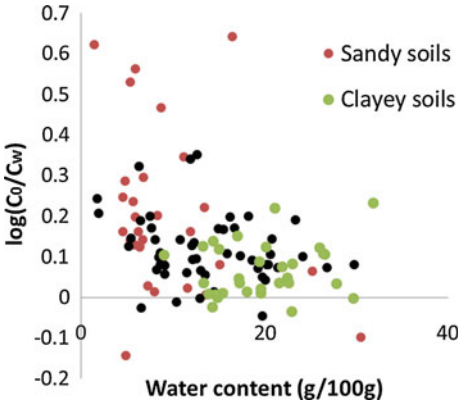

Fig. 5.4 The relationship between soil water content and the ratio of Fe concentration of air-dried samples (C_0) and field-moist samples (C_w). Here, a clayey soil refers to a clay content of >40 %. Loamy, intermediate textures are shown in *black*

Table 5.1 Mean and standard deviation of the 240 observations of Fe concentration as measured by pXRF under field-moist and air-dry conditions

	Mean of observations (mg/kg)	Std. dev of observations (mg/kg)	Average std. dev of measurements (mg/kg)	Average CV of measurements
Field-moist	32,859	22,980	169.7	0.58
Air-dry	39,263	27,528	209.3	0.60

Each observation is the mean of three measurements. The average standard deviation and coefficient of variation of measurements are also presented

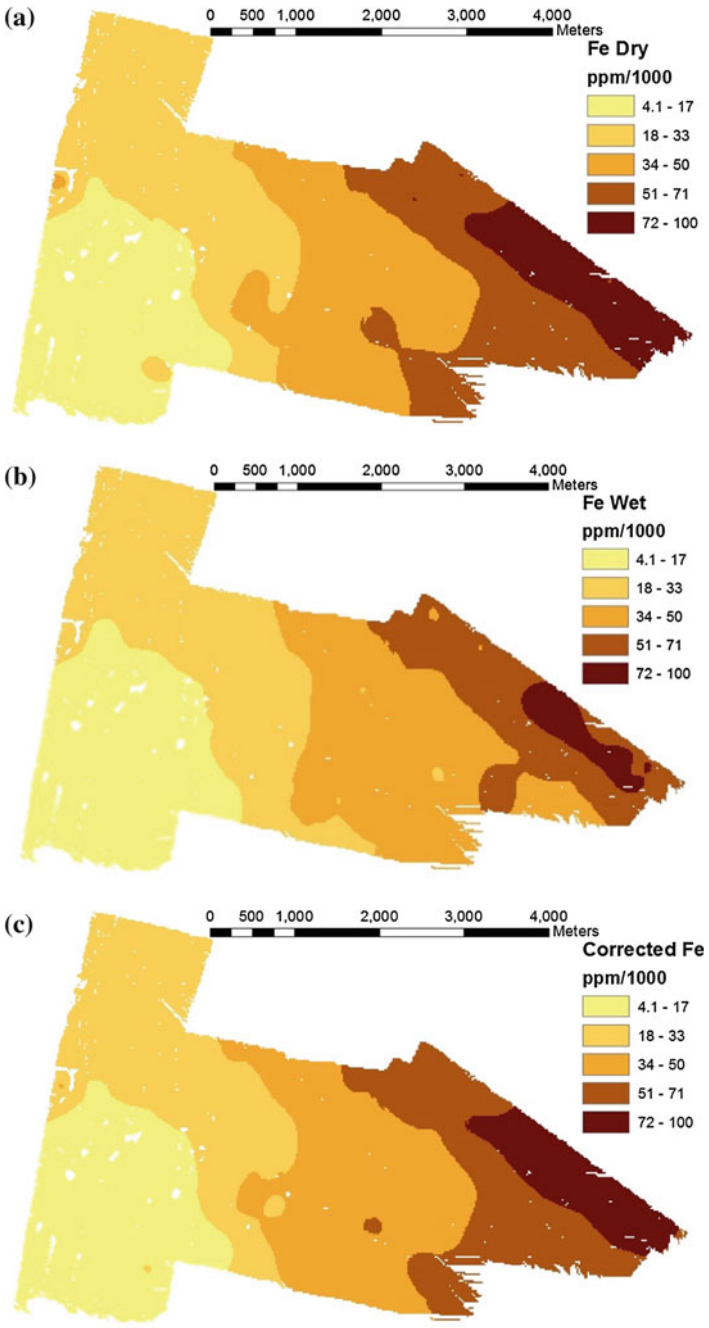

Fig. 5.5 Maps of Fe concentration in g/kg as measured using pXRF under **a** air-dried condition, **b** field-moist condition, and **c** field-moist corrected to air-dried condition. The maps were created using ordinary kriging of 240 top soil samples collected at Nowley Farm (2083 ha)

similar. Since the relationship of Fe content between field and air-dried conditions is linear, we can correct the observed offset using an empirical relationship. We selected 10 samples from the whole range of Fe concentrations and fitted a linear relationship:

$$\text{Fe(air-dried)} = 1103 + 1.12 * \text{Fe (field-moist)}, \quad \left(R^2 = 0.99\right)$$

This relationship is applied to the field-moist map, which results in an air-dried corrected map (Fig. 5.5c) that is identical to the map produced using samples scanned in air-dried condition. Thus in practice, we can derive such correction functions from field measured data by selecting a subsample (e.g. 10 samples) covering the whole elemental concentration. These subsamples were air-dried and ground and remeasured under laboratory conditions, and thus, a correction function can be derived.

5.4 Conclusions

The response of XRF intensity to soil moisture content is affected by mineralogy and clay content. The correction factor proposed by Ge et al. (2005) does not apply for soil with varying clay content and mineralogy. The effect of moisture dampens the X-ray intensity resulting in lower elemental concentrations. The effect of soil moisture on Fe content is more pronounced for clayey soils than sandy soils. Furthermore, the relationship between air-dried and field-moist Fe concentrations is linear. As the coefficient of variation between air-dry and field-moist measurements is similar, we can measure elemental concentrations directly in the field. We propose a pragmatic way to correct for the moisture effect during field pXRF measurement by taking representative samples (from high to low elemental concentration), and subsequently preparing and measuring those samples under air-dried condition. From this, a linear correction factor can be developed to correct for field-moist measurements.

References

Bastos RO, Melquiades FL, Biasi GEV (2012) Correction for the effect of soil moisture on in situ XRF analysis using low-energy background. X-Ray Spectrom 41(5):304–307

Ge L, Lai W, Lin Y (2005) Influence of and correction for moisture in rocks, soils and sediments on in situ XRF analysis. X-Ray Spectrom 34:28–34. doi:10.1002/xrs.782

Hartemink AE, Minasny B (2014) Towards digital soil morphometrics. Geoderma 230–231: 305–317

Horta A, Malone B, Stockmann U, Minasny B, Bishop TF, McBratney B, Pallasser R, Pozza L (2015) Potential of integrated field spectroscopy and spatial analysis for enhanced assessment of soil contamination: a prospective review. Geoderma 241–242:180–209

Hürkamp K, Raab T, Völkel J (2009) Two and three-dimensional quantification of lead contamination in alluvial soils of a historic mining area using field portable X-ray fluorescence (FPXRF) analysis. Geomorphology 110(1):28–36

Kalnicky DJ, Singhvi R (2001) Field portable XRF analysis of environmental samples. J Hazard Mater 83:93–122

Laiho JVP, Perämäki P (2005) Evaluation of portable X-ray fluorescence (PXRF) sample preparation methods. Special Paper of the Geological Survey of Finland 73–82

Markowicz AA (2008) Quantification and correction procedures. In: Potts PJ, West M (eds) Portable X-ray fluorescence spectrometry: capabilities for in situ analysis. The Royal Society of Chemistry, Cambridge, pp 13–38

Maruyama Y, Ogawa K, Okada T, Kato M (2008) Laboratory experiments of particle size effect in X-ray fluorescence and implications to remote X-ray spectrometry of lunar regolith surface. Earth Planet Space 60:293–297

Parsons C, Grabulosa EM, Pili E, Floor GH, Roman-Ross G, Charlet L (2013) Quantification of trace arsenic in soils by field-portable X-ray fluorescence spectrometry: considerations for sample preparation and measurement conditions. J Hazard Mater 262:1213–1222

Tjallingii R, Röhl U, Kölling M, Bickert T (2007) Influence of the water content on X-ray fluorescence core-scanning measurements in soft marine sediments. Geochem Geophys Geosyst 8(2)

Chapter 6
Estimating Soil Texture from a Limited Region of the Visible/Near-Infrared Spectrum

Elisângela Benedet Silva, Alexandre ten Caten, Ricardo Simão Diniz Dalmolin, André Carnieletto Dotto, Walquiria Chaves Silva and Elvio Giasson

Abstract Soil particle size is an attribute of fundamental importance when defining soil horizons. Proximal soil sensors can facilitate the acquisition of a larger amount of soil data using a faster and less laborious technique. Thus, the objective of this study is to evaluate the capacity of a limited spectral acquisition region (325–1075 nm) for estimating soil texture. Soil samples were collected in the southwest part of Marombas river watershed located near the center of Santa Catarina State, south of Brazil. A total of 42 soil profiles were sampled according to the GlobalSoilMap specification. A dataset of 166 samples was used for model calibration and another set of 71 samples was used for model validation. Diffuse reflectance spectroscopy of sieved samples (2 mm) was collected with a spectrometer FieldSpecHandHeld II (ASD Inc.). Savitzky–Golay second derivatives were calculated and used in partial least-squares regression modeling. Calibration and validation datasets showed

E.B. Silva (✉)
Epagri—Agricultural Research and Rural Extension Corporation of Santa Catarina, Federal University of Rio Grande do Sul, Avenida Bento Gonçalves, 7712, Porto Alegre, RS 91540-000, Brazil
e-mail: elisbenedetsilva@gmail.com

A. ten Caten
Biology and Veterinary Science Department, Federal University of Santa Catarina Campus Curitibanos, Ulysses Gaboard Highway, km3, Curitibanos SC 89520/000, Brazil
e-mail: alexandre.ten.caten@ufsc.br

R.S.D. Dalmolin
Soil Department, Federal University of Santa Maria, Avenida Roraima, 1000, Santa Maria, RS 97105-900, Brazil
e-mail: dalmolin@ufsm.br

A.C. Dotto
Federal University of Santa Maria, Avenida Roraima, 1000, Santa Maria, RS 97105-900, Brazil
e-mail: andrecdot@gmail.com

A.E. Hartemink and B. Minasny (eds.), *Digital Soil Morphometrics*, Progress in Soil Science, DOI 10.1007/978-3-319-28295-4_6

statistically similar mean and variance. The root-mean-square error of prediction for sand, silt, and clay content is 5.47, 5.18, and 5.39 g 100 g^{-1}, respectively. The R^2 for validation is 0.30, 0.59, and 0.69 for the same attributes. Partitioning the model by depth did not improve the predictions significantly. The results show that estimating soil texture from a limited spectral region is promising and can contribute toward the development of cheaper spectrometers or infrared cameras that can be used for digital soil morphometrics.

Keywords Diffuse reflectance spectroscopy · Soil reflectance · Proximal soil sensing · Soil attribute · Digital soil morphometrics

6.1 Introduction

During the last two decades, a growing interest on the quantification of soil attributes by means of soil sensing techniques has emerged (Ramirez-Lopez et al. 2014; Vasques et al. 2008) using visible–near-infrared (Vis–NIR) diffuse reflectance spectroscopy to provide data for digital soil mapping (Viscarra Rossel and Behrens 2010; Wetterlind et al. 2010) and soil morphometrics. Visible and near-infrared spectroscopy (Vis–NIR, 400–2500 nm) can be used as a tool to acquire more data rapidly and consequently increases mapping accuracy. Vis–NIR has potential to analyze several soil attributes simultaneously without considerable increase in costs (Viscarra Rossel and Lark 2009; Wetterlind et al. 2010), time and with less production of reagents residues (Viscarra Rossel et al. 2006; Demattê and da Silva Terra 2014).

Vis–NIR spectra contain information on minerals, organics, water, color, and particle size, which are fundamental components of the soil (Viscarra Rossel and Chen 2011). Reflectance spectroscopy can be very useful in the assessment of soil variations in depth (from different layers and/or horizons) due to the interaction of light with soil attributes reflecting intrinsic data related with soil (Demattê and da Silva Terra 2014).

Recent studies also investigated the relationships between soil attributes and its spectral reflectance aiming into predicting physical–chemical soil attributes (Summers et al. 2011). Using a laboratory spectrometer, Demattê et al. (2012)

W.C. Silva
Federal University of Santa Catarina Campus Curitibanos,
Ulysses Gaboardi Highway, km3, Curitibanos, SC 89520/000, Brazil
e-mail: walquiria.chs@gmail.com

E. Giasson
Federal University of Rio Grande do Sul, Avenida Bento Gonçalves,
7712, Porto Alegre, RS 91540-000, Brazil
e-mail: giasson@ufrgs.br

analyzed the relation between the reflected electromagnetic energy and soil attributes. They observed features between 450 and 600 nm caused by subtle differences in the absorption intensity, which can be used to separate the subhorizons in the field from their color.

The studies of soil reflectance spectra across the whole visible, near-infrared, and shortwave infrared (Vis–NIR–SWIR) have been successfully applied by Dotto et al. (2014) who developed models using multiple linear regression analysis to predict the content of sand, silt, and clay. The models produced good results, explaining 77 and 72 % of the variance for sand and clay, respectively. In a study carried out by Viscarra Rossel et al. (2006), the authors have shown that a spectrometer operating in visible region of the spectra (400–700 nm) can be used for soil organic carbon prediction. Their results achieved a RMSE of 0.18 % and R^2 of 0.60. The authors highlighted that the predictions using only the visible part of the spectra can be comparably accurate and not as expensive as the infrared spectrometer.

Considering that spectrum of the visible region (400–700 nm) is used for morphological in field soil classification, this paper has the hypothesis that, even using a spectrometer capable of acquiring a limited region of the spectrum, the soil signatures collected with such equipment is suitable for estimating soil texture. Thus, the main objective of the paper is to predict soil texture using second derivatives of the reflectance in a limited region of the spectrum (325–1075 nm). It is anticipated that lower-cost near-infrared camera or spectrometer with a limited range of spectra can be used for digital soil morphometrics.

6.2 Materials and Methods

6.2.1 Soil Sampling and Laboratory Analysis

Samples were collected in the southwest part of Marombas river watershed, located near the center of Santa Catarina State, south of Brazil (Fig. 6.1). Parental material in the region consists mainly of basaltic igneous rocks of Serra Geral formation. A small area of the watershed, located toward east, consists in consolidated sedimentary rocks of the Botucatu Formation. The climate is subtropical with mild summer and mean annual temperatures of 16 °C. Köppen climate classification system for the area is Cfb. Annual precipitation is about 1600 mm. Altitude of watershed varies from 900 to 1300 m above sea level. Natural vegetation belongs to the mixed ombrophylous forest. The total area of the watershed is approximately 950 km^2, and predominant land cover consists of 22 % of agriculture (garlic, onion, soy beans, and maize), 37 % of cultivated forest (*Pinus taeda*), 33 % of natural forest (with *Araucaria angustifolia*), and 8 % of grassland and pasture. Prevalent soil types in the area are Oxisols, Inceptisols, and Entisols (Latossolos, Cambissolos, and Neossolos in the Brazilian classification system).

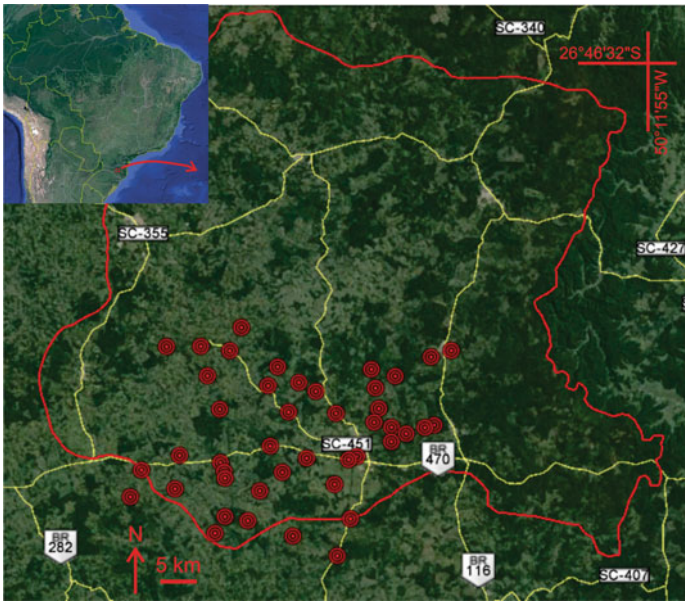

Fig. 6.1 Study area and sampling locations (*dots*) in the Marombas river watershed (*red polygon*). Small *inbox* shows the location of the watershed in south of Brazil

A total of 42 soil profiles were sampled following the GlobalSoilMap specifications (Arrouays et al. 2014). In every profile, samples were collected until 2 m depth (when possible) in the intervals of 0–5, 5–15, 15–30, 30–60, 60–100, and 100–200 cm. Soil analyses were conducted in the Pedology Laboratory of the Federal University of Santa Maria (Santa Maria, RS, Brazil). Soil organic carbon (SOC) and soil texture were determined for the 237 soil samples after air-dried, ground, and sieved through a 2-mm mesh according to Embrapa (1997). Sand, silt, and clay (g kg^{-1}) were determined by the pipette method, and SOC (g kg^{-1}) by Walkley–Black wet digestion as described by Tedesco et al. (1995).

6.2.2 Spectral Analysis

In the laboratory, in a controlled setting, the 237 air-dried grounded samples were scanned using a FieldSpec HandHeld II (ASD Inc.) spectrometer, with a spectrum range acquisition of 325–1075 nm and spectral resolution of <3 nm at 700 nm. Soil scanning was conducted inside a black painted box (dimensions L/750 × H/400 × W/400 mm), to allow for a controlled light illumination. Inside the box, soil samples were put in a Petri dish. Spectrometer was installed on top of the box with a conical field of view of 10° at a distance of 400 mm from samples. With this configuration, the spectrometer sampling area in the Petri dish was 40.7 cm^2.

A light source of 70 W quartz–tungsten–halogen lamp with integrated reflector was placed inside the box. Light source was placed 400 mm away from the soil sample and inclined 30° from lamp nadir. Four composite scans (each one is an average of 100 internal scans) were obtained for each sample from the four quadrants of Petri dish by rotating it 90°. Reference spectrum using a white Spectralon® panel was collected prior to the first scan and at every new group of samples from a different profile. Final spectrum was calculated by averaging the four composite scans.

6.2.3 Spectral Data Analysis

This study applied three preprocessing steps to soil reflectance spectra. First, spectra with high noise-to-signal ratio at the edges were removed (325–400 and 980–1075 nm) which were confirmed by visual observation. Second, the reflectance spectra were smoothed by a Savitzky–Golay second-order polynomial using a moving window of nine values (Savitzky and Golay 1964). Third, to reduce the dimensionality of the data, the reflectance values were averaged across a 5-nm window. This pretreatment reduced the soil spectral curves to 116 reflectance values (400–980 nm) which were then used for modeling.

Savitzky–Golay second derivatives were calculated on the 116 soil reflectance spectral values using a second-order polynomial across a 9-nm window. This derivative procedure followed the recommendation by Vasques et al. (2008). The modeling dataset was formed by sand, silt, and clay values and second derivatives of the air-dried grounded samples, using partial least-squares regression (PLSR) with The Unscrambler®X 10.3 software (CAMO Inc., Woodbridge, NJ).

6.2.4 Partial Least-Squares Regression Modeling

For each Vis–NIR spectral pretreatment, a PLSR model was tested. PLSR is the most common algorithm used to calibrate Vis–NIR spectra to soil properties (Viscarra Rossel et al. 2006) where there are many predictor variables that are highly collinear (Viscarra Rossel and Behrens 2010). PLSR handles this multicollinearity and is robust in terms of data noise and missing values (Summers et al. 2011; Viscarra Rossel et al. 2006). The PLSR algorithm integrates the compression and regression steps, and it selects successive orthogonal factors that maximize the covariance between predictor and response variables (Viscarra Rossel and Behrens 2010).

Dataset was also further partitioned in three subsets related to soil depth. In all PLSR models, the quality of prediction was assessed by randomly dividing the datasets in two groups (70:30 split) for calibration (C) and validation (V). Thus, there were four groups of data formed by soil texture and reflectance second derivatives: whole dataset (i.e., 166C/77 V), 0–15 cm (i.e., 59C/25 V), 15–60 cm

(i.e., 58C/24 V), and 60–200 cm (i.e., 51C/20 V). For modeling, soil texture clay, silt, and sand content were expressed in g 100 g^{-1} or %. Models were evaluated based on the coefficient of determination of validation (R^2, Eq. (6.1)). Complementary error statistics were also provided, including the root-mean-square error (RMSEP, Eq. (6.2)) for models accuracy, and mean error (ME, Eq. (6.3)) for its bias:

$$R^2 = \sum_{i=1}^{n} (\hat{y}i - \bar{y})^2 \Big/ \sum_{i=1}^{n} (yi - \bar{y})^2 \tag{6.1}$$

$$\text{RMSEP} = \sqrt{\sum_{i=1}^{n} (\hat{y}i - yi)^2 \Big/ n} \tag{6.2}$$

$$\text{ME} = \frac{1}{n} \sum_{i=1}^{n} (\hat{y}i - yi) \tag{6.3}$$

where $\hat{y}$ = predicted values, $\bar{y}$ = mean of observed values, y = observed values, and n = number of predicted/observed values with $i = 1, 2, \ldots, n$.

Homogeneity of variance test, between soil texture calibration and validation sets, was carried out with Levene's test. Following results of homogeneity of variance (i.e., groups had equal or unequal variances), a comparison between the mean was conducted with Student's t test. All tests were done with a critical p-value of 0.05 (95 % confidence).

6.3 Results and Discussion

6.3.1 Descriptive Statistics

Soil textures in the Marombas river watershed are predominantly clay and silty clay (Fig. 6.2). There are also a few samples of clay loam and silty clay loam. Those soils are deeply weathered with strong presence iron oxides with particles diameter less than 0.002 mm. Soil clay content of the 237 samples ranges from 31.79 to 78.48 % and sand content ranges from 1.38 to 35.48 % (Table 6.1). The mean clay content increases from 51.73, 56.49, and 63.82 % within the increasing soil depth of 0–15, 15–60, and 60–200 cm, respectively. This small increase in clay with depth is due to translocation. The dominant minerals are calcic plagioclase and pyroxene basalt which weathered completely and formed clay minerals through oxidation process of the parental material contributing to this fine texture. The profiles were classified as Oxisols (Latossolos in Brazilian classification).

Sand, silt, and clay contents were tested for normality with Shapiro–Wilk test at a 0.05 significant level. The test indicates that sand, silt, and clay were normally

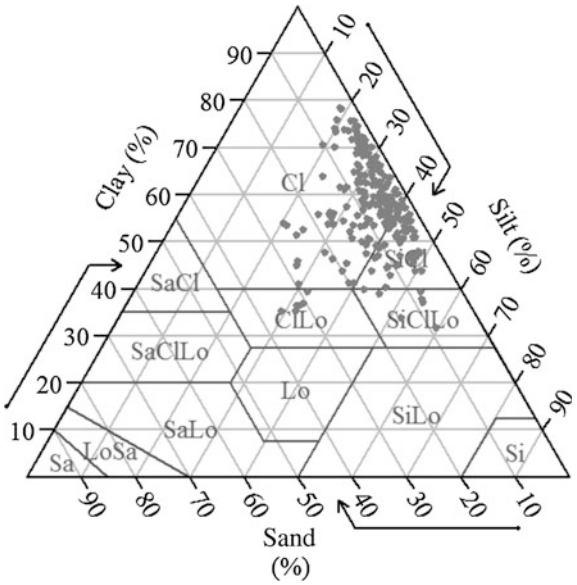

Fig. 6.2 Soil texture of the samples following the USDA triangle

distributed, and thus, no transformation was applied to the attribute datasets before modeling. To verify whether there was similarity between calibration and validation datasets, tests of homogeneity of variance (Levene's test) and comparison of the mean (Student's t test) were carried out with a 0.05 significant level. The Levene's test indicated no homogeneity of variance between sand datasets for depth of 0–15 and 60–200 cm (Table 6.2). All remain groups of data had equality of variances between calibration and validation samples. Due to the lack of homogeneity of variance, the Student's t test for comparison of the mean in those two groups (0–15 and 60–200 cm) was carried out with non-equal variance assumption. Comparison between the mean for sand, silt, and clay values for calibration and validation sets did not show a significant difference (Table 6.2). Sand, silt, and clay are compositional data which needs to sum to 100 %. In this study, we model the components independently to study the relative predictability of the content using NIR. Future work will look into additive log-ratio transformation.

6.3.2 *Qualitative Description of the Spectral Data*

Spectra of all soils were similar with minor features apparent in visible and near-infrared region. An increase in soil reflectance could be noticed toward deeper soil samples (Fig. 6.3a). Samples located near the surface have higher SOC content which absorbs radiation. Sousa Junior et al. (2011) found similar results on correlation between soil attributes and its reflectance showing that soil organic matter has a high influence on the spectral behavior, resulting in a significant negative

Table 6.1 Entire and segregated by depth datasets descriptive statistics

Descriptive statistics (%)	Sand	Silt	Clay	Sand	Silt	Clay
	Calibration			Validation		
	Whole dataset					
	***n* = 166**			***n* = 71**		
Min	1.38	18.91	31.79	1.38	18.50	33.85
Q1	3.32	28.51	52.09	3.00	29.37	50.87
Median	5.12	33.26	57.92	6.09	36.77	56.78
Mean	7.82	34.12	58.06	7.60	35.59	56.81
Q3	9.19	38.67	66.19	10.98	40.82	62.89
Max	32.81	59.40	78.16	35.48	52.76	78.48
Range	31.43	40.49	46.37	34.10	34.27	44.62
SD	7.05	7.52	10.05	6.29	8.03	9.69
	Depth 0–15 cm					
	***n* = 59**			***n* = 25**		
Min	3.00	20.27	33.85	2.60	25.93	39.51
Q1	5.12	33.20	46.57	4.26	33.11	47.89
Median	6.77	38.26	53.30	6.39	37.91	53.69
Mean	10.51	37.75	51.73	7.86	37.91	54.23
Q3	12.86	41.19	56.93	9.08	43.86	58.17
Max	35.48	51.94	69.48	19.91	52.76	70.39
Range	32.48	31.67	35.62	17.31	26.83	30.87
SD	8.25	6.49	8.54	4.72	7.27	8.13
	Depth 15–60 cm					
	***n* = 58**			***n* = 24**		
Min	2.00	18.50	36.78	1.56	24.10	38.90
Q1	3.62	29.47	52.48	2.58	31.18	51.71
Median	5.65	34.74	57.90	4.79	34.66	56.22
Mean	7.66	34.80	57.54	8.43	35.07	56.49
Q3	9.50	39.59	63.00	10.69	40.02	63.04
Max	30.61	48.52	78.48	28.69	47.12	73.36
Range	28.61	30.02	41.70	27.14	23.02	34.46
SD	6.14	6.51	8.52	8.40	6.31	9.02
	Depth 60–200 cm					
	***n* = 51**			***n* = 20**		
Min	1.38	18.91	31.79	1.38	19.06	37.05
Q1	2.25	24.79	59.34	2.35	23.50	60.85
Median	3.23	28.38	64.86	3.09	27.62	68.35
Mean	5.60	30.58	63.82	4.42	29.79	65.79
Q3	6.64	36.14	71.42	6.25	35.27	72.70
Max	25.29	59.40	78.16	10.21	54.38	74.62
Range	23.91	40.49	46.37	8.83	35.32	37.57
SD	5.74	8.22	9.23	2.74	8.51	9.11

correlation in all evaluated bands. The organic matter can also mask features of the reflectance (Demattê et al. 2012).

The SOC content varied from 0.03 to 8.32 % in the dataset of 237 samples. High SOC presence is due to constant supply of new organic material in vegetated areas. The altitude of the region has annual average temperature to be around 16 °C,

Table 6.2 Values of p for the tests of homogeneity of variance and comparison of the mean

p at 0.05	Sand	Silt	Clay
	Whole dataset		
Homogeneity of variance	0.90	0.31	0.44
Comparison of the mean	0.98	0.75	0.66
	Depth 0–15 cm		
Homogeneity of variance	0.03[a]	0.30	0.63
Comparison of the mean	0.07	0.92	0.21
	Depth 15–60 cm		
Homogeneity of variance	0.07	0.74	0.68
Comparison of the mean	0.64	0.86	0.62
	Depth 60–200 cm		
Homogeneity of variance	0.04[a]	0.89	0.87
Comparison of the mean	0.25	0.72	0.42

[a]Indicates no significance

thus maintaining a high SOC content on top layers. Clay soil texture also plays a role in protecting organic carbon from decomposition through physical protection. The 71 samples from depth of 60–200 cm showed an amount of 0.03 to 3.78 % of SOC, indicating a decrease of SOC with depth.

First and second spectra derivatives highlighted features related to soil samples mineralogical composition (Fig. 6.3b, c). According to Torrent and Barrón (2002), soil reflectance of weathered Oxisols shows features related to the presence of iron oxides goethite and hematite around 480 and 530 nm, respectively. Those features are a product of various electronic or vibrational transitions in the atoms and molecules of minerals. In the case of Oxisols, this is of decisive influence for morphological description and soil color determination. Summers et al. (2011) found some contributions from the visible (400–700 nm) and near-infrared region (700–1300 nm) in the clay absorption feature at 2200 nm and the features at 1400 and 1900 nm, indicating there may be some covariation between the clay content and the color of the soil. The second derivative spectra showed similar behavior in all depth except for the presence of different amounts of SOC. Samples with higher amount of SOC showed smaller amplitude. Another effect of increasing amounts of SOC is the obliteration of a concavity feature around 880 nm which is related to the presence of iron oxides (Fig. 6.3a). Demattê et al. (2004) reported that the depth of this concavity is related to the degree of the crystallization of iron oxides, and the presence of SOC will diminish this spectral feature.

Second derivative (Fig. 6.3c) shows the absence of goethite from the concavity around 450–480 nm. On the other hand, a strong peak in the second derivative values near 540–560 nm is related to the samples that reach content of hematite (Fig. 6.3c). These features can be used for soil texture and spectral signature modeling with PLSR.

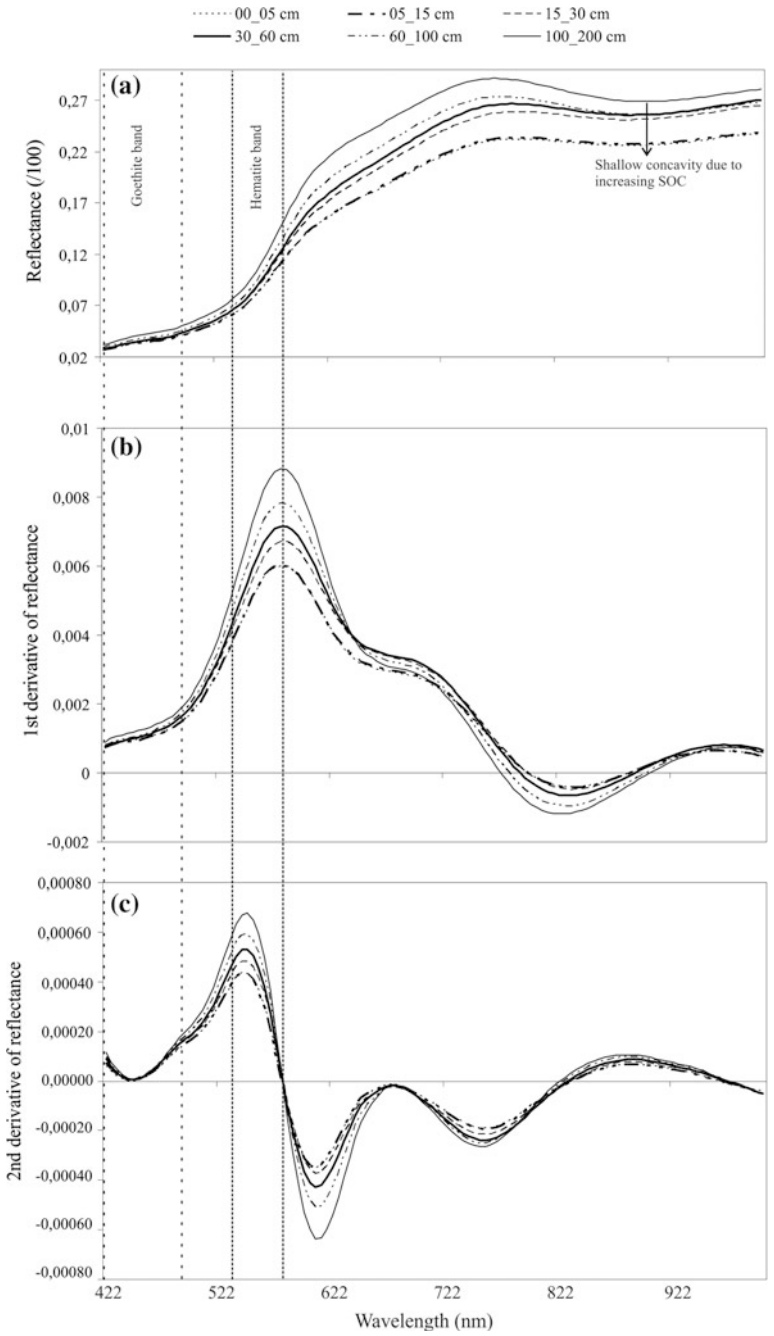

Fig. 6.3 Reflectance data and 1st and 2nd derivatives. Data collected in 6 depths at soil profile number 1

6.3.3 Development of Calibration Model

Overall, best PLSR predictive values were achieved for clay (mean R^2 = 0.58), followed by silt (mean R^2 = 0.56), with worst predictive values achieved for sand (mean R^2 = 0.24) (Table 6.3).

Considering PLSR results separately in each of the four datasets, the best predictive values can be achieved by modeling soil clay content using data from all depths. When this whole dataset was used, the R^2 = 0.69, RMSEP(%) = 5.39 and ME(%) = −0.01. Small bias was found when the validation set is carried out on samples very similar to the ones which have used for calibration procedures. Worst results for clay PLSR prediction is obtained for soil samples from 60 to 200 cm, with R^2 = 0.46, RMSEP(%) = 6.56 and a clay underestimation of ME(%) = −0.86. Those results are somehow the opposite of what was expected. Since at this depth, SOC is lower, it was expected that a less interference of organic molecule on the spectra would allow a higher clay content prediction. However, one has to bear in mind that the 60–200 cm dataset had only 51 samples for calibration and 20 samples for validation of the models, with similar clay content, thus causing the model to underperform due to the lack of the representativeness of the information. Clay variability remained high in this dataset shown by the range values of 46.37 and 37.57 % for 51C and 20 V, respectively (Table 6.1).

For sand prediction, poor performance with R^2 = 0.09, RMSEP(%) = 4.14, and ME(%) = 0.26 was found for soil samples form 60 to 200 cm depth. This might also be due to the smaller amount of information in this dataset. Nevertheless, when modelled using the whole dataset (237 samples), PLSR for sand prediction also achieved poor results with R^2 = 0.30, RMSEP(%) = 5.47 and ME(%) = 0.59. Future work should rely on datasets with a broader range of sand content. This could be an evidence that sand prediction in Oxisols, using a limited spectral region, could be a challenge. Model adjustment might demand higher sample datasets to cope with soil variability, in addition, the high soil clay content might coat the sand particles, thus making sand prediction more difficult.

In PLSR modeling, a specific region of the spectrum may be important for modeling of soil attributes. Such attributes are identified by large PLS regression

Table 6.3 Statistics of PLSR modeling

Soil attribute	R^2	RMSEP (%)	ME	Factor (no.)	R^2	RMSEP (%)	ME	Factor (no.)
	Whole dataset				**Depth 00–15 cm**			
Sand	0.30	5.47	0.59	7	0.10	5.30	−0.48	6
Silt	0.59	5.18	−0.58	6	0.72	4.27	−0.73	7
Clay	0.69	5.39	−0.01	5	0.60	5.07	0.09	2
	Depth 15–60 cm				**Depth 60–200 cm**			
Sand	0.45	6.14	0.19	7	0.09	4.14	0.26	7
Silt	0.53	4.37	1.09	6	0.38	6.52	0.03	3
Clay	0.58	5.84	−1.23	7	0.46	6.56	−0.86	3

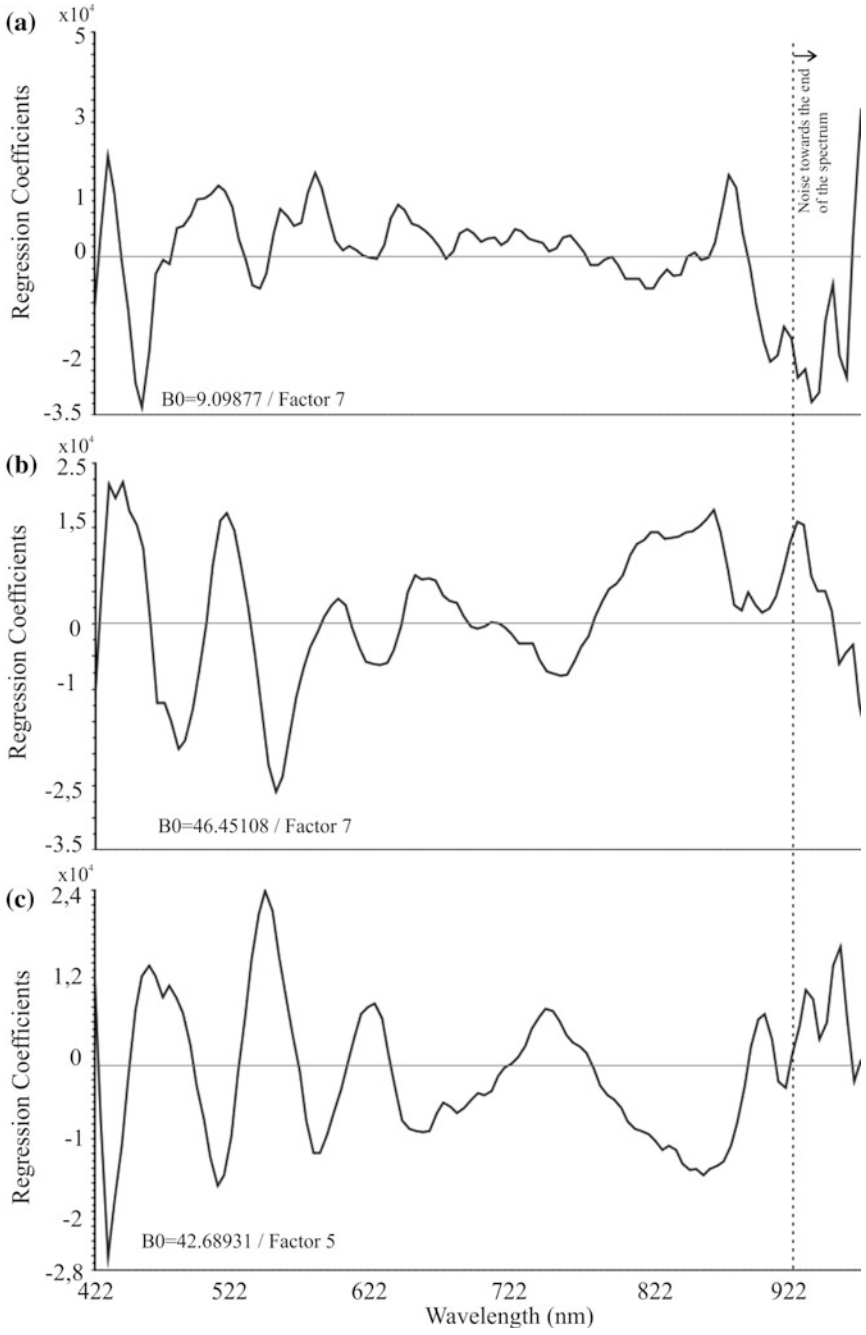

Fig. 6.4 Regression coefficients of the partial least-squares regression model with whole dataset for soil attributes: **a** sand, **b** silt, and **c** clay

coefficients. The regression coefficients for the three soil attributes are shown in Fig. 6.4. The magnitude of those regression coefficients, negative or positive, represents the importance of the reflectance band in terms of the explanation of variance in soil analysis data. Positive peaks are due to the component of interest, while negative peaks correspond to interfering components (Haaland and Thomas 1988). Spectra with a coefficient near zero do not have predictive capability.

For sand prediction, regression coefficients with positive values can be found at 432, 512, 582, and 882 nm. A significant negative peak can be seen at 457 nm. Looking into the whole spectrum of clay regression coefficients (Fig. 6.4c), its peaks are much better defined than the ones for sand and silt (Fig. 6.4a, b). This could be due to the strong presence of iron oxide characteristics (i.e., soil color within 400–700 nm) in the analyzed Oxisols samples. For clay prediction, positive regression coefficients were 462, 547, 627, and 752 nm. On the other hand, negative coefficients were located at 492, 512, 587, 662 and 867 nm. This last negative peak around 867 nm could be associated with the presence of higher amounts of SOC in the soil surface. The presence of organic material diminishes the perception of the iron oxide concavity around 880 nm, which in turn makes it more difficult to the PLSR models to predict clay content. All the negative and positive peaks of regression coefficients are spectral regions which deserve more attention toward selecting, and possible model recalculation, focusing in more significant variables for PLSR models.

6.4 Conclusions

Soil attribute prediction with PLSR using a limited spectral region (325–1075 nm) performed poorly for sand. The results were more promising when considering the capabilities to predict silt and clay.

The application of visible and part of the near-infrared region (400–980 nm) for clay prediction in Oxisols achieved relative good results when all dataset (n = 237) was used for modeling with no stratification by depth with R^2 = 0.69, RMSEP (%) = 5.39, and ME = −0.01 %. Regression coefficients showed good relation to the spectral behavior of weathered soils in visible and near-infrared region. They should be used in future studies as a filtering approach toward selecting more significant variables (i.e., spectral regions) for modeling.

Acknowledgments This study was supported by the Foundation for Research Support of Santa Catarina State (FAPESC) No. 2012000094 with funds for equipment acquisition and soil analysis. The National Council of Technological and Scientific Development (CNPq) financed the research grant (Universal No. 442718/2014-4) for coauthor (2). First author acknowledges support of the Coordinating Office for the Advancement of Higher Education (CAPES) for graduation fellowships and Federal University of Rio Grande do Sul (UFRGS) for support paper presentation at Global Workshop 2015—Digital Soil Morphometrics. We also thank the editors for their comments and suggestions on this paper.

References

Arrouays D, McKenzie NJ, Hempel JW, de Forges A, McBratney AB (eds) (2014) GlobalSoilMap. Basis of the global spatial soil information system. In: Proceedings of the first GlobalSoilMap conference, Orleans, France, 7–9 Oct 2014. Taylor & Francis, Balkema

Chang C, Laird DA, Mausbach MJ, Hurburgh CR (2001) Near infrared reflectance spectroscopy: principal components regression analysis of soil properties. Soil Sci Soc Am J 65:480–490

CAMO Technologies Inc. (2006) The Unscrambler appendices: method references. PDF document. Available at: http://www.camo.com/TheUnscrambler/Appendices/The%20Unscrambler%20Method%20References.pdf

Demattê JAM, da Silva Terra F (2014) Spectral pedology: a new perspective on evaluation of soils along pedogenetic alterations. Geoderma 217–218:190–200

Demattê JAM, Campos RC, Alves MC, Fiorio PR, Nanni MR (2004) Visible-NIR reflectance: a new approach on soil evaluation. Geoderma 121:95–112

Demattê JAM, Terra FDS, Quartaroli CF (2012) Spectral behavior of some modal soil profiles from São Paulo State, Brazil. Bragantia, (ahead), 0–0

Dotto AC, Dalmolin RSD, de Araújo Pedron F, ten Caten A, Ruiz LFC (2014) Mapeamento digital de atributos: granulometria e matéria orgânica do solo utilizando espectroscopia de reflectância difusa. R Bras Ci Solo 38:1663–1671

Empresa Brasileira de Pesquisa Agropecuária E (1997) Manual de Métodos de Análise de Solo, 2nd edn. Rio de Janeiro

GlobalSoilMap.net products (2011) GlobalSoilMap.net. Specifications: Version 1 GlobalSoilMap.net products, Release 2.1. 1–48. Viewed in 29 May 2015, http://www.globalsoilmap.net/specifications

Haaland DM, Thomas EV (1988) Partial least-squares methods for spectral analyses. 1. Relation to other quantitative calibration methods and the extraction of qualitative information. Anal Chem 60(11):1193–1202

Ramirez-Lopez L, Schmidt K, Behrens T, van Wesemael B, Demattê JAM, Scholten T (2014) Sampling optimal calibration sets in soil infrared spectroscopy. Geoderma 226–227(1):140–150

Saeys W, Mouazen AM, Ramon H (2005) Potential for onsite and online analysis of pig manure using visible and near infrared reflectance spectroscopy. Biosyst Eng 91:393–402

Savitzky A, Golay MJE (1964) Smoothing and differentiation of data by simplified least squares procedures. Anal Chem 36:1627–1639

Sousa Junior JG, Demattê JAM, Araújo SR (2011) Modelos espectrais terrestres e orbitais na determinação de teores de atributos dos solos: Potencial e custos. Bragantia 70(3):610–621

Summers D, Lewis M, Ostendorf B, Chittleborough D (2011) Visible near-infrared reflectance spectroscopy as a predictive indicator of soil properties. Ecol Ind 11:123–131

Tedesco MJ, Gianello C, Bissani CA, Bohnen H, Volkweiss SJ (1995) Análises de solo plantas e outros materiais. Porto Alegre, Universidade Federal do Rio Grande do Sul, 174 p

Torrent J, Barrón V (2002) Diffuse reflectance spectroscopy of iron oxides. Encyclopedia of surface and colloid science. Taylor and Francis, New York, pp 1438–1446

Vasques GM, Grunwald S, Sickman JO (2008) Comparison of multivariate methods for inferential modeling of soil carbon using visible/near-infrared spectra. Geoderma 146:14–25

Viscarra Rossel RA, Behrens T (2010) Using data mining to model and interpret soil diffuse reflectance spectra. Geoderma 158(1–2):46–54

Viscarra Rossel RA, Chen C (2011) Digitally mapping the information content of visible-near infrared spectra of surficial Australian soils. Remote Sens Environ 115(6):1443–1455

Viscarra Rossel RA, Lark RM (2009) Improved analysis and modeling of soil diffuse reflectance spectra using wavelets. Eur J Soil Sci 60(3):453–464

Viscarra Rossel RA, Walvoort DJJ, McBratney AB, Janik LJ, Skjemstad JO (2006) Visible, near infrared, mid infrared or combined diffuse reflectance spectroscopy for simultaneous assessment of various soil properties. Geoderma 131(1–2):59–75

Wetterlind J, Stenberg B, Söderström M (2010) Increased sample point density in farm soil mapping by local calibration of visible and near infrared prediction models. Geoderma 156(3–4):152–160

Chapter 7
Estimating Soil Properties with a Mobile Phone

Matt Aitkenhead, David Donnelly, Malcolm Coull and Richard Gwatkin

Abstract Several soil properties can be used to estimate soil health and suitability for specific land use. These properties include, but are not restricted to, organic matter content, pH, cation exchange capacity, C/N ratio, texture and structure. These properties provide broad information about the capacity of the soil to provide nutrients, water and physical support to crops. They also provide information about soil erosion and compaction risk. The measurement of these properties is traditionally carried out through laboratory analysis which delays decision-making. Some of these properties can be estimated from an understanding of the soil-forming characteristics and visual analysis of the soil profile. Here, a method is presented that automates estimating soil fertility properties using image analysis of field-based topsoil images, including image morphometrics. A database of Scottish soil samples has been used to generate a model, which links spatial data sets and image analysis to produce estimates of soil fertility properties. A mobile phone app has been produced that provides an estimate of soil organic matter rapidly and for free.

Keywords Soil fertility · Indicators · Mobile phone · Apps · Image analysis

7.1 Introduction

The use of spectral information for estimating soil characteristics is a rapidly growing research area, with much of the current effort directed at infrared or visible–near-infrared wavelengths. The use of visible wavelength light alone has been demonstrated to be useful (Liles et al. 2013; Ibanez-Asensio et al. 2013). Soil colour attributes have been measured using a number of different ways, ranging from naked eye comparison with Munsell colour charts (Aitkenhead et al. 2013) to electronic measurement (e.g. Gunal et al. 2008). Proximal sensing of soil with

M. Aitkenhead (✉) · D. Donnelly · M. Coull · R. Gwatkin
The James Hutton Institute, Aberdeen AB15 8QH, Scotland, UK
e-mail: matt.aitkenhead@hutton.ac.uk

A.E. Hartemink and B. Minasny (eds.), *Digital Soil Morphometrics*,
Progress in Soil Science, DOI 10.1007/978-3-319-28295-4_7

digital cameras has also been used. Mausel et al. (1997) explored the potential of digital photography for identifying spectrally distinct soil types. Levin et al. (2005) used colour indices from digital photography to estimate iron oxide content and textural parameters in sandy soils, whereas Gregory et al. (2006) estimated soil organic matter content using a digital camera with visible and near-infrared wavelength capacity.

There are some examples of research directed towards the engineering design of soil proximal sensing systems, for example Rossel et al. (2008), but most are targeted at soil or remote sensing scientists. Some work has considered the design and practicalities of soil imaging systems from an agricultural perspective (e.g. Chung and Joh 2012). There is also some research that crosses the boundaries between standard digital cameras with visible wavelength range and the use of sophisticated and expensive hyperspectral imaging systems (e.g. Zhao et al. 2012). The field protocols, parameters estimated, data interpretation and presentation of results tend to overlap between these two techniques, and it is mainly the cost of the equipment and sometimes the quality of the results that separates them.

The use of mobile phone cameras with their additional functionality can add processing capacity and other data interpretation and transmission abilities. Moonrungsee et al. (2015), for example, demonstrated colorimetric analysis of soil water using indicators for estimating available phosphorus, while El Kaoutit et al. (2013) achieved something similar for mercury concentrations. Gomez-Robledo et al. (2013) investigated the use of smartphone camera as a soil colour sensor, using it to determine Munsell colour of soil samples. Field-based investigation of soil biology has also been experimented with, for example Bogoch et al. (2013) who used a smartphone coupled with a basic microscope to detect helminth species from soil samples. Aitkenhead (2013) demonstrated a smartphone app linking camera, image analysis and server-side processing for the estimation of soil carbon.

In this paper, an overview of the use of image colour and texture for characterising soil, along with a discussion of image colour calibration and mobile phone sensors, is given. This is followed by the use of spatial covariates and their integration into modelling frameworks for estimating soil characteristics. The development of mobile phone apps that incorporate these modelling frameworks is described, with examples given of systems that have been developed and for ongoing work. Lastly, potential applications are explored.

7.2 Colour and Soil Character

Traditionally, soil scientists have determined the colour of a sample in the field by matching a soil aggregate against a series of colour patches first produced by Albert H. Munsell in the early twentieth century (www.munsell.com). The effects of lighting are assumed to be the same on a Munsell colour card patch and a soil of the same colour, eliminating the effects of lighting. There is some subjectivity in the Munsell soil colour assessment.

Complexity of soil colour–character relationships means that it is necessary to have information regarding the soil-forming factors (e.g. topography, climate, vegetation, parent material and land use). Modelling using legacy data is an important component of this work. If no legacy data are available that include colour and the parameter(s) of interest, then additional field sampling effort is needed. Soil colour and other parameters are included in several national and international data sets including the ISRIC–World Soil Information data set.

Soil parameters that have been estimated using colour include organic matter content (Aitkenhead et al. 2013; Liles et al. 2013), texture (Ibanez-Asensio et al. 2013), water table depth (Humphrey et al. 2011), iron oxide (Gunal et al. 2008) and others. Recent and ongoing work at the James Hutton Institute in the UK has demonstrated the ability to estimate a number of soil physical and chemical properties using soil colour and spatial covariates.

7.3 Mobile Phone Sensors

A number of sensors exist as standard in modern mobile phones that can be used to provide sensor data for soil monitoring. Below, we describe the sensors a smartphone/tablet device is equipped with, how they are relevant and how they can be used to further this goal. The long-term goal of much of the work described in this paper is to optimise the use of these sensors and the data they produce for real-time soil and general environmental characterisation—turning the smartphone into a *Star Trek*-style 'tricorder'.

7.3.1 GPS

GPS (Global Positioning System) is a navigation system using satellite signals, with the first fully working system being developed by the US military. Most models of smartphone and tablet have GPS circuitry installed, giving them the same functionality as a standard GPS device. The basic GPS location information is given in latitude/longitude rather than in individual national grid reference systems and so may need to be converted to match spatial data sets.

GPS positioning allows the user's location to be captured at the time of making other sensor readings. This positional information is then inserted into the header of any photographs that are uploaded and can be extracted and used to determine the parameter values of spatial covariates at the user's location. This eliminates the need for the user to record anything other than the image/sensor reading that they are interested in and allows automation of site characterisation.

The accuracy of smartphone GPS locations is less than standard GPS devices, largely due to the limited size of the built-in antenna. With a mid-range smartphone, the location accuracy is usually within 35–40 m more than 95 % of the locations.

This level of accuracy is smaller than the spatial resolution of most of the spatial data sets that are being used in parallel with the positional information, and so it is considered acceptable for this kind of work.

7.3.2 Camera

Improvements to digital cameras in smartphones have resulted in high-quality and consistent imaging. The number of pixels in a smartphone camera is now more than needed to simply determine the soil colour although for texture there is never a lower limit of requirement (some soil particles will always be smaller than the imaging capabilities of a commercial digital camera). The spectral range of cameras is an issue as they only provide colour information across broad spectral ranges. This limits their application for spectroscopic analysis. Spectral sensitivity or the response curve of the camera's light-detecting sensors to different wavelengths is another issue, as these response curves vary between devices and so do not produce a uniform colour response.

Without specialist equipment, the shortest minimum focus distance varies from approximately 5 to 20 cm across smartphone/tablet cameras. This means that the minimum image pixel resolution that can be achieved is around 10 microns with up to 100 microns for older models. Smartphone cameras are unable to produce images that capture the full range of silt particle size and cannot acquire images of clay particles.

Automatic image adjustment can present a problem, as the camera's internal software will attempt to adjust contrast and focus in ways that alter the colour response. There are also implications of the digital sensor array design due to the distribution of spectral filters on the pixel array. This can mean that the true RGB (red, green, blue) characteristics of individual pixels are inaccurate as they contain information from surrounding pixels.

So while cameras on smartphones and tablets can provide imagery of soil, they are unable to satisfy all the requirements in terms of spectral resolution and spatial scale, and are variable in terms of the images that will be acquired. It is necessary therefore to consider methods that can deal with this relatively coarse and inconsistent imagery.

7.4 Calibrating Image Colour

7.4.1 Why Calibrate Image Colour?

The need for a colour 'absolute' standard in imaging soil is necessary if colour information is to be used as a predictor of soil properties. Without this standardisation, it is impossible to tell whether colour variation is due to differences in the

appearance of the soil, or in the device used to image it. Spectral response is measured in terms of the quantum efficiency (proportion of incoming light that is detected) at different wavelengths, with response curves due to the filter/sensor architecture and design usually having three distinct curves in the red, green and blue sections of the visible spectrum. The shape of these curves varies between devices and can alter over time in the same device, so calibration is required.

Loss of data from using multispectral instead of hyperspectral imaging systems is considered likely to reduce the accuracy of soil property estimation. Many of the comparisons that have been carried out (few of which have involved soil) have used hyperspectral imaging systems with a different, usually greater, spectral range than the multispectral system. Examples include Garrido-Novell et al. (2012), who looked at automated grading of apples, and Taghizadeh et al. (2011), who examined the quality evaluation of mushrooms.

A number of colour spaces exist (Munsell, RGB, LAB, etc.), often implying a need to convert from the initial colour description of the soil to the colour space of the model/calibration being used. Translation tables between the different colour spaces are readily available online, but this translation can sometimes result in a degradation of the colour information as colour spaces vary in the level of detail with which they cover different parts of the represented colour space.

7.4.2 Lighting Conditions

The effects of lighting conditions on the digital image are various, difficult to predict in advance and often seen in combination with one another. Lighting intensity is obvious, with cameras operating within a fairly broad range of light intensity. If light levels drop below a certain level, the camera will not produce images with pixel intensities across the full range available, resulting in a loss of data. For light levels that are too high, overexposure and glare from reflective surfaces will produce a restricted intensity range at the upper levels. In photographing soil, we have found that during daylight hours (preferably with the Sun well above the horizon), it is possible to produce adequate photographs.

The spectral distribution of daylight varies not only in maximum intensity but also in distribution. The angle of the Sun above the horizon plays a major factor with daylight being shifted towards the redder end of the spectrum when the Sun is low. Overcast skies also produce a slightly different wavelength distribution, with this variation depending on cloud thickness and other conditions. Below, we have four images of soils photographed with the same device at different dates and times within north-east Scotland. A colour correction card with the James Hutton Institute logo is also shown in each photograph, and it is clear that there is substantial colour variation between the images due to the lighting conditions (Fig. 7.1).

Fig. 7.1 Examples of topsoil images taken of soils under different lighting conditions

7.4.3 Photography Requirements

A number of effects to be avoided can be easily produced in photography of soil. These include shadows caused by trees or the observer themselves. Image calibration becomes problematic if there are inconsistent lighting levels across the

scene being photographed. Blurring caused by the movement of the camera while taking the photograph will be a problem if image analysis is to be carried out but is not an issue if only colour is being measured. Image focus will have a strong influence on image morphology, but not on the soil colour.

Contrast in the image can be a problem for very low or high lighting levels, or if there are highly reflective objects in the image that cause glare. If these problems are avoided, then the automatic colour calibration will resolve variable contrast levels. This means that automatic contrast adjustments made by the camera are more of a help than a hindrance, as they tend to produce image intensity distributions that are suitable for working with.

Some camera-induced image artefacts include faulty or damaged devices where false image signals are caused by misalignment or poor operation of the optical components. If an image contains unevenly distributed colours or rainbow-like image artefacts, it is best to use another camera as these are difficult to remove from the image.

File format effects can also be seen with devices that use Joint Photographic Experts Group (JPEG) image compression although the use of the uncompressed (RAW) file format is becoming more common. The JPEG compression format reduces file size and thus makes it easier to upload and use, but can result in a loss of image data and reduction in image quality. This is a problem with measurements of image morphology, as the compression algorithm introduces image artefacts at the pixel scale that cannot be distinguished from real image features.

7.4.4 Calibration Methodology

Colour calibration is required to produce a standard 'true' colour image that is independent of lighting conditions, camera spectral response and other. The way to do this is to determine the relationship of image colour to a standard colour sample within the image and to use this relationship to adjust the colour distribution of the rest of the image. We have developed an approach that uses a colour calibration card containing a standard distribution of RGB pixel values and which can also be used to determine the pixel resolution of the image.

The James Hutton Institute's app development team has used two different colour calibration cards for different apps. The first used the Institute logo as it provided values across the RGB colour space while at the same time served as promotional material for the Institute (see below). The calibration results achieved with this card were good, but it did not provide a broad range of colour intensity values. The second card contains several greyscale bands, each of which has known RGB ratios while providing a range of reflectance values. This provides a spectral response curve that can be matched to the values received in an image (Fig. 7.2).

Colour card recognition in the image is necessary and requires identification of the edges of the card in order to isolate the pixels to be used for colour correction. The approach that we have used is to identify lines and rows within the image that

Fig. 7.2 Examples of images taken incorrectly and correctly with a colour correction card

contains more than a certain number of 'white' pixels—that is, pixels for which the red, green and blue values were all above 95 % of the maximum image intensity. Once these lines and rows had been identified, it was relatively trivial to identify the

'bounding box' of the colour correction card as the colour correction card's outer surround is a large white area. Some trial and error was required to ensure that the threshold value of 'white' pixels was set at a value that allowed the correction card to be identified consistently. Calibration pixel extraction is carried out by selecting specific areas within this bounding box and identifying the mean RGB values from these areas. Development of the RGB calibration curve is done by calculating the ratios between known colour values for the calibration pixels and the values acquired from the image. This is done for a large number of pixels (several hundred distributed across the colour space—we used between 200 and 1000 depending on the colour correction card size in the image) to allow the correction across the full range of RGB values. Accuracy of the calibration process for RGB values was determined across a number of different lighting conditions, by comparing calibration pixels with target values. It is estimated that for imagery acquired under moderate and good lighting conditions, the RGB pixel value error is consistently reduced to less than 10 % of precalibration values. Under lighting conditions that are very dark or very light, the correction is less even but was found to always result in some improvement in the RGB value distribution.

7.5 Image Texture

Several image texture analysis approaches exist that can provide information about the relationships between the spatial distribution of image pixel intensity values and soil characteristics. These include wavelets (detection of specific frequencies in intensity variation within the image), GLCM (grey-level co-occurrence matrix) (spatial relationships of similar greyscale values), edge detection and the calculation of statistical parameters describing intensity values (e.g. range, mean, maximum, standard deviation, entropy) within a moving window of selected size within the image.

Removing non-soil pixels is the first step in the image analysis, followed by the reduction of the image colour space to greyscale. The implementation of image texture mapping with depth down the soil profile is carried out by calculating the GLCM texture parameters across the whole image, at a number of different scales. The image is sequentially reduced in pixel resolution by 2 (five times) and subjected to texture analysis, resulting in six sets of image texture data. This was done in order to capture variation in image texture with scale, which may be important for characterising the soil texture.

Measuring image scale using the colour correction card allows the image texture parameters to be given values in relation to real scales, which is important when comparing soils with different structural properties. The procedure for this is to measure image texture at the pixel/multipixel resolution, determine the resolution of a single pixel in the image and then fit the curve of measured texture values to a logarithmic range of preselected spatial scales. The scale values used in the work

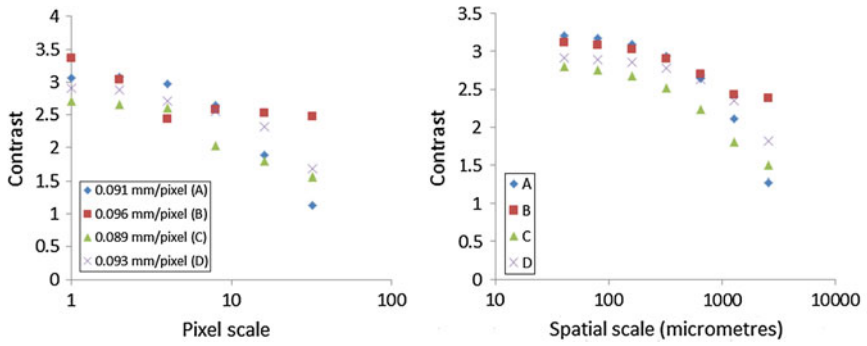

Fig. 7.3 Examples of image texture-scale curves adjusted to constant scale values. Raw textural measurement of a parameter (contrast) is on the *left*, and the values derived from *fitted curves* for different scales are on the *right*

demonstrated here were 40, 80, 160, 320, 640, 1280 and 2560 μm, and the curve fitting was carried out by fitting a third-order polynomial curve to the values (Fig. 7.3).

7.6 Integration of Site Descriptors

7.6.1 SCORPAN

The concept of SCORPAN, which is an acronym of soil, climate, organisms, topography, parent material, age and N (for geographical location), is an adaptation of the concept described by Hans Jenny (Jenny 1994).

Nonlinear relationships between covariates and soil character make the implementation of SCORPAN within a modelling framework difficult. In practice, it is used as a conceptual model rather than as an approach for predicting soil properties (McBratney et al. 2003). Effects of non-SCORPAN drivers can confuse the issue, with, for example, burial of a soil profile by sediments which cannot easily be predicted.

7.6.2 Spatial Covariates

Examples of covariates that can be derived from spatial data sets and used in SCORPAN-derived predictive models of soil character include elevation and slope (topography), parent material from geological maps, vegetation classes from land cover maps, monthly or annual mean temperature and rainfall (climate). Land management and historical land cover data are also useful. Normalisation of

covariate values is often necessary, particularly for parameters that are biased within their distribution (e.g. elevation, slope) or that have discontinuities in value (e.g. aspect, in which the difference between 359° and 0° should have the same impact as between 0° and 1°).

Location is useful because it allows other information about the soil's environment to be included in a calibration model. The link with mobile device geolocation is useful, because it provides a system that incorporates image capture, geolocation and either onboard processing or transmission to a processing server. Accuracy requirements of the geolocation are difficult to define as soil varies, but normal operating accuracies of a few tens of metres or less are considered sufficient —the spatial data sets used are not usually of finer resolution than this in any case. Speed of response is also a consideration for real-time soil monitoring in the field. The SOCIT (Soil Organic Carbon Information Technology) app provides an estimate of soil organic matter content within 10–30 s, most of which is taken up by transmitting the image (in compressed form) to the processing server.

7.6.3 Spatial Data sets

Global data sets that allow covariates to be derived include topography (e.g. SRTM (Shuttle Radar Topography Mission), Aster GDEM (global digital elevation map), WorldDEM), climate (e.g. WorldClim, NOAA (National Oceanic and Atmospheric Administration) data), soil (Food and Agriculture Organisation Harmonized World Soil Database (FAO HWSD)—this also provides some information on parent material) and land cover (e.g. Joint Research Centre (JRC) Global Land Cover). Many other data sets exist at national and even local level, usually at smaller spatial resolution/larger scale than these global ones. A number of high-quality spatial data sets of relevant parameters exist for Scotland and were used in the work described here (see Sect. 7.9.1). Preparation requirements for the data sets include the reclassification of categorical maps, normalisation for bias in the range of values, extraction of additional parameters (e.g. slope and aspect from elevation maps) and spatial coregistration of the multiple data sets used.

The spatial data sets should not be on the device, because trying to put all of the necessary data onto a smartphone or tablet would require a data storage capacity beyond even modern devices. It would also mean that the developer was sharing data acquired from other sources, generally under restricted licence agreements. This would put these data sets onto devices from which they could be extracted, violating intellectual property. A solution is to use server-side processing, with all data and models stored at a single location and with the minimum of functionality on the device itself.

The concept of server-side processing is one that reduces the device-based processing requirements and gives the developer more options, but does introduce the need for developing a framework for passing data between the field device and the server. It also adds complexity to the processing chain while at the same time

allowing the information derived to be recorded and stored for later use by the developer. One requirement when working with spatial covariates is that the specific site characteristics must be extracted and fed into any integrative model rapidly. This means that sequential reading of large spatial files to find the correct location is inappropriate, and the spatial data must be organised or split to allow more rapid access.

Once the spatial covariates have been parameterised, they can be linked to the image-derived data to generate input values for models developed to predict soil characteristics. Sample number versus parameter count must be appropriate, with large numbers of model parameters and low sample count resulting in what is known as the 'curse of dimensionality'. The distribution curves of all parameter values must be as close to normal as possible, either through sample selection or through parameter normalisation. It is useful to attempt to reduce the number of model parameters by checking for high correlation values between input variables. For real-world soil data sets, there are often missing values and outliers due to analytical error that must be estimated using some imputation approach or removed from the data set, respectively.

7.7 Modelling Frameworks

Strong linear correlations between SCORPAN/image data input parameters and soil characteristics of interest are not common, so sophisticated methods of mapping between inputs and outputs are required. These can include multivariate correlation, decision trees, neural networks, Bayesian statistics, partial least squares or a number of others. There is no single method for developing models with complicated, noisy data sets, and so the approach used is generally decided based on preference, software availability and experience with specific approaches or familiarity with similar work. It is not that the methods themselves are not successful—merely that there is rarely a clear winner in terms of capability. In the case of the James Hutton Institute's app development team, preference is to use neural networks as they are easily implemented, relatively intuitive and sufficiently flexible to be used for almost all soil-related data sets. We have also experimented with partial least squares, multivariate regression and decision trees. These and other approaches may provide an improvement of a few percentage points, but it is difficult to identify when one approach will be better than another.

It is possible to produce good predictive results that turn out to be meaningless due to inadequate model training. One of the most fundamental considerations is the splitting of the available data into training and testing data sets. A simple split into one subset for training and one for testing is valid if done robustly (i.e. the data points in each subset are representative of the full data set while at the same time avoiding the placing of replicates into different subsets). One of the commonly used approaches is k-means cross-validation, in which the data set is split at random into k approximately equal subsets, and k models are developed, each of which is tested

on a separate subset. This has the advantage of using all of the data efficiently while at the same time producing an ensemble of models that can be used together at a later point. A further consideration for additional robustness is the testing of the model using a verification subset that is independently developed and unrelated to the training data set. We have used this approach to validate the model developed for the SOCIT app described later.

7.8 Mobile Phone Apps

7.8.1 Server Processing

The principal coding languages and environments for mobile devices are Java and Android Studio (for Android devices) and Objective-C and Xcode (for Apple devices). Additional coding languages may be used for server-side support of applications; there is a large number of these, and each coder will have their own preference, but they include PHP, which is useful for providing a connection between the app and a server-side database and languages such as Visual Basic or Visual C++, which can be used for running software to generate outputs from server-side data sets.

There are two security considerations: protection of the user and their device and protection of the server. Apps should be designed to use the minimum set of functions required to operate, in order to risk exposing the mobile device to electronic attack. For example, WebViews in Android apps support JavaScript and this can be exploited in malicious attacks. On the server side, the type of security implemented will reflect the application, e.g. databases must be protected against Structured Query Language (SQL) injection attacks, white lists can be used to permit allowed options, and secure passwords can be used and careful database administration, including mirroring and views can all be effective.

Online processing is the obvious choice for rapid field assessment of soils using the approach detailed here, but is not always possible, usually due to poor mobile phone reception. It is possible to send the imagery at a later date, as the location of the user is irrelevant—it is the location stored in the image that is used.

7.8.2 User and Design Requirements

User requirements include stability of the app, response speed and accuracy of the soil parameter estimates given. The issue of ergonomics and usability of apps is complex as the diversity of devices increases. An app must be designed to work on both low- and high-resolution devices with screen sizes from 9 to 25 cm and work with landscape and portrait screen orientations. It requires careful design to ensure legibility and that software buttons are large enough to touch. Also, while tools

exist to help designers cope with multiple devices, there remains considerable effort required in producing graphics (logos, images and textures) for each of the required resolutions.

Design team expertise requirements for developing this kind of system cover four main areas: (1) soil science, particularly in the subfield of soil modelling; (2) data management; (3) programming (in any one of a number of appropriate languages—we have found Python works well, but there are other options); and (4) app interface development.

The intellectual property of all components in an app must be duly acknowledged and also communicated to the user through the End User License Agreement (EULA). The EULA is intended to make explicit the rights which the owner of the app confers on the user and what the user may and may not do with the app. It is written to satisfy the requirements of any relevant legislation and any health and safety implications.

Agreement to the EULA can be enforced from within the app. On current James Hutton Institute apps, the user is presented with the EULA when the app is first run. The user must click an acceptance, or the app will terminate. After acceptance, the EULA is only displayed if the user clicks on a button to show it.

Keeping the app simple in design means that less effort is required in the development and also avoids confusing the user with overambitious design. A simple design is usually most easily reused for later work if other apps are to be developed. Another important rule is to keep it free, as attempting to make profit from an app that uses underlying spatial data sets can cause legal issues.

A number of criteria exist for measuring the success of any app, and information on these can usually be obtained from analytics available through the app provider. These include the number of downloads of the app itself, the number of times it has been used and feedback that has been sent. Additionally, the availability of user-provided data for later use can also be considered a criterion of success.

Licences associated with the data used in any model/app framework must be considered, to ensure that all requirements are being met. Some form of licence must be considered for the model and app itself, to protect the IP of the developers. Server-side protection of the data is a sensitive issue, and the app design should make it impossible for malicious users to use the app to access the data directly. This is also true of the user-derived data, which should be made invisible unless a deliberate decision is made to share this information.

7.9 Examples

7.9.1 SOCIT

The SOCIT app originated through the existing work for QMS (Quality Meat Scotland), on estimating soil organic matter in grassland soils based on spatial

covariates. A software package for desktop PCs was anticipated, before realisation that a smartphone app would be a better option and would provide a link with institutional priorities in relation to digital soil mapping and the use of legacy data for improving our understanding of the soils of Scotland.

The Scottish Soils Database provided data on soil organic matter content and colour from hundreds of sites sampled across Scotland. The majority of data used in the database came from NSIS1, the first National Soil Inventory of Scotland. Parameters used from the database included LOI (loss on ignition), spatial location of the sample site and Munsell colour estimated under field conditions.

The decision to use organic matter content (in reality LOI) rather than soil organic carbon content was made for two reasons: primarily, land managers were found to be more familiar with the concept of 'organic matter content' than with 'carbon content' and stated a preference for using this parameter; secondly, Scottish soils almost all contain very little carbonate (based on the evaluation of the Scottish Soils Database), and so the LOI values could be reasonably assumed to equate to organic matter content. Converting Munsell colour to RGB was carried out using an online conversion table (Boronkay 2013).

Topographical data included elevation, slope, aspect and curvature derived from the 50-m resolution DEM from the UK Ordnance Survey (OS). Land cover data included Land Cover of Scotland 1988 (LCS88) and Land Cover Map 2007 (LCM2007) data sets, reclassified to produce a simple categorisation of ten land cover classes. Soil map information was taken from the 1:250,000 Scottish Soil Map generated by the Macaulay Land Use Research Institute (MLURI). Parent material data were derived from the soil maps. Climate data used included mean monthly temperature and rainfall, from gridded UK Meteorological Office observations between 1971 and 2000.

The app requires rapid access to specific information about sites of interest. To facilitate this, the spatial data were used to produce a set of data strips as separate files, each of which contained the relevant parameter values for a strip of data 100 m wide across the country. These smaller files could then be read quickly to access data relevant for specific locations.

A neural network model was used to estimate soil organic matter content from the various input parameters. This model was kept simple, using the backpropagation error minimisation algorithm and using the k-means cross-validation approach to create a robust consensus model. Validation accuracy measurements for a model trained with all LOI values less than 20 % for agricultural, grassland and forestry soils gave an R^2 value of 0.79, a root mean square error (RMSE) of 1.58 % and a mean absolute error of 1.12 %.

The apps produced by the James Hutton Institute have been designed using the client–server paradigm where the client device is the mobile device and the server is at the James Hutton Institute. The app is designed to enable and guide the user to structure an appropriate request for information and to send that to the server. The server processes the query, runs the required software, generates an output and returns it to the mobile device. The device receives the response for the query and

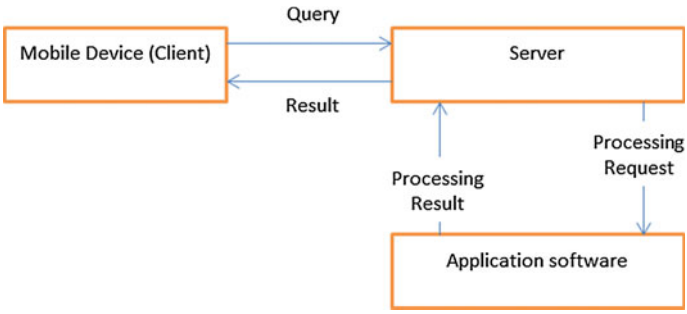

Fig. 7.4 Framework for client–server information flow used in James Hutton Institute apps

interprets and processes it into a form suitable for display on the mobile device (Fig. 7.4).

The main processing thread of the app that responds to inputs from the user must continue while a second, and the so-called asynchronous thread must be created to communicate with the server. There are time delays between the client sending the request for information and receiving the result from the server, and if this process were to remain on the main processing thread, the operating system or the user could interpret the wait as a software error. In the time between sending a request and receiving a response the device must still be usable (e.g. the user might wish to take a phone call), the user must understand that the process is ongoing and the device must be in a state whereby it can receive the response from the server and process it appropriately.

Implementation of the neural network model, coordinate transformation and image analysis scripts was made using Python, as was that of the controlling 'master code' that coordinated the activity of the various subroutines. The app was tested in the field but was hampered occasionally by the lack of signal. It was found that the model was much more accurate (in terms of RMSE and mean absolute error) when developed for soils under agriculture, seminatural grassland and forestry only. Inclusion of organic soils and heathland areas resulted in a model with poorer prediction ability.

Having selected a location, a small inspection hole is dug to a depth sufficient to expose the subsoil, a supplied colour correction card is placed in the hole, and a photograph is taken. The georeferenced photograph is sent to a server for processing, where code uses the colour correction card to determine the colour of the sample in red/green/blue colour space. The neural network model then uses this colour value, along with attributes determined from the geographical location, to estimate organic matter content which is returned to the user.

Getting the colour correction card is relatively easy—you can request it directly using the app, by providing an email address and delivery address. This is useful information for the developers, as it gives an indication of the geographical distribution of people interested in the app. When the address is not in Scotland, we email back to inform the contact that the app does not work where they are.

Interpreting the results is straightforward, as the app provides two numbers—estimates of organic matter and organic carbon in the topsoil. The ratio between these two values is variable but normally lies within the range 1.5–2.0 in Scotland (based on values in the Scottish Soils Database).

7.9.2 Visual Structural Assessment (VSA)

As soil structure affects the ability of roots to penetrate soil and access water and nutrients, it is an important property of soils that is of direct relevance to many land users. A simple, rapid, field-based assessment has been developed that allows users to obtain a measure of structure (Guimaraes et al. 2011).

As the basic principle of the method is that soil is naturally found in some sort of aggregate (although these can be difficult to see where soil compaction has occurred) and that larger soil aggregates can be broken into smaller ones, image analysis techniques can be used to detect and classify aggregates; where the scale can be determined with reference to some standard of known size (see the colour correction card example above) this information can be used to estimate aggregate structure (size and structural strength). Soil textural and structural parameters might be predictable using an app similar to SOCIT system described above, although with different image analysis.

Field imagery was acquired using a number of different smartphones and tablets, including Apple and Android devices. An example of the images acquired is given below (note the different colour correction card, which gives better correction accuracy over the full pixel intensity range). Soil analysis was carried out using wet chemistry for a number of exchangeable cations, LOI for organic matter content, laser diffraction analysis for particle distribution and visual structural assessment in the field for the VSA scoring. Spatial data sets used for the VSA model were the same as those used for the development of the SOCIT app model (Fig. 7.5).

Colour calibration is similar to the SOCIT app, followed by GLCM image texture analysis and the scaling of image texture as explained earlier. Site descriptor values are derived using the data strips developed for SOCIT, to provide model input/output data. The number of input parameters for the model is greater than that for the soil organic matter model, as image texture analysis provides a larger number of parameters than colour. Image colour has been shown to have some impact on the estimation of soil structure, possibly through the detection of organic matter levels. Of the GLCM parameters derived from the imagery, it appears that contrast provides the strongest link and that it is the variance in contrast (measured in horizontal pixel lines across the profile) at different scales that provide an indication of structure.

Fig. 7.5 Example of image acquired of topsoil profile for visual soil assessment model

7.9.3 From Scotland to Europe

The geographical expansion of the SOCIT model concept seemed a natural progression, and one of the data sets to use for this is LUCAS (Tóth et al. 2013). The one disadvantage of this data set is that it does not contain information on soil colour in situ and only has spectroscopy data from dried and milled samples. A proportion of the work carried out so far has involved developing an approach using spectroscopy data to estimate an 'absolute' soil colour that can also be derived in the field.

Soil carbon data were the main target of this work, although the other parameters measured for LUCAS have also been investigated. Early results confirmed that splitting the data into mineral/organic subsets decreased the R^2 values of predictive models but also greatly improved the RMSE and mean error values.

The creation of data 'strips' for EUSOCIT has resulted in the generation of 10 rows of data, each 5° of longitude wide and extending from 37°N to 71°N. The first of these rows begins at 15°W, and the last ends at 35°E. Within each row, represented by a folder, there are 35 subfolders for each degree of latitude, and within each subfolder, there are 1200 files, each of which represents 5 degrees of longitude

and 3 arcseconds in latitude. Each file (of which there are 444,000) contains in sequence 80 environmental parameter values for each of the 6000 3-arcsecond points along the 5° strip.

Now, we can access the environmental descriptors (topography, climate, soil, land cover and geology) for any location with 3 arcseconds (approximately 90 m or less) precision, with a search time of no more than 3 s. This information can then be formatted and used as input data for the EUSOCIT model to provide an estimate of soil organic matter.

The other information that is needed for EUSOCIT to work is soil colour. As LUCAS does not contain soil field colour, we have to rely on the spectroscopy data. For this, the visible range values have been extracted for each sample point and converted to RGB values by averaging over the relevant wavelength ranges.

First indications of predictive accuracy for the EUSOCIT model trained with different partitioning give an R^2 value of 0.82 and a mean absolute error (MAE) value of 2.3 % when using all data, and lower R^2 values of 0.57–0.65 and MAE values of 0.9–1.2 % (6.3 % for organic soils) when the data are split between different land cover types. This indicates that using several models rather than one, with each model linked to a specific land cover, will produce more robust prediction accuracy. The use of spatial covariates definitely improves model performance over the use of colour alone.

7.9.4 Potential Applications

Soil colour has been shown to be related to a number of soil properties (e.g. Aitkenhead et al. 2013; Moritsuka et al. 2014). It should be possible to devise a series of apps which would give the user a quick 'health check' of their soil against a common set of health or quality indicators (e.g. organic matter content, pH, texture, structure, available water capacity). Additionally, while some of the underlying data sets used by the neural network model for national-scale predictions are of a coarse resolution (i.e. >5 km pixel size), where higher-resolution data sets exist for a specific geographical area, there is potential to use this approach in applications such as precision agriculture.

Extension from mobile devices to custom low-cost sensors is a possible area of development. The type of information would be the same, but it would allow more rugged and field-capable sensors to be used.

Free and rapid estimation of soil characteristics in the field fits well with citizen science activities, as it provides the user with information while at the same time automatically recording estimates on the process server. The SOCIT app provides a template for future work in this area. Caution about estimation versus direct measurement is an issue that must be made clear to the potential user of these data.

Upload of data from citizen scientists/field surveyors for Web mapping services is an option. With appropriate consideration of data protection issues, it is possible to include Web mapping services on standard app implementations. ESRI has

produced a development kit for both platforms and this makes the coding of apps with WMS and other mapping functions more straightforward. An existing online presence giving an indication of what this could look like is MySoil, produced by the British Geological Survey (BGS) under the UK Soil Observatory umbrella (http://www.ukso.org/home.html).

7.10 Discussion

Points of advice to focus on during the development of a model/app system of the kind described here include the following:

- Keep the team small and focused on the bare bones of the functionality in the first instance.
- Multidisciplinary work is important for this kind of project—scientists, software developers and data managers are required.
- Keep your communications and legal expert colleagues close—they can save a lot of effort and prevent you from reinventing what already exists.
- Conversely, keep your communications and legal teams at arms' length where required—their instinct may be to 'overbrand' the outputs and make things more legally complex than they really need to be.
- The apps that are produced must be at all times simple, clear to understand and free to use.
- The End User License Agreement is vitally important but must not intrude on the user's experience of the app.

7.11 Conclusions

What can be achieved using this suite of approaches? Direct estimation of soil characteristics in the field is possible for some soil properties such as organic matter content, texture, structure, pH, nitrogen, base saturation and some elements (Ca, Mg, Fe, Al). Our work has shown that these soil properties can be estimated with accuracy levels suitable for soil monitoring requirements (ongoing). Potassium and phosphorus remain difficult (for us, using the methods described here) to estimate from colour and site descriptors, as do most of the heavier elements that have been measured within soil samples listed in the Scottish Soils Database. This work is ongoing, and the links between model inputs and outputs in these cases need to be further investigated.

Acknowledgments The authors would like to thank Willie Towers of the James Hutton Institute for his assistance in preparing this work.

References

Aitkenhead MJ (2013) The E-SMART project. http://www.hutton.ac.uk/research/groups/information-and-computational-sciences/esmart

Aitkenhead MJ, Coull M, Towers W, Hudson G, Black HIJ (2013) Prediction of soil characteristics and colour using data from the National Soils Inventory of Scotland. Geoderma 200:99–107. doi:10.1016/j.geoderma.2013.02.013

Bogoch II, Andrews JR, Speich B, Utzinger J, Ame SM, Ali SM, Keiser J (2013) Short report: mobile phone microscopy for the diagnosis of soil-transmitted Helminth infections: a proof-of-concept study. Am J Trop Med Hyg 88(4):626–629

Boronkay G (2013). Colour Conversion Centre. http://ccc.orgfree.com/

Chung S-O, Joh G-H (2012) Effect of light illumination and camera moving speed on soil image quality. J Agric Sci 39(3):407–412. doi:10.7744/cnujas.2012.39.3.407

El Kaoutit H, Estevez P, Garcia FC, Serna F, Garcia JM (2013) Sub-ppm quantification of Hg(II) in aqueous media using both the naked eye and digital information from pictures of a colorimetric sensory polymer membrane taken with the digital camera of a conventional mobile phone. Anal Meth 5(1):54–58

Garrido-Novell C, Perez-Martin D, Amigo JM, Fernandez-Novales J, Guerrero JE, Garrido-Varo A (2012) Grading and color evolution of apples using RGB and hyperspectral imaging vision cameras. J Food Eng 113(2):281–288. doi:10.1016/j.jfoodeng.2012.05.038

Gomez-Robledo L, Lopez-Ruiz N, Melgosa M, Palma AJ, Capitan-Vallvey LF, Sanchez-Maranon M (2013) Using the mobile phone as Munsell soil-colour sensor: an experiment under controlled illumination conditions. Comput Electron Agric 99:200–208. doi:10.1016/j.compag.2013.10.002

Gregory SDL, Lauzon JD, O'Halloran IP, Heck RJ (2006) Predicting soil organic matter content in southwestern Ontario fields using imagery from high-resolution digital cameras. Can J Soil Sci 86(3):573–584

Guimaraes RML, Ball BC, Tormena CA (2011) Improvements in the visual evaluation of soil structure. Soil Use Manag 27(3):395–403

Gunal H, Ersahin S, Yetgin B, Kutlu T (2008) Use of chromameter-measured color parameters in estimating color-related soil variables. Commun Soil Sci Plant Anal 39(5–6):726–740. doi:10.1080/00103620701879422

Humphrey CP, O'Driscoll MA (2011) Evaluation of soil colors as indicators of the seasonal high water table in coastal North Carolina. International Journal of Soil Science 6(2):103–113

Ibanez-Asensio S, Marques-Mateu A, Moreno-Ramon H, Balasch S (2013) Statistical relationships between soil colour and soil attributes in semiarid areas. Biosyst Eng 116(2):120–129. doi:10.1016/j.biosystemseng.2013.07.013

Jenny H (1994) Factors of Soil formation. A system of quantitative pedology. Dover Press, New York Reprint of the 1941 McGraw-Hill publication

Levin N, Ben-Dor E, Singer A (2005) A digital camera as a tool to measure colour indices and related properties of sandy soils in semi-arid environments. Int J Remote Sens 26(24):5475–5492. doi:10.1080/01431160500099444

Liles GC, Beaudette DE, O'Geen AT, Horwath WR (2013) Developing predictive soil C models for soils using quantitative color measurements. Soil Sci Soc Am J 77(6):2173–2181. doi:10.2136/sssaj2013.02.0057

Mausel PW, Wilson JS, Venugopal G (1997) The use of high spatial resolution multispectral digital camera data in soil applications. Videography and Color Photography Resour Assess. 245–245

McBratney AB, Mendonça Santos ML, Minasny B (2003) On digital soil mapping. Geoderma 117(1–2):3–52

Moonrungsee N, Somkid P, Jaroon J (2015) Colorimetric analyser based on mobile phone camera for determination of available phosphorus in soil. Talanta 136:204–209

Moritsuka N, Matsuoka K, Katsura K, Sano S, Yanai J (2014) Soil color analysis for statistically estimating total carbon, total nitrogen and active iron contents in Japanese agricultural soils. Soil Sci Plant Nutr 60(4):475–485

Rossel RAV, Fouad Y, Walter C (2008) Using a digital camera to measure soil organic carbon and iron contents. Biosyst Eng 100(2):149–159. doi:10.1016/j.biosystemseng.2008.02.007

Taghizadeh M, Gowen AA, O'Donnell CP (2011) Comparison of hyperspectral imaging with conventional RGB imaging for quality evaluation of Agaricus bisporus mushrooms. Biosyst Eng 108(2):191–194

Tóth G, Jones A, Montanarella L (2013) LUCAS Topsoil Survey methodology, data and results. JRC Technical Report EUR 26102. Publications Office of the European Union, Luxembourg. DOI: 10.2788/97922

Zhao T-J, Sakai K, Higashi T, Komatsuzaki M (2012) Assessing soil organic carbon using portable hyper-spectral camera in Andisols. J Agric Sci Appl 1(4):131–137. doi:10.14511/jasa.2012.010407

Part II
Soil Profile Imaging

Chapter 8
Advances Towards Quantitative Assessments of Soil Profile Properties

Pierre Roudier, Andrew Manderson and Carolyn Hedley

Abstract In this paper, we present some advances in digital soil morphometrics techniques in New Zealand. A soil monolith extractor has been developed in house and facilitates the application of digital soil morphometrics techniques. Three distinct soil profiles have been sampled using the monolith extractor to test new ways to collect information from the soil profile. Digital images have been collected on these soil monoliths and calibrated using a set of reference colour chips. The spectral resolution of these images has been enhanced by combining the spatial resolution of the CCD images (1 mm) with the spectral resolution and range of an ASD FieldSpec 3 visible–NIR spectrometer (1 nm between 350 and 2500 nm). A processing chain combining image processing methods such as principal component (PC) analysis and image segmentation has been developed to support the delineation of soil horizons and collect information about the soil structure.

Keywords Digital soil morphometrics · Quantitative pedology · Regression-kriging · Sensor fusion · Image segmentation · Hierarchical classification

8.1 Introduction

The soil profile has been the key support for soil observation since the inception of pedology. A soil profile is an exposed vertical section of a soil from the ground surface down to the underlying parent material. For practical reasons, soil profiles are usually examined in situ by excavating a large hole to accommodate the pedologist making close visual inspection of the profile surface. The process can be physically demanding and time-consuming. Traditionally, pedologists would look at the soil profile and use their senses—sight, touch, hear—to infer properties about the soil that is being observed. Some of the information collected during the soil

P. Roudier (✉) · A. Manderson · C. Hedley
Landcare Research, Private Bag 11052, Manawatu Mail Centre,
Palmerston North 4442, New Zealand
e-mail: roudierp@landcareresearch.co.nz

A.E. Hartemink and B. Minasny (eds.), *Digital Soil Morphometrics*,
Progress in Soil Science, DOI 10.1007/978-3-319-28295-4_8

profile may be subjective, and the emergence of a wide range of infield technologies is opening opportunities to update the way soil profiles are observed and described. Digital soil morphometrics, the framework leveraging these developments, aims for a more quantitative and objective way to collect data, derive information, and assess properties from the soil profile (Hartemink and Minasny 2014).

A diverse range of dedicated proximal soil sensing techniques has been tested on soil profiles in the field and allows to estimate many of its properties beyond the visible range of the spectrum (Hartemink and Minasny 2014). Examples include X-ray fluorescence (XRF, Weindorf et al. 2012) and visible/near-infrared (Vis-NIR) spectroscopy (Ben-Dor et al. 2008; Roudier et al. 2015) and imaging (Steffens and Buddenbaum 2013). RGB data have been captured using simpler, cheaper devices, such as a mid-range digital camera (Aitkenhead et al. 2015), or a chromameter (Liles et al. 2013). Other authors have used digital photography (O'Donnell et al. 2010). The high spatial resolution of the images opens opportunity beyond the pixel-wise classification tools and analyses the shape of elements sensed from the soil profile (Anderson and Bouma 1973).

The in situ examination of the soil profile limits the choice of instrumentation because of the lack of control over ambient conditions (such as lightning and soil moisture conditions) and the amount of time available for controlled measurements. Soil monoliths are extracted whole profiles for transport and subsequent preparation, examination, and measurement under controlled conditions. Traditional box-fitting techniques (Berger and Muckenhirn 1945; Brown 1963) are time-consuming to implement, and modern hollow flight auguring techniques require heavy machinery and capture a small profile width (Haddad et al. 2009).

The aim of this study was to develop a portable, low cost, and comparatively quicker system of extracting and preparing soil profile monoliths for quantitative morphometric analysis. The second aim of the study was to investigate ways to derive quantitative information from the soil profile. Digital images were collected on these soil monoliths and calibrated using a set of reference colour chips. The spectral resolution of these images has been enhanced by combining the spatial resolution of the images with the spectral resolution of Vis–NIR spectroscopy. From these enhanced images, a series of spectral and morphological metrics were derived and classified. The results were compared to a traditional, qualitative analysis of the profile.

8.2 Material and Methods

8.2.1 Sampling Sites

Monolith samples were collected from three permanent pasture sites. The first site, "Kairanga", is located within a pastoral beef and horse farming property (WGS84: −40.36242, 175.46558), on the edge of a large, low-lying, alluvial deposition basin that is subject to occasional flooding and ponding. The soil sampled at this site was

classified as a Fluvic Gleysol (New Zealand Soil Classification: Typic Recent Gley Soil). Elevation is 10.9 m above sea level; annual rainfall is 860 mm/year, while air temperature averages 13.2 °C. The second site, "Ohakea", is located within an extensive Aeolian sand country belt that runs along the lower and western side of New Zealand's North Island (WGS84: −40.28186, 175.30732). This soil profile is a Gleyic Luvisol (New Zealand Soil Classification: Fragic Perch-gley Pallic Soil), which was formed from quartzo-feldspathic loess overlying more than 2 m of tephric material. Land use is predominantly sheep and beef grazing. Altitude is 27 m above sea level, the average rainfall is 900 mm/year, and annual air temperature is 13.0 °C. The third site, "Manawatu", is located on a sheep-grazed pasture located within the immediate levee forming area of the Manawatu River (WGS84: −40.38320, 175.60639). The soil is a well-drained Eutric Fluvisol (New Zealand Soil Classification: Weathered Fluvial Recent Soil) formed from historical flood deposition of sands and silts. The altitude is 27.7 m above sea level, with annual rainfall and air temperatures averaging 930 mm and 13.4 °C, respectively.

8.3 Extraction of Soil Monoliths

8.3.1 Monolith Sampling Frame

A soil monolith sampling tool was developed to speed up access to the soil profile and facilitate the application of soil morphometrics techniques. The monolith sampling frame was constructed from high-tensile 2-mm stainless steel folded and welded to produce a box with the size of 1200 × 300 × 50 mm (Fig. 8.1). The cutting edge was bevelled inwards to minimise the risk of outwards splaying when the extractor is put under load. A steel frame (20 mm × 20 mm high-tensile boxing tube) was constructed and welded to the back to provide reinforcing. Shallow box designs would be more suitable for dense soils, while deeper designs would be more suitable for poorly cohesive soils.

8.3.2 Extraction

Preliminary, site examinations were undertaken with a Dutch auger to identify a suitable and representative profile for extraction. Vegetation was trimmed to ground level, and a 400 × 250 × 1300 mm hole was dug to provide sufficient clearance to insert both the sampling frame and two 2-tonne capacity scissor jacks (positioned near the top and base of the hole). The low bulk density soils required extra bracing for the jacks. Each jack was opened in alternating stages, and the sampling frame was gradually cut into the profile face under load. When full cutting depth was achieved, the jacks were unwound to a state that provides support but without compressive load. A second hole was excavated at the front of the sampling frame,

Fig. 8.1 Soil monolith sampling tool

Fig. 8.2 Soil monolith sampling tool in place and ready to be extracted

the dimensions of which depend on soil characteristics. For easily dug soils (e.g. low bulk density, low percentage or absence of gravels, absence of impeding horizons), this may be a spade's width, but soils with dense or compacted subsoils required a larger soil pit. In both cases, the pit was carefully excavated to produce a profile face that was 30–50 mm of the monolith sampling frame (Fig. 8.2). Starting

at the base, the sides of the profile were carefully trimmed and cut. Eventually, the frame was then tilted and extracted from the hole.

8.3.3 Surface Preparation

Soil profile monoliths are often collected for display purposes, and the surface is prepared and preserved in a manner that highlights aggregate structure and pattern. Our purpose required a flat and clean surface suitable for image and spectral analysis. This proved difficult as manual techniques (knives, cutting wire, and saws) were labour-intensive and produced variable levels of quality. Mechanical approaches were considered (freezing and sawing, diamond saws, horizontal band saws, ultrasonic knives, water jet cutters, thickness planers), but these were discarded as too expensive, unavailable, or having an unknown risk of failure relative to the level of development required. Our solution was a modified high-speed router fitted with a 30-mm tungsten carbide bit, implemented across the profile using a fixed height jig. This produced a consistently flat surface without the imperfections experienced using manual techniques (tearing and pocking associated with concretions, roots, differences in density and consistence, and complete dislodgement of entire peds especially in topsoils). Light smearing and small concentric ridges resulted on horizons with a higher percentage of clay, but this was manually removed with cutting spatulas. As a final step, each profile was tilted and lightly washed with a mist spray. This removed any fine particles and remnant smearing (especially in regard to high chroma mottles and soft <1 mm concretions), improved colour prominence, and for two of the soils improved the definition of horizons with contrasting textures (water soaked into coarse-textured horizons making them wetter, darker, and more distinctive). Horizon boundaries were identified and recorded and compared with the spectral and image analysis.

8.4 Data Collection

8.4.1 Photography

Each profile was photographed (RAW format) under natural daylight conditions using a DSLR camera (Canon 1200D, 18 MP) with an 18–55 mm lens (Canon EF-S 18–55 mm f/3.5-5.6 III). An X-Rite ColorChecker Passport (X-Rite, 2015) was positioned and captured as part of each image. Profiles were mounted on a bench and tilted to receive full exposure from direct midday sunlight. RAW images were converted to digital negative format (DNG), and colour correction profiles were constructed using Adobe DNG Profile Editor (Adobe Systems, 2012). White balance correction and colour profile assignment were undertaken in Camera Raw

(Adobe Systems, 2015), and the results were exported as 16-bit TIFF images in the system RGB colour space (sRGB). Each image was then georeferenced in Cartesian coordinate space (with the origin set as the bottom left corner of the profile) and clipped to the extents of the sampling frame. The resolution of the image (usually around 0.3 mm) was resampled to 1 mm using bilinear interpolation.

8.4.2 Spectroscopy

Spectra Collection

For each soil profile, 120 soil spectra were collected on a 50 × 50 mm grid by an ASD FieldSpec 3 spectrometer (formerly ASD, Inc., now PANalytical Boulder, Boulder, Colorado, USA) using the visible and near-infrared ranges. The spectral reflectance of the surface of the washed soil monolith was measured between 350 and 2500 nm at a resolution of 1 nm. The spectra collection was done using the ASD contact probe fitted with the soil light bulb, whose field of view is a 10-mm-radius disc. The sensor was optimised and calibrated with a Spectralon white reference panel every 10 acquisitions. Each spectrum was an average of 30 acquisitions (50 for the white reference) calculated by the IndicoPro acquisition software.

Preprocessing

The raw reflectance data were exported as text files using IndicoPro and further processed using the R statistical environment (R Core Team 2015). First, the reflectance values (R) have been converted into absorbance (A) using the $A = 1/\log(R)$ formula. Then, additive noise has been removed by the multiple scatter correction (MSC). Finally, the spectra were downsampled by a factor of 10 for further data reduction.

Principal Component Analysis

For each soil profile, a principal component analysis (PCA) of the preprocessed spectra was used to analyse the data set. The PCA was computed in R (R Core Team 2015) and by singular value decomposition. This operation reduced the high dimensionality and collinearity of the spectral data and compressed its variance into a limited number of orthogonal principal components (PCs). The variance captured by the first principal component (PC1) was largest, and subsequent principal components (PC2-PCn) account for decreasingly smaller part of the data set's overall variance. In this study, the first three PCs were retained.

8.5 Fusion of Soil Profile Image and Observations

The data collected by spectroscopy and the digital image have different supports: the Vis–NIR spectrometer was captured at a relatively coarse scale data, whereas the sRGB image captures data at a fine spatial resolution. Sensor fusion is a technique of quantitative image analysis that merges data collected by different sensors to improve the data. In particular, downscaling (or sharpening) is an image fusion process that combines the spatial resolution of a sensor with the spectral resolution of another sensor. This is routinely used in remote sensing, where the coarse resolution multi-spectral bands are resampled using a fine-resolution panchromatic band. In this study, the soil profile image was used to improve the spatial resolution of the Vis–NIR data. Regression-kriging was used as the fusion method (Odeh et al. 1995). Using regression-kriging for image fusion offers advantages such as avoiding spectral distortion (Meng et al. 2010). In order to improve the performance of the regression step, the sRGB image was converted to the CIE Lab colour space (Liles et al. 2013).

8.5.1 Regression

The principal components of the spectra were predicted from the image of the soil monolith. To take into account the spatial footprint of the sensors, and the uncertainty of positioning of the probe, CIE Lab values were averaged over a disc of radius 6 mm centred on the sampling grid used for the vis–NIR spectra collection. The random forest regression method was used in the first stage of the regression-kriging as implemented in the randomForest package (Liaw and Wiener 2002). The model was calibrated using all the available observations and using a repeated tenfold cross-validation with 30 repeats using the caret package (Kuhn 2015) to assess its performance. The number of trees in the forest was set to 500, and the number of variables randomly sampled as candidates at each split of the random forest was determined so to minimise the cross-validated root-mean-square error (RMSE).

8.5.2 Kriging of the Residuals

The autocorrelation of the residuals from the regression step was analysed using gstat (Pebesma 2004). Three variogram models were tested: spherical, exponential, and linear. The model minimising the sum of squared errors was chosen and used to interpolate the residuals onto the 1-mm grid of the soil profile image using ordinary kriging. The interpolated residuals were then combined with the original predictions from the regression model.

8.6 Object-Oriented Analysis

8.6.1 Segmentation

The sharpened PC1, PC2, and PC3 images were collated in GRASS GIS (Neteler et al. 2012) for image segmentation. Segmentation is the process that groups pixels into unique and coherent objects (also called segments). Unlike classification, the segmentation process produces contiguous objects and allows for analysis of the morphology of the delineated segments (Roudier et al. 2008).

In this study, we used a region growing and merging segmentation method (Bins et al. 1996), as implemented in the i.segment module of GRASS GIS. All pixels are considered as initial segments. Then, the similarity between any given segment and each of its neighbours is computed using the Euclidean distance. Two segments are merged if the similarity distance is smaller than to any other neighbour, and if the similarity distance is lower than the threshold given by the user (in this study, we chose a threshold of 0.05). This process is run iteratively. Finally, segments smaller than the minimum size are merged with their most similar neighbour (in this study, we chose a minimum size of 100 mm^2). For each segment delineated by the segmentation routine, the average and the standard deviation of PC1, PC2, and PC3 were computed. Additionally, the morphology of the segments was assessed using a range of indicators available in the v.to.db module in GRASS GIS: area (A), perimeter (P), compactness, computed as $C = P/(2 \times \sqrt{\pi \times A})$, and fractal dimension, computed as $\mathrm{FD} = 2 \times \log(P)/\log(A)$.

8.6.2 Hierarchical Classification

The segments were classified using an agglomerative hierarchical classification of their attributes (average of PC1, PC2, PC3 and standard deviation of PC1, PC2, PC3, compactness of the segments). The method used was the flexible UPGMA (Belbin et al. 1992) using a dissimilarity matrix computed using the Gower distance. These steps were implemented using the cluster package for *R* (Maechler et al. 2015).

8.7 Results and Discussion

8.7.1 Profile Observations

Soil Profile Images

The three soil profile images collected on the monoliths are shown in Fig. 8.3. The soil sampled at the Kairanga site (Gleysol) exhibits clear depositional layering of

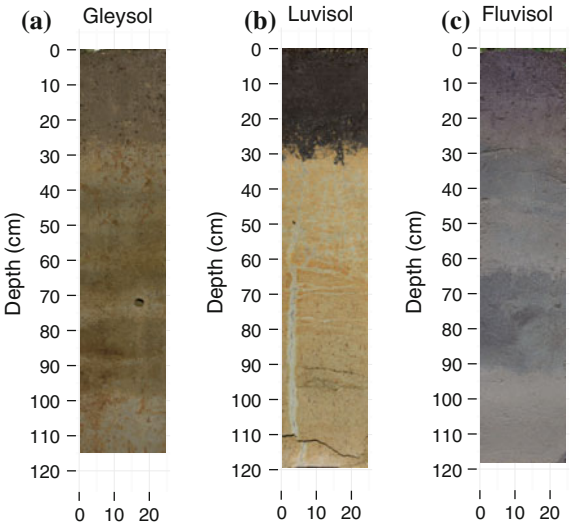

Fig. 8.3 sRGB images collected on each of the three soil monoliths

sands and silts from historical flood and deposition events. The Ohakea profile (Luvisol) has fragic and humic characteristics and exhibits distinctive net reticulate patterns in the subsoil. It is suspected the site represents a former surface that has been exhumed from surrounding Aeolian sands as the result of dune mobilisation activity approximately 500–1000 years ago. Finally, the soil profile sampled at the Manawatu site (Fluvisol) presents layering patterns due to a succession of flood depositions from the nearby river.

8.8 Principal Component Analysis of the Vis–NIR Spectra

The PCA of the spectra collected on each of the three soil monoliths allowed to reduce the dimensionality of the Vis–NIR data sets significantly (Table 8.1). For each profile, the first principal component (PC) accounted for more than 75 % of the total variance. For the remaining part of the analysis, we restrained the spectral data sets to the first three PCs. Cumulatively, these represented 97.4, 99.5, and 99.1 % of the total variance of the Vis–NIR data sets. The summary statistics of PC1, PC2, and PC3 are also reported in Table 8.2.

Table 8.1 Proportion of variance (%) captured by the first 3 principal components (PC) of the spectra collected on each soil monolith

Profile	PC1	PC2	PC3	Cumulative
Gleysol	77.80	14.63	4.98	97.41
Luvisol	96.55	2.25	0.74	99.54
Fluvisol	84.13	13.75	1.22	99.09

The cumulative proportion of the variance (%) is also reported

Table 8.2 Summary statistics of PC1, PC2, and PC3

Profile	Attribute	Min.	Mean	Median	Max.	SD	Skewness	Kurtosis
Gleysol	PC1	−1.84	0	−0.05	2.07	0.79	0.34	−0.11
	PC2	−0.90	0	0.14	0.48	0.34	−0.94	−0.46
	PC3	−0.42	0	−0.03	0.83	0.20	0.98	1.95
Luvisol	PC1	−8.82	0	1.13	4.60	3.31	−1.15	0.06
	PC2	−0.89	0	−0.12	1.66	0.50	0.71	0.39
	PC3	−0.78	0	0.01	0.81	0.29	0.05	0.47
Fluvisol	PC1	−2.49	0	−0.15	2.42	1.24	0.16	−0.97
	PC2	−1.40	0	0.21	0.51	0.50	−1.40	0.51
	PC3	−0.30	0	−0.01	0.48	0.15	0.63	0.90

The first PC of each soil profile is plotted (Fig. 8.4), and the PCA scores are plotted in Fig. 8.5. On the Gleysol profile, PC1 shows a succession of layers, which is linked with the deposition processes involved in the pedogenesis (Fig. 8.4), while PC2 is discriminating the topsoil from the subsoil (Fig. 8.5). On the Luvisol profile, PC1 is discriminating strongly between the topsoil and the subsoil (Figs. 8.4 and 8.5). For the Fluvisol profile, PC1 is discriminating the lowest part of the soil profile (below 900 mm, Figs. 8.4 and 8.5), while PC2 is discriminating the topsoil from the subsoil (Fig. 8.5).

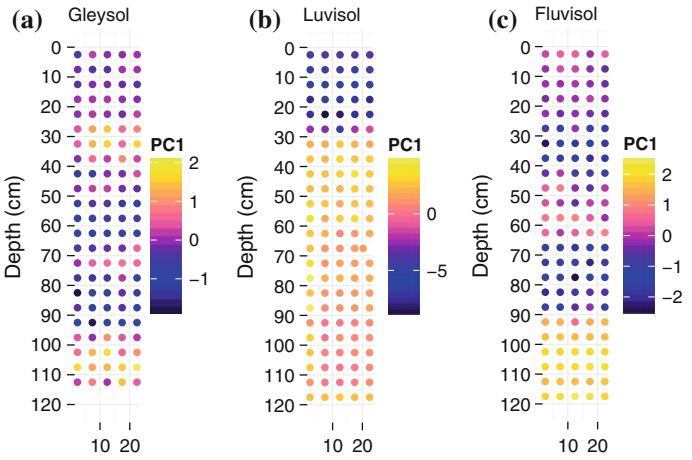

Fig. 8.4 First principal component values (PC1) of the Vis–NIR spectra collected on each soil profile

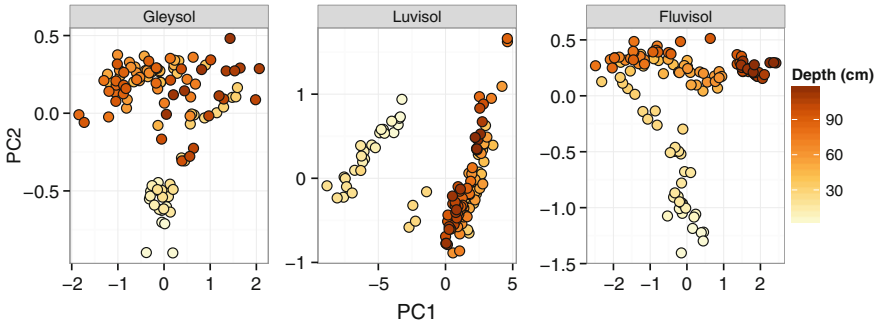

Fig. 8.5 Distribution of the scores of the PCA analysis for each soil profile in the space defined by the first two principal components. Soil depth is indicated by the colour scale

8.9 Sensor Fusion

8.9.1 Prediction of Vis–NIR Principal Components from the Soil Profile Image

The results of the regression step of the sensor fusion procedure are shown in Table 8.3. The R^2 values of the regression of PC1, PC2, and PC3 from the CIE Lab bands of the soil profile image range from 0.35 to 0.95 (average: 0.68, standard deviation: 0.22). As the first PC of the spectra focuses on most of the variance, it is important to note the performance of the regression of PC1 for each profile: 0.56 for the Gleysol profile, 0.95 for the Luvisol profile, and 0.81 for the Fluvisol profile. In contrast to PC1, the performance of the regression of PC3 was less successful: 0.43 for the Gleysol profile, 0.57 for the Luvisol profile, and 0.35 for the Fluvisol profile. However, this variable contributed marginally to the overall variance expressed in the initial Vis–NIR data set.

Table 8.3 Repeated tenfold cross-validation results of the prediction of PC1, PC2, and PC3 for the three soil monoliths

Profile	Attributes	RMSE	R^2	CCC	Bias
Gleysol	PC1	0.54	0.56	0.66	0.00
	PC2	0.15	0.82	0.88	0.00
	PC3	0.15	0.43	0.54	0.00
Luvisol	PC1	0.76	0.95	0.97	−0.04
	PC2	0.29	0.69	0.78	0.00
	PC3	0.19	0.57	0.66	0.00
Fluvisol	PC1	0.54	0.81	0.88	−0.01
	PC2	0.13	0.93	0.95	0.01
	PC3	0.13	0.35	0.42	0.00

Table 8.4 Variogram models fitted on the residuals of the PC1, PC2, and PC3 regression results for the three soil monoliths

Profile	Attributes	Model	Nugget	Sill	Range (mm)
Gleysol	PC1	Sph	0.0398	0.0310	183.4041
	PC2	Sph	0.0018	0.0026	101.9186
	PC3	Exp	0.0050	0.0006	506.0284
Luvisol	PC1	Sph	0.0939	0.0333	285.4767
	PC2	Sph	0.0117	0.0066	202.6782
	PC3	Sph	0.0033	0.0055	130.3721
Fluvisol	PC1	Sph	0.0420	0.0335	285.0122
	PC2	Sph	0.0015	0.0016	107.2548
	PC3	Sph	0.0026	0.0019	470.4335

8.9.2 Kriging of the Residuals

The variogram models used in the kriging of the residuals from the regression step are given in Table 8.4. Most models showed some spatial structure in the residuals. An exception is the residuals from the PC3 model on the Gleysol profile, which shows mainly nugget effect.

8.9.3 False Colour Composite Visualisation

For each soil profile, the three principal components retained in the analysis are conveying a different aspect of the variance. It is possible to visualise PC1, PC2, and PC3 by using a false colour composite (FCC), i.e. affecting PC1, PC2, and PC3 to the red, green, and blue channel of a RGB image. The FCC for the Gleysol, Luvisol, and Fluvisol profiles is presented in Fig. 8.6.

8.10 Image Segmentation

The output of the segmentation of the PC1, PC2, and PC3 images is presented in Figs. 8.7 and 8.8. The segmentation created 718 segments for the Gleysol profile, 949 segments for the Luvisol profile, and 683 segments for the Fluvisol profile. Figure 8.6 shows the shape of the objects delineated by the segmentation algorithm, along with a FCC visualisation of the average PC1, PC2, and PC3 in each segments. The horizon boundaries assessed by the pedologist have been added to these visualisations.

A visual inspection of the segments reveals that these are variable in shape and in size (Fig. 8.7). This can be observed in all three profiles, but particularly in the Fluvisol profile. On this alluvial soil, the layering effects seem to impact the area and shape of the segments. Between 65 and 90 cm, the difference between the right and the left side of the horizon seems to be detected as the area of the segments is

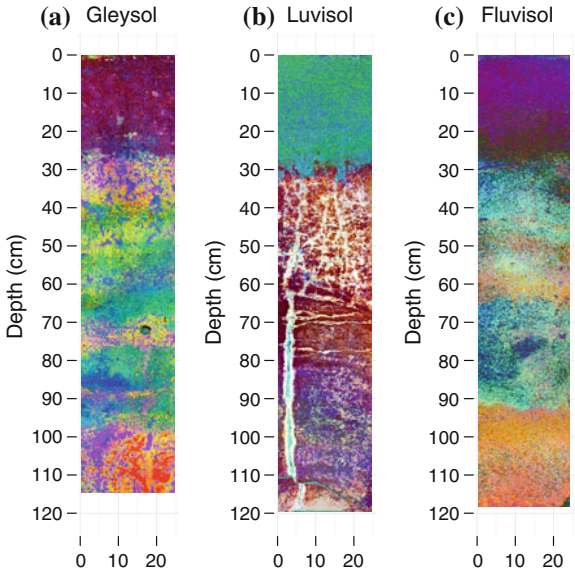

Fig. 8.6 False colour composite visualisations of PC1, PC2, and PC3 for the three soil profiles

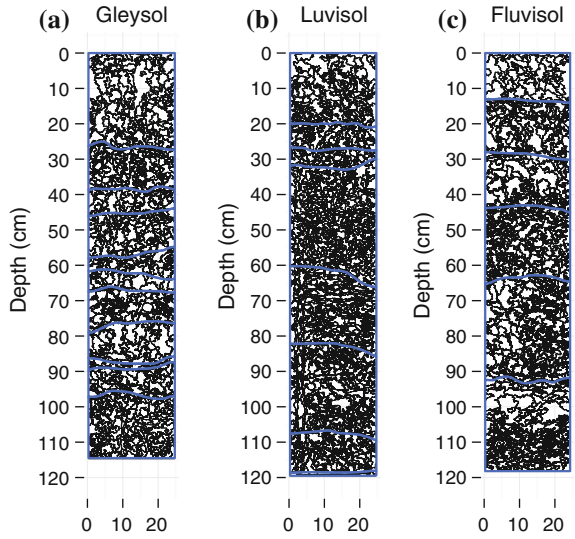

Fig. 8.7 Results of the segmentation of the principal component images for each soil profile. The *blue lines* show the horizon boundaries drawn by the pedologist on each soil profile

smaller on the right-hand side. This corresponds to a difference in texture that was also noted by the pedologist on the monolith inspection. We also found that coarse-textured horizons (sand and loamy sand) appear to result in relatively larger segments (especially horizons 3 and 5 for the Fluvisol profile).

Figure 8.8 combines the segmentation results with the sharpened data, by populating each segment with the average PC1, PC2, and PC3 values. By doing so,

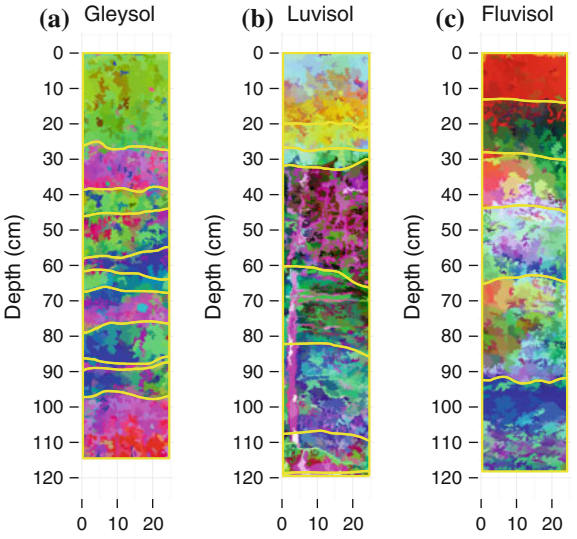

Fig. 8.8 False colour composite of the average PC1, PC2, and PC3 values in each segment. The *yellow lines* show the horizon boundaries drawn by the pedologist on each soil profile

the speckle effects of the sharpened image are reduced and highlight some morphological effects detected by the image segmentation. The visualisation corresponds with the horizons delineated by the pedologist. The PC segments appear to provide a more objective and precise basis for assigning boundaries when horizon transitions are diffuse or mixed. While some of the horizon boundaries are distinct (A/B horizon boundary of the Gleysol profile), others are transitions and not so sharp. There is also evidence that the data recorded by the PC offer further detail not captured by the pedologist, especially in regard to additional differentiation of topsoil horizons (Luvisol and Gleysol), transitional A/B horizons (Fluvisol), and possibly new horizons (e.g. at the base of Fluvisol).

8.11 Variations of the Radiometric and Morphometric Indices

Figure 8.8 shows that the FCC visualisations are helpful in the analysis of a soil profile. They also indicate variation in the horizons. Figure 8.9 shows the variations in radiometry and morphology of the segments with depth for each profile. The mean, along with the spread distribution around that central tendency, is plotted for PC1, PC2, PC3, compactness, and fractal dimension. The plots show variation of the indices along the soil profiles, and the standard deviation of these indices is variable with depth. In particular, the Luvisol profile is showing more variations at depth than the two other profiles. This can be explained by the vertical veining pattern that is present in the subsoil (Figs. 8.3 and 8.8).

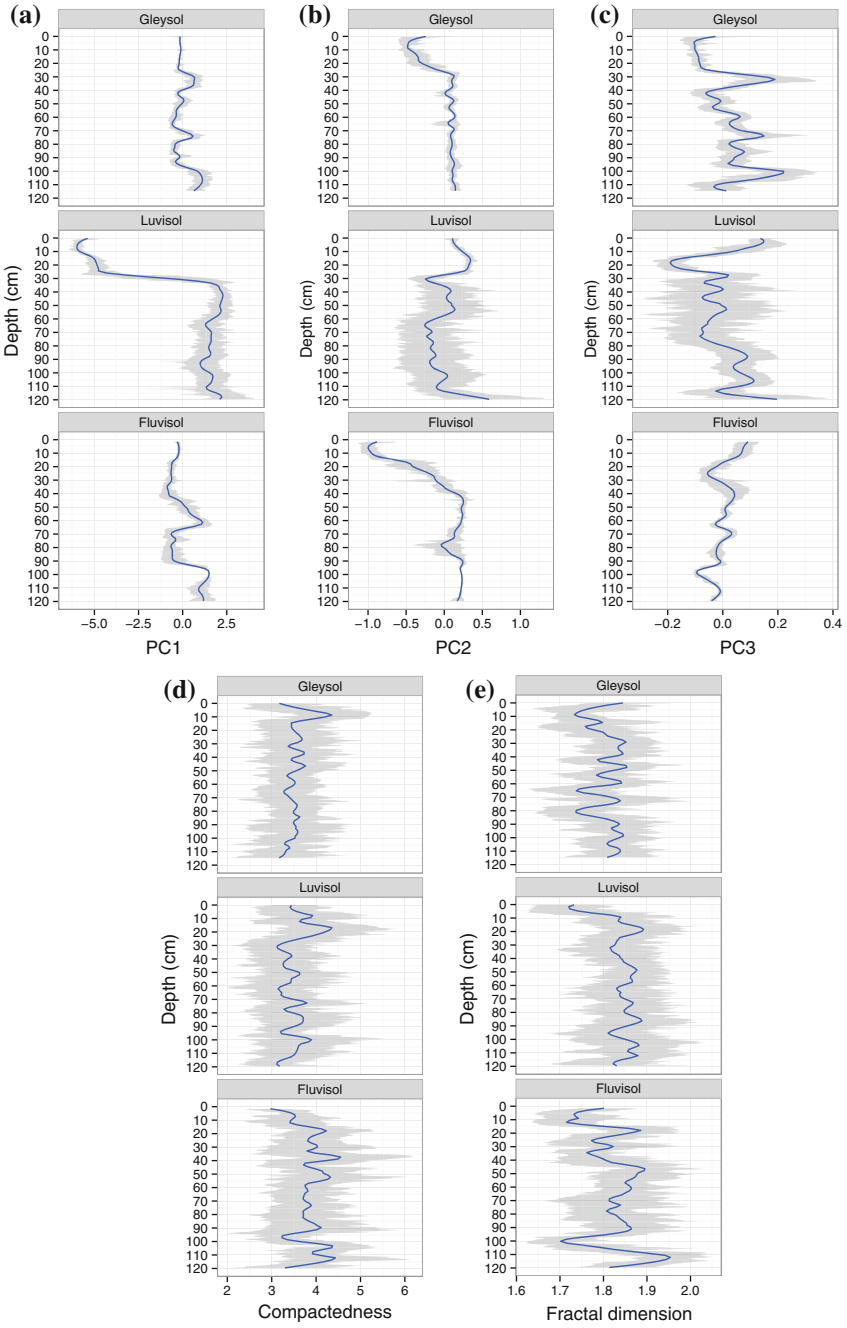

Fig. 8.9 Evolution of the PCs and fractal dimension of segments with depth. The *blue line* shows loess smoothing of the values. The *grey ribbon* indicates the mean ±1 standard deviation

The relative variations in these metrics can indicate changes in the soil horizons along with their associated uncertainties. In the lower part of the Gleysol profile (below 100 cm depth), the values for PC1 and PC3 are changing significantly. Higher up in the profile, the A/B transition is marked by variations in PC1, PC2, and PC3. A change in the morphology of the segments can be observed between 5 and 15 cm and mark a change in texture. The A/B transition on the Luvisol profile is marked on the PC1 plot, while horizon transitions in the subsoil are captured by PC2, PC3, compactness, and fractal dimension. The spread of values around the mean in the subsoil shows that those transitions are mixed. On the Fluvisol profile, the gradual topsoil to subsoil transition is captured by PC2 and fractal dimension and to some extent by the compactness. Other transitions in the subsoil can be located using PC1, PC3, fractal dimension, and compactness. In particular, these indices seem to indicate a horizon transition around 100 cm that was not observed by the pedologist.

8.12 Hierachical Classification

The hierarchical classification process is attempting to automatically characterise the main features of the soil profile by combining the radiometric and the morphological data. The dissimilarity matrix was computed on the aggregate statistics of PC1, PC2, and PC3 for each segment and on the morphology of those segments. Figures 8.10 and 8.11 show the result of the hierarchical classification of the Luvisol profile. Figure 8.10 is the hierarchical tree obtained by agglomerative clustering, and the leaves of the tree have been merged until 6 classes were left. Figure 8.11 mapped the location of each class (1–6) in the soil profile.

The hierarchical tree provides a multi-scale visualisation of the classification process. At the coarsest scale of the tree, two groups are distinguished: classes 1 and 2 and classes 3–6. These groups correspond to the distinction between the topsoil and the subsoil, and the hierarchical tree gives this distinction the most important weight. Given the choice of classes retained, this figure focuses on the second scale of the hierarchy. In the topsoil, class 1 represents the majority of the topsoil. This corresponds to the Ah horizon. Class 2 is a transition layer between the topsoil and the subsoil and corresponds to the A/B1 and A/B2 horizons of the soil profile. In the subsoil, 4 different classes have been distinguished. Class 6 differs significantly from the 3 other subsoil classes and corresponds to a deep crack in the fragipan that fills with water during summer months, giving this feature high clay content. At the bottom of the soil profile, another set of segments are classified as class 6 and correspond to the parent material (C horizon). Classes 3 and 4 correspond to two different horizons of the subsoil. Class 4 is the Bg horizon, while class 3 is a fragipan. Class 5 corresponds to mottles that are common throughout the subsoil.

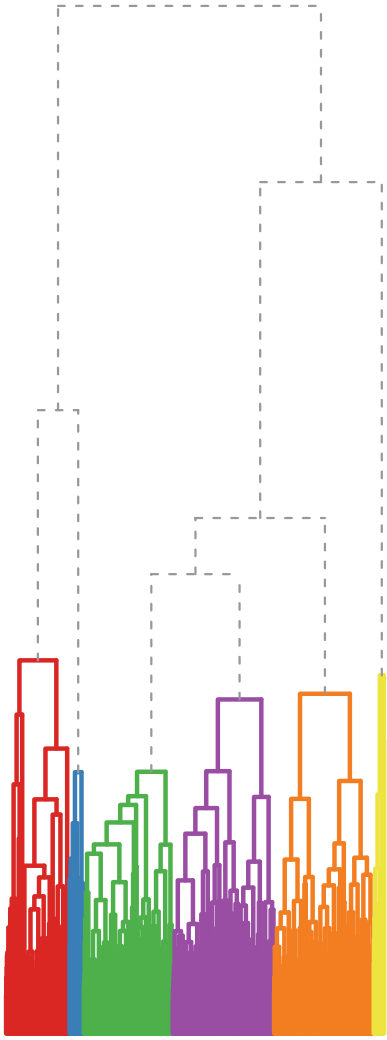

Fig. 8.10 Hierarchical classification of the radiometric and morphological metrics of the segment delineated for the Luvisol profile

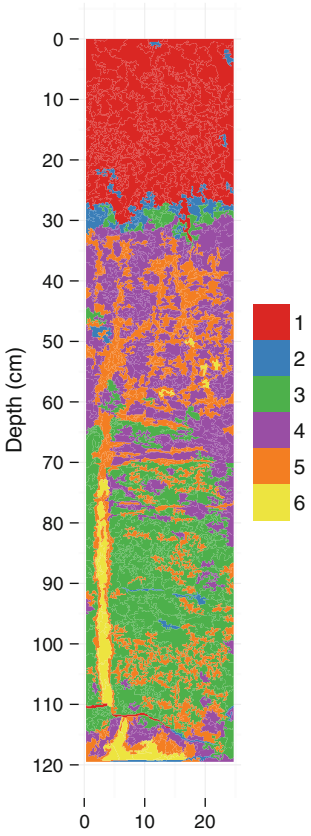

Fig. 8.11 Results of the hierarchical classification mapped on the soil profile

8.13 Conclusions

This study presented a new protocol to explore imaging techniques of the soil profile. An extraction tool was developed and tested to sample field condition soil profiles to facilitate and speed up the application of imaging techniques directly on the profile. The prototype in this paper worked well on the three soil types for the development and testing of new digital morphometrics approaches. In particular, obtaining the soil profile out of the soil pit facilitated the normalisation of the lightning conditions for digital photography, which is the most affordable technology for the quantitative pedologist. It became evident that this technique is not successful for soils that would be too loose (very sandy soils, very stony soils) and could be challenging in conditions where the soil is very hard (dry, heavy clays).

The use of regression-kriging allowed us to fuse high spatial resolution data (RGB image converted to CIE Lab) with high spectral resolution data (recorded by a hand-held spectrometer). These data were used as an input to a segmentation algorithm, which finds objects within the soil profile. We found this object-oriented

visualisation to be useful, as it provides a level of detail between the speckled raw imagery and the generalised visual delineation of horizons. It provided an opportunity to capture quantitatively the veining and gamut structures observed on the Luvisol profile. While these could be noted as a soil characteristic, they would not be captured using traditional horizons. Additionally, the creation of segments allowed deriving morphological metrics such as the area of the segments, their compactness, and fractal dimensions. Future work will focus how well the multi-scale analysis of these segments can relate to soil profile properties such as texture and structure.

Overall, the application of these soil profile imaging techniques offers a more objective and precise method to delineate soil horizons. It also offers a new method of depicting soil profiles and horizons that provides a mid-point level of generalisation with more detail but still retains the advantage of easy visual interpretation.

References

Aitkenhead M, Donnelly D, Sutherland L, Miller D, Coull M, Black H (2015) Predicting Scottish topsoil organic matter content from colour and environmental factors. Eur J Soil Sci 66:112–120

Anderson JL, Bouma J (1973) Relationships between saturated hydraulic conductivity and morphometric data of an argillic horizon. Soil Sci Soc Am J 37:408–413

Belbin L, Faith DP, Milligan GW (1992) A comparison of two approaches to beta-flexible clustering. Multivar Behav Res 27:417–433

Ben-Dor E, Heller D, Chudnovsky A (2008) A novel method of classifying soil profiles in the field using optical means. Soil Sci Soc Am J 72:1113–1123

Berger KC, Muckenhirn RJ (1945) Soil profiles of natural appearance mounted with Vinylite Resin. Proc Soil Sc Soc Am 10:368–370

Bins LS, Fonseca LMG, Erthal GJ, Ii FM (1996) Satellite imagery segmentation: a region growing approach. Simpósio Brasileiro de Sensoriamento Remoto 8:677–680

Brown LN (1963) Lacquer cement method of making soil monoliths. Division of Agricultural Sciences, University of California, California Agricultural Experiment Station

Haddad N, Lawrie R, Eldridge S (2009) Improved method of making soil monoliths using an acrylic bonding agent and proline auger. Geoderma 151:395–400

Hartemink AE, Minasny B (2014) Towards digital soil morphometrics. Geoderma 230:305–317

Kuhn M (2015) caret: classification and regression training

Liaw A, Wiener M (2002) Classification and regression by randomForest. R News 2:18–22

Liles GC, Beaudette DE, O'Geen AT, Horwath WR (2013) Developing predictive soil C models for soils using quantitative color measurements. Soil Sci Soc Am J 77:2173–2181

Maechler M, Rousseeuw P, Struyf A, Hubert M, and Hornik K (2015) Cluster: cluster analysis basics and extensions

Meng Q, Borders B, Madden M (2010) High-resolution satellite image fusion using regression kriging. Int J Remote Sens 31:1857–1876

Neteler M, Bowman MH, Landa M, Metz M (2012) GRASS GIS: a multi-purpose open source GIS. Environ Model Softw 31:124–130

Odeh IO, McBratney A, Chittleborough D (1995) Further results on prediction of soil properties from terrain attributes: heterotopic cokriging and regression-kriging. Geoderma 67:215–226

O'Donnell TK, Goyne KW, Miles RJ, Baffaut C, Anderson SH, Sudduth KA (2010) Identification and quantification of soil redoximorphic features by digital image processing. Geoderma 157:86–96

Pebesma EJ (2004) Multivariable geostatistics in S: the gstat package. Comput Geosci 30:683–691
R Core Team (2015) R: a language and environment for statistical computing. R Foundation for Statistical Computing, Vienna, Austria
Roudier P, Tisseyre B, Poilvé H, Roger J-M (2008) Management zone delineation using a modified watershed algorithm. Precision Agric 9:233–250
Roudier P, Hedley C, Ross C (2015) Prediction of volumetric soil organic carbon from field-moist intact soil cores. Eur J Soil Sci
Steffens M, Buddenbaum H (2013) Laboratory imaging spectroscopy of a stagnic luvisol profile—high resolution soil characterisation, classification and mapping of elemental concentrations. Geoderma 195:122–132
Weindorf DC, Zhu Y, McDaniel P, Valerio M, Lynn L, Michaelson G, Clark M, Ping CL (2012) Characterizing soils via portable X-ray fluorescence spectrometer: 2. Spodic and Albic horizons. Geoderma 189:268–277

Chapter 9
Computer Graphics Procedural Modeling of Soil Structure

Hansoo Kim, Minerva J. Dorantes, Darrell G. Schulze and Bedrich Benes

Abstract Soil scientists in the USA have created a large national database of written soil profile descriptions that follow a well-defined set of rules for describing soil morphological properties. Interpreting these soil descriptions is a skill that requires considerable practice and experience. While writing a soil description is straightforward, recreating a visual representation of a soil profile from a written description is very difficult. So far, there is no generalized approach for translating written or tabular soil descriptions into visual representations. We propose a novel procedural modeling approach inspired by procedural models commonly used in the field of computer graphics. Our framework takes tabular soil morphological data (i.e., soil profile descriptions) as textual input and translates it into visual features based on parametric models. These models can be used to generate two-dimensional soil profiles or to generate three-dimensional interactive models that allow rotation, scaling, and other forms of visual explorations. The procedural modeling technique enables the user to generate the soil profile visual representation with only a small amount of data. The images do not need to be stored because they are generated as needed.

Keywords Tabular soil morphological data · Procedural modeling · Computer graphics

H. Kim · B. Benes
Department of Computer Graphics Technology, Purdue University, West Lafayette, IN 47907, USA

M.J. Dorantes · D.G. Schulze (✉)
Agronomy Department, Purdue University, West Lafayette, IN 47907, USA
e-mail: dschulze@purdue.edu

A.E. Hartemink and B. Minasny (eds.), *Digital Soil Morphometrics*, Progress in Soil Science, DOI 10.1007/978-3-319-28295-4_9

9.1 Introduction

Soil scientists have developed detailed terminology for describing the morphological properties of soil profiles. In the USA, there are large national databases of soil profile descriptions that follow a well-defined set of rules (Schoeneberger et al. 2012). With training and practice, writing a soil profile description is a fairly straightforward process, with the result that different trained soil scientists will write similar, but not necessarily identical, descriptions of the same soil profile. Interpreting written descriptions, however, is a skill that requires considerable practice and experience. Experienced soil scientists can draw on their experience to mentally visualize soil profiles based on written descriptions, but to students and the vast majority of more casual users of soils information, soil profile descriptions, whether in tabular or narrative form, can be inscrutable.

Soil profile descriptions, however, contain large amounts of information that can be used to reconstruct an image of the soil originally described. Some soil properties, such as horizon depth and dominant color, are easy to represent in simple, schematic profile diagrams. The Soil Web Apps produced by the California Soil Resource Lab (http://casoilresource.lawr.ucdavis.edu) take this approach. The resulting profiles, however, do not really look like soil profiles, although they do provide information and context to trained soil scientists. There is currently no generalized approach for translating written soil profile descriptions into visual representations that one would recognize as soil profiles, primarily because soil structure is so difficult to represent.

The field of computer graphics has developed very efficient and effective methods for data visualization and representation. *Procedural methods* have recently found a prominent place among traditional techniques that take existing data and display them in different forms (Ebert et al. 2002). Procedural methods have been used in areas ranging from modeling of cities (Parish and Müller 2001), plants (Prusinkiewicz et al. 1990), to entire virtual worlds (Smelik et al. 2014). The basic idea of procedural methods is to represent an image, which in soil science is the image of a soil profile, as a computer program with specific input parameters. Then, when the image is needed, the code is executed and the image is generated. An obvious advantage of procedural representations is the huge data compression, variability of the output since one code can generate various images, and versatility. Very recently, the *inverse problem* has become important in various fields. The inverse problem attempts to answer the question, 'given existing data, for example, a written soil profile description, what is the code that can generate it?' This is a very complex problem, and several solutions have been found so far for virtual plants (Stava et al. 2014), models of cities (Vanegas et al. 2012), and procedural art (Stava et al. 2010).

Here, we apply the inverse procedural modeling approach to the field of soil science. We propose a novel procedural modeling approach that takes tabular soil morphological data (i.e., soil profile descriptions) as textual input and then translates that data into visual features based on parametric models. The output of these models can then be displayed as 2-dimensional images of soil profiles, or as three-dimensional (volumetric) interactive models that can be rotated, scaled, and explored visually in other ways. The procedural modeling technique enables the user to generate a visual representation of a soil profile with only a small amount of data, and the images do not need to be stored because they are generated as needed.

9.2 System Overview

The overview of our system is depicted in Fig. 9.1. The system takes tabular soil data as input. The *visualizer* selects the appropriate procedural model according to the tabular soil data and applies the appropriate parameters. In this step, the procedural models produce a magnitude map, which is a three-dimensional array of points (x, y, z) where x and y give the location of a point in a right Cartesian coordinate system, and z is the height above the x-y plane. The magnitude map is equivalent to the digital elevation model (DEM) used in geographic information system (GIS) software. The *renderer* then generates the final image using user-defined rendering methods equivalent to hill shading in GIS. The renderer converts the cloud-like image produced by the procedural model into an image of the highlights and shadows of a solid surface illuminated by a light source. Details of each step are described below.

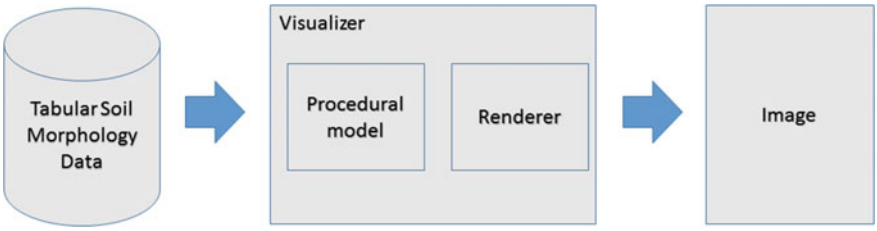

Fig. 9.1 System overview

9.3 Procedural Modeling of Tabular Soil Morphology Data

9.3.1 Data

Our goal is to use the Official Soil Series Descriptions (OSDs) available from the USDA Natural Resource Conservation Service (http://www.nrcs.usda.gov/wps/portal/nrcs/site/soils/home/) for input data. The OSDs consist of a national collection of more than 20,000 detailed soil series descriptions. Particularly, we focus on the soil structural descriptions in the OSDs. While properties such as color, depths, or boundary patterns are easily visualized by connecting them to quantitative parameters and values (e.g., converting the Munsell color designations to the RGB system), structural descriptions are difficult to quantify because they implicitly include many qualitative visual aspects. For instance, when a horizon description mentions 'subangular blocky,' we cannot clearly define its quantitative properties in a straightforward way, which is a crucial part of reconstructing a visual representation. Standardized soil structural terminology is commonly used for soil profile descriptions, so the task is to translate that terminology into images that look like the feature being described. For our initial work, we are focusing on 'granular,' 'subangular blocky,' 'prismatic,' and 'platy' soil structural keywords.

Soil structural keywords contain considerable qualitative information that is too subtle or vague to model directly by simple geometric techniques. For example, subangular blocky structure has properties of 'cubic structural units' and 'rounded edges,' but a model that simply filled space with cubes having rounded edges would not look like subangular blocky soil structure. 'Rounded edges' does not specify curvature, length, or direction, for example, and neither are global aspects of the 'cubic structural units' specified in terms of position, size, and transitions among units. In addition, these properties must have a degree of randomness in order to appear natural. To address the problem, we employ procedural noise functions (Fig. 9.2) and match their properties with structural keywords.

9.3.2 Procedural Modeling

As discussed above, there are several advantages in using procedural models. First, they generate seamless images because they are functions that can be evaluated at any point in a given domain (i.e., one-, two-, or three-dimensional space). Therefore, there are no 'empty' points in the output, and the entire output domain is controlled by the functions. This is especially beneficial when we map a reconstructed appearance onto a three-dimensional model because there are no undesirable discontinuities. Second, procedural noise functions can generate various

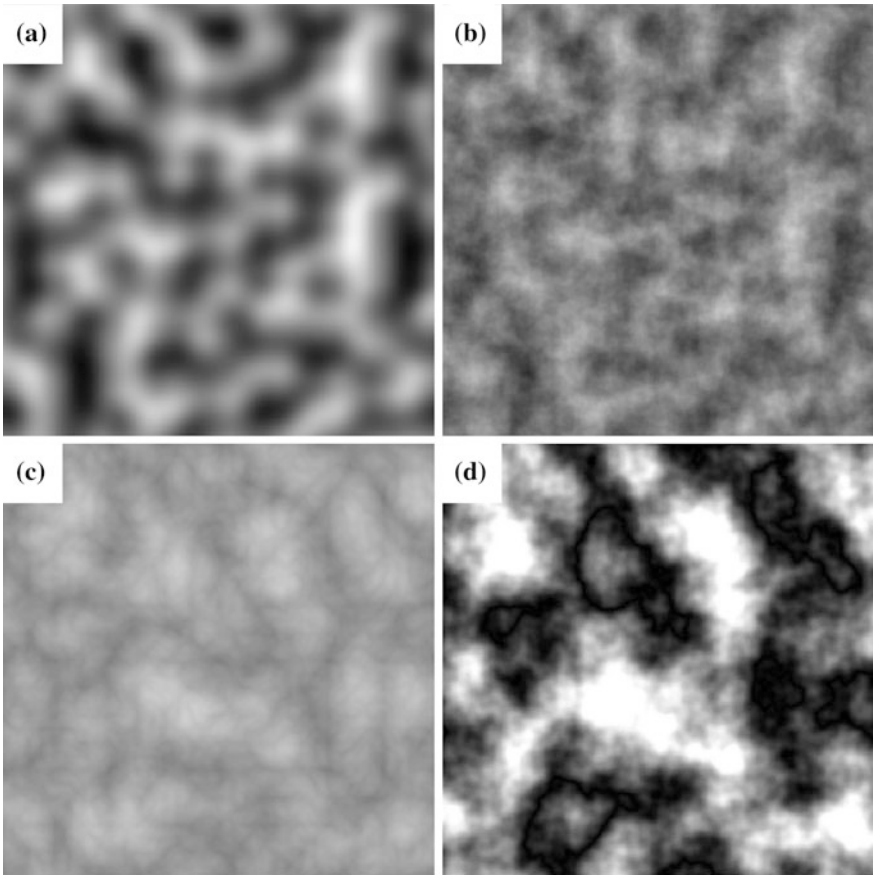

Fig. 9.2 The output from four different procedural models. **a** *Gradient Noise* has very high contrast and distinct structures. **b** *Fractal Synthesis* has a cloud-like appearance, medium contrast, and smooth but noticeable structures. **c** *Turbulence* has low contrast, smooth boundaries, and small rounded sub-patterns. **d** *Trigonometric Jittering* has distinct structure and high contrast

types of patterns by changing just a few input parameters. For example, trigonometric jittering, also known as 'Perlin Marble,' mainly creates distinguishable, but smoothly blended structures (Fig. 9.2d). On the other hand, fractal synthesis generates regularly distributed and smoother appearances (Fig. 9.2b). We are able to adjust the size, smoothness, and width–height ratio by using less than four input parameters. Third, procedural models are fast, and a 512 × 512 pixel, two-dimensional image is generated in tens of microseconds on today's computers. This enables interactive visualization, which is a crucial aspect for images that will be used for teaching and learning.

Table 9.1 Parameters of the four procedural models

Parameter	Description
X seed	Unit evaluation interval in the horizontal direction (0.0–1.0). Greater values generate smoother horizontal appearances
Y seed	Unit evaluation interval in the vertical direction (0.0–1.0). Greater values generate smoother vertical appearances
Octave	Applies to all models except gradient noise (1–16). The value determines the amount of detail to be added. Octave value is actually the number of repetitions for adding high frequency values
Frequency	Only applies to trigonometric jittering (2.0–10.0). The value defines the 'jitter' value at each octave

We currently use four procedural models (Fig. 9.2). They all are the simplest types of procedural noise functions and are employed for several reasons. First, while we are able to obtain more complex and sophisticated appearances using more complicated procedural methods, they take a significantly longer time to generate an output. Second, they require only a few input parameters (Table 9.1) that can be correlated with soil structural terms that describe the size, grade, and shape of soil structural aggregates. The output of a procedural model can be adjusted using only a few parameters. For example, by changing the *X* seed and *Y* seed, we are able to achieve many different appearances (Fig. 9.3). Finally, we have good intuition about the structures in the generated output image, because they consist of only a few interpolation equations. Since we must conduct numerous trial and error tests to find input parameters that generate images that look like soil structures, simple procedural functions accelerate the process. The result of our user-assisted process is shown in Table 9.2.

9.3.3 Visualization

While procedural models generate desired structures with randomness, the resulting outputs look different from the soil structure one sees in a soil profile. We apply additional hill shading (Horn 1981) to the results generated by the procedural models. Hill shading is a grayscale, image-space shading technique that takes into account the light source's position in order to model the pattern of highlights, shadows, and gray scale gradients that result from light shining on an opaque surface. Hill shading is frequently used for visualizing DEMs in GIS software.

The use of hill shading provides additional advantages. First, it converts excessively smooth boundaries into sharp edges by emphasizing high frequency details of procedural noise images that are hardly recognizable in the original output from the procedural models (Fig. 9.4). Although octave values greater than four do

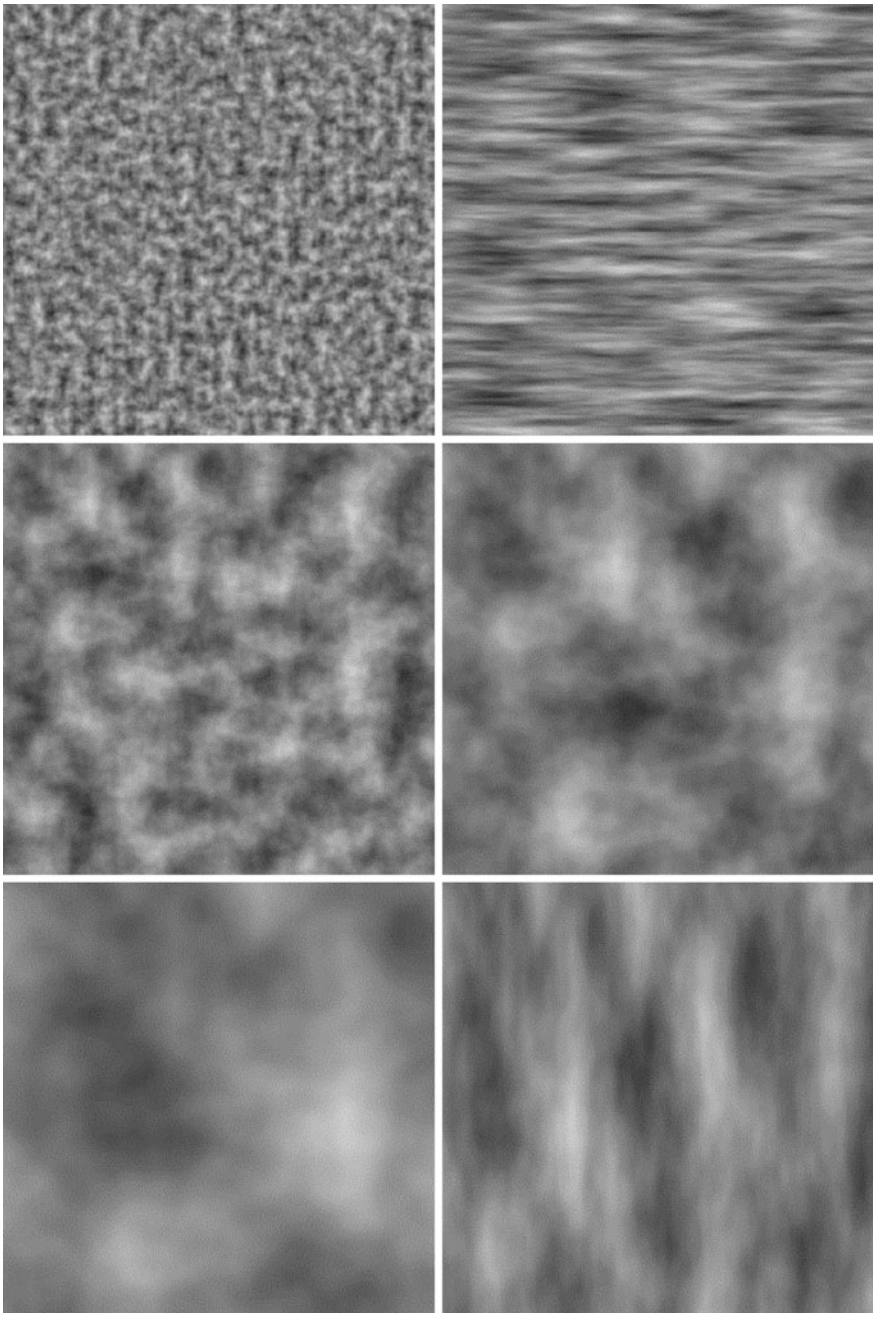

Fig. 9.3 Variations of fractal synthesis that result from different input parameters

Table 9.2 Relationships between structural keywords and procedural model parameters

Structure keyword	Features	Procedural model
Granular	• Small and rounded aggregates	• Model: any model is acceptable • *X* and *Y* seed: smaller than 0.04
Subangular blocky	• Cubic (or similar) structural units • Rounded edges	• Model: fractal synthesis or trigonometric jittering • *X* seed: 0.25–0.75 • *Y* seed: 0.25–0.75 • Octave: 4–16 • Frequency: 2.0∼ (trigonometric jittering only)
Prismatic	• Cubic (or similar) structural units • Structural units are taller than they are wide	• Model: fractal synthesis • *X* seed: 0.25–0.55 • *Y* seed: 0.3–0.6, but greater than the *X* seed • Octave: 4–16
Platy	• Structural units are wider than they are tall	• Model: fractal synthesis or trigonometric jittering • *X* seed: greater than 0.5 • *Y* seed: smaller than 0.5 • Octave: 4–16

not add clearly noticeable details in the raw output of procedural noise images, hill shading makes these details visible so that we are able to obtain better appearance (Fig. 9.4).

9.4 Results and Discussion

Figure 9.5a, b shows an example of the recreation of a granular structure. We use small values for both *X* and *Y* seeds in order to achieve fine unit structures. Figure 9.5c, d shows recreation of platy soil structure using a greater *X* seed value than *Y* seed value. Figure 9.6a is a photograph of subangular blocky structure. Since subangular blocky structure has cube-like rounded shapes, we use trigonometric jittering as the procedural model (Fig. 9.6b). A high octave value adds further details. Figure 9.6c, d shows the regeneration of prismatic structure. Note that *Y* seed value is greater than *X* seed value to generate vertical structure. All results were generated at 1024 by 1024 pixel resolution and took <2 s to generate, but a 512 by 512 pixel image, which is sufficient for many purposes, can be generated in <1 s.

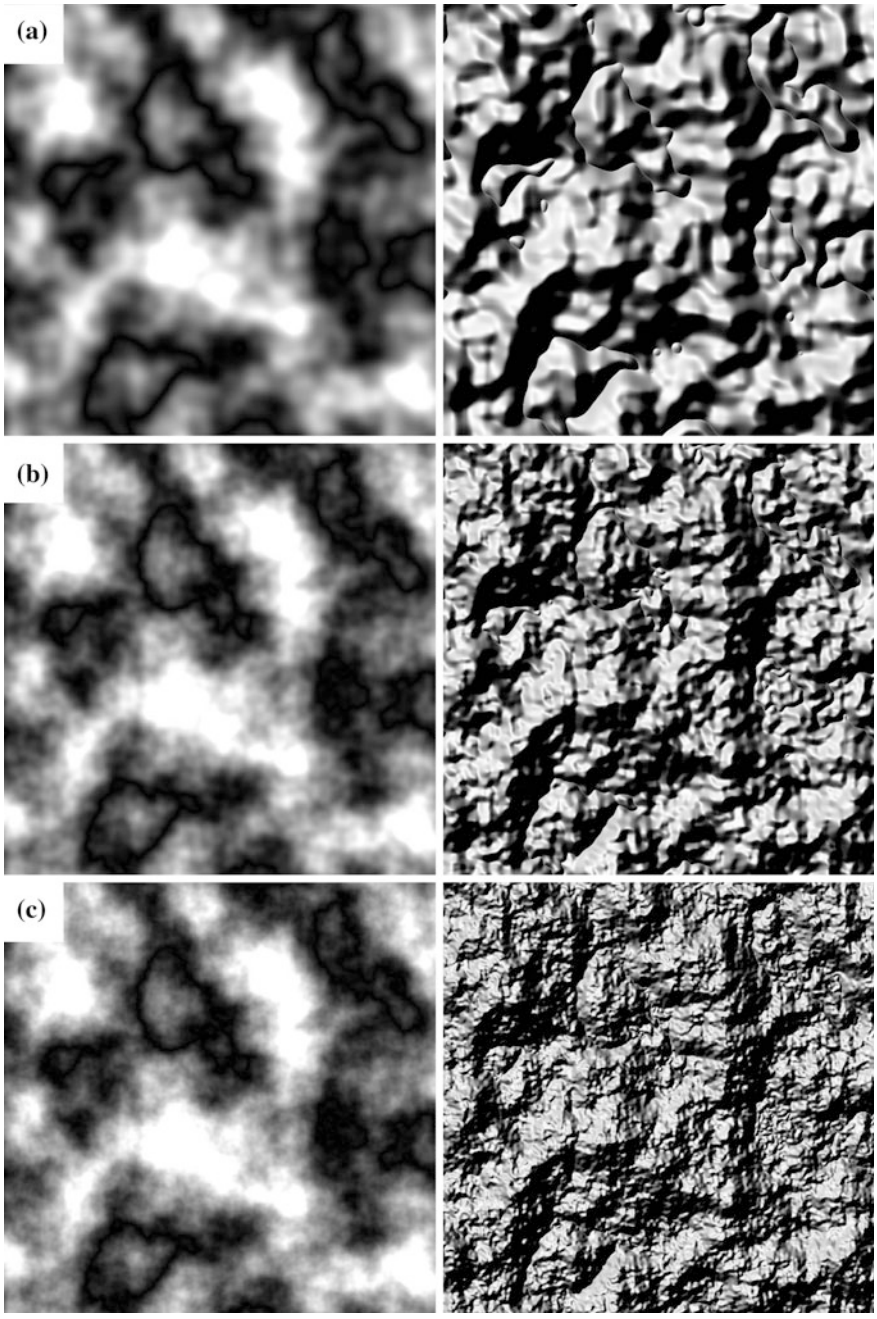

Fig. 9.4 Comparison between raw procedural noise (*left image*) and hill shading of the raw output (*right image*) for different octave values. **a** Octave value 4. **b** Octave value 5. **c** Octave value 6

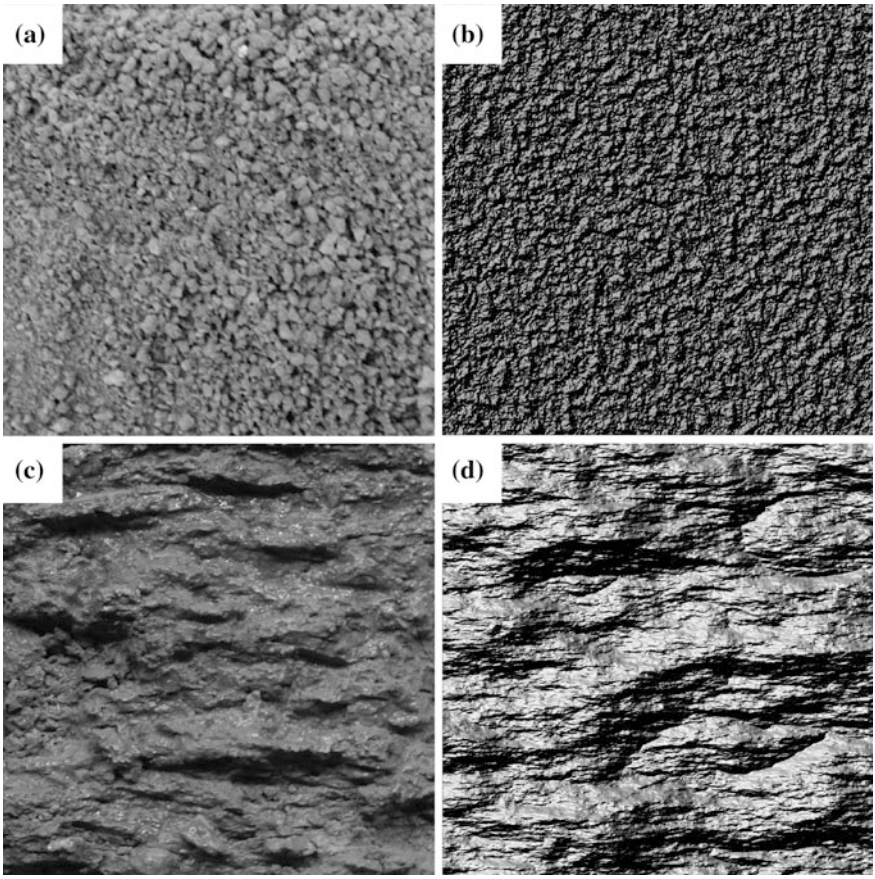

Fig. 9.5 **a** Photograph of granular soil structure. **b** Procedural model of granular structure using fractal synthesis (X seed = 0.037, Y seed = 0.037, octave = 6). **c** Photograph of platy soil structure. **d** Procedural model of platy soil structure using trigonometric jittering (X seed = 0.82, Y seed = 0.375, octave = 16, frequency = 2.17)

The procedural models described above have some drawbacks, however. First, due to the innate properties of the procedural approach, local feature control (i.e., controlling macrostructure) is very difficult. Adding specific macrostructure, for example a large prism, will require a redesign of the entire model so that pre-generated data will not be necessary. Second, the approach currently does not take into account blending between two different structures. Structure transitions in a soil profile are a subtle but important feature of soil profiles and we cannot yet depict it by using interpolations.

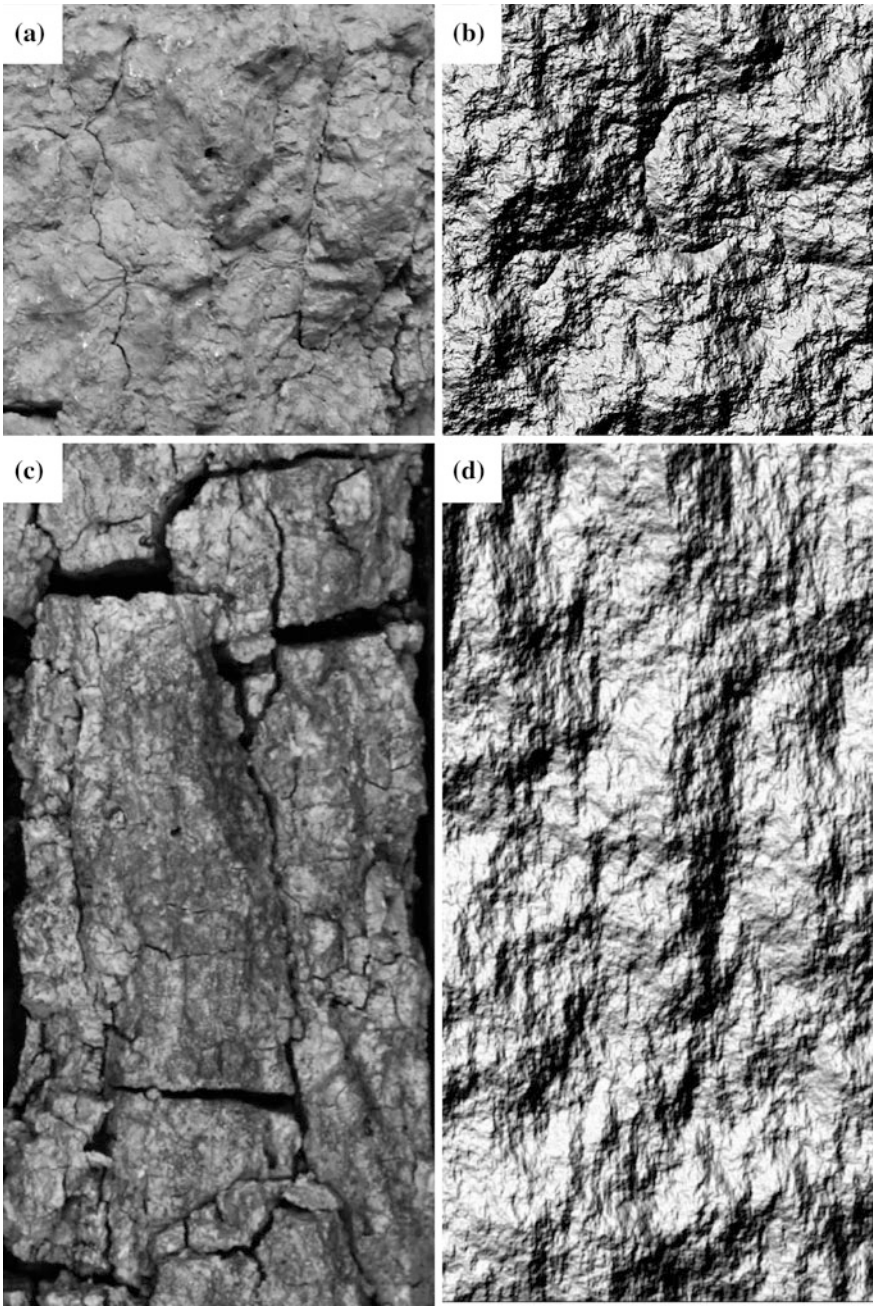

Fig. 9.6 **a** Photograph of subangular blocky soil structure. **b** Procedural model of subangular blocky soil structure using trigonometric jittering (X seed = 0.25, Y seed = 0.25, octave = 16, frequency = 2.17). **c** Photograph of prismatic soil structure. **d** Procedural model of prismatic soil structure using fractal synthesis (X seed = 0.25, Y seed = 0.375, octave = 10)

9.5 Conclusions and Future Work

We introduce a procedural model reconstruction framework for soil morphology data. Our framework takes tabular soil morphological data and converts it into visual features utilizing procedural models. The models generate appropriate procedural noise images that are then processed by a visualizer that applies hill shading to obtain images that are close approximations to actual soil structures. This approach will enable users to reconstruct soil structures with a minimum of data overhead.

There are several possible avenues for future work. As mentioned above, support for macrostructure would be useful. Also, good blending options to produce appropriate transitions from one type of soil structure to the next are still needed in order to simulate transitions between soil horizons.

So far, we have used user intuition to find appropriate procedural models and input parameters to generate images that look like different soil structures. In future work, we would like to investigate automatic inverse procedural approaches that would match an actual image of soil structure to an image generated by an appropriate procedural model. This may open the way to automatically quantifying soil structure without having to rely on the judgment of human observers.

Acknowledgements This material is based upon work supported by the Cooperative State Research, Education, and Extension Service, U.S. Department of Agriculture, under Award No. 2013-70003-20924. Any opinions, findings, conclusions, or recommendations expressed in this publication are those of the author(s) and do not necessarily reflect the view of the U.S. Department of Agriculture.

References

Ebert DS, Musgrave FK, Peachey D, Perlin K, Worley S (2002) Texture & modeling: a procedural approach. 3rd ed. Morgan Kaufmann

Horn BKP (1981) Hill shading and the reflectance map. In: Proceedings of the IEEE, vol 69, pp 14–47

Parish YI, Müller P (2001) Procedural modeling of cities. In: Proceedings of the 28th annual conference on computer graphics and interactive techniques. ACM, pp 301–308

Prusinkiewicz ALP, Lindenmayer A, Hanan JS, Fracchia FD, Fowler D (1990) The algorithmic beauty of plants. Springer, New York

Schoeneberger PJ, Wysocki DA, Benham EC, Soil Survey Staff (2012) Field book for describing and sampling soils, Version 3.0. Natural Resources Conservation Service, National Soil Survey Center, Lincoln, NE

Smelik RM, Tutenel T, Bidarra R, Benes B (2014) A survey on procedural modelling for virtual worlds. Comput Graph Forum 33(6):31–50

Stava O, Pirk S, Kratt J, Chen B, Měch R, Deussen O, Benes B (2014) Inverse procedural modelling of trees. Comput Graph Forum 33(6):118–131

Stava O, Benes B, Měch R, Aliaga DG, Krištof P (2010) Inverse procedural modeling by sutomatic generation of L-systems. Comput Graph Forum 29(2):665–674

Vanegas CA, Garcia-Dorado I, Aliaga DG, Benes B, Waddell P (2012) Inverse design of urban procedural models. ACM Trans Graph 31(6):168

Chapter 10
Soil Profile Imaging for Estimating the Depth Distributions of Clay, Iron, and Hydrological Conditions of Soils Under Rice in Northern Taiwan

Shih-Hao Jien, Zeng-Yei Hseu, Chen-Chi Tsai and Zueng-Sang Chen

Abstract Soil color variation, clay illuviation, and translocation of Fe and Mn are influenced by hydrological conditions. Soil profile imaging has been considered to predict the distribution of clay, Fe and Mn oxides, and hydrological conditions. Ten Ultisol and Alfisol profiles were selected at elevations ranging from 15 m to 40 m a.s.l. at Chungli Terrace, northern Taiwan. Sixty soil horizons were collected for redoximorphic features (RMFs) identification and analysis of soil texture and selective extraction of Fe and Mn oxides. All soil properties were correlated with the RMFs. There was a significantly positive correlation between gray mottle (GM) (value ≥5, chroma ≤3) amounts and annual reduction duration (ARD) ($r = 0.80^{**}$, $p < 0.01$) and a negative correlation between red mottle (RM) (value ≥4, chroma ≥3) amounts and ARD ($r = 0.75^{**}$, $p < 0.01$) at surface horizons (within 30 cm). A significantly positive correlation was also found between RM and clay content ($r = 0.32^{*}$, $p < 0.05$), indicating clay might determine the formation of RM. Moreover, the ratios of iron activity (Fe_o/Fe_d) and iron crystalline ($(Fe_d\text{-}Fe_o)/Fe_t$) could also be good indices for ARD prediction. The Mn_d/Fe_d seemed an index of frequent fluctuation of water table in soil profiles. Using image analysis technique, replacing naked eye identification of RMF could improve correlations between soil color and hydrological conditions.

Keywords Pedogenesis Hydrological condition · Redoximorphic feature · Soil color · Digital soil morphometrics

S.-H. Jien
Department of Soil and Water Conservation, National Pingtung University of Science and Technology, Pingtung 91201, Taiwan

Z.-Y. Hseu · Z.-S. Chen (✉)
Department of Agricultural Chemistry, National Taiwan University, Taipei 10617, Taiwan
e-mail: soilchen@ntu.edu.tw

C.-C. Tsai
Department of Forestry and Natural Resources, National Ilan University, I-Lan 26047, Taiwan

A.E. Hartemink and B. Minasny (eds.), *Digital Soil Morphometrics*,
Progress in Soil Science, DOI 10.1007/978-3-319-28295-4_10

10.1 Introduction

Digital soil morphometrics is defined as the application of tools and techniques for measuring and quantifying soil profile attributes (horizons, texture, color, structure, moisture, mottles, consistence, carbonates, rock fragments, pores, and roots) and deriving continuous depth functions (Hartemink and Minasny 2014). Technologies that can rapidly characterize the entire soil profile are necessary (Ben-Dor et al. 2008; Demattê et al. 2004; Stockmann et al. 2014; Viscarra Rossel and Webster (2011). Several digital techniques, including ground penetrating radar (GPR), electrical resistivity (ER), cone penetrometer, hyperspectral core scanner, and X-ray fluorescence (XRF), have been developed to supplement traditional ones to characterize soil profiles (Hartemink and Minasny 2014).

Soil color is considered a common property to depict soil horizons and classify soils. Soil color (matrix color/redoximorphic features, RMFs) could be used as an indicator of soil organic carbon content, drainage, aeration, iron content, or mineralogy, particularly in soils with lowland rice and frequent fluctuation of groundwater. The rice-growing soil is a hydric soil, which is defined as soils formed under conditions of sufficient saturation or flooding during the growing season to develop an anaerobic condition in the upper part of the soil. The rice-growing hydric soils are characterized by hydrological conditions and various soil colors in their matrix (Hseu and Chen 2001; Jien et al. 2010). The development of suitable color indices or a good digital technique for color descriptions in situ could effectively identify soil moisture regimes (SMR) and be helpful for the classification of hydric soils.

Generally, gray mottles (GMs) or depleted matrix (chroma 2) has been considered as generally indicators for extensive duration of saturation and reduction (Daniel et al. 1971; Simonson and Boersma 1972; Cox et al. 1996; Jien et al. 2010). Franzmeier et al. (1983) found that GMs with chroma 2 indicated saturation for 30 % of the year for loamy soils in Indiana, USA. Cycles of reduction and oxidation in soils over prolonged periods and the consequent mobility and accumulation or depletion of Fe and Mn resulted in the formation of RMFs (Fanning and Fanning 1989; Vepraskas 1992; Hseu and Chen 1996; Jien et al. 2004, 2010). Studies have tested the application of RMFs as SMR indicators in various environments. High levels (7.5 %) of Fe and Mn concretions were found in the upper B horizons of soils along hydrosequences in Bavaria, Germany (Schwertmann and Fanning 1976). In a study of five fine-silty soils in Indiana, iron depletions with chroma 2 indicated >30 % saturation at a depth of one meter (Franzmeier et al. 1983). In hardwood forest areas in Louisiana, USA, soils with chroma <2 with redox concentrations below the A horizon generally indicated hydric conditions constituting saturation and reduction >25 % of the growing season (Faulkner and Patrick 1992).

The relationship between soil color and SMR might be failed because of wrong judgment of soil colors by naked eyes. The digital techniques for soil morphometrics might improve judgments. Recently, soil color has been measured indirectly using Vis–NIR. Viscarra Rossel et al. (2009) used Vis–NIR to measure soil color

in situ and in the laboratory. Measurements were compared to the Munsell color chart readings. There was fair agreement between spectroscopic estimates of soil color and Munsell readings although Vis–NIR tended to be slightly darker and more yellow. Ben-Dor et al. (2008) used Vis–NIR field spectrometer and an accessory to read subsoil reflectance to examine soil color in Alfisols, Inceptisols, and Vertisols. The results were compared to traditional soil descriptions, and it was possible to describe quantitatively and objectively the soil profile color in situ using optical instruments.

Quantitative descriptions of RMFs associated with hydromorphology for the rice-growing soils in Taiwan have been studied by Hseu and Chen (1996, 2001) and Jien et al. (2004, 2010). Soils had high chroma matrix colors, Fe (chroma 6) and Mn (chroma 1) concentrations, and chroma 1 depletions > horizons that were saturated for considerable periods were reduced for a much shorter time. Some problems exist regarding long-term assessment and interpretation of the criteria, particularly in seasonally saturated rice-growing soils. This study attempts (1) to compare the RMFs of rice-growing soils with different elevations, (2) to clarify the correlations between soil colors and local hydrology condition of lowland rice-growing soils in Taiwan, (3) to compare the digital data, including types and quantities of RMFs, identified by naked eyes and image analysis.

10.2 Materials and Methods

10.2.1 Site Description

The study area is located inside the Chungli Terrace in northern Taiwan, about 40 km southwest of Taipei city (Fig. 10.1). The altitude ranges from 20 to 40 m above sea level. The soil is developed on an alluvial terrace from Quaternary, with a minimum thickness of 5 m (Ho 1988). The mean air temperature is 27 °C in summer and 13 °C in winter. Average annual rainfall is 1560 mm, and the annual rainfall exceeds the annual evapotranspiration.

Ten representative rice-growing soils were selected for this study. Plinthite was found only in Pingchen soil, and other soils contained plinthitic feature (Fig. 10.2). All pedons were close (∼2 km) to the seashore. Slopes range from 2 to 6 % over 2 km. All soils are classified as Ultisols or Alfisols according to the Keys to Soil Taxonomy (Soil Survey Staff 2010), and specifically, they are Oxyaquic Paleudult (Pingchen), Plinthitic Paleudalf (Tachuwei), Plinthaquic Paleudult (Lungchung), Typic Plinthaqualf (Chuwei-1), Typic Plinthaquult (Luchu, Hsinwu, and Houhu-1), and Typic Paleaquult (Houko, Chuwei-2 and Houhu-2). The Pingchen, Lungchung, and Tachuwei series are the farthest from the seashore (about 4 km) and are situated at the highest elevation (around 40 m) in this study area. The Houhu-1, Houko, Chuwei-2, and Houhu-2 series are the nearest to the seashore and have the lowest elevation (15–20 m). The Chungli Terrace has been used for rice (*Oryza sativa* L.)

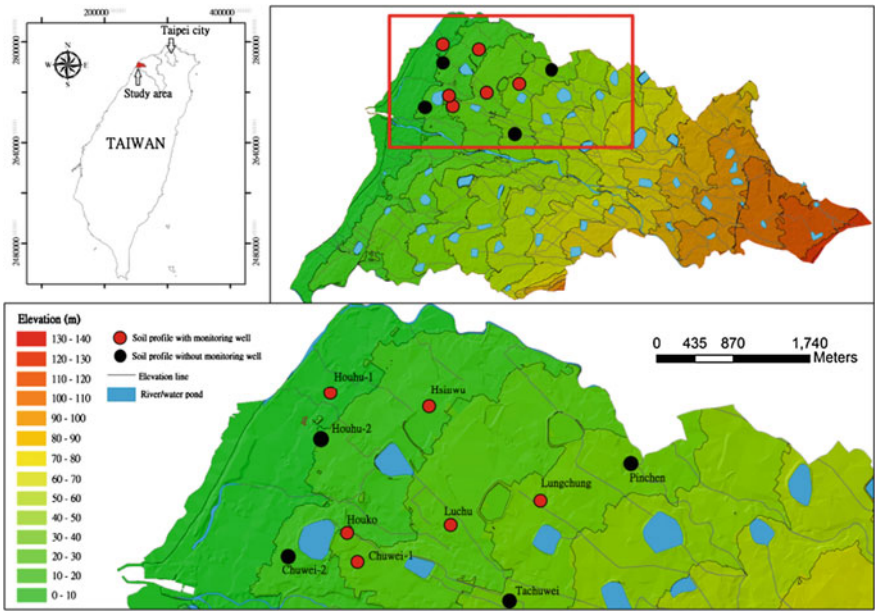

Fig. 10.1 Locations of the studied pedons at Chungli Terrace in northern Taiwan

cultivation since the 1950s. Each year, rice is harvested during the March to October growing season, and the soils are fallowed in winter. The soils are seasonally flooded by irrigation water and groundwater.

10.2.2 Soil Analyses

Soil pits were excavated in 1996 and in 2002 and 2003. The description included morphological characteristics and RMFs based on the Soil Survey Manual (Soil Survey Staff 1993). The soil properties are given in Hseu and Chen (2001) and Jien et al. (2004, 2010). Fe oxides (Fe_d) and Mn oxides (Mn_d) were extracted by the dithionite–citrate–bicarbonate (DCB) method (Mehra and Jackson 1960). Amorphous Fe (Fe_o) and Mn (Mn_o) were extracted by 0.2 M ammonium oxalate (pH = 3.0) (AAO) (McKeague and Day 1966). All elements were determined using an atomic adsorption spectrometer (Hitachi, 180-30 type). Total contents of Fe (Fe_t) and Mn (Mn_t) were measured after digestion with HF–$HClO_4$–H_2SO_4–HCl on a hot plate (200 °C) (Hossner 1996). The bulk density of each size fraction of the ferromanganiferous nodules was also determined by the paraffin clod method (Blake and Hartge 1986). Bulk density was determined on six samples for 2- to 5-mm nodules and three samples for other, larger size fractions. All soil analyses were performed in triplicate.

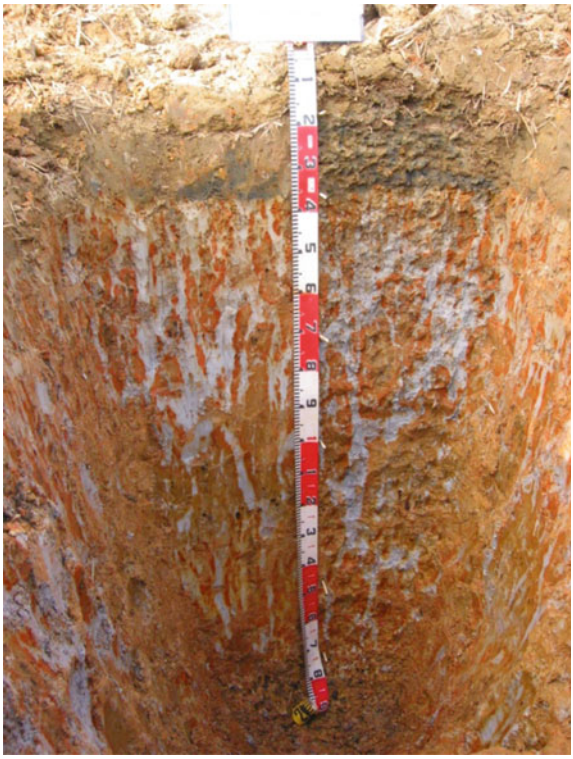

Fig. 10.2 The plinthitic feature of rice-growing soils in our study area. The photograph is Chuwei-1 pedon

10.2.3 Hydrological Monitoring

In six of the ten soils, a 7 × 7 m plot was established to monitor hydrological conditions over two years, which Lungchung–Hsinwu–Houhu-1 monitored during 1996–1997, and Luchu–Chuwei-1—Houko monitored during 2004–2005. The following data were recorded at biweekly intervals: (1) water table level, (2) soil water tension at depths of 25, 75, 100 and 200 cm, and (3) soil redox potential at depths of 25, 75, 100, and 200 cm. All data were recorded in triplicates. Hydrological data at other pedons were used for the nearest pedons in which no measurements were made.

Plowing in lowland rice forms compact subsurface layers, and perched water appears during the growing seasons. These compact layers exhibit lower saturated hydraulic conductivity than the overlying horizon and water tends to accumulate above them, creating a perched zone of saturation. Wells were constructed to measure the perched water table, and it piezometers were used to determine water table depths. Tensiometers and platinum electrodes were installed at predetermined depths and used to monitor saturation and redox potential (Eh). The voltage reading was recorded after the drift decreased to equilibrium, characterized by less than

5 mV of change during a 10-s period. The field reading was adjusted by adding +200 mV in order to correct for reference electrode potential. The threshold Eh value for the reduction of Fe (III) to Fe (II) was estimated from an Eh–pH diagram and equation, 1235–177 pH (for pH < 7.5), which was provided by Ponnamperuma (1972). Also, the range of pH (5.0–6.0) in the studied soils was measured to establish pH-corrected redox threshold levels for Fe (II). Instruments were constructed in triplicate for each study site (including wells, piezometers, and tensiometers). All measurements were made at biweekly intervals and in triplicate at each monitoring time.

10.2.4 Identification of Redoximorphic Features by Image Analysis

Five aluminum boxes measuring 10 × 10 × 8 cm were used for collecting the soil blocks from each soil horizon of the pedons of Luchu, Chuwei-1, and Houko. Fresh soil blocks from two boxes were taken out for image analysis, and other three boxes were oven-dried at 105 °C for 24 h to remove water before sieving the ferromanganiferous nodules. A stainless wire was used to cut the soil blocks with an interval of 1 cm. Eight soil pieces were extracted from each soil block, and pictures were taken for image analysis. ERDAS Imagine 8.4 (ERDAS, USA) was used for image analysis.

10.3 Results and Discussion

10.3.1 Soil Morphology and Hydrological Conditions

The soils were divided into three groups based on their soil morphological characteristics (Table 10.1). The first group (around 40 m a.s.l.) included Pingchen, Tachuwei, and Lungchung soils, which had no plinthite or plinthite ranged from 2 to 50 % within 150 cm depth. The soils of Luchu, Hsinwu, Chuwei-1, and Houhu-1 are located at the elevation around 20–40 m.a.s.l. and characterized by plinthite, and most soil horizons (20–200 cm in depth) contained plinthite. The third group (15–20 m a.s.l.) included Houko, Chuwei-2, and Houhu-2 soils, and the morphological features were different as gleyzation was the dominant soil forming process due to long-term high groundwater table. The Btg as the major soil horizon and the reduced matrix (chroma ≤2) of the Ap and Btg horizons indicated strongly reduced conditions.

All pedons had a perched water table during the growing season from March to November. Table 10.2 shows the annual duration of saturation and reducing conditions at different depths. In the first soil group, the least annual reduction duration (∼5 %) was found in the lower soil horizons, which corresponded with the color

Table 10.1 Morphological characteristic of ten pedons in study area

Horizons	Depth (cm)	Moist color	Soft masses[†]	Depletions	Texture	Boundary[‡]
Pinchen (Oxyaquic Paleudult)						
Ap	0–20	10YR 4/4	FP 5YR 5/8 (15 %)[§]	–[¶]	–	–
AB	20–40	10YR 4/4	FP 5YR 5/8 (15 %)	–	–	–
Bt1	40–60	7.5YR 5/8	–	MP 5Y 5/3 (15 %)	–	–
Bt2	60–100	10R 3/6	MP 10YR 5/6 (40 %)	M&FP 5Y 5/3 (<2 %)	–	–
Bt3	100–130	10R 3/6	M&CP 10YR 7/4 (30 %)	–	–	–
Bt4	130–160	2.5YR 4/8	M&CP 10YR 7/4 (30 %)	–	–	–
Bt5	160–200	2.5YR 4/8	M&CP 10YR 7/4 (30 %)	MP 2.5Y 8/2 (20 %)	–	–
Tachuwei (Plinthitic Paleudalf)						
Ap	0–35	10YR 5/6	FP 10R 4/6 (2 %)	–	L	–
AB	35–60	2.5Y 6/6	MP 10R 4/8 (40 %)	–	C	–
Bt1	60–80	2.5YR 4/8	MP 7.5YR 6/8 (25 %)	–	SiL	–
Bt2	80–120	10YR 7/8	MP 2.5YR 4/8 (30 %)	–	SiL	–
Bt3	120–150	2.5YR 3/6	MP 7.5YR 5/8 (20 %)	MP 5YR 7/2 (30 %)	SiL	–
Lunchung (Plinthaquic Paleudult)						
Ap	0–20	2.5Y 4/2	–	–	SiCL	as
Bw	20–41	10YR 5/2	CD 5YR 5/8 (5 %)	–	SiC	aw
2A	41–56	10YR 4/2	CP 2.5YR 3/4 (5 %)	–	SiCL	cw
2Bt	56–85	10YR 4/4	CD 7.55YR 5/6 (10 %)	–	SiC	d
2Btv1	85–100	10YR 5/3	CP 2.5YR 5/8 (30 %)	CD 2.5YR 2.5/2 (5 %)	SiC	as
2Btv2	100–140	10YR 6/2	MP 2.5 YR 5/6 (20 %)	CP 2.5YR 2.5/2 (5 %)	SiC	d
2Btv3	140–180	10YR 6/1	MP 2.5 YR 5/8 (20 %)	CP 2.5YR 6/1 (20 %)	SiC	d
2Btv4	>180	10YR 6/1	MP 2.5 YR 5/8 (30 %)	CP 2.5YR 6/1 (15 %)	SiC	–
Luchu (Typic Plinthaquult)						
Ap	0–20	5Y 4/2	–	M&Cf 5YR 6/2 (20 %)	CL	cs
Btv1	20–50	2.5Y 6/1	M&Cd 2.5Y 5/6 (30 %); M&Cp 10YR 5/4 (10 %)	–	CL	d
Btv2	50–75	5Y 7/1	C&VCp 10YR 6/8 (30 %); M&Cp 5YR 5/8 (15 %)	–	CL	d
Btv3	75–104	5Y 8/1	M&Cp 5YR 5/8 (15 %); M&Cd 2.5Y 6/6 (20 %)	–	CL	d

(continued)

Table 10.1 (continued)

Horizons	Depth (cm)	Moist color	Soft masses[†]	Depletions	Texture	Boundary[‡]
Btv4	104–124	2.5Y 7/1	M&Cd 2.5Y 6/6 (25 %)	–	C	d
Btv5	124–160	5Y 7/1	F&Mp 2.5YR 4/8 (10 %); Md 2.5Y 6/6 (30 %)	–	C	d
Hsinwu (Typic Plinthaquult)						
Ap	0–15	2.5Y 4/3	–	–	SiL	cs
AB	15–26	2.5Y 4/1	–	CF 2.5Y 4/2 (10 %)	SiL	cs
Bt1	26–45	10YR 5/4	CD 7.5YR 4/4 (10 %); FF 10YR 5/8 (5 %)	–	SiC	d
Bt2	45–75	10YR 5/6	CD 5YR 5/8 (15 %); FF 10YR 5/8 (5 %)		SiC	aw
Btv1	75–107	10YR 5/2	MP 2.5YR 4/4 (25 %); MF 10YR 5/3 (5 %)	–	CL	d
Btv2	107–133	2.5YR 4/8	CD 10YR 6/3 (5 %)	CP 10YR 6/2 (5 %)	C	d
Btv3	133–160	2.5YR 4/8	CD 2.5YR 2/1 (5 %)	CP 10YR 6/2 (10 %)	C	d
Chuwei-1 (Typic Plinthaqualf)						
Ap	0–18	10YR 4/3	VF&Fp 10YR 6/8 (15 %)	–	C	cs
AB	18–36	2.5Y 3/2	VFp 7.5Y 6/8 (15 %)	–	CL	d
Btv1	36–70	2.5Y 7/1	M&Cp 5YR 4/8 (20 %); M&Fp 10YR 5/4 (10 %)	–	C	d
Btv2	70–110	2.5Y 7/1	M&Cd 2.5YR 4/8 (35 %); M&Fp 10YR 5/6 (25 %)	–	C	d
Btv3	110–145	2.5Y 7/1	C&VCp 10YR 5/8 (50 %); Cp 10YR 6/8 (30 %)	–	C	d
Btv4	145–170	2.5Y 7/1	V&VCp 2.5Y 5/8 (20 %); Mp 7.5YR 6/8 (45 %)	–	C	d
Btv5	170–200	2.5Y 7/2		–	C	d
Houhu-1 (Typic Plinthaquult)						
Ap	0–34	2.5Y 4/2	MP 5YR 4/4 (30 %)	–	CL	as
AB	34–47	2.5Y 4/1	CP 7.5YR 5/8 (10 %)	–	SiCL	cs
Bt1	47–66	10YR 4/3	MP 7.5YR 5/8 (10 %)	–	SiCL	cs
Btv1	66–82	10YR 5/3	MP 7.5YR 5/8 (10 %)	CD 10YR 6/1 (10 %)	SiC	g
Btv2	82–102	10YR 6/1	MP 2.5YR 5/8 (25 %)	–	SiC	d
Btv3	102–122	7.5YR 6/1	MD 2.5YR 5/8 (25 %)	MD10YR 7/1 (10 %)	SiC	d
Btv4	>122	7.5YR 6/1	MD 5YR 5/8 (30 %); MF 7.5YR 5/6 (20 %)	–	C	d

(continued)

Table 10.1 (continued)

Horizons	Depth (cm)	Moist color	Soft masses[†]	Depletions	Texture	Boundary[‡]
Houko (Typic Paleaquult)						
Ap	0–20	10YR 4/4	p 2.5YR 5/8 (10 %)	–	C	gs
Bt1	20–50	2.5Y 4/2	F&Mp 5YR 5/6 (10 %)	F&Md 2.5Y 6/1 (15 %)	SiC	gw
Bt2	50–75	10YR 4/1	F&Mp 5YR 6/8 (10 %)	M&Cd 2.5Y 6/1 (15 %)	SiC	gw
Bt3	75–110	5Y 5/1	M&Cp 2.5YR 4/6 (30 %)	–	SiC	d
Btg1	10–130	10BG 4/1	F&Mp 10YR 6/6 (10 %)	–	SiC	d
Btg2	130–170	10BG 4/1	F&Mp 10YR 6/6 (2 %)	–	C	d
Btg3	170–200	10BG 4/1	F&Mp 10YR 6/6 (2 %)	–	C	d
Chuwei-2 (Typic Paleaquult)						
Ap	0–35	7.5YR 4/6	CP 7.5YR 5/8 (10 %); FP 2.5YR 5/8 (<2 %)	–	SiL	–
AB	35–65	10YR 5/4	CP 7.5YR 6/8 (15 %)	–	SiL	–
Btg1	65–90	5G 5/1	MP 10YR 7/8 (30 %)	–	SiCL	–
Btg2	90–105	5PB 6/1	CP 10YR 7/8 (10 %)	–	SiCL	–
Btg3	105–120	5PB 6/1	CP 2.5Y 7/6 (4 %)	–	SiC	–
Houhu-2 (Typic Paleaquult)						
Ap	0–25	10YR 6/2	FP 5YR 5/8 (10 %)	–	SiCL	–
Bt1	25–45	2.5Y 4/4	MP 5YR 5/8 (10 %)	–	SiC	–
Btg2	45–70	2.5Y 6/2	MP 5YR 5/8 (40 %)	–	SiC	–
Btg3	70–110	10YR 6/1	MP 2.5YR 5/8 (40 %)	–	SiC	–
Btg4	110–140	5 PB 6/1	MP 10YR 5/8 (20 %); MP 2.5YR 5/8 (20 %)	–	SiC	–

[†]F = fine, M = medium, C = coarse, p = prominent, d = distinct, f = faint

[‡]a = abrupt, c = clear, d = diffuse, g = gradual, s = smooth, w = wavy

[§]The value in parentheses is quantity of redoximorphic features

[¶]None

Table 10.2 Annual saturation and reduction duration of the studied soils

Soils	Elevations (m)	Soil depth (cm)	Annul saturation duration (%)	Annul reduction duration (%)
Pinchen (Oxyaquic Paleudult)	50	25	75	70
		50	60	70
		100	40	5
		200	35	5
Tachuwei (Plinthitic Paleudalf)	40	25	75	70
		50	60	70
		100	40	5
		200	35	5
Lungchung (Plinthaquic Paleudult)	40	25	75	70
		50	60	70
		100	40	5
		200	35	5
Luchu (Typic Plinthaquult)	25–30	25	68	36
		50	50	21
		100	27	21
		200	27	25
Hsinwu (Typic Plinthaquult)	30	25	40	10
		50	45	30
		100	50	30
		200	55	10
Chuwei-1 (Typic Plinthaquult)	23	25	51	63
		50	41	33
		100	45	40
		200	63	48
Houhu-1 (Typic Plinthaquult)	20	25	53	75
		50	33	55
		100	21	80
		200	38	75
Houko (Typic Paleaquult)	20	25	57	69
		50	34	53
		100	21	76
		200	38	65
Chuwei-2 (Typic Paleaquult)	18	25	55	95
		50	65	100
		100	70	100
		200	80	100
Houhu-2 (Typic Paleaquult)	15	25	55	95
		50	65	100
		100	70	100
		200	80	100

morphormetrics. In the second soil group, the highest amounts of redox concentrations (≥30 %) were found in the Btv horizons with about 20–60 % annual saturation duration and 10–80 % annual reduction duration. These depths were probably the transitional zones between the fluctuating depths of perched irrigated water and groundwater table (Tables 10.1 and 10.2). The presence of plinthite

implied that the saturated conditions from Btv horizons are the result of long-term seasonal fluctuation of the groundwater (Daugherty and Arnold 1982). Red (2.5YR 3/6 or 4/6) and hard ferromanganiferous nodules were prevalent in these horizons. In the third soil group, the prevailing redox depletions corresponded to high annual duration of saturation (21–80 %) and reducing conditions (55–100 %) (Table 10.2). The discrepancy between ASD and ARD could be probably attributed to the clayey texture of the soils; the reduced conditions prevailed as the water table lowered. In the Luchu soil, annual duration of saturation was higher than that of reduction at a depth of 200 cm which can be attributed to the high dissolved oxygen content in groundwater under oxyaquic conditions (Hseu and Chen 2001; Jien et al. 2010).

10.3.2 Relationship Between Soil Redoximorphic Features and Hydrology

Several studies have found significant correlations between soil color and moisture regimes (Hseu and Chen 1996, 2001; Jien et al. 2004, 2010). Jien et al. (2004) found that the saturation duration of the horizon above 50 cm was not significantly correlated to soil chroma index (CI) or soil reduction duration. These results implied that the pedoturbation of the surface 50 cm resulted from human irregation during the growing season occured. The Fe depletions in the A horizon was difficult to identify and should be regarded as color affected by organic matter. The soil color index within 50 cm from surface soil is difficult for predicting the soil wetness condition in rice-growing soils. Significant correlations were found between the soil color index and soil saturation duration ($r = -0.43^{**}$, $p < 0.01$) and reduction duration ($r = -0.52^{**}$, $p < 0.01$) for 50–100 cm soil depth. The RMFs at this depth were affected by groundwater table and by perched water. The reduction and saturated time at this depth were >25 and >35 % of a year, and the contents of the Fe depletion ranged from 5 to 40 %. This result confirms the results of Daniel et al. (1971) and Evans and Franzmeier (1986), who found soil chroma to correlate with soil saturation at a depth of 30–60 cm.

In this study, we also divided soil layers into <30 and 30–100 cm and divided soil RMFs into GMs (value ≥5, chroma ≤3) and red mottles (RM) (value ≥4, chroma ≥3) to assess the correlation between soil color and soil wetness conditions including the annual saturation and reduction durations. For the surface soils (≤30 cm), the results revealed that neither GM nor RM existed significant correlation with annual saturation or reduction duration (Fig. 10.2). There was no obvious correlation between GM or RM and annual saturation duration in horizons below 30 cm. The significantly positive relationship existed between GM and annual reduction duration, and negative relationship was found between RM and annual reduction duration (Fig. 10.3) in horizons below 30 cm.

Soil color index provided a good morphology index for predicting soil wetness conditions at depths below 30 cm for the rice-growing soils in Taiwan, particularly

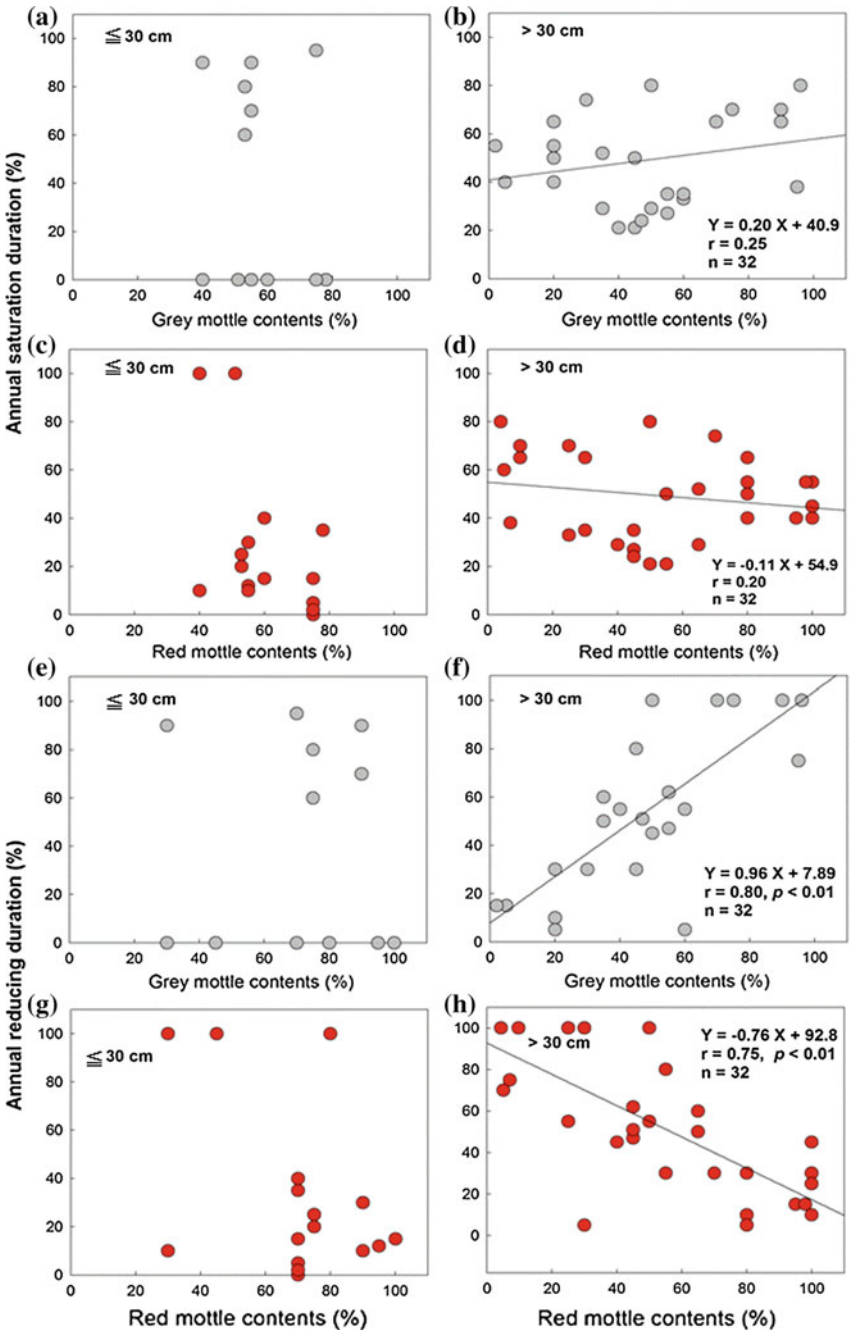

Fig. 10.3 Correlations between soil wetness conditions and redoximorphic features: **a–d** annual saturation duration (%); **e–h** annual reduction duration (%)

for annual reduction duration. The surface soil is pedoturbated resulting from rice-growing cultivation and the accumulation of rice straw residual. These phenomena create difficulties in identifying the RMFs and cause errors in correlation establishment. New digital techniques should be developed to describe and quantify RMFs to improve the correlations between soil color and soil wetness conditions.

10.3.3 Fe, Al, and Mn and Hydrology

Levels of iron and manganese were changing with SMR. We can use instruments, e.g., portable XRF, to estimate distribution of Fe and/or Mn in situ to predict SMR or variances of groundwater table within soil profiles.

In our studied sites, oxalate- and DCB-extractable fractions and total contents of Fe and Mn were determined in bulk soils to assess the effects of different moisture regimes for the three soil groups. Extractions of Fe and Mn were performed on some of selected pedons. The Fe extraction data suggested that the soil matrix of all analytical pedons are a source of Fe that can be reduced, translocated, and concentrated in RMFs (Table 10.3), particularly in soils of the second group. In the pedon with the highest reducing conditions (>70 % of the year), the Houko soil (the 3rd group), the contents of Fe_d were lower than those of the other two soils. The Fe_o in the Houko soil was however much higher than the other two sites, suggesting that the crystallization of free Fe was retarded by the duration of reducing conditions. This was also found by Khan and Fenton (1996). Consequently, iron activity ratio (Fe_o/Fe_d) might be suggested as an index for prediction soil moisture regimes. Table 10.4 shows a positive correlation between annual reduction duration (ARD) and Fe_o ($r = 0.31^{**}$, $p < 0.01$) and Fe_o/Fe_d ($r = 0.47^{**}$, $p < 0.01$). A significantly negative correlation ($r = -0.54^{**}$, $p < 0.01$) was also found between ARD and Fe crystalline ratio ($(Fe_d\text{-}Fe_o)/Fe_t$), indicating an estimation of soil moisture regimes by Fe contents.

The ratio of Mn_d/Fe_d in nodules is a good indicator for prediction of soil depths where the water table fluctuated, because Mn accumulated and was well crystallized at these depths. It was also found that the maximum Mn_d/Fe_d ratios of soils are found at depths of fluctuating water table. The results are corresponded with Khan and Feton (1996), who found that the highest Mn_d/Fe_d ratio was correlated with the zones where frequent wetting and drying cycles occurred. In the Chuwei soil, the highest ratio of Mn_d/Fe_d (0.19–0.44) was in the Btv5 horizon (170–200 cm) where the groundwater table fluctuated frequently (Tables 10.1 and 10.3). In the Luchu soil, the Mn_d/Fe_d ratio ranged from 0 to 0.03 (Table 10.5). The maximum ratio was found in the Ap horizon (0–20 cm) where perched irrigated water fluctuated. The next highest ratio was found in the Btv6 horizon (160–180 cm) and the Btv3 horizon (75–104 cm) where the water table frequently fluctuated.

Table 10.3 Selected extraction of Fe and Mn of the studied pedons

Horizon	Depth	Oxalate		DCB		Total		Fe_o/Fe_d	$(Fe_d-Fe_o)/Fe_t$	Mn_d/Fe_d
		Fe_o	Mn_o	Fe_d	Mn_d	Fe_t	Mn_t			
Lunchung										
Ap	0–20	2.5	0.0	39	0.1	30	0.0	0.06	1.22	0.26
Bw	20–41	1.6	0.0	82	0.1	18	0.0	0.02	4.47	0.12
2A	41–56	2.3	0.0	42	0.1	24	0.1	0.05	1.65	0.24
2Bt	56–85	0.9	0.0	61	0.3	30	0.1	0.01	2.00	0.49
2Btv1	85–100	0.6	0.2	58	0.3	24	0.1	0.01	2.39	0.52
2Btv2	100–140	0.4	0.1	37	0.3	42	0.3	0.01	0.87	0.81
2Btv3	140–180	1.4	0.3	71	1.5	–	–	0.02	–	2.11
2Btv4	>180	1.3	0.2	72	2.0	–	–	0.02	–	2.78
Luchu										
Ap	0–20	2.7	0.2	20	0.3	45	0.5	0.14	0.38	1.50
Btv1	20–50	1.1	0.2	24	0.2	50	0.5	0.05	0.46	0.83
Btv2	50–75	0.9	0.2	22	0.1	48	0.4	0.04	0.44	0.45
Btv3	75–104	1.5	0.2	25	0.2	40	0.3	0.06	0.59	0.80
Btv4	104–124	1.6	0.2	29	0.1	47	0.3	0.06	0.58	0.34
Btv5	124–160	1.5	0.2	27	0.1	40	0.3	0.06	0.64	0.37
Btv6	160–180	1.9	0.2	28	0.3	44	0.4	0.07	0.59	1.07
Hsinwu										
Ap	0–15	2.2	0.2	36	0.1	39	0.3	0.06	0.87	0.28
AB	15–26	1.0	0.3	36	0.2	–	–	0.03	–	0.56
Bt1	26–45	0.5	0.3	45	0.2	47	0.5	0.01	0.95	0.44
Bt2	45–75	0.5	0.3	58	0.2	60	0.5	0.01	0.96	0.34
Btv1	75–107	0.8	0.2	48	0.2	50	0.4	0.02	0.94	0.42
Btv2	107–133	1.2	0.3	52	0.3	54	0.6	0.02	0.94	0.58
Btv3	133–160	1.4	0.3	52	0.3	56	0.6	0.03	0.90	0.58
Chuwei-1										
Ap	0–18	2.6	0.1	22	0.1	22	0.2	0.12	0.88	0.45
AB	18–36	2.5	0.1	26	0.1	26	0.2	0.10	0.90	0.38
Btv1	36–70	1.7	0.4	32	0.4	39	0.6	0.05	0.78	1.25
Btv2	70–110	1.5	0.2	37	0.2	34	0.3	0.04	1.04	0.54
Btv3	110–145	0.9	0.3	22	0.2	23	0.3	0.04	0.92	0.91
Btv4	145–170	0.5	0.0	27	0.0	29	0.1	0.02	0.91	0.00
Btv5	>170	2.6	7.2	60	6.9	66	9.2	0.04	0.87	11.5
Houhu-1										
Ap	0–34	2.4	0.1	29	0.1	32	0.1	0.08	0.83	0.34
AB	34–47	0.7	0.1	32	0.1	31	0.3	0.02	1.01	0.31
Bt1	47–66	0.4	0.2	45	0.2	30	0.3	0.01	1.49	0.44
Btv1	66–82	0.5	0.4	53	0.3	44	0.1	0.01	1.19	0.57
Btv2	82–102	0.6	0.3	56	0.5	56	0.7	0.01	0.99	0.89
Btv3	102–122	1.0	0.3	61	0.3	63	0.7	0.02	0.95	0.49
Btv4	122–150	0.8	0.3	52	0.3	56	0.5	0.02	0.91	0.58
Houko										
Ap	0–20	5.2	0.1	26	0.2	35	0.3	0.20	0.59	0.77
Bt1	20–50	2.4	0.3	23	0.1	74	0.5	0.10	0.28	0.43
Bt2	50–75	3.6	0.2	21	0.2	49	0.4	0.17	0.36	0.95
Bt3	75–110	8.3	0.2	24	0.2	76	0.4	0.35	0.21	0.83
Btg1	110–130	17	0.3	18	0.2	39	0.5	0.94	0.03	1.11
Btg2	130–170	3.1	0.1	36	0.2	74	0.3	0.09	0.44	0.56

–: Not available

Fe_d: DCB extraction (g/kg)

Fe_o: Oxalate extraction (g/kg)

Fe_t: Total amount of elements (g/kg)

Table 10.4 Pearson correlation coefficient among soil properties, soil wetness conditions, and redoximorphic feature amounts

	Clay	Fe_d	Mn_d	Fe_o	Mn_o	Fe_t	Mn_t	Fe_o/Fe_d	$(Fe_d\text{-}Fe_o)/Fe_t$	ASD	ARD	GM	RM
Clay	1.00												
Fe_d	0.24	1.00											
Mn_d	0.34*	0.28*	1.00										
Fe_o	−0.04	−0.35**	−0.01	1.00									
Mn_o	0.30*	0.21	0.98**	0.01	1.00								
Fe_t	0.01	0.66**	0.21	−0.05	0.19	1.00							
Mn_t	0.29*	0.29*	0.99**	0.00	0.98**	0.29*	1.00						
Fe_o/Fe_d	−0.07	−0.43**	−0.07	0.98**	−0.05	−0.15	−0.06	1.00					
$(Fe_d\text{-}Fe_o)/Fe_t$	0.24	0.48**	0.13	−0.62**	0.07	−0.24	0.07	−0.62**	1.00				
ASD	−0.23	0.16	0.06	−0.12	0.06	0.17	0.08	−0.14	0.10	1.00			
ARD	−0.08	−0.34*	−0.02	0.41**	0.04	0.06	0.01	0.37**	−0.54**	0.26*	1.00		
GM	0.27	0.02	0.02	0.16	0.01	0.41*	0.03	0.12	−0.32*	−0.23	0.25	1.00	
RM	0.32*	0.06	0.32*	0.14	0.30	0.07	0.32*	0.13	−0.01	−0.12	−0.16	−0.01	1.00

–: Not available; Fe_d: DCB extraction; Fe_o: oxalate extraction; Fe_t: total amount of elements; ASD: annual saturation duration; ARD: annual reduction duration; GM: gray mottle amounts; RM: red mottles

*$p < 0.05$

**$p < 0.01$

Table 10.5 Types and quantities of redoximorphic features identified by naked eye and image analysis

Chuwei pedon	Matrix color	Fe depletions		Fe concretions		
		Gray (%)	Light yellow (%)	Yellow (%)	Yellow (%)	Red (%)
Naked eye						
Ap	10YR 4/3 (95)	2.5Y 3/1 (1)	–	10YR 6/8 (2)	–	5YR 5/8 (2)
AB	10YR 4/1 (91)	2.5Y 3/1 (2)	–	7.5YR 5/8 (2)	–	5YR 5/8 (5)
Btv1	N 6/0 (35)	–	–	10YR 5/8 (20)	–	5YR 5/8 (45)
Btv2	N 6/0 (55)	–	10YR 7/8 (20)	7.5YR 6/8 (25);	–	–
Image analysis						
Ap	10YR 4/3 (43)	10YR 6/1 (5)	7.5YR 6/3 (19)	5YR 6/8 (16)	–	10R 4/8 (17)
AB	10YR 4/1 (45)	10YR 6/1 (10)	–	7.5YR 7/8 (23)	2.5YR 4/8 (10)	10R 4/8 (12)
Btv1	10YR 7/1 (54)	–	10YR 7/3 (13)	7.5YR 7/6 (15)	–	2.5YR 5/8 (18)
Btv2	10YR 6/1 (42)	–	10YR 7/3 (24)	7.5YR 6/8 (34)	–	–

– : None

10.3.4 Digitize Redoximorphic Features

There was significant correlation between ARD and CI (Jien et al. 2004), as well as ARD and GM/RM contents (Fig. 10.3). Jien et al. (2004) indicated that the presence of organic carbon would lead to misjudgment and content misestimate of RMFs in upper soil horizons (<50 cm depth) if we identified and quantified the features by naked eyes in situ. A digital technique could be developed to precisely describe and quantify soil morphologies like applying image analysis techniques or spectroscopic estimates though Vis–NIR (Viscarra Rossel et al. 2009).

This study collected soil blocks (10 × 10 × 10 cm) from each horizon and then cut each block into 10 soil pieces (1 cm thick) for image analysis by IMAGIN 8.4. From the image analysis, the detail information of types and amounts of RMF was acquired. For Chuwei-1 soil, Table 10.5 compares with the identified types and amounts of RMFs by methods of naked eye and image analysis. Large differences of RMFs identification were found in Ap and AB horizons. The gray (10YR 6/1), reddish yellow (5YR 6/8 or 7.5YR 7/8), and red (10YR 4/8) seem to be misjudged by naked eye (Table 10.5), and the largest amounts of the misjudged RMFs ranged

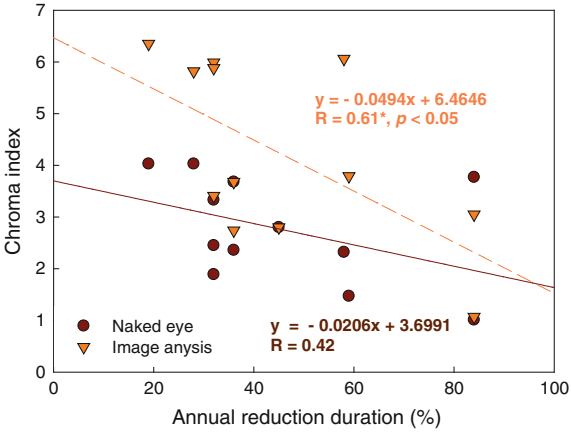

Fig. 10.4 Regression correlations between chroma index (*CI*) and annual reduction duration: *orange line* is image analysis method, and *brown line* is naked eye method

from 46 to 52 % in this study. Such misjudgments might be the major reason why soil colors fail to correlate to moisture regimes in surface soils (<30 cm). Our hypothesis is demonstrated in Fig. 10.4, in which significant negative correlation between ARD and CI was calculated from identified RMFs by image analysis. The CI values from RMFs identified by naked eye method failed to correlate to ARD in surface soils.

10.4 Conclusions

Digital soil morphometrics can help measuring and quantifying soil profile attributes and deriving continuous depth functions for further soil understanding. This study established correlations between soil color and wetness condition in rice-growing soils in Taiwan to help us in clarifying the SMR and develop criteria for classifying these soils. The study indicated that soil color could be used to assess soil wetness within soil profile as well as selective extraction of Fe and Mn. Digital soil morphometrics using image analysis significantly increased precision in quantifying and qualifying soil morphology.

Acknowledgements The authors would like to thank the Ministry of Science and Technology of the Republic of China (Taiwan) for financially supporting this research under Contract No. MOST 103-2313-B-020-007-MY2.

References

Ben-Dor E, Heller D, Chudnovsky A (2008) A novel method of classifying soil profiles in the field using optical means. Soil Sci Soc Am J 72:1113–1123

Blake GR, Hartge KH (1986) Bulk density. In: Klute A (ed) Methods of soil analysis. Part 1, 2nd edn., ASA and SSSA, Madison, WI, pp 363–375 (Agron. Monogr. 9)

Cox JW, Fritsch E, Fitzpatrick RW (1996) Interpretation of soil features produced by ancient and modern process in degraded landscapes VII. Water duration. Aust J Soil Res 34:803–824

Demattê JAM, Campos RC, Alves MC, Fiorio PR, Nanni MR (2004) Visible–NIR reflectance: a new approach on soil evaluation. Geoderma 121:95–112

Daniel RB, Gamble EE, Nelson LA (1971) Relations between soil morphology and water-table levels on a dissected North Carolina Coastal Plain surface. Soil Sci Soc Am Proc 35:781–784

Daugherty LA, Arnold RW (1982) Mineralogy and iron characterization of plinthitic soils on alluvial landforms in Venezuela. Soil Sci Soc Am J 46:1244–1252

Evans CV, Franzmeier DP (1988) Color index values to represent wetness and aeration in some Indiana soils. Geoderma 41:353–363

Fanning DS, Fanning MCB (1989) Gleization. Soil morphology, genesis, and classification. Wiley, New York, pp 110–125

Faulkner SP, Patrick WH Jr (1992) Redox processes and diagnostic wetland indicators in bottomland hardwood forests. Soil Sci Soc Am J 56:856–865

Franzmeier DP, Yahner JE, Steinhardt GC, Sinclair HR (1983) Color patterns and water table levels in some Indiana soils. Soil Sci Soc Am J 47:1196–1202

Hartemink A, Minasny B (2014) Towards digital soil morphometrics. Geoderma 230–231:305–317

Ho CS (1988) An introduction to the geology of Taiwan and explanation text of the geological map of Taiwan, 2nd ed. The Ministry of Economics Affairs, Republic of China, Taipei, Taiwan

Hossner LR (1996) Dissolution for total elemental analysis. In: Sparks DL et al (eds) Methods of soil analysis, Part 3. Chemical methods. ASA and SSSA, Madison, WI, USA, pp 49–64

Hseu ZY, Chen ZS (1996) Saturation, reduction, and redox morphology of seasonally flooded Alfisols in Taiwan. Soil Sci Soc Am J 60:941–949

Hseu ZY, Chen ZS (2001) Quantifying soil hydromorphology of a rice-growing Ultisol toposequence in Taiwan. Soil Sci Soc Am J 65:270–278

Jien SH, Hseu ZY, Chen ZS (2004) Relations between morphological color index and soil wetness condition of anthraquic soils in Taiwan. Soil Sci 169:871–882

Jien SH, Hseu ZY, Chen ZS (2010) Hydropedological implications of ferromanganiferous nodules in rice-growing plinthitic Ultisols under different moisture regimes. Soil Sci Soc Am J 74:880–891

Khan FA, Fenton TE (1996) Secondary iron and manganese distributions and aquic conditions in a Mollisol catena of central Iowa. Soil Sci Soc Am J 60:546–551

Mehra OP, Jackson ML (1960) Iron oxides removed from soils and clays by a dithionite-citrate system buffered with sodium bicarbonate. Clays Clay Miner 7:317–327

McKeague JA, Day JH (1966) Dithionite- and oxalate-extractable Fe and Al as aids in differentiating various classes of soils. Can J Soil Sci 45:49–62

Ponnamperuma FN (1972) The chemistry of submerged soils. Adv Agron 24:29–96

Schwertmann U, Fanning DS (1976) Iron and manganese concretions in hydrosequences of soils in loess in Bavaria. Soil Sci Soc Am J 40:731–738

Simonson GH, Boersma L (1972) Soil morphology and water table relations. II. Correlation between annual water fluctuations and profile features. Soil Sci Soc Am Proc 36:649–653

Soil Survey Staff (1993) Examination and description of soils in the field. In: Soil survey manual, Issued Oct 1993. Handbook No. 18. USDA-SCS, Washington, D.C, pp 59–196

Soil Survey Staff (2010) Keys to soil taxonomy. USDA-NRCS, 11th edn. U.S. Gov. Print. Office, Washington, D.C.

Stockmann U, Minasny B, McBratney AB (2014) How fast does soil grow? Geoderma 216:48–61

Vepraskas MJ (1992) Redoximorphic features for identifying aquic conditions. Tech. Bull. 301. North Carolina Agric. Res. Serv., North Carolina State Univ., Raleigh

Viscarra Rossel RA, Cattle SR, Ortega A, Fouad Y (2009) In situ measurements of soil colour, mineral composition and clay content by vis–NIR spectroscopy. Geoderma 150:253–266

Viscarra Rossel RA, Webster R (2011) Discrimination of Australian soil horizons and classes from their visible-near infrared spectra. Eur J Soil Sci 62:637–647

Chapter 11
Variation of Soil Properties in a Mollisol Profile Wall

Jenna R. Grauer-Gray and Alfred E. Hartemink

Abstract Soil variation was investigated in a Mollisol soil profile wall in south central Wisconsin, USA. The soil was classified as a fine-loamy, mixed, superactive, mesic Pachic Argiudolls. Data were collected from a 1 × 1 m soil profile wall that was divided into a 10 × 10 cm raster. The following measurements were made: volumetric moisture content, soil pH, soil organic carbon (SOC) concentration, and elemental analysis of Al, Ca, Fe, Mn, P, Si, Ti, and Zr by portable X-ray fluorescence (pXRF). Spatial variation of soil properties was analyzed and mapped. All the soil properties demonstrated horizontal variation within the soil profile. The extent of horizontal variation changed with depth. The magnitude and direction of these changes showed no general pattern, differing between the soil properties. The SOC concentration showed constant horizontal variation at all depths except 70–80 cm. The soil pH demonstrated the lowest horizontal variation in the top 30 cm of the profile. The horizontal variation of Fe concentration tended to increase with depth. Soil property depth functions showed considerable variation between vertical transects. Only the SOC concentration and the soil pH demonstrated fairly consistent responses to changes in depth. The soil showed spatial variation within soil horizons. The soil pH and the Fe concentration showed low within-horizon variation in all soil horizons. SOC concentration showed moderate within-horizon variation in the Ap1 horizon and high within-horizon variation in the Bt horizon. Overall, the Bt horizon contained the greatest spatial variation. All soil horizons contained high within-horizon variation of at least one soil property. These results have some implications for sampling pedons.

Keywords Soil variation · Soil pit wall · Soil profile · Morphometrics · Soil horizon

J.R. Grauer-Gray · A.E. Hartemink (✉)
Department of Soil Science, F.D. Hole Laboratory, University of Wisconsin—Madison, 1525 Observatory Drive, Madison, WI 53706, USA
e-mail: alfred.hartemink@wisc.edu

A.E. Hartemink and B. Minasny (eds.), *Digital Soil Morphometrics*,
Progress in Soil Science, DOI 10.1007/978-3-319-28295-4_11

11.1 Introduction

Soil scientists characterize a soil profile by dividing the profile into horizons based on soil properties observed in the field (Hartemink and Minasny 2014). These properties generally include color, texture, structure, and redoximorphic features. After soil horizon designation, one soil sample is taken from each horizon for laboratory analysis. As a result, only vertical variation of a soil profile is measured.

We used a raster approach to characterize horizontal and vertical variation of a Mollisol profile wall. A raster contains equally spaced data points (Goodchild 1992). Rasters are used to obtain, predict, and communicate spatial data in soil science. Digital soil mapping uses raster data and prediction rasters to produce rastered maps of soils and soil properties depicting the spatial variation of soils across landscapes (McBratney et al. 2003). However, few studies have used rasters to study spatial variation in a soil profile.

The objectives of our research were (i) to study horizontal and vertical variation of soil properties within a soil profile wall, (ii) to investigate within-horizon and between-horizon variation of soil properties in the soil profile, (iii) to utilize soil profile maps of soil properties to investigate patterns in the spatial variation of soil properties, (iv) to examine the homogeneity of soil horizons, and (v) to assess whether a soil profile can be accurately characterized with a one-dimensional, vertical sampling scheme.

11.2 Materials and Methods

11.2.1 Site Description

The soil was located at latitude 43° 4′ 2.88″ N and longitude 89° 32′ 8.10″ W at the University of Wisconsin-Madison West Madison Research Station in Verona, Wisconsin, USA (Fig. 11.1). The altitude of the site was 330 m.a.s.l. This area has a mean annual temperature of 7.8 °C and a mean annual precipitation of 840 mm.

The soil was formed in loess over outwash covering dolomite bedrock of Ordovician age at approximately 3.5 m depth. The vegetation was mainly grass and alfalfa. Though not cultivated at the time of this study, the site had been under agricultural use since the mid-1800s. The soil was located at the footslope landscape position and contained a buried A horizon at 59 cm depth due to the sedimentation of soil eroded from upper parts of the soilscape. An argillic horizon at 77 cm depth contained redoximorphic features.

The soil was classified as a fine-loamy, mixed, superactive, mesic Pachic Argiudolls (Troxel silt loam series). To 100 cm soil depth, the soil contained five horizons, all formed in loess (Table 11.1).

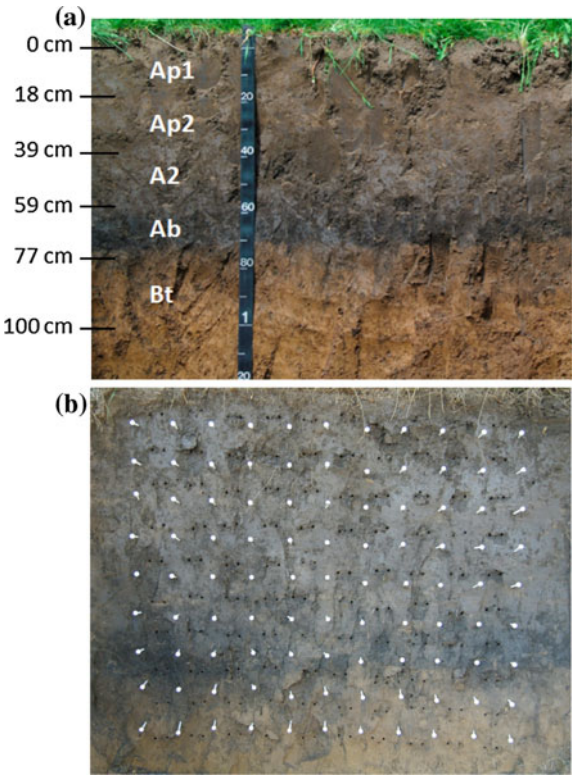

Fig. 11.1 Soil profile of a fine-loamy, mixed, superactive, mesic Pachic Argiudolls in Wisconsin, USA. **a** Soil profile with horizon designations and horizon depths indicated. **b** Soil profile rastered for field measurements and soil sampling (10 × 10 cm)

Table 11.1 Profile description of the soil (characterized to 100 cm soil depth), a fine-loamy, mixed, superactive, mesic Pachic Argiudolls located at the University of Wisconsin-Madison West Madison Research Station in Verona, Wisconsin, USA

Horizon	Depth (cm)	Dry color	Moist color	Structure	Texture	SOC (g/kg)	N (g/kg)
Ap1	0–18	Very dark brown (10YR 2/2)	Dark grayish brown (10YR 4/2)	Granular	Silt	22	2.3
Ap2	18–39	Very dark brown (10YR 2/2)	Dark grayish brown (10YR 4/2)	Platy	Silt loam	18	1.8
A2	39–59	Very dark brown (10YR 2/2)	Dark grayish brown (10YR 4/2)	Subangular blocky	Silt loam	22	2.1
Ab	59–77	Black (10YR 2/1)	Dark grayish brown (10YR 4/2)	Subangular blocky	Silt loam	27	2.3
Bt	77+	Dark yellowish brown (10YR 3/4)	Yellowish brown (10YR 5/4)	Angular blocky	Silty clay loam	8	1.6

11.2.2 Soil Sampling and Analysis

The soil profile wall was divided into a 1 × 1 m raster of 10 × 10 cm squares up to 1 m depth (Fig. 11.1). Volumetric moisture content was measured in the field in the center of each square using a time-domain reflectometer (Spectrum FieldScout TDR 300). Soil samples of approximately 200 g were collected from the center of each raster square.

Laboratory samples were air-dried. Dry and moist color measurements were taken using Munsell soil color charts. Samples were finely ground. The concentrations of Al, Ca, Fe, Mn, P, Si, Ti, and Zr were measured in the laboratory using portable X-ray fluorescence (pXRF). A Delta Professional pXRF Analyzer (Olympus Scientific Solutions Americas, Inc.) was used to scan the soil samples. The pXRF analyzer was calibrated using a 316 stainless steel calibration check reference coin. The soil organic carbon (SOC) and nitrogen concentrations were determined by LECO dry combustion. The soil pH was measured in 1:1 soil to water.

11.2.3 Data Analysis

Boxplots for each soil property were made to examine property variation within and between depth intervals and within and between soil horizons. Individual plots were created for each property. The boxplots show the median, the quartiles (excluding outliers), and the outliers at each depth or within each horizon. Property depth function plots were created by combining the soil property depth functions of the ten vertical transects of the soil profile on one plot. Depth function plots were created for every studied soil property except Ti and Zr concentrations. The midpoint of each depth interval was used as the depth value for the property measurement in that depth interval.

Soil profile maps were created for every soil property except volumetric moisture content and Ti and Zr concentrations by locating the soil property measurements of each soil sample in the center of its raster square then spatially interpolating the soil property values over the soil profile wall using block kriging and global variograms in VESPER (Minasny et al. 2005).

Statistics by depth and by horizon were calculated using the “doBy” package (Højsgaard and Halekoh 2014) within the R statistical package (R Core Team 2013). Coefficients of variation (CVs) by horizon were calculated by dividing the standard deviation by the mean.

11.3 Results

11.3.1 Variation of Soil Properties with Depth

SOC

The SOC concentration showed constant horizontal variation at all depths except at 70–80 cm soil depth (Fig. 11.2). The standard deviation was 7 g C/kg at 70–80 cm soil depth, whereas at all other depths it was below 2 g C/kg. The SOC depth functions all followed the same pattern. At 0–30 cm soil depth, the SOC concentration tended to decrease slightly with depth. At 30–70 cm soil depth, the SOC concentration tended to increase with depth. At 60–70 cm soil depth, the direction of the depth functions changed, and below 70 cm, the depth functions showed a tendency of decreasing SOC concentration with depth. The SOC depth functions all tended to have similar rates of change with depth except at 60–80 cm soil depth. At 60–80 cm soil depth, the SOC depth functions demonstrated the most dissimilarity due to varying rates of change in SOC concentration; the magnitude of the decrease in SOC concentration from 60 cm soil depth to 80 cm soil depth ranged from 0.3 g C/kg to 20 g C/kg.

pH

The lowest horizontal variation of soil pH occurred in the top 30 cm of the soil profile with standard deviations below 0.1 (Fig. 11.2). The soil pH at depths with high pH did not vary more than the soil pH at depths with low pH. The highest horizontal variation of soil pH occurred at 90–100 cm soil depth with a standard deviation exceeding 0.2. The soil pH depth functions generally followed the same pattern. The soil pH increased with depth at 0–20 and 80–100 cm soil depth. At 40–60 cm, the soil pH tended to decrease with depth. At 20–40 and 60–80 cm soil depth, the soil pH depth functions fluctuated slightly with depth and the changes did not follow a consistent pattern.

Volumetric Moisture Content

The horizontal variation of the volumetric moisture content increased with depth in the top 30 cm of the soil profile, decreased with depth until 70 cm soil depth, then stayed constant at 70–100 cm soil depth (Fig. 11.2). The highest horizontal variation of volumetric moisture content occurred at 10–40 cm soil depth with standard deviations exceeding 5 %.

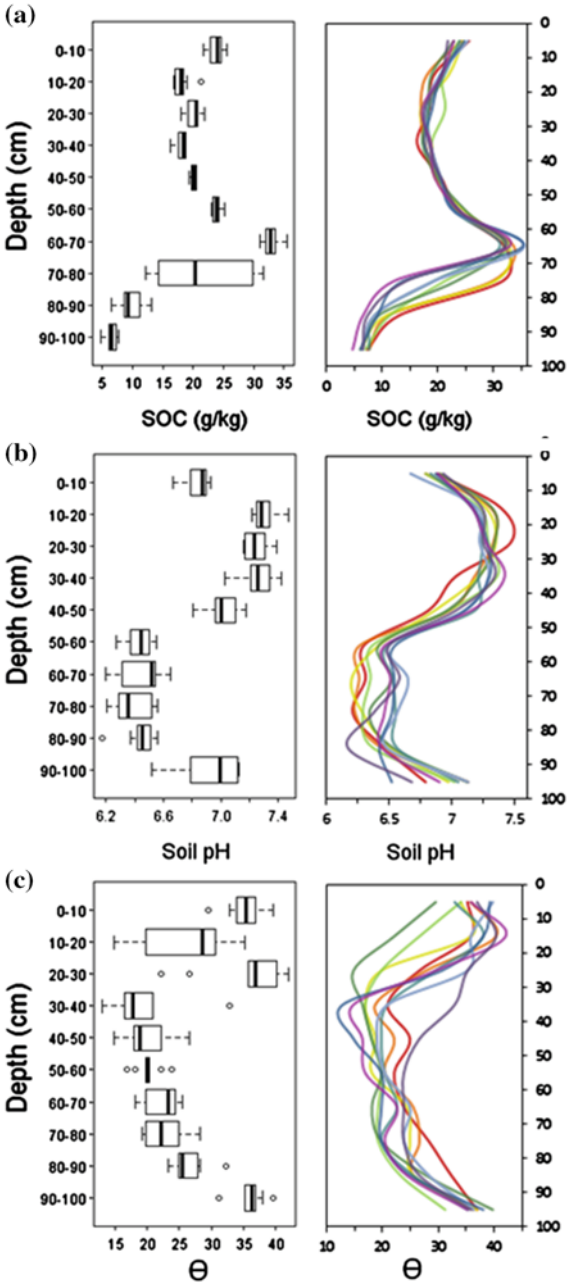

Fig. 11.2 Boxplots and depth function plots showing the horizontal and vertical variation of soil properties at each depth interval studied in a 1 × 1 m profile wall of a fine-loamy, mixed, superactive, mesic Pachic Argiudolls in Wisconsin, USA. The depth function plots contain ten individual depth functions, obtained from the ten vertical transects studied in the soil profile wall. Ten soil samples from the center of 10 × 10 cm raster squares were taken at each depth interval and from each vertical transect. **a** SOC concentration and **b** pH were obtained in the laboratory. **c** Volumetric soil moisture content (θ) was measured in the field

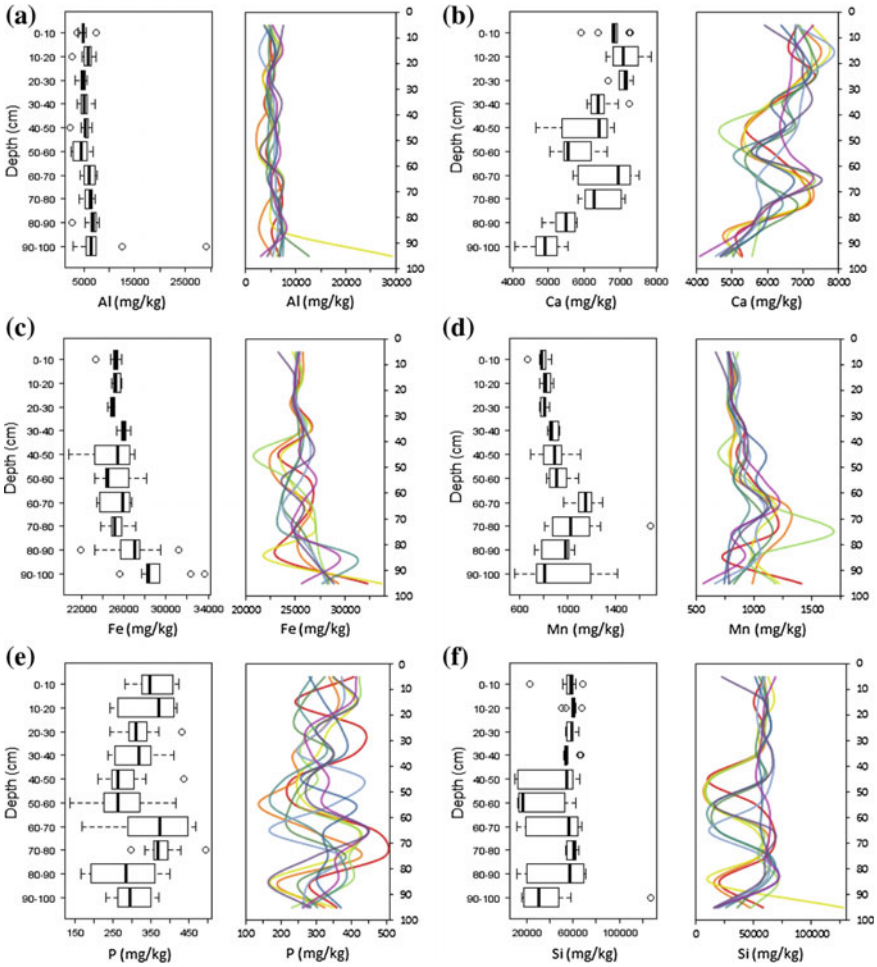

Fig. 11.3 Boxplots and depth functions showing the horizontal and vertical variation of soil properties at each depth interval studied in a 1 × 1 m profile wall of a fine-loamy, mixed, superactive, mesic Pachic Argiudolls in Wisconsin, USA. The depth function plots contain ten individual depth functions, obtained from the ten vertical transects studied in the soil profile wall. Ten soil samples from the center of 10 × 10 cm raster squares were taken at each depth interval and from each vertical transect. Elemental concentrations of **a** Al, **b** Ca, **c** Fe, **d** Mn, **e** P, and **f** Si were obtained on air-dried soil samples using pXRF

Al

The Al concentration showed relatively constant horizontal variation at all depth intervals except at 90–100 cm soil depth (Fig. 11.3). At 90–100 cm soil depth, the standard deviation was 8000 mg Al/kg; at other depths, the standard deviations were between 800 and 2000 mg Al/kg. The median Al concentrations ranged from 4000 mg Al/kg at 50–60 cm soil depth to 7000 mg Al/kg at 80–90 cm soil depth.

Ca

The horizontal variation of the Ca concentration fluctuated with depth (Fig. 11.3). The greatest horizontal variation occurred at 40–50 cm soil depth and 60–70 cm soil depth with standard deviations exceeding 700 mg Ca/kg. The lowest horizontal variation occurred at 20–30 cm soil depth with a standard deviation of 200 mg Ca/kg. The median Ca concentration ranged from 5000 mg Ca/kg at 90–100 cm soil depth to 7000 mg Ca/kg at 60–70 cm soil depth.

Fe and Mn

The horizontal variation of Fe and Mn concentrations tended to increase with depth (Fig. 11.3). The lowest horizontal variation occurred in the top 40 cm of the soil profile with standard deviations of 200–700 mg Fe/kg and of 20–50 mg Mn/kg. The horizontal variation increased below 40 cm soil depth with standard deviations of 1000–3000 mg Fe/kg and 90–300 mg Mn/kg. The median Fe and Mn concentrations stayed relatively constant with depth in the upper 60–80 cm of the soil profile with median concentrations of around 25,000 mg Fe/kg at 0–80 cm soil depth and median concentrations of around 800 mg Mn/kg at 0–60 cm soil depth. Below 80 cm soil depth, the median Fe concentration increased to 28,000 mg Fe/kg at 90–100 cm. The highest median Mn concentration occurred at 60–70 cm soil depth (1000 mg Mn/kg).

P

The horizontal variation of P concentration fluctuated with depth (Fig. 11.3). The highest horizontal variation of P concentration occurred at 60–70 cm soil depth with a standard deviation exceeding 100 mg P/kg. At other soil depths, the standard deviations ranged from 40 to 90 mg P/kg. The median P concentration ranged from 260 mg P/kg at 40–60 cm to 370 mg P/kg at 10–20 cm soil depth and 60–80 cm soil depth.

Si

The horizontal variation of Si concentration fluctuated with depth (Fig. 11.3). The lowest horizontal variation of Si concentration occurred at 0–40 cm soil depth and at 70–80 cm soil depth with standard deviations below 20,000 mg Si/kg. The highest horizontal variation occurred at 90–100 cm soil depth with a standard deviation exceeding 30,000 mg Si/kg. The median Si concentrations were relatively constant at all depths except at 50–60 cm soil depth and 90–100 cm soil depth.

Ti

The lowest horizontal variation of Ti concentration occurred in the top 40 cm of the soil profile with standard deviations below 150 mg Ti/kg. At other depths, the standard deviations ranged from 200 to 470 mg Ti/kg. The lowest median Ti concentration occurred at 50–60 cm soil depth (2900 mg Ti/kg). At other depths, the median Ti concentration remained fairly constant, ranging from 3200 to 3500 mg Ti/kg.

Zr

The highest horizontal variation of Zr concentration occurred at 70–80 cm soil depth with a standard deviation of 30 mg Zr/kg (Fig. 11.4). At other soil depths, standard deviations were below 20 mg Zr/kg. The lowest horizontal variation of Zr concentration occurred at 0–40 cm soil depth. The median Zr concentration at 0–40 cm soil depth ranged from 290 mg Zr/kg to 310 mg Zr/kg. The median Zr concentration at 40–70 cm soil depth was below 280 mg Zr/kg. The median Zr concentration at 70–100 cm soil depth exceeded 350 mg Zr/kg.

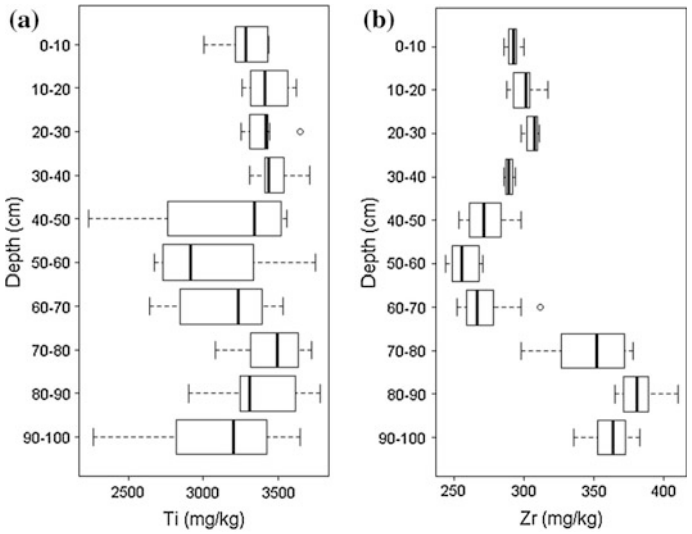

Fig. 11.4 Boxplots showing the horizontal and vertical variation of soil properties at each depth interval studied in a 1 × 1 m profile wall of a fine-loamy, mixed, superactive, mesic Pachic Argiudolls in Wisconsin, USA. Ten soil samples from the center of 10 × 10 cm raster squares were taken at each depth interval. Elemental concentrations of **a** Ti and **b** Zr were obtained on air-dried soil samples using pXRF

Table 11.2 Amount of within-horizon variation of soil properties: soil organic carbon (SOC), soil pH, volumetric moisture content (Θ), elemental concentrations of Al, Ca, Fe, Mn, P, and Si

Horizons	n	SOC	pH	Θ	Al	Ca	Fe	Mn	P	Si
Ap1	20	±	−	±	+	−	−	−	±	±
Ap2	20	−	−	+	±	−	−	−	±	−
A2	20	−	−	±	+	±	−	±	+	+
Ab	10	−	−	±	+	±	−	−	+	+
Bt	20	+	−	±	+	−	−	+	+	+

All properties except Θ were measured on air-dried soil samples in the laboratory. Amount of variation measured using coefficients of variation (CVs).
− = CV < 10 %, ± = CV 10–20 %, + = CV > 20 %

11.3.2 Variation Within Soil Horizons

The samples from 0 to 20 cm soil depth are from the Ap1 horizon, from 20 to 40 cm soil depth are from the Ap2 horizon, from 40 to 60 cm soil depth are from the A2 horizon, from 60 to 70 cm soil depth are from the Ab horizon, and from 80 to 100 cm soil depth are from the Bt horizon. The Bt horizon contained five soil properties demonstrating high (CV > 20 %) within-horizon variation (Table 11.2). The A2 and Ab horizons each contained three soil properties demonstrating high within-horizon variation. The Ap1 and Ap2 horizons contained mainly low (CV < 10 %) and moderate (CV 10–20 %) within-horizon soil property variation.

SOC

The within-horizon SOC concentrations consisted of three non-overlapping ranges (Fig. 11.5). The lowest SOC concentrations occurred in the Bt horizon (5–13 g C/kg). The Ap1, Ap2, and A2 horizons contained SOC concentrations between 16 and 26 g C/kg. The highest SOC concentrations occurred in the Ab horizon (31–35 g C/kg). The lowest within-horizon variation of SOC occurred in the Ap2 and Ab horizons (CV < 6 %). The Ap1 and A2 horizons had CVs of about 10 %. The highest within-horizon variation of SOC concentration occurred in the Bt horizon (CV 30 %).

pH

The highest soil pH occurred in the Ap1 and Ap2 horizons (Fig. 11.5). The pH showed low within-horizon variation in all the horizons with CVs lower than 5 %. The lowest within-horizon variation occurred in the Ap2 and Ab horizons.

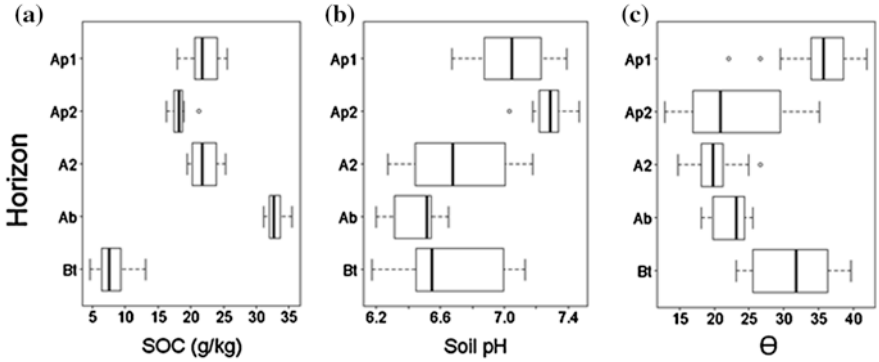

Fig. 11.5 Boxplots showing within- and between-horizon variation of soil properties in the five horizons studied in a 1 × 1 m profile wall of a fine-loamy, mixed, superactive, mesic Pachic Argiudolls in Wisconsin, USA. Soil samples were collected from the center of 10 × 10 cm raster squares and **a** SOC concentration and **b** soil pH were measured in the laboratory. **c** Volumetric soil moisture content (θ) was measured in the field in the center of 10 × 10 cm raster squares

Volumetric Moisture Content

Volumetric moisture content demonstrated moderate to high within-horizon variation with CVs ranging from 11 % to 31 % (Fig. 11.5).

Al

The lowest median Al concentrations occurred in the Ap1, Ap2, and A2 horizons with median concentrations of 5000 mg Al/kg (Fig. 11.6). The Ab horizon had a median concentration of 6000 mg Al/kg, and the Bt horizon had a median Al concentration of 7000 mg Al/kg. The highest within-horizon variation of Al concentration occurred in the Bt horizon (CV > 70 %). The other soil horizons contained moderate to high within-horizon variation of Al concentration with CVs below 30 %.

Ca

The lowest median Ca concentrations occurred in the Ab and Bt horizons with median concentrations below 6000 mg Ca/kg (Fig. 11.6). The Ap1, Ap2, and Ab horizons had median Ca concentrations of 7000 mg Ca/kg. The Ap1 and Ap2 horizons had the lowest within-horizon variation of Ca with CVs lower than 7 %. The A2, Ab, and Bt horizons had CVs around 10 %.

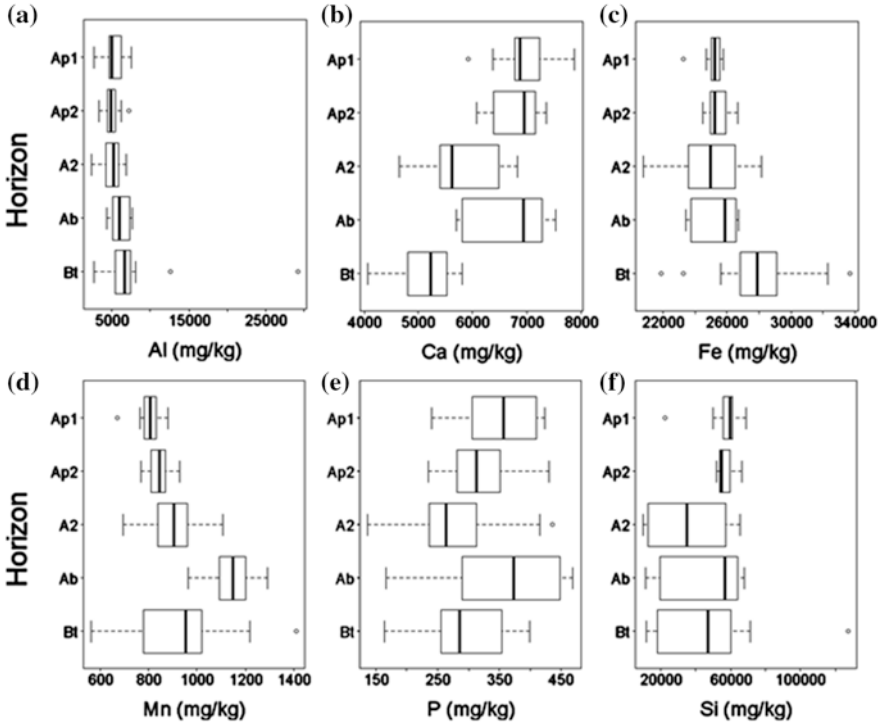

Fig. 11.6 Boxplots showing within- and between-horizon variation of soil properties in the five horizons studied in a 1 × 1 m profile wall of a fine-loamy, mixed, superactive, mesic Pachic Argiudolls in Wisconsin, USA. Soil samples were collected from the center of 10 × 10 cm raster squares and the following elemental concentrations were measured in the laboratory: **a** Al, **b** Ca, **c** Fe, **d** Mn, **e** P, **f** Si

Fe

The highest Fe concentration occurred in the Bt horizon with a median concentration of 28,000 mg Fe/kg (Fig. 11.6). The other horizons contained median concentrations of about 25,000 mg Fe/kg. The lowest within-horizon variation of Fe concentration occurred in the Ap1 and Ap2 horizons (CV < 3 %). The highest within-horizon variation of Fe concentration occurred in the Bt horizon (CV 10 %).

Mn

The highest median Mn concentration occurred in the Ab horizon with a median concentration exceeding 1000 mg Mn/kg (Fig. 11.6). The Ap1, Ap2, A2, and Bt horizons contained median concentrations of 800–1000 mg Mn/kg. The Ap1 and Ap2 horizons had the lowest within-horizon variation of Mn concentration

(CV < 6 %). The Bt horizon had the highest within-horizon variation of Mn concentration with a CV exceeding 20 %.

P

The lowest P concentration occurred in the A2 horizon with a median concentration of 260 mg P/kg (Fig. 11.6). The highest median P concentrations occurred in the Ap1 and Ab horizons with median concentrations exceeding 350 mg P/kg. The lowest within-horizon variation of P concentration occurred in the Ap1 and Ap2 horizons. The highest within-horizon variation of P concentration occurred in the Ab horizon (CV 30 %).

Si

The lowest median Si concentration occurred in the A2 horizon with a median concentration of 35,000 mg Si/kg (Fig. 11.6). The Bt horizon had a median concentration of 47,000 mg Si/kg. The highest median Si concentrations occurred in the Ap1, Ap2, and Ab horizons with median concentrations between 55,000 and 60,000 mg Si/kg. The lowest within-horizon variation of Si concentration occurred in the Ap2 horizon (CV 8 %). High within-horizon variation of Si concentration occurred in the Ab horizon (CV 50 %) and the highest within-horizon variation of Si concentration occurred in the A2 and Bt horizons with CVs exceeding 60 %.

11.3.3 Variation Between Soil Horizons

Between the Ap1 and the Ap2 horizons, three soil properties demonstrated little (ΔCV 1–5 %) change in within-horizon variation and one soil property demonstrated medium (ΔCV 5–10 %) change in within-horizon variation (Table 11.3). One soil property demonstrated large (ΔCV 10–20 %) change in within-horizon variation between the Ap1 and Ap2 horizons, between the Ap2 and the A2 horizons and between the A2 and the Ab horizons. One soil property demonstrated very large (ΔCV > 20 %) change in within-horizon variation between the Ap2 and the A2 horizons. Between the Ab and the Bt horizons, four soil properties demonstrated large or very large changes of within-horizon variation.

Within-horizon variation of SOC concentration and Al concentration showed little change between all adjacent horizons except the Ab and Bt horizons. Between the Ab and the Bt horizons, the within-horizon variation of SOC and Al concentrations demonstrated very large changes. The within-horizon variation of Si concentration and Mn concentration demonstrated large changes between the Ab and the Bt horizons.

Table 11.3 Change in within-horizon variation of soil properties between adjacent horizons

Horizons	SOC	pH	Θ	Al	Ca	Fe	Mn	P	Si
Ap1 → Ap2	↓	↓	↑↑↑	↓	≈	≈	≈	≈	↓↓
Ap2 → A2	↑	↑	↓↓↓	↑↑	↑	↑	↑↑	↑↑	↑↑↑↑
A2 → Ab	↓	↓	↓	↓	≈	↓	↓	↑	↓↓↓
Ab → Bt	↑↑↑↑	↑	↑↑	↑↑↑↑	↓	↑	↑↑↑	↓↓	↑↑↑

≈: change of <1 %, ↑/↓: increase/decrease of 1–5 %, ↑↑/↓↓: increase/decrease of 5–10 %, ↑↑↑/↓↓↓: increase/decrease of 10–20 %, and ↑↑↑↑: increase of >20 %

11.3.4 Soil Profile Maps of SOC Concentration and Soil pH

The soil profile map of SOC concentration divided the profile into four layers: a layer of medium SOC concentration between 0 and about 57 cm soil depth, a layer of high SOC concentration between about 57 and 72 cm soil depth, another layer of medium SOC concentration between about 72 and 81 cm soil depth, and a layer of low SOC concentration below 81 cm soil depth (Fig. 11.7). A nearly level horizontal boundary occurred between the first and the second layers of the soil profile map. Wavy boundaries occurred between the second and third layers, and the third and fourth layers of the soil profile map.

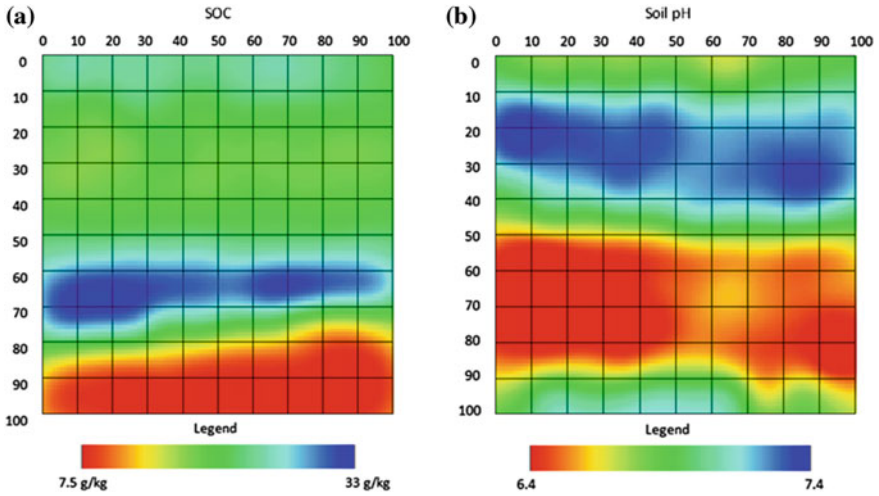

Fig. 11.7 Soil profile maps showing spatial variation of a mixed, superactive, mesic Pachic Argiudolls in Wisconsin, USA. Soil samples (n = 100) sampled from the center of 10 × 10 cm raster squares. **a** SOC concentration and **b** soil pH were obtained in the laboratory. Soil profile maps were created for each soil property by locating the measured values of each soil sample in the center of its column and depth interval then spatially interpolating the soil property values over the soil profile wall using block kriging and global variograms in Vesper 1.6 (Australian Center for Precision Agriculture)

The soil profile map of soil pH consisted mainly of two layers: a layer of high soil pH at about 10–40 cm soil depth and a layer of low soil pH at 50–90 cm soil depth (Fig. 11.7). Thin layers of medium soil pH occurred at about 0–10 cm, 40–50 cm, and 90–100 cm soil depth. An area of medium-high soil pH occurred at about 90–100 cm soil depth. All of the layers had wavy boundaries.

11.3.5 Soil Profile Maps of Elemental Concentrations

Al

The soil profile map of Al concentration showed a pattern of increasing Al concentration with depth in the horizontal range of 0–80 cm (Fig. 11.8). At 80–100 cm

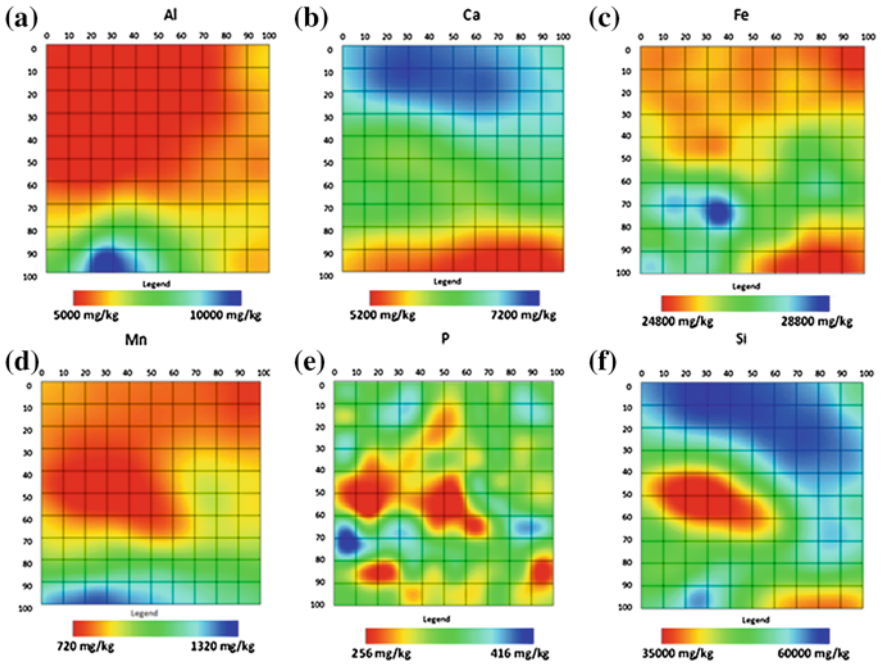

Fig. 11.8 Soil profile maps showing spatial variation of a mixed, superactive, mesic Pachic Argiudolls in Wisconsin, USA. Soil samples (n = 100) from the center of 10 × 10 cm raster squares. Elemental concentrations of **a** Al, **b** Ca, **c** Fe, **d** Mn, **e** P, and **f** Si were obtained in the laboratory using pXRF. Soil profile maps were created for each soil property by locating the measured values of each soil sample in the center of its column and depth interval then spatially interpolating the soil property values over the soil profile wall using block kriging and global variograms in Vesper 1.6 (Australian Center for Precision Agriculture)

horizontally, the Al concentration remained relatively constant with depth. The increase in Al concentration with depth occurred irregularly. The greatest increase in Al concentration with depth occurred at 20–40 cm horizontally.

Ca

The soil profile map of Ca concentration showed a pattern of decreasing Ca concentration with depth (Fig. 11.8). The soil profile map of Ca concentration had three main layers: a top layer of high Ca concentration, a middle layer of medium Ca concentration, and a bottom layer of low Ca concentration. The top layer had an irregular lower boundary, beginning at 20–30 cm soil depth at 0–10 cm horizontally then decreasing in depth and becoming more diffuse. The middle layer had a less irregular but still wavy lower boundary. Also, a few areas of increasing Ca concentration with depth occurred: at 70–100 cm horizontally at 0–20 cm soil depth, at 0–40 cm horizontally at 40–60 cm soil depth, and at 50–60 cm horizontally at 50–80 cm soil depth.

Fe

The soil profile map of Fe concentration had two large areas: an area of low Fe concentration in the upper 30–50 cm of the soil profile and an area of medium concentration located between 30 cm and 100 cm soil depth (Fig. 11.8). Small areas of high Fe concentration occurred between 60 cm and 80 cm soil depth. An area of low Fe concentration occurred below 70 cm soil depth at 50–100 cm horizontally.

Mn

The soil profile map of Mn concentration contained three main layers: a layer of low Mn concentration at about 0–70 cm soil depth, a layer of medium Mn concentration at about 70–100 cm soil depth, and a layer of high Mn concentration at about 90–100 cm soil depth (Fig. 11.8). The boundary between the top and the middle layers occurred at 60–80 cm soil depth at 0–60 cm horizontally and at 90–100 cm horizontally. At 60–90 cm horizontally, the layer of medium Mn concentration had a tongue-shaped extension, which stretched up to about 40 cm soil depth. At 20–70 cm horizontally, the boundary between the middle and the bottom layers occurred at 80–90 cm depth, but the boundary occurred at 90–100 cm depth elsewhere in the profile.

P

The soil profile map of P concentration showed an apparently random distribution of P content in the profile (Fig. 11.8). The map had scattered areas of high, medium, and low P concentration.

Si

The soil profile map of Si concentration showed a pattern of decreasing Si concentration with depth in the top 70 cm of the profile (Fig. 11.8). A region of high Si concentration occurred in the top 0–50 cm of the soil profile. Small areas of medium-high to high Si concentration occurred below 50 cm soil depth. Areas of low Si concentration occurred between 30 and 70 cm soil depth and below 90 cm soil depth.

11.4 Discussion

11.4.1 Application of Digital Soil Morphometrics

In this study, we applied digital soil morphometrics to quantitatively measure soil profile properties, to create continuous depth functions, and to investigate spatial variation of soil properties in a soil profile wall (Hartemink and Minasny 2014). The technique of rastering allowed us to study horizontal and vertical variation at fixed depth increments and to create soil property depth functions and soil profile maps showing the variation of soil properties. We used the pXRF analyzer and the TDR to obtain rapid measurements of elemental concentrations and volumetric soil moisture content. A similar approach was used by Adhikari et al. (2016) who applied soil profile wall rastering, TDR, pXRF, and spatial interpolation to study soil profile properties. In a study of soil hydrology, Netto et al. (1999) used a grid method to study horizontal and vertical variation, sampling every 10 cm horizontally over a 1.2 m distance, and sampling nine depth ranges (5–6 cm deep) between 0 and 1.05 m soil depth. Schwen et al. (2014) used a three-dimensional raster sampling scheme to study solute movement and soil physical properties in soil pedons, sampling every 10 cm in each dimension.

Digital soil morphometrics enables investigation of variation within soil profiles, variation that would be overlooked when using traditional methods. Buddenbaum and Steffens (2012) imaged an undisturbed soil profile in the laboratory using high-resolution vis-NIR (400–1000 nm) spectroscopy. They detected spatial variation within the profile using the resulting images. Steffens et al. (2014) used the same technique to identify SOM fractions in a visually uniform organic soil profile. Roudier et al. (2016) collected spectroscopic (350–2500 nm) images of three soil

profiles in the laboratory. Using principal component analysis and segmentation, they created false color images showing horizontal variation within the profile. They also found vertical variation within horizons and the presence of a possible horizon boundary not detected when horizonating the soil profile using traditional characterization tools and techniques.

11.4.2 Horizontal Variation of Soil Properties

All studied soil properties demonstrated horizontal variation within the soil profile. The extent of horizontal variation changed with depth. The magnitude and direction of these changes showed no general pattern, differing between soil properties. In their study of a Psamment soil profile, Adhikari et al. (2016) observed considerable horizontal variation and soil property-dependent patterns of variation. Netto et al. (1999) observed considerable horizontal variation of volumetric soil moisture content in coarse-textured soil profiles.

Cultivation and Bioturbation

The lowest horizontal variation of soil pH occurred in the top 30 cm of the soil profile, and the lowest horizontal variation of Al, Fe, Mn, Si, Ti, and Zr concentrations occurred in the top 40 cm of the soil profile. The Al, Fe, Mn, Si, Ti, and Zr concentrations also demonstrated low vertical variation between 0 and 40 cm soil depth. This 0–40 cm depth range corresponded to the location of the Ap1 and Ap2 horizons, the horizons that have undergone haploidization due to plowing and sedimentation. Other studies have found low spatial variation in the top 30–40 cm of soil profiles with a history of cultivation. Adhikari et al. (2016) noted that the lowest spatial variability occurred in the top 40 cm of their soil profile. Franklin et al. (2003) found no difference between the concentrations of Al, Fe, Mn, Zr, and Ti and twenty other elements between the 0–15 cm and the 15–30 cm soil depth ranges in 27 soil profiles with a history of cultivation.

Haploidization due to cultivation of the top 40 cm cannot completely explain the spatial variation of soil pH at the 0–40 cm soil depth. The soil pH demonstrated vertical variation at 0–40 cm soil depth and horizontal variation at 30–40 cm soil depth. Soil haploidization due to bioturbation may have contributed to low horizontal variation of pH. Bioturbation can reduce variation in soil and tends to occur most intensely near the soil surface (Hole 1981; Wilkinson et al. 2009).

SOC

The SOC concentration increased with depth at 30–70 cm soil depth, possibly due to a decreasing rate of decomposition of soil organic matter (SOM). With increasing

soil depth, SOM decomposition rates tend to decrease (Gregorich et al. 1998; Helgason et al. 2014). The horizontal variation of SOC concentration was more or less constant at all depths except 70–80 cm soil depth. The higher horizontal variation of SOC at 70–80 cm resulted from the presence of the boundary between the Ab horizon and the subsoil (Bt horizon). This boundary effect seems to increase spatial variation of SOC concentration. Mapping a soil profile using high-resolution vis-NIR spectroscopy, Steffens and Buddenbaum (2013) found larger spatial variability in the transition zone between the topsoil (A) and the subsoil (E) horizons of their profile than within the individual horizons.

Volumetric Moisture Content

The volumetric moisture content demonstrated horizontal variation with standard deviations between 2 and 8 %. Netto et al. (1999) found moderate horizontal variation (CV 5–20 %) in a coarse-textured soil profile and non-significant correlation of the volumetric moisture content horizontally.

Al and Si

The Al and Si concentrations demonstrated increasing horizontal variation with depth at 70–100 cm soil depth, the depth range containing the Bt horizon. The increasing variation probably reflects increasingly irregular distribution of illuviated aluminosilicate clays with depth. The low spatial variation of Al and Si concentrations in the top 40 cm of the soil profile may result from an even distribution of aluminosilicate clay. At 40–70 cm soil depth, Al concentration showed low spatial variation, but Si concentration showed high spatial variation. A factor other than distribution of aluminosilicate clays is needed to explain the variation of Al and Si concentrations at 40–70 cm soil depth.

11.4.3 Utility of Soil Depth Functions

Soil profile studies have used soil depth functions to help characterize soil profiles and identify soil processes (e.g. Gaikawad and Hole 1965; Eswaran and Bin 1978). Minasny et al. (2016) used soil depth functions to derive soil horizon boundaries. However, the soil property depth functions in our soil profile changed between vertical transects. Sampling the vertical transect at 0–10 cm horizontally resulted in different depth functions for most soil properties than sampling the adjacent vertical transect at 10–20 cm horizontally or sampling the vertical transect at 90–100 cm horizontally. Only the depth functions of SOC concentration and soil pH maintained relatively constant shapes across the ten vertical transects.

11.4.4 Ti and Zr

The Ti concentration remained relatively constant throughout the soil profile. The Zr concentrations divided the soil profile into three zones: a region of medium Zr concentration at 0–40 cm soil depth, a region of low Zr concentration at 40–70 cm soil depth, and a region of high Zr concentration at 70–100 cm soil depth. Since Zr is relatively immobile in the soil, changes in Zr concentrations may reflect differences in parent material (Schaetzl 1998). The top 100 cm of this soil profile formed in loess, but loess from different depositional events may differ in chemical composition (Muhs and Bettis 2000). The decrease in Zr concentration at 40 cm soil depth may result from the loess parent material having a different chemical composition as compared to the 40–70 cm soil depth. The 40–70 cm soil depth contained the majority of the buried A horizon with approximately 20 cm of deposited material above it. This 20 cm of deposited material may have been transported from nearby areas with the same type of loess parent material as the buried A horizon. The increase in Zr concentration at 70–80 cm soil depth may result from a different loess parent material.

11.4.5 Variation Within and Between Soil Horizons

We found that soil properties show considerable horizontal and within-horizon variation, variation that cannot be detected using one-dimensional vertical sampling schemes. We found moderate to very high spatial variation of at least three soil properties within all horizons studied. This high within-horizon variation implies that horizon characterization using one sample per horizon does not always estimate the average value of a soil property within the horizon.

Stolt et al. (1993) found considerable variation of soil properties within soil horizons. They used four soil samples from the corners of 1 × 1 m lateral horizon cross sections. They found an average CV of 10 % and a maximum CV of 40 % for extractable Al and Fe within Bt horizons. They suggested taking multiple samples from a soil horizon to increase the accuracy of soil profile characterization.

SOC, Al, and Si

In our soil profile, the SOC, Al, and Si concentrations demonstrated high within-horizon variation in the Bt horizon. The high variation of Al and Si concentrations may result from the uneven distribution of illuviated aluminosilicate clays. SOM may have been transported into the Bt horizon in conjunction with clay, contributing to high variation of SOC in the Bt horizon. SOC can be transported within a soil profile as clay-humus chelates (Miedema et al. 1999). Another factor that could have contributed to the high variation of SOC may be spatially localized sources of SOM, for example, plant roots and fungal hyphae.

The high to very high increase in within-horizon variation of Al and Si concentrations between the Ab and the Bt horizons may occur because of the lower concentration and possibly more even distribution of clay and of clay-associated SOM in the Ab horizon. This may also partly explain the change in within-horizon variation of SOC concentration. However, most of the SOC in the Ab horizon resulted from the horizon being a former surface horizon. The low within-horizon variation of SOC concentration in the Ab horizon may result from bioturbation that occurred when the horizon was at the soil surface.

The increase in SOC concentration between the A2 and the Ab horizons probably results from the preservation of SOC in the Ab horizon. As the surface horizon of a Mollisol, the Ab horizon would have contained high SOC concentration, and the burial of the horizon probably resulted in very low SOM decomposition rates, thus preserving SOC. SOM decomposition rates tend to decrease with increasing depth from the soil surface (Gregorich et al. 1998; Helgason et al. 2014).

A decrease in the SOM decomposition rates with depth may have contributed to the increase in SOC concentration between the Ap2 horizon and the A2 horizon. Increased decomposition rates in the Ap2 horizon due to tillage may also have contributed to the increase in SOC concentration between the Ap2 horizon and the A2 horizon. Tillage generally increases the rate of SOM decomposition, thus reducing SOC concentration (Martel and Paul 1974; Tisdall and Oades 1982; Puget and Lal 2005).

Fe and Mn

The Fe and Mn concentrations demonstrated the highest within-horizon variation in the Bt horizon. Much of this variation resulted from the occasional saturation of this horizon, as evidenced by the presence of redoximorphic features. Mobility of Fe and Mn tends to increase with soil saturation due to decreased oxygen concentration, reducing Fe and Mn concentrations in parts of the soil horizon (Christensen et al. 1951; Callebaut et al. 1982; Patrick and Jugsujinda 1992). Conversely, Fe and Mn precipitate when the horizon drains and reoxidizes, thus increasing Fe and Mn concentrations in parts of the soil horizon (Gotoh and Patrick 1972, 1974; Atta et al. 1996). The low density of redoximorphic features in the Bt horizon implies that the soil horizon primarily experienced short-term saturation. The predominant short-term saturation explains the high within-horizon variation of Mn and the low within-horizon variation of Fe in the Bt horizon. Mn becomes mobile in less reducing conditions than Fe and thus is transported in periods of saturation too short to produce the degree of reduction needed to transport Fe (Olomu et al. 1973; Patrick and Jugsujinda 1992).

11.4.6 Interpretations of Soil Profile Maps

SOC

The soil profile map of SOC concentration confirmed the presence of three main horizons: an A horizon formed in material deposited by soil erosion, the buried A horizon, and the Bt horizon. The third layer we designated as a transition zone between the Ab and the Bt horizons because the Ab/Bt horizon boundary occurred in this layer and because based on the high horizontal variation of SOC concentration at 70–80 cm depth, the sampling occurred around the Ab/Bt boundary. The wavy boundaries of this transition zone imply a wavy Ab/Bt boundary.

pH and Ca

The soil profile map of soil pH divided the soil profile differently than the soil profile map of SOC concentration. The high soil pH of the second layer likely resulted from liming and incorporation of lime by tillage, and the top layer probably had a similar soil pH when the soil was regularly limed and plowed. The medium soil pH of the top layer likely resulted from a decrease in soil pH due to acidification processes such as additions of acids to the soil by rainfall and production of organic acids by plant roots and microbes (Gerretsen 1948; Jones and Darrah 1994). Together these top two layers corresponded to the A horizons that showed evidence of cultivation, the Ap1 and Ap2 soil horizons. The bottom layers of the soil profile map did not correspond with soil horizons. The thin third layer is a transition zone between the second and the fourth layers, the two main layers of the soil profile map. The fourth layer, a layer of low pH, probably resulted from this soil being below the region of lime incorporation. The increase in pH at around 85 cm soil depth may have resulted from the upward movement of water through underlying calcareous material, although the lowest Ca concentrations in the soil profile also occurred in this region.

The soil profile map of Ca concentration divided soil profile differently than the soil profile maps of SOC concentration and soil pH. The high Ca concentration in the top layer probably resulted from the application and incorporation of lime. The high horizontal variation of Ca concentration in the top layer may result from spatially differing levels of Ca removal by plant uptake and leaching. The second layer of the profile map may contain the Ca concentration of the soil with minimal additions through liming. However, Ca leached from above may have raised the Ca concentration in this layer. This could help explain the decrease in Ca concentration below the second layer. The lower layer of the profile map occurred within the Bt horizon, which had a finer texture than the horizons above. This change in texture would slow downward movement of water, reducing the amount of Ca received through leaching. However, part of the Bt horizon was located within the middle layer. Preferential flow increasing the amount of Ca received through leaching or reducing the amount of Ca removed by leaching may explain this discrepancy.

11.5 Conclusions

A raster sampling scheme can be used to examine horizontal and vertical variation within a soil profile, as well as within- and between-horizon variation of soil properties. However, this sampling scheme can also result in sampling at horizon boundaries, thus obtaining samples containing soil from two different horizons.

Profile maps of soil properties can be used to detect patterns in spatial distribution of soil properties. Distribution of SOC concentration has potential for establishing the location of horizon boundaries. Distribution of Ca concentration has potential for establishing the location of boundaries between an A horizon and a subsoil horizon of Mollisol.

The studied soil properties demonstrated horizontal variation within the distance of 1 m. SOC concentration and pH demonstrated fairly consistent responses to changes in depth within the distance of 1 m. The other soil properties demonstrated different responses to changes in depth depending on the vertical raster column studied. To accurately characterize soil property changes with depth, depth functions may require several vertical sampling transects of the soil profile.

Within-horizon variation occurred in all the soil horizons. The magnitude of the variation depended on the soil horizon and the soil property. Overall, the within-horizon variation of the soil properties studied was highest in the Bt horizon and lowest in the Ap2 horizon. The soil pH and the Fe concentration exhibited low within-horizon variation. The Al concentration and the volumetric moisture content were the only soil properties which did not demonstrate low within-horizon variation in any horizon. The volumetric moisture content and the SOC, Al, Mn, P, and Si concentrations each exhibited high within-horizon variation in at least one horizon. The lowest within-horizon variation of Ca, Mn, and Si concentrations occurred in the cultivated horizons (Ap1 and Ap2) of this profile. The surface horizon (Ap1) contained high within-horizon variation of Al concentration and moderate within-horizon variation of volumetric moisture content and SOC, P, and Si concentrations. Below the surface horizon, the within-horizon variation tended to increase with depth.

Acknowledgements This research was supported by a Hatch project of the National Institute of Food and Agriculture, United States Department of Agriculture, accession number 1003083. We wish to thank Kabindra Adhikari, Benito Bonfatti, Corey Breseman, Luis Reyes-Rojas, and Jenifer Yost for their support and their assistance in obtaining the data used in this study.

References

Adhikari K, Hartemink AE, Minasny B (2016) Mapping a profile wall of a typic udipsamments from the Central Sands, WI, USA. In: Hartemink AE, Minasny B (eds) Digital soil morphometrics. Springer, Dordrecht

Atta SK, Mohammed SA, VanCleemput O, Zayed A (1996) Transformations of iron and manganese under controlled E(h), E(h)-pH conditions and addition of organic matter. Soil Technol 9:223–237. doi:10.1016/s0933-3630(96)00013-x

Buddenbaum H, Steffens M (2012) The effects of spectral pretreatments on chemometric analyses of soil profiles using laboratory imaging spectroscopy. Appl Environ Soil Sci 2012:1–12. doi:10.1155/2012/274903

Callebaut F, Gabriels D, Minjauw W, De Boodt M (1982) Redox potential, oxygen diffusion rate, and soil gas composition in relation to water table level in two soils. Soil Sci 134:149–156. doi:10.1097/00010694-198209000-00001

Christensen PD, Toth SJ, Bear FE (1951) The status of soil manganese as influenced by moisture, organic matter, and pH. Soil Sci Soc Am Proc 1950:279–282. doi:10.2136/sssaj1951.036159950015000C0064x

Eswaran H, Bin WC (1978) Study of a deep weathering profile on granite in peninsular Malaysia. 1. Physicochemical and micro-morphological properties. Soil Sci Soc Am J 42:144–149. doi:10.2136/sssaj1978.03615995004200010033x

Franklin R, Duis L, Smith B, Brown R, Toler J (2003) Elemental concentrations in soils of South Carolina. Soil Sci 168:280–291. doi:10.1097/00010694-200304000-00005|10.1097/01.ss.0000064891.94869.el

Gaikawad ST, Hole FD (1965) Characteristics and genesis of a gravelly brunizemic regosol. Soil Sci Soc Am Proc 29:725–728. doi:10.2136/sssaj1965.03615995002900060035x

Gerretsen FC (1948) The influence of microorganisms on the phosphate intake by the plant. Plant Soil 1:51–81. doi:10.1007/bf02080606

Goodchild M (1992) Geographical data modeling. Comput Geosci 18:401–408. doi:10.1016/0098-3004(92)90069-4

Gotoh S, Patrick WH (1972) Transformation of manganese in a waterlogged soil as affected by redox potential and pH. Soil Sci Soc Am Proc 36:738–742. doi:10.2136/sssaj1972.03615995003600050018x

Gotoh S, Patrick WH (1974) Transformation of iron in a waterlogged soil as influenced by redox potential and pH. Soil Sci Soc Am J 38:66–71. doi:10.2136/sssaj1974.03615995003800010024x

Gregorich EG, Greer KJ, Anderson DW, Liang BC (1998) Carbon distribution and losses: erosion and deposition effects. Soil Tillage Res 47:291–302. doi:10.1016/s0167-1987(98)00117-2

Hartemink AE, Minasny B (2014) Towards digital soil morphometrics. Geoderma 230:305–317. doi:10.1016/j.geoderma.2014.03.008

Helgason BL, Konschuh HJ, Bedard-Haughn A, VandenBygaart AJ (2014) Microbial distribution in an eroded landscape: buried A horizons support abundant and unique communities. Agric Ecosyst Environ 196:94–102. doi:10.1016/j.agee.2014.06.029

Højsgaard, S, Halekoh U, Robison-Cox J, Wright K, Leidi AA et al (2014) doBy: Groupwise statistics, LSmeans, linear contrasts, utilities. R package version 4.5–13. Url:http://CRAN.R-project.org/package=doBy

Hole FD (1981) Effects of animals on soil. Geoderma 25:75–112. doi:10.1016/0016-7061(81)90008-2

Jones DL, Darrah PR (1994) Role of root derived organic acids in the mobilization of nutrients from the rhizosphere. Plant Soil 166:247–257. doi:10.1007/bf00008338

Martel YA, Paul EA (1974) Effects of cultivation on the organic matter of grassland soils as determined by fractionation and radiocarbon dating. Can J Soil Sci 54:419–426. doi:10.4141/cjss74-056

McBratney AB, Santos M, Minasny B (2003) On digital soil mapping. Geoderma 117:3–52. doi:10.1016/S0016-7061(03)00223-4

Miedema R, Koulechova IN, Gerasimova MI (1999) Soil formation in Greyzems in Moscow district: micromorphology, chemistry, clay mineralogy and particle size distribution. Catena 34:315–347. doi:10.1016/s0341-8162(98)00105-2

Minasny B, McBratney AB, Whelan BM (2005) VESPER version 1.6. Australian Centre for Precision Agriculture, McMillan Building A05, The University of Sydney, NSW 2006. url: http://www.usyd.edu.au/su/agric/acpa

Muhs DR, Bettis EA (2000) Geochemical variations in Peoria Loess of western Iowa indicate paleowinds of midcontinental North America during last glaciation. Quatern Res 53:49–61. doi:10.1006/qres.1999.2090

Minasny B, Stockmann U, Hartemink AE, McBratney AB (2016) Measuring and modelling soil depth functions. In: Hartemink AE, Minasny B (eds) Digital soil morphometrics. Springer, Dordrecht

Netto AM, Pieritz RA, Gaudet JP (1999) Field study on the local variability of soil water content and solute concentration. J Hydrol 215:23–37. doi:10.1016/s0022-1694(98)00259-5

Olomu MO, Racz GJ, Cho CM (1973) Effect of flooding on the Eh, pH, and concentrations of Fe and Mn in several Manitoba soils. Soil Sci Soc Am Proc 37:220–224. doi:10.2136/sssaj1973.03615995003700020019x

Patrick WH, Jugsujinda A (1992) Sequential reduction and oxidation of inorganic nitrogen, manganese, and iron in flooded soil. Soil Sci Soc Am J 56:1071–1073. doi:10.2136/sssaj1992.03615995005600040011x

Puget P, Lal R (2005) Soil organic carbon and nitrogen in a Mollisol in central Ohio as affected by tillage and land use. Soil Tillage Res 80:201–213. doi:10.1016/j.still.2004.03.018

R Core Team (2013) R: A language and environment for statistical computing. R foundation for statistical computing, Vienna, Austria. url:http://www.R-project.org/

Roudier P, Manderson A, Hedley C (2016) Advances towards more quantitative assessments of soil profile properties. In: Hartemink AE, Minasny B (eds) Digital soil morphometrics. Springer, Dordrecht

Schaetzl RJ (1998) Lithologic discontinuities in some soils on drumlins: theory, detection, and application. Soil Sci 163:570–590. doi:10.1097/00010694-199807000-00006

Schwen A, Backus J, Yang Y, Wendroth O (2014) Characterizing land use impact on multi-tracer displacement and soil structure. J Hydrol 519:1752–1768. doi:10.1016/j.jhydrol.2014.09.028

Steffens M, Buddenbaum H (2013) Laboratory imaging spectroscopy of a stagnic Luvisol profile—high resolution soil characterisation, classification and mapping of elemental concentrations. Geoderma 195:122–132. doi:10.1016/j.geoderma.2012.11.011

Steffens M, Kohlpaintner M, Buddenbaum H (2014) Fine spatial resolution mapping of soil organic matter quality in a Histosol profile. Eur J Soil Sci 65:827–839. doi:10.1111/ejss.12182

Stolt MH, Baker JC, Simpson TW (1993) Soil-Landscape Relationships in Virginia: I. Soil Variability and Parent Material Uniformity. Soil Sci Soc Am J 57:414–421. doi:10.2136/sssaj1993.03615995005700020022x

Tisdall JM, Oades JM (1982) Organic matter and water-stable aggregates in soils. J Soil Sci 33:141–163. doi:10.1111/j.1365-2389.1982.tb01755.x

Wilkinson M, Richards P, Humphreys G (2009) Breaking ground: pedological, geological, and ecological implications of soil bioturbation. Earth Sci Rev 97:257–272. doi:10.1016/j.earscirev.2009.09.005

Chapter 12
Mapping a Profile Wall of a Typic Udipsamments from the Central Sands in Wisconsin, USA

Kabindra Adhikari, Alfred E. Hartemink and Budiman Minasny

Abstract We measured and mapped the spatial distribution of Al, Si, Fe, Mn, Ca, pH, soil moisture content (θ), and color of a soil profile wall of a Typic Udipsamments. A 10 × 10 cm grid was laid on the soil profile wall, and 70 soil samples were collected from the grid centers. The spatial distribution of these properties was mapped with block kriging. The kriged values of the elements and red color were used in *k*-means clustering to identify soil horizons. Variation in the profile was considerable, but we observed that Fe, Mn, Ca, pH, and θ decreased with soil depth, while red color increased. The concentration of Al and Si increased at depth between 30 and 60 cm from the soil surface. The *k*-means clustering was able to locate three soil horizons in the profile, which was comparable to the standard soil profile description. We found that pXRF and soil color index coupled with clustering could be useful in digital soil morphometrics for the identification of soil horizons.

Keywords Digital soil morphometrics · Soil horizons · pXRF · *k*-means clustering

12.1 Introduction

Soil profiles comprise of a number of layers or horizons, which are often parallel to the land surface and are less heterogeneous in terms of properties and processes by which they are formed. The horizons are more or less continuous one to another in geographic, temporal, and character space (FitzPatrick 1988). Generally, soil horizons are

K. Adhikari (✉) · A.E. Hartemink
Department of Soil Science, FD Hole Soils Lab, University of Wisconsin-Madison, Madison, WI 53706, USA
e-mail: kabindra.adhikari@wisc.edu

B. Minasny
Department of Environmental Sciences, The University of Sydney, Biomedical Building C81, Sydney, NSW 2006, Australia

A.E. Hartemink and B. Minasny (eds.), *Digital Soil Morphometrics*, Progress in Soil Science, DOI 10.1007/978-3-319-28295-4_12

formed by the addition or removal of materials and its translocation or transformation within the profile. In most profiles, horizons are distinct in color with sharp boundaries making it straightforward to differentiate, but in many soils, the color or other diagnostic property changes gradually so that the boundaries are difficult to establish (Brady and Weil 1996). Delineation of horizons in a soil profile needs a careful examination of soil properties, understanding of the physicochemical and biologic processes involved, and information on soil–landscape relations of the area where the profile is located. Bridges (1993) stated that it is impossible to ignore soil horizon designations, as they have become an integral part in soil science communications from local, national, and international levels.

In pedology, where describing soil profiles and horizons is important (Bockheim et al. 2005; Butler 1980; Kellogg 1974), a number of tools and techniques have been developed to observe and measure soil properties in situ or in the laboratory. The application of such tools and techniques for measuring and mapping soil properties, such as texture, structure, color, carbonates, moisture, mottles and redoximorphic features, pores and roots, and horizon depth and boundaries, is called digital soil morphometrics (Hartemink and Minasny 2014). Digital morphometrics employs tools such as electrical resistivity, ground-penetrating radar, portable X-ray florescence spectrometry (pXRF), Vis–NIR, digital cameras, and profile cone penetrometer to measure soil properties and in the identification and mapping of soil horizon depths and boundaries (e.g., Chaplot et al. 2001; Doolittle and Collins 1995; Fajardo et al. 2015; Rooney and Lowery 2000; Steffens and Buddenbaum 2013; Tabbagh et al. 2000; Weindorf et al. 2012). Among all, pXRF offers a way of quantifying elemental concentration in the soils and has been used for soil horizon identification (Weindorf et al. 2012). Similarly, usefulness of Vis–NIR coupled with fuzzy clustering has been reported to recognize soil morphological horizons from Australia (Fajardo et al. 2015). As the soil varies continuously with depth, modeling and mapping soil depth functions is important in digital soil morphometrics. Minasny et al. (2016) provide some insights into the distribution of soil properties as a function of depth, and Adhikari et al. (2013, 2014) report some examples of modeling and mapping soil properties' depth functions.

Soil profile data collected with different morphometric tools and its grouping or clustering based on similarities could be used to identify soil horizon boundaries. The use of *k*-means clustering has been used in soil horizon classification (McBratney and Gruijter 1992; Triantafilis et al. 2001). Data clustering is mostly done for grouping soil class on a lateral spatial extent. For example, Webster (1973) determined soil boundaries along transects automatically by calculating the Mahalanobis distance of the soil properties along a width "window." We use this principle for identifying horizon boundaries based on vertical measurements of a profile wall. This study aims to map the soil profile wall of a Typic Udipsamments using digital soil morphometrics. The objectives were (i) to map the spatial distribution of Al, Si, Fe, Mn, Ca, pH, θ, and soil color in the soil profile wall of 100 cm × 70 cm dimension and (ii) to use elemental concentration and soil color to identify soil horizons.

12.2 Materials and Methods

12.2.1 Study Site Description

The study site was located in Adams County in the central-south part of Wisconsin, USA (latitude 43° 53′ 41.82″N; longitude 89° 41′ 30.66″W). The area is known as Central Sands where soils are developed on glacial outwash and are relatively young (<15,000–17,000-year-old). Soils of this area were Plainfield series and classified as Mixed, mesic Typic Udipsamments (USDA 1999). A typical soil profile of a Plainfield series consists of four to five soil horizons: Ap (∼0–18 cm), Bw1 (∼18–41 cm), Bw2 (∼41–71 cm), BC (∼71–92 cm), and C (>92 cm). We have found that these soils under intensive agriculture have a topsoil depth of 29 cm. Topography in the study area is flat (1 % slope) with an elevation of about 325 m asl. These soils are under agriculture with sweet corn, potatoes, and soybean as main crops. The soils are irrigated with 200–300 mm of water annually. Figure 12.1 displays the location of the study site in the Central Sands with the distribution of entisols, including Udipsamments, in Wisconsin.

12.2.2 Soil Sampling

A soil profile of 1 m^3 dimension was opened in July. A 10 × 10 cm grid net was laid down on the profile wall covering 0.7 m^2 area, and the grid corners were marked with pegs (Fig. 12.1). Soils were sampled from each grid center and in total 70 samples were collected from the profile. Colors were determined with the Munsell color chart, and volumetric soil moisture content (θ) was measured with a time-domain reflectometry (TDR) (Spectrum FieldScout TDR 300). Each sample was air-dried, ground, and scanned in the laboratory with a Delta Professional pXRF Analyzer (Olympus Scientific Solutions Americas, Inc.) for 30 s in geochemical mode, and the data on elemental concentration of aluminum (Al), silica (Si), iron (Fe), manganese (Mn), and calcium (Ca) were collected. For the color, hue, value, and chroma obtained from the Munsell color chart were converted to red, green, and blue color coordinate using the algorithm for quantitative pedology package (Beaudette et al. 2013). Samples were analyzed for soil pH measured in water at a soil-to-water ratio of 1:1.

12.2.3 General Statistics and Mapping

The distribution of soil properties by depth was analyzed considering mean, standard deviation, median, CV, and interquartile range. Box plots of each soil property at each 10-cm soil depth interval were generated (SAS Institute Inc. 2013).

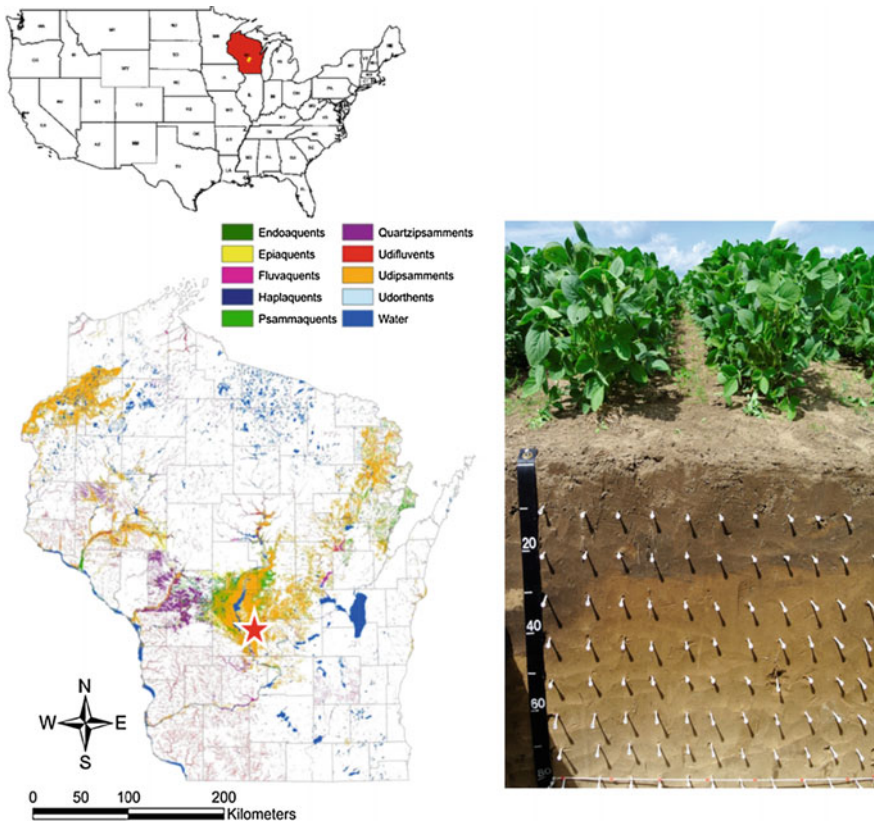

Fig. 12.1 Distribution of Udipsamments and the location of soil profile in Wisconsin. The profile wall displays the 10 × 10 cm grid net established for soil sampling

Autocorrelation and spatial distribution of the selected soil properties on the profile wall were analyzed and mapped using isotropic variogram and block kriging using Vesper (Minasny et al. 2005). We used block kriging of 10 cm × 10 cm size over the point kriging because we assumed it represents the average value of the property for that grid. Spatial dependency of the soil properties was evaluated with nugget-to-sill ratio (*NSR*) with $NSR < 0.25$, strong; $0.25 < NSR > 0.75$, moderate; and $NSR > 0.75$, weak spatial dependence (Cambardella et al. 1994).

$$NSR = \frac{C_0}{C_0 + C_1} \tag{12.1}$$

where C_0 and C_1 are the nugget and partial sill of the variogram model.

12.2.4 k-*Means Clustering*

We grouped the values of the measured soil properties based on similarities using *k*-means clustering algorithm (MacQueen 1967). The *k*-means is a common unsupervised learning algorithm to classify a given data set through a certain number of clusters fixed a priori. The objective function of the *k*-means aims at minimizing the squared error function (Eq. 12.2):

$$J = \sum_{j=1}^{k} \sum_{i=1}^{k} \left\| x_i^{(j)} - c_j \right\|^2 \tag{12.2}$$

where $\left\| x_i^{(j)} - c_j \right\|^2$ is a chosen distance measured between data point $x_i^{(j)}$ and the cluster center c_j and indicates the distance of the n data points from their respective cluster centers.

The clustering analysis was done in JMP software (SAS Institute Inc. 2013) using the block-kriged values of Al, Si, Fe, Mn, Ca, and red color as inputs. The procedure was as follows:

1. Define the number of clusters or seeds (*k*-cluster);
2. Assign each observation to the closest cluster;
3. Calculate the centroid of each cluster (*k* centroid);
4. Replace seeds with centroid and reassign the observations; and
5. Continue until the clusters are stable.

We clustered the soil properties' values with the initial cluster set to two and then repeated the process with subsequently increasing the cluster numbers to five assuming two to five soil horizons within 70 cm depth.

12.2.5 *Selecting the Cluster*

Once the values were partitioned into four different cluster sets ($k = 2, 3, 4, 5$), they were displayed as corresponding cluster maps. Among the four different cluster maps, the best map that represents the observed soil horizon boundaries was selected using the cubic clustering criterion (*CCC*). The *CCC* can be used to estimate the optimum number of clusters in *k*-means clustering. It compares the R^2 of clusters with the R^2 of a uniformly distributed set of points with the highest *CCC* value for the most optimal cluster set. The *CCC* can be computed from the observed R^2.

$$CCC = \ln\left[\frac{1 - E(R^2)}{1 - R^2}\right] \frac{\sqrt{\frac{np^*}{2}}}{(0.001 + E(R^2))^{1.2}} \tag{12.3}$$

where $E(R^2)$ the expected value of R^2 derived from extensive simulations, n the number of observations, and p^* the between cluster variation.

12.3 Results

12.3.1 Soil Properties

Descriptive statistics of soil properties from the soil profile wall are given in Table 12.1. Among the soil properties, Mn was most highly variable (CV = 48 %) followed by Al and Si (CV = 33 and 32 %, respectively), whereas the pH was least variable (CV = 5 %). Average Fe content of the profile was 5197 mg kg^{-1} with a CV of 32 % which is comparable to Si (CV = 32 %) but was slightly higher than that of Ca (CV = 26 %). With soil depth, the average value of Al and Si increased to 50/60 cm below the surface and decreased thereafter. The Fe levels decreased with soil depth, but the decrease was gradual with the lowest Fe levels at 60–70 cm depth. The levels of Mn and Ca were high in the surface layer and decreased with depth. The maximum variation of Fe and Ca was observed at 0–10 cm depth. Similarly, pH and soil moisture were higher and less variable in the surface layers, but variation increased below 30 cm. The red color was at lowest and more variable in the surface and increased sharply with depth, with maximum values at 60–70 cm soil depth. The variation of Al and Si was maximum at 20–30 cm soil depth and minimum at 30–40 cm. Figure 12.2 shows the box plots of the soil properties at 0–70 cm depth.

12.3.2 Maps of Soil Properties

The variogram parameters used for each soil property mapping are listed in Table 12.2. The levels of Ca showed a short limited variation compared to other

Table 12.1 Descriptive statistics of measured soil properties from the profile wall (dimension 100 cm × 70 cm)

Soil property	Aluminum (mg/kg)	Silica (mg/kg)	Iron (mg/kg)	Manganese (mg/kg)	Calcium (mg/kg)	Red color index	pH	Moisture (cm^3/cm^3)
Minimum	3000	15,018	1955	0	2522	111	5.3	6.2
Maximum	11,800	104,300	10,890	479	8480	201	6.5	18.1
Mean	7267	73,726	5197	121	3947	152	5.9	12.1
(± SD)	(±2451)	(±23,518)	(±1608)	(±107)	(±1033)	(±26)	(±0.3)	(±2.5)
CV, %	33.7	31.9	30.9	48.7	26.2	17.1	5.3	21.1
Median	7600	81,950	5715	98	3619	148	5.8	12.5
IQ range	4275	23,049	1893	213	1114	33	0.5	4.1

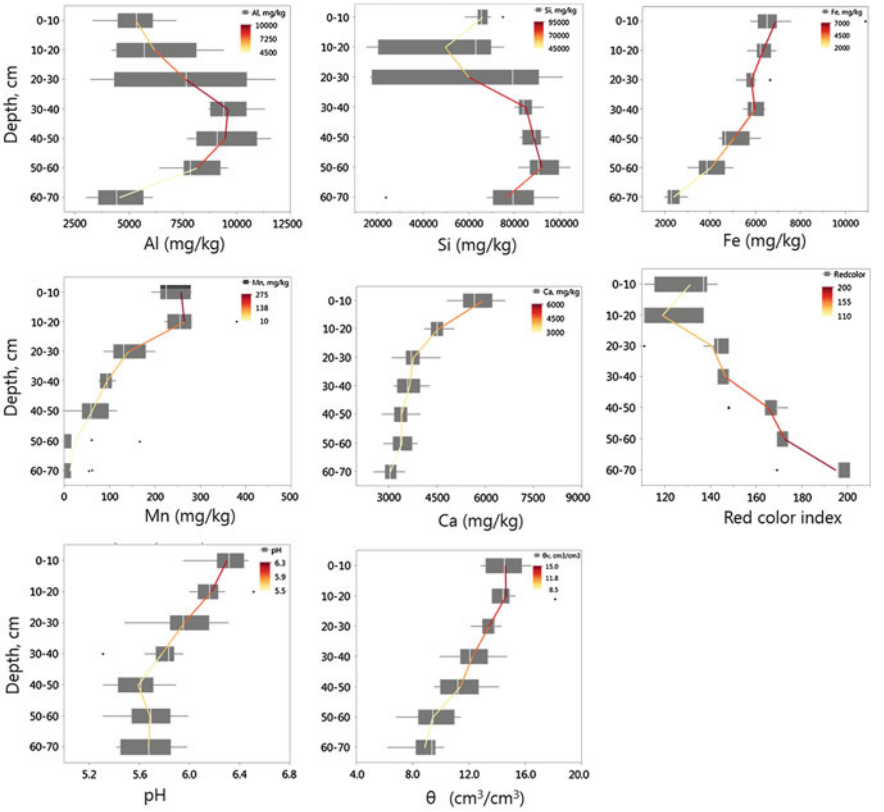

Fig. 12.2 Box plots showing the depthwise distribution of aluminum (Al), silica (Si), iron (Fe), manganese (Mn), calcium (Ca), red color index, pH, and soil moisture (θ) at each 10 cm depth increment in the soil profile. The continuous line represents the average value of measured soil properties and the values increases from yellow to dark red

Table 12.2 Variogram parameters of soil properties

Soil property	Variogram model	C_0^a (mg/kg)^2	C_1^a (mg/kg)^2	A, cm	NSR^a
Aluminum	Exponential	851,364	6,002,548	37	0.12
Silica	Spherical	209×10^5	377×10^5	39	0.26
Iron	Gaussian	208,183	3,249,967	38	0.06
Manganese	Gaussian	1689	15,787	42	0.10
Calcium	Gaussian	2262	10,000	33	0.18
Red color index	Gaussian	80	1006	45	0.07
pH	Spherical	0.01	0.12	50	0.08
Soil moisture	Gaussian	0.62	8.6	35	0.07

[a]C_0 nugget; C_1 partial sill; A range; and NSR nugget-to-sill ratio

elements, all sharing a comparable range between 33 and 42 cm, but pH had the highest range of 60 cm and was least variable (CV = 5.3 %). All soil properties had strong spatial dependence (NSR < 0.25) except for Si which showed a moderate spatial dependence (NSR = 0.36). The predicted maps (Fig. 12.3) of Ca, Mn, and Fe showed that these elements were mostly confined to the surface horizons with Ca mostly within the top 20 cm, Mn to 40 cm, and Fe to 50 cm depth. The red color increased with depth where maximum values were recorded below 60 cm. The concentration of Si, and Al, was higher at 25–60 cm, and a lower level of Al was also recorded below 60 cm. Soil pH was higher at 0–20 cm and decreased below 30 cm. The pH map was irregular and patchy. Soil moisture showed a similar pattern with higher values at the surface. The soil moisture map also reflected the crop row (soybean) influence with relatively lower moisture content between the crop rows.

12.3.3 Cluster Maps and Soil Horizons

Clustering of the kriged values of soil properties produced four maps (Fig. 12.4), each for one set of a defined cluster (k = 2, 3, 4, and 5). For cluster two and three, the first horizon boundary is at a depth of about 30 cm (Fig. 12.4a, b) and the second horizon boundary at about 55 cm depth (Fig. 12.4b). Cluster four divides each of the first and second horizons of cluster two (Fig. 12.4a) into two new horizons (Fig. 12.4c). Cluster five defined a small portion of the first horizon as a possible new horizon (Fig. 12.4d). For all cluster maps except cluster two, the last horizon boundary is at a same depth of about 55–60 cm from the soil surface.

Among the four cluster maps, the highest CCC was found for cluster three (CCC = 49.6) (Fig. 12.5a). Cluster two had the lowest CCC of about 15 and that for cluster five was 46. Cluster three was selected to represent soil horizon boundaries in the profile. Figure 12.5b plots the points and clusters in the first two principle components of the input data (i.e., PC1 and PC2) that exceeded the eigenvalue of 1. The eigenvalues for PC1 and PC2 were 4.2 and 1.4, respectively. Soil properties falling along PC1 axis were Ca, Mn, and red color index, whereas those along PC2 were Al and Si with higher loadings of these elements. Fe content, however, was between the two PCs with a moderate loading.

For the selected cluster, Table 12.3 lists the mean and standard deviation of the soil properties in each cluster. For cluster one, Mn was the most variable element (CV = 75 %) followed by Fe (CV = 25 %). Ca and red color index both shared a similar variability (CV = 4.3 %). Cluster one had the maximum average for red color index, whereas cluster two had the lowest Si but highest Fe, Mn, and Ca. A maximum level of Si and Al was present in cluster three.

A positive correlation was found between the elements Al and Si, and Fe with Mn and Ca. Red color index had a negative correlation with Mn, and Ca, and a positive correlation with Si. Similarly, both Al and Si were negatively correlated with Ca and Mn. The Al levels showed no relation with Fe, with the red color index (Fig. 12.6).

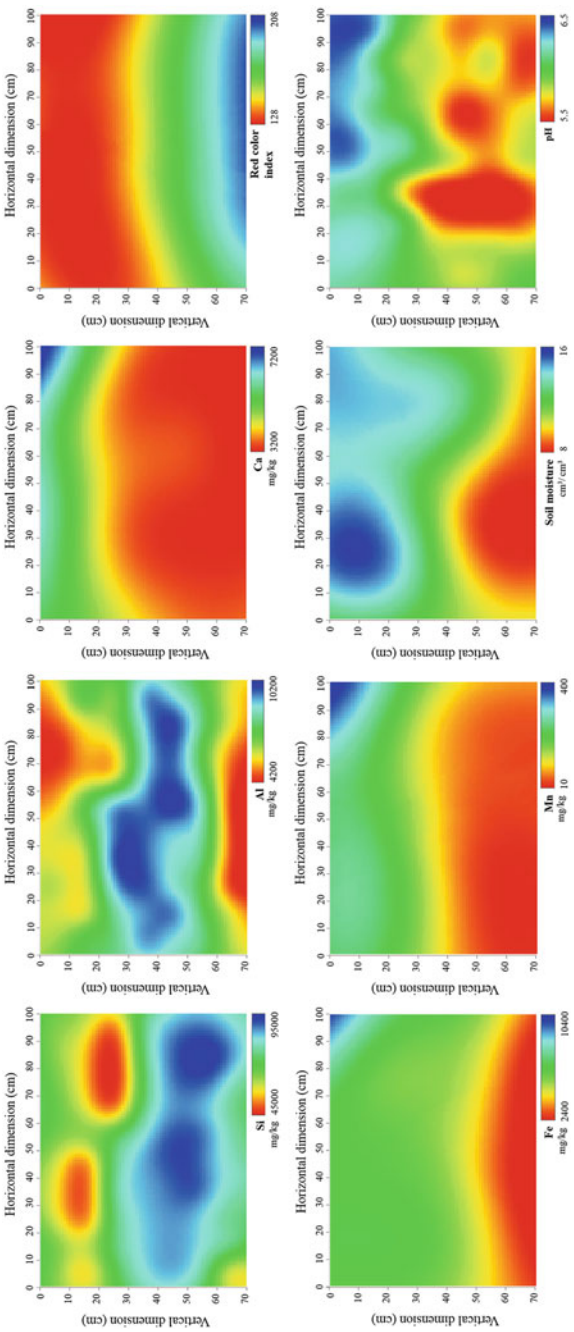

Fig. 12.3 Kriged maps showing the spatial distribution of measured soil properties in the soil profile (dimension 100 cm × 70 cm)

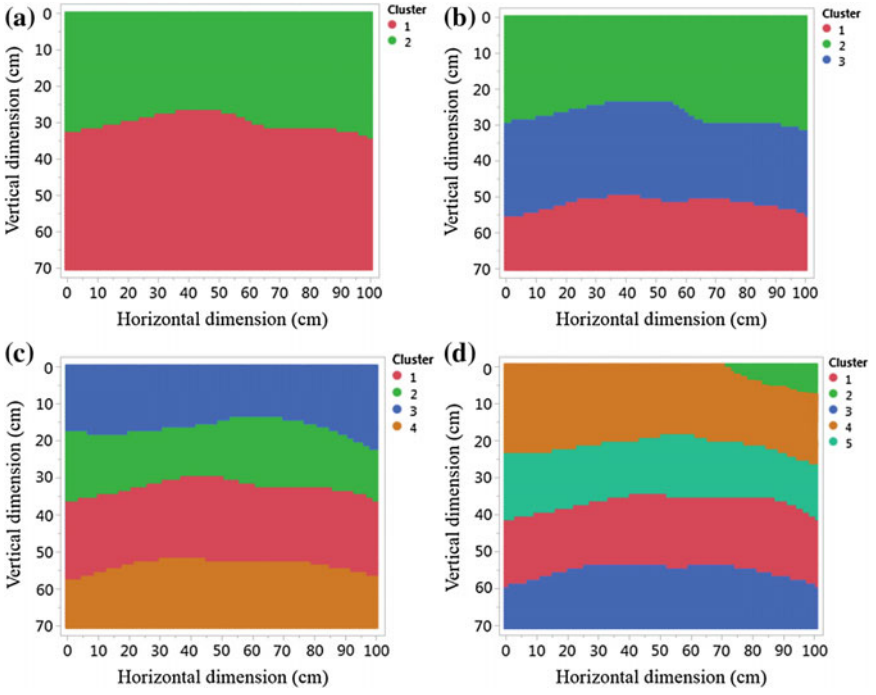

Fig. 12.4 Map of four different sets of *k*-clusters; **a** $k = 2$; **b** $k = 3$; **c** $k = 4$; and **d** $k = 5$, showing possible horizon boundaries in the profile wall

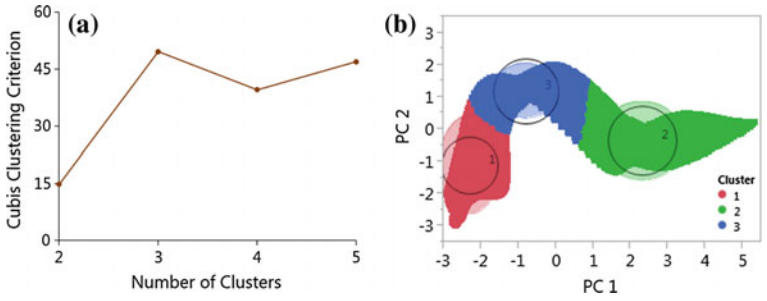

Fig. 12.5 **a** Plot of cubic clustering criterion versus number of *k*-cluster sets and **b** the first two principle components (PCs) of the points (*dark color*) and of the most appropriate cluster set ($k = 3$) indicated as *light color*

Based on the observations, the soil profile had three horizons, namely Ap (~0–18 cm), Bw1 (~18–41 cm), and Bw2 (~41–71 cm). The cluster map suggested the three horizons, but the depth of these horizon boundaries was deeper than that of the observed horizon depth. We found that the depth of Ap horizon ranged between 0 and 27/30 cm, Bw1 between 27 and 30/54 cm, and Bw2 from 54 to >70 cm (Fig. 12.4b).

Table 12.3 Mean and standard deviation of soil properties for the selected cluster set (k = 3)

Cluster	Aluminum		Silica		Iron		Manganese		Calcium		Red color index	
	Avg.[a] (mg/kg)	Stdev.[a] (mg/kg	Avg. (mg/kg	Stdev. (mg/kg	Avg. (mg/kg	Stdev. (mg/kg	Avg. (mg/kg	Stdev. (mg/kg	Avg. (mg/kg	Stdev. (mg/kg	Avg. (mg/kg	Stdev. (mg/kg
1	6230.9	1363.1	82,142.2	7513.6	3057.5	771.7	19.5	14.8	3223.2	139.9	186.0	8.1
2	6212.1	1062.1	59,937.1	6837.4	6449.4	647.3	227.1	47.8	4892.5	735.2	129.6	4.0
3	9094.7	630.5	82,654.0	7276.3	5389.7	557.2	82.1	40.1	3505.7	194.3	154.1	11.3

[a]*Avg*. mean value; *Stdev*. standard deviation

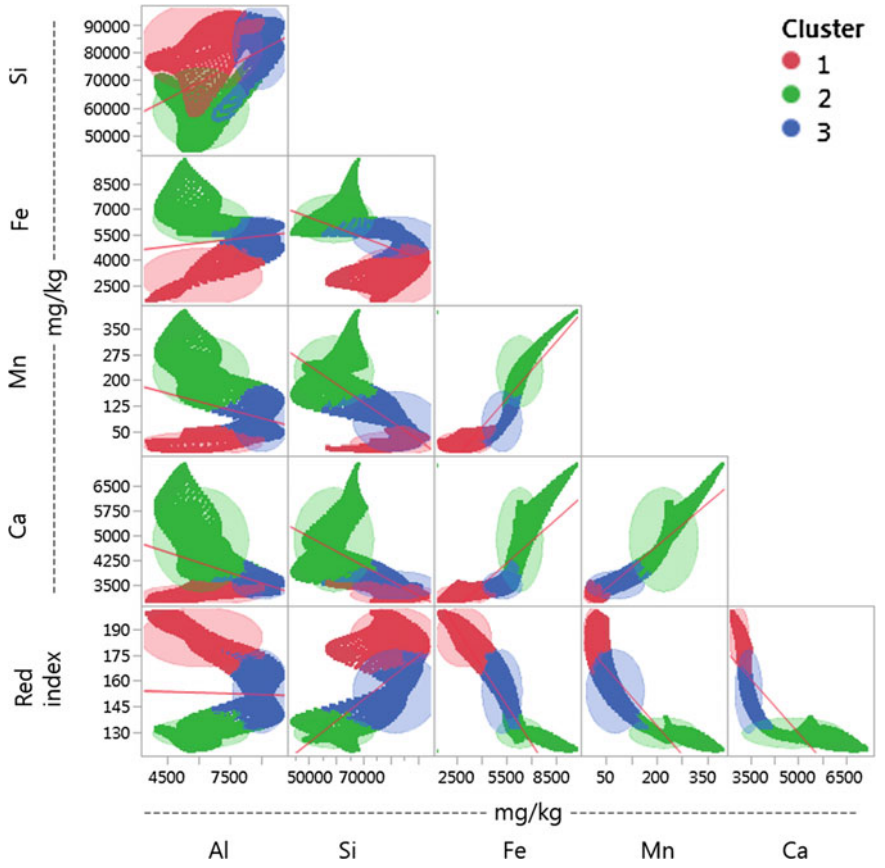

Fig. 12.6 Scatterplot matrix of soil attributes for the most appropriate cluster ($k = 3$). *Light color* represents the cluster of the points in *darker color*

12.4 Discussion

12.4.1 Digital Soil Morphometrics

This study applied digital soil morphometric tools and techniques to collect soil data and identify soil horizon boundaries of an Udipsamments profile wall. A grid-based soil sampling design ensured capturing the variations of soil properties across the profile wall. Data collection using pXRF and TDR helped to understand soil properties' variations in a profile wall both in horizontal and in vertical dimensions. The use of pXRF in soil properties' data collection and evaluation has been reported in other studies (e.g., Grauer-Gray and Hartemink 2016; Stockmann et al. 2016; Weindorf et al. 2012). A benefit of using morphometrics is in the exploration of within-horizon soil variations, which is often

overlooked in traditional soil pit descriptions. As an example, the first 27 or 30 cm of our soil profile was identified as Ap horizon, but the distribution of Ca concentration within this horizon was heterogeneous; the mean value ranged between 5908 mg kg^{-1} at 0–10 cm and 3753 mg kg^{-1} at 20−30 cm. Similarly, the mean pH also dropped from 6.3 at 0−10 cm to 5.9 at 20–30 cm. In case of Si, the upper 10 cm of Ap horizon was least variable (CV = 7 %) than the lower most 10 cm of it where the maximum variation was found (CV = 62 %). Grauer-Gray and Hartemink (2016) reported similar within-horizon variations in soil properties of a Mollisol profile wall.

Use of geostatistics, which is common in soil science (Burgess and Webster 1980; Goovaerts 1999), allowed us to evaluate autocorrelation and spatial variations of soil properties in the profile wall. Spatial prediction with block kriging represented our sample grid dimension. Grouping similar values of soil properties into more homogeneous classes is a key to clustering and it has been used in soil classification studies (e.g., Fajardo et al. 2015; McBratney and Gruijter 1992; Powell et al. 1992; Webster 1973).

12.4.2 Variation in Soil Profile Wall

Soil properties were variable in the profile wall and displayed a well spatial structure. Top 30 cm of the profile showed higher variation compared to lower horizons. All elements and θ displayed short-range variations compared to pH and red color which had a maximum range. All properties except Si had a strong spatial dependence. The level of Al and Si was lower in the surface and higher at 20 to 60 cm, whereas the levels of Fe, Mn, Ca, pH, and θ gradually decreased. Grauer-Gray and Hartemink (2016) found a lower Al in the surface soil horizons where the levels of Ca and soil pH were higher. The nature of Al and Si, which are related to clay minerals and their distribution in the profile, indicated that these soils have lost some clay from the surface horizons, which is illuviated below 40 cm. A second explanation is that the subsoils are enriched with aluminosilicate minerals through mineral weathering. The higher levels of Mn, Fe, Ca, and pH in the surface and their reduction with depth might be due to fertilizer application, irrigation, liming or leaching. Similar effect of liming and leaching on the depth function of pH and soil development has been reported from Denmark (Adhikari et al. 2014; Madsen and Munk 1987). Likewise, higher moisture in the surface could be linked to the irrigation. Although soil moisture is a dynamic property that is related to texture, structure, soil carbon, irrigation, and precipitation, its content as measured in the field is related to variation in soil texture and water-holding capacity (Mulla 1988; Reynolds 1970).

12.4.3 Identifying Horizon Boundaries

The *k*-means clustering identified three soil horizons in the profile. The boundary between cluster two (horizon Ap) and three (horizon Bw1) was determined by the levels of Si, Al, and Ca. Horizon Ap had the lowest levels of Al, and Si, but the highest level of Fe, Mn, and Ca. Horizon Bw1 was associated with the highest concentration of Al and Si. Horizon Bw2 had minimum Fe, Mn, and Ca. These findings suggest that aluminosilicate minerals, which are mostly related to clay content, were leached from Ap and illuviated in lower horizons, mostly in Bw1 or in situ formation of such minerals. The clustering technique was able to capture the influence of agricultural activities such as fertilization, irrigation, and liming that has increased the levels of Fe, Ca, and Mn on the surface soils for horizon boundary designation.

12.5 Conclusions

This study demonstrated the usefulness of digital soil morphometrics for mapping a profile wall with emphasis on the soil horizon boundary identification. The methodology presented is a way of identifying and locating soil horizon boundaries that would complement our pedological understanding. Based on the study, the following can be concluded:

- Fe, Mn, Ca, pH, and soil moisture decreased with soil depth, while red color value increased. Al and Si increased at a depth between 30 and 60 cm.
- Clusters of the kriged values of soil properties were able to locate three most probable soil horizons in the soil profile.
- The pXRF and soil color can be useful tools for soil horizon delineation.

References

Adhikari K, Kheir RB, Greve MB, Bøcher PK, Malone BP, Minasny B, McBratney AB, Greve MH (2013) High-resolution 3-D mapping of soil texture in Denmark. Soil Sci Soc Am J 77:860–876

Adhikari K, Kheir RB, Greve MB, Greve MH, Malone BP, Minasny B, McBratney AB (2014) Mapping soil pH and bulk density at multiple soil depths in Denmark. In: Arrouays D, McKenzie NJ, Hempel J, de Forges AR, McBratney AB (eds) GlobalSoilMap: basis of the global spatial soil information system. CRC Press/Balkema, Leiden, p 155

Beaudette DE, Roudier P, O'Geen AT (2013) Algorithms for quantitative pedology: a toolkit for soil scientists. Comput Geosci 52:258–268

Bockheim J, Gennadiyev A, Hammer R, Tandarich J (2005) Historical development of key concepts in pedology. Geoderma 124(1):23–36

Brady NC, Weil RR (1996) The nature and properties of soils. Prentice-Hall Inc.

Bridges EM (1993) Soil horizon designations; past use and future prospects. CATENA 20(4):363–373

Burgess TM, Webster R (1980) Optimal interpolation and isarithmic mapping of soil properties. 1. The semi-variogram and punctual kriging. J Soil Sci 31(2):315–331

Butler BE (1980) Soil classification for soil survey. Clarendon Press, Oxford

Cambardella CA, Moorman TB, Novak JM, Parkin TB, Karlen DL, Turco RF, Konopka AE (1994) Field-scale variability of soil properties in central Iowa soils. Soil Sci Soc Am J 58 (5):1501–1511

Chaplot V, Walter C, Curmi P, Hollier-Larousse A (2001) Mapping field-scale hydromorphic horizons using radio-MT electrical resistivity. Geoderma 102(1):61–74

Doolittle JA, Collins ME (1995) Use of soil information to determine application of ground penetrating radar. J Appl Geophys 33(1):101–108

Fajardo M, McBratney A, Whelan B (2015) Fuzzy clustering of Vis–NIR spectra for the objective recognition of soil morphological horizons in soil profiles. Geoderma (In press)

FitzPatrick EA (1988) Soil horizon designation and classification. International Soil Reference and Information Centre, ISRIC, Wageningen

Goovaerts P (1999) Geostatistics in soil science: state-of-the-art and perspectives. Geoderma 89(1–2):1–45

Grauer-Gray JR, Hartemink AE (2016) Variation of soil properties in a Mollisol profile wall. In: Hartemink AE, Minasny B (eds) Digital soil morphometrics. Springer, Dordrecht

Hartemink AE, Minasny B (2014) Towards digital soil morphometrics. Geoderma 230–231:305–317

Kellogg CE (1974) Soil genesis, classification, and cartography: 1924–1974. Geoderma 12 (4):347–362

MacQueen J (1967) Some methods for classification and analysis of multivariate observations. In: Proceedings of the fifth Berkeley symposium on mathematical statistics and probability. Oakland, CA, USA, pp 281–297

Madsen HB, Munk I (1987) The influence of texture, soil depth and geology on pH in farmland soils: a case study from southern Denmark. Acta Agriculturae Scandinavica 37(4):407–418

McBratney A, Gruijter JD (1992) A continuum approach to soil classification by modified fuzzy k-means with extragrades. J Soil Sci 43(1):159–175

Minasny B, McBratney AB, Whelan BM (2005) VESPER version 1.62. Australian Centre for Precision Agriculture, McMillan Building A05, The University of Sydney. NSW

Minasny B, Stockmann U, Hartemink AE, McBratney A (2016) Measuring & modelling soil depth functions. In: Hartemink AE, Minasny B (eds) Digital soil morphometrics. Springer, Dordrecht

Mulla D (1988) Estimating spatial patterns in water content, matric suction, and hydraulic conductivity. Soil Sci Soc Am J 52(6):1547–1553

Powell B, McBratney AB, MacLeod DA (1992) Fuzzy classification of soil profiles and horizons from the Lockyer Valley, Queensland. Australia. Geoderma 52(1–2):173–197

Reynolds S (1970) The gravimetric method of soil moisture determination part III an examination of factors influencing soil moisture variability. J Hydrol 11(3):288–300

Rooney D, Lowery B (2000) A profile cone penetrometer for mapping soil horizons. Soil Sci Soc Am J 64(6):2136–2139

SAS Institute Inc. (2013) Using JMP 11. Cary, NC, SAS Institute Inc.

Steffens M, Buddenbaum H (2013) Laboratory imaging spectroscopy of a stagnic Luvisol profile—high resolution soil characterisation, classification and mapping of elemental concentrations. Geoderma 195–196:122–132

Stockmann U, Jun Jang H, Minasny B, McBratney AB (2016) The effect of soil moisture and texture on Fe concentration using portable X-ray fluorescence spectrometers. In: Hartemink AE, Minasny B (eds) Digital soil morphometrics. Springer, Dordrecht

Tabbagh A, Dabas M, Hesse A, Panissod C (2000) Soil resistivity: a non-invasive tool to map soil structure horizonation. Geoderma 97(3):393–404

Triantafilis J, Ward W, Odeh I, McBratney A (2001) Creation and interpolation of continuous soil layer classes in the lower Namoi valley. Soil Sci Soc Am J 65(2):403–413

USDA (1999) Soil taxonomy: a basic system of soil classification for making and interpreting soil surveys, 436. US Department of Agriculture, Soil Conservation Service

Webster R (1973) Automatic soil-boundary location from transect data. J Int Assoc Math Geol 5 (1):27–37

Weindorf DC, Zhu Y, Haggard B, Lofton J, Chakraborty S, Bakr N, Zhang W, Weindorf WC, Legoria M (2012) Enhanced pedon horizonation using portable X-ray fluorescence spectrometry. Soil Sci Soc Am J 76(2):522–531

Chapter 13
Comparative Analysis of Saturated Hydraulic Conductivity (K_{sat}) Derived from Image Analysis of Soil Thin Sections, Pedotransfer Functions, and Field-Measured Methods

Zamir Libohova, Philip Schoeneberger, Phillip R. Owens, Skye Wills, Doug Wysocki, Candiss Williams and Cathy Seybold

Abstract Saturated hydraulic conductivity (K_{sat}) is an important soil parameter that governs water movement through horizons, pedons, and soil landscapes. K_{sat} is infamous for its spatial and temporal variability, which contributes to the difficulty and considerable expense in measuring or otherwise quantifying it. Consequently, predictive methods such as pedotransfer functions (PTFs) that use physical soil properties, such as texture and bulk density, have been developed to derive K_{sat} values. Soil texture and structure are key factors influencing K_{sat} because of their direct relationship to pore size distribution. Quantitatively defining the combined effects of texture and structure on pore size distribution in a PTF is a difficult task. The objectives of this research were to: (i) estimate K_{sat} based on pore characteristics derived from soil thin sections via image analysis; and (ii) compare the resultant values with field-measured K_{sat} and with K_{sat} estimated by a PTF using soil texture and bulk density parameters. We digitally scanned 39 thin sections from 11 pedons of soils derived from loess over till and/or over weathered sandstone. Soil voids were classified based on their size and shape. K_{sat} was measured in the field using a Compact Constant-head Permeameter (Amoozemeter) and estimated using a Rosetta PTF. Simple and multiple linear regression (MLR) analyses were used to relate pore indexes and soil physical properties with measured and estimated K_{sat}. The mean measured K_{sat} was 0.74 cm h^{-1}, whereas the PTF-estimated K_{sat} from Rosetta and MLR were 0.36 cm h^{-1} and 0.49 cm h^{-1}, respectively. The addition of pore characteristics into the model improved K_{sat} predictions compared

Z. Libohova (✉) · P. Schoeneberger · S. Wills · D. Wysocki · C. Williams · C. Seybold
USDA-NRCS, Lincoln, NE, USA
e-mail: zamir.libohova@lin.usda.gov

P.R. Owens
Purdue University—Agronomy Department, West Lafayette, IN, USA

A.E. Hartemink and B. Minasny (eds.), *Digital Soil Morphometrics*,
Progress in Soil Science, DOI 10.1007/978-3-319-28295-4_13

to predictions using Rosetta alone. The estimated K_{sat} based on the model with added pore characteristics was better correlated with field-measured K_{sat} ($r = 0.82$) than that based on Rosetta ($r = 0.62$). The addition of pore characteristics can improve K_{sat} predictions. However, thin section void analysis from additional parent materials is needed.

Keywords Saturated hydraulic conductivity (K_{sat}) · Thin sections · Image analysis · Pedotransfer functions · Soil porosity

13.1 Introduction

The success of hydrology modeling predictions depends on the accurate representation of the spatial and temporal variability of major external drivers such as weather, land use, land management, geomorphic surface, and soil hydrological properties (Pachepsky et al. 2008). Saturated soil hydraulic conductivity (K_{sat}) is one of the most important soil parameters in hydrological modeling because it characterizes water movement through soils with direct and substantive impact on streamflow timing and volume (Guber et al. 2006). Unfortunately, K_{sat} is also one of the most difficult properties to accurately evaluate due to its variability over short-range distances (Oosterbaan and Nijland 1994) and over time. The presence of structural and/or root macropores has been identified as one of the major contributors to K_{sat} variability (White 1985; Perret et al. 1999, 2003; Watson and Luxmoore 1986). The terms "preferential flow" and "bypass flow" have been applied by many researchers to acknowledge the presence and the mechanisms of soil water movement through macropores (White 1985).

Although by definition K_{sat} is evaluated under saturated soil moisture conditions, the presence of macropores combined with the effects of "boundary conditions" between wet and dry soil matrices contributes to the variability in K_{sat} measurements and results in overestimations of K_{sat} (Bouma et al. 1989). Many field (in situ) and laboratory methods have been developed to overcome such limitations (Reynolds and Elrick 1985). Some of the field measurement methods include lysimeters (Barkle et al. 2010) and various constant or falling head permeameters (Amoozegar and Warrick 1986; Amoozegar 1989). Whether K_{sat} is measured in situ or in laboratory conditions, the methods have limitations related to the determination of an appropriate representative soil volume. A representative soil volume is needed to reduce the measurement variability due to preferential flow and wet/dry boundary conditions (Bouma et al. 1989; Mohanty and Mousli 2000). Techniques such as X-ray computed tomography (CT) have been developed to better evaluate the effects of macropores on K_{sat} by characterizing their size and distribution over a larger volume of soil and in a nondestructive manner (Anderson et al. 1990; Peyton et al. 1992, 1994). However, few studies exist on X-ray computed tomography (CT) methodology that link their results with other soil physical properties for

predictive K_{sat} (Peyton et al. 1994) and likewise other field methods are not very practical for routine measurements.

Most K_{sat} field methods and techniques are expensive and time-consuming and require many K_{sat} measurements over large areas and extended time periods to capture spatial and temporal variability. Bouma et al. (1989) discuss some of the morphological techniques for estimating the appropriate soil volume for representative measurements of K_{sat} in the field. They also recognized the challenges for upscaling such soil hydrological parameters for modeling (Bouma 2006). Different approaches to upscaling have been developed by researchers, but mostly rely on pedotransfer functions (PTFs) (Guber et al. 2006). McKenzie and Jacquier (1997) used successfully field soil morphological characteristics such as field texture, grade of structure, areal porosity, bulk density, dispersion index, and horizon type for K_{sat} predictions. Both visual and quantitative estimates of areal porosity provided satisfactory results, with the quantitative method performing slightly better (McKenzie and Jacquier 1997). The USDA-NRCS Kellogg Soil Survey Laboratory (KSSL) has approximately 8000 soil thin sections that offer a unique opportunity to quantify the role of porosity in improving K_{sat} predictions. Thin sections represent a small soil area and like in situ field K_{sat} measurements are scale limited. However, the incorporation of pore characteristics in modeling could potentially improve K_{sat} predictions. This chapter aimed to: (i) assess the use of soil thin sections to characterize the K_{sat} at the soil horizon level; and (ii) compare K_{sat} derived from thin sections with measured values and with values derived from a published PTF.

13.2 Materials and Methods

13.2.1 Study Sites and Soils

The two study sites selected for this research are in Wabash and Dubois Counties, Indiana. Soils in Wabash County are in the Northern Moraine and Central Till Plain Physiographic Region which is characterized by low-relief landscapes (Franzmaier et al. 2004). Soils in Dubois County are in the Southern Hills and Lowland Physiographic Region (Franzmaier et al. 2004), which is characterized by high-relief, bedrock-controlled hills (Franzmaier et al. 2004) (Fig. 13.1). Soils in study area formed predominantly in loess over till (Wabash County) or in loess over weathered materials from the underlying sandstone, siltstone, or shale (Dubois County) (Wingard et al. 1980). The texture class for the study soils is silt loam, silty clay loam, silty clay, or clay (Table 13.1).

The dominant soil series include Pewamo, Glynwood, and Blount in Wabash County and Wellston and Gilpin in Dubois County. Soil characterization analyses were conducted at the Kellogg Soil Survey Laboratory (KSSL) of USDA-NRCS, Lincoln, Nebraska.

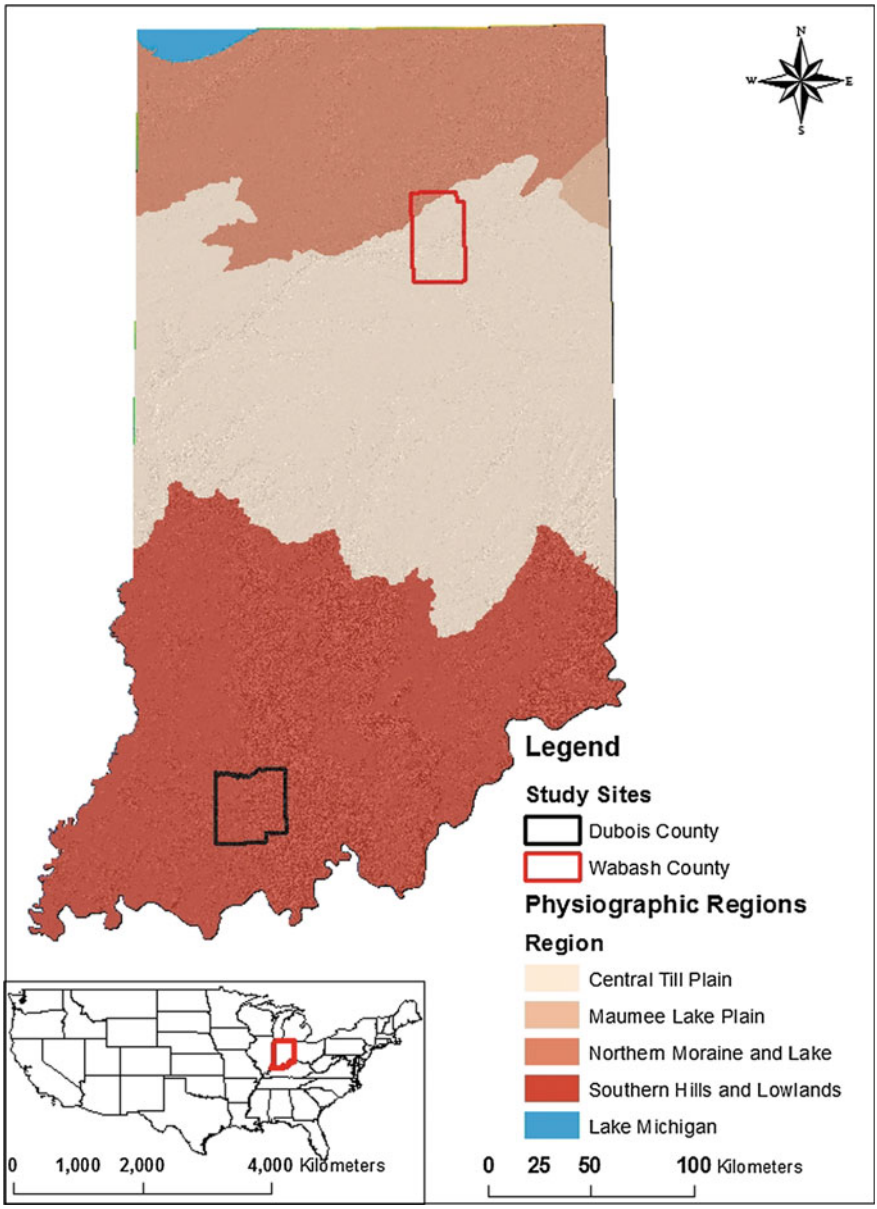

Fig. 13.1 Study site locations and physiographic regions of Indiana

Table 13.1 Measured physical characteristics of soils used for thin sections

County	Soil series	Texture class	Soil horizon	Particle size (<2 mm)			Bulk density		Water content	
				Clay (%)	Silt (%)	Sand (%)	33 kPa (g cm^{-3})	Oven Dry (g cm^{-3})	33 kPa (%wt)	1500 kPa (%wt)
Dubois	Wellston	SIL	Ap	20.3	76.9	2.8	1.46	1.52	24	8.7
	Wellston	SIL	Bt1	25.7	72.6	1.7	1.42	1.52	25.2	10.8
	Wellston	SIL	Btx	23.4	67.1	9.5	1.55	1.63	20.8	10.7
	Wellston	SIL	BA	25.5	72.8	1.7	1.45	1.58	24.8	11.2
	Wellston	SIL	Bt1	27.6	71.1	1.3	1.32	1.42	27.5	12.8
	Wellston	C	2Bt4	71.9	26.1	2	1.46	1.82	28.3	24
	Gilpin	SIL	Ap	23.9	68.5	7.6	1.49	1.61	23.1	12.7
	Gilpin	SICL	Bt1	28.2	64.2	7.6	1.48	1.58	23.7	13.3
	Gilpin	C	2Bt3	50.5	15.8	33.7	1.6	1.8	21.9	18.2
	Gilpin	SIL	Ap	24.6	56.9	18.5	1.38	1.49	26.1	11
	Gilpin	CL	Bt1	33	43.8	23.2	1.45	1.57	23.5	13.5
	Gilpin	CL	Bt3	34.2	44.6	21.2	1.59	1.78	21.4	13.3
	Gilpin	SIL	Ap	21	68.3	10.7	1.41	1.53	27.8	12.5
	Gilpin	SIL	2Bt1	25.9	58.8	15.3	1.53	1.67	21.6	9.6
	Gilpin	SIL	Ap	21.7	75.7	2.6	1.28	1.4	27.8	10.6
	Gilpin	SICL	Bt1	28	70.1	1.9	1.33	1.51	27.9	11.9
	Gilpin	SIL	2Btx	22.5	56.3	21.2	1.6	1.81	20.3	7.9
	Gilpin	C	3Bt1	38.7	34.1	27.2	1.53	1.85	24.6	15.1
	Gilpin	SIL	Ap	22.3	75	2.7	1.43	1.55	26.3	10.1
	Gilpin	SIL	Bt1	25	72.8	2.2	1.4	1.49	25.6	10.5
	Gilpin	SIL	Btx1	20.7	60.2	19.1	1.49	1.58	21.3	8.3
	Gilpin	SIL	Ap	20.9	75	4.1	1.48	1.61	24.3	10.3
	Gilpin	SIL	Bt1	22.6	67.7	9.7	1.49	1.56	21.9	8.8
	Gilpin	SICL	2Btx1	27.9	58.7	13.4	1.52	1.66	22.6	10.1

(continued)

Table 13.1 (continued)

County	Soil series	Texture class	Soil horizon	Particle size (<2 mm)			Bulk density		Water content	
				Clay (%)	Silt (%)	Sand (%)	33 kPa (g cm^{-3})	Oven Dry (g cm^{-3})	33 kPa (%wt)	1500 kPa (%wt)
Wabash	Pewamo	SICL	Ap1	29.4	52.6	18	1.53	1.64	20.2	15.3
	Pewamo	SIC	Btg2	45	43.9	11.1	1.49	1.72	24.4	18.2
	Pewamo	SIC	BCdtk	54.2	38.1	7.7	1.59	1.82	23.2	20.1
	Pewamo	C	Cdk2	54.1	38.9	7	1.64	1.88	23.2	20.4
	Glynwood	SICL	Ap1	28	53.1	18.9	1.69	1.83	18.9	12.7
	Glynwood	SICL	Bt2	34.6	37.7	27.7	1.51	1.73	22.1	16.9
	Glynwood	SIC	BCdtk	34.4	42.7	22.9	1.51	1.73	23.9	14.2
	Glynwood	SIC	Cdk2	35.3	42.9	21.8	1.8	1.94	17.4	14.4
	Glynwood	SICL	Ap	26.4	54.4	19.2	1.57	1.7	19.3	12.4
	Glynwood	CL	Bt2	49	38.7	12.3	1.46	1.73	24.3	20.3
	Glynwood	CL	Cdtk	40.9	42.3	16.8	1.63	1.88	20.4	16
	Glynwood	CL	Cdk2	25.9	51.1	23	1.8	1.9	15.4	11.2
	Blount-Del Rey	SICL	Ap	35.4	46.9	17.7	1.71	1.89	18.7	14.8
	Blount-Del Rey	C	Bt2	51.8	38.6	9.6	1.54	1.88	24.7	18.7
	Blount-Del Rey	SIC	Cdk1	52.1	40.3	7.6	1.64	1.88	22.5	18.3
	Blount-Del Rey	SIC	Cdk3	49.7	41.5	8.8	1.69	1.91	21.4	18.9

13.2.2 Thin Section Image Processing and Analysis

We selected 39 horizons with prepared thin sections from 11 pedons. The horizons were grouped as Ap (surface), Bt (subsurface), and C horizons (deepest). The thin section dimensions were 2.0 × 3.5 cm, but we avoided the section edges during scanning to minimize sample preparation artifacts. We analyzed pores via a three-step process:

Step 1 Thin sections were scanned with an HP Officejet 6310 and edited with HP Photosmart Software before image analysis. The scanned image resolution was set at 7200 dpi and saved in "bmp" format, which is compatible with ENVI (Environment for Visualizing Images, Version 3.2, Research Systems Inc., Boulder, Colorado) image analysis software. We performed an image enhancement before exporting the image to ENVI (Fig. 13.2a). The enhancement process included brightness and contrast adjustments to highlight pores by increasing contrast between the soil matrix and the voids. This enhancement allowed a simple and efficient image classification

Step 2 We imported the enhanced image into ENVI as RGB and transformed it to hue, saturation, and value (HSV) formats (Fig. 13.2b). The density slicing

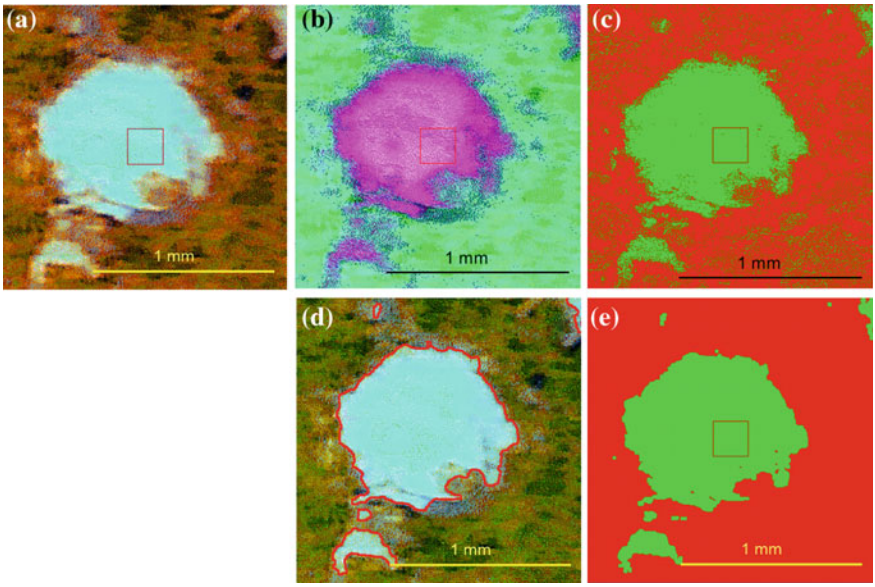

Fig. 13.2 A portion of a thin section illustrating the processing steps: **a** enhancement; **b** RGB to HSV density slicing; **c** unsupervised classification; **d** filtering; and **e**) vectorization used to derive pore characteristics

function was used to define the wavelength ranges for major colors (red, green, blue, yellow, cyan, magenta maroon, and sea green) of HSV-converted thin sections. Color ranges for the voids were identified and the image was segmented, which yielded an image of two contrasting colors that represented either the soil matrix or voids

Step 3 We used an unsupervised classification to evaluate the image and then a "sieve" function to remove isolated pixels (Fig. 13.2c). The binary image (matrix and voids) was further processed using majority filter (kernel size = 5), clumped (kernel size = 5), and majority filter (kernel size = 11) (Fig. 13.2d). The resulting binary image was converted to a vector file using ENVI and exported as a shape file (Fig. 13.2e). The polygon shape file was further processed in ArcMap (ESRI 2009) for soil pore classification

13.2.3 Soil Pore Classification

After image processing, small isolated polygons (outliers) were either combined with adjacent polygons or eliminated. There is no agreement in pore size classifications used for distinguishing between micropores and macropores (Bouma et al. 1979). Moreover, the naming convention is inconsistent: Some authors use a two-term "micro-" and "macro"-pores distinction (Jongerius 1957; Bouma et al. 1977), whereas others use a multi-term description such as "very fine," "fine," "coarse," etc. (Russell 1973; Soil Survey Division Staff 1993). The equivalent cylindrical diameter (ECD) ranges associated with pore size categories are also inconsistent across studies. In all of the studies we reviewed, pore size is based on ECD rather than mean equivalent square (MEC), which is the shape of pixels and the resulting polygons produced by thin section image analysis. To remove the remaining small square polygons, we calculated the area of a single pixel based on the 7200 dpi resolution and dimensions. The area of a pixel was calculated to be 12.0 μm^2, which is approximately a 3.44 × 3.44 μm square. To use ECD for distinguishing micropores and macropores, the square pixel dimension was assumed to also represent a circular pore diameter. The ECD was calculated based on the "area" column in the polygon attribute shape file and the pixel dimensions derived from the image resolution. A threshold value of 200 pixels was used to separate micropores from macropores. Polygons with an area greater than 200 pixels were further classified into three major shapes, as per Bouma et al. (1977), using void area (A)/void perimeter (P^2) ratio with A/P2 > 0.04 classified as "rounded"; A/P2 < 0.04 and >0.015 as "intermediate"; and A/P2 < 0.015 as "elongated" voids.

13.2.4 Soil-Saturated Hydraulic Conductivity (K_{sat})

Field-Measured K_{sat}

The K_{sat} values were determined from in situ measurements using a Compact Constant-Head Permeameter (Amoozometer) (Amoozegar 1989; Amoozegar and Warrick 1986). The in situ K_{sat} was determined for major soil horizons from which the thin sections were extracted, each in five replicates. The major horizons were (i) surface or near surface horizons (Ap, E, AB, BE); (ii) subsurface horizons (Bt1, Bt3); and (iii) deeper restrictive horizons (Btx, 3Bt, Cr). The replicates were spaced approximately 1 m apart and aligned along topographic contours.

Pedotransfer Function (PTF) Estimated K_{sat}

We used a pedotransfer function software Rosetta V1.0 to estimate K_{sat} based on soil texture (sand, silt, clay), bulk density, and water content at 33 and 1500 kPa water tension (Schaap et al. 1998). The soil input parameters for Rosetta were measured values from the KSSL characterization data. In addition to Rosetta, we also estimated K_{sat} using a step-wise multiple linear regression (MLR) model that included porosity characteristics (total porosity and pore shape) as well as soil texture (sand, silt, clay), bulk density, and water content at 33 and 1500 kPa water tension.

13.2.5 Statistical Analysis

We used Pearson's correlation coefficient to assess the relationship between measured K_{sat} and estimated K_{sat} from Rosetta and step-wise multiple linear regression (MLR) analysis. We also employed forward step-wise regression analysis to determine the best K_{sat} predictors. We evaluated R^2, RMSE (root-mean-square error), and Akaike Information Criterion (AIC) (Akaike 1974, 1976) criteria to select the best K_{sat} predictive model. LSMeans Tukey's HSD test was used to compare mean K_{sat} between different soil horizons. The mean comparison test was done on the log-transformed data due to non-normal distribution. The null hypotheses were rejected at a significance level of 0.05. The statistical analysis was conducted in JMP (SAS Institute Inc. 2003).

13.3 Results and Discussions

13.3.1 Pore Size Distribution from Thin Sections

We grouped soil horizons into three major layers (L1, L2, L3) based on morphological, physical, and chemical characteristics (Table 13.2). There were no differences in mean pore radius between surface (L1), intermediate (L2), and deepest horizons (L3). Similar results are reported by Bouma et al. (1977) who found no specific, significant trends with depth for the three macropore types. Total porosity for the surface layer was slightly higher than that for the intermediate layer; however, both layers (L1, L2) had lower total porosity than the deepest layer (L3).

The proportions of different pore shapes relative to total porosity showed mixed trends with soil depth, especially for the deepest layer. Differences were slight for the upper and intermediate layers and greatest for the deepest layer. For example, proportions of elongated pores in the deepest layer (L3) were higher than those of the upper layers (L1, L2), whereas proportions of rounded pores and, especially, intermediate pores in the deepest layer (L3) were less than half of those of the upper layers (L1, L2). Bouma et al. (1977) observed similar tendencies of increasing proportions of elongated pores with depth and determined that the water flow along structural channels was the main mechanism for water movement.

13.3.2 Estimated K_{sat} from Step-Wise Multiple Regression Analysis

In addition to the Rosetta parameters used for predicting K_{sat} (sand, silt, clay, bulk density, and water content at 33 kPa and 1500 kPa), we added the following parameters to the model: pore characteristics derived from thin section image analysis (total porosity, pore radius, elongated/total porosity ratio, rounded/total porosity ratio, and intermediate/total porosity) (Table 13.3).

Table 13.2 Pore characteristics from image analysis of thin sections

Grouped soil horizons	Genetic soil horizons	Pore radius (μm)	Total porosity (%)	Elongated/total porosity	Rounded/total porosity	Intermediate/total porosity
L1	Ap, Ap1, BA	5.5 (0.37)	12.4 (3.02)	68.2 (5.00)	3.8 (0.97)	28.1 (4.29)
L2	Bt1, Bt2, 2Bt1, 2Btx, 2Btx1, BCdtk, Cdk2	5.4 (0.30)	10.7 (2.54)	67.9 (4.20)	3.9 (0.81)	28.0 (3.61)
L3	Bt3, Btg, Bt3, 2Bt4, 3Bt1, BCdtk, Cdtk, Cdtk (1, 2, 3)	5.9 (0.40)	18.8 (3.31)	82.4 (4.48)	3.1 (1.06)	14.5 (4.70)

Numbers in parentheses are standard error values

Table 13.3 Parameter estimates and significance from step-wise multiple regression (MLR) analysis and Rosetta PTF for predicting saturated soil hydraulic conductivity (K_{sat})

Predictive parameter	Step-wise MLR					Rosetta		
	Full	Texture	Texture Bd	Texture Bd/WC	Porosity	Texture	Texture Bd	Texture Bd/WC
Pore_radius (μm)	x				x			
Total porosity (%)	x*				x			
Elongated/total (%)	x				x			
Rounded/total (%)	x*				x			
Intermediate/total (%)	x*				x			
Clay (%)	x	x	x	x		x	x	x
Silt (%)	x	x	x	x		x	x	x
Sand (%)	x*	x	x	x		x	x	x
Bd at 33 kPa (g cm^{-3})	x*		x	x			x	x
Bd oven dry (g cm^{-3})	x		x	x			x	x
WC at 10 kPa (%wt)	x*			x				x
WC at 33 kPa (%wt)	x			x				x
WC at 1500 at kPa (%wt)	x*			x				x
R^2	0.82	0.04	0.10	0.12	0.10	0.01	0.09	0.05
RMSE	1.64	2.36	2.30	2.28	2.43	2.41	2.32	2.36

Texture refers to clay, silt, and sand fractions; Bd is the soil bulk density; WC is the soil water content
*Parameters significant at p value = 0.05

This model yielded the highest R^2 (0.82) (adjusted R^2 = 0.70). The resultant prediction equation is given as:

$$K_{sat} = 238 + -0.12 * TP + 0.82 * R/T + -0.28 * I/T + -2.85 * \text{Sand} + -94.88 * \text{Bd33} + -3.71 * \text{WC10} + 0.35 * \text{WC1500} + 12.12 * \text{WC33}$$

where TP is the total porosity; R/T is the ratio of rounded pores over total pores; I/T is the ratio of intermediate pores over total pores; Sand is the total sand (%); Bd33 is the bulk density (g cm^{-3}) at 33 kPa water tension; WC10 is the water content (wt%) at 10 kPa tension; WC1500 is the water content (wt%) at 1500 kPa tension; and WC33 is the water content (wt%) at 33 kPa tension. Interestingly, both step-wise multiple linear regression (MLR) and Rosetta showed similar performance when

only soil texture, bulk density, and water content were used for K_{sat} predictions (Table 13.3). Also, when the statistical parameters of the step-wise MLR model included only pore characteristics, the resulting R^2 was 0.10 and RMSE was 2.43. It is possible that the use of a larger number of parameters in the step-wise MLR model resulted in better predictions compared to Rosetta PTF. Unfortunately, for this study we did not have a way to compare both models using all parameters including porosity, as Rosetta PTF was developed based on soil texture, bulk density, and water content only. Also, the comparisons between step-wise MLR and Rosetta models were based on a small sample size (n = 39). We recognize the unfairness with regard to the use of porosity for the step-wise MLR and a small sample size for both models. These are especially critical for Rosetta that was developed on much larger sample size and did not incorporate as many parameters as step-wise MLR. However, the results indicate that a combination of both physical soil properties and pore characteristics is needed to improve K_{sat} predictions. More data are needed on thin sections and other described soil morphological characteristics that relate to structure and pore size as shown by McKenzie and Jacquier (1997).

13.3.3 Measured Versus Estimated K_{sat} from Rosetta and Step-Wise Multiple Linear Regression Analysis

There were significant differences in mean K_{sat} values between grouped soil horizons (L1, L2, L3), especially for the deepest layer (L3). With the exception of the Rosetta PTF model, the K_{sat} values decreased exponentially with depth (Table 13.4). The decrease in K_{sat} by an order of magnitude with soil depth, especially between the surface and the subsurface layers, has been observed by others (Lin 2006). The measured K_{sat} values were more variable compared to those from the Rosetta PTF and Step-Wise MLR models, as shown by standard error values in parentheses in Table 13.4. This is to be expected due to the fact that measured K_{sat} values derived at field point scale are more prone to local variability in actual measured soil volume surrounding the instrument, which depends upon soil structure and, more specifically, pore size and distribution (Bouma et al. 1989).

Rosetta PTF and, to a lesser degree, the step-wise MLR model over-fit the data, resulting in less variability in predicted K_{sat} values compared to measured values. The role that soil structure, especially pore size, shape, and distribution, plays in predicting K_{sat} is well documented (Bouma et al. 1989; White 1985; Perret et al. 1999, 2003). However, one of the major limitations of Rosetta PTF is the lack of soil structure input parameters. The Rosetta PTF model uses soil texture, bulk density, and soil water retention characteristics to predict K_{sat} (Schaap 1999; Schaap et al. 1998), none of which is a direct representation of the soil structure. The addition of pore characteristics to the model may improve the prediction of K_{sat} values (Fig. 13.3).

Table 13.4 Mean comparisons between measured K_{sat} and those derived from Rosetzta PTF, and step-wise multiple linear regression model

Grouped soil horizons	Genetic soil horizons	Measured		Rosetta		Step-Wise MLR	
		Mean** (cm h^{-1})	Sig* (cm h^{-1})	Mean** (cm h^{-1})	Sig* (cm h^{-1})	Mean** (cm h^{-1})	Sig* (cm h^{-1})
L1	Ap, Ap1, BA	2.10 (0.98)	a	0.51 (0.08)	a	1.04 (0.23)	a
L2	Bt1, Bt2, 2Bt1, 2Btx, 2Btx1, BCdtk, Cdk2	0.22 (0.81)	a	0.39 (0.06)	a	0.27 (0.09)	b
L3	Bt3, Btg, 2Bt3, 2Bt4, 3Bt1, BCdtk, Cdtk, Cdtk (1, 2, 3)	0.04 (1.40)	b	0.15 (0.03)	b	0.05 (0.02)	c
		0.74 (0.38)	**a**	**0.36 (0.04)**	**a**	**0.49 (0.12)**	**a**

The reported values are in their "native" format but the mean comparisons are based on log-transformed values. Numbers in parentheses are standard error values

*Significant at p value = 0.05

**Mean values within the same method followed by same letters are not significantly different. Mean values between methods (bold) followed by same letters are not significantly different

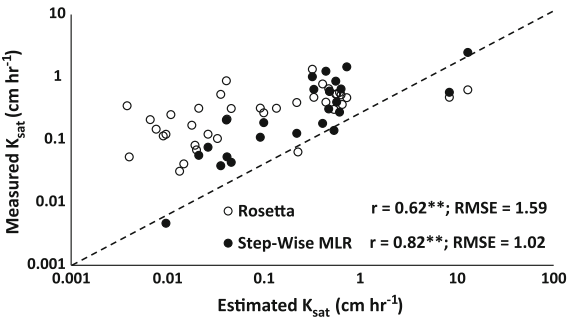

Fig. 13.3 Estimated versus measured K_{sat} values based on Rosetta and step-wise multiple regression model (MLR)

The results are promising. However, they are based on a small data set and broader evaluation is needed. The K_{sat} method we developed from thin sections has limitations like any other proxy method used to measure or estimate K_{sat}. Thin sections represent a small soil area and do not show three-dimensional pore continuity patterns, particularly for macropores, which control K_{sat} at horizon and pedon scales (Bouma et al. 1977). Whether measured K_{sat} is determined in situ or in a laboratory setting, identifying the appropriate representative soil volume, which is needed to reduce the variability due to preferential macropore flow, is challenging

(Bouma et al. 1989; Mohanty and Mousli 2000). Techniques such as X-ray computed tomography (CT) have been developed to better evaluate the effects of macropores on K_{sat} by characterizing their size, distribution, and, especially, connectivity over a large volume of soil in a nondestructive manner (Anderson et al. 1990; Peyton et al. 1992, 1994). However, X-ray computed tomography (CT) despite advantages is expensive. In addition, there is no extensive data available to our knowledge with both X-ray computed tomography (CT) analysis and soil physical properties for developing predictive K_{sat} models.

13.4 Conclusions

Soil-saturated hydraulic conductivity (K_{sat}) is one of the most important properties used to describe soil water movement. However, K_{sat} is highly variable and measuring it in the field is expensive. Pedotransfer functions (PTFs) such as Rosetta use soil physical properties (texture and bulk density) to predict K_{sat}. Soil morphological properties, especially porosity, can be added to PTF models to improve K_{sat} prediction. We used soil thin sections and image analysis to help quantify pore size and shape from soils for which measured K_{sat} values were available.

Pore characteristics alone explained 10 % of the predicted K_{sat} variability. Including them in PTF models with the other soil physical properties improved the K_{sat} predictions for loess-derived soils in our study area. The pore numerical quantification from thin sections is limited because of the lack of an appropriate representative soil volume, which is needed to overcome the high variability of K_{sat} due to preferential flow as related to the presence of soil macropores.

The results from this study show the potential of pore characteristics to improve K_{sat} prediction, but additional studies are needed on soils derived from other parent materials and with texture ranges wider than loess. The USDA-NRCS Kellogg Soil Survey Laboratory (KSSL) has over 8000 soil thin sections that could be used to assess the potential of using pore characteristics to improve K_{sat} predictions.

References

Akaike H (1974) A new look at the statistical model identification. IEEE Trans Autom Control 19:716–723

Akaike H (1976) An information criterion (AIC). Math Sci 14:5–9

Amoozegar A (1989) A compact constant-head permeameter for measuring saturated hydraulic conductivity of the vadoze zone. Soil Sci Soc Am J 53:1356–1361

Amoozegar A, Warrick AW (1986) Hydraulic conductivity of saturated soils: field methods. In: A. Klute (ed) Methods of soil analysis. Part I. Physical and mineralogical methods. 2nd edn. Agronomy Series, vol. 9, American Society Agronomica, pp. 735–770

Anderson SH, Peyton RL, Gantzer CJ (1990) Evaluation of constructed and natural soil macropores using X-ray computed tomography. Geoderma 46:13–29

Barkle GF, Wöhling Th, Stenger R, Mertens J, Moorhead B, Wall A, Clague J (2010) Automated equilibrium tension lysimeters for measuring water fluxes through a layered, volcanic vadose profile in New Zealand. Vadose Zone J 10:747–759. doi:10.2136/vzj2010.0091

Bouma J (2006) Hydropedology as a powerful tool for environmental policy research. Geoderma 131:275–286

Bouma J, Jongerius A, Boersma O, Jager A, Schoonderbeek D (1977) The function of different types of macropores during saturated flow through four swelling soil horizons. Soil Sci Soc Am J 41:945–950

Bouma J, Jongerius A, Schoonderbeek D (1979) Calculation of hydraulic conductivity using micromorphometric data. Soil Sci Soc Am J 43:261–264

Bouma J, Jongmans AG, Stein A, Peek G (1989) Characterizing spatially variable hydraulic properties of a boulder clay deposit in The Netherlands. Geoderma 45:19–29

ESRI (2009) ArcGIS desktop: release 9. Environmental Systems Research Institute, Redlands, CA

Franzmaier DP, Steinhardt GC, Schulze DG (2004) Indiana soil and landscape evaluation manual, version 1.0. Purdue University, Agronomy Department

Guber AK, Pachepsky YA, van Genuchten MTh, Rawls WJ, Simunek J, Jacques D, Nicholson TJ, Cady RE (2006) Field-scale water flow simulations using ensembles of pedotransfer functions for soil water retention. Vadose Zone J 5:234–247

Jongerius A (1957) Morphologic investigations of soil structure. Bodemkundige Studies No. 2. Mededelingen van de Stickting voor Bodemkartering, Wageningen, The Netherlands

Lin H (2006) Temporal stability of soil moisture spatial pattern and subsurface preferential flow pathways in the Shale Hills catchment. Vadose Zone J 5(1):317–340

McKenzie N, Jacquier D (1997) Improving the field estimation of saturated hydraulic conductivity in soil survey. Aust J Soil Res 35(4):803–827

Mohanty BP, Mousli Z (2000) Saturated hydraulic conductivity and soil water retention properties across a soil-slope transition. Water Resour Res 43(11):3311–3324

Oosterbaan RJ, Nijland HJ (1994) Determining the saturated hydraulic conductivity, chapter 12. In: Ritzema HP (ed) Drainage principles and applications. International Institute for Land Reclamation and Improvement (ILRI), Pub. 16, 2nd revised edn. Wageningen, The Netherlands, ISBN 90 70754 3 39

Pachepsky YA, Gimenez D, Lilly A, Nemes A (2008) Promises of hydropedology. Perspect Agric Vet Sci Nutri Nat Resour 3:2–19

Perret JS, Prasher SO, Kantzas A, Langford C (1999) Three-dimensional quantification of macropore networks in undisturbed soil cores. Soil Sci Soc Am J 63:1530–1543

Perret JS, Prasher SO, Kacomov AR (2003) Mass fractal dimension of soil macropores using computed tomography: From the box-counting to the cube-counting algorithm. Europ J Soil Sci 54:569–579

Peyton RL, Haeffner BA, Anderson SH, Gantzer CJ (1992) Applying X-ray CT to measure macropore diameters in undisturbed soil cores. Geoderma 53:329–340

Peyton RL, Gantzer CJ, Anderson SH, Haeffner BA, Pfeifer P (1994) Fractal dimension to describe soil macropore structure using X-ray computed tomography. Water Resour Res 30 (3):691–700

Reynolds WD, Elrick DE (1985) In-situ measurement of field saturated hydraulic conductivity, sorptivity, and the a-parameter, using the Guelph permeameter. Soil Sci 140(4):292–302

Russell EW (1973) Soil conditions and plant growth, 10th edn. Longmans, London

SAS Institute Inc. (2003) JMP®, Version 11.0.0. Cary, NC

Schaap MG (1999) Rosetta (http://www.ussl.ars.usda.gov/MODELS/rosetta/rosetta.htm)

Schaap MG, Leij FJ, van Genuchten MTh (1998) Neural network analysis for hierarchical prediction of soil water retention and saturated hydraulic conductivity. Soil Sci Soc Am J 62:847–855

Soil Survey Division Staff (1993) Soil survey manual. Soil conservation service. U.S. Department of Agriculture Handbook 18

Watson KW, Luxmoore RJ (1986) Estimating macroporsity in a forest watershed by use of a tension infiltrometer. Soil Sci Soc Am J 50:578–582

White RE (1985) The influence of macropores on the transport of dissolved and suspended matter through soil. Adv Soil Sci 3:95–120

Wingard RC, Bernard JR, Coulter GW, Hudson GL (1980) Soil survey of Dubois County, Indiana. United States Department of Agriculture, National Cooperative Soil Survey. U.S. Government Printing Office 299-473/87, 117 p

Part III
Soil Depth Functions

Chapter 14
Measuring and Modelling Soil Depth Functions

Budiman Minasny, Uta Stockmann, Alfred E. Hartemink and Alex B. McBratney

Abstract Hans Jenny stated that the anisotropy of soil with depth means that the soil has a unique profile. Therefore, naturally every soil property has its specific depth function. The changes of soil particle size distribution in a soil profile can be used as an indicator of soil formation and processes and has been used as a proxy for soil age or degree of development. Uniform, gradational and rapidly changing (duplex) soil textures are examples of soil profile forms used for soil classification in Australia. Various parametric and nonparametric depth functions have been used to describe the variation of soil properties with depth. We have identified 7 typologies of depth functions: uniform, gradational, exponential, wetting front, abrupt, peak and minima–maxima. These depth functions are related to soil-forming processes. To test these functions, a proximal soil sensor was used to perform in situ digital morphometrics by which soil properties are measured along a soil profile wall at small depth increments. We explore the possibility of horizon boundary detection based on the changes in elemental concentrations. It was concluded that digital morphometrics enables soil scientists to measure the soil's depth functions and weathering history quantitatively directly in the soil pit and assists in more objective delineation of soil horizons.

Keywords In situ pXRF analysis · Soil depth functions · Weathering indices · Soil profile development · Soil horizons

B. Minasny (✉) · U. Stockmann · A.B. McBratney
Faculty of Agriculture and Environment, The University of Sydney, New South Wales 2006, Australia
e-mail: budiman.minasny@sydney.edu.au

A.E. Hartemink
Department of Soil Science, University of Wisconsin—Madison, FD Hole Soils Lab, 1525 Observatory Drive, Madison, WI 53706, USA

A.E. Hartemink and B. Minasny (eds.), *Digital Soil Morphometrics*, Progress in Soil Science, DOI 10.1007/978-3-319-28295-4_14

14.1 Introduction

Hans Jenny (1941) noted that naturally, every soil property has its own vertical distribution pattern or specific "depth function". Most soil scientists work on data collected from soil horizons. Jenny (1941) and (Arkley 1976) stated that the assignment of horizons and their names is difficult and can be subjective. Jenny suggested the use of the soil indicatrix (a laterally isotropic 3-D depth function) for clarification and refinement of soil profile descriptions.

Measurements of soil properties in a soil profile are usually made based on the horizons, or defined depth intervals. Samples or measurements are usually bulked based on the horizons, resulting in "stepped" data which may mask the continuity of soil properties (Hartemink and Minasny 2014). Soil scientists also measure soil properties at fixed depth intervals (e.g. every 10 cm) to reveal the depth functions of certain soil physical and chemical properties [e.g. (Walker and Green 1976)]. For example, soil organic carbon and total nitrogen, representing biotic components, commonly decrease exponentially with depth, whereas clay and iron, representing mineral components, can be low in the A horizon and highest in the B horizon. Colwell (1970) noted that most chemical properties show continuous trends throughout the soil profile. Depth function characterisation of soil properties is thus needed to show profile trends in addition to particular horizons.

This paper first reviews soil depth functions found in the literature, from pedological observations, to mechanistic models. We then suggest some common soil depth function typologies and reason how they relate to soil-forming processes. We will present examples of depth functions of soil elemental concentration measured in the field using a pXRF instrument.

14.2 A Review of Soil Depth Functions

14.2.1 Pedological Models

Northcote (1971) introduced principal soil profile forms resulting from his observations of many soil profiles in Australia. His book *Factual Key for the Recognition of Australian Soils*' first division of soil profile is based on its primary profile forms: organic, uniform, gradational and duplex. Mineral soils are distinguished by the depth trend in texture. Uniform profiles have little or no change in texture; gradational profiles show a steady increase of clay content with depth, and duplex profiles have layers of contrasting texture within the solum (Fig. 14.1). The profile forms also imply the degree of soil development from minimum development (uniform), to moderate development with some illuviation process (gradational), and pronounced development with heavy illuviation (duplex).

For young soils developed from till (Madsen and Munk 1987), as reported in Adhikari et al. (2014), the degree of soil development can be estimated from the

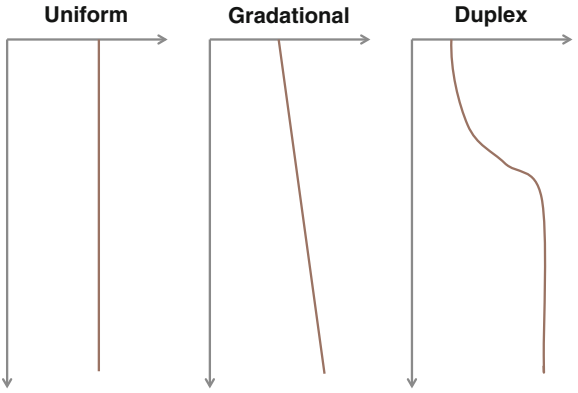

Fig. 14.1 Principal soil profile form as recognised by Northcote (1971)

trend of pH with depth. A soil after the deposition of carbonate rich parent material will have a uniform high pH and was considered young (Fig. 14.2a). With time, leaching of carbonates created a gradational (b) and duplex (c) soil pH which increased with depth. When these soils (b and c) are limed, the depth function changed towards profile (d and e), respectively (Adhikari et al. 2014).

14.2.2 Analytical Models

Kirkby (1977) proposed several depth functions which relate to the distribution of organic material, water, and evaporation and transpiration processes. The shapes of the functions included the following: exponential decay, convex and minima–maxima (Fig. 14.3). The exponential function assumes the distribution of organic

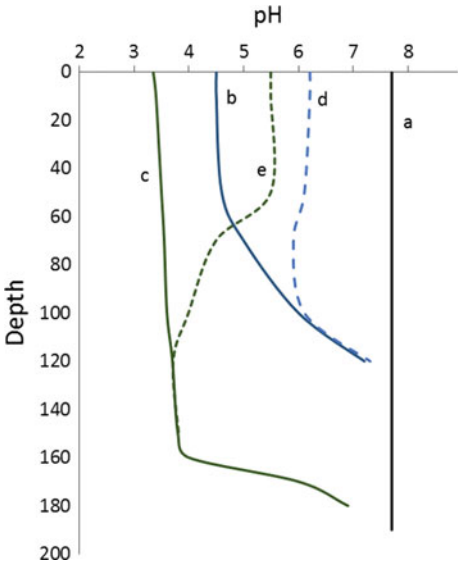

Fig. 14.2 Leaching and liming effect on soils developed in lime-rich till in Denmark. Soil profile **a** newly deposited till; **b** weakly leached soil; **c** strongly leached soil; **d** soil **b** limed; and **e** soil **b** limed (adapted from Madsen and Munk 1987)

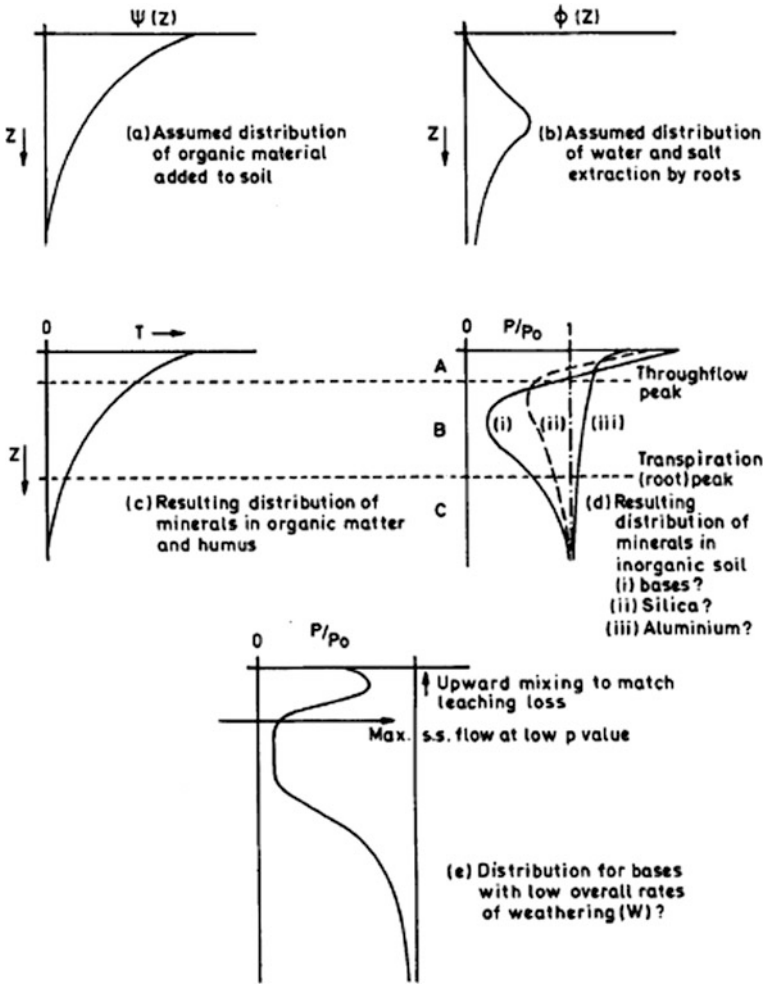

Fig. 14.3 Features of equilibrium soil profile predicted by an analytical soil profile development model [from Kirkby (1977)]

matter that was added to soil via plant litter or decaying of roots. The bell-shaped function assumes the distribution of water and the movement of solutes, and their extraction by plant roots. Mixing in the surface layer can create minimum–maximum peaks. We will discuss these functions in the next sections.

14.2.3 Exponential or Power Functions

The most widely used model for soil depth functions is the exponential or power function, which is mainly used to describe the distribution of soil organic matter or

organic carbon content with depth. The function describes the decline of soil organic matter or carbon with depth (highest in the A horizon, and low in the subsequent horizons). Russell and Moore (1968) proposed a simple exponential function:

$$C(z) = C_0 \exp(-kz)$$

where C_0 is the carbon concentration at the soil surface and k is the rate of decrease, and z is depth. They mentioned that this function is similar to the profile depth of biological properties, e.g. plant roots. This function can model a range of shapes, from a highly exponential to a linear decrease of concentration with depth. Variations of this exponential function have been proposed to describe the decrease of soil carbon with depth (Bernoux et al. 1998). A power function can also display such trend with depth (Fig. 14.4):

$$C(z) = C_0 z^b$$

The soil organic carbon content in the plough layer of cultivated fields is often relatively uniform, and a constant can be introduced for that zone as shown in Fig. 14.4b (Mikhailova et al. 2000; Meersmans et al. 2009). In spodosols, a second maxima of SOC often occurs in the spodic horizon (Webster 1978). A similar pattern also occurs in the presence of buried horizons and in palaeosols (Fig. 14.4c) (Grauer-Gray and Hartemink 2016).

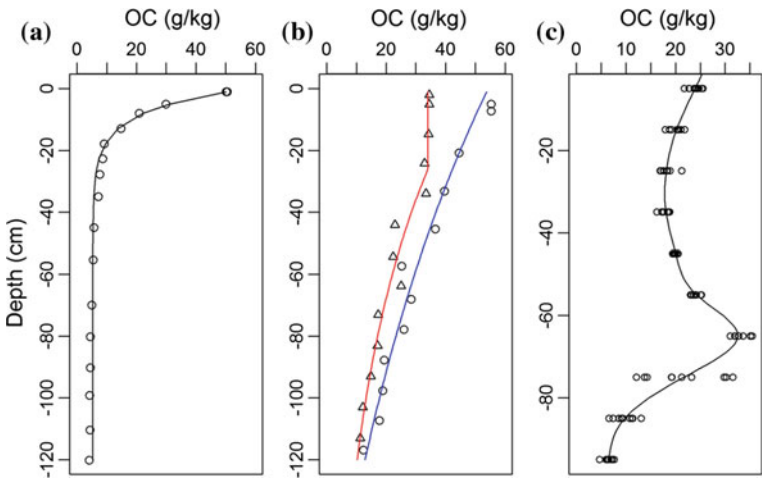

Fig. 14.4 Depth function of soil organic carbon, **a** an exponential function in an alluvial soil in New South Wales, Australia (Walker and Green 1976), **b** a grassland (*circle*) and a continuously cropped field (*triangle*) of Chernozems from Russia (Mikhailova et al. 2000), and **c** a Mollisol with a buried A horizon at 70 cm depth from South Central Wisconsin, USA (Grauer-Gray and Hartemink 2016)

The negative exponential depth function can also be used to describe soil temperature as an analytical solution to heat transport. The incorporation of organic matter through bioturbation in soil modelled as a diffusion process often results in an exponentially shaped depth function. The depth-exponential relation is also found in the soil production function, where the soil weathering rate decreases with increasing soil thickness (Stockmann et al. 2014).

14.2.4 Wetting Front

The movement of water through a soil profile creates wetting front-type depth functions. A mechanistic model by Kirkby (1985) with diffusion processes results in the weathering profile that resembles a wetting front. Brantley et al. (2008) observed that most chemical and mineralogical profiles display reaction fronts that show depletion of leachable elements or minerals (Fig. 14.5). They modelled the depth function in the form of a sigmoidal function:

$$C(z) = \frac{C_m}{1 + \frac{C_m - C_0}{C_0} \exp(\alpha\, z)}$$

where C is the concentration at depth z, with an empirical parameter α.

Beaudette et al. (2016) modelled the depth distribution of soil horizons using a proportional odds logistic regression which has a form similar to the sigmoid

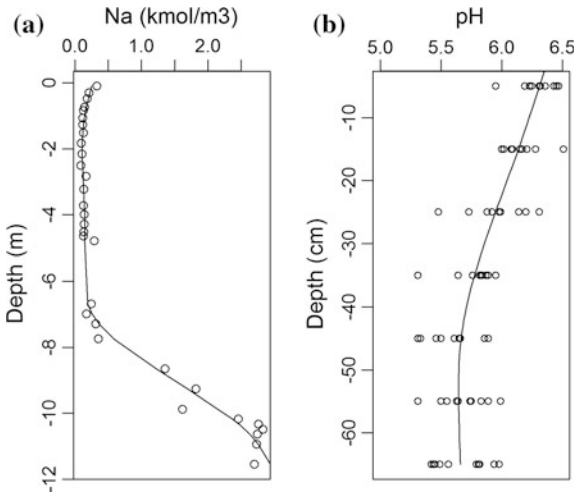

Fig. 14.5 Wetting front-type depth functions for: **a** Concentration of Na in Panola granite soil in the Piedmont Province of Georgia, USA, exposed to weathering for approximately 250–500 ka [data from Brantley et al. (2008)], **b** Soil pH from an intensely cultivated Udic Psamments from the Central Sands of Wisconsin, USA (Adhikari et al. 2016)

function. Leblanc et al. (2016) found a wetting front-type depth function for gleyed horizons, but a peak function for spodic horizons.

14.2.5 Peak Functions

Some soil properties such as clay content show accumulation (maxima) with depth as a result of eluviation and illuviation processes, in situ formation or discontinuity in soil parent materials. This accumulation can depict a bell-shaped curve, which is a characteristic of solute transport. Solute transport in soil can exhibit a normal distribution for dispersion and diffusion processes (Wetselaar 1962) or a lognormal distribution function for convective processes (Jury 1982) (Fig. 14.6). The analytical solution for a convective-diffusion transport during weathering by (Kirkby 1985) suggests a double exponential function. Myers et al. (2011) observed that some soil profiles showed highly asymmetric peak-shaped depth distributions for some soil properties. The asymmetry occurred mainly due to the gravitational vector of profile weathering and development. They proposed the use of the Pearson-type IV (PIV) asymmetric probability density function or logistic peak function. The parameters of the model can be related to properties' maximum, depth to the maximum, abruptness, and profile anisotropy. Peak functions can also indicate compaction, and anthropogenic influences can create variations such as multiple peaks (Fig. 14.7a).

An extension of the peak model is observed in properties such as clay content or electrical conductivity (Bishop et al. 1999), where its value reaches a minimum and increases to a maximum (Fig. 14.7b). This minima–maxima (minimax) depth function can be related to mixing processes in the surface and translocation to the

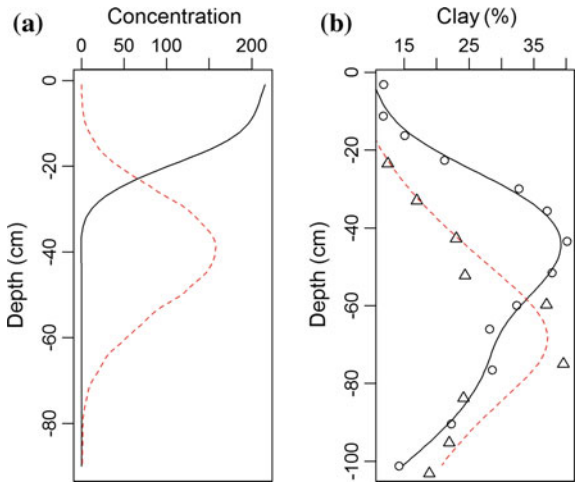

Fig. 14.6 **a** Theoretical depth distribution of solute transport in soil; solute initially follows the wetting front and displays a bell-shaped distribution following convection–dispersion processes. **b** An example of peak distribution function for clay content

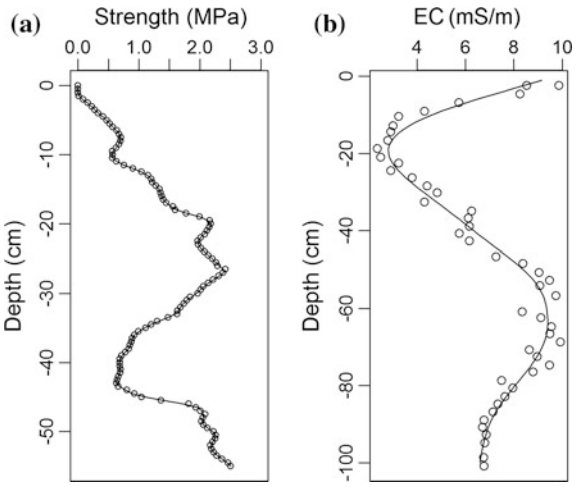

Fig. 14.7 **a** Penetration resistance from a cone penetrometer for a cultivated field showing multiple peaks [data from (Minasny 2012)], and **b** electrical conductivity from a *red* podzolic soil (Alfisol) in New South Wales, Australia, showing a minima–maxima pattern [from Bishop et al. (1999)]

subsurface, through excessive bioturbation, or textural discontinuities resulting from different parent materials within the soil profile.

14.2.6 Abrupt or Lithologic Discontinuity

Abrupt changes in the soil properties in the profile can be due to changes in the lithology of soil parent materials (Schaetzl 1998). When they occur within or near the solum, they can impact pedogenesis. Sudden increase in coarse sand or layers of gravel are common indicators of lithologic discontinuity. In environments with sharp discontinuities due to deposition or human influences, the depth functions of soil properties change abruptly. Kempen et al. (2011) modelled the depth functions for soil organic carbon of soils that have composite or stacking of discontinued horizons, where each horizon has either a linear or an exponential function. This resulted in discontinuous depth functions with abrupt boundaries.

14.2.7 Polynomials and Splines

Linear regression and orthogonal polynomials of 2nd-degree to 5th-degree have been fitted to soil depth data (Colwell 1970). This allows a degree of variation within the depth, but there are disadvantages as there is no theory from which to determine a suitable degree of polynomial and local variation can affect the quality of fit elsewhere in the soil profile (Webster 1978). Erh (1972) proposed the use of splines as a flexible function that can fit a piece wise a series independent polynomial functions over small intervals of a soil profile and also produces a

continuous derivative function. Webster (1978) demonstrated that the spline interpolators are better for some organic matter profiles of soils in Britain, especially for Spodosols where the exponential decrease assumption is invalid.

Ponce-Hernandez et al. (1986) pointed out that many of the proposed methods fit the depth functions or curves through the depth of horizon averages. This can produce unreliable results as it smoothens out the variance of the data. The fitted curves can be smoother than the true variation of the properties with depth. They proposed equal-area splines to reconstruct profiles more accurately from stepped data and the approach was used by Slater (1994) to reconstruct soil horizon data into a more regular depth interval for a continuous classification. Bishop et al. (1999) proposed the equal-area quadratic smoothing splines and tests of their model indicated the superiority of equal-area splines in prediction of depth functions.

The development of proximal soil sensors allows measurements of soil properties at small depth increments with depth. Invasive, in situ technologies include penetrometer with penetration resistance measurement (Arriaga et al. 2016) which can be coupled with moisture content and bulk electrical conductivity sensors.

14.2.8 Typologies of Depth Functions

Based on the above review, we have identified common typologies of soil depth functions. The shape of the functions imply physical processes as described above. In essence, there are 7 typologies that describe soil property change with depth: uniform, gradational, exponential, wetting front, abrupt, peak, and minima–maxima (minimax) (Fig. 14.8). The curves have mirror images reflecting properties that

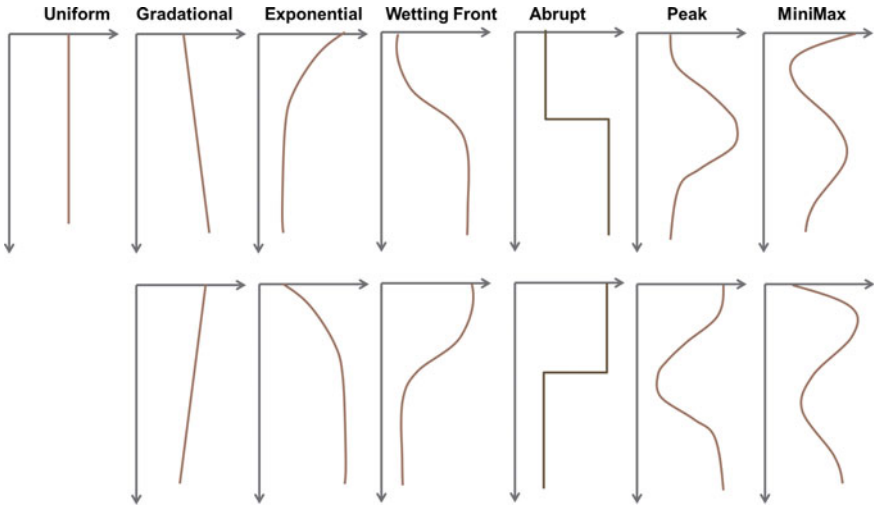

Fig. 14.8 General typologies of depth functions

might be compositional or complementary. The patterns may or may not reflect soil horizon boundaries.

14.3 Profile Development Indices

Pedologists study the depth functions to infer soil processes and development. Profile development indices were developed based on the horizons' morphological and chemical data as quantitative measures of stages of soil profile development. For example, Harden (1982) developed a soil profile development index that was related to the age of the soil. The index was calculated as a sum of field and laboratory data weighted by the horizon thickness.

Another index related to profile development is the Index of Profile Anisotropy (IPA) was developed by Walker and Green (1976) which provides a single value to describe the anisotropy of a profile with laboratory-measured soil data. When a soil is very young, its properties are assumed to be isotropic in nature (such as a uniform texture). When a soil matures and is more intensely weathered, the anisotropy value is increased. IPA is defined as follows:

$$\text{IPA} = |\text{Deviation}|/\text{mean}$$

At time = 0 soil properties are isotropic; with time, soil properties change with depth, the degree of anisotropy increases with time. The depth functions can now be used to calculate these indices as a quantitative measure the degree of soil profile development.

14.4 Soil Depth Function Examples

To demonstrate the idea of depth functions, we show the measurement of elemental concentration of soils in the field. Measurements were made every 5 cm along the profile wall of an Alfisol and an Entisol in Wisconsin, USA, using an Olympus pXRF operated in GEOCHEM mode.

14.4.1 Mollic Hapludalfs

The Mollic Hapludalfs from West Madison has developed in loess over coarse and calcareous outwash and the soil has 5 soil horizons. The plough layer is 24 cm deep with a silt loam followed by a silty clay loam Bt horizon (24–55 cm). There is a transitional BC horizon (55–91 cm) adjacent to the outwash (horizon 2 C) where the texture is a loamy sand. Figure 14.8 shows depth functions of some major elements measured in the soil pit. The Al and Fe concentrations show a similar pattern with a peak in the Bt horizon, indicating that there is enrichment with

alumino-silicates—an indication of clay illuviation. The Mn concentration varies gradually down the profile with an increase in the Bt horizon. There is a colour and morphology change from the Ap to the Bt horizon, but most elements measured by pXRF varies smoothly down the profile.

Elemental concentration from pXRF allows calculation of soil chemical weathering indices that were developed for pedological studies (Sauer et al. 2007). The main assumption of these indices is that the concentration and movement of chemical elements are controlled by the degree of weathering. It is assumed that during the weathering process, major oxides such as TiO_2 and Fe_2O_3 and Al_2O_3 are considered immobile, and Si_2O, K_2O, Na_2O, MgO and CaO are mobile. Most of these weathering indices are expressed as a ratio of molecular or weight percentage between different elements or groups of major oxides (Sauer et al. 2007). The simplest weathering index is SiO_2/Al_2O_3 (Ruxton 1968) which captures the loss of silica during weathering. It is assumed that the amount of alumina in weathered soil is immobile and constant and the amount of oxides (zirconia, titanium and total iron oxides) is constant. The index ranges from a high value (around 10 for unweathered material) to a low for weathered soil. It is mostly used for studying highly weathered soils. Another index is the Ti/Zr ratio, and these immobile elements are highly correlated and have been used to test the homogeneity of parent materials (Maynard 1992). The Ti/Zr ratio is not much affected by primary alteration or weathering and can be used as indicator of major igneous rock types.

We calculated these two weathering indices for the Alfisol (Fig. 14.9). Although the 2C horizon is a parent material discontinuity (starting at 60 cm), most elements did not reflect this abrupt change except for elemental Ca concentrations. The Zr concentration shows a wetting front-type depth function with a constant value to a depth of 50 cm and gradually decreasing at 80 cm depth where the Zr concentrations are low. The Ti/Zr ratio shows a convex or peak function with a spike at the horizon boundary at 90 cm depth. The SiO_2/Al_2O_3 ratio is low and around 5 up to 80 cm soil depth and increases from 8 to 14 to a depth of 150 cm. The elemental concentration that mostly shows a smooth variation across the 2 parent materials indicates that there has been mixture through diffusion process.

14.4.2 Typic Udipsamments

The Typic Udipsamments from the Wisconsin central sand plain is characterised by a blanket of sandy and gravelly outwash. The soil is the plainfield sand series consists of very deep excessively drained soils formed in sandy drift on outwash plain, glacial lake basins, stream terraces, and moraines.

The profile has an Ap horizon of 24 cm which is reflected in the variation of Fe and Mn. The depth function of Fe shows a constant value for the Ap horizon followed by a peak at 60 cm. The depth function of P follows an exponential form, decreases with depth, with P sourced from inorganic fertiliser input. The Al and Si concentrations show a bowl-shaped depth function indicating some mixture of

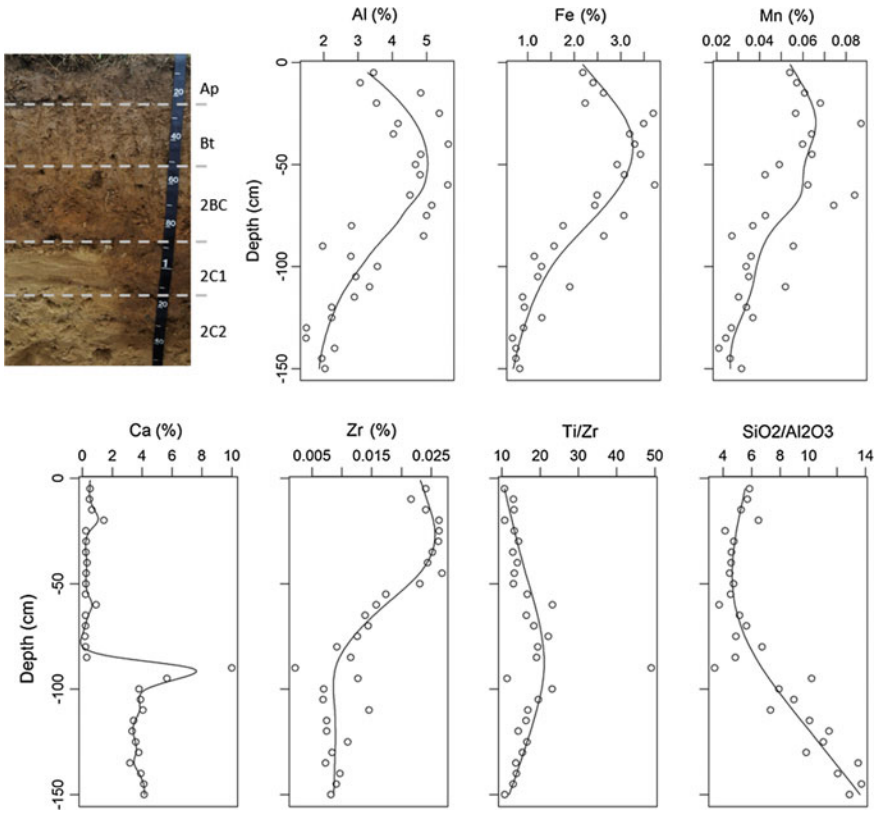

Fig. 14.9 Depth functions of a Mollic Hapludalfs from West Madison, Wisconsin, USA. Concentration of Al, Fe, Ca, Zr, Ti/Zr and SiO_2/Al_2O_3 was measured using a pXRF in the field at 5-cm-depth intervals along the soil profile wall. The lines are fitted smoothing splines

materials in the Ap horizon, leaching of materials in the Bw1 and Bw2 horizons and unweathered materials in Bw3. This pattern is reflected in the SiO_2/Al_2O_3 ratio, where the pattern is a reverse of a weathered soil profile (increasing weathering down the profile). The index reflects leaching of Si, and the assumption of Al as constant is invalidated. The Ruxton index may not be suitable for this soil as an indication of weathering. The Ti/Zr ratio is uniform throughout the profile with an increasing value in the Bw3 horizon indicating less weathered soil materials (Fig. 14.10).

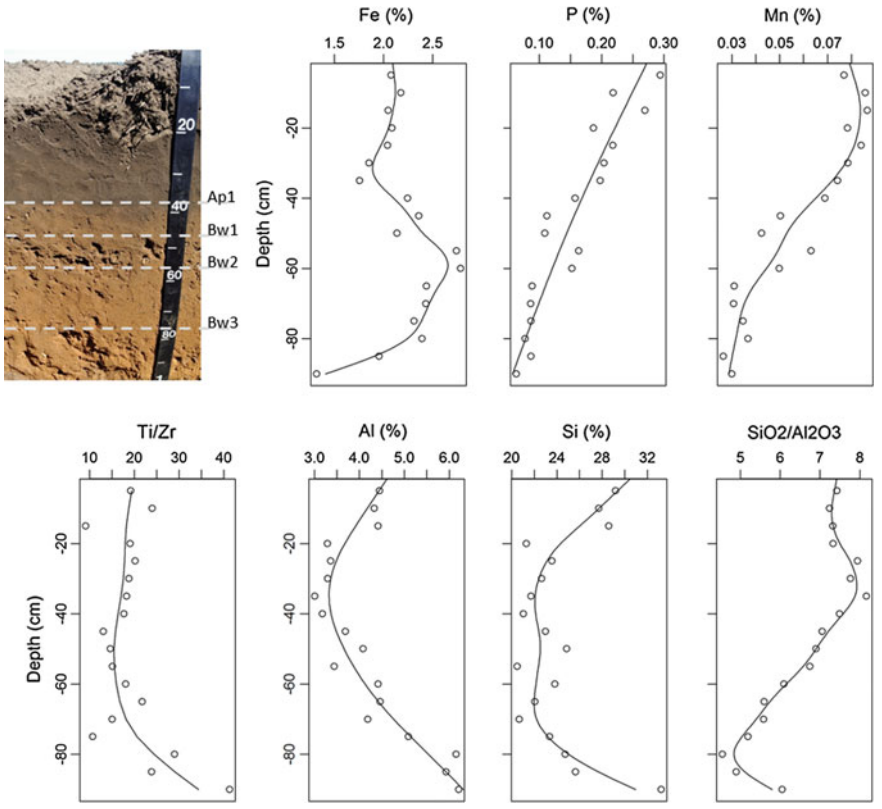

Fig. 14.10 Depth functions of a Typic Udipsamments from the Central Sands, Wisconsin, USA. Concentration of Fe, P, Mn, Ti/Zr, Si, Al and SiO_2/Al_2O_3 was measured using a pXRF at 5-cm-depth intervals along a soil profile wall. The lines are fitted smoothing splines

14.4.3 Horizon Boundary Detection Using Soil Depth Function Data

The depth functions of the elements are mostly continuous as opposed to the discrete appearance and assumptions in soil horizons. We can use pedometric techniques to segment these into layers and reconcile the layers with field observed horizons (Weindorf et al. 2012). The depth functions can be treated as transect with multivariate measurements of elemental concentration. The horizon boundaries can be identified based on the Mahalanobis distance of a split moving window approach of (Webster 1973) or the difference between subsequent pXRF readings as proposed by (Weindorf et al. 2012). We can also apply a fuzzy k-means clustering of the elemental concentration to create soil material classes (Fajardo et al. 2015). In this example, fuzzy k-means clustering was applied to identify layers of similar characteristics within each profile. In our example (Fig. 14.11), both profiles were

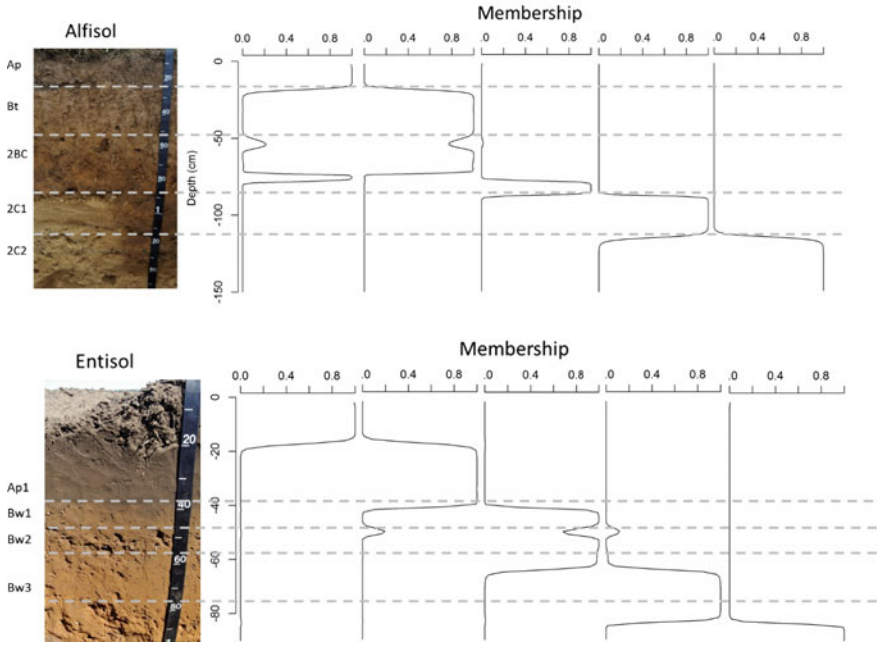

Fig. 14.11 Elemental concentration data (Fe, Mn, Al, Ca, Si) for each profile were grouped using a fuzzy k-means clustering method. The data for each profile were clustered into 5 classes individually, and the plot shows the membership for each of the class

grouped individually into 5 classes based on their elemental concentration. The membership for each class occupied a unique layer within the profile, and some of the numerical classes correspond to the horizons observed in the field. For example in the Alfisol, the numerical class corresponds to the Ap, (Bt + BC), BC, 2C1 and 2 C2. Whereas in the Entisol, the Ap horizon is separated into 2 classes.

14.5 Conclusions

We identified 7 typologies of soil depth functions: uniform, gradational, exponential, wetting front, abrupt, peak/convex and minima–maxima. These depth functions represent major soil processes. Field measurements using tools such as pXRF and NIR allow measurement of soil properties and elemental concentration at small depth increments and thus enable estimation of depth functions readily and rapidly without the need to collect bulk soil samples from horizons. The examples presented here showed that most soil elemental concentration vary continuously with depth. Although the data are few, the depth functions reflect the age of the soil, some major soil processes, parent materials, and soil textural changes. Horizon

boundaries based on elemental concentration can be derived using, for example, moving window Mahalanobis distance or fuzzy k-means clustering. Proximal soil sensors allow measurement of soil development indices in the field, which has the potential for a more objective delineation of soil horizons and description of the soil profile. A more objective measurement of the soil properties can lead to a better understanding of soil processes and within soil horizon variation.

References

Adhikari K, Hartemink AE, Minasny B (2016) Mapping a profile wall of a typic Udipsamments from the Central Sands, WI, USA. In: Hartemink AE, Minasny B (eds) Digital soil morphometrics. Springer, Dordrecht

Adhikari K, Kheir RB, Greve M, Greve MH, Malone MB, Minasny B, McBratney A (2014) Mapping soil pH and bulk density at multiple soil depths in Denmark. In: Arrouays D, McKenzie N, Hempel J, de Forges AR, McBratney AB (eds) GlobalSoilMap: basis of the global spatial soil information system. Taylor & Francis, London, pp 155–160

Arkley RJ (1976) Statistical methods in soil classification research. Advances in Agronomy. Academic Press, New York, NY, pp 37–69

Arriaga FJ, Lowery B, Reinert D, McSweeney K (2016) Cone penetrometers as a tool for distinguishing soil profiles and mapping soil erosion. In: Hartemink AE, Minasny B (eds), Digital soil morphometrics. Springer, Dordrecht, p. (this volume)

Beaudette DE, Roudier P, Skovlin J (2016) Probabilistic representation of genetic soil horizons. In: Hartemink AE, Minasny B (eds), Digital soil morphometrics. Springer, Dordrecht, p. (this volume)

Bernoux M, Arrouays D, Cerri CC, Bourennane H (1998) Modeling vertical distribution of carbon in oxisols of the Western Brazilian Amazon (Rondonia). Soil Sci 163:941–951

Bishop TFA, McBratney AB, Laslett GM (1999) Modeling soil attribute depth functions with equal-area quadratic smoothing splines. Geoderma 91:27–45

Brantley SL, Bandstra J, Moore J, White AF (2008) Modelling chemical depletion profiles in regolith. Geoderma 145:494–504

Colwell J (1970) A statistical-chemical characterization of four great soil groups in southern New South Wales based on orthogonal polynomials. Soil Res 8:221–238

Erh K (1972) Application of the spline function to soil science. Soil Sci 114:333–338

Fajardo M, McBratney A, Whelan B (2015) Fuzzy clustering of Vis–NIR spectra for the objective recognition of soil morphological horizons in soil profiles. Geoderma

Grauer-Gray JR, Hartemink AE (2016) Variation of soil properties in a Mollisol profile wall. In: Hartemink AE, Minasny B (eds) digital soil morphometrics. Springer, Dordrecht

Harden JW (1982) A quantitative index of soil development from field descriptions: Examples from a chronosequence in central California. Geoderma 28(1):1–28

Hartemink AE, Minasny B (2014) Towards digital soil morphometrics. Geoderma 230:305–317

Jenny H (1941) Factors of soil formation. A system of quantitative pedology. McGraw-Hill, New York

Jury WA (1982) Simulation of solute transport using a transfer function model. Water Resour Res 18:363–368

Kempen B, Brus DJ, Stoorvogel JJ (2011) Three-dimensional mapping of soil organic matter content using soil type-specific depth functions. Geoderma 162:107–123

Kirkby M (1977) Soil development models as a component of slope models. Earth Surf Process 2:203–230

Kirkby MJ (1985) A basis for soil profile modelling in a geomorphic context. J Soil Sci 36:97–121

Leblanc MA., Gagné G, Parent LE (2016) Numerical clustering of soil series using profile morphological attributes for potato. In: Hartemink AE, Minasny B (eds) Digital soil morphometrics. Springer, Dordrecht, p. (this volume)
Madsen HB, Munk I (1987) The influence of texture, soil depth and geology on pH in farmland soils: a case study from southern Denmark. Acta Agricul Scand 37:407–418
Maynard J (1992) Chemistry of modern soils as a guide to interpreting Precambrian paleosols. J Geol 279–289
Meersmans J, van Wesemael B, De Ridder F, Van Molle M (2009) Modelling the three-dimensional spatial distribution of soil organic carbon (SOC) at the regional scale (Flanders, Belgium). Geoderma 152:43–52
Mikhailova E, Bryant R, Vassenev I, Schwager S, Post C (2000) Cultivation effects on soil carbon and nitrogen contents at depth in the Russian Chernozem. Soil Sci Soc Am J 64:738–745
Minasny B (2012) Contrasting soil penetration resistance values acquired from dynamic and motor-operated penetrometers. Geoderma 177–178:57–62
Myers DB, Kitchen NR, Sudduth KA, Miles RJ, Sadler EJ, Grunwald S (2011) Peak functions for modeling high resolution soil profile data. Geoderma 166:74–83
Northcote K (1971) A factual key for the recognition of Australian soils. CSIRO/Rellim, Glenside, South Australia
Ponce-Hernandez R, Marriott FHC, Beckett PHT (1986) An improved method for reconstructing a soil profile from analyses of a small number of samples. J Soil Sci 37:455–467
Russell J, Moore A (1968) Comparison of different depth weightings in the numerical analysis of anisotropic soil profile data. Transactions of the 9th International Congress of Soil Science, pp. 205–213
Ruxton BP (1968) Measures of the degree of chemical weathering of rocks. J Geol 518–527
Sauer D, Schellmann G, Stahr K (2007) A soil chronosequence in the semi-arid environment of Patagonia (Argentina). Catena 71:382–393
Schaetzl RJ (1998) Lithologic discontinuities in some soils on drumlins: theory, detection, and application. Soil Sci 163:570–590
Slater BK (1994) Continuous Classification and visualization of soil layers: a soil-landscape model of Pleasant Valley Wisconsin. University of Wisconsin, Department of Soil Science, Madison, Wisconsin
Stockmann U, Minasny B, McBratney AB (2014) How fast does soil grow? Geoderma 216:48–61
Walker P, Green P (1976) Soil trends in two valley fill sequences. Soil Res 14:291–303
Webster R (1973) Automatic soil-boundary location from transect data. J Int Assoc Math Geol 5:27–37
Webster R (1978) Mathematical treatment of soil information. Transactions of the 11th International Congress of Soil Science, pp 161–190
Weindorf DC, Zhu Y, Haggard B, Lofton J, Chakraborty S, Bakr N, Zhang W, Weindorf WC, Legoria M (2012) Enhanced pedon horizonation using portable X-ray fluorescence spectrometry. Soil Sci Soc Am J 76:522–531
Wetselaar R (1962) Nitrate distribution in tropical soils. Plant Soil 16:19–31

Chapter 15
Electrical Conductivity Depth Functions for Delineating Paleosols

Glenn Borchardt

Abstract Soil weathering and leaching lead to increased salt concentrations at the wetting front in soils of semiarid and Mediterranean climates. Burial of silty alluvial fan deposits may preserve these salt signatures in paleosols, with the base of each solum being delineated by high electrical conductivity. The buried layer must be thick enough to prevent destruction of the initial signature via leaching. The identification of alluvial strata as paleosol horizons helps to confirm age estimates derived from standard soil descriptions. Several examples illustrate the use of conductivity in delineating late Quaternary soils and paleosols. A soil profile along the Hayward fault had a soil underlain by three paleosols instead of the four paleosols as was first assumed by visual examination. Estimates of soil and paleosol ages were sufficient to assure that no surface fault rupture had occurred during the last 24,000 years. Background conductivity was about 200 μS/cm, while maxima for the soil and three paleosols were 560, 580, 630, and 590 μS/cm, respectively. It was concluded that field electrical conductivity measurements can be used to delineate paleosols.

Keywords Pedochronology · Faulting · Tectonics · Electrical conductivity · Depth functions

15.1 Introduction

Soil weathering and leaching lead to increased salt concentrations at the wetting front in soils. In uniform, fine-textured soil measurements of electrical conductivity (EC) within soil solutions may indicate the extent of this process (Frinkl 1979; Pozdnyakova 1999; Golovko et al. 2007; Son et al. 2010). However, due to the great solubility of salts released from minerals, concentrations typically are low and ephemeral, particularly in soils of the humid regions.

G. Borchardt (✉)
Soil Tectonics, Berkeley, CA, USA
e-mail: gborchardt@gmail.com

A.E. Hartemink and B. Minasny (eds.), *Digital Soil Morphometrics*,
Progress in Soil Science, DOI 10.1007/978-3-319-28295-4_15

In California, EC measurements have been used to aid in pedochronology (soil dating), which we use in assessing the age of fault movement. State law prohibits most construction on earthquake faults that had surface fault rupture (SFR) during the Holocene (Bryant and Hart 2007). To gauge the hazard, geologists excavate 3 to 6-m-deep trenches perpendicular to suspect fault traces across potential building sites. As a pedochronologist, I estimate the ages of soils and any associated faulting exposed in these trenches. Although the modern soil in many of the trenches may have begun developing less than the required 11,000 years, we sometimes find paleosols beneath them. EC measurements may help to confirm that such soils indeed are paleosols. Soil development durations are estimated from peak heights in combination with other age-related characteristics such as color, B horizon thickness and structure, clay film development, and calcite stage.

15.2 Materials and Methods

We generally describe soil profiles that represent the oldest, most complete record of soil development in the trench excavations that geologists use to evaluate the presence of hazardous faults. If a fault is discovered, this may necessitate sampling, measuring, and describing soils about a meter on either side of the suspect fault. Vertical channel samples of each horizon are obtained as representative.

In the laboratory, EC and pH are measured after representative subsamples are mixed with an equal amount of water by weight. EC measurements can be performed in the field or laboratory with a handheld meter (Fig. 15.1). EC values could be used to produce in situ analog depth functions that could help in delineating soil horizons. However, EC and its inverse, electrical resistivity are influenced by the amount of moisture present (Ozcep et al. 2010). The water to soil ratio must be controlled. Dry soils do not yield EC measurements (Brevik et al. 2006), as demonstrated by the Phoenix Mars Lander, which failed to get a response even though there was ice within 5 cm of the probe (Zent et al. 2009). Coarse soils and sediments generally do not trap salts. Although this low EC response may aid in the identification of sand and gravel lenses (Fig. 15.2), it may also prevent the development of an EC peak that would indicate the extent of the wetting front.

15.3 Results

15.3.1 Holocene Soil (10 ka)

Although soil weathering was minimal in California during the Holocene, we can detect its occurrence by performing EC measurements. Depth functions for EC indicate that a particular soil has received sufficient precipitation to induce soil

Fig. 15.1 Simple, typical handheld electrical conductivity meter

formation. Leaching from the A horizon generally removes salts released from soil minerals. These salts move to the wetting front. A typical soil has received rainfall with carbonic acid formed from carbon dioxide in the atmosphere. This naturally acidifies and decalcifies the soil, with surface horizons countering that trend as they accumulate Ca-laden vegetative matter (Fig. 15.3). EC measurements follow a similar pattern (Fig. 15.4). The soil pH was lowest at the 140 cm depth, which also was the depth that the EC began to increase. The upper 33 cm of the soil was imported artificial fill.

15.3.2 Pleistocene–Holocene Transition

The climate change from humid to subhumid that occurred as a result of the Pleistocene–Holocene transition in northern California has provided valuable information for pedochronology. Holocene soils tend to be about a meter thick, while soils formed during the Pleistocene can be up to several meters thick. When there is associated colluvial or alluvial deposition, EC depth functions sometimes reflect both soil moisture regimes (Fig. 15.5).

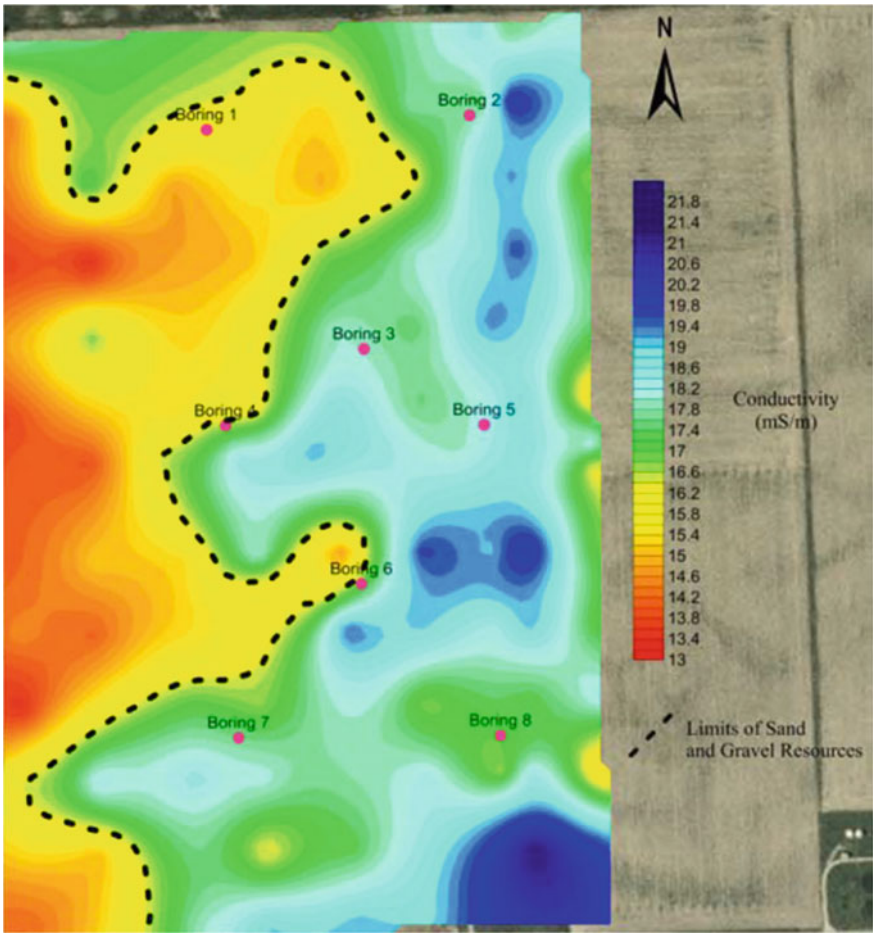

Fig. 15.2 EC measurements showing the effect of particle size. Reddish areas have low EC in the sand and gravel areas (Mundell and Associates, Inc. 2015)

Micropedology sometimes can be used to confirm the transition from one climate to another or, alternatively, the effect of alluvial deposition or erosion. For instance, peds that were coated with clay films during the Pleistocene can be subsequently coated with soluble salts that demonstrate that the wetting front has risen in the profile. Figure 15.6 shows gypsum coating a ped formed when the landscape was subject to much greater water percolation.

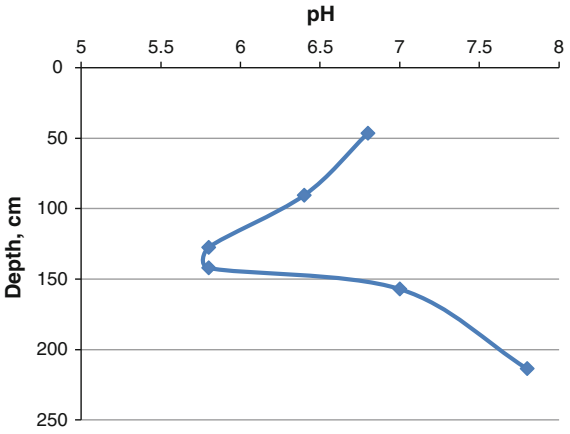

Fig. 15.3 Depth function for pH in Soil Profile No. 1 in Trench EFT-1 on Toro Vista Court (10 ka/70 ka; MAP = 551 mm/year) (Borchardt 2007, Fig. 2). Note that the upper 33 cm of this profile was artificial fill

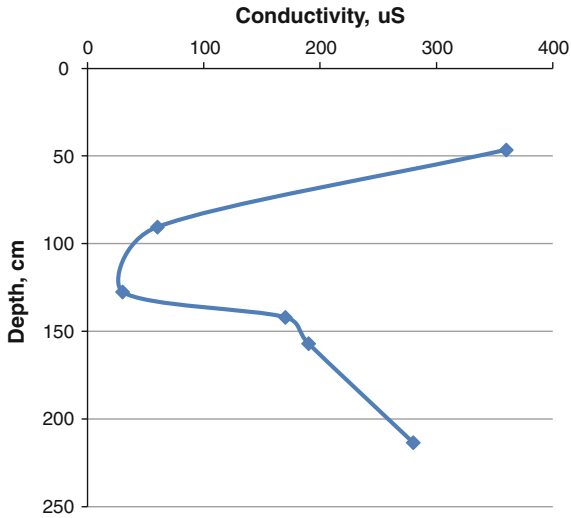

Fig. 15.4 Depth function for EC in Soil Profile No. 1 in Trench EFT-1 on Toro Vista Court (10 ka/70 ka; MAP 551 mm/year) (Borchardt 2007, Fig. 3). Note that the upper 33 cm of this profile was artificial fill

15.3.3 Sangamon Soil (122 ka)

Relict paleosols considered to be Sangamon age (the last time sea level was higher than at present, Chen et al. 1991) sometimes exist on stable surfaces devoid of significant degradation or aggradation during the Pleistocene/Holocene transition. Salts are left behind as the wetting front gradually retreats toward the surface when the climate becomes increasingly dry (Fig. 15.7). Such uniform behavior is dependent on a relatively uniform fine soil texture. Salt concentrations in coarse horizons tend to be low due to their low water holding capacity and high permeability (Figs. 15.2 and 15.8). In the Sangamon paleosol, the upper two silt loam horizons have been leached extensively during the Holocene (Fig. 15.7), while the

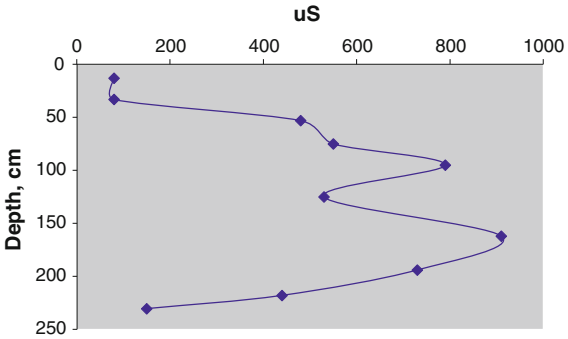

Fig. 15.5 Depth function for EC in Soil Profile No. 3 at the Lakes at Fountain Grove, Santa Rosa, CA. The two high EC peaks may represent two distinct phases of soil development, with paleosol development during the Pleistocene being interrupted by the colluviation that contributed parent material for the modern soil (10 ka/80 ka; MAP 1067 mm/year) (Borchardt 2003, Fig. 6)

Fig. 15.6 Close-up of clay-coated ped face surrounded by gypsum in the Etyb1 horizon of a paleosol near the Calaveras fault. The clay films were deposited first and the gypsum second. View SE (16 ka; MAP 578 mm/year) (Borchardt 2008, Fig. 5)

underlying 2-m-thick silty clay Bt horizon that formed during the Pleistocene remains preserved beneath the E horizon (Fig. 15.9).

California state law prohibits construction on faults having had surface fault rupture during the Holocene for residential housing developments. Even though this soil was much older than that, it had experienced several fault offsets since 122 ka. These totaled about 1 m and probably were the results of several earthquakes. During that period, the subparallel San Andreas fault about 6 km to the east had undergone 3000 m of lateral offset. The faults at this site had negligible activity. In addition, there was no offset of the surface topography, as is generally the case with hazardous faults. The analysis of the SFR hazard at the site indicated that up to

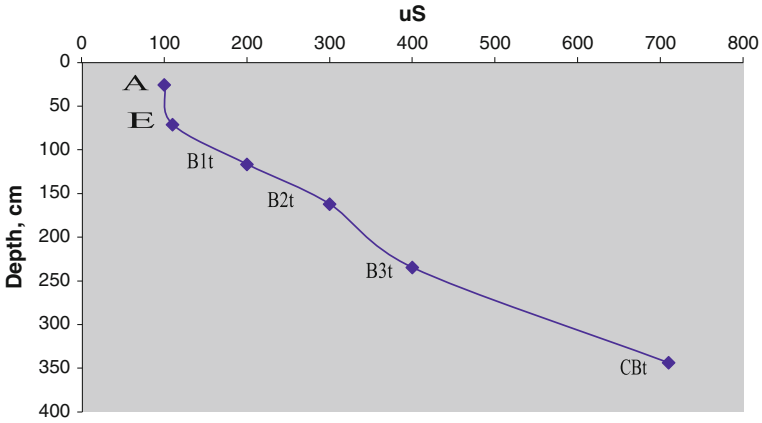

Fig. 15.7 Depth function for EC in a Pleistocene soil at Paradise Valley, Bolinas, California (122 ka; MAP = 914 mm/year) (Borchardt 2005, Fig. 2)

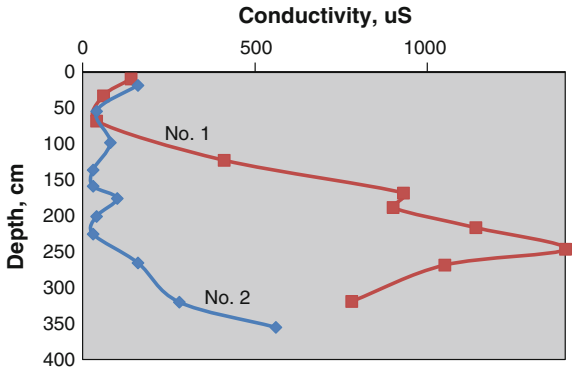

Fig. 15.8 Depth function for EC in Soil Profile Nos. 1 and 2 at Alamo, California. The high EC beneath the 130 cm depth in Soil Profile No. 1 reflects the presence of high amounts of gypsum beneath the present-day wetting front. The gravelly nature of Soil Profile No. 2 allows clays and salts to penetrate to much greater depths than they do in the silt of Soil Profile No. 1 (22 ka; MAP = 578 mm/year) (Borchardt 2008, Fig. 9)

24 cm of vertical and horizontal offset could occur in a single event (Dwyer et al. 2010). We selected 1.2 m as the maximum possible horizontal offset, which would be 20 % of what occurred on the San Andreas in 1906 (Lawson 1908; Hoexter 1992).

Fig. 15.9 Pleistocene soil at Bolinas showing the E horizon overlying the yellowish brown Bt horizon (122 ka; MAP = 914 mm) (Borchardt 2005, Fig. 3)

15.3.4 Multiple Paleosols in Young Alluvium (24 ka)

EC depth functions are useful in detecting and confirming the presence of paleosols in young alluvial fans. A change in salt concentration may convey age-related information. At a prospective building site on the southwest side of the Hayward fault, EC measurements indicated that there was a Holocene soil underlain by three short-lived paleosols (Fig. 15.10). During initial description of this soil profile, an additional paleosol was assumed when viewing the faunal bone in the section (Fig. 15.11). Bones, like most charcoal specimens, are often found at the surfaces of paleosols, similar to lag deposits. In this soil, however, a bone was in the midst of a weak, Bt horizon, which was one reason it had survived the relatively short period

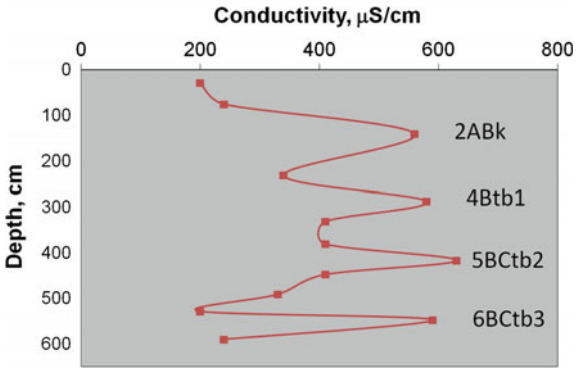

Fig. 15.10 Depth function for EC showing maxima for the modern soil and three underlying paleosols along the Hayward fault (24 ka; MAP = 640 mm/year) (Borchardt 2015, Fig. 7)

Fig. 15.11 View of the 5B2tb2 horizon from Soil Profile No. 3 showing a bone fragment at the 405 cm depth (Borchardt 2015, Fig. 4)

Table 15.1 Comparison of pedochronological estimates derived from the profile description with estimates derived from the relative areas of EC peaks

Horizon	Duration of soil development (t_d) (ky)	
	Borchardt (2015)	EC peak area
2ABk	11.0[a]	10.0[b]
4Btb1	4.0	4.9
5BCtb2	5.0	3.5
6BCtb3	4.0	5.4
Profile t_o, ka	24.0	23.8

[a]Pedochronological estimates based on available information. All ages should be considered subject to ±50 % variation unless otherwise indicated (Borchardt 1992)
[b]Peak areas were calculated by multiplying half the height of the EC peak (μS/cm) times the width of the base of the peak (cm)
t_o = date when soil formation or aggradation began, ka
t_b = date when soil or strata were buried, ka
t_d = duration of soil development or aggradation, ky

(5 ky) of weathering. Background EC was about 200 μS/cm, while maxima for the soil and three paleosols were 560, 580, 630, and 590 μS/cm, respectively (Fig. 15.10). These results reflect the relatively high average deposition rate (0.24 mm/year) necessary to safeguard EC maxima from dissolution by percolation from overlying deposits.

There is a possibility that the actual quantity of soluble salt preserved in these soils and paleosols is correlative with the amount of time each was exposed to pedogenesis. For instance, in the above example, I calculated the areas of the four EC peaks after performing the usual qualitative estimates of development durations (Table 15.1). The two methods appear to be somewhat correlative, showing that quantitative measurements of soluble salts, along with more detailed EC measurements, may have promise in future pedochronological studies.

15.4 Conclusions

These results highlight the use of EC measurements in pedochronology and the estimation of soil age. Salts dissolved from weathering minerals percolate in soil solutions and are generally deposited at the wetting front. This mostly occurs in Mediterranean and semiarid to arid climates where salts are not leached from fine-textured soils. With sufficient aggradation, salt accumulations can be preserved, providing evidence for previous soil formation in the form of paleosols. Unlike pH measurements, changes in EC may appear minuscule, but they can be important indicators of pedogenesis. EC measurements can help in descriptions of paleosols that provide valuable information on previous landscapes and climates. Salt concentrations as indicators of soil weathering should receive more attention than they are normally given, particularly in areas subject to semiarid and Mediterranean climates, where salts tend to tarry on their way to the sea.

Acknowledgments I thank M.J. Dwyer, Certified Engineering Geologist, Santa Rosa, California, and Alfred Hartemink, University of Wisconsin-Madison, Department of Soil Science, for many helpful suggestions that improved the manuscript.

References

Borchardt G (1992) Pedochronology along the Hayward fault. In: Borchardt G, Hirschfeld SE, Lienkaemper JJ, McClellan P, Williams PL, Wong IG (eds) Proceedings of the second conference on earthquake hazards in the Eastern San Francisco Bay Area, 25–29 March 1992, Hayward, California, California Department of Conservation, Division of Mines and Geology Special Publication 113, pp 111–117

Borchardt G (2003) Pedochronological report for The Lakes at Fountain Grove, Santa Rosa, California, Unpublished consulting report prepared for RGH Geotechnical and Environmental Consultants, Santa Rosa, California, RGH Project No. 1780.02.08.1, Berkeley, California, Soil Tectonics, A-1 to A-16

Borchardt G (2005) Pedochronological report for the Osterweis Property, Paradise Valley Road, Bolinas, California, in Samrad, LA, Dwyer, MJ (eds) Fault trench investigation: Osterweis Property, APN 188-140-11 (5.8 Acres) & APN 188-120-31 (66 Acres), Paradise Valley Road, Bolinas, California: Unpublished consulting report prepared for Mr. John Osterweis, Osterweis Capital Management, San Francisco, California, Miller Pacific Engineering Group Project No. 1147.02: Novato, California, Miller Pacific Engineering Group, C-1 to C-27

Borchardt G (2007) Pedochronological report for 2785 Toro Vista Court, Morgan Hill, California, in Connelly, SF (ed) Fault investigation: APN 817-70-007, 2875 Toro Vista Court, Morgan Hill, California: Unpublished consulting report prepared for Mr. Tony Duong, Milpitas, California, Project #0722: San Jose, California, Steven F. Connelly, C.E.G., A-1 to A-22

Borchardt G (2008) Pedochronological report for the Gordon Ball property, Camille Avenue, Alamo, California, Unpublished consulting report prepared for ENGEO, Inc., San Ramon, California, Project No. 8442.000.001, Berkeley, California, Soil Tectonics, A-1 to A-31

Borchardt G (2015) Pedochronological report for the southeast parking lot at Camp Sweeney, San Leandro, California, Unpublished consulting report for Kleinfelder, Inc., Santa Rosa, California, Berkeley, CA, Soil Tectonics, A-1 to A-33

Brevik EC, Fenton TE, Lazari A (2006) Soil electrical conductivity as a function of soil water content and implications for soil mapping. Precis Agric 7(6):393–404. doi:10.1007/s11119-006-9021-x

Bryant WA, Hart EW (2007) Fault-rupture hazard zones in California: Alquist-Priolo Earthquake Fault Zoning Act with index to Earthquake Fault Zones maps, California Geological Survey Special Publication 42, 41 p

Chen JH, Curran HA, White B, Wasserburg GJ (1991) Precise chronology of the last interglacial period: ^{234}U-^{230}Th data from fossil coral reefs in the Bahamas. Geol Soc Am Bull 103:82–97

Dwyer MJ, Samrad LA, Borchardt G, Pappas B (2010) Construction on secondary traces of the San Andreas fault at Bolinas. AEG News 53:22–25

Frinkl Jr CW (1979) Electrical conductivity. In: Fairbridge RW, Frinkl Jr CW (eds) The encyclopedia of soil science, Part 1. Physics, chemistry, biology, fertility, and technology. Dowden Hutchinson & Ross, Stroudsbug, PA, pp 97–99

Golovko L, Pozdnyakov AI (2007) Electrical geophysical methods in agriculture. In: Proceedings of the 4th international symposium on intelligent information technology in agriculture (ISIITA), 26–29 Oct 2007, Beijing, China, China National Engineering Research Center for Information Technology in Agriculture, pp 457–471

Hoexter DF (1992) Potential for triggered slip on secondary faults in the East Bay: implications for the planning process. In: Borchardt G, Hirschfeld SE, Lienkaemper JJ, McClellan P, Williams PL, Wong IG (eds) Proceedings of the second conference on earthquake hazards in

the Eastern San Francisco Bay Area: California Department of Conservation, Division of Mines and Geology Special Publication 113, pp 153–158

Lawson AC (ed) (1908) Report of the State Earthquake Investigation Commission: Washington, DC, Carnegie Institute of Washington, 2 vol, vol 1, 451 p

Mundell & Associates, Inc. (2015) Conductivity mapping to locate sand and gravel resources. Access date: 25 April 2015. http://0101.nccdn.net/1_5/207/368/181/Conductivity-Mapping-to-Locate-Sand-and-Gravel-Resources.pdf

Ozcep F, Yıldırım E, Tezel O, Asci M, Karabulut S (2010) Correlation between electrical resistivity and soil-water content based artificial intelligent techniques. Int J Phys Sci 5(1):47–56. http://www.academicjournals.org/journal/IJPS/article-abstract/F30B4EB22327

Pozdnyakova L (1999) Electrical properties of soils. PhD thesis, Laramie, WY, University of Wyoming, 138 p

Son Y, Oh M, Lee S (2010) Estimation of soil weathering degree using electrical resistivity. Environ Earth Sci 59:1319–1326

Zent AP, Hecht MH, Cobos DR, Campbell GS, Campbell CS, Cardell G, Foote MC, Wood SE, Mehta M (2009) Thermal and electrical conductivity probe (TECP) for Phoenix. J Geophys Res Planets 114(E3):E00A27

Chapter 16
Numerical Clustering of Soil Series Using Profile Morphological Attributes for Potato

Michaël A. Leblanc, Gilles Gagné and Léon E. Parent

Abstract Potato fertilization response models have been developed for 46 soil series in the province of Québec, Canada. This study aimed to create a set of representative soil classes based on morphological data so that they reflect suitable soil properties for growing potato. Data of modal soil profiles of soil series contain morphological attributes from master horizons (including bedrock) with diagnoses indicating the absence (0), weak expression (0.5) or presence (1) of specific properties (pedogenetic features), and particle-size distribution. A distance matrix was calculated to represent the dissimilarity between the soil profiles. Using multidimensional scaling technique, soil profiles distributed in a feature space were clustered using the fuzzy k-means with extragrades algorithm to allow expressing soil groups as continuous variables, hence facilitating modeling. The dissimilarity measure between soil profiles computed using soil descriptions (e.g., color, pH, and C content) at experimental sites showed that genetic horizon indices can be used as a basis to compare and allocate soil profiles to existing classes. In conclusion, numerical clustering provided a quantitative basis to integrate soil profile descriptions into crop response models.

Keywords Numerical soil classification · Soil series · Soil profile · Morphology · Continuous classification · Pedometrics

M.A. Leblanc · L.E. Parent (✉)
Department of Soils and Agri-Food Engineering, Université Laval, Paul-Comtois Building, Québec, QC G1V 0A6, Canada
e-mail: Leon-Etienne.Parent@fsaa.ulaval.ca

G. Gagné
Centre de Référence en Agriculture et Agroalimentaire du Québec (CRAAQ), Delta 1 Building, Québec, QC G1V 2M2, Canada

A.E. Hartemink and B. Minasny (eds.), *Digital Soil Morphometrics*,
Progress in Soil Science, DOI 10.1007/978-3-319-28295-4_16

16.1 Introduction

Soil classification systems have been traditionally oriented toward agricultural applications. Crop productivity is influenced by the soil's capacity to supply sufficient amounts of water, nitrogen, and mineral nutrients in interaction with climatic conditions and soil management. However, the morphological soil properties used as taxonomic criteria at the soil series level such as texture, carbonates, and lithic contact and the properties that influence the agronomic soil potential cannot be generalized consistently at the highest hierarchical levels of the Canadian system of soil classification such as orders and great groups (Soil Classification Working Group 1998). An alternative numerical procedure must be developed to synthesize a large number of input variables provided by soil surveys for use in agronomic models.

Morphometrics techniques allow deriving depth functions from quantified soil profile attributes to support numerical soil classification (Hartemink and Minasny 2014). Usually, a soil series is represented by one or more modal soil profiles, described by a sequence of horizons with different morphological characteristics. From deriving depth functions, soil profiles can be clustered into continuous soil classes using the degree of similarity between soil profiles and the principles of fuzzy classification (Carré and Jacobson 2009; Odgers et al. 2011). Such groups with fuzzy memberships can be integrated as continuous variables into crop response models allowing a more realistic expression of the gradual nature of soils (McBratney and De Gruijter 1992).

The aim of this work was to aggregate soil series commonly used for potato cropping in Québec, Canada, into a number of representative classes. New profile observations can be allocated to those classes to run a potato fertilizer response models.

16.2 Materials and Methods

16.2.1 Legacy Database of Profile Descriptions of Soil Series

Soil surveys conducted in Québec between 1943 and 2005 described 649 series of mineral soils as shown in the updated file of soil names (Lamontagne and Nolin 1997). The genetic horizon code and the clay (0–0.002 mm), silt (0.002–0.05 mm), and sand (0.05–2 mm) contents determined by sedimentation techniques are some of the properties recorded in the 1657 modal profiles from 547 soil series, representing 92 % of the mapped area. Horizon designations were harmonized to the current Canadian system (Soil Classification Working Group 1998) by expert knowledge and the clay and silt measurements separated at 0.005 mm in soil

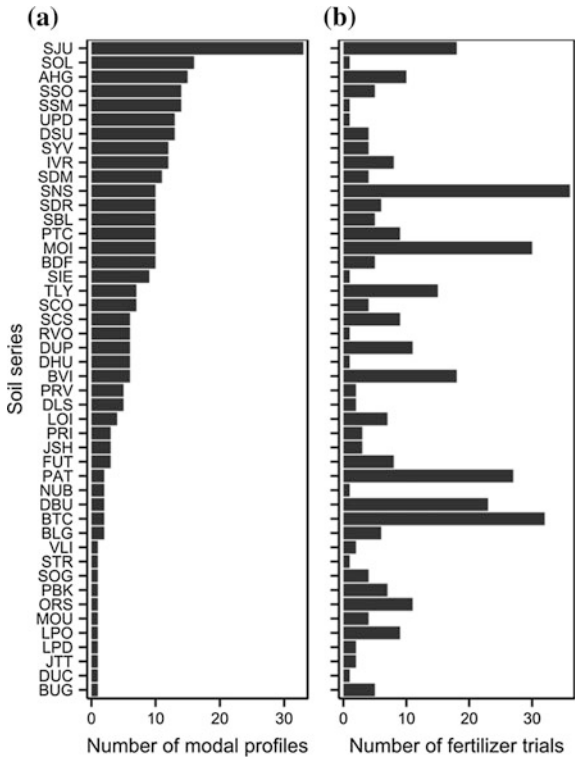

Fig. 16.1 Number of modal soil profiles (**a**) and fertilizer trial sites (**b**) by soil series. Soil series code refers to the updated file of soil names of Québec (Lamontagne and Nolin 1997). For brevity, soil series variants were amalgamated into the corresponding soil series

surveys before 1957 were transformed into the current system using regression equations (unpublished).

The potato fertilizer trials (N, P, and K treatments) archived in Québec (1958–2014) have been conducted on 46 soil series associated with 310 modal profiles (Fig. 16.1). The profiles located in the Saguenay-Lac Saint-Jean and the St. Lawrence Lowlands were mainly developed on fluviatile, lacustrine, and marine deposits ranging from very rapidly to poorly drained and classified as Podzols, Brunisols (Cambisols), and Gleysols.

16.2.2 Transformation of Morphological Data

Genetic Horizons

Pedometric approach that compares soil taxa quantitatively using the key attributes of modal soil profiles as central entities has been applied to derive metric distances between genetic soil horizons (Láng et al. 2013; Mazaheri et al. 1995; Minasny and McBratney 2007). The diagnostic horizons were transformed into eight indices of 0,

Table 16.1 Indexing value of selected genetic horizons of the Canadian system of soil classification

Horizon	Morphologic features	Suffix	Index
Eluviated (Elu)	Horizon characterized by the eluviation of clay, Fe, Al, or organic matter alone or in combination.	e	1
		ej	0.5
		–	0
Illuviated (Ili)	Illuvial horizon enriched with silicate clay.	t	1
		tj	0.5
		–	0
Podzolized (Pod)	Horizon enriched with amorphous material, principally Al, and Fe combined with organic matter.	f	1
		fj	0.5
		–	0
Podzolized (Hom)	Horizon (B) enriched with organic matter.	h	1
		–	0
Altered (Alt)	Horizon slightly altered by hydrolysis, oxidation, or solution, or all three.	m	1
		–	0
Gleyed (Gle)	Horizon characterized by gray colors, or prominent mottling, or both, indicating permanent or periodic intense reduction.	g	1
		gj	0.5
		–	0
Carbonated (Car)	Denotes the presence of carbonate as indicated by HCl-effervescence reaction.	k	1
		kj	0.5
		–	0
Hardened (Har)	Strongly cemented or high-density pedogenic horizon.	c, x	1
		cj, cc, xj	0.5
		–	0

0.5, and 1 indicating, respectively, the absence, weak expression, and the presence of specific properties as pedogenetic features (Table 16.1). For example, we characterized a podzolized, weakly gleyed, and cemented soil horizon showing the secondary distinction of *fcgj* in the Canadian system by a vector [0, 0, 1, 0, 0, 0.5, 0, 1] in the order reported in Table 16.1.

Soil Textural Components

Sand, silt, and clay contents are compositional data (proportions constrained between zero and 100 % or 1000 g kg^{-1}). Their conventional statistical analysis can create distortions caused by redundancy, scale dependency, and inherent non-normal distribution (Filzmoser et al. 2009). The log ratio transformations avoid such problems (Aitchison 1986; Egozcue et al. 2003; Filzmoser and Hron 2011). Soil textural components were thus transformed into isometric log ratios (ilr) according to a sequential binary partition (SBP) (Table 16.2) as follows (Egozcue and Pawlowsky-Glahn 2006):

$$\mathrm{ilr}_i = \sqrt{\frac{r_i s_i}{r_i + s_i}} \ln \frac{g(x^+)}{g(x^-)}, \tag{16.1}$$

Table 16.2 Sequential binary partitioning of soil textural components

ilr	Sand	Silt	Clay
ilr_1	+1	−1	−1
ilr_2	0	+1	−1

where ilr_i is the ith balance of a D-part composition, $i \in [1, D-1]$, r_i, and s_i are the numbers of components in the + (numerator) and − (denominator) groups, respectively, and $g(x^+)$ and $g(x^-)$ are the geometric means across components in the + and − groups, respectively. The SBP consists of dividing sequentially the composition into two groups of parts which are indicated by +1 and −1 until all groups are made of a single part. Label 0 indicates that this part is not involved in the partition at this order (Egozcue and Pawlowsky-Glahn 2006). To support the interpretation of principal coordinate analysis, textural components were transformed into centered log ratio (clr) (Aitchison 1986) making their interpretation possible in terms of the original compositional parts in the principal coordinate analysis (Filzmoser and Hron 2011):

$$\mathrm{clr}_i = \ln \frac{x_i}{g(x)}, \tag{16.2}$$

where x_i is the ith part of the composition and $g(x)$ is the geometric mean. As proposed by Martín-Fernández et al. (2011), the zeroes can be replaced by a fraction of the detection limit (e.g., $0.65 \cdot 10\ \mathrm{g\ kg^{-1}} = 6.5\ \mathrm{g\ kg^{-1}}$) to compute log ratios while minimizing the impact of zeroes on the covariance structure of the compositional dataset.

Data Scaling

A classification should be performed using variables of equal weights (Sneath and Sokal 1973). To assign a common footing to the pedogenetic variables ranging between 0 and 1, the ilr-transformed textural components were centered by subtracting the mean and scaling to two times the standard deviation (Gelman 2008). We preferred this option instead of the standardization of all variables, i.e., mean centered and scaled to their standard deviation, because variables showing low values of standard deviations (e.g., carbonated index) were upscaled, and that of minimum–maximum transformation because textural variables scaled in the range [0–1] were de-emphasized compared to genetic horizon variables.

Fertilizer Trials Experimental Sites

In addition to the soil series, soil profiles from 49 experimental sites were characterized by moist colors of matrix and mottles using the Munsell soil color chart, pH in $CaCl_2$ (Hendershot et al. 1993), and C content (dry combustion in the

Leco-CNS instrument). Munsell color code (hue, value, and chroma) was projected into the L-a-b color space (Viscarra Rossel et al. 2006). Contrast of mottles was defined as a Euclidean distance between the mottle and matrix L-a-b coordinates. In the absence of mottles, the distance was reported as zero (Malone et al. 2014).

16.2.3 Dissimilarity Measure Between Soil Profiles

The soil horizon attributes of each soil profile were disaggregated (segmented) to a common depth to allow pairwise comparisons of soil profiles by a 5-cm slice (Beaudette et al. 2013). The dissimilarity measure (d_{xy}) between soil profiles x and y, where d_{xy} is the element of the distance matrix D of size $p \times p$ and p is the number of soil profiles, was calculated as the mean Euclidean distance between the ith slice of each soil profile, with $i \in [1, N]$, as follows:

$$d_{xy} = \frac{1}{N}\sum_{i=1}^{N}\sqrt{\sum_{j=1}^{M}(v_{xj} - v_{yj})^2}, \tag{16.3}$$

where v_j is the jth soil morphological property of the slice, with $j \in [1, M]$. Non-soil material (e.g., bedrock) that has no soil morphological attribute was defined as the maximum between-slice dissimilarity to reflect the fact that soil and non-soil materials are very different (Beaudette et al. 2013). A distance of zero was imputed between corresponding slices of non-soil material.

Usually, soil series are conceptualized using soil properties of the sub-surface layers. The legacy dataset includes modal soil profile descriptions from cultivated and undisturbed areas. To avoid the influence of land use on this classification, dissimilarity measures were computed for soil layers at depths ranging from 30 to 100 cm. Disregarding the first 30 cm is justified by the fact that more detailed information of surface layer (e.g., texture, Mehlich-III extracts) can be integrated into the crop response models.

16.2.4 Continuous Classification of Soil Profiles

The distance matrix of the soil profiles was projected into a Cartesian framework using the multidimensional scaling technique. Briefly, after transforming the eigendecomposition of the dissimilarity matrix D by Gower's centering, we computed principal coordinates by scaling the eigenvectors to lengths equal to the square roots of their eigenvalues (Legendre and Legendre 2012).

The fuzzy k-means with extragrades (FKMe) clustering algorithm (McBratney and De Gruijter 1992) was performed on the principal coordinates to partition the soil profile distribution into clusters (defined by their centroids) that shared similar morphological descriptions. The FKMe is an unsupervised clustering procedure that accommodates, in an extragrade cluster, the soil profiles with atypical properties located in the periphery of the soil distribution to decrease their effect on the normal (intragrade) clusters. Briefly, the FKMe algorithm finds the position of cluster centroids in the space of coordinates by minimizing its objective function using the distance between individuals and centroids. The algorithm considers three parameters: the number of classes (k) and the fuzziness exponent (ϕ) which were determined from relationships with the fuzziness performance index, and the derivative of the fuzzy k-mean objective function with respect to ϕ (Odeh et al. 1992), and the parameter that defines the contribution of the extragrade class (α) which was set by iteration to allocate 5 % of the total population in the extragrade cluster (95 % in the intragrade clusters) creating a confidence region about the intragrade clusters.

After completing the classification, the closest modal profiles of each cluster centroid were defined as exemplars (highest membership to a class). Using a real profile rather than a centroid, a new profile can be classified without principal coordinates calculation. The fuzzy memberships of soil profiles were computed by the dissimilarity measure to the exemplars using allocation equations (McBratney 1994).

16.2.5 Statistics of the Aggregated Depth Functions

According to the principle of working on coordinates (ilr) (Mateu-Figueras et al. 2011) for each 1-cm slice, the average and standard deviation were calculated for the ilr-transformed textural components and back-transformed to the original domain (i.e., 0 to 100 %). Genetic horizon indices (index value of 0, 0.5, or 1) and their counterparts (i.e., 1-index) were also transformed individually into isometric log ratio before computing descriptive statistics. As explained above, the zeroes were replaced by a fraction of the detection limit of 1 % (i.e., $0.65 \cdot 0.01 = 0.0065$).

The numerical clustering process summarized in Fig. 16.2 was conducted using the FuzME software (Minasny and McBratney 2002) for the FKMe classification and the R statistical environment (R Development Core Team 2011) using packages "aqp" (Beaudette and Roudier 2015) for soil profile data manipulation, "compositions" (Van den Boogaart et al. 2014) for compositional data transformation, "ggplot2" (Wickham and Chang 2015) for data visualization, and "plyr" (Wickham 2015) for summary statistics.

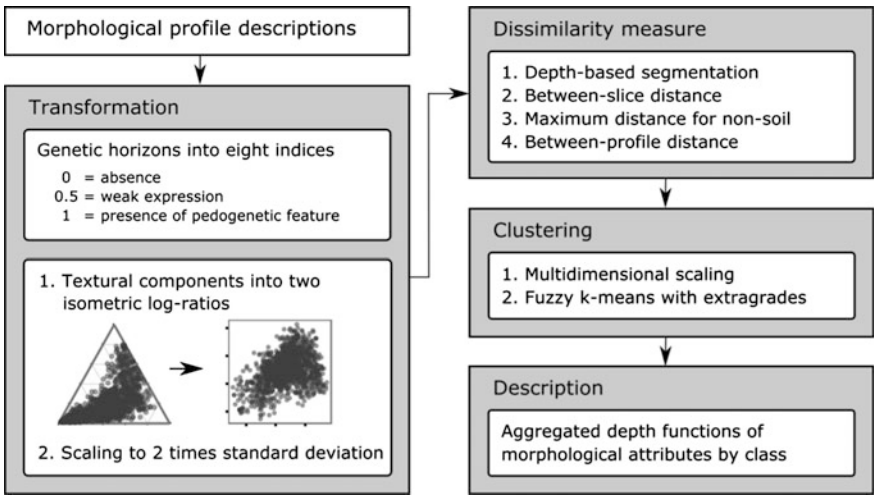

Fig. 16.2 Summary of the numerical clustering process of soil profiles

16.3 Results and Discussion

16.3.1 Clustering of Modal Soil Profiles

FKMe clustering was carried out on modal soil profiles of soil series where fertilizer trials have been conducted (Fig. 16.3). The algorithm was set with $k = 3$ and $\phi = 1.6$ (Odeh et al. 1992) and with a $\alpha = 0.6$ leaving 4.9 % of the modal profiles as extragrades. A small k value restricted the number of variables in the potato fertilization models.

The soil profile distribution along the first two principal coordinates that explained 51 % of the variance was mainly correlated with the textural components and the pedogenetic variables Pod and Gle (Fig. 16.3). The elliptical areas of classes A, B, and C were thus consistent with the textural gradient and the gleying and podzolization processes. Those morphological characteristics were aggregated into depth functions by soil classes (Fig. 16.4). The depth functions of the podzolized (Pod) horizons followed a peak function, while the gleyed horizon followed a wetting front function (Minasny et al. 2016).

Class A is dominated by sandy soil profiles with podzolized (Pod) horizons down to 60 cm. Those soils are well to very well-drained and classified as Podzols or Brunisols. They are susceptible to nitrate leaching during intensive precipitation events, and rain-fed crops are vulnerable to water stress during dry periods.

Soil profiles of class B are composed of sandy gleyed horizons. That group also includes soil profiles with podzolized (Pod) horizons to a depth ranging from 20 to 40 cm, sometimes showing both Gle and Pod features (i.e., Bfg) or both Hom and Pod (i.e., Bhf). Soil profiles in class B are imperfectly to poorly drained and

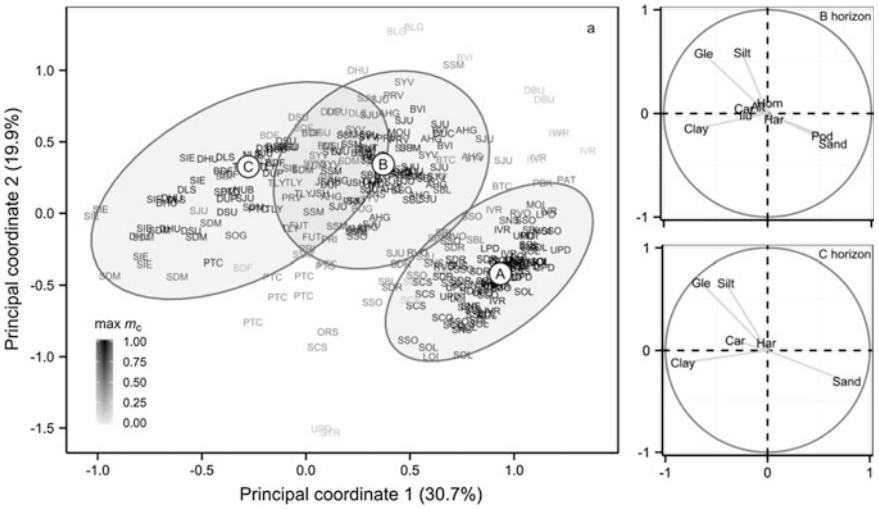

Fig. 16.3 Distribution of the maximum fuzzy membership (max m_c) to clusters A, B, and C of modal soil profiles in fertilizer trials (*a*) and correlation circles of clr-transformed textural components and pedogenetic features (see Table 16.1 for descriptions) of B and C horizons along the first two principal coordinates. Filled white circles represent exemplar positions and elliptical shaded areas cover 95 % of the theoretical distribution of clusters A, B, and C

classified as Gleysols and gleyed Podzols. Potato crops grown on such soils are less affected by water stress compared to class A soils.

Soil profiles of class C are fine-textured ranging from loam to silty clay loam that also include shallow sandy soil overlying clay materials. Textural variability is slightly higher in class C compared to classes A and B. Although some profiles show altered or weakly podzolized (Pod) horizons, gleying is the dominant pedogenic feature of class C soils. Some profiles also have carbonates in deeper horizons. Soil profiles of class C are moderately well to poorly drained and classified as Gleysols, gleyed Podzols, or Brunisols. In general, water storage and fertility are higher in soils of class C compared to those of classes A and B, but crops could be affected by prolonged wet periods.

Partitioning the data into three soil classes, the soil profiles characterized by low-frequency morphological features (e.g., Har and Alt) that are weakly correlated for the first two principal coordinates (Fig. 16.3) were not discriminated. Soil profiles with hardened horizons (strongly cemented or high-density pedogenetic) were allocated to classes A and B while profiles with altered horizons were classified in classes A and C. However, low-frequency features were kept rather than excluded by cluster analysis in order to classify new specimens correctly. Hence, soil profiles far from the cluster centers could be located in the periphery of the soil distribution (extragrades). On the other hand, with additional fertilizer trials increasing the degrees of freedom to run the crop response models, the classification could be refined with a higher number of soil classes to account for a higher degree

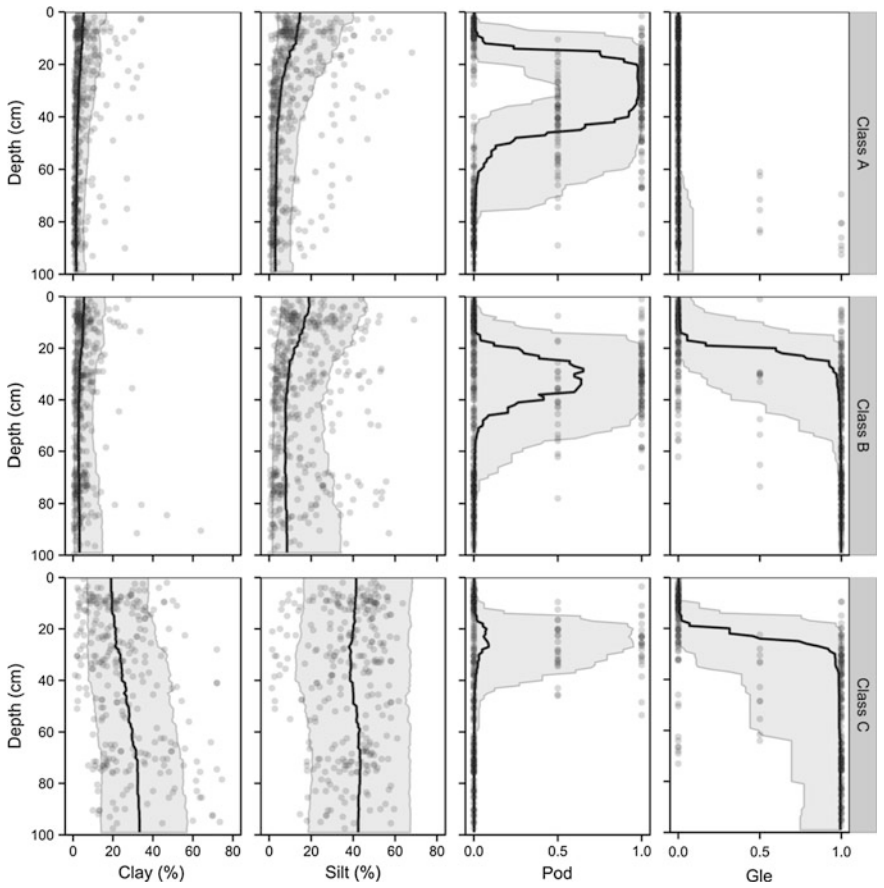

Fig. 16.4 Aggregated depth functions of morphological variables (see Table 16.1 for descriptions) by soil classes (A, B, and C) of trial-associated modal profiles. Black lines represent the mean and shaded area coverage ± standard deviation computed for each 1-cm layer. Dots represent observed values at midpoint of genetic horizons

of soil heterogeneity. Uncertainty analysis of the models can also be used to identify soil classes requiring more field trials.

16.3.2 Cluster Memberships of Individual Soil Series

Most fertilizer trial sites are often associated with a single soil series name without profile description. To allocate a set of fuzzy memberships to each of the soil series, the soil profile closest to the centroid of individual soil series was identified as the exemplar. In our opinion, the exemplar profile is more appropriate to represent a soil series than a combination of average depth functions of variables, because a

given combination could represent a nonexistent profile. A soil profile can be allocated to this numerical class without the need to designate the soil series.

On the other hand, the soil series concepts elaborated over a long period (1943–2005) evolved differently across soil surveys. Although a soil series represented by many soil profiles from different soil surveys is more indicative of the soil series concepts variability, their allocation to soil classes could be also performed individually. Furthermore, as discussed by Láng et al. (2013), the taxonomic distance between modal soil profiles is an important quantitative tool to correlate and harmonize soil series that arise from different soil surveys.

16.3.3 Domain Limit of the Clusters

All soil profiles (n = 1657) of soil series were classified into clusters A, B, C, and extragrade. Therefore, potato fields with soil series not associated with fertilizer trials can be supported by the crop response models. However, the prediction models are not appropriate when extrapolating to cases far from the calibration domain (Tranter et al. 2010). The domain limit of the clustering was defined by the extragrade class that delineates a confidence region about intragrade clusters (Fig. 16.5). Because soil profile distribution is not normally distributed in the

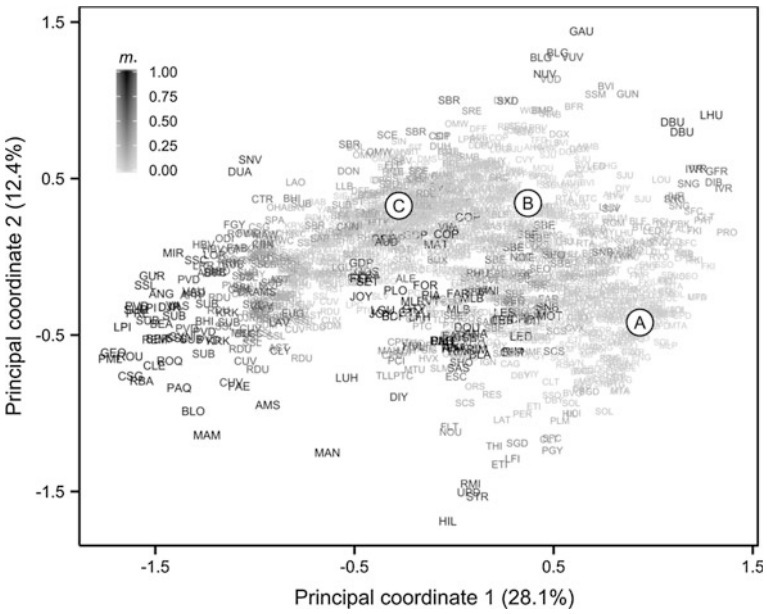

Fig. 16.5 Distribution of the fuzzy membership to the extragrade cluster ($m*$) for all modal profiles of soil series along the first two principal coordinates. Filled white circles represent exemplar positions for clusters A, B, and C

principal coordinate space, the extragrade region is more appropriate as a domain limit compared to an arbitrary distance cutoff from a centroid. Indeed, 15.4 % of the soil profiles (22.5 % of soil series) were classified as extragrades. Most of them presented unsuitable properties for potato cropping (clayed, carbonated, shallow soil profiles).

16.3.4 Comparison of Genetic Horizons Indexed with Basic Properties

Principal component analysis was conducted on the basic soil attributes of horizons (n = 160) of soil profiles from the surveyed fertilization experimental sites (Fig. 16.6). The distribution of podzolized to gleyed horizons was correlated with color coordinates and contrast of mottles, which is consistent with the field identification of genetic horizons broadly based on color, arrangement of particles (structure and consistence), and the HCl-effervescence reaction. However, their genetic horizons overlapped. Basic properties, such as colors that are sensitive to the intensity of pedological development and related to the nature of soil material (geological origin), can be more informative compared to genetic horizon designations and can explain the overlapping distributions. A correlation coefficient of

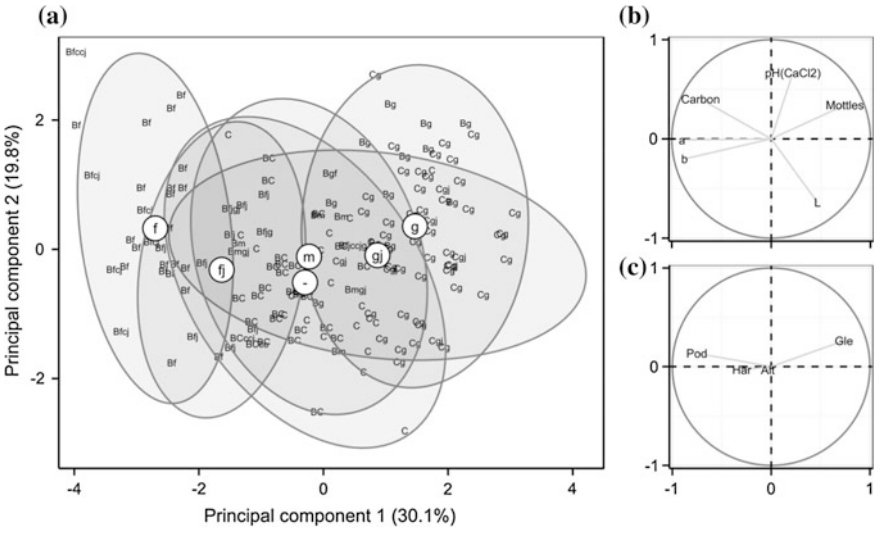

Fig. 16.6 Principal component analysis of genetic horizons of soil profiles of experimental sites using variables of **b** (**a**). Correlation circles of color and chemical variables (**b**) and pedogenetic features (**c**) (see Table 16.1 for descriptions) along the first two principal components. Filled white circles represent centroid and elliptical shaded areas cover 95 % of the theoretical distribution of genetic horizon suffixes

0.548 ($p < 0.001$) was obtained between profile distances computed either from basic properties or from genetic horizons indices. Indexing conceptual horizons is thus consistent with basic properties to compare soil profiles quantitatively.

16.4 Conclusions

Numerical clustering allowed aggregating of soil series based on the degree of similarity between modal soil profiles. Using both quantitative and qualitative information on soil horizons, the textural gradient and the two major pedogenic processes of potato soil profiles were partitioned into three continuous soil classes. With the upgrading of soil legacy databases, the grouping of soil series could be refined using more exhaustive descriptions (e.g., sand fractions, coarse fragments, and mineralogical composition). Using soil profile databases from soil surveys, this study showed that tools of pedometrics can synthesize the soil profile information into continuous indices to facilitate running site-specific crop response models.

Acknowledgements We wish to thank Alex B. McBratney and Budiman Minasny from the University of Sydney, Australia, and their team research, especially Philip A. Hughes, for their support to develop the numerical classification process of this work. This study is part of the soil quality module of the research project entitled "Implementing means to increase potato ecosystem services" (CRDPJ 385199–09) funded by Natural Sciences and Engineering Research Council of Canada (NSERC) as well as farm partners as follows: Cultures Dolbec Inc., St-Ubalde, Québec, Canada; Groupe Gosselin FG Inc., Pont Rouge, Québec, Canada; Agriparmentier Inc. and Prochamps Inc., Notre-Dame-du-Bon-Conseil, Québec, Canada; Ferme Daniel Bolduc et Fils Inc., Péribonka, Québec, Canada.

References

Aitchison J (1986) The statistical analysis of compositional data. Chapman and Hall, London

Beaudette DE, Roudier P (2015) "aqp": algorithms for quantitative pedology. R package version 1.8-6. R Found. Stat. Comput., Vienna, Austria

Beaudette DE, Roudier P, O'Geen AT (2013) Algorithms for quantitative pedology: a toolkit for soil scientists. Comput Geosci 52:258–268

Carré F, Jacobson M (2009) Numerical classification of soil profile data using distance metrics. Geoderma 148:336–345

Egozcue JJ, Pawlowsky-Glahn V (2006) Simplicial geometry for compositional data. Geol Soc London Spec Publ 264:145–159

Egozcue JJ, Pawlowsky-Glahn V, Mateu-Figueras G, Barceló-Vidal C (2003) Isometric logratio transformations for compositional data analysis. Math Geol 35:279–300

Filzmoser P, Hron K (2011) Robust statistical analysis. In: Pawlowsky-Glahn V, Buccianti A (eds) Compositional data analysis: theory and applications. John Wiley and Sons, New York, pp 57–72

Filzmoser P, Hron K, Reimann C (2009) Univariate statistical analysis of environmental (compositional) data: problems and possibilities. Sci Total Environ 407:6100–6108

Gelman A (2008) Scaling regression inputs by dividing by two standard deviations. Stat Med 27:2865–2873

Hartemink AE, Minasny B (2014) Towards digital soil morphometrics. Geoderma 230–231: 305–317

Hendershot WH, Lalande H, Duquette M (1993) Soil reaction and exchangeable acidity. In: Carter MR (ed) Soil sampling and methods of analysis. Lewis Publication, Boca Raton, Florida, pp 141–145

Lamontagne L, Nolin MC (1997) Dossier des noms de sols du Québec. SISCan. Agriculture et Agroalimentaire Canada, Sainte-Foy, Québec, Canada

Láng V, Fuchs M, Waltner I, Michéli E (2013) Soil taxonomic distance, a tool for correlation: as exemplified by the hungarian brown forest soils and related WRB reference soil groups. Geoderma 192:269–276

Legendre P, Legendre L (2012) Numerical ecology, 3rd edn. Elsevier, Amsterdam

Malone BP, Hughes P, McBratney AB, Minasny B (2014) A model for the identification of terrons in the Lower Hunter Valley, Australia. Geoderma Reg 1:31–47

Martin-Fernandez JA, Palarea-Albaladejo J, Olea RA (2011) Dealing with zeroes. In: Pawlowsky-Glahn V, Buccianti A (eds) Compositional data analysis: theory and applications. John Wiley and Sons, New York, pp 43–58

Mateu-Figueras G, Pawlowsky-Glahn V, Egozcue JJ (2011) The principle of working on coordinates. In: Pawlowsky-Glahn V, Buccianti A (eds) Compositional data analysis: theory and applications. John Wiley and Sons, New York, pp 31–42

Mazaheri SA, Koppi AJ, McBratney AB (1995) A fuzzy allocation scheme for the Australian great soil groups classification system. Eur J Soil Sci 46:601–612

McBratney A (1994) Allocation of new individuals to continuous soil classes. Aust J Soil Res 32:623–633

McBratney AB, De Gruijter JJ (1992) A continuum approach to soil classification by modified fuzzy k-means with extragrades. J Soil Sci 43:159–175

Minasny B, McBratney AB (2002) FuzME version 3.0. Australian Centre for Precision Agriculture. The University of Sydney, Australia

Minasny B, McBratney AB (2007) Incorporating taxonomic distance into spatial prediction and digital mapping of soil classes. Geoderma 142:285–293

Minasny B, Stockmann U, Hartemink AE, McBratney AB (2016) Measuring and modelling soil depth functions. In: Hartemink AE, Minasny B (eds) Digital Soil Morphometrics, Springer

Odeh IOA, Mcbratney AB, Chittleborough DJ (1992) Soil pattern recognition with fuzzy-c means: Applications to classification and soil-landform interrelationships. Soil Sci Soc Am J 56:505–516

Odgers NP, McBratney AB, Minasny B (2011) Bottom-up digital soil mapping II. Soil series classes. Geoderma 163:30–37

R Development Core Team R (2011) R: A language and environment for statistical computing. R Foundation for Statistical Computing, Vienna, Austria

Sneath PHA, Sokal RR (1973) Numerical taxonomy: The principles and practice of numerical classification. Freeman and Company, San Francisco, W.H

Soil Classification Working Group (1998) The Canadian system of soil classification, 3rd edn. Agriculture and Agri-Food Canada. Publication 1646

Tranter G, Minasny B, McBratney AB (2010) Estimating pedotransfer function prediction limits using fuzzy k-means with extragrades. Soil Sci Soc Am J 74:1967–1975

Van den Boogaart KG, Tolosana-Delgado R, Bren M (2014) "compositions": compositional data analysis. R package version 1.40-1. R Found Stat Comput, Vienna, Austria

Viscarra Rossel RA, Minasny B, Roudier P, McBratney AB (2006) Colour space models for soil science. Geoderma 133:320–337

Wickham H (2015) "plyr": tools for splitting, applying and combining data. R package version 1.8.1. R Found Stat Comput, Vienna, Austria

Wickham H, Chang W (2015) "ggplot2": an implementation of the grammar of graphics. R package version 1.01. R Found Stat Comput, Vienna, Austria

Chapter 17
Digital Summaries of Pedon Descriptions

Stephen Roecker, Jay Skovlin, Dylan Beaudette and Skye Wills

Abstract Soil scientists have been describing and analyzing pedons for over a hundred years. In the USA, a small portion of this data has been captured in the National Soil Information System (NASIS). While NASIS serves as a data repository, its analytical capabilities are limited, and the data are underutilized. In order to facilitate the analysis of soil horizon data in NASIS, we have used R to develop R Markdown (Rmd) reports. These Rmd reports are designed to provide numerical and graphical summaries of soil horizon data used for soil survey activities, such as the development of Official Series Descriptions and soil map unit components.

Keywords Soil series · Range in characteristics · NASIS · Pattern matching

17.1 Introduction

Pedon data consist of field estimates, observations, and laboratory measurements. Unlike the soil map unit polygons and their associated attribute data (component data), pedon data represent point data from individual soil observations. In support of soil surveys during the last 100 years, the National Cooperative Soil Survey (NCSS) has collected a substantial amount of pedon data. Since the introduction of the National Soil Information System (NASIS) in 1994 (Fortner and Price 2012), approximately 400,000 field pedons and approximately 63,000 laboratory pedons have been digitized (Ferguson, 2015, personal communication). Although

S. Roecker (✉)
USDA-Natural Resource Conservation Service, Indianapolis, IN 46278, USA
e-mail: stephen.roecker@in.usda.gov

J. Skovlin
USDA-Natural Resource Conservation Service, Missoula, MT 59808, USA

D. Beaudette
USDA-Natural Resource Conservation Service, Sonora, CA 95370, USA

S. Wills
USDA-Natural Resource Conservation Service, Lincoln, NE 68508, USA

A.E. Hartemink and B. Minasny (eds.), *Digital Soil Morphometrics*,
Progress in Soil Science, DOI 10.1007/978-3-319-28295-4_17

significant, this represents only a small portion of total field pedons ever described (Fig. 17.1). For digital soil mapping and updates to soil surveys, these pedon data are an invaluable resource.

In order to store soil data compactly and efficiently, NASIS has a hierarchical data structure (Fig. 17.2). One branch of the data structure stores point data—observations of site and pedon data, with soil horizons as the basic element. Aggregated data about soil map units and their soil components are stored in another part of the structure. Each aggregated soil component is made up of

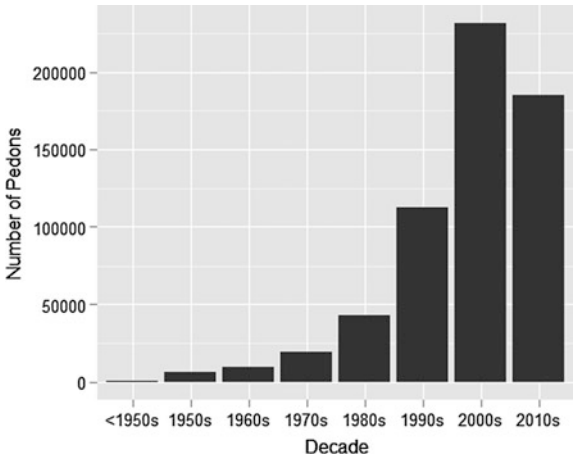

Fig. 17.1 Number of pedons sampled per decade recorded in NASIS

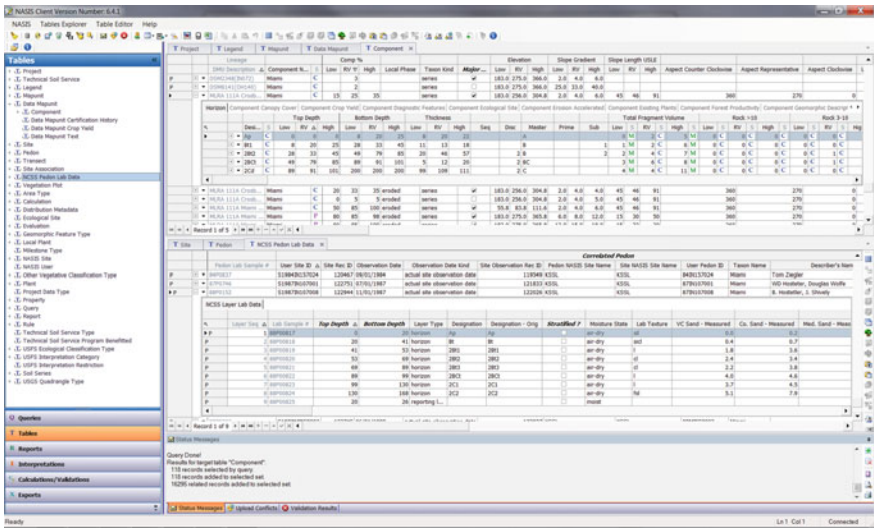

Fig. 17.2 Screenshot of the NASIS database interface, and the component and laboratory tables

generalized soil horizons based on a sample of pedon observations. Also linked to each horizon record are additional child tables. Each of these nested child tables may include several related child tables in order to capture heterogeneous soil conditions within each soil horizon. The dominant condition is specified as the representative value (RV). For numeric component data, it is also possible to specify a range with low (L) and high (H) values. This makes it possible to characterize the distribution or variation of a particular soil variable, such as clay content. Using this database structure, it is possible to capture soil horizonation, aggregate the data, and then generate spatial predictions by linking it to the soil polygons.

Soil mapping involves aggregating horizon descriptions from field and laboratory pedons into component horizon data. While there are standards that guide the process of describing individual sites and pedons in the Soil Survey Manual (Soil Survey Division Staff 1993) and the Field Book for Describing and Sampling Soils (Schoeneberger et al. 2012), there are no guidelines for the process of aggregating point/pedon observations into their component database elements. The NCSS guidelines either address developing Official Series Descriptions (OSDs) (USDA 2015), or how component ranges relate to the OSD (USDA 2013). Historically, the process of determining the ranges (L, RV, H) for various soil properties has been done with pencil and paper or spreadsheets and then selected by expert knowledge. This is a practice that continues today for a variety of reasons:

1. Familiarity with existing protocol,
2. Inconsistency among the existing data,
3. Additional workload involved in digitizing data,
4. Perceived or real software limitations,
5. Lack of training in new software and statistical methods.

Prior to the advent of NASIS, there were many early attempts at estimating low, RV, and high values for soil properties (Young et al. 1991; Jansen and Arnold 1976). These earlier attempts looked at estimates for portions of the soil profile, such as surface texture or subsoil clay content, and utilized parametric estimates (i.e., mean and confidence intervals). They also demonstrated the disconnect between the limits set for taxonomic units and those observed within map unit components. This issue is now addressed by Soil Survey Technical Note 4 (USDA 2003), which allows the range (i.e., low and high) of map unit components to extend beyond those specified by the OSD.

It is possible to manipulate and summarize pedon data directly in NASIS with reports and pivot tables, but the majority of summary functions within NASIS have been designed to analyze and evaluate component-level aggregate data. Data can be exported from NASIS to other software (Table 17.1), but these other software do not provide the same concise summary of data as do the reports designed for component data in NASIS. New reports can be added to NASIS, but complex reports are difficult to write because NASIS supports a limited implementation of the Structured Query Language (SQL) which has few functions for performing statistical analysis. Here, we advocate exporting pedon data to R (R Core

Table 17.1 Sample of tools for analyzing soil data sorted by user sophistication

Tabular analysis
1. Pencil and paper
2. Excel spreadsheets
3. PedonPC and AnalysisPC (microsoft access databases)
4. NASIS
5. R
Spatial analysis
1. SoilWeb
2. Web soil survey
3. Soil data viewer
4. SSURGO file geodatabases
5. R

Development Team 2015). R now supports R Markdown (Rmd) reports that provide access to report-writing capabilities (Xie 2014; Allaire et al. 2015) and user-contributed functions specifically designed for digital soil morphometrics, such as the aqp (Beaudette et al. 2012), soilDB (Beaudette and Skovlin 2015), and soil texture (Moeys 2015) packages.

17.2 Methods

To generate Markdown documents, RStudio was used. RStudio is an integrated development environment (IDE) for R and provides a minimalist graphical user interface (GUI) that organizes the R environment into four task-oriented windows. The initial start-up process of using RStudio and R to run the reports requires the user to install several R packages and their dependencies and setup an ODBC connection to NASIS. These steps are documented online at the NRCS Soils job-aid page, and readers are pointed to these reference documents for full details. R is an extendable environment and is in constant development, so installing additional packages is a common practice as packages are updated or new packages become available.

In order to access NASIS data for use in R, a user must first load a selected set of field or laboratory pedons in NASIS. A selected set is a view or virtual table that is created via a query, and serves as a working subset of a user's local NASIS database. NASIS has numerous queries to accomplish this. Once the data is loaded in NASIS, it can be imported into R via an ODBC connection using the fetchNASIS() function in the soilDB package. The user only needs to modify the report script by entering the name of the text file (e.g., "Miami") containing the GHL rules that correspond to the pedons loaded in the selected set. The report script is then run, and an HTML document is generated by pressing the Knit button in

RStudio. The necessary analysis steps are programmed into the report script, and the output is formatted to HTML using Rmd.

To develop a list of GHL, the user must specify which horizons are similar enough to be aggregated (Fig. 17.3). This is accomplished by mapping the existing horizon designations for each horizon and matching them to a generalized (i.e., simplified) horizonation sequence for each soil series or component. The assumption is made that the existing horizon designations accurately reflect the soil morphology and the corresponding soil properties of the horizons. For established soil series, the Official Series Description (OSD) can be used as a starting point for determining the appropriate GHL to assign to the horizons for the soil in question. The OSD provides a sample of likely horizons within either the typical pedon described or the range in characteristics (RIC) sections. For example, multiple Bt horizons might be aggregated or grouped together if it is determined that they are similar in clay content and other characteristics and that such an aggregation is not going to affect the use or interpretation of that soil. Also, Bw and Btk horizons might be aggregated if the development of the Btk horizons is incipient and does not meet the definition of an argillic or calcic diagnostic horizon. Another approach is to examine the frequency with which each horizon occurs (Fig. 17.4). Horizons that occur frequently are likely to be the most representative.

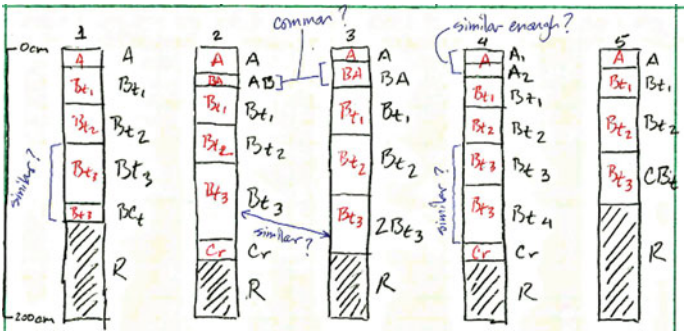

Fig. 17.3 Hand drawn illustration of the decision making (e.g., question asking) process soil scientists go through when determining the best selection of GHL for several similar soil descriptions

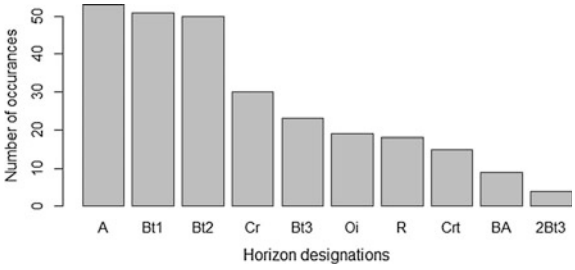

Fig. 17.4 Example of the original horizon designations sorted by frequency of occurrence for the Miami soil series

Once appropriate GHL have been determined for the collection of pedons, pattern matching is used to assign the new GHL to each horizon. The process uses functions designed to parse the text from each horizon designation and match it to the new GHL. The function searches for any combination of characters before or after the specified pattern. Patterns that do not match any of the GHL are labeled "not used." Special meta-characters serve as anchors or anti-wildcards for the beginning (i.e., caret "^") and end (i.e., dollar sign "$") of the given pattern. For example, the GHL pattern "Bt" will match any permutation of Bt, such as 2Bt or Bt1. To exclude 2Bt horizons, a more specific pattern of "^Bt" would be necessary. Conversely, to exclude Bt1 horizons, a pattern of "Bt$" would be used. If a user wishes to match special character like the caret "^" symbol, which is also used for human-transported material, it is necessary to append it with two backslashes like so, "\\^." As the GHL rules are developed, they are stored in a text file and later referenced by the Rmd report. If the user is satisfied with the resulting GHL designations, they can upload it to the comp layer ID field in the horizon table in NASIS where it is stored for future use.

Example of the GHL rules for the aqp loafercreek sample data set:

- **A**: ^A$|Ad|Ap
- **Bt1**: Bt1$
- **Bt2**: ^Bt2$
- **Bt3**: ^Bt3|^Bt4|CBt$|BCt$|2Bt|2CB$|^C$
- **Cr**: Cr
- **R**: R

Embedded in the reports are numerical and graphical summarizes of the data elements typically collected and used to differentiate dissimilar soils. Numerical variables are summarized by percentiles (i.e., quantiles), instead of the mean and confidence intervals, because they provide nonparametric estimates of a distribution and are less influenced by skewness which is common for most soil properties. Also percentiles provide a neat and compact summary. The percentiles used can be adjusted by the user, but the default is set to the five number summary (i.e., 0, 25, 50 % or median, 75, and 100 %) (Tables 17.3 and 17.4). Additionally, the percentiles are appended with the number of observations (n) (e.g., (0, 25, 50 % or median, 75, and 100 %)(n)), to inform the user of the sample size. The standard graphics used are box plots which provide a similar summary and interpretation (outliers, ~5, ~25, 50 % or median, ~75, ~95 %, outliers) of the data (Fig. 17.5). To summarize categorical variables, frequency tables (i.e., contingency tables) are used which cross-tabulate the number of occurrences of matching pairs (Tables 17.5 and 17.6).

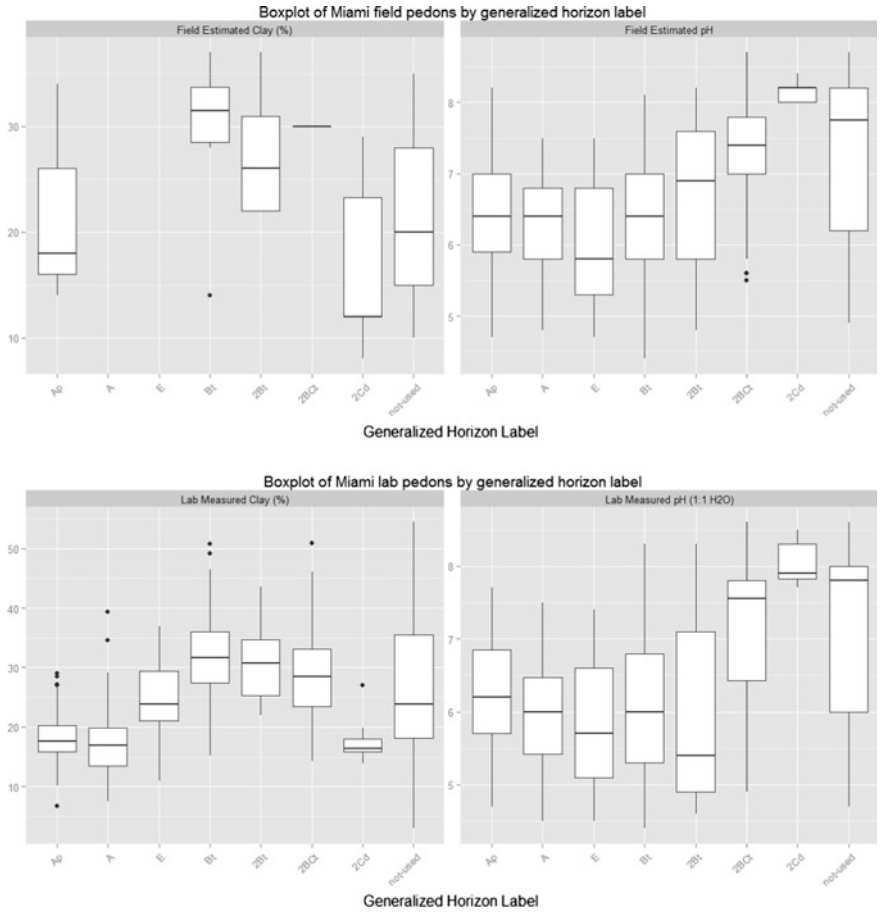

Fig. 17.5 Box plots of field (*top*) and laboratory (*bottom*) measurements for clay (%) and pH

17.3 Results and Discussion

The full field and laboratory reports are not shown here due to space limitations. The list below summarizes their content followed by sample excerpts and a discussion of the field and laboratory report content.

- Field pedon report content:
  - General map of georeferenced pedon locations overlaid on county boundary outlines;
  - Table of identifying information: pedon id, soil series, etc.,
  - Soil profile plots (Fig. 17.6),
  - Surface rock fragments,

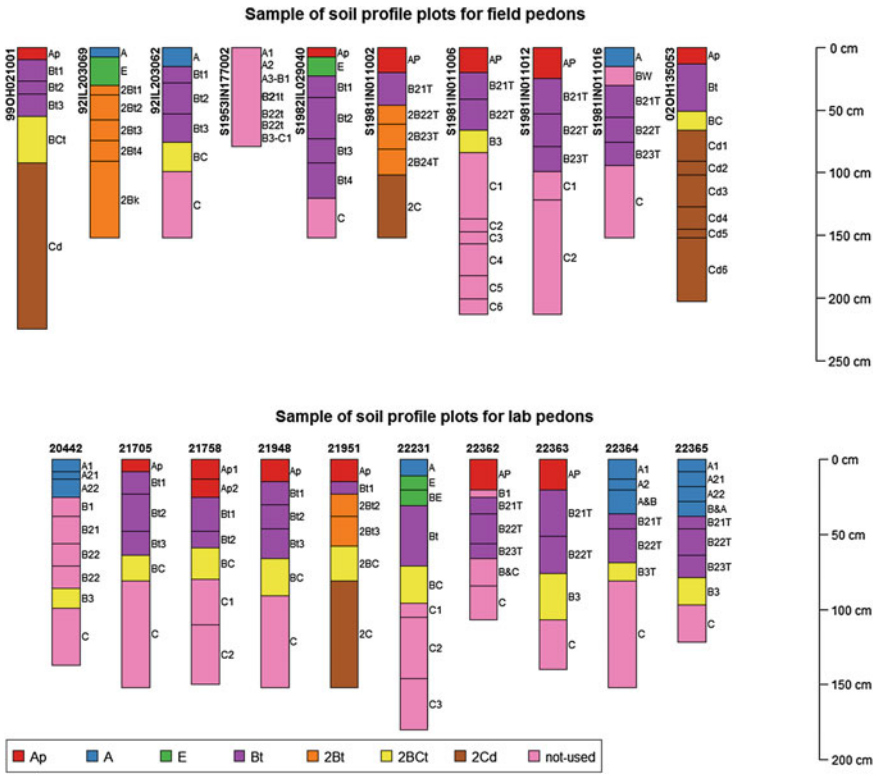

Fig. 17.6 Example of soil profile plots of the field (*top*) and laboratory (*bottom*) pedons for the Miami soil series. Horizons are colored according to their GHL

  - Depths and thickness of diagnostic horizons,
  - Comparison of GHL versus original horizon designations (Table 17.2),
  - Depth and thickness distribution of GHL,
  - Numeric variables: clay content, rock fragments, pH, etc., (Table 17.3)
  - Soil texture and texture class modifier summarized by GHL (Table 17.5),
  - Soil color hue summarized by GHL,
  - Elevation, slope gradient, and slope aspect,
  - Parent material versus landform,
  - Slope shape (down slope vs. across slope shape),
  - Drainage class versus hillslope position.

- Laboratory pedon report content:

  - General map of georeferenced laboratory pedon locations overlaid on county boundary outlines,
  - Table of identifying information: pedon id, soil series, etc.,
  - Soil profile plots (Fig. 17.6),

Table 17.2 Number of the GHL versus the original horizon designations for the Miami series

	Ap	Bt1	BC	Bt2	AP	B21T	B22T	B3	BE	A	E	A1	Bt3	A2	B23T	2Bt2	2Bt3	2C	BT3	1Bt1
Ap	54	0	0	0	29	0	0	0	0	0	0	0	0	0	0	0	0	0	0	0
A	0	0	0	0	0	0	0	0	0	23	0	16	0	14	0	0	0	0	0	0
E	0	0	0	0	0	0	0	0	24	0	17	0	0	0	0	0	0	0	0	0
Bt	0	36	0	35	0	27	26	0	0	0	0	0	16	0	14	0	0	0	7	6
2Bt	0	0	0	0	0	0	0	0	0	0	0	0	0	0	0	8	7	0	0	0
2BCt	0	0	35	0	0	0	0	26	0	0	0	0	0	0	0	0	0	0	0	0
2Cd	0	0	0	0	0	0	0	0	0	0	0	0	0	0	0	0	0	7	0	0
Not-used	0	0	0	0	0	0	0	0	0	0	0	0	0	0	0	0	0	0	0	0

Table 17.3 Percentile summaries of field estimates of clay (%) and pH

genhz	Clay	phfield
Ap	(14, 16, 18, 26, 34)(3)	(4.7, 5.9. 6.4, 7, 8.2)(77)
A	(NA, NA, NA, NA, NA)(0)	(4.8, 5.8, 6.4, 6.8, 7.5)(54)
E	(NA, NA, NA, NA, NA)(0)	(4.7, 5.3, 5.8, 6.8, 7.5)(41)
Bt	(14, 28, 32, 34, 37)(6)	(4.4, 5.8, 6.4, 7, 8.1)(206)
2Bt	(22, 22, 26, 31, 37)(5)	(4.8, 5.8, 6.9, 7.6, 8.2)(30)
2BCt	(30, 30, 30, 30, 30)(1)	(5.5, 7, 7.4, 7.8, 8.7)(70)
2Cd	(8, 12, 12, 23, 29)(6)	(8, 8, 8.2, 8.2, 8.4)(17)
Not-used	(10, 15, 20, 28, 35)(29)	(4.9, 6.2, 7.8, 8.2, 8.7)(146)

Table 17.4 Percentile summaries of laboratory measurements of clay (%) and pH

genhz	Claytot	ph1to1h20
Ap	(7, 16, 18, 20, 29)(83)	(4.7, 5.7, 6.2, 6.9, 7.7)(83)
A	(7.5, 13.5, 17, 19.9, 39.4)(53)	(4.5, 5.4, 6, 6.5, 7.5)(54)
E	(11, 21, 24, 29, 37)(45)	(4.5, 5.1, 5.7, 6.6, 7.4)(45)
Bt	(15.2, 27.4, 31.6, 36, 50.7)(155)	(4.4, 5.3, 6, 6.8, 8.3)(155)
2Bt	(22, 25.3, 30.7, 34.7, 43.6)(13)	(4.6, 4.9, 5.4, 7.1, 8.3)(13)
2BCt	(14.3, 23.4, 28.4, 33.2, 50.9)(86)	(4.9, 6.4, 7.5, 7.8, 8.6)(86)
2Cd	(14, 16, 16, 18, 27)(10)	(7.7, 7.8, 7.9, 8.3, 8.5)(10)
Not-used	(3, 18.1, 23.8, 35.5, 54.4)(298)	(4.7, 6, 7.8, 8, 8.6)(299)

- Weighted averages for the particle size control section,
- Depths and horizon thickness for the particle size control section,
- Comparison of GHL versus original horizon designations (Table 17.2),
- Depth and horizon thickness of GHL,
- Numeric variables: particle size fractions, pH, base saturation, carbon content, etc. (Table 17.4),
- Laboratory soil texture summarized by GHL (Table 17.6).

Much of the information contained in the reports is used to summarize data for developing OSD and aggregated map unit soil components. Evaluating the graphics and tables within the reports quickly show where there are possible errors, narrow or wide ranges in values, or where data gaps exist due to insufficient data. One of the first outputs of the report that should be examined is the contingency table of the GHL versus the original horizon designations (Table 17.2). This shows the results of the pattern matching and should be examined to confirm whether the GHL assignments aggregate the soil horizons appropriately. For example, GHL that are labeled as "not used" did not match any of the given patterns and were not included in the data summaries. The user may in some cases wish to further examine these horizons and decide whether or not to refine the GHL rules to include/exclude them from the summaries.

Table 17.5 Number of GHL versus field textures

	cos	s	ls	lfs	si	fsl	l	sil	si	scl	cl	sicl	sc	sic	c	Sum
Ap	0	0	0	0	0	1	13	74	1	1	7	1	0	0	0	98
A	0	0	0	0	0	2	10	50	0	0	1	3	0	0	0	66
E	0	0	0	0	0	0	7	25	0	0	1	16	0	0	0	49
Bt	0	0	0	0	0	1	25	9	0	5	141	30	0	3	9	223
2Bt	0	0	0	0	0	0	8	0	0	0	22	6	0	0	0	36
2BCt	0	0	0	0	1	3	35	1	0	4	34	11	0	0	5	94
2Cd	0	0	0	0	0	0	27	1	0	0	1	0	0	0	0	29
Not-used	1	1	1	1	6	11	172	24	0	2	40	35	1	4	32	331
Sum	1	1	1	1	7	18	297	184	1	12	247	102	1	7	46	926

The values represent the frequency of occurrence (counts) for combinations of GHL and texture

Table 17.6 Number of GHL versus laboratory textures

	cos	si	fsl	l	sil	si	scl	cl	sicl	sc	sic	c	Sum
Ap	0	1	1	13	63	0	1	3	1	0	0	0	83
A	0	0	2	5	42	0	0	2	2	0	0	0	53
E	0	0	0	6	24	0	0	7	8	0	0	0	45
Bt	0	0	1	24	6	0	7	85	14	0	2	16	155
2Bt	0	0	0	4	1	0	0	5	2	0	0	1	13
2BCt	0	0	3	30	0	0	4	36	5	0	1	7	86
2Cd	0	0	1	8	0	0	0	1	0	0	0	0	10
Not-used	1	2	14	147	13	1	2	60	15	1	6	37	299
Sum	1	3	22	237	149	1	14	199	47	1	9	61	744

The values represent the frequency of occurrence (counts) for combinations of GHL and texture

As an example, the following tables and figures show excerpts from all the field and laboratory data labeled as the Miami soil series within NASIS (Tables 17.3, 17.4, 17.5, and 17.6) (Figs. 17.2, 17.4, 17.5, and 17.6). The example shows that the field estimates of clay content are missing for A horizons. Given the age of the data set, which ranges from 1951 to 2014, this is not surprising, as it has not always beencommon practiceto record field estimates for clay content. The laboratory data by comparison have numerous measurements of clay content. By examining the box plots, we can see a clay increase in the Bt and 2Bt horizons and a decrease in the 2Cd horizon. The box plots for pH show a wide interquartile range and a slight decrease in the median pH with depth. The subsoil (i.e., 2BCt and 2Cd) shows a much narrow interquartile range and higher median pH. Examining the contingency tables of GHL versus texture, we can see a greater frequency of silty textures in the A and E horizons (Table 17.5 and 17.6). The Bt horizon has a higher frequency of clay loam textures. If silty textures are indicative of the loess cap associated with the Miami soil series, numerous Bt horizons should be relabeled as 2Bt horizons. The report's summaries allow soil scientists to examine their data quickly particularly when the data are viewed in aggregate.

17.4 Conclusion

Here, we have presented an effort to efficiently analyze the large volume of soil horizon data present in the NASIS database. We have developed R Markdown reports that provide univariate summarizes of the data elements typically used to develop OSD and soil map unit components. Using the relational structure of the NASIS database combined with the extensible data handling and statistical analysis capabilities of R, it is possible to generate powerful graphical and tabular summaries for collections of pedon data bundled into one report. Summarizing pedon data by horizon is a critical and time-consuming step in the soil survey workflow. Because we can typically only investigate soil variability by examining several soil profiles and comparing multiple descriptions, viewing the data in aggregate allows us to approximate the representative values and ranges for soil horizons (i.e., polypedons), which are the building blocks of soil map unit components.

Acknowledgements The methodology presented here has benefited from the input from numerous individuals. Those that stand out include Alena Stephens and John Hammerly who assisted in testing different iterations of the reports, and Henry Ferguson, Paul Finnell, Carrie-Ann Houdeshell, and Samuel Indorante who provided valuable feedback.

References

Allaire JJ, Cheng J, Xie Y, McPherson J, Chang W, Allen J, Wickham H, Hyndman R (2015) rmarkdown: dynamic documents for R. R package version 0.6.1. http://CRAN.R-project.org/package=rmarkdown

Beaudette DE, Roudier P, O'Geen AT (2012) Algorithms for quantitative pedology: a toolkit for soil scientists. Comput Geosci 52:258–268

Beaudette DE, Skovlin JM (2015) soilDB: soil database interface. R package version 1.5–2. http://CRAN.R-project.org/package=soilDB

Fortner JR, Price AB (2012) United States soil survey databases. In: Huang PM, Li Y, Sumner ME (eds) Handbook of soil sciences: resource management and environmental impacts 2nd edn. CRC Press, pp 1–12

Jansen IJ, Arnold RW (1976) Defining ranges of soil characteristics. Soil Sci Soc Am J 40:89–92

Moeys J (2015) soiltexture: functions for soil texture plot, classification and transformation. R package version 1.3.3. http://CRAN.R-project.org/package=soiltexture

R Development Core Team (2015) R: a language and environment for statistical computing. R foundation for statistical computing. Vienna, Austria. ISBN3-900051-07-0

Schoeneberger PJ, Wysocki DA, Benham EC, Soil Survey Staff (2012) Field book for describing and sampling soils, Version 3.0. Natural resources conservation service, National Soil Survey Center, Lincoln, NE

Soil Survey Division Staff (1993) Soil survey manual. Soil conservation service. U.S. Department of Agriculture Handbook 18

U.S. Department of Agriculture (USDA) (2003) Natural resources conservation service. Technical note 4, populating map unit data: taxonomic classes and map unit componnents. http://www.nrcs.usda.gov/wps/portal/nrcs/main/soils/ref/. Feb 2013

U.S. Department of Agriculture (USDA) (2015) Natural resources conservation service. National soil survey handbook, title 430-VI. Available online. Accessed 24 June 2015

Xie Y (2014) knitr: a comprehensive tool for reproducible research in R. In Stodden V, Leisch F, Peng RG (eds) Implementing reproducible computational research. Chapman and Hall/CRC. ISBN 978-1466561595

Young FJ, Maatta JM, Hammer RD (1991) Confidence intervals for soil properties within map units. In: Mausbach MJ, Wilding LP (eds) Spatial variabilities of soils and landforms. SSSA Special Publication Number 28, Soil Science Society of America, pp 213–229

Chapter 18
Probabilistic Representation of Genetic Soil Horizons

D.E. Beaudette, P. Roudier and J. Skovlin

Abstract Published soil survey reports typically describe soil series concepts in the form of aggregated information: ranges in soil properties, interpretations, and limitations that are derived from a collection of field-described soil profiles. While aggregated soil properties are readily estimated via standard statistical functions (mean, median, etc.), an aggregated representation of horizonation (e.g., genetic or functional horizon designation and depth) is typically difficult to construct. Variation in horizon designation use among soil scientists and different soil description systems, changes in horizon designation standards over time, variable depths at which horizons occur, and the uncertainties associated with these are all factors that complicate the process of delivering an aggregated representation of horizonation. In this chapter, we propose alternatives to the typical "representative profile," e.g., the selection of a single soil profile to represent a collection. Two possible methods for aggregating a collection of soil profiles into synthetic profiles are presented, describing depth-wise probability functions for each horizon. Both methods rely on an expert-guided description of generalized horizon designation (e.g., a subset of horizon designation labels that convey a reasonable "morphologic story") along with associated rules (regular expression patterns) used to correlate field-described to generalized horizon designation. The first method is based on (1-cm interval) slice-wise evaluation of generalized horizon designation; the second is based on a proportional-odds logistic regression model fit to depth-slices. These methods are demonstrated using USDA-NRCS soil survey data (USA).

Keywords Soil series · Soil survey · Depth-function · Aggregated soil data · Expert knowledge · Soil morphology

D.E. Beaudette (✉)
USDA-NRCS, Sonora, CA, USA
e-mail: dylan.beaudette@ca.usda.gov

P. Roudier
Landcare Research, Lincoln, New Zealand

J. Skovlin
USDA-NRCS, Missoula, MT, USA

A.E. Hartemink and B. Minasny (eds.), *Digital Soil Morphometrics*,
Progress in Soil Science, DOI 10.1007/978-3-319-28295-4_18

18.1 Introduction

Published soil survey reports typically describe soils in terms of *aggregated* information, i.e., soil properties, interpretations, and limitations that are based on a collection of field-described soil profiles. While aggregated soil properties are readily estimated via standard statistical functions (mean, median, etc.), an aggregated representation of *horizonation* (e.g., genetic horizon designation and depth) is typically difficult to construct (Beaudette et al. 2013). Variation in horizon designation "style" among different soil scientists, changes in horizon designation standards over time, variable depths at which genetic horizons occur, and the possible lack of a specific genetic horizon are all factors that complicate the process of delivering an aggregated representation of horizonation. The process of designating horizons by soil scientists can be somewhat subjective; even a second description of the same volume of soil can lead to a slightly different set of horizon designations and depths (Holmgren 1988). In addition to human sources of variability, it is understood that most of the variation between profile descriptions is due to real differences between soils observed at different locations (Wilding et al. 1964).

This complex combination of variability in morphologic horizon designation and depths is rarely acknowledged from a numerical standpoint at the soil series or soil component level. Boundaries between horizons, expressed as horizon depths, are generally considered as "crisp" numbers, while in actuality they represent "fuzzy" numbers due to varying distinctness of the horizon boundaries and how abruptly characteristics change at horizon boundaries.

Soil profiles and their corresponding soil horizons represent a record of soil formation and encapsulate significant information about soil morphology. Although new tools and technologies may make continuous depth-measurements of soils possible, horizon designation nomenclature has historically been the common pedological language used to annotate observations of changes in soil properties with depth (Hartemink and Minasny 2014; Myers et al. 2011; Kempen et al. 2011). The use of horizon designation nomenclature has inherent interpretation and meaning and allows useful comparisons to be made among soil profiles in a collection (Soil Survey Manual 1951).

The soil survey programs of many countries have historically used the "modal pedon" or "modal soil" concept to convey a reasonable example of morphologic central tendency. Several authors have expressed concern with this approach (Jones 1959; Hudson 1990) due to the loss of information on a complex natural body that exhibits continuous gradation in space. While the "modal pedon" concept fails as a true aggregated representation of a collection, it does offer the soil survey user a concrete example (of one possible realization) that can be visited and sampled as needed.

We demonstrate two possible methods for aggregating a collection of soil profiles into "representative conceptual profiles"; describing depth-wise probability functions for each genetic horizon. Both methods rely on an expert-guided

description of generalized horizon designation (e.g., horizon designations that are deemed representative) along with associated rules (regular expression patterns) used to correlate field-described to generalized horizon designation. The first method is based on (1-cm interval) slice-wise evaluation of generalized horizon designation; the second is based on a proportional-odds logistic regression (McCullagh 1980) model fit to depth-slices. Specialized classes for soil profile collections and depth-slicing algorithms are implemented in the **aqp** package for R (Beaudette et al. 2013).

18.2 Materials and Methods

18.2.1 Soil Profile Data

A collection of (63) soil profiles from the Sierra Foothill Region of California were used to demonstrate two approaches for determining an aggregated representation of genetic horizon boundaries. This collection of soil profile data represents the work of 13 different soil scientists, and is included within the **soilDB** package for R (Beaudette and Skovlin 2015). These soils are associated with the Loafercreek soil series (fine-loamy, mixed, superactive, thermic Ultic Haploxeralfs); moderately deep soils formed in colluvium and residuum from metavolcanic rocks (greenschist) (Fig. 18.1). The climate is characterized by hot, dry summers and cool, wet winters. Mean annual air temperature is approximately 16 °C and mean annual precipitation

Fig. 18.1 Eight photographs of the Loafercreek soil series, collected in Tuolumne and Calaveras counties, CA, USA. How would you combine the wide range in morphology from these profiles into an aggregated concept?

is 760 mm. The native vegetation is blue oak and annual grass savannah. Land uses for this soil series include range, vineyards, recreation, and wildlife habitat.

The methods described in this chapter are based on field descriptions: observations based on (experienced) visual and tactile investigation of the soil profile. Given sufficient laboratory characterization data, these same methods could be refined to use a combination of field and laboratory data.

18.2.2 Horizon Generalization

Generalized horizon labels (GHL) represent an expert-guided selection of horizon designations that were consistently observed in the field, and meaningful in terms of soil morphology and management. These designations were determined to convey the "morphologic story" or conceptual framework of most-likely horizons typically observed in a suite of soil profiles associated with a specific soil series or map unit soil component. The Official Series Description (OSD) (Soil Survey Staff 2015) of the Loafercreek series typical pedon and range in characteristics defines this soil series concept. In this case, the OSD provided a useful GHL template, however, older OSDs or those based on a very limited set of data may not adequately convey an appropriate morphologic story.

Once a set of GHL have been determined (in the case of the sample data set: Oi, A, BA, Bt1, Bt2, Bt3, Cr, R), it is necessary to create and apply a set of rules that map the field-described designations to corresponding GHL. When working with a set of pedons that have been described by a small number of individuals over a short period of time (i.e., consistency in both designation application and standards), it is possible to use regular expression (REGEX) pattern matching to apply GHL. This process typically requires review of: (1) regional patterns in horizonation style, (2) morphologic property differences by groups of field-described designation, and (3) patterns of horizonation and properties with depth. We used a combination of field-described clay content, rock fragment volume, moist Munsell color value, and horizon midpoint to evaluate GHL assignments and determine the final set of REGEX rules. Due to this iterative process, local experience with these soils and their properties is (mostly) preserved within the REGEX rules and corresponding GHL. It should be noted that there are some cases where pattern matching alone is not enough and manual adjustment of GHL on a horizon-by-horizon basis is needed. For simplicity, only REGEX-based assignment of GHL was used in this study.

At present, there are limited means for capturing this type of soil horizon "micro-correlation" information developed in the application of GHL to soil horizon data. The authors suggest that future studies maintain a record of original horizon designations, GHL suitable for aggregation, and the rules used to apply these labels. Such a record would be useful should more data on a soil be collected or laboratory data be included in the horizon data set. A convenient, quantitative evaluation of GHL assignments can be performed using the silhouette width metric

(Rousseeuw 1987). This metric, commonly used to assess clustering labels, can be used to address the basic question of GHL assignment: "given a set of data and labels, how well do these labels split differences within the data?"

Aggregation of Generalized Horizon Labels

Aggregation of horizons as defined by GHL was performed using empirical probabilities, estimated along regular depth-slices from 0 to 150 cm (Beaudette et al. 2013). The "sliced" GHL data were then aggregated using proportional-odds logistic regression (Fig. 18.2). All computation was performed with the R package for statistical computing (R Core Team 2013).

A sequence of morphologic soil horizon designations can be modeled as an ordinal-scale variable: categorical by definition and ordered along a common gradient—depth. Within the set of GHL associated with our sample data, "Bt2" horizons always occur after "Bt1" horizons and before "Bt3" horizons. The proportional-odds logistic regression model (cumulative link model with logit link) (McCullagh 1980) is a convenient framework for estimating the probability of encountering a GHL, as conditioned by depth. The proportional-odds logistic regression (PO-LR) model can be defined as follows:

$$P[Y \geq j|X] = \frac{1}{1 + \exp[-(\alpha_j + X\beta)]}$$

where $P[Y \geq j|X]$ is the estimated probability of encountering GHL j, X is a set of predictor variables, and β is a vector of fitted regression coefficients (Harrell 2001). In this study, the PO-LR model was fit to "sliced" horizon data; 1-cm slices of GHL and slice top depth (Fig. 18.2). Restricted cubic spline (RCS) basis functions (Harrell 2001; Hastie et al. 2009) with 4 knots located at the 5th, 35th, 65th, and

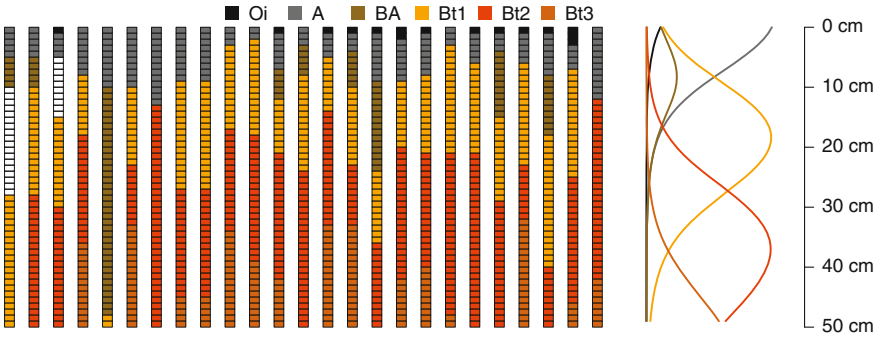

Fig. 18.2 Demonstration of a selection of Loafercreek soil profiles sliced into 1-cm chunks to a depth of 50 cm, colored by GHL, and associated probability estimates from the fitted PO-LR model

95th percentiles of slice top depth were used to accommodate nonlinearity. An empirical index of model stability was calculated by repeatedly refitting the PO-LR model to 25 randomly selected profiles (out of 63 total), 250 times.

18.2.3 Most-Likely Horizon Boundaries

Continuous estimates of GHL probability with depth are a convenient approach to communicating variability; however, there are still cases where discrete horizon depths are either required (e.g., database limitations) or sufficient for end-users. For example, the USDA-NRCS Official Series Description pages are used by a wide range of individuals that may not need continuous estimates of horizon probability. We used a simple strategy for converting these depth-functions into a discrete set of "most-likely" GHL boundary depths. At each depth-slice, the GHL with the highest probability is selected. Most-likely boundary depths are determined by locating upper and lower depths from contiguous sets of slices that share a common GHL. Within a collection of highly similar pedons, the most-likely boundary depths closely correspond to crossings of the GHL probability depth-functions.

18.2.4 Model Assessment

We used Shannon Entropy to quantify the relative amount of information present within GHL predictions at any given depth. Shannon Entropy was calculated according to (Kempen et al. 2009):

$$H = -\sum_{i=1}^{n} p_i \log_n(p_i)$$

where H is an index of entropy associated with predicted probabilities, p, of encountering GHL i through n at any given depth. Values range from 0 (maximum information, minimum entropy) to 1 (minimum information, maximum entropy). Entropy values were computed along each 1-cm depth-slice from predictions generated by the PO-LR model.

We used Brier scores (Harrell 2001) to quantify agreement between observed GHL and probabilities of predicted GHL:

$$B = \frac{1}{n}\sum_{i=1}^{n}(p_i - y_i)^2$$

where B is an index of agreement between predicted probabilities, p, and observed horizons, y, over depth-slices i through n associated with a specific horizon. Larger values suggest less agreement between probabilities and observed horizon labels.

18.3 Results

18.3.1 Generalized Horizon Labels

A graphical representation of the association between field-described horizon designation and associated GHL is presented as a box and whisker plot in Fig. 18.3. Assignment of GHL to the top- (A) and bottom-most (Cr and R) genetic horizons by REGEX pattern matching resulted in the most internally consistent groups of data. Transitional horizons near the surface (AB, BA, etc.) and lower Bt horizons (2Bt3, Bt4, BCt, etc.) were generally the most variable and thus difficult to place within a GHL by pattern matching. Further investigation of select soil properties and associated ranges (Table 18.1) made it possible to refine REGEX rules.

The apparent gap (Fig. 18.3) in horizon midpoints between Cr and R GHL is related to various depths to which Cr material was excavated and cases where an R horizon was not described. By convention, R horizon bottom depths are commonly extended to 150 or 200 cm. The degree of overlap in GHL concepts can be expressed in terms of measured soil properties (in this case, a limited set of field-described properties), summarized by GHL (Table 18.1).

18.3.2 Probabilistic Representation of GHL

A graphical comparison of empirical and PO-LR-predicted GHL probabilities is presented in Fig. 18.4. The empirical probability curves are an exact representation of the 63 pedons within our sample data set; however, these curves are not likely a generalized representation of all possible soils correlated with the Loafercreek series. At the expense of a small amount of accuracy (as evaluated using the sample data set), the smoother and more generalized shape of the PO-LR-derived GHL probabilities are better candidates for describing the central tendency of a soil series concept (Fig. 18.4). When samples sizes are too small to support fitting a stable PO-LR model, the empirical probabilities can provide a reasonable alternative.

The PO-LR probabilities were the least accurate within the very thin Oi (Brier Score of 1.40) and infrequently occurring BA horizons (Brier Score of 1.22). Accuracy was greatest in the most consistently defined horizons which were not surprisingly found at the “top” (A horizons) and “bottom” (R horizons) of the

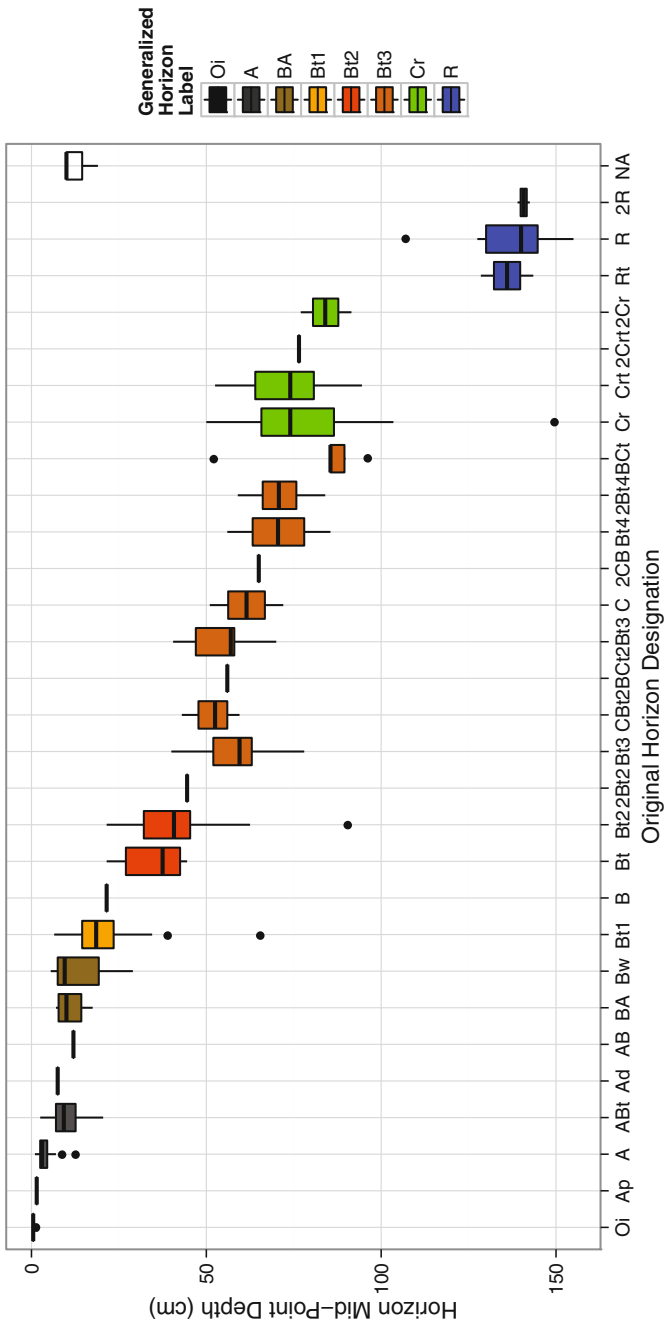

Fig. 18.3 Original horizons designations (*x*-axis), GHL assignments (*colors*), and associated ranges in depth. Standard box-whisker conventions are used in this figure: *box* contains the median bounded by the inter-quartile range (IQR), whiskers extend from upper and lower quartiles to ±1.5 times the IQR, and filled *circles* represent values outside the whisker range

Table 18.1 Evaluation of GHL via field-described soil properties

GHL	Clay (%)	Horizon midpoint (cm)	Total RF[a] volume (%)	Moist Munsell color value
Oi	–	0.7 (0.4)	–	–
A	16 (3.3)	4.2 (3.2)	7 (7.3)	3.3 (0.6)
BA	18 (3.7)	12.1 (6.2)	10 (6.5)	3.6 (0.7)
Bt1	21 (4.5)	19.9 (9.3)	13 (12.5)	3.7 (0.6)
Bt2	25 (5.0)	39.6 (11.3)	24 (21.8)	4.0 (0.7)
Bt3	29 (6.3)	60.9 (13.6)	35 (23.9)	4.4 (0.6)
Cr	–	77.0 (16.4)	–	–
R	–	137 (11.5)	–	–

Reported values are means with standard deviation in parenthesis. Values marked as "–" are the result of missing or insufficient data
[a]RF: rock fragment percent by volume

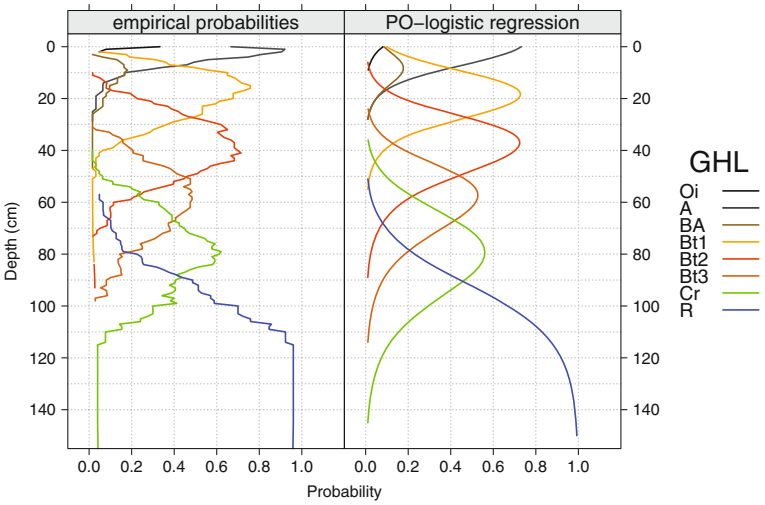

Fig. 18.4 Comparison of empirical GHL probabilities, evaluated over 1-cm depth-slices, and predictions from the PO-LR model. Probabilities less than 0.01 have been removed for clarity

profiles. The degree of overlap in GHL concepts was greatest (as defined by Shannon Entropy) near the surface where Oi, A, and BA horizons spanned similar depth ranges, and lower in the profile where Bt3 and Cr horizons spanned large ranges in depth (Fig. 18.5).

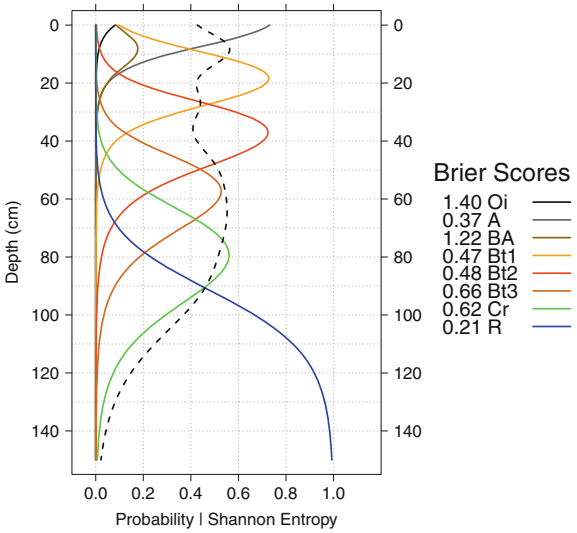

Fig. 18.5 PO-LR-predicted GHL probabilities *solid lines*, Shannon entropy *dashed line*, and associated Brier scores (values printed in legend)

18.3.3 Model Fit and Stability

The fitted PO-LR model had a reasonably high coefficient of determination ($R^2 = 0.83$). Removal of RCS basis functions from the model resulted in an R^2 of 0.79. Deviations between empirical and modeled probabilities were greatest in horizons near the surface and smallest in the lower-most horizons (Fig. 18.6). Discrepancies between the two sets of probabilities can be attributed to two main factors: (1) lack of model fit, and (2) generalization (e.g., smoothing) of empirical probabilities by the PO-LR model.

The stability of the PO-LR model was evaluated by iteratively refitting the model (250 times) using a random subset of 25 pedons (out of 63 total) within each iteration. The predictions from each iteration are presented in Fig. 18.7. Mean model R^2 was 0.89 and ranged from 0.81 to 0.91. Variation between iterations appears to results in a range in predicted probabilities of about 0.2 probability units near the peaks associated with each generalized horizon label. The combination of predictions from the full model combined with many realizations of a reduced model could be a useful way to convey uncertainty in predictions of GHL probabilities at any given depth.

18.3.4 ML Horizon Depths

The "most-likely" (ML) horizon depths extracted from empirical probabilities were quite similar to those extracted from PO-LR model predictions (Table 18.2). ML horizon depths represent one possible way in which probabilistic estimates of GHL

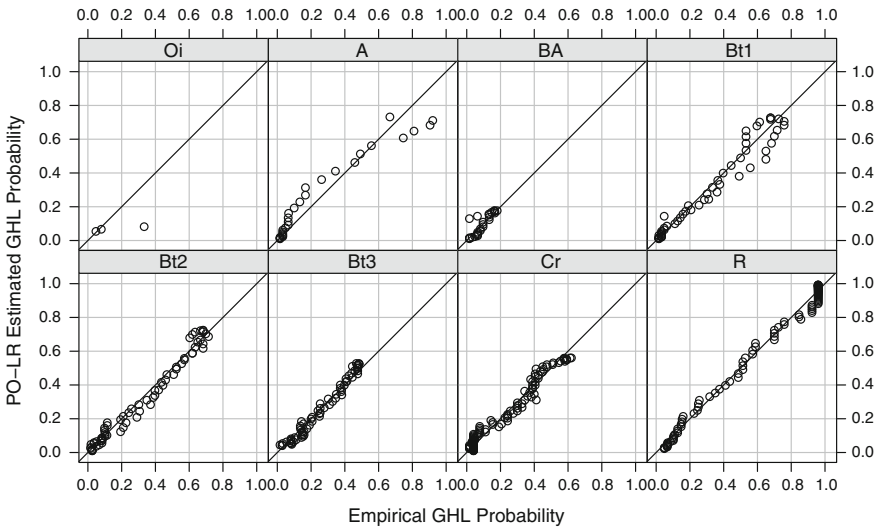

Fig. 18.6 Scatterplot comparison of empirical GHL probabilities and PO-LR-estimated GHL probabilities. *Solid lines* represent a 1:1 agreement

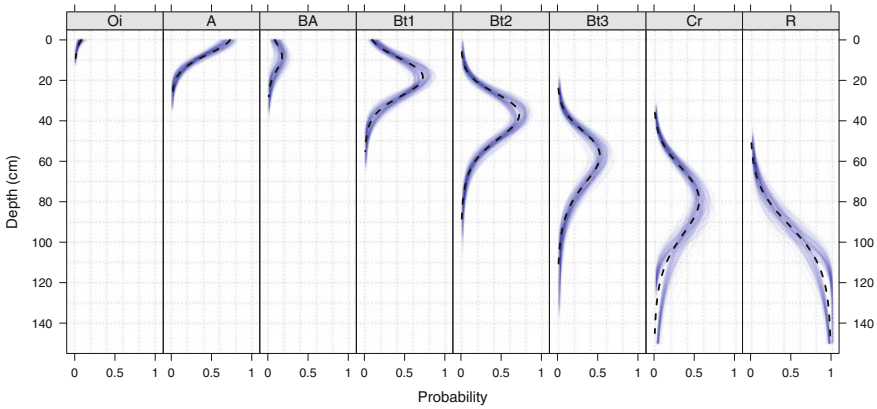

Fig. 18.7 Predicted GHL probability depth-functions from 250 iterations of model fitting, based on a reduced data set. *Dashed lines* are predictions from the full model

occurrence can be simplified into a format that is more familiar to users of existing soil survey products. ML horizon depths could also serve as a template by which aggregated soil properties (clay, pH, CEC, etc.) are organized within soil survey reports. The Brier scores (Table 18.2) serve as an indication of how well each set of ML horizon depths fits the original collection of pedons. For example, predictions associated with the ML horizon depths for "A" horizons more consistently overlap with field-observed "A" horizons (e.g., smaller Brier scores) as compared to "Bt3"

Table 18.2 Most-likely GHL boundary depths and associated Brier scores, computed from empirical probabilities and PO-LR predictions

Empirical probabilities				PO logistic regression			
Horizon	Top	Bottom	Brier	Horizon	Top[a]	Bottom[a]	Brier[b]
A	0	8	0.20	A	0-**0**-0	7-**9**-10	0.26
Bt1	8	28	0.23	Bt1	7-**9**-10	25-**28**-31	0.23
Bt2	28	51	0.25	Bt2	25-**28**-31	47-**50**-54	0.23
Bt3	51	68	0.44	Bt3	47-**50**-54	63-**67**-73	0.39
Cr	68	90	0.36	Cr	63-**67**-73	85-**91**-100	0.36
R	90	203	0.05	R	85-**91**-100	151-**151**-151	0.08

All depths are in cm

[a]5th, 50th, and 95th percentiles of ML horizon boundaries derived from 250 iterations of model fitting, based on a reduced data set

[b]Brier scores calculated using full PO-LR model

horizons (e.g., larger Brier scores). In all cases except "Bt2" and "Bt3" horizons, Brier scores associated with the PO-LR model were equal to or greater than those associated with empirical probabilities; not surprising as predictions from the PO-LR model are much smoother than the over-fit empirical probabilities. The similarity in ML horizon depths and small differences in Brier scores suggest that the PO-LR model is a reasonable generalization of the GHL concepts defined for this collection of pedons.

18.4 Conclusions

Describing and sampling soil by genetic horizon represents an efficient approach that has provided a common pedological language used among soil scientists and classification systems for nearly 100 years. Yet, deriving an aggregate representation of soil morphology (e.g., to support a soil series concept or similar task) from a suite of similar soil profile descriptions has been challenging. For this reason, soil series concepts have historically been defined using the modal profile; a single, field-observed pedon selected as a "representative" demonstration of central tendency. Advances in soil morphometrics are poised to change our understanding of what it means to describe soil profiles. Continuous depth-functions of soil properties will further our understanding of how soil properties vary with depth, adding rich content to the existing genetic horizon framework.

In this chapter, we have outlined an approach for deriving continuous depth-functions of groups of field-described genetic horizon probabilities. Correlation of horizon designation to a subset of GHL is fundamental to this approach and represents a series of "micro-correlation" decisions that could support a wide range of soil data aggregation tasks. The two aggregation methods described in this chapter yield similar results; selection of an appropriate method depends on

sample size; use of empirical probabilities is recommended for small collections of pedons (less than 10 pedons), and PO-LR-derived probabilities are recommended for large collections.

The methods presented in this chapter represent progress toward a quantitative description of soil morphology. Future application of these methods will depend on development of guidelines related to: minimum sample sizes, PO-LR model fitting parameters, model diagnostics, and recommendations on pedogenic interpretation of model coefficients. In addition, more work needs to be done on incorporating *depth-wise* correlation into the PO-LR model to support more realistic estimates of coefficient standard errors.

References

Beaudette DE, Skovlin J (2015) soilDB: Soil Database Interface. http://CRAN.R-project.org/package=soilDB

Beaudette DE, Roudier P, O'Geen AT (2013) Algorithms for quantitative pedology: a toolkit for soil scientists. Comput Geosci 52:258–268

Harrell FE (2001) Regression modeling strategies. Springer Series in Statistics. Springer, New York, NY

Hartemink AE, Minasny B (2014) Towards digital soil morphometrics. Geoderma 230–231: 305–317. doi:10.1016/j.geoderma.2014.03.008

Hastie T, Tibshirani R, Friedman J (2009) The Elements of Statistical Learning. Springer, Berlin

Holmgren GGS (1988) The point representation of soil. Soil Sci Soc Am J 52:712–716

Hudson BD (1990) Concepts of soil mapping and interpretation. Soil Surv Horizons 31:36–72

Jones TA (1959) Soil classification–a destructive criticism. J Soil Sci 10:196–200

Kempen B, Brus DJ, Heuvelink GBM, Stoorvogel JJ (2009) Updating the 1:50,000 Dutch soil map using legacy soil data: a multinominal logistic regression approach. Geoderma 151: 311–326. doi:10.1016/j.geoderma.2009.04.023

Kempen B, Brus DJ, Stoorvogel JJ (2011) Three-dimensional mapping of soil organic matter content using soil type specific depth functions. Geoderma 162:107–123. doi:10.1016/j.geoderma.2011.01.010

McCullagh P (1980) Regression models for ordinal data. J Roy Stat Soc B 42:109–142

Myers DB, Kitchen NR, Sudduth KA, Miles RJ, Sadler EJ, Grunwald S (2011) Peak functions for modeling high resolution soil profile data. Geoderma 166(1):74–83

R Core Team (2013) R: a language and environment for Statistical computing. R Foundation for statistical computing. Vienna, Austria. http://www.R-project.org/

Rousseeuw PJ (1987) Silhouettes: a grapical aid to the interpretation and validation of cluster analysis. J Comput Appl Math 20:53–65

Soil Survey Staff (1951) Soil Survey Manual. U.S.D.A. Handbook 18. U.S. Govt. Printing Office, Washington, D.C

Soil Survey Staff (2015) "Official Soil Series Descriptions." Edited by Natural Resources Conservation Service, United States Department of Agriculture. https://soilseries.sc.egov.usda.gov/OSD_Docs/L/LOAFERCREEK.html

Wilding LP, Scafer GM, Jones RB (1964) Morley and blount soils: a statistical summary of certain physical and chemical properties of some selected profiles from Ohio. Soil Sci Soc Proc 28:674–679

Chapter 19
Using Soil Depth Functions to Distinguish Dystric from Xanthic Ferralsols in the Landscape

Helena Saraiva Koenow Pinheiro, Waldir de Carvalho Jr., Cesar da Silva Chagas, Lucia Helena Cunha dos Anjos and Phillip Ray Owens

Abstract The soil texture is a key parameter and is widely used as input in predictive models to estimate other soil properties. The general goal was creating numerical parameters to describe the variability of soil particle size (sand, silt, and clay) components using continuous depth functions to characterize Ferralsols from Guapi-Macacu watershed in Rio de Janeiro State (Brazil). The profile collection comprises fifteen profiles, seven classified as Haplic Ferralsols (Dystric) and eight as Haplic Ferralsols (Xanthic). The analysis was performed in the R software through "aqp" package (Algorithms for Quantitative Pedology) and using equal-area quadratic spline function. A numerical aggregation of soil texture components was used to build a mean, a median, and spline depth functions, fitting the dataset to six predefined depths (GlobalSoilMap project) and to most-likely horizon depths. The analysis revealed sand and silt content with decreasing values with soil depth and the opposite trend for clay. The topsoil layer (0–30 cm) had

H.S.K. Pinheiro (✉) · L.H.C. dos Anjos
Soils Department—Agronomy, Federal Rural University of Rio de Janeiro,
BR 465, Km 47, Seropédica, RJ CEP 23890-000, Brazil
e-mail: lenask@gmail.com

L.H.C. dos Anjos
e-mail: lanjos@ufrrj.br

W. de Carvalho Jr. · C. da Silva Chagas
Embrapa Solos, Rua Jardim Botânico 1.024, Jardim Botânico, RJ 22460-000, Brazil
e-mail: waldir.carvalho@embrapa.br

C. da Silva Chagas
e-mail: cesar.chagas@embrapa.br

P.R. Owens
Lilly Hall of Life Sciences, Purdue University,
915 West State Street, West Lafayette, IN 47907-2054, USA
e-mail: prowens@purdue.edu

A.E. Hartemink and B. Minasny (eds.), *Digital Soil Morphometrics*,
Progress in Soil Science, DOI 10.1007/978-3-319-28295-4_19

dominantly a clay loam texture (32–40 % clay; 49–53 % sand; and 15–20 % silt). The most-likely diagnostic B-horizon (45–150 cm depth) presented clayey texture (43–47 % of clay and 40–55 % of sand). Ferralsols usually have low silt contents; and the silt range was from 10 to 20 % in the soil profile collection. The organized data can be useful to many purposes, including profile database harmonization and soil classification.

Keywords Soil depth functions · Soil texture components · Digital mapping of soil properties · Spline · Algorithm for quantitative pedology

19.1 Introduction

Ferralsols have a large distribution in Brazil covering almost one-third of the territory and are important for agriculture and pasture production (Dick et al. 2005). The mineralogy of these soils is mainly composed of low activity clays (kaolinite) and Fe and Al-oxides (hematite, goethite and gibbsite); thus, they have a low cation exchange capacity (Sposito 1989; Santos et al. 2013). The soil profiles are in general deep and they have a well-developed soil structure, showing yellowish and reddish colors indicating good drainage conditions.

The soil texture, or composition of mineral particle size, is a highly variable soil physical characteristic, which has an essential role for growing crops, engineering projects, and land protection and conservation. The effects of the soil texture on land capability, storage of water and nutrients, distribution and composition of vegetation are well known globally (Klingebiel 1963; Jenny 1980; Silver et al. 2000; Fernandez-Illescas et al. 2001). The soil texture information is a key parameter widely used as input in predictive models to estimate hydrologic parameters (Thompson et al. 2012). Due to those facts, digital soil mapping (DSM) efforts have been made to obtain information about soil particle size fraction distribution (Moore et al. 1993; Arrouays et al. 1995; McBratney et al. 2000).

Field evaluation of a soil profile and the description of horizons/layers are usually performed according to morphological characteristics related to pedogenetic processes (alteration of parental material, eluviation/illuviation of clay, organic matter and salts distribution, hydromorphic features, iron content, among others). In the soil surveys, the information and data from soil evaluation are related to narrative, tabulated, or presented in sketches drawings. However, the lack of data standardization and quantitative parameters turns it difficult to transmit the information to other users (Beaudette et al. 2013).

The organized data can be useful to many purposes; however, the analysis of large soil profile collections is affected by changes in soil classification over time and among taxonomic systems, regardless of standard soil data issues and differences of analytical procedures. Addressing the issue of variability of soil properties along profile depths, the global consortium of soil survey (GlobalSoilMap project) proposed standard intervals to compound the database of soil properties (Hartemink

et al. 2010). The six predefined depths correspond to the following layers: 0–5, 5–15, 15–30, 30–60, 60–100, and 100–200 cm (Arrouays et al. 2014).

The general goal was creating numerical parameters to describe the variability of soil particle size (sand, silt, and clay) components using continuous depth functions to characterize Ferralsols from Guapi-Macacu watershed in Rio de Janeiro State (Brazil). The analysis comprised soil depth functions (spline and slicewise aggregation) and relations among soil texture components and diagnostic horizons. To accomplish the proposed goal, a numerical approach, fitting the dataset to predefined depths (GlobalSoilMap project) and according to most-likely inferred horizon depths, was applied aiming to set the representative functions and characterize the texture of soils studied in the watershed.

19.2 Materials and Methods

19.2.1 Study Area

The Guapi-Macacu watershed is located at southeast region of Brazil, in Rio de Janeiro State (Fig. 19.1). The climate is classified as tropical rainy with dry winter (Aw) according to Köppen classification (Köppen 1948). The mean temperature is 23 °C, with low temperatures in winter. The average annual rainfall exceeds

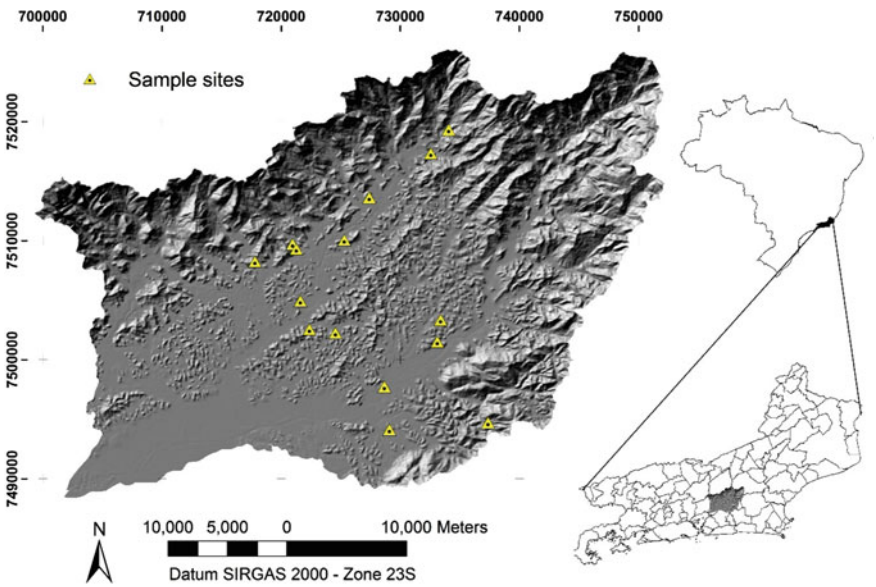

Fig. 19.1 Location of Ferralsols profiles in the Guapi-Macacu watershed, Rio de Janeiro (Brazil)

1200 mm, and it can reach 2600 mm in the watershed divisors (Projeto Macacu 2010; Dantas et al. 2008). The region is part of the Atlantic rainforest biome, with different types of natural vegetation, such as the altitude grasslands, dense forests, mangroves, swamps, and estuaries (Pedreira et al. 2009).

The maximum altitudes are observed in the escarpments of the "Serra do Mar," with gneiss/granite rocks as the predominant lithology. The transition area between the escarpment and the coastal plains, at sea level, comprises of a series of hills and slopes with elevations below 1000 m. Geologically, the region is located in the central portion of the Guanabara Graben, classified as Macacu Sedimentary Basin, formed by several depositional sequences from tectonic events in the early Tertiary (Ferrari 2001). The consequences of geological events that gave rise to the Guanabara Graben induced geomorphological features related to depositional events, such as alluvial fans and fluvial and lacustrine deposits.

The soils were surveyed in 2011 and 2012, and approximately one hundred soil profiles were described and collect. For this study, fifteen profiles of Ferralsols were selected from the collection. Figure 19.1 shows the location of Ferralsols profiles in the Guapi-Macacu watershed in Rio de Janeiro State, Brazil.

Total sand, silt, and clay contents were measured according to Embrapa (1997) procedures. The analytical results of particle size, corresponding to the depths described in the soil survey (genetic horizons), were used to identify the diagnostic horizons, and the soil classification was performed according to the Brazilian System of Soil Classification—SiBCS (Santos et al. 2013) and correspondent criteria in the World Reference Base for Soil Resources—WRB (IUSS Working Group 2014).

19.2.2 Soil Profile Data and Depth Functions

The dataset selected to perform the analysis comprises fifteen Ferralsols: seven profiles classified as Haplic Ferralsols (Dystric) and eight as Haplic Ferralsols (Xanthic). The statistical procedures were implemented in the R software (R Development Core Team 2013). The R program is an open source and free software. Operating procedures in this program are conducted by command lines (scripts) and require the prior installation of packages to read certain types of data and run specific analysis.

The analysis of the soil profile data comprises aggregation of profiles by soil texture properties by slicewise aggregation algorithm (Beaudette et al. 2013) and harmonization of soil depth by equal-area spline function (Ponce-Hernandez et al. 1986). The analysis by slicewise aggregation was performed using Algorithm for Quantitative Pedology (AQP) package, developed by Beaudette et al. (2013). The "aqp" stable version of the package is available on CRAN (http://cran.r-project.org/web/packages/aqp/). The aggregation algorithm allows the estimative of central

tendency according to each depth slice (1 cm) and computing statistic for each segment, reconstructing the profile data at predefined depths, as a single "representative depth function" (Beaudette et al. 2013). Slicing the soil profiles in layers with 1 cm thickness allows calculating the average and median values of each layer as a vector of segment boundaries, allowing reassemble the average profile and the median, through the syntax below:

$$\text{slab}\ (\text{data},\ \sim \text{clay}\ +\ \text{silt}\ +\ \text{sand},\ \text{slab.fun} = \text{mean/median},\ \text{na.rm} = \text{TRUE})$$

A function to summarize soil texture data according certain depths can be extracted from the dataset created by slicing the soil profile in 1 cm layers. The aggregation of continuous data was based on the distribution of soil particle size fractions (sand, clay, and silt) at the predefined depths (0–5, 5–15, 15–30, 30–60, 60–100, 100–200 cm) and most-likely inferred horizon depths.

Soil depth functions were applied to fit the data to the proposed intervals, which act as coefficients for a spline function. The spline function proposed by Ponce-Hernandez et al. (1986) represents a nonparametric function, called an equal-area spline, appropriated to model soil attributes (Bishop et al. 1999; Malone et al. 2009). The function equal-area spline considers each horizon as the predefined interval and the knots of each horizon lie between horizon boundaries, with one inflexion in each interval. The knots should lie as near as possible to the inflexion and as far of boundaries as possible, which in essence, preserve the mean value of the soil property. In this sense, the area at left of the fitted curve above the horizon mean value is the same than the area at the right of the spline curve, below the horizon mean (Odgers et al. 2012). This mechanism provides continuous values to soil properties varying according to the depth in a soil profile, which allows compose a database where all points can have a value in a certain depth.

The slicewise aggregation algorithm was applied to create a new dataset from the original profile collection to support soil depth functions analysis, allowing to distribute the data by one-centimeter layers and posteriori aggregation by horizons/layers. This algorithm is based on the premise: "*a representative depth function for some soil property (e.g., clay content) can be generated from a collection of soil profiles by summarizing this property along depth slides*" (Beaudette et al. 2013). In this sense, depth-slice probabilities were generated based on data frequency by major horizon (most-likely horizon depth), revealing quantitative trends of the soil texture components according Ferralsols profiles horizons. The probabilities for each slice (1 cm) are syntax:

$$S_{k.i} = \text{frequency}\ (S_{k.i})/j;$$

where "$S_{k.i}$" corresponds to the inferred value of the soil property to each 1 cm slice, and "k" is the class of the categorical variable (sand, silt, and clay), "i" is the slice counter and "j" is the number of profiles contributing to the calculation.

19.2.3 Similarity Between Soil Profiles

The pairwise similarity between soil profiles was based on soil classification diagnostic criteria, where a quantitative comparison between soil profiles must account the variability of diagnostic horizons thickness associated with soil properties (Webster and Oliver 1990). The regular layer slices of the dataset allow calculating the dissimilarity between profiles, comparing then through a dissimilarity matrix for each depth slice (Beaudette et al. 2013). A dissimilarity between Ferralsols was computed using "profile compare ()" function considering sand, clay, and content to a maximum depth and depth-weighting coefficient of 0.01. The contributing fraction values returned for each depth slice describe the number of soil profiles used in the computation and that value can be understood as an aggregate measure of soil depth probability.

A function to rendering soil profiles in simple sketches was applied using "profile plot ()" function, turning the visualization and comparison between taxonomic relationships based on the soil profiles' properties easier to observe and analyze (Beaudette et al. 2013).

19.3 Results and Discussion

19.3.1 Characterization of Ferralsols and Soil Texture Data

The Guapi-Macacu watershed presented substantial variability of soils, predominantly Ferralsols (28 %), Acrisols (24 %), Cambisols (18 %), and Gleysols (15 %). Haplic Ferralsols (Xanthic)—FRxa and Haplic Ferralsols (Dystric)—FRdy represent the Ferralsols, which showed a wide distribution with 58 and 41 % of the soil observations in the watershed (Pinheiro et al. 2013). The main taxonomic difference between these classes is expressed by the color criteria, which reflect differences in the clay mineralogy and moisture regime, where Xanthic soils have greater content of hydrated Fe-oxides (goethite), and Dystric soils have more hematite and better soil drainage. These differences are generally related to landscape features, hydrological conditions, and parental material.

Haplic Ferralsols (Dystric) are largely observed under pasture and Atlantic rainforest, in varied slope conditions but predominantly in less hilly areas. In the mountainous areas, these soils occur in association with regosols and cambisols. Haplic Ferralsols (Xanthic) commonly occupy the footslopes of the watershed. Such soil sequence is typical in the east and south of the watershed, along a band of NE-SW-oriented gneiss rocks of Precambrian age. Besides their occurrence at the lower part of hills with granite/gneiss parental material, Haplic Ferralsols (Xanthic) were also observed related to sedimentary rocks, in the Southeast areas of the watershed. The Haplic Ferralsols (Xanthic) land coverage is usually of grassland, secondary forest vegetation, and urban areas.

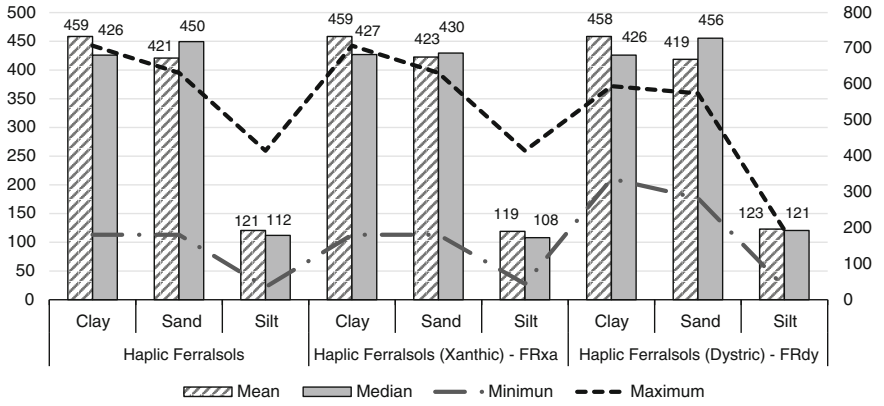

Fig. 19.2 Distribution of minimum, maximum, mean, and median values of particle size components in the Ferralsols profiles (scale at *left* side is representing the mean/median values; and at *right* side, the minimum/maximum values)

From the soil survey dataset, fifteen chosen Ferralsols had all horizons described, sampled, and the particle size analyzed; thus, the dataset (70 horizons) presented no missing data. Based on the selected dataset, soil depth functions were created and further analysis was performed. The descriptive values to the soil texture, of the seven profiles (30 horizons) of Haplic Ferralsols (Dystric) and eight profiles (40 horizons) of Haplic Ferralsols (Xanthic), are presented in Fig. 19.2. Observing the trends of minimum and maximum values, all Ferralsols have the same patterns and they show high clay content, followed by sand and silt (scale on the right side of Fig. 19.2).

In general, the Dystric Ferralsols showed less amplitude of values to all particle size components when compared with the Xanthic Ferralsols. Regarding the clay content, Ferralsols Xanthic and Dystric showed no difference among them; however, both soil types had higher values to the mean when compared with median parameter. Sand content had slightly smaller values compared to clay for all Ferralsols, and the same pattern was observed for both classes (FRxa and FRdy), with median higher than mean values. Silt was the fraction with less contribution in the particle size of Ferralsols, and the values were also similar among soil classes.

Summarizing, Fig. 19.2 shows that both Ferralsols classes are similar regarding the particle size components, although the mean and median values for sand and silt contents were slightly higher in the Haplic Ferralsols (Dystric)—FRdy. Further analysis, based on the vertical distribution of particle size in the soil profile through the soil depth functions, is needed to separate these classes quantitatively.

The visualization by standard sketches allows detecting similarities/dissimilarities among the soil profile collection, as observed in Fig. 19.3a, b. The P72 and P89 revealed a similar trend of particle size along the soil profiles in addition to the profiles P84 and P86, which also showed high content of clay and low values of sand. This kind of approach can be useful to support the

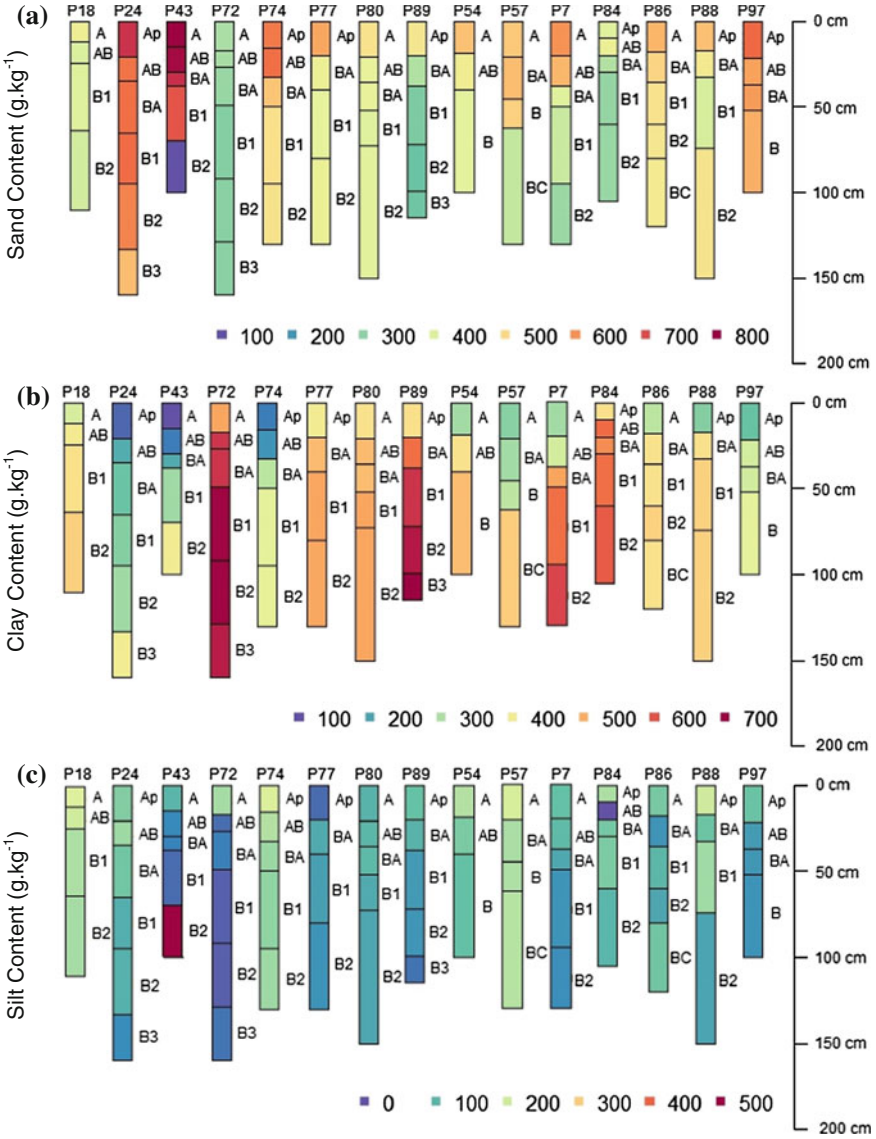

Fig. 19.3 Sand, clay, and silt distribution of Ferralsols profile collection

definition of lower taxonomic levels in soil classification (families and series), or even to define typical soil sequences based on relief, time, and parental material (toposequences, chronosequences, and lithosequences, respectively).

Sketches representing soil properties observed in the field are widely used and a very useful tool to soils scientists, particularly to report soil stratigraphy (horizons and transitions) and morphological features (Beaudette et al. 2013). However, those

plots are not to scale and without standard legends and symbols; thus, they are subjective and not easily transmitted to other researchers and users in general. The distribution of sand, clay, and silt in the Ferralsols, according to horizon depth, is illustrated in Fig. 19.3. The sketches of profiles highlight the particle size components (sand, clay, and silt) in classes of 100 g kg^{-1} intervals (Fig. 19.3a–c). As expected, the deeper soils show more homogeneous texture composition along the profile (P24, P72, P74, P77, P80, P7, and P88), showing a sequence of overlaid B-horizons with smooth transitions. On the other hand, the shallowest profiles show remarkable differences between horizons, and when compared with the "modal" profile referred in soil classification systems, this pattern is related to the granite/gneiss parental material properties.

Looking at dissimilarities, an example is the profile P43, which is shallow compared to the other soils and shows the lowest values of sand content in contrast with the highest values of silt. Further investigation is needed, but a reasonable explanation is the local influence of parental material, which is corroborated by the thickness of soil profile. Regarding soil classification systems, this spline approach could be useful to set regional series or family of soils; or to propose new criteria to describe the soil series, which is a way improving the information associated with soil mapping units and their design.

19.3.2 Soil Depth Functions and Data Aggregation

Analysis of Profile Data (Components of Texture and Relation with Horizon Depth)

Corroborating the field observations and the characterization of the particle size in the soil horizons, sand and silt content in the Ferralsols tends to decrease with depth up to 100 cm (Fig. 19.4) which is within the control section used to define the diagnostic horizons. However, the clay content shows a distinct increase around 20 cm, which is usually the transition from the A to B-horizon. This trend was noticed particularly on the Haplic Ferralsols (Dystric), as observed in Fig. 19.4c. The Haplic Ferralsols (Dystric) have also a small contribution of profiles deeper than 150 cm depth to compound the estimative of a median profile at this depth, less than 14 % of the dataset. This can be related to the conditions of occurrence of these soils, particularly related to steep slopes in the mountainous areas of the watershed, inhibiting the formation of typical deep weathered B-horizons. Some of the Haplic Ferralsols (Dystric) showed a transitional BC horizon, in the sampled depth, similar to the one in the Haplic Cambisols (Dystric), but differing mainly in smaller content of easily weatherable minerals (biotite, montmorillonite, and feldspar).

Regarding soil depth and silt content relation, high silt values were observed in the 0–25 cm depths (Fig. 19.4). Haplic Ferralsols (Xanthic) also presented subtle increases in median silt values related to 70–100 cm depth, probably related to transition between horizons in the soils developed from colluvium deposits

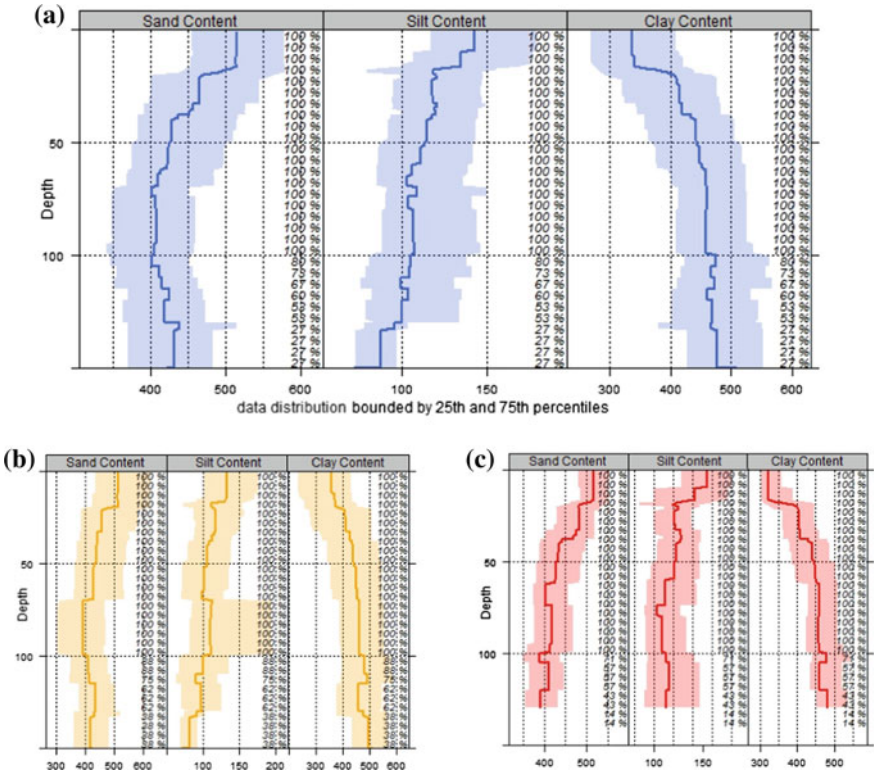

Fig. 19.4 Median distribution of sand, silt, and clay content along profile depth; **a** Ferralsols collection (15 Profiles); **b** Haplic Ferralsols (Xanthic); **c** Haplic Ferralsols (Dystric)

originated from the granite/gneiss materials. The variability in silt content, particularly below 80 cm depth, can also be correlated to parental material. The presence of BC horizons starting at this depth (80 cm) was observed in two soil profiles, both classified as Haplic Ferralsols (Dystric). The analysis of the graphs reveals how many profiles from the dataset were contributing to calculate the parameters, which give important information about the original dataset.

At the bottom of the soil profile (below 150 cm), the data contributing to the calculation were less than 27 % of the entire collection, which reduces the confidence of the estimative for the Haplic Ferralsols (Dystric). However, the soil information applied to orient land use and for taxonomic purposes is usually obtained to a depth of 1.5 m, where the subsurface diagnostic horizons express themselves in most soil classes (*solum*).

For comparative purposes, a harmonization of the dataset was performed based on the six predefined depth intervals suggest by the GlobalSoilMap project (Arrouays et al. 2014). According to Bishop et al. (1999), equal-area spline functions showed superiority over other soil depth functions (exponential, polynomials)

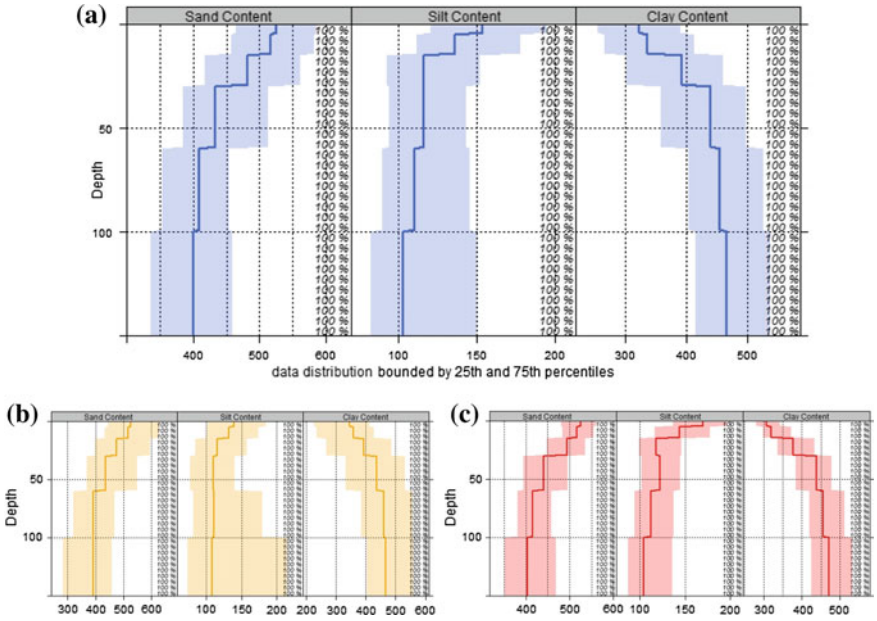

Fig. 19.5 Distribution of sand, silt, and clay content according spline depth function fitted to predefined depth; **a** Ferralsols collection; **b** Haplic Ferralsols (Xanthic); **c** Haplic Ferralsols (Dystric)

to predict the soil properties pH, clay content, water content. Thus, the spline function was applied to harmonize the data in six layers (Fig. 19.5).

The spline functions reveal the same trend for the components, in both soil classes, with values of sand and silt decreasing with depth, while the clay content increases (Fig. 19.5). Observing the Haplic Ferralsols (Dystric), there is a remarkable difference in texture component (mainly, sand, and clay content) below 30 cm depth, when compared to Haplic Ferralsols (Xanthic) in which the changes in soil properties are smoother along the soil profile.

Most-Likely Diagnostic Horizons Probability as a Function of Particle Size Data

The most-likely horizons based of the frequency of particle size data from Ferralsols profile collection are presented in Fig. 19.6. The six columns on the left of Fig. 19.6 represent individual probability per horizon, identified with a black line representing the most-likely (i.e., modal) horizon, and the red line corresponds to the horizon probability fitted to the dataset, considering the contributing factor to each depth. On the right side of Fig. 19.6, the horizons are represented by assorted colors and plotted in a single column.

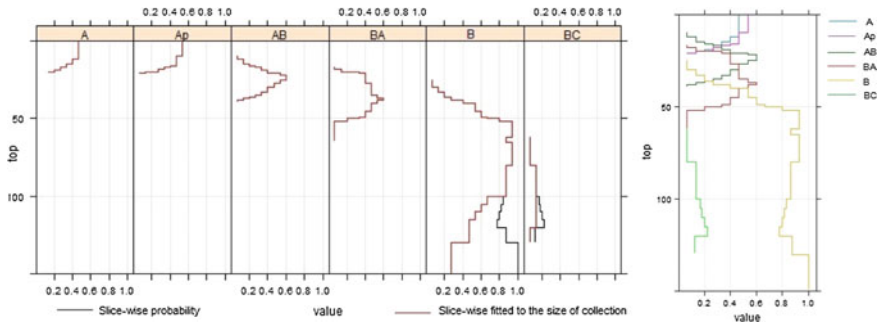

Fig. 19.6 Probability of most-likely horizon depths by slicewise aggregation technique

The A and Ap horizons have similar thickness pattern, both up to 10 cm depth. However, Ap horizons have a tendency of being shallowest, mostly due to erosion favoured by the slope (degree and form) and land use observed in the area. Below 10 cm, the occurrence of transitional horizons (AB, BA) was observed, with peaks of occurrence around 20 cm for AB and 40 cm for BA, not necessarily occurring together in the profile. In the field, the transitional horizons were mostly separated based on color, structure, and biological activity, related to the organic material deposition in the topsoil layer. In general, the transitional horizons (AB, BA) occurred at the 20–30 cm depth.

According to the slicewise aggregation (Fig. 19.6), the Ferralsols diagnostic B-horizon was observed from 25 to 150 cm and below, in deep soil profiles with a sequence of B-horizons, always with the main diagnostic B-horizon in the 50–100 cm layer. Simultaneously, in this layer, transition BC horizons were found in two profiles: their presence is not common in Ferralsols and may imply a different response for soil management and hydrology, indicating a layer of impediment, such as shallow altered bedrock.

The slicewise probabilities organized by major horizon types can enhance the quantitative characterization of site patterns, such as topsoil thickness or presence of compact layers, bedrock contact, among other important terrain characteristics (Beaudette et al. 2013). For example, soil depth functions aggregated by horizon may help in establishing limiting values and standard deviation of collected data, assisting to create mean/median taxonomic sections; and allowing comparison with modal profiles, as described in the soil taxonomic systems (Pereira et al. 1984). Furthermore, this technique can be useful to compare soil data among profiles classified in different taxonomic systems.

The estimated horizon midpoint depth from Ferralsols profiles, as well the midpoint to clay, sand, and silt content related to the genetic horizons is presented in Fig. 19.7.

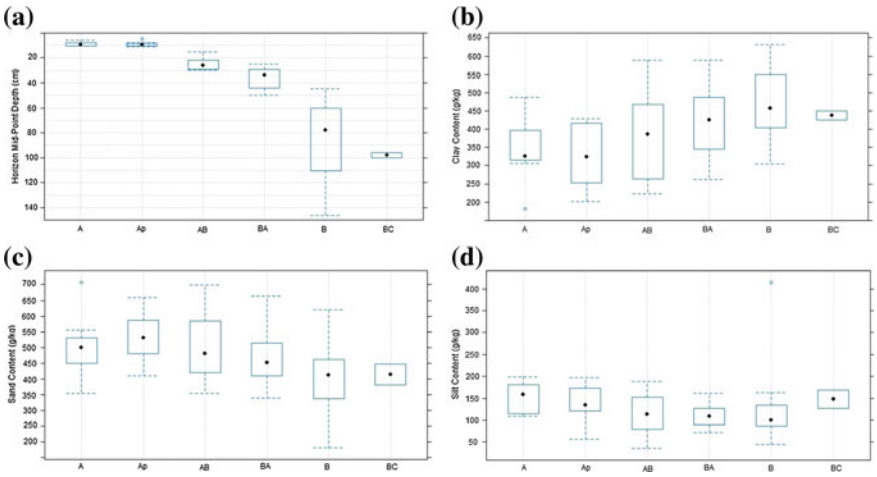

Fig. 19.7 Midpoint: **a** depth of horizons; **b** clay content; **c** sand content; **d** silt content

The boxplot graph for the horizons midpoint depth shows small differences for A and Ap horizons, since they occupy the same position in the profile (Fig. 19.7a). The transitional AB and BA horizons presented the midpoint depth closer to 25 and 30 cm, respectively, ranging between 15 and 45 cm. The generalized depth considering the consistence of data (frequency) is highlighted by the boxplot graph on 25–75th percentiles. The diagnostic B-horizons have the greatest range, mostly because the Ferralsols show a sequence on sub B-horizons (B1, B2, B3). All the estimative related to the BC horizon had contribution from two profiles of the entire dataset (less than 14 %), which means that BC is not commonly observed before the 200 cm depth.

Regarding the clay, sand, and silt contents, the distribution of the midpoints along the soil profile showed the same trends of median depth function (Fig. 19.4), where clay content slightly increases with the depth, in contrast to sand and silt. However, the boxplot graph (Fig. 19.7) better represents the range of values beyond the frequency of data. According to Fig. 19.7c, d, sand and silt content decreased with depth, although the variability of sand in the diagnostic horizons (A and B) was greatest. Generally, the AB horizon showed greater particle size variability, when compared with other horizons, even the BA, which by definition is similar to the B-horizon regarding to morphological properties.

Based on the analysis and observations from field survey, the most-likely horizon depth can be generalized as the following: A (0–15 cm), AB (15–30 cm), BA (30–45 cm), B (45–150 cm), and BC (85–200 cm). The superposition of B and BC horizons will be addressed by aggregation soil data with different depth intervals. Nevertheless, the lower probability of BC horizon occurrence has to be considerate based on the frequency of data from the collection.

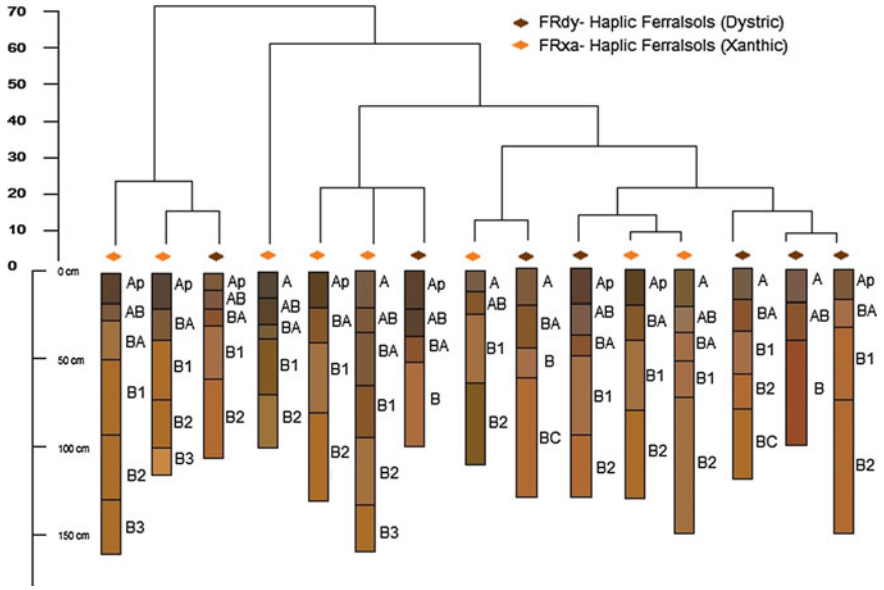

Fig. 19.8 Similarity among the fifteen Ferralsols from Guapi-Macacu watershed, Rio de Janeiro

Representative Soil Profile (Similarity and Variability of Soil Texture Parameters)

The comparison of the taxonomic classes can be based on similarity analysis between soil profiles through divisive hierarchical clustering, assuming that a soil order represents a large collection of profiles that can be split into smaller groups (Kaufman and Rousseeuw 2005; Beaudette et al. 2013). In this sense, dendrograms and sketches were created to compare the soil profiles supporting analysis of similarities and differences between the two Ferralsols taxonomic classes (Fig. 19.8). The horizontal axis (*X*) of Fig. 19.8 organizes the pairwise dissimilarities based on clay, sand, and silt contents, while the vertical (*Y*) represents the depths of horizons according to field soil horizon description. The upper scale on the left side corresponds to numerical dissimilarity based on sand, silt, and clay content.

The Haplic Ferralsols (Xanthic)—FRxa usually show deeper profiles than the Haplic Ferralsols (Dystric)—FRdy, in the data collection from the Guapi-Macacu watershed. In addition, FRxa showed a sequence of B-horizons, extending beyond 150 cm depth, with small variability of the particle size parameters. In contrast, FRdy presented shallowest profiles, in some cases, with BC horizon showing signs of the altered granite/gneiss parental material.

Analysis of similarity among profiles can contribute to quantitative comparison between soils and landscape conditions. In that way, it may be a useful tool to individualize taxonomic subgroups and review the outline and composition of soil

mapping units; always supported by additional analyses due to the scale and regional characteristics of landscape. Quantitative methods based on soil profile characteristics (morphometrics), combined with terrain analysis could also improve the designation of criteria for family and series in taxonomic systems, such as in the Brazilian Soil Classification System, where these taxonomic levels are still undeveloped. Furthermore, this approach makes easier to include legacy data through the taxonomic correspondence to representative profiles, even with data from different classification systems.

The particle size parameters of "modal" Ferralsols in the Guapi-Macacu watershed, with values of mean, median, and harmonized (spline function) data, aggregated at predefined depths and as most-likely inferred horizon depths are presented in Table 19.1.

The Ferralsols topsoil layer can be generalized to the 30 cm depth, corresponding to the first three layers of harmonized dataset with GlobalSoilMap project (six predefined depths), and first two most-likely inferred horizon (corresponding to A/Ap horizons plus the transitional AB). Consequently, the subsurface horizon is placed from 30 to 150 cm depth, where the characteristics reflecting pedogenesis are more intensively expressed. In this sense, texture components as described by layers B1, B2, B3, and B4 (45–150 cm depth) are representing the modal B-horizon used as a diagnostic criterion to soil classification.

The soil properties values from the deepest layer in both aggregation procedures (150–200 cm) are representing less than half of dataset collection. Thus, the occurrence of a transitional horizon BC is considered, as well as, the probability of a sequence of B-horizons. Particular conditions of parental material exposure and landscape forms observed on the field survey were the main factors defining soil thickness.

The clay content in the topsoil layer (0–30 cm depth or A/Ap plus AB horizon) varies between 32 and 40 %, while sand values range from 49 to 53 % (less than 50 g kg^{-1} variation). The combination of soil particle size components shows dominance of clay loam texture in the Ferralsols topsoil layer. The transitional AB and BA horizons (15–45 cm depth) showed, in general, a slight increase in clay (around 3% more clay), with relative values ranging from 38 to 43 %. At the same time, sand values ranged from 49 (AB) to 42 % (BA), showing more variability in the transitional layers (around 7 %).

The diagnostic B-horizons had clay values clay from 43 to 47 % in the subsurface (45–150 cm). When a large sequence of B-horizons was observed, the clay values reached up to 50 % in the deepest horizons (below 1.5 m depth). Sand content, in general, showed slightly decreasing values with depth, varying from 40 to 55 % in the subsurface layers (Ferralsols diagnostic horizons).

The silt content varied from 15 to 20 % in the topsoil, and from 10 to 13 % in the subsurface, showing a linear trend with depth. Below the sequence of B-horizons, the probability of the occurrence of a transitional BC horizon (around 1 m depth), related to a slight increase of silt content, has to be considered, but it is usually restricted to a particular soil-landscape condition. However, the silt content had low contribution to soil texture when compared with other particle sizes. The

Table 19.1 Values of mean, median, and harmonized (spline function) data, aggregated at predefined depths and as most-likely inferred horizon depths

Modal profile texture values—GlobalSoilMap project predefined depths												
*	Sand content (g/kg)				Clay content (g/kg)				Silt content (g/kg)			
	Mean	Median	Spline	Range	Mean	Median	Spline	Range	Mean	Median	Spline	Range
1	519.5	510.0	527.5	510.0–527.5	335.7	325.0	320.1	320.1–335.7	144.7	138.0	152.4	138.0–152.4
2	519.6	510.0	522.3	510.0–522.3	340.1	325.0	337.8	325.0–340.1	140.3	134.5	139.9	134.5–140.3
3	490.7	487.0	492.7	487.0–492.7	387.6	408.0	385.8	385.8–408.0	121.7	120.0	121.4	120.0–121.7
4	449.6	421.0	451.3	421.0–451.3	434.5	428.0	433.7	428.0–434.5	155.9	113.0	115.0	113.0–115.9
5	410.0	413.0	408.8	408.8–413.0	465.8	450.0	466.0	450.0–466.0	124.2	105.0	125.1	105.0–125.1
6[a]	419.1	413.0	387.9	387.9–419.1	480.4	450.0	478.7	450.0–480.4	100.5	98.0	133.4	98.0–133.4
Modal profile texture values—most-likely horizon depth												
**	Sand content (g/kg)				Clay content (g/kg)				Silt content (g/kg)			
	Mean	Median	Spline	Range	Mean	Median	Spline	Range	Mean	Median	Spline	Range
A	519.6	510.0	524.0	510.0–524.0	338.6	325.0	331.9	325.0–338.6	141.8	138.0	144.1	138.0–144.1
AB	490.7	487.0	492.7	487.0–492.7	387.6	408.0	385.8	385.8–408.0	121.7	120.0	121.4	120.0–121.7
BA	458.0	431.0	451.3	431.0–458.0	423.6	428.0	433.7	423.6–433.7	118.4	114.0	115.0	114.0–118.4
B1	441.3	415.0	451.3	415.0–451.3	445.4	445.0	433.7	433.7–445.4	113.3	112.0	115.0	112.0–115.0
B2	414.6	411.0	408.8	408.8–414.6	464.2	450.0	466.0	450.0–466.0	121.2	102.0	125.1	102.0–121.2
B3	402.4	413.0	408.8	402.4–413.0	468.4	450.0	466.0	450.0–468.4	129.2	105.0	125.1	105.0–129.2
B4[b]	419.0	413.0	387.9	387.9–419.0	479.0	450.0	478.7	450.0–479.0	102.0	98.0	133.4	98.0–133.4
B5[c]	421.5	421.5	387.9	387.9–421.5	506.5	506.5	478.7	478.7–506.5	72.0	72.0	133.4	72.0–133.4

*Aggregate data as GlobalSoilMap project depth. 1: 0–5 cm, 2: 5–15 cm, 3: 15–30 cm, 4: 30–60 cm, 5: 60–100 cm, 6: 100–200 cm. **Aggregate data as probability intervals (most-likely inferred horizon). A: 0–15 cm, AB: 15–30 cm, BA: 30–45 cm, B1: 45–60 cm, B2: 60–85 cm, B3: 85–100 cm, B4: 100–150 cm, B5: 150–200 cm. Contributing fraction to mean and median functions corresponding to: [a]0.4333; [b]0.4933; [c]0.1333. Other layers = 1.0

combination of sand, clay, and silt showed a trend of clay texture related to the subsurface layer of Ferralsols in Guapi-Macacu watershed.

The type of horizon transition (contrast and thickness) is key information for taxonomic purposes, highlighting gradients between morphological and physical properties, contributing to characterize diagnostic horizons and modal profiles. As observed on Table 19.1 and Fig. 19.7 (midpoints depth analysis), the Ferralsols transitional horizons were omitted, or misinterpreted, when the aggregation procedure is based on the six predefined depths as suggested by the GlobalSoilMap project, instead when the data are aggregated by most-likely horizon depth. The results show that the slicewise method can be used to balance the variability of soil horizons by depth considering the natural distribution of soil properties along the profile.

The predefined depths as proposed by the global consortium are useful to support decisions regarding land use and management. However, for soil taxonomic purposes, a different approach may be needed to represent the diagnostic horizons criteria, considering variability of soil properties with depth. As example, the transitional horizons of the Ferralsols showed no necessary correspondence with the predefined depths (GlobalSoilMap project), justifying a different approach, such as aggregation based on most-likely horizons probability.

The slicewise aggregation allowed to study different "representative depth functions" to characterize sand, silt, and clay content of the Ferralsols profiles. This approach contributed to transpose the concept of modal soil profile into an assemblage of representative depth functions, as suggested by Beaudette et al. (2013).

In this sense, soil depth models to represent the variability of properties with depth is a promising tool to taxonomic purposes and to support land usage decisions, improving the products obtained from soil surveys and reaching a greater number of users.

19.4 Conclusions

The process of examining data using the slicewise aggregation method and equal-area spline function was useful for comparing soil properties and taxonomic classification. The mid-depth horizon and soil properties depth function analysis showed the most-likely horizons of Ferralsols in the Guapi-Macacu watershed corresponding to: A (0, 15 cm), AB (15–30 cm), BA (30–45 cm), B (45–150 cm), and BC (85–200 cm). In general, the Haplic Ferralsols (Xanthic) showed deeper soil profiles and with more clay in subsurface horizons, compared with the Haplic Ferralsols (Dystric).

The Ferralsols topsoil layer presents commonly clay loam texture, and the subsurface is clayey. The modal profile showed representative values varying between 32 and 50 % of clay, 40 and 55 % of sand, and 10 and 20 % of silt.

The application of depth functions to evaluate the particle size variability of Ferralsols in Guapi-Macacu watershed showed that the slicewise aggregation technique can elucidate the distribution of continuous properties and to support definition of representative functions and their relationship with diagnostic horizons.

Haplic Ferralsols (Xanthic) and Haplic Ferralsols (Dystric) have a wide occurrence in the watershed, and they diverge mostly by landscape and parental material resulting in morphological and morphometric differences in color, texture, and thickness. The visualization by sketches and pairwise dissimilarity of the fifteen soil profiles showed a potential application of the procedure for soil taxonomy and mapping.

The evaluation of particle size variation and content as criteria of Ferralsols diagnostic horizons helps to build quantitative parameters to improve the Brazilian Soil Classification System and other taxonomic systems as well.

References

Arrouays D, Vion I, Kicin JL (1995) Spatial analysis and modeling of topsoil carbon storage in temperate forest humic loamy soils of France. Soil Sci 159:191–198

Arrouays D, McKenzie N, Hempel J, de Forges AR, McBratney AB (eds) (2014) GlobalSoilMap: basis of the global spatial soil information system. CRC Press

Beaudette DE, Roudier P, O'Geen AT (2013) Algorithms for quantitative pedology: a toolkit for soil scientists. Comput Giosci 52:258–268

Bishop TFA, McBratney AB, Laslett GM (1999) Modelling soil attribute depth functions with equal-area quadratic smoothing splines. Geoderma 91:27–45

Dantas JRC, Almeida JR, Lins GA (2008) Environmental impacts in the watershed of Guapi-Macacu and its consequences for the water supply in the municipalities of eastern Guanabara Bay. (In Portuguese). Série Gestão e Planejamento Ambiental. (Coleção Artigos Técnicos nº7). CETEM/MCT. Rio de Janeiro, RJ. 26 p

Dick DP, Gonçalves CN, Dalmolin RSD, Knicker H, Klamt E, Kögel-Knabnerc I, Simões ML, Martin-Neto L (2005) Characteristics of soil organic matter of different Brazilian Ferralsols under native vegetation as a function of soil depth. Geoderma 124(3–4):319–333. doi:10.1016/j.geoderma.2004.05.008

Empresa Brasileira de Pesquisa Agropecuária. EMBRAPA. Centro Nacional de Pesquisa de Solos (1997) Manual de métodos de análise de solo. Rio de Janeiro: Centro Nacional de Pesquisa de Solos—CNPS. 212p. (Embrapa-CNPS. Documentos. 1)

Fernandez-Illescas CP, Porporato A, Laio F, Rodriguez-Iturbe I (2001) The ecohydroogical role of soil texture in a water-limited ecosystem. Water Resour Res 37(12):2863–2872

Ferrari AL (2001) Evolução Tectônica do Gráben da Guanabara. Tese de Doutoramento. Instituto de Geociências, USP, São Paulo

Hartemink AE, Hempel J, Lagacherie P, McBratney A, McKenzie N, MacMillan RA, Zhang GL (2010) GlobalSoilMap.net–a new digital soil map of the world. In: Digital soil mapping. Springer, Netherlands, pp. 423–428

IUSS Working Group WRB (2014) World reference base for soil resources 2014. World Soil Resources Reports No. 106. FAO, Rome. World Reference Base for Soil Resources. WRB. World Reference Base for Soil Resources (2014) FAO, Rome. 191 p. (World Soil Resources Reports, No. 106)

Jenny H (1980) The soil resource, origin and behaviour. Springer, New York. 377 p

Kaufman L, Rousseeuw PJ (2005) Finding groups in data an introduction to cluster analysis. Wiley-Interscience

Klingebiel AA (1963) Land classification for use in planning. Agriculture Yearbook. U.S. Department of Agriculture, Washington, DC, pp 399–407

Köppen W (1948) Climatologia: com un estudio de los climas de la tierra. (In Espanish). Fondo Cultura Econômica. Panuco, México. 479 p

Malone BP, Minasny B, McBratney AB (2009) Mapping continuous soil depth functions in the Edgeroi District, NSW, Australia, using terrain attributes and other environmental factors, proceedings of geomorphometry. Malone

McBratney AB, Odeh I, Bishop T, Dunbar MS, Shatar TM (2000) An overview of pedometric techniques for use in soil survey. Geoderma 97:293–327

Moore ID, Gessler PE, Nielsen GA, Peterson GA (1993) Soil attribute prediction using terrain analysis. Soil Sci Soc Am J 57:443–452

Odgers NP, Libohova Z, Thompson JA (2012) Equal-area spline functions applied to a legacy soil database to create weighted-means maps of soil organic carbon at a continental scale. Geoderma 189–190:153–163p

Pedreira, BCCG, Fidalgo ECC, Abreu MB (2009) Mapeamento do uso e cobertura da terra da bacia hidrográfica do rio Guapi-Macacu, RJ. Anais XIV Simpósio Brasileiro de Sensoriamento Remoto, pp 2111–2118, Natal, Brasil, INPE, 25–30 Apr 2009

Pereira W, Tanaka OK (1984) Elementos de estatística. McGraw-Hill do Brasil, São Paulo, p 309p

Pinheiro HSK, Anjos LHC, Chagas CS (2013) Mapeamento Digital de Solos por Redes Neurais Artificiais -Estudo de Caso: Bacia Hidrográfica do Rio Guapi-Macacu, RJ. NovasEdiçõesAcadêmicas—NEA. OmniScriptumGmbH & Co. Saarbrücken, Germany

Ponce-Hernandez R, Marriott FHC, Beckett PHT (1986) An improved method for reconstructing a soil profile from analyses of a small number of samples. J Soil Sci 37:455–467

Projeto Macacu (2010) Strategic plan to the hydrographic region of Guapi-Macacu and Caceribu-Macacu rivers. (In Portuguese). UFF/FEC. Niterói, RJ. 544 p

R Development Core Team (2013) R: a language and environment for statistical computing. R Foundation for Statistical Computing, Vienna. Available at: http://www.r-project.org/isbn3-900051-07-0. Accessed 8 May 2013

Santos HG, Jacomine PKT, Anjos LHC, Oliveira VA, Lumbreras JF, Coelho MR, Almeida JA, Cunha TJF, Oliveira JB (2013) Sistema Brasileiro de Classificação de Solos -SiBCS (Brazilian System of SoilClassification) 3rd edn. Rio de Janeiro. Embrapa Solos, Rio de Janeiro, Brazil

Silver WL, Neff J, McGroddy M, Veldkamp E, Keller M, Cosme R (2000) Effects of soil texture on belowground carbon and nutrient storage in a lowland Amazonian forest ecosystem. Ecosystems 3:193–209. doi:10.1007/s100210000019

Sposito G (1989) The chemistry of soils. Oxford Univ. Press, New York, 215 p

Thompson JA, Roecker S, Grunwald S, Owens PR (2012) Digital soil mapping: interactions with and applications. In: Hydropedology. 1st edn. pp 665–709

Webster R, Oliver M (1990) Statistical methods in soil and land resource survey. Oxford University Press

Chapter 20
Comparing Soil C Stocks from Soil Profile Data Using Four Different Methods

Benito R. Bonfatti, Alfred E. Hartemink and Elvio Giasson

Abstract Soil organic carbon (SOC) concentration differs by depth, soils, and distinct land uses. Different methods have been used to calculate SOC stocks, and here, we used data from 10 pedons from Southern Brazil to compare four methods: horizon values with discrete data, exponential function, equal-area exponential function, and equal-area quadratic spline function. SOC stocks were calculated up to 30 cm and 100 cm depth from (i) the original data, (ii) the standardized data based on equal mass, (iii) the standardized data based on equal mass minus coarse fragments (gravels). Results were compared calculating SOC stocks up to 30 and 100 cm depth. Discrete values by horizon produced mean SOC stocks for 30 and 100 cm depth of 6.9 and 14.6 kg/m^2 for original values, 6.5 and 14.1 kg/m^2 for standardized values by mass, and 6.3 and 13.5 kg/m^2 for standardized values by mass minus gravels. Negative exponential functions produced mean values of 6.1 and 14.1 kg/m^2 for original values, 5.6 and 13.3 kg/m^2 for standardized values by equal mass, and 5.4 and 12.9 kg/m^2 for standardized values by equal mass minus gravels. Equal-area exponential function had mean values of 7.1 and 14.5 kg/m^2 for original values, 6.6 and 13.9 kg/m^2 for standardized values by equal mass, and 6.4 and 13.5 kg/m^2 for standardized values by equal mass minus gravels. Equal-area spline produced SOC averages of 6.8 and 14.7 kg/m^2 for original values, 6.3 and 14.2 kg/m^2 for standardized values by equal mass, and 6.1 and 13.7 kg/m^2 for standardized values by equal mass minus gravels. From the comparison, we found that negative exponential functions produced lower SOC stocks than horizons in the

B.R. Bonfatti · E. Giasson
Universidade Federal do Rio Grande do Sul, UFRGS—Faculdade de Agronomia,
Av. Bento Gonçalves, 7712, Porto Alegre, RS 91540-000, Brazil
e-mail: brbonfatti@yahoo.com.br

B.R. Bonfatti · A.E. Hartemink (✉)
Department of Soil Science, FD Hole Soils Lab, University of Wisconsin—Madison,
1525 Observatory Drive, Madison, WI 53706, USA
e-mail: hartemink@wisc.edu

B.R. Bonfatti
CAPES Grand Holder—Process BEX 3095/14-2, CAPES Foundation,
Ministry of Education of Brazil, Brasília, DF 70040-020, Brazil

A.E. Hartemink and B. Minasny (eds.), *Digital Soil Morphometrics*,
Progress in Soil Science, DOI 10.1007/978-3-319-28295-4_20

upper layers and higher stocks than horizons in the lower layers; equal-area exponential produced SOC stocks that are statistically similar to horizon values; equal-area spline function produced values up to 30 cm depth statistically similar to horizon values and statistically different up to 100 cm depth. We can conclude that different methods for calculating SOC stocks by depth produce significantly different results and values derived from equal-area exponential and equal-area splines are more similar to those of the horizons.

Keywords SOC · Spline · Exponential function · Soil equal mass

20.1 Introduction

The levels of soil organic carbon (SOC) and its distribution by depth are related to the climate, vegetation cover, soil type, geomorphology, and agricultural activities. High-precipitation areas commonly with dense vegetation result in the accumulation of soil carbon. The opposite occur in soils of dry areas which, in addition to not having enough moisture, the carbon is bound to calcium and immobile (Schaetzl and Anderson 2005). There is considerable variation in SOC levels across the landscape. Valleys' bottoms may receive erosional sediments from upper areas, forming deep soil profiles with buried A horizons. Agricultural activities largely affect carbon stocks. Tillage and no-tillage practices result in different SOC distribution (Angers and Eriksen-Hamel 2008; Sisti et al. 2004).

There are only few studies that consider carbon up to 100 cm depth (Minasny et al. 2013). Most studies have data up to 30 cm soil depth, which is the standard IPCC depth and relevant to agriculture crops. To assess the amount of carbon below 30 cm it is needed to comprehend the SOC dynamics under different tillage systems (Angers and Eriksen-Hamel 2008; Sisti et al. 2004) or its distribution by depth under different land uses (Guo and Gifford 2002; Jobbágy and Jackson 2000).

Comparison of SOC under different environmental conditions is complicated as the data are often from discrete horizons. Knowledge and interpretation about carbon accumulation is facilitated when data are continuous across the soil. The continuous distribution of properties can give a new insight into diagnostic horizons and may even result in the formation of new classes (Hartemink and Minasny 2014).

Representing SOC by mathematical functions provides continuous values by depth and gives SOC for fixed or ranges of depths. Recent studies have used the equal-area spline function (Adhikari et al. 2014; Malone et al. 2009; Odgers et al. 2012), which models local quadratic polynomials functions (Bishop et al. 1999; Ponce-Hernandez et al. 1986). Other methods have used exponential decay functions (Minasny et al. 2006; Mishra et al. 2009; Zinn et al. 2005), and they assume that carbon concentration decreases exponentially with depth. Studies have also used exponential functions based on horizon data, considering area equivalence similar to equal-area splines (Kempen et al. 2011).

The quantification of SOC stocks includes the variation of bulk density and the content of coarse fragments (e.g., gravel). Miscalculation of SOC stocks occurs when bulk density is altered by compaction or when a reduction in bulk density following tillage is not considered. The SOC stocks under different bulk densities must be corrected by thickness variance (Ellert and Bettany 1995) or standardized by cumulative mass coordinates (Gifford and Roderick 2003). Moreover, when calculating SOC stocks, the amount of coarse fragments should be considered.

This study analyzed four methods for calculating soil carbon stocks up to 30 and 100 cm depth: (a) distribution by horizon, (b) distribution by exponential function, (c) distribution by equal-area exponential function, and (d) distribution by equal-area spline function. The discrete values by horizon use data directly from the database, and the functions use midpoint data from each horizon. The methods were separated into 3 groups: (I) original values, (II) values standardized by equal mass, and (III) values standardized by equal mass minus gravels.

20.2 Materials and Methods

20.2.1 The Soils

We have used the SOC and bulk density data from 10 soil profiles collected in Vale dos Vinhedos (Vineyard Valley) in northeastern Rio Grande do Sul State, Brazil. This area has a mean annual precipitation of 1736 mm and mean annual temperature of 17.2 °C. The climate is classified as Cfb (EMBRAPA 2008). Some of the soils are gravelly (Flores et al. 2012) and dominant soils are Inceptisols, and smaller areas with Ultisols, Mollisols, Entisols, Alfisols, and Oxisols. Most soils are covered by forest or used as vineyards.

The data of 10 profiles (Table 20.1) were extracted from the soil survey report by Flores et al. (2012) and complemented with soil bulk density measurements made in 2014. The bulk density was measured in different soils and land uses (vineyard, forest/planted forest, pasture, arable crops, and fallow). The soils were sampled by soil horizon and SOC was analyzed by Walkley-Black (Flores et al. 2012; Santos et al. 2006).

20.2.2 Methods

In this study, we used four methods for calculating carbon stocks up to 30 and 100 cm depth. The punctual bulk density values were interpolated by smooth splines and the results were calculated using each centimeter. The values were average and assigned to each respective horizon. The horizons' midpoints were used to interpolate the functions. Details of each method are presented below.

Table 20.1 Description of the 10 pedons from the study area in Vale dos Vinhedos in Rio Grande do Sul, Brazil

Pedon	Reference Pedon (Flores et al. 2012)	Horizon	Depth (cm)	SOC (g/kg)	Bulk density[a] (Mg/m^3)	Coarse fragments (%)	Soil class	Land use
1	4	Ap	0–15	19.8	1.15	16	Orthents	Vineyard
		CR	15–35	15.1	1.17	6		
2	5	Ap	0–16	16.7	1.17	0	Udepts	Vineyard
		Bi	16–36	7.4	1.21	0		
		BC	36–50	5.5	1.22	0		
3	27	Ap	0–23	13.8	1.14	1	Udults	Vineyard
		AB	23–55	5.7	1.21	19		
		Bt1	55–74	3.9	1.23	0		
		Bt2	74–120	2.9	1.25	0		
4	28	Ap	0–30	14.7	1.20	0	Humults	Vineyard
		Bt1	30–72	13.8	1.24	1		
		Bt2	72–120/140	8.6	1.17	0		
		C	120/140–200	2.8	1.17	0		
5	53	Ap1	0–30	37.3	0.97	0	Udoxs	Forest
		A2	30–55	26.7	1.06	0		
		Bt1	55–90	14.4	1.18	0		
		Bt2	90–200	6	1.23	0		
6	78	Ap	0–35	25.5	1.03	0	Udepts	Forest
		Bi	35–90	22.6	1.19	0		
		CR	90–150	15	1.28	75		
7	99	Ap	0–28	12.3	1.15	28	Udalfs	Pasture
		Bt	28–61	5.9	1.21	0		
		BC	61–100	4.3	1.25	0		
8	118	Ap	0–39	17.2	1.33	0	Humults	Arable crops
		AB	39–73	12.5	1.37	0		
		Bt1	73–120	10.4	1.28	0		
		Bt2	120–200	6.7	1.28	0		
9	119	Ap	0–24	43.3	1.20	0	Udepts	Fallow
		Bi	24–55	5.2	1.29	23		
		C1	55–85	2.5	1.30	0		
		C2	85–150	2	1.17	0		
10	141	Ap	0–30	21.2	1.09	0	Humults	Planted forest
		BA	30–60	11.8	1.25	0		
		Bt1	60–110	11.1	1.38	0		
		Bt2	110–200	6.2	1.30	0		

[a]Bulk density samples were taken at different depths; values in the table correspond to derivate values for each horizon, from smooth spline functions

Discrete Values by Horizon

In this method, we used the discrete horizon values from the database, without interpolations. Bulk density, carbon content (g/kg), and thickness (up to 30 and 100 cm) from each horizon were multiplied for getting the SOC stocks.

Exponential Function

The exponential function has been used in mapping carbon by depth because of its mathematical ease and apparent similarity to soil profile changes with depth found for most soil properties (Minasny et al. 2006). The negative exponential function can summarize the profile data in three parameters allowing the use of more easy measured or widely available data (Minasny et al. 2006).

The negative exponential function is given as follows:

$$C = C_a \exp(-kz) + C_b \tag{20.1}$$

With conditions C_a, C_b, $k > 0$, where C is the organic carbon content in volume basis (kg/m^3), z is the absolute value of depth from the soil surface, C_a is the difference in carbon content between the surface and the lowest depth, $(C_a + C_b)$ is the carbon content at the soil surface, C_b is the carbon content at the bottom of the profile, and k is the rate of carbon decrease with depth.

To apply the equation, the bulk density values (kg/m^3) were multiplied by SOC concentration (kg C/kg). The calculated SOC (kg/m^3) were used as input values to the function, which parameter k was fitted by nonlinear least squares.

Equal-Area Exponential Function

The equal-area exponential functions have similarities with the equal-area smoothing spline where for each horizon the area fitted to the left of the fitted curve is equal to the area to the right, so the function represents the average value for a horizon. It does not always guarantee mass conservation as in equal-area splines, but it has better mass-conserving properties than a decay exponential function fitted to the midpoints of the soil horizons (Kempen et al. 2011).

For this approach, first the components C_a and k were fitted, minimizing the sum of squared differences between the observed and the predicted SOC stocks for each horizon, by the model:

$$0 = \sum_{i=1}^{n} \left[\left(\frac{C_a}{k} \right) \left[\exp\left(-kz^*_{Li}\right) - \exp\left(-kz^*_{Ui}\right) \right] - C_{li} \right]^2 \tag{20.2}$$

where z^*_{Li} is the depth of the lower boundary of soil horizon i in a soil profile, n is the number of soil horizon, z^*_{Ui} is the depth of the upper boundary soil horizon i, and C_{li} is the observed SOC stock of horizon i.

The exponential function was defined with the fitted C_a and k values, by the equation:

$$C = C_a \exp(-kz) \tag{20.3}$$

The equation needs at least three points to be solved. For soil profile 1 that has only two horizons, the deepest horizon was divided into two parts and the midpoint of each part was taken.

Equal-Area Spline Function

The equal-area spline function produces a continuous function showing the SOC distribution by depth and attempts to negate the damping effects of using discrete data from horizons (Bishop et al. 1999; Ponce-Hernandez et al. 1986). The key characteristics described by Bishop et al. (1999) are as follows:

1. It consists of a series of local quadratic polynomials with the "knots" or positions of joins being located at horizon boundaries.
2. For each horizon, the area to the left of the fitted spline curve above the horizon average (X) is equal to the area to the right of the fitted spline curve below the horizon average (Y), thus ensuring the mean value of the horizon is maintained.

Malone et al. (2009) used the equal-area smoothing spline, which is a generalization of the quadratic spline model of Bishop et al. (1999). First, the spline functions produce continuous data, then the values are again combined in different depth intervals, by averages.

In the spline method, summarily, $f(x)$ represents a spline depth function and can be solved by minimizing the following:

$$\frac{1}{n}\sum_{i=1}^{n}\left(y_i - \overline{f_i}\right)^2 + \lambda \int_{x_0}^{x_n} [f'(x)]^2 \mathrm{d}x, \tag{20.4}$$

$$\text{where} \quad y_i = \overline{f_i} + e_i \tag{20.5}$$

The first term of Eq. (20.4) represents the fit to the data, and the second, the roughness of spline function. The parameter λ controls the trade-off between the fit and the roughness penalty; n is the number of layers in a soil profile; depth is denoted by x. The y_i represents the measurement of bulk sample from layer i, and $\overline{f_i}$ is the mean value of $f(x)$ over each layer. The errors e_i in Eq. (20.5) are assumed independent, with mean 0 and common variance σ^2 (Bishop et al. 1999). The function $f(x)$ and its first derivative $f'(x)$ are both continuous and $f'(x)$ is square integrable.

In our study, the spline functions were solved similarly to the method described in Malone et al. (2009) and using $\lambda = 1$. Spline functions were calculated for SOC content (g/kg), bulk density (g/cm^3), and coarse fragments (%), for each of the 10 soil profiles.

20.2.3 Correcting for Mass and Coarse Fragments

SOC stocks were calculated for each method until 30 and 100 cm depth. Then, the values were combined in three different groups. The first groups had the original calculated values. The second group had the values standardized by equal mass, and in the third group the values were standardized by mass minus coarse fragments (gravel).

Standardization by mass was used to make comparisons possible among soils with different bulk densities. We used the method described by Gifford and Roderick (2003) with a cumulative mass coordinates approach. Cumulative soil mass (kg/m^2) was calculated by multiplying the soil bulk density and thickness of each horizon (or 1 cm when using continuous functions). Similarly, it was used to determine cumulative SOC stocks. The soil mass under forest was chosen as a reference. Hence, cumulative mass of the two profiles under forest (profiles 5 and 6) was averaged and the value was used in the following equation for correcting SOC stocks applied to each horizon or 1 cm:

$$c_s(t) = c_s(z_a) + \frac{c_s(z_b) - c_s(z_a)}{m_s(z_b) - m_s(z_a)}(m_s(t) - m_s(z_a)) \tag{20.6}$$

where $c_s(t)$ is the value of cumulative SOC stocks corrected by mass; $c_s(z_a)$ and $m_s(z_a)$ are the values of cumulative SOC stocks and mass, respectively, from the lower boundary of the horizon above it; $c_s(z_b)$ and $m_s(z_b)$ are the cumulative SOC stocks and mass of the lower boundary of the current horizon (or centimeter); $m_s(t)$ is the cumulative soil mass from the lower depth of the reference horizon. For the continuous functions, the values were determined by each centimeter, instead of horizons.

The third group of SOC calculations used the cumulative SOC stocks corrected by coarse fragments (gravels and stones) to standardize by mass using the procedure described above.

20.2.4 Statistical Analysis

Two statistical ways were used to compare the total SOC stocks up to 30 and 100 cm depth, considering the four different methods: (a) assigned by horizon, (b) negative exponential function, (c) equal-area exponential function, and (d) equal-area spline function, and divided into 3 groups: (1) original values, (2) values standardized by mass, and (3) values standardized by mass minus gravels (coarse fragments).

The first analysis compared different methods within the same group using repeated measure ANOVA as the samples are dependent. For paired comparisons, the post hoc Bonferroni test and multiple dependent t-test for paired samples were used. The second analysis compared the same method in different groups using the post hoc Bonferroni test for paired comparisons.

20.3 Results and Discussion

The different methods used to interpolate carbon with depth showed distinct curve (Fig. 20.1). Results differ significantly depending on how the function fits to the SOC variation.

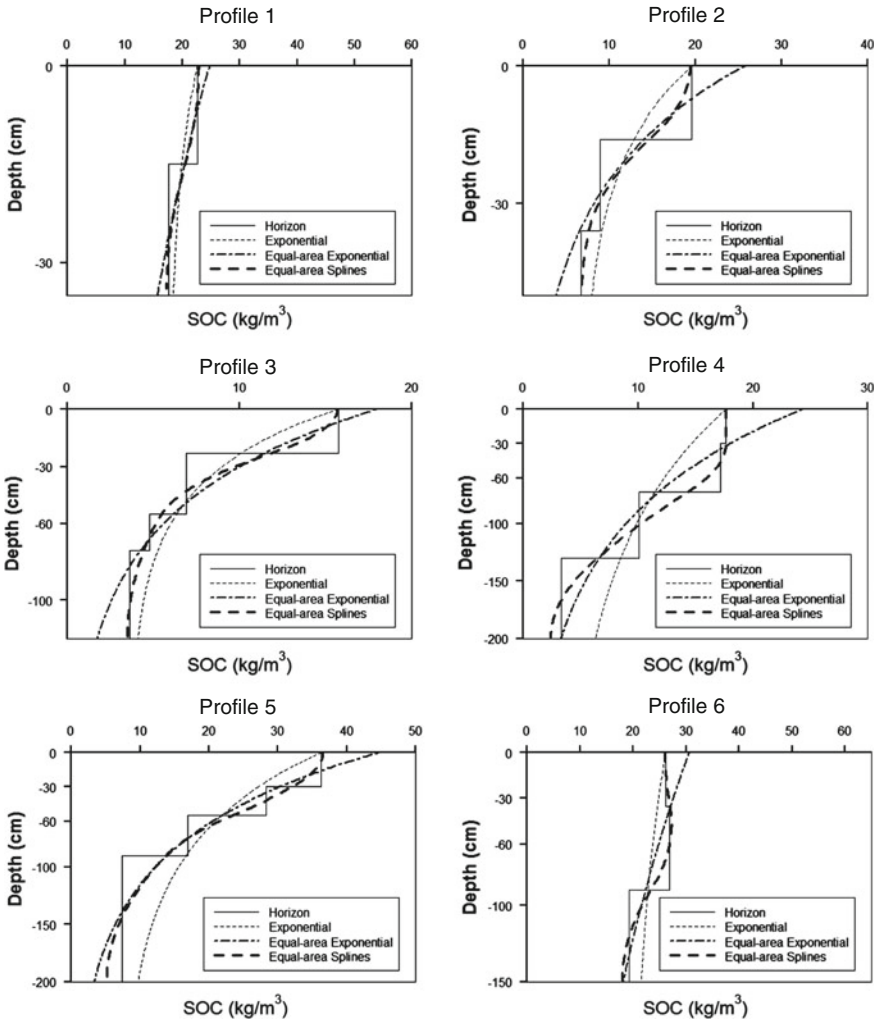

Fig. 20.1 SOC concentration (kg/m^3) by four different methods

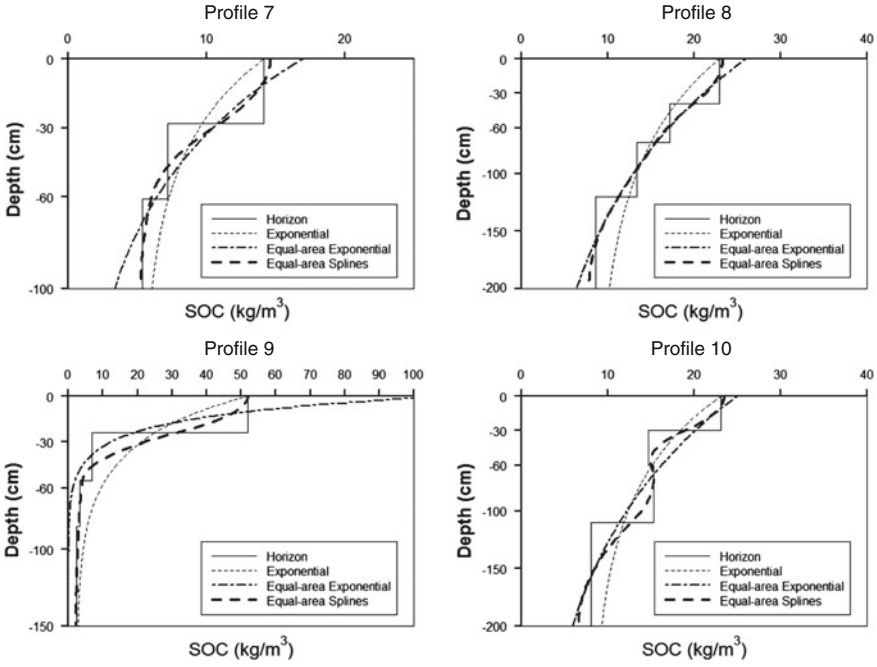

Fig. 20.1 (continued)

20.3.1 The 4 Methods

Discrete Values by Horizon

This method used information directly from SOC analysis by horizon. The graphs assume the aspect of "stairs" (Fig. 20.1) which make it difficult to view the smoothness of carbon variation by depth.

The averages of SOC stocks up to 30 and 100 cm depth were, respectively, 6.9 and 14.6 kg/m^2 for original values, 6.5 and 14.1 kg/m^2 for standardized values by mass, and 6.3 and 13.5 kg/m^2 for standardized values by mass minus coarse fragments.

Exponential Function

The exponential function shows a continuous exponential decrease of carbon with depth. The equation is less complex than equal-area exponential or spline method but the curve adjusting is more limited. It initializes at 0 cm depth interpolating with values of mid-horizon. The curves show lower values than horizons for upper

depths and higher for lower depths (Fig. 20.1) producing a lower average of total SOC stocks (Fig. 20.3).

This approach produced the lowest SOC stocks up to 30 cm depth or 100 cm depth. The averages of SOC stocks up to 30 and 100 cm depth were, respectively, 6.1 and 14.1 kg/m^2 for original values, 5.6 and 13.3 kg/m^2 for standardized values by mass, and 5.4 and 12.9 kg/m^2 for standardized values by mass minus coarse fragments.

Equal-Area Exponential Function

The equal-area exponential function showed SOC stocks very similar to stocks calculated by horizons up to 30 cm and up to 100 cm. Starting points of the curves have values higher than SOC values of top horizons. In some soils, as in profile 9, the initial values look exaggerated. For other profiles considering continuous SOC variation with depth, the initial values seem more reasonable.

This approach produced the highest SOC stocks up to 30 cm. The averages of SOC stocks up to 30 and 100 cm depth were, respectively, 7.1 and 14.5 kg/m^2 for original values, 6.6 and 13.9 kg/m^2 for standardized values by mass, and 6.4 and 13.5 kg/m^2 for standardized values by mass minus coarse fragments.

Equal-Area Spline Function

The equal quadratic splines show that curves fit well to discrete distribution (Fig. 20.1). The curves start at or very close to surface with the SOC value from the top horizon. This approach produced the highest SOC stocks up to 100 cm depth. The averages of SOC stocks up to 30 cm and 100 cm depth were, respectively, 6.8 and 14.7 kg/m^2 for original values, 6.3 and 14.2 kg/m^2 for standardized values by mass, and 6.1 and 13.7 kg/m^2 for standardized values by mass minus coarse fragments.

20.3.2 Correction by Mass and Coarse Fragments

The values of SOC stocks were corrected by mass (Fig. 20.2) and for coarse fragments. The 30 and 100 cm depths were marked to facilitate comparisons. Horizontal lines show total SOC stocks up to 30 and 100 cm depth for the reference soil mass. There is a difference between original values and standardized values by mass. Observing the points stressing the values up to 30 and 100 cm depth, the SOC stocks have lower values when using standardized mass.

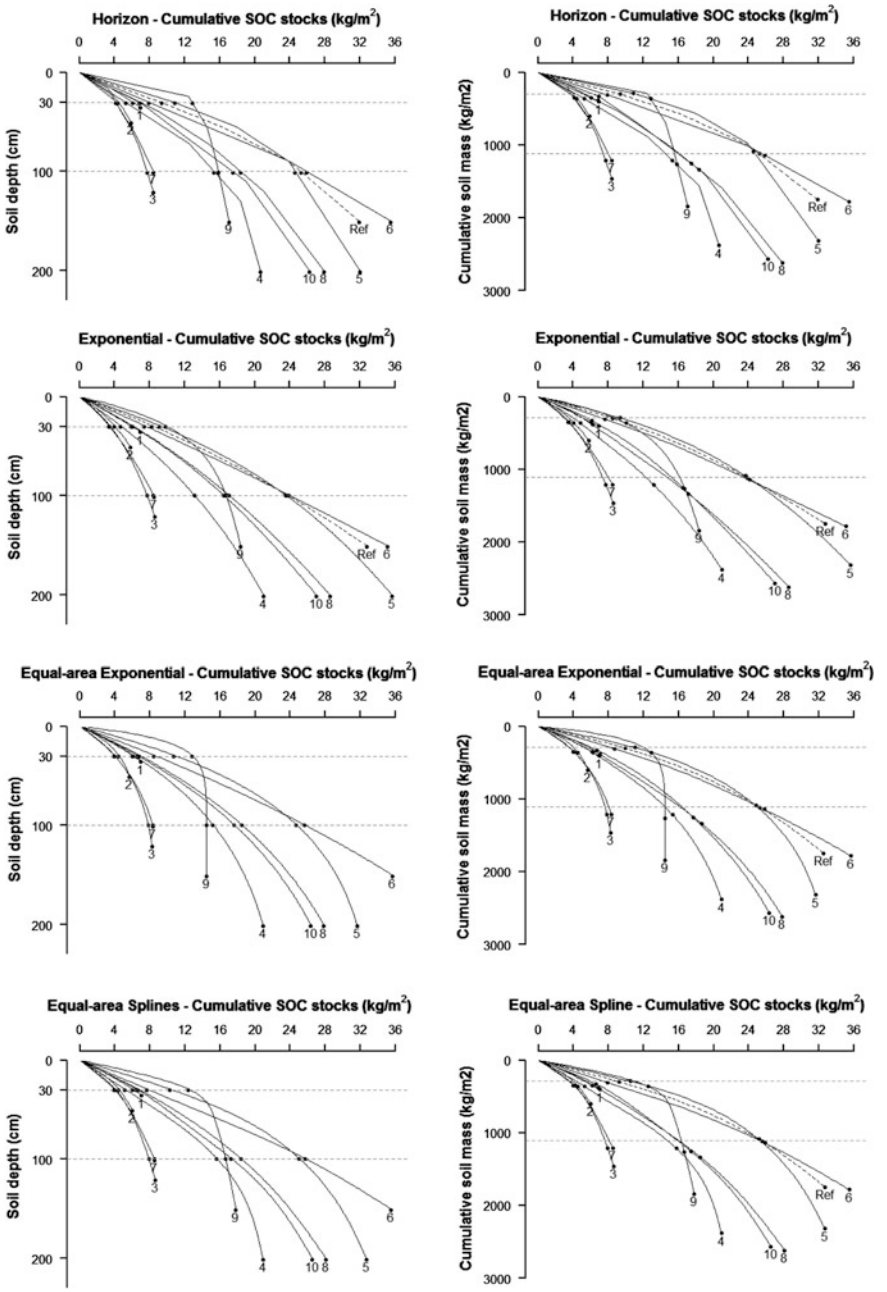

Fig. 20.2 SOC stocks standardized by cumulative mass for 10 soil profiles. The reference line (Ref) is the average of profiles 5 and 6 (under forest) used for SOC stocks comparisons by same accumulate mass. *Horizontal dashed lines* show the cumulative soil mass for 100 and 30 cm of the reference depth. The points indicate the SOC stocks on the 30, 100 cm and depth of each profile

20.3.3 Statistical Analysis

The average total SOC stock is different for each method and group. The highest average total SOC stock up to 30 cm depth, 7.1 kg/m^2, was found using original values interpolated by equal-area exponential function. The lowest average SOC stock up to 30 cm depth, 5.4 kg/m^2, was calculated using standardized values by mass minus gravels and the exponential function. The highest average total SOC stock up to 100 cm depth, 14.7 kg/m^2, was found using original values interpolated by equal-area spline function. The lowest average SOC stock up to 100 cm depth, 12.9 kg/m^2, was calculated using standardized values by mass minus gravels and the exponential function. This considerable difference between different methods and standardization results in significantly different quantification of SOC stocks.

The first analysis compared the four different methods within the same group. In the group with original values, the repeated measured ANOVA with multiple *t*-test showed similarity between the horizon values and the equal-area exponential and spline functions, until 30 cm (Fig. 20.3). When considering the depth up to 100 cm,

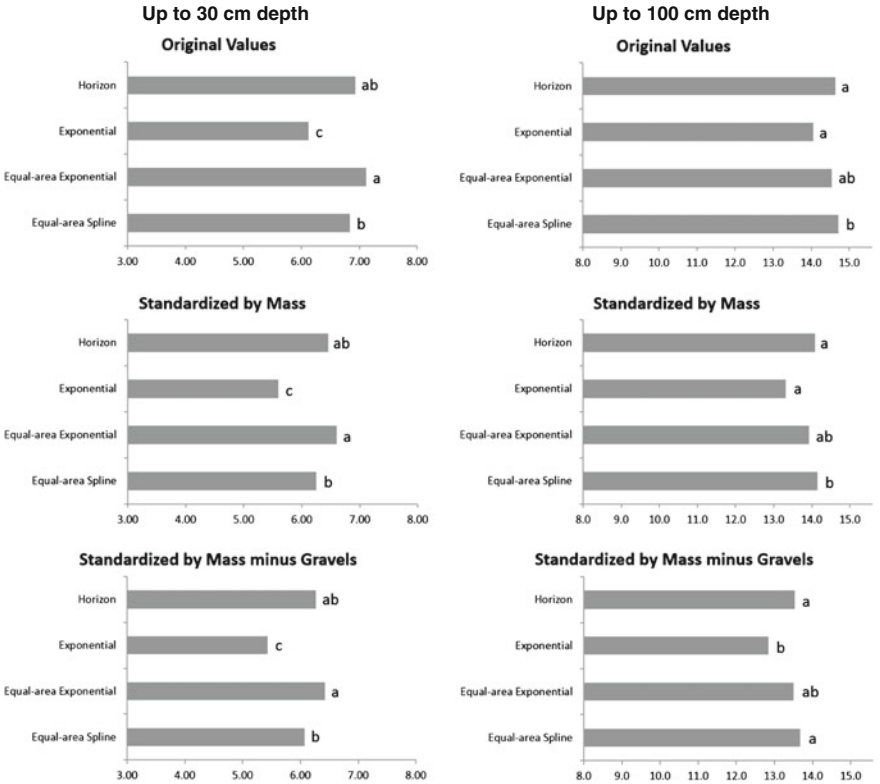

Fig. 20.3 Average SOC stocks (kg/m^2) of 10 soil profiles and statistical comparison between four different methods combined in three groups. Multiple dependent *t*-test for paired samples was used for statistical analysis

equal-area exponential function and discrete values by horizon yield similar results. However, the equal-area spline function is not similar to horizon values as in depth up to 30 cm. The equal-area spline curve, for some profiles, was cut on 100 cm depth, sectioning the interpolation next to half horizon. This considers only the initial part of the fitted curve at respective horizon and the values were not balanced by the final part. As the initial part has higher values than the final, a higher average was found. This difference was reduced when the values were standardized by mass and corrected by gravels.

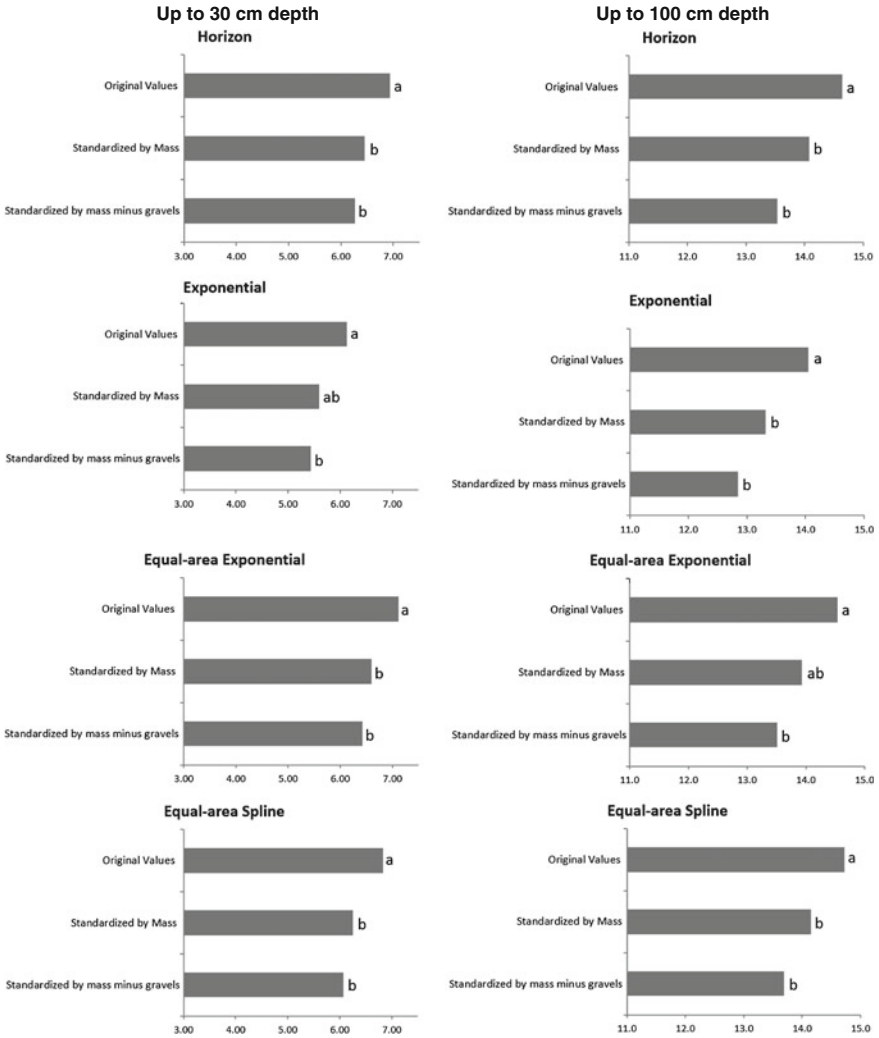

Fig. 20.4 Average SOC stocks (kg/m^2) of 10 soil profiles for each method by different groups. Repeated measure ANOVA with post hoc Bonferroni correction was used for statistical analysis

The results found in values standardized by mass and standardized by mass minus gravels were similar.

The second analysis comparing the same methods in different groups showed that the values standardized by mass and mass minus gravels are statistically similar (Fig. 20.4). When both are compared to the original values, the results differ.

The analysis is complementary and confirms that original data produced significantly different results than standardized data. Different functions can produce different results, independently of the standardization.

The characteristic of each function needs to be considered during the choice of the function and interpretation of the results. When using discrete values, the continuous carbon variation on the profiles is not considered. Negative exponential function tends to produce lower values than horizons in upper layers and higher values at greater depths and lower SOC stocks of the profile. Equal-area exponential and equal-area splines produce SOC stocks similar to horizon values. Differences may appear when the function is not considering the initial and the final balance part of the curve and this generally increases the values.

20.4 Conclusions

From this analysis, the following can be concluded:

- Different functions for calculating SOC by depth produce significantly different results.
- The highest average total SOC stock up to 30 cm depth, 7.1 kg/m^2, was found in the original values interpolated by equal-area exponential function. The lowest average SOC stock up to 30 cm depth, 5.4 kg/m^2, was calculated using standardized values by mass minus gravels and the exponential function.
- The highest average total SOC stock up to 100 cm depth, 14.7 kg/m^2, was found in original values interpolated by equal-area spline function. The lowest average SOC stock up to 100 cm depth, 12.9 kg/m^2, was calculated using standardized values by mass minus gravels and the exponential function.
- Equal-area exponential and equal-area splines produce SOC stocks similar to horizon values, primarily when considering the initial and final parts of the fitted curve by each horizon.
- Values standardized by mass and mass minus gravels yield significantly different results compared to original values.

References

Adhikari K, Hartemink AE, Minasny B, Bou Kheir R, Greve MB, Greve MH (2014) Digital mapping of soil organic carbon contents and stocks in Denmark. PLoS ONE 9:e105519. doi:10.1371/journal.pone.0105519

Angers DA, Eriksen-Hamel NS (2008) Full-inversion tillage and organic carbon distribution in soil profiles: a meta-analysis. Soil Sci Soc Am J 72:1370–1374

Bishop TFA, McBratney AB, Laslett GM (1999) Modelling soil attribute depth functions with equal-area quadratic smoothing splines. Geoderma 91:27–45

Ellert BH, Bettany JR (1995) Calculation of organic matter and nutrients stored in soils under contrasting management regimes. Can J Soil Sci 75:529–538. doi:10.4141/cjss95-075

EMBRAPA (2008) Normal Climatológica: Estação Agroclimática da Embrapa Uva e Vinho, Bento Gonçalves, RS. Período de 1961 a 1990. http://www.cnpuv.embrapa.br/

Flores CA, Pötter RO, Sarmento EC, Weber EJ, Hasenack H (2012) Os Solos do Vale dos Vinhedos. EMBRAPA, Brasília, DF, Brazil

Gifford RM, Roderick ML (2003) Soil carbon stocks and bulk density: spatial or cumulative mass coordinates as a basis of expression? Glob Change Biol 9:1507–1514

Guo LB, Gifford RM (2002) Soil carbon stocks and land use change: a meta analysis. Glob Change Biol 8:345–360. doi:10.1046/j.1354-1013.2002.00486.x

Hartemink AE, Minasny B (2014) Towards digital soil morphometrics. Geoderma 230–231:305–317. doi:10.1016/j.geoderma.2014.03.008

Jobbágy EG, Jackson RB (2000) The vertical distribution of soil organic carbon and its relation to climate and vegetation. Ecol Appl 10:423–436

Kempen B, Brus DJ, Stoorvogel JJ (2011) Three-dimensional mapping of soil organic matter content using soil type–specific depth functions. Geoderma 162:107–123. doi:10.1016/j.geoderma.2011.01.010

Malone BP, McBratney AB, Minasny B, Laslett GM (2009) Mapping continuous depth functions of soil carbon storage and available water capacity. Geoderma 154:138–152. doi:10.1016/j.geoderma.2009.10.007

Minasny B, McBratney AB, Mendonça-Santos ML, Odeh IOA, Guyon B (2006) Prediction and digital mapping of soil carbon storage in the Lower Namoi Valley. Aust J Soil Res 44:233. doi:10.1071/SR05136

Minasny B, McBratney AB, Malone BP, Wheeler I (2013) Digital Mapp Soil Carbon 118:1–47. doi:10.1016/b978-0-12-405942-9.00001-3

Mishra U, Lal R, Slater B, Calhoun F, Liu D, Van Meirvenne M (2009) Predicting soil organic carbon stock using profile depth distribution functions and ordinary kriging. Soil Sci Soc Am J 73:614. doi:10.2136/sssaj2007.0410

Odgers NP, Libohova Z, Thompson JA (2012) Equal-area spline functions applied to a legacy soil database to create weighted-means maps of soil organic carbon at a continental scale. Geoderma 189–190:153–163. doi:10.1016/j.geoderma.2012.05.026

Ponce-Hernandez R, Marriott FHC, Beckett PHT (1986) An improved method for reconstructing a soil profile from analyses of a small number of samples. J Soil Sci 37:455–467

Santos HG, Jacomine PK, dos Anjos LHC, de Oliveira VA, de Oliveira JB, Coelho MR, Lumbreras JF, Cunha TJF (2006) Sistema Brasileiro de Classificação de Solos, 2nd edn. Embrapa Solos, Rio de Janeiro

Schaetzl RJ, Anderson S (2005) Soils genesis and geomorphology. Cambridge University Press, Cambridge

Sisti CPJ, dos Santos HP, Kohhann R, Alves BJR, Urquiaga S, Boddey RM (2004) Change in carbon and nitrogen stocks in soil under 13 years of conventional or zero tillage in southern Brazil. Soil Tillage Res 76:39–58. doi:10.1016/j.still.2003.08.007

Zinn YL, Lal R, Resck DVS (2005) Texture and organic carbon relations described by a profile pedotransfer function for Brazilian Cerrado soils. Geoderma 127:168–173. doi:10.1016/j.geoderma.2005.02.010

Chapter 21
Evaluation of Pedotransfer Equations to Predict Deep Soil Carbon Stock in Tropical Podzols Compared to Other Soils of the Brazilian Amazon Forest

O.J.R. Pereira, C.R. Montes, Y. Lucas and A.J. Melfi

Abstract According to the soil measurement procedures proposed by the Intergovernmental Panel on Climate Change (IPCC), the sampling depth for SOC stock estimation is centred on the upper soil horizons where root biomass and organic matter inputs are concentrated, depending on soil type and ecosystem, typically between 0 and 0.3 m. However, recent research in areas of Amazonian Podzols has shown that these soils store a great amount of carbon in thick spodic horizons (Bh). The amount of carbon stored in deep Bh horizons of Podzols (down to 3 m) may exceed 80 kg C m^{-2} in some regions of the Amazon. Thus, a better understanding of the vertical distribution of the SOC in Amazonian soils is an urgent matter considering the volume of carbon stored in Podzols, in a context of global climate change. Given this, the main goal of this research was to test and to propose pedotransfer functions based on several Amazonian soil profiles in order to estimate SOC stock and evaluate different soil attributes that could be used to infer indirectly, soil bulk density. For this propose, we selected around 320 pedons that were collected in the region of the Rio Negro Basin, to model the vertical distribution of SOC stock using a series of negative exponential profile depth functions and parametric/nonparametric functions for Podzols. The derived function parameters were used to predict carbon stock in deep horizons for all studied profiles and to explain the vertical behaviour of the SOC stock in Podzol profiles. The soil bulk density of Amazonian soils was properly modelled by symbolic regression, considering pH, clay content and SOC as the most relevant variables likely to affect soil bulk density values. We observed that the SOC stored in deep horizons of non-podzolic soils can be modelled by exponential decay equations. However, in Podzol, the vertical distribution of carbon stock is highly complex with a

O.J.R. Pereira (✉) · C.R. Montes
CENA, NUPEGEL, Universidade de São Paulo, Piracicaba, São Paulo, Brazil
e-mail: ojrpereira@cena.usp.br

Y. Lucas
PROTEE, Université de Toulon, La Garde, Provance, France

A.J. Melfi
IEE, ESALQ, Universidade de São Paulo, São Paulo, Brazil

A.E. Hartemink and B. Minasny (eds.), *Digital Soil Morphometrics*,
Progress in Soil Science, DOI 10.1007/978-3-319-28295-4_21

significant increase in deep horizons, which cannot be explained by negative exponential functions. Our findings have shown that the SOC stock of Amazonian soils, excluding Podzols, can be predicted by fitted exponential functions (RMSE: 0.9 kg C m^{-2}). However, the vertical variation of SOC stored in Podzol profiles can be modelled just by complex equations (equal-area spline RMSE: 13.6 kg C m^{-2}; Fourier RMSE 15.9 kg C m^{-2} and Sum of Sines RMSE: 15.0 kg C m^{-2}) with a large number of parameters. According to the results achieved in this research, we concluded that the SOC stock of Podzols can be indirectly estimated for the whole soil profile by integrating the Sum of Sines and Fourier equations, which is not possible when applying an equal-area spline fitting due to the absence of model parameters. Moreover, spodic horizons store most of the carbon pool of podzolic regions and the Podzols have more than twice of the capability of storing carbon when compared to other Amazonian soils.

Keywords Soil organic carbon stock · Podzols · Amazon forest · Pedotransfer equations

21.1 Introduction

The Brazilian tropical Podzols cover 1.36 10^5 km^2 of the Amazon forest, which represents 2.7 % of the total area of the Amazon biome and around 20 % of the soils of the Rio Negro Basin. The other important soil group in this region comprises ferralitic soils (Acrisols and Ferralsols) that cover 55 % of the Rio Negro Basin. The remaining soil groups are related to alluvial and litholic soils as well as scattered hydromorphic Plinthosols. Such diversity of soil types reflects on the capacity of the Amazon biome on storing soil organic carbon (SOC), especially in regions of Podzols. According to recent research, the Amazonian Podzols (Montes et al. 2011) store about 13.6 ± 1.1 PgC, which is at least 12.3 PgC higher than previous estimations (Bernoux et al. 2002; Batjes and Dijkshoorn 1999) that have considered soil depths down to 0.3 m.

Several surveys have investigated the capability of soils to store and retain SOC (Post et al. 1982; Buringh 1994; Kimble 1990; Eswaran et al. 1993; Batjes 1996), but present research usually considers a fixed soil depth, typically based on the topsoil 0.2 or 0.3 m, where the highest SOC concentrations usually occur (Burke et al. 1989). Batjes (1996) reported a 60 % increase in the global SOC pool when the second metre of soil was included, taking into account the FAO (2012) soil classification system. A few studies of the Amazon forest (Montes et al. 2011; Pereira et al. 2015) have described the capability of Podzols in storing high amounts of C in deep spodic (Bh) horizons. These soils have an average stock of 70 kg C m^{-2} and around 80.9 % of its C is stored in thick deep Bh horizons in depths ranging from 2 m to more than 5 m (Montes et al. 2011; Pereira et al. 2015).

The vertical pattern of SOC content in Podzols is highly complex when compared to other Amazonian soils, with a significant increase in thick Bh horizons (Montes et al. 2011). Negative depth exponential function has been successfully applied in several mineral soils to model and predict C stock. However, any local variation affects the quality of the exponential fit everywhere else in the soil profile, as observed by Webster (1978). In this context, the modelling of Podzol SOC stock can be carried out by nonparametric depth function (e.g. equal-area spline) that can result in satisfactory adjustment, but with the disadvantage of not providing any parameters that would allow model generalizations (Bishop et al. 1999). The summarization of the model by parameters is essential to allow an indirect estimation of the SOC in Podzols and to explain the behaviour of C along the soil profile, by means of a general approach.

Traditionally, the amount of *C* stored in soil is obtained as *C* mass per unit area according to a specific profile depth (T_p). The calculation is carried out by summing the *C* stock (kg C m^{-2}) of the measured soil layers (*1, 2, ..., N*). Thus, the content of C to a given soil profile can be obtained by the following equation:

$$C_s = \sum_{p=1}^{N} \left(C * \rho_p\right) * T_p \tag{21.1}$$

where C_s is the carbon stock (kg C m^{-2}) to a given profile; *C* is the carbon content in mass basis (kg C kg^{-1}); ρ_p is the soil bulk density (g cm^{-3}); and T_p is the layer thickness. Another option to obtain the C_s value is through the application of a profile depth function fitted to the soil C data in a volumetric basis (kg C m^{-3}) according to specific measured soil layers (T_p). The integration of the function is applied in order to obtain the SOC stock (kg C m^{-2}) for the whole profile. The expression of C content as depth function is useful to estimate the C stock down to certain depths and to standardize databases where soil depths are sampled to layers randomly distributed (Arrouays and P'elissier 1994; Minasny et al. 2006).

Parametric Pedotransfer functions (PTF) are widely used in soil science to predict several soil attributes based on the empirical equations that result in function parameters that can be easily applied to measure soil attributes (Mcbratney et al. 2003). Given this, the main goal of this research was to test and to propose PTF in several Amazonian soil profiles (IBGE 2008; EMBRAPA 2014) in order to estimate SOC stock (C_s) and evaluate different soil attributes that could be used to infer indirectly, soil bulk density (ρ_p).

21.2 Methodology

The methods adopted in this research are divided into two general steps. The indirect estimation of soil bulk density by the evaluation of traditional PTF (Bernoux et al. 1998; Tomasella and Hodnett 1998; Benites et al. 2007) was

compared to the ones developed in the frame of this research. The second step was focused on the estimation of SOC stock by the application of curve-fitting models based on different approaches, taking into account the behaviour of SOC along the soil profiles of Podzols and other Amazonian soils.

21.2.1 Field Sample Data

The studied area is located in the Amazonia State, Brazil (Fig. 21.1). The soil database used in this study was provided by IBGE (2008) and EMBRAPA (2014) as well as collected in the field surveys developed by this research (Fig. 21.1).

The soil profiles in Fig. 21.1 are divided into three groups. The "Podzol Sample Areas" represent the profiles collected by this study in the regions of equatorial Podzols of the Rio Negro Basin (393 sampled layers in 18 profiles). The "soil bulk density PTF" profiles (Fig. 21.1) refer to the soil profiles provided by EMBRAPA (2014), which were used to develop the soil bulk density PTF (668 sampled layers in 129 profiles). Due to the scarcity of samples in Rio Negro Basin, we decided to use soil profiles in the entire Amazon state to validate the bulk density PTF. The SOC stock was estimated in profiles limited to the region of the Rio Negro Basin based on database provided by IBGE (2008), illustrated in Fig. 21.1 by the "SOC PTF" group (1442 sampled layers in 324 profiles).

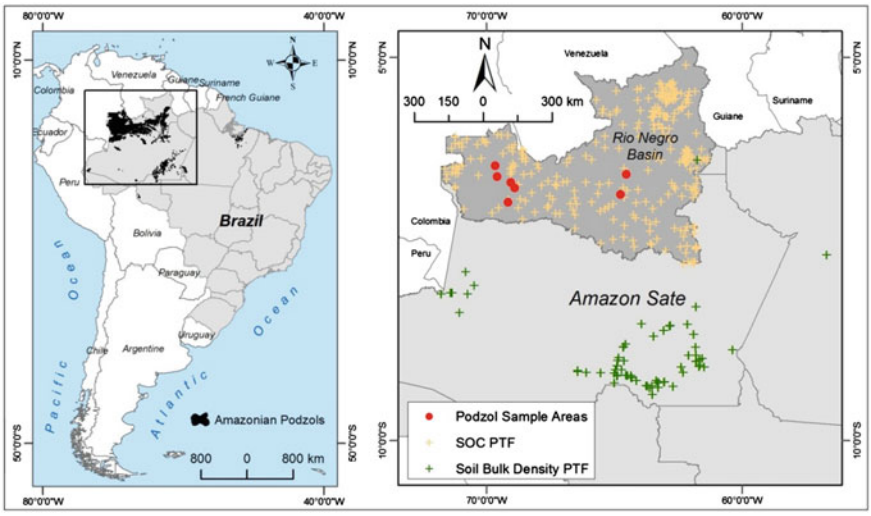

Fig. 21.1 Situation of the studied area highlighting the location of the soil sample profiles used in this study

EMBRAPA Soil Database

All samples provided by EMBRAPA contain values of soil pH (water and KCl); organic carbon by dichromate method (SOC); total nitrogen by Kjeldahl digestion; iron oxide (Fe_2O_3); titanium oxide (TiO_2); aluminium oxide (Al_2O_3) and silicon oxide (SiO_2) by strong acid digestion; exchangeable cations (Ca^{2+}, Mg^{2+}, and Al^{3+}) by 1 N KCl; soluble potassium and phosphorus by Mehlich 1 method (0.05 N HCl in 0.025 N H_2SO_4). Soil physical data consisted of particle size measurements, comprising sand (2.00–0.05 mm), silt (0.05–0.002 mm) and clay (<0.002 mm) measured by the hydrometer method using Na-hexametaphosphate as chemical dispersant; soil bulk density by the core method and water dispersible clay (WDC). A complete description of the EMBRAPA soil database can be found in EMBRAPA (2011).

IBGE Soil Database

The IBGE (2008) soil database was developed in the frame of the "Systematization of Natural Resources Information" project coordinated by the Natural Resources and Environmental Studies division/IBGE (CREN). The information of each soil sample was standardized in a harmonized soil geodatabase, which allows interface with GIS (Geographic Information Systems). The samples are divided by horizons according to the Brazilian Soil Classification System (EMRAPA 2011). The database contains the same information presented in the EMBRAPA soil database (EMBRAPA 2011). However, there are no soil bulk density values available for any of the sampled profiles. A full description of the IBGE soil database can be found in IBGE (2008).

21.2.2 Estimation of Soil Bulk Density

In Podzol region (Fig. 21.1), the soil bulk density was directly determined by the Kopeck ring method described by Blake et al. (1986). The remaining soil orders have their bulk density values estimated and validated based on the EMBRAPA (2014) database. Two aspects were considered to select the most reliable PTF: the versatility of the proposed equation and the soil information available in the two databases used in this study (IBGE 2008; EMBRAPA 2014). The PTF equations were developed and evaluated using the artificial programming tool *Eureqa* (Schmidt and Lipson 2009). The database was divided into two datasets (training Dataset 1 and validation Dataset 2).

Table 21.1 Descriptive statistics of the soil attributes of the training and validation datasets (Datasets 1 and 2)

	Dataset 1					Dataset 2				
Soil attribute	Valid cases	Min	Max	Mean	S.D.[a]	Valid cases	Min	Max	Mean	S.D.[a]
Corse sand (g kg^{-1})	654	1.0	704.0	162.6	160.1	230	10.0	620.0	201.7	134.6
Fine sand (g kg^{-1})	654	1.0	883.0	219.3	206.0	230	10.0	620.0	243.1	174.8
Total sand (g kg^{-1})	654	2.0	988.0	381.8	284.9	230	20.0	950.0	444.9	266.4
Silt (g kg^{-1})	654	2.0	806.0	214.6	168.1	230	20.0	482.0	116.1	91.1
Clay (g kg^{-1})	654	10.0	880.0	403.6	228.7	230	20.0	960.0	439.1	246.8
pH	654	3.3	7.4	4.9	0.7	230	3.6	7.3	5.3	0.9
K^+ ($cmol_c$ kg^{-1})	654	0.0	1.0	0.1	0.1	230	0.0	1.0	0.1	0.2
SiO_2 (g kg^{-1})	654	0.0	325.0	109.5	65.2	230	8.7	379.0	147.7	93.2
Al_2O_3 (g kg^{-1})	654	0.0	426.0	129.3	72.6	230	6.9	345.1	150.9	101.3
Fe_2O_3 (g kg^{-1})	654	0.0	467.0	55.5	50.6	230	1.4	259.0	60.9	59.1
SOC (g kg^{-1})[b]	654	0.2	115.5	8.5	10.7	230	0.2	46.7	8.0	7.8
N (g kg^{-1})	654	0.1	4.7	0.9	0.8	230	0.1	10.0	0.9	1.2
C/N (%)	654	0.0	96.0	8.3	7.4	230	0.1	27.0	10.0	4.7
ρ_p (g cm^{-3})[c]	654	0.8	1.9	1.3	0.2	230	0.9	1.8	1.3	0.2

[a]Standard deviation
[b]Total organic carbon
[c]Measured soil bulk density

The independent soil dataset 2 was used in order to compare the proposed model (Dataset 1) with the ones presented in the previous research (Bernoux et al. 1998; Tomasella and Hodnett 1998; Benites et al. 2007). Therefore, there is no redundancy between Datasets 1 and 2. The Dataset 2 contains 230 soil samples of profiles collected in different regions of Brazilian Amazon forest (EMBRAPA 2014) excluding the samples collected in the region of the Amazonia state. The descriptive statistics of the soil attributes used to generate the PTF are summarized in Table 21.1.

Unlike previous studies regarding the development of PTF in the Amazon region (Bernoux et al. 1998; Tomasella and Hodnett 1998; Benites et al. 2007), we applied symbolic regression (SR) analysis (Koza 1992) in order to generate PTF equations. SR is a powerful machine-learning modelling technique introduced by Koza (1991). Different from linear and nonlinear regression methods, symbolic regression searches both the parameters and the form of equations, which allows the automatic generation of symbolic regression functions (Schmidt and Lipson 2009).

We used the coefficient of determination (r^2), the mean squared error (MSE), the root mean square error (RMSE) and Akaike's Information Criterion (AIC) in order to access the accuracy of the proposed PTF against the ones presented in previous

research, considering the independent Dataset 2 (Table 21.1). MSE, RMSE and AIC are defined as follows:

$$\mathrm{MSE} = \frac{1}{n}\sum_{i=1}^{n}(\hat{\rho}_i - \rho_i) \tag{21.2}$$

$$\mathrm{RMSE} = \sqrt{\frac{1}{n}\sum_{i=1}^{n}(\rho_i - \hat{\rho}_i)^2} \tag{21.3}$$

$$\mathrm{AIC} = \mathrm{Nln}\left[\frac{1}{n}\sum_{i=1}^{n}(\rho_i\hat{\rho}_i)^2\right] + 2P \tag{21.4}$$

where $\hat{\rho}_i$ and ρ_i are the observed and predicted soil bulk density values, respectively, i is the soil sample, P is the number of parameters used, n is the total number of observations and Nln is the natural logarithm. The better model is with MSE and RMSE values closer to 0 and the smaller AIC value.

21.2.3 Modelling the Vertical Distribution of SOC

The prediction of soil bulk density values based on PTF was critical to allow the estimation of SOC stock in the region of Rio Negro Basin due to the absence of ρ_p values in IBGE soil database (IBGE 2008). The ρ_p values were applied to convert SOC content from a mass basis (kg C kg^{-1}) to a volume basis (kg C m^{-3}). The resulting values were used to predict SOC stock (kg C m^{-2}) in selected profiles (Fig. 21.1). We divided the database into two datasets according to the fitting functions applied to model the vertical distribution of SOC stock: (i) Dataset A which comprises soil profiles that can have their SOC stock modelled by exponential decay equations; (ii) Dataset B, referent to samples collected in field (Podzols), where the vertical distribution of SOC stock cannot be explained by exponential decay equations. The methods concerning each dataset are described below.

Exponential Depth Function: Dataset A

The following negative exponential function was fitted for each sample point in the calibration dataset from the surface to variable soil depth according to each soil profile:

$$C = C_i * \exp^{\left(\frac{-z}{b}\right)} + y_0 \tag{21.5a}$$

where C_i is the SOC content in volume basis (kg C m^{-3}); z is the soil depth (m) for a given horizon; b is the SOC decay constant and y_0 is the absolute value of depth (m). The integral of Eq. 21.5a (Eq. 21.5b) represents C stock to depth z (d_z):

$$C_t = \int_0^{d_z} \left(C_i * \exp^{\left(\frac{-z}{b}\right)} + y_0 \right) \tag{21.5b}$$

where C_t is the amount of organic C stored per unit area (kg C m^{-2}). Integrating Eq. 21.5b, the C stock from the soil surface to depth $z(d_z)$ is given by the Eq. 21.5c:

$$C_t = -C_i b \exp^{\left(\frac{-z}{b}\right)} + y_0 d_z + C_i b \tag{21.5c}$$

Equation 21.5c was applied to estimate C stock in all profiles excluding regions of Podzols. The equation parameters (C_i, z, b and y_0) were predicted individually for each profile with variable d_z values according to the soil depth of each observed profile. We used 25 soil profiles provided by IBGE (2008) to validate the negative exponential function (Eq. 21.5c). Thus, the parameters for the 25 validation profiles were generated to 1 m soil depth in order to predict SOC stock to a 3 m soil depth. The validation was based on measured values (IBGE 2008) down to 3 m soil depth.

Podzol Depth Functions: Dataset B

The soil samples provided by the two systematic databases available in the Amazon (IBGE 2008; EMBRAPA 2014) have an insignificant number of profiles collected in Podzol areas. Moreover, the sampling soil depth is always up to 2 m, which is limited to the topsoil (O/A horizons), elluvial (E) horizon and the first centimetres of the spodic horizon (Bh). Given this, we collected samples in different regions of Podzols, totalizing 18 soil profiles (Fig. 21.1). For each profile, we have collected from 12 to 36 samples (layers), taking into account deep/thick spodic horizons (from 4.5 to 6 m soil depth).

The vertical distribution of SOC stock was modelled according to three fitting models: (i) Nonparametric equal-area splines (Bishop et al. 1999); parametric; (ii) Sum of Sines; and (iii) Fourier periodic fitting models (Renshaw and Ford 1984). It is important to highlight that periodic fitting models were not applied in previous researches related to vertical distribution of SOC stock. Usually, soil attributes have a vertical behaviour that cannot be explained by periodic models. However, we observed that Podzols can have their vertical SOC content distribution fitted in these models due to a specific pattern along the soil horizons. A brief description of the Podzol fitting models is presented below.

Equal-area splines: The spline model assumes that soil attributes vary smoothly with depth, which is translated into mathematical terms by denoting depth by z, and the depth function describing the true attribute values by $f(z)$. Given this, $f(z)$ and its first derivative $f_0(z)$ are both continuous, and $f_0(z)$ is square integrable. The depths

of the boundaries of the n layers or soil horizons are given by z_0 ($<z_1$; …; $< z_n$). Thus, the measurements of C_i ($i = 1$; …; n) are mathematically modelled as follows:

$$C_i = \bar{f}_i + e_i, \tag{21.6}$$

where $\bar{f}_i = \int_{z_{i-1}}^{z_i} f(z)dz/(x_i x_{i-1})$ is the mean value of $f(z)$ considering the interval $(x_i x_{i-1})$. The errors are assumed independent, with mean 0 and common variance σ^2. $f(z)$ denotes a spline function that can be determined by minimizing:

$$\frac{1}{n}\sum_{i=1}^{n}(C_i - f_i)^2 + \lambda \int_{z_0}^{z_n} f'(z^2)dz \tag{21.7}$$

The first term describes the model fit to data and the second one measures the roughness of function $f(z)$, expressed by its first derivative $f_0(z)$. Parameter λ controls the trade-off between the fit and the roughness penalty. The solution is a linear–quadratic smoothing spline (Bishop et al. 1999). The values of SOC were included on the model as volumetric basis (kg C m^{-3}). The total SOC stock of each profile (kg C m^{-2}) was calculated summing the resulting values of the fitted model. Bishop et al. (1999) has already discussed the methods to establish a proper λ value. Given this, we considered a standardized λ value of 0.1.

Fourier series fitting: Specific Fourier models were developed for each Podzol profile, considering the sums of sine and cosine functions (Eq. 21.8) assuming the behaviour of SOC along the profile as a periodic signal to a limited soil depth. The Fourier series to n terms is given by:

$$C = a_0 + \left(\sum_{i=1}^{n} a_i \mathrm{COS}(iwz) + b_i \mathrm{SEN}(iwz)\right) \tag{21.8}$$

where a_0 models an intercept term in the data and is associated with the $i = 0$ cosine term, w is the fundamental frequency of the signal, n is the number of terms in the series and limited to $1 \leq n \leq 8$, z is the soil depth interval. We applied four terms in order to achieve the best model adjustment. The resulting parameters were used to estimate the SOC stock in the whole profile, after applying the integration of the Fourier series (Eq. 21.9).

$$C_t = \int_0^{d_z} \left(a_0 + \sum_{i=1}^{n} \mathrm{a}_i \mathrm{COS}(iwz) + b_i \mathrm{SEN}(iwz)\right) \tag{21.9}$$

where C_t is the amount of organic C stored per unit area (kg C m^{-2}) and d_z refers to the profile depth. After integrating the 4 terms of the Fourier series function to d_z depth, we obtained the following equation:

$$C_t = \frac{0.25a_4 \sin(4wd_z)}{w} - \frac{0.25b_4 \cos(4wd_z)}{w} + \frac{0.333a_3 \sin(3wd_z)}{w} - \frac{0.333b_3 \cos(3wd_z)}{w} + \frac{0.5a_2 \sin(2wd_z)}{w} - \frac{0.5b_2 \cos(2wd_z)}{w} + \frac{1a_1 \sin(wd_z)}{w} - \frac{1b_1 \cos(wd_z)}{w} + 1a_0 d_z + \frac{0.25b_4}{w} + \frac{0.333b_3}{w} + \frac{0.5b_2}{w} + \frac{1b_1}{w} \tag{21.10}$$

where the parameters a_0, a and b are given for each Fourier term, with 95 % confidence bounds.

Sum of Sines fitting: The Sum of Sines is similar to the Fourier fitting. However, it includes the phase constant and does not include a constant term. The Sum of Sines function is represented by the following equation:

$$C = \sum_{i=1}^{n} a_i \sin(b_i z + c_i) \tag{21.11}$$

where a is the amplitude, b is the frequency, and c is the phase constant for each sine wave term. n is the number of terms in the series. We also included four terms to fit the SOC stock in Podzol profiles. The integration to d_z soil depth is shown in Eq. 21.12.

$$C_t = \int_0^{d_z} \left(\sum_{i=1}^{n} a_i \sin(b_i x + c_i) \right) \tag{21.12}$$

After integrating the four terms of the Sum of Sines fitting to d_z, we obtained the Eq. 21.13 as follows:

$$C_t = \frac{-(a_4 \cos(b_4 d_z + c_4))}{b_4} - \frac{a_3 \cos(b_3 d_z + c_3)}{b_3} - \frac{a_2 \cos(b_2 d_z + c_2)}{b_2} - \frac{a_1 \cos(b_1 d_z + c_1)}{b_1} + \frac{a_4 \cos(c_4)}{b_4} + \frac{a_3 \cos(c_3)}{b_3} + \frac{a_2 \cos(c_2)}{b_2} + \frac{a_1 \cos(c_1)}{b_1} \tag{21.13}$$

The parameters a, b and c are given for each Sum of Sines term with 95 % confidence bounds. The evaluation of results was carried out by comparing observed and predicted SOC stock values, considering the coefficient of determination (r^2), MSE, RMSE and AIC.

21.3 Results

21.3.1 Predicting Soil Bulk Density in Amazonian Soils

In the first attempt to generate a PTF (Dataset 1), we considered all soil attributes presented in Table 21.1. The best model was achieved (Model 1: Eq. 21.14) with the following input data: fine sand, silt, clay, total N and C/N. The symbolic regression analysis considering all input data returned a generalized equation (21.14) that explained 70 % of the soil bulk density variance (Fig. 21.2a). The MSE and RMSE between predicted and observed values were 0.011 and 0.108 g cm^{-3}, respectively.

$$\begin{aligned}\rho_p = {} & 1.463 + 0.1998\tan(1.044 - 0.002(\text{clay}))\cos(0.125 + 0.135(\text{C/N}) + \left(3.543\,10^{-5}\right)\left(\text{silt}^2\right) \\ & -0.013(\text{silt}))\cos(0.004(\text{fine sand})\cos(0.315 + \tan(0.005(\text{clay}) - 2.317)) \\ & -1.065\cos(0.315 + \tan(0.005(\text{clay}) - 2.317))) - 0.144(\text{total N})\end{aligned} \tag{21.14}$$

Arithmetic and trigonometric operators were selected by the user and automatically added to the final equation. As pointed out by Benites et al. (2007), a better correlation between N and $\rho_{p,}$ when compared to SOC content is observed in EMBRAPA (2014) database. That might be related to the total SOC measurement procedure (acid-dichromate $FeSO_4$ titration procedure) adopted by EMBRAPA. The use of C/N and N values on the resulting symbolic regression equation (21.14) might poses a problem towards the proposition of a general PTF equation for Amazonian soils due to the lack of such data in most of soil databases currently available. Thus, we used the following input data to train the symbolic regression model (Model 2: Eq. 21.15; Fig. 21.2b): total sand, silt, clay, pH and SOC.

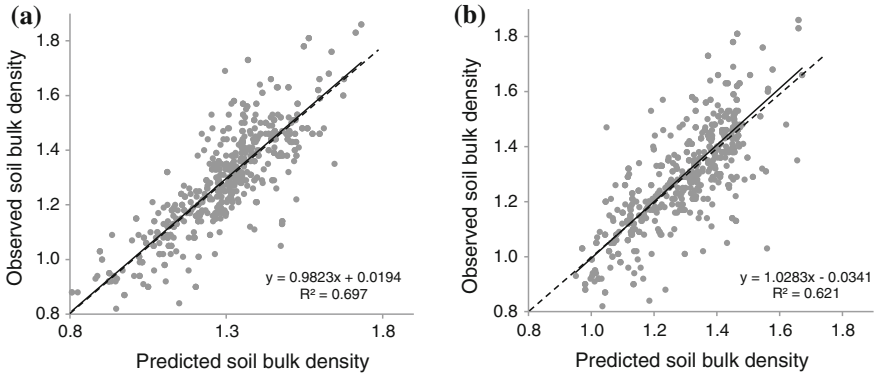

Fig. 21.2 Plot of the predicted data against the observed data. **a** Model 1; **b** Model 2. *Dashed lines* are the 1:1 lines

$$\rho_p = 1.326 + 0.315\ \sin(1.045 - 0.001(\text{clay}) - 0.052(\text{SOC})) + 0.0003(\text{clay})\ \sin(\sin(2.561 + 1.287(pH) - 0.006(\text{clay}))) - 0.134\ \sin(\sin(2.561 + 1.287(\text{pH}) - 0.006(\text{clay}))) \quad (21.15)$$

The Model 2 (Eq. 21.15) had a lower correlation with the observed dataset (Fig. 21.2); however, It takes into account three soil attributes that are widely available in most of systematic soil databases (EMBRAPA and IBGE legacy data). Therefore, Model 2 was applied in order to predict values of soil bulk density. The Model 2 had an MSE and RMSE of 0.015 and 0.123 g cm^{-3}, respectively. The validation was based on the independent Dataset 2, as described below.

Symbolic Regression Model Validation

The proposed Model 2 (Fig. 21.3) has shown the best performance, among the evaluated PTF, with MSE and RMSE closest to 0 and the lower AIC value. However, the model proposed by Benites et al. (2007) has a similar behaviour with close MSE, RMSE and AIC indices. Thus, we observed that Benites' et al. (2007) model could be applied to estimate soil bulk density in Amazonian soils, but with the disadvantage of demanding Fe_2O_3 values, which are not available in most of the soil profiles provided by IBGE (2008).

Clay content and SOC content have been reported in previous studies as the most relevant attributes to explain soil bulk density variability (Bernoux et al. 1998; Benites et al. 2007). Given the availability of soil textural fraction, pH and SOC data in the applied soil databases (IBGE 2008; EMBRAPA 2014), we decided to use the Model 2 in order to estimate soil bulk density values. It is important to highlight that this model was developed based on soil samples limited to the region of the Amazon Basin, which might detail its application in areas outside Amazon biome.

21.3.2 Modelling the Vertical Distribution of SOC Stock in Amazonian Soils

The main soil orders in Rio Negro Basin are Ferralsols (34 % of the region); Acrisols (22 % of the region) and Podzols (19 % of the region). The remaining orders comprise Gleysols (6 %) and Plinthosols (5 %). Arenosols, Nitisols and Planosols account to less than 10 % of the soils of Rio Negro Basin. In the first 0.3 m soil depth, we observed that Ferralsols and Acrisols have a mean SOC content of 1.8 ± 1.4 % and 1.5 ± 1.1 %, respectively. Below 0.3 m (0.3–0.8 m), the SOC content in these soils decays to 0.57 ± 0.5 % in Ferralsols and 0.44 ± 0.6 % in Acrisols. The superficial horizons of Podzols have a higher carbon concentration (0–0.3 m: 2.7 ± 1.5 %). The same pattern was observed in deep thick Bh horizons (1–3 m soil depth) where the mean carbon content is 2.31 ± 2.1 %.

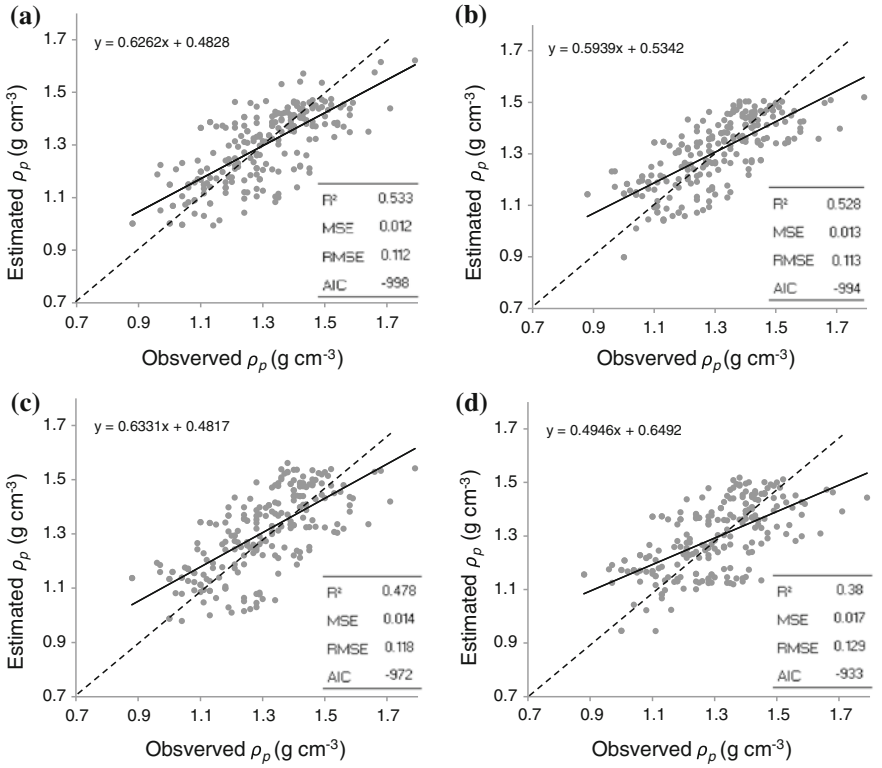

Fig. 21.3 Scatterplots and goodness-of-fit indexes of proposed and previous soil bulk density PTF. **a** Proposed Model 2; **b** Benites et al. (2007); **c** Bernoux et al. (1998) and **d** Tomasella and Hodnett (1998). *Dashed lines* are the 1:1 lines

All soils that had their SOC stock modelled by exponential depth functions were grouped together (Dataset A). After integration (Eq. 21.5c), the exponential functions showed a mean r^2 value of 0.99 and a RMSE of 0.85 kg m^{-2} between the observed and the fitted SOC stock (Fig. 21.4a). These results indicate that the exponential depth functions fitted the data very well, with an r^2 closer to 1 and an RMSE below 1 kg C m^{-2}. It is important to highlight that 5 % of the soil profiles originally provided by IBGE (2008) were not fitted to exponential equations due to the low number of observed soil layers (2.4 % of profiles) or because of the occurrence of high amounts of SOC content in horizons below 0.3 m (2.6 % of profiles).

As shown in Fig. 21.4b, the predicted SOC values fitted well to the observed data with an RMSE of 2.5 kg C m^{-2} considering a 3 m soil depth, which allows the prediction of SOC stock in Amazonian soils in deeper horizons (below 1 m). The validation dataset comprises soil profiles of Acrisols and Ferralsols, which are dominant in Amazon Basin. Therefore, exponential depth functions offer a feasible

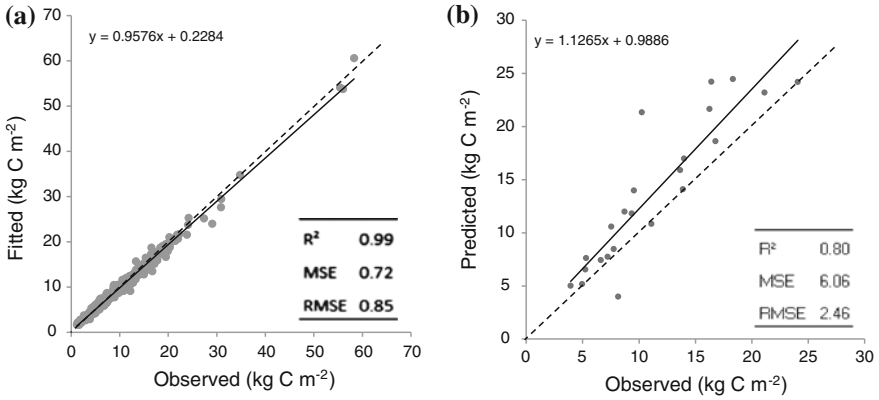

Fig. 21.4 **a** Observed and fitted exponential depth function SOC; **b** Observed and predicted exponential depth function, based on the validation dataset. *Dashed line* is the 1:1 line

way to estimate SOC stock in Amazon biome. However, this assumption is not valid for Podzols due to the peculiar distribution of SOC along the profile (Fig. 21.5).

The pedogenitic processes involving the formation of Podzols have already been investigated by several studies in Amazon (Lucas et al. 1984, 1988, 1996; Chauvel et al. 1987; Bravard and Righi 1989; Dubroeucq and Volkoff 1998; Nascimento et al. 2004; Montes et al. 2007; Patel-Sorrentino et al. 2007; Fritsch et al. 2009; Montes et al. 2011). All researches developed in this region have described the occurrence of sandy soil materials (E horizon) that lead to the leaching of Al and Fe organic matter complexes, resulting in the dissolution of clay minerals, Al-hydroxides and Fe-oxides or Fe-oxyhydroxides, causing the formation of illuvial deep Bh-rich-SOC horizons. These characteristics allowed us to segment Podzol profiles in four systematic horizons according to their SOC content: (1) SOC-rich topsoil horizon (A/O); (2) Elluvial sandy horizon with insignificant amount of SOC; (3) Deep thick SOC-rich Bh horizon; and (4) C horizon with a gradual decrease in SOC content (Fig. 21.5).

We observed a clear periodical pattern that fit very well in Sum of Sines and Fourier models (Table 21.2). Nevertheless, spline models have generated the best predicted values when compared to measured data (Table 21.2). It is important to emphasize that the establishment of λ (lambda) values is laborious and depends on the availability of several soil samples for each soil profile, which allows an appropriate representation of the soil attribute to be measured. Given this, we decided to apply the λ value of 0.1 as suggest by Bishop et al. (1999). The periodical models were fitted to the observed data with 2, 3 and 4 terms. The best fitting was achieved with 4 terms in both Fourier and Sum of Sines models.

The curve fitting of Dataset B was created considering all measured layers of each Podzol profile as shown in the example of Fig. 21.6. We observed a complex distribution of SOC along a typical Podzol profile. As shown in Fig. 21.5, the SOC

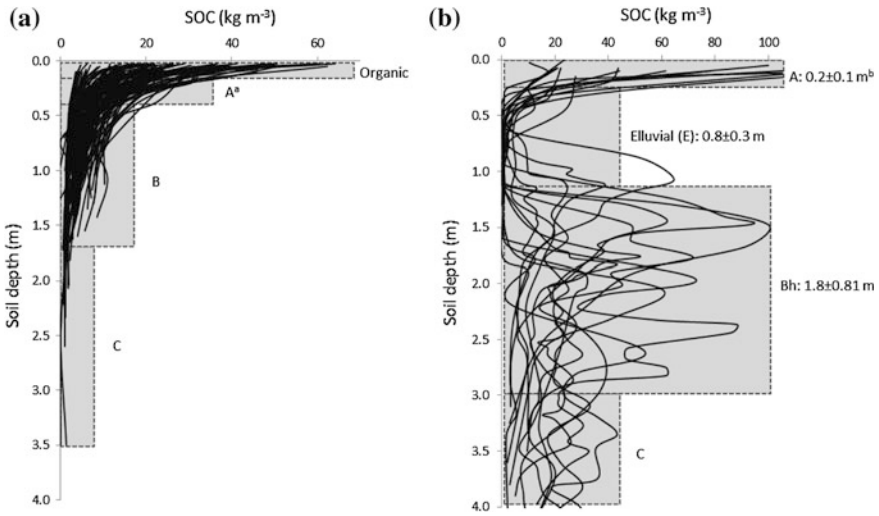

Fig. 21.5 Measured SOC stock. **a** Dataset A (Ferralsols and Acrisols); **b**: Dataset B (Podzols). [a]Typical Ferralsol horizons. [b]Typical Podzol horizons with average thickness for evaluated Podzol profiles

Table 21.2 Evaluation indices for the three fitting models considering Dataset B (Podzols)

Fitting model	Observations	R^2	MSE (kg C m^{-2})	RMSE (kg C m^{-2})	AIC
Equal-area spline	18	0.85	187.21	13.68	96.06
Sum of sines	18	0.82	225.38	15.00	99.40
Fourier	18	0.79	255.12	15.97	101.63

content in Bh horizon is highly variable with abrupt changes in depth intervals lower than 0.05 m (Fig. 21.5). The variation in C content within Bh horizon is explained by pedogenitic processes of this horizon. What is observed here is a process of reduction and reoxidation of organometallic complexes leading to the selective accumulation of different amounts of C in Bh horizon.

Considering the parametric equations, we observed a better performance of the Sum of Sines fitting, confirmed by the quality evaluation indices (Table 21.2). Thus, the integration of the Sum of Sines model to the observed soil depth (Eq. 21.13) was capable of representing the complex distribution of SOC stock within Bh horizons (Fig. 21.5), which justifies the application of a 4-term Sum of Sines model. It is interesting to highlight that Sum of Sines, as well as Fourier models, deals with trigonometric and circular functions, usually applied to describe attributes with clear periodical behaviour. In this context, we assumed that SOC stock in Podzols has a periodical pattern, which implies in modelling the profile to a limited range according to the observed data, where the assumption of periodicity is attested. Therefore, the prediction of values is limited to the measured soil depth,

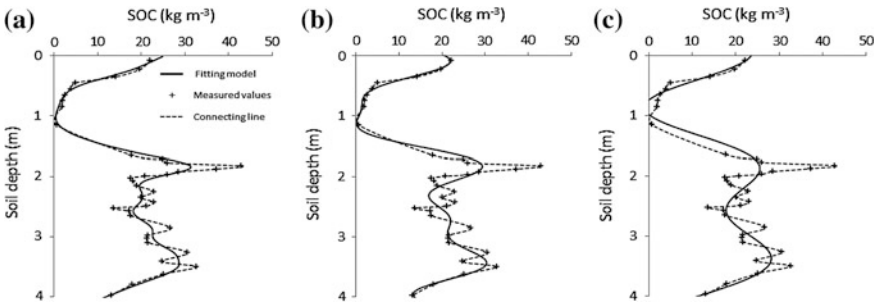

Fig. 21.6 Example of fitting models to a typical Podzol profile. **a** Equal-area spline; **b** sum of sines; **c** fourier

which means that we cannot predict SOC stock values beyond the measured layers considering the three fitting models: Spline, Sum of Sines and Fourier.

21.3.3 The SOC Stock in Datasets A and B

In Dataset A, we observed that a significant portion of the SOC stock is located in the first 0.3 m soil depth with an average stock of 8.2 ± 5.0 kg C m^{-2}. Such value represents 41 % of the total SOC stock to a 3 m soil depth. In the first soil metre, we observed that the profiles evaluated in Dataset A store about 15.2 ± 6.2 kg C m^{-2}, which is 76 % of the total SOC stored in profiles up to 3 m soil depth. Finally, if we take into account the entire soil profile (3 m soil depth), the SOC stock increases to a value of 19.2 ± 10.7 kg C m^{-2}. Thus, the carbon stored in deep soil horizons, from 2 to 3 m soil depth, represents about 19.2 % of the total SOC stored in the first 3 m soil depth of Dataset A. We observed high standard deviation values due to the grouping of different soil orders into the same dataset in order to compare the vertical behaviour of SOC stock distribution in Dataset A against Dataset B (Podzols). Different from other Amazonian soils, Podzols have shown a high capacity of storing huge amounts of SOC in deep thick horizons (Bh), with a complex vertical distribution that was not evaluated in previous studies.

In Podzols, the organic (O/A) horizon stores higher amounts of C when compared to other Amazonian soils due to the prevalence of hydromorphic conditions that leads to the accumulation of fresh MOS in surface. In O/A horizon, the average SOC stock is 17.9 ± 11 kg C m^{-2} to a 0.3 m soil depth. In elluvial sandy horizons (E), the SOC stock abruptly decays to an average value of 4.8 ± 2.7 kg C m^{-2}. The thickness of E horizon is variable ranging from 0.5 to 1.5 m, depending on the observed profile. The Bh horizon stores a mean SOC value significantly high with an average stock of about 83.2 ± 15.5 kg C m^{-2} to a 2-m horizon thickness. It is important to highlight that the upper and bottom limits of Bh horizon are variable which implies in different Bh thickness according to the observed profiles; however, the values

presented above were taken to a 3 m soil depth. Nevertheless, Bh horizons might extend to a 5 m soil depth, which would increase the average SOC stock of Podzols.

21.4 Conclusions

The good performance of the exponential depth function was attested to a 3 m soil depth based on the validation dataset. Thus, the application of exponential models to predicted SOC stock in Amazonian soils has proven to be efficient, considering the availability of measured values to the first soil metre. Nevertheless, information of soil bulk density was essential to allow the systematic estimation and prediction of SOC stock. The prediction of soil bulk density data was possible by the application of PTF equations developed according to symbolic regression analysis, which generated a dynamic model suited to predicting soil bulk density specifically in soils in the Amazon region. Soil bulk density PTF models and exponential depth functions have allowed the estimation of SOC stock in Amazon soils where the assumption of SOC content exponential decay was attested. The prediction of SOC stock by exponential decay equations is simple and can be carried out indirectly by integrating the exponential model to a desired soil depth, which is helpful to estimate deep SOC stock in Amazon soils.

In Podzols, the SOC stock is significantly higher than that in other Amazonian soils, especially below 1 m soil depth. The vertical variation of SOC was successfully modelled by parametric and nonparametric fitting models. The nonparametric equal-area spline model returned the best predicted values. Moreover, the fitted spline curves are not affected by local variations, due to the possibility of fitting piece-wise a series of local independent functions over small intervals (soil depths). However, the application of parametric models might be helpful to allow the indirect prediction of SOC stock in Podzols and to describe the general behaviour of SOC along the soil profile. In this matter, we observed that Sum of Sines models, yet poorly explored in predicting soil attributes, can be properly applied to describe and estimate the SOC stock distribution in Amazonian Podzols with deep thick Bh horizons.

Funding This work was funded by grants from Brazilian FAPESP (São Paulo Research Foundation. Process number: 2012/12882-5) and CNPq, as well as French ARCUS (joint programme of Région PACA and French Ministry of Foreign Affairs).

References

Arrouays D, P'elissier P (1994) Modeling carbon storage profiles in temperate forest humic loamy soils of France. Soil Sci 157:185–192. doi:10.1097/00010694-199403000-00007

Batjes NH (1996) Total carbon and nitrogen in the soils of the world. Eur J Soil Sci 47:151–163. doi:10.1111/j.1365-2389.1996.tb01386.x

Batjes NH, Dijkshoorn JA (1999) Carbon and nitrogen stocks in the soils of the Amazon Region. Geoderma 89:273–286. doi:10.1016/S0016-7061(98)00086-X

Benites VM, Machado P, Fidalgo ECC, Coelho RM, Madari EB (2007) Pedotransfer functions for estimating soil bulk density from existing soil survey reports in Brazil. Geoderma 39:90–7. doi:10.1016/j.geoderma.2007.01.005

Bernoux M, Arrouays D, Cerri C, Volkoff B, Jolivet C (1998) Bulk densities of Brazilian Amazon soils related to other soil properties. Soil Sci Soc Am J 162:743–749

Bernoux M, Carvalho MDS, Volkoff B, Cerri CC (2002) Brazil's soil carbon stocks. Soil Sci Soc Am J 66:888–896. doi:10.2136/sssaj2002.8880

Bravard S, RIGHI D (1989) Geochemical differences in an oxisolspodosol toposequence of Amazonia (Brazil). Geoderma 44:29–42. doi:10.1016/0016-7061(89)90004-9

Bishop TFA, Mcbratney AB, Laslett GM (1999) Modelling soil attribute depth functions with equal-area quadratic smoothing splines. Geoderma 91:27–45. doi:10.1016/S0016-7061(99)00003-8

Blake G, Hartge K, Klute A (1986) Bulk density. Methods Soil Anal Part 1: Phys Mineral Methods 363–375

Buringh P (1994) Organic carbon in the soils of the world. In Woodwell G (ed) The role of terrestrial vegetation in the global carbon cycle: measurement by remote sensing, SCOPE, vol 23. Wiley, NY, pp 91–109

Burke IC, Yonker CM, Parton WJ, Cole CV, Flach K, Schimel DS (1989) Texture, climate, and cultivation effects on soil organic matter content in U.S. grassland soils. Soil Sci Soc Am J 53:800–805. doi:10.2136/sssaj1989.03615995005300030029x

Chauvel A, Lucas Y, Boulet R (1987) On the genesis of the soil mantle of the region of Manaus, Central Amazonia, Brazil. Experientia 43:234–241. doi:10.1007/BF01945546

Dubroeucq D, Volkoff B (1998) From oxisols to spodosols and histosols: evolution of the soil mantles in the Rio Negro Basin (Amazonia). Catena 32:245–280. doi:10.1016/S0341-8162(98)00045-9

EMBRAPA (2011) Empresa Brasileira de Pesquisa Agropecuária. Centro Nacional de Pesquisas de Solos. Manual de métodos de análises de solos. 2 ed. Embrapa Solos, Rio de Janeiro, 230 p

EMBRAPA (2014) Digital soils system information (Brazilian soils database) Rio de Janeiro. Accessed 25 Oct 2014. http://www.bdsolos.cnptia.embrapa.br/consulta_publica.html

Eswaran H, Van Den Berg E, Reich P (1993) Organic carbon in soils of the world. Soil Sci Soc Am J 57:192–194. doi:10.2136/sssaj1993.03615995005700010034x

FAO/IIASA/ISRIC/ISSCAS/JRC (2012) Harmonized world soil database (version 1.2). FAO, Rome, Italy and IIASA, Laxenburg, Austria

Fritsch E, Allard T, Benedetti MF, Bardy M, do Nascimento NR, Li Y, Calas G (2009) Organic complexation and translocation of ferric iron in podzols of the Negro River watershed. Separation of secondary Fe species from Al species. Geochim Cosmochim Acta 73:1813–1825. doi:10.1016/j.gca.2009.01.008

IBGE. Geoscience Department (DGC) (2008) Coordenação de Recursos Naturais e Estudos Ambientais (CREN). Mapas georreferencias de recursos naturais. Scale 1:250:000, Digital Format: shp. Rio de Janeiro. Accessed 15 Aug 2014. ftp://geoftp.ibge.gov.br/mapas/

Kimble JM, Heath LS, Birdsey R, Lal R (1990) The potential of US. Forest soils to sequester carbon and mitigate the greenhouse effect. CRC Publishers, Boca Raton, FL, 429. ISBN:9781566705837

Koza J (1991) Evolving a computer program to generate random numbers using the genetic programming paradigm. In Proceedings of the fourth international conference on genetic algorithms, Morgan Kaufmann, La Jolla, CA

Koza J (1992) Genetic programming: on the programming of computers by means of natural selection. The MIT Press

Lucas Y, Chauvel A, Boulet R, Ranzani G, Scatolini F (1984) Transição latossolos-podzois sobre a formação Barreiras na região de Manaus, Amazônia. Rev. Bras. Cienc. Solo 8:325–335

Lucas Y, Boulet R, Chauvel A (1988) Intervention simultanée des phénomènes d'enfoncement vertical et de transformation latérale dans la mise en place de systèmes de sols de la zone

tropicale humide. Cas des systèmes sols ferrallitiques – podzols de l'Amazonie Brésilienne. C R Acad Sci Paris Ser lla 306:1395–1400

Lucas Y, Nahon D, Cornu S, Eyrolle F (1996) Genèse et fonctionnement des sols en milieu equatorial. C R Acad Sci Paris Ser IIa 322:1–16

Mcbratney AB, Mendonça-Santos ML, Minasny B (2003) On digital soil mapping. Geoderma 117:3–52. doi:10.1016/S0016-7061(03)00223-4

Minasny B, Mcbratney AB, Mendonça-Santos ML, Odeh IOA, Guyon B (2006) Pre-diction and digital mapping of soil carbon storage in the Lower Namoi Valley. Aust J Soil Res 44:233–244

Montes CR, Lucas Y, Melfi AJ, Ishida DA (2007) Systèmes sols ferrallitiques–podzols et genèse des kaolins. C R Geosci 339:50–56. doi:10.1016/j.crte.2006.11.001

Montes CR, Lucas Y, Pereira OJR, Achard R, Grimaldi M, Melfi AJ (2011) Deep plant-derived carbon storage in Amazonian podzols. Biogeosciences 8:113–120. doi:10.5194/bg-8-113-2011

Nascimento NR, Bueno GT, Fritsch E, Herbillon AJ, Allard T, Melfi A, Astolfo R, Boucher H, Li Y (2004) Podzolization as a deferralitization process: a study of an Acrisol-Podzol sequence derived from Palaeozoic sandstones in the northern upper Amazon Basin. Eur J Soil Sci 55:523–538

Patel-Sorrentino N, Lucas Y, Eyrolles F, Melfi AJ (2007) Fe, Al and Si species and organic matter leached off a ferrallitic and podzolic soil system from Central Amazonia. Geoderma 137:444–454. doi:10.1016/j.geoderma.2006.10.002

Pereira OJR, Montes CR, Lucas Y, Santin RC, MelfI AJ (2015) A multisensor approach for mapping plant-derived carbon storage in Amazonian podzols. Int J Remote Sens 36(8):2076–2092. doi:10.1080/01431161.2015.1034896

Post WM, Emanuel WR, Zinke PJ, Stangenberger AG (1982) Soil carbon pools and world life zones. Nature 298:156–159

Renshaw E, Ford ED (1984) The description of spatial pattern using two-dimensional spectral analysis. Vegetatio 56:75–85

Schmidt M, Lipson H (2009) Distilling free-form natural laws from experimental data. Science 324(5923):81–85

Tomasella J, Hodnett MG (1998) Estimating soil water retention characteristics from limited data in Brazilian. Soil Sci 163:190–202. doi:10.1097/00010694-199803000-00003

Webster R (1978) Mathematical treatment of soil information'. In Proceedings of the 11th international congress of soil science. Edmonton, Canada, vol 3, pp 161–190

Part IV
Digital Soil Morphometrics—Use and Applications

Chapter 22
The Next Generation of Soil Survey Digital Products

Jon Hempel, David Hoover, Robert Long, Erika Micheli, Vincent Lang and Alex McBratney

Abstract Advances in computer technology (within the past two decades) and access to geographically accurate digital environmental data (i.e., elevation and its derivatives, geology, land use, climate, parent material, and remotely sensed spectral data) have created enormous advancements in our ability to produce soil information at fine spatial resolutions (10–90 m). The data contained in each of these grid cells are data rich in nature and include probability and uncertainty information that allow the modeling of the soil continuum. The same advances in computer technology and digital information are now being applied to data capture for pedon descriptions. Coined "digital morphometrics," this set of methodologies provide the potential to collect pedon soil property information that defines the continuum of the soil column, no longer restricting pedon information to aggregated "blocks" of data. Potentials and application of this new data model for pedon descriptions will be examined, studied, and presented in this paper.

Jon Hempel: Retired.

J. Hempel (✉) · D. Hoover
USDA-NRCS, National Soil Survey Center, Lincoln, NE, USA
e-mail: jhempel82@gmail.com

D. Hoover
e-mail: david.hoover@lin.usda.gov

R. Long
USDA-NRCS, St. Johnsbury Soil Survey Office, St. Johnsbury, VT, USA
e-mail: robert.long@vt.usda.gov

E. Micheli · V. Lang
Szent Istvan University, 2100 Gödöllő, Hungary
e-mail: Micheli.Erika@mkk.szie.hu

V. Lang
e-mail: Lang.Vincent@mkk.szie.hu

A. McBratney
The University of Sydney, Sydney, Australia
e-mail: alex.mcbratney@sydney.edu.au

A.E. Hartemink and B. Minasny (eds.), *Digital Soil Morphometrics*,
Progress in Soil Science, DOI 10.1007/978-3-319-28295-4_22

Keywords Analogue · Digital · Continuum · Digital morphometrics

22.1 Introduction

The US Soil Survey Program has used the same data presentation for its information for over 100 years. This information is based on the concept of an aggregated data model. For both spatial soil survey information (soil maps) and pedon (soil profile data or horizons), the data are based on one value for each polygon (soil survey maps) representing the dominant component and one value for all analyzed soil properties within each horizon (soil profiles). Soil survey map units are designed to be multicomponent in nature (typically three to seven components defining a map unit), but due to scale restrictions, it has been impossible to display the locations of each distinct component, thereby restricting data presentation to the dominant component or components in the case of complexes. With this data presentation, it is not possible to show the natural continuum or gradation between soil map units as these concepts and the soil properties represented within the soil map units are "hard breaks" at each polygon boundary.

Much like polygon soil maps, soil profiles, and the individual horizons within the profile are described and sampled in an aggregated fashion, the layers are "bulk sampled" without taking into account variability in the horizons. The presentation for this data model is one aggregated sample per horizon (typically there are four to eight horizons that make up a pedon).

The present technology for documenting soil survey profile descriptions dates back to the early 1900s. Kellogg (1936) documented the importance of describing soil color, texture, structure, and colloidal movement within the soil profile as well as subhorizons within the A, B, C sequence. Figure 22.1 documents the state of soil structure in 1935. Note that our propensity for recognizing for soil structure types has not changed in 80 years, and in fact, we recognize fewer types now than in 1935.

In the early 1990s, the concept of presenting soils' information on the continuum became a reality through the technology of digital soil mapping. This technology has revolutionized how soils are mapped and presented.

22.2 Evolution of Spatial Data Presentation

For the last 60 years, the data model, in the US Soil Survey Program, has been based on data aggregation. One set of data represents the entire polygon, even though soil surveys have good documentation that the number of components that make up map units is typically 3–8. Figure 22.2 documents the analogue presentation of the soil vector model (one set of data representing the entire polygon).

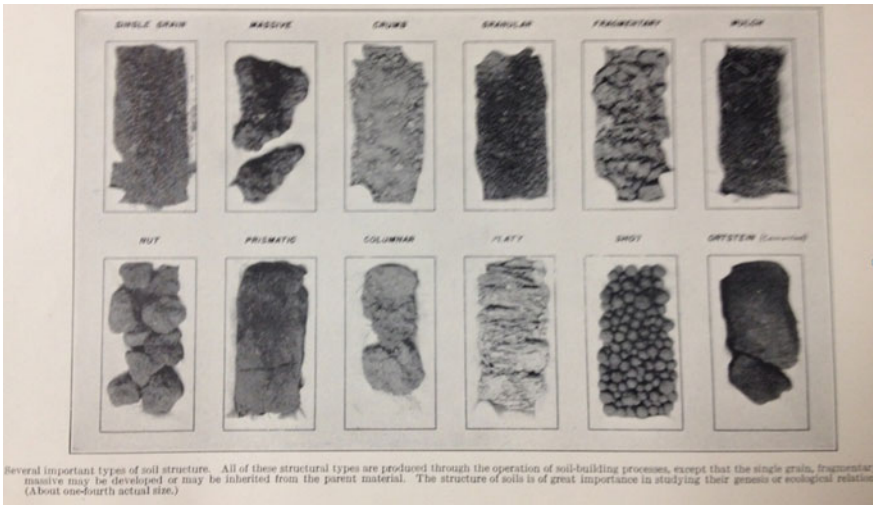

Fig. 22.1 Soil structure types recognized in 1935

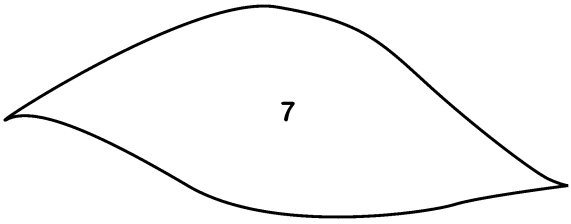

Fig. 22.2 Soil vector model, one set of data representing the entire soil polygon

As the soil survey program has continued moving toward data presentation for documenting the soil landscape on the continuum, the "first generation" of digital soil data was developed. The gridded SSURGO or gSSURGO contains a set of 10-m grids that have the same map unit identifier as the vector polygons they were derived from. In other words, each grid cell has the same data within a polygon. Figure 22.3 documents the gSSURGO data model.

The "second generation" of documenting the soil landscape continuum with raster-based products will portray the location of documented soil components (or inclusions) within the original soil vector polygon. Figure 22.4 documents the disaggregation and presentation of soil components within a soil polygon. This adds to the definition of soil survey information and is relevant for soil management decisions.

The "third generation" of documenting the soil landscape continuum with raster-based products will assign soil values to cells regardless of existing vector soil line placement. It will represent the true continuum of soil properties and components as they occur naturally and will be based on rule sets developed for

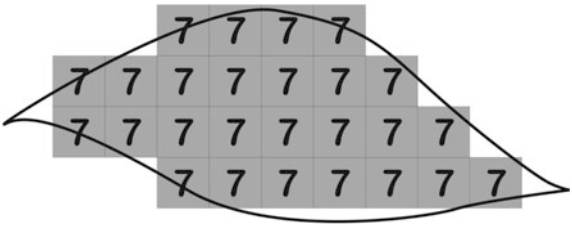

Fig. 22.3 gSSURGO data model documenting the set of 10-m grids each with the same data as the soil vector model they were derived from

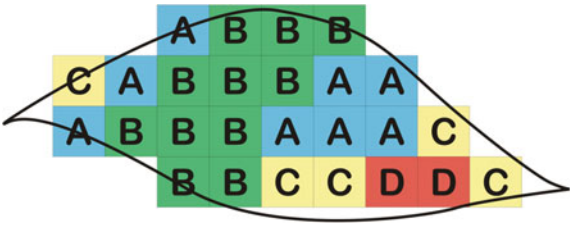

Fig. 22.4 Disaggregated components within the soil polygon

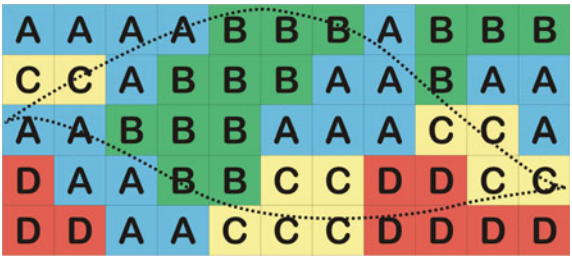

Fig. 22.5 Generation 3 documents the soil continuum regardless of existing vector soil line placement, a true portrayal of the soil landscape continuum

individual soil polygons as well as landscape, landform, and geomorphic concepts. Figure 22.5 documents the soil continuum regardless of existing vector soil line placement, a true portrayal of the soil landscape continuum.

22.3 Map Presentation Examples

An example of map presentation is given in Fig. 22.6 showing the state of soil mapping in 1970 in Custer County, Nebraska (courtesy of Custer County Soil Conservation District). This map represents the analogue presentation of soil survey

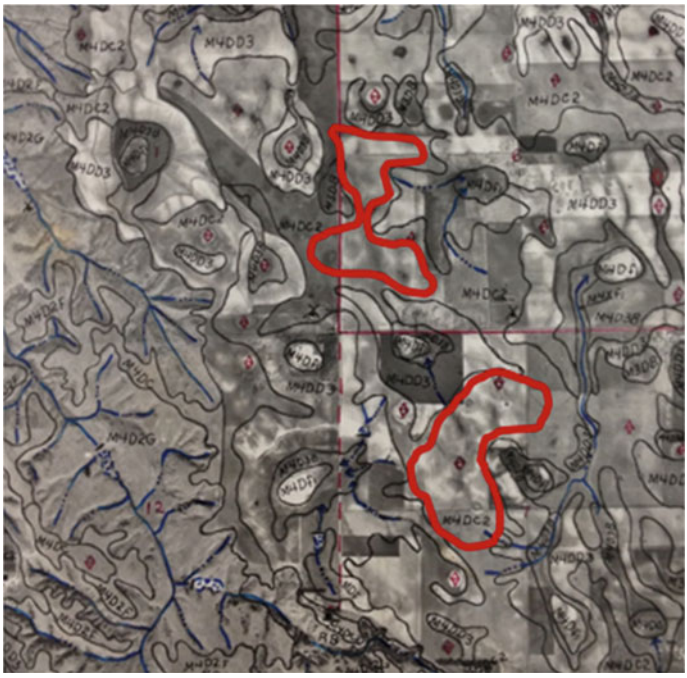

Fig. 22.6 Analogue presentation of soil survey information in Broken Bow County, Nebraska, circa 1970

information, whereby one set of data represents the entire polygon. Note the highlighted areas of the map where more than one component is evident within the polygons.

Data from the Web Soil Survey (May, 2015a) were downloaded for the Ozaukee County Soil Survey in Wisconsin (September, 1970) (Fig. 22.7). Forty-five years after the Broken Bow, Nebraska map was produced the soil survey continues to utilize the same analogue data model; of one set of soil data representing the entire polygon. Note the highlighted areas of the map where more than one component occurs within the polygons.

Digital soil mapping technology is available to move soil survey information into the next generation of digital products (generation two and three). Figure 22.8, from the Essex County, Vermont soil survey (July, 2015b), represents the next generation of soil survey products: disaggregated and continuous categorical information superimposed on a polygon-based map for the USA.

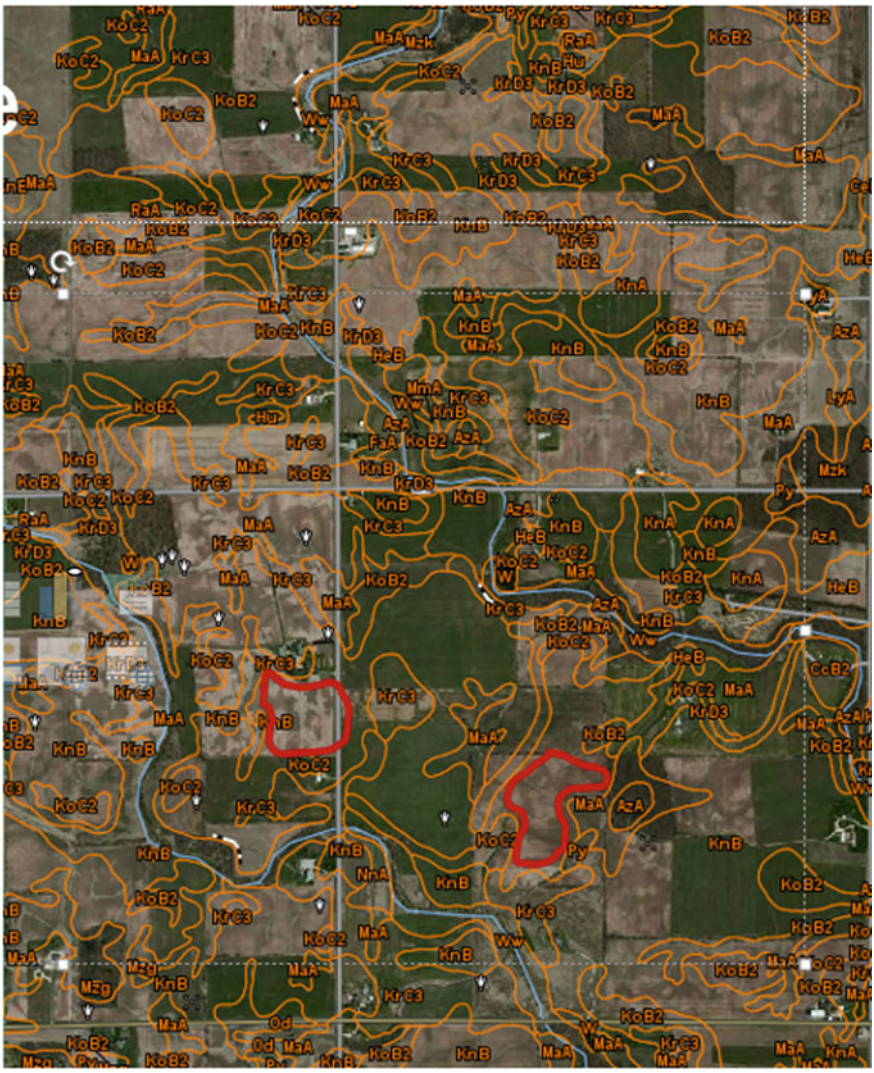

Fig. 22.7 Analogue presentation of soil survey information in Ozaukee County, Wisconsin, generated from the Web Soil Survey

22.4 Digital Presentation of Soil Profiles

In the manner that soil survey maps are produced using an aggregated data model, information regarding soil profile descriptions are also generated using an aggregated model. An example of this is given in Fig. 22.9a. Soil horizons for the state soil of Wisconsin, the Antigo silt loam, are portrayed as they are described in the Official

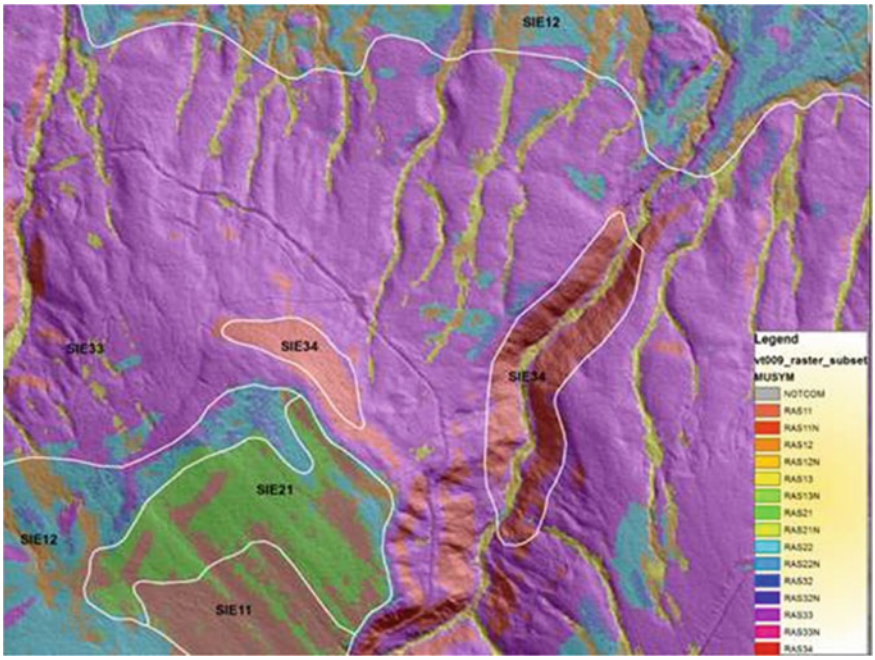

Fig. 22.8 Disaggregated and continuous categorical digital information from Essex County, Vermont

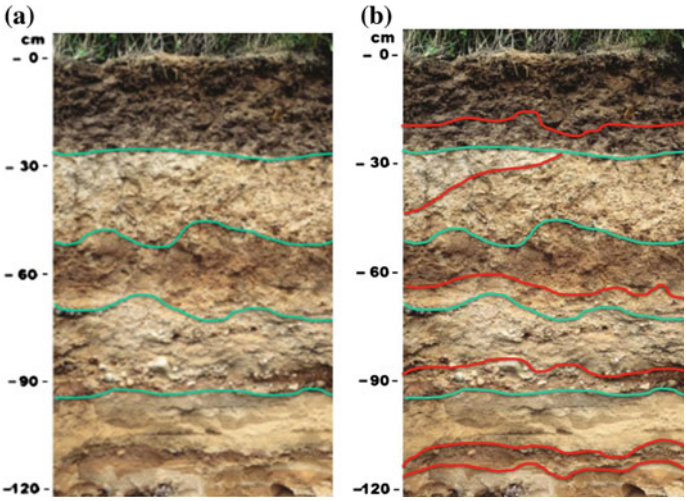

Fig. 22.9 **a** Horizons of the Antigo Silt Loam as portrayed from the Official Series Description. **b** Additional subhorizons portrayed that are lost due to bulk sampling of the major horizons

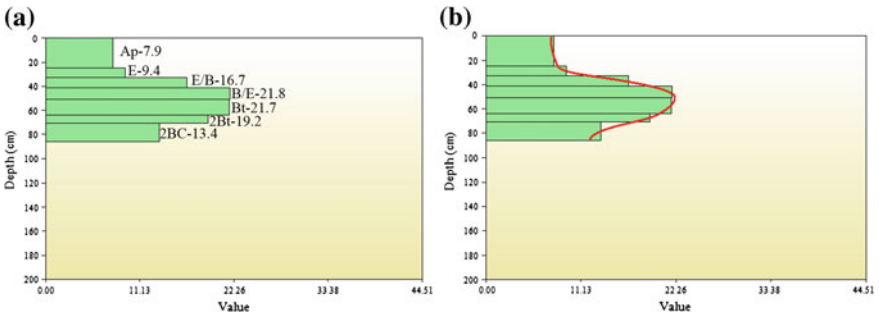

Fig. 22.10 **a** Horizon designations and depths and the bulk sample percentages for clay Antigo silt loam, clay percentage. **b** Bulk-sampled horizons with a continuous depth function that portrays more natural distribution of clay in the soil profile

Series Description for the Antigo Silt Loam. Figure 22.9b portrays the Antigo silt loam with the subhorizons defined that would be part of the bulk sampling of the major horizon. This type of definition is lost in soil profile descriptions due to bulk soil sampling.

Bulk sampling of horizons creates hard limits of soil property information at the soil horizon boundaries. The continuous nature of soil properties in the soil profile are disrupted. Figure 22.10a depicts clay distribution of bulk-sampled horizons for a profile of Antigo silt loam. Each layer has a "hard boundary" at the top and the bottom.

Figure 22.10b is the Antigo silt loam soil profile with a continuous depth function for clay percentage. This is a more natural representation of clay distribution in a soil profile. Through the science and tools in "digital soil morphometrics," we now have the technology to provide information for continuous depth functions of soil properties within a soil profile by actual measurements as well as by modeling. Hartemink and Minasny (2014) document a variety of technologies such as X-ray fluorescence (XRF), visible and near infrared (Vis-NIR), digital cameras, X-ray computed tomography (X-ray CT), hyperspectral scanning, ground-penetrating radar (GPR), and scanning electron microscope (SEM) that can be used effectively and efficiently to provide more detailed information about the soil profile. This is a significant step forward in providing accurate and functional information for a more natural description and interpretation of the properties of a soil profile.

Utilizing the tools of digital morphometrics, there is now the distinct potential to provide new insights into the soil property continuum, which can provide new information on how soils form, how they can be classified, interpreted and used.

Fig. 22.11 Soil pit face illustrating variation in range of characteristics of horizons (and their associated properties) dependent on where in the pit face the soil is described

22.5 Horizontal and Vertical/Lateral Soil Profile Descriptions

There is a vertical continuum of soil properties in the soil profile, but there is also a continuum in the horizontal sense. In a typical soil description, an area of the "soil pit," usually 25–40 cm wide, is chosen as the representative area where the soil is described and sampled. This representative area is selected using expert knowledge. With such a small area chosen for the soil description, much of the variation in the overall soil pit is not captured. Figure 22.11 portrays a soil pit with the horizons delineated that illustrates how horizon dimensions and proportions can vary along a soil pit face. (Note the difference in the horizons in the two defined areas along the pit face).

With the advent of the tools within the digital morphometrics concept, it becomes feasible to investigate the entire pit face and develop data for the lateral extent for the full range of characteristics for depths and properties within each horizon.

22.6 Digital Soil Morphometrics and Universal Soil Classification

The International Union of Soil Sciences Working Group for Universal Soil Classification has spent the last three years developing an overarching conceptual Universal Soil Classification system that is based on numerical classification concepts.

1-coarse fragments	12-CaCO3
2-clay content	13-pH in water
3-Silt content	14-Cation Exchange Capacity
4-Sand content	15-Ca
5-r (color)	16-Mg
6-g, (color)	17-Na
7-b, (color)	18-K
8- Presence of redox features (evidence of water)	19-Acidity
9- Presence of permafrost (evidence of ice)	20-Base Saturation
10-Bulk Density	21-Electrical Conductivity
11-Organic Carbon	22-Gypsum

Fig. 22.12 Twenty-two soil properties were analyzed to create Universal Soil Classification Data Centroids

The concept of this Universal Soil Classification system is based on a soil property data centroid approach. This concept involves analyzing databases from across the world, using a set of accepted soil properties, to make allocations into logical clouds or clusters of points that recognize "Great Soil Groups" or "Mesotaxa." This level will be equivalent to the great group level from US Soil Taxonomy, along with similar levels in the World Reference Base, Australian Soil Classification, and other soil classification systems.

Point data have been assembled from available databases across the world including 42,000 profiles from the US National Cooperative Soil Survey database, 3000 profiles from the ISRIC-WISE 3.1 dataset, 11,000 profiles from the AFSIS legacy database, an additional 1200 profiles assembled from the Hungarian database, and 680 profiles from the Russian database.

As a starting point for developing the "centroid" concept, only pedons from the US National Cooperative Soil Survey were analyzed. Figure 22.12 documents the set of soil properties that were used to define the data centroids. A data "centroid" was calculated for each great group within the soil taxonomy system and a central concept for the 22 properties was produced.

Since the universal system is based solely on properties, there is a need to document important diagnostic and morphological information that is important to soil classification that is not captured in physical soil properties. Morphological information such as clay films, slickensides, and redoximorphic features are important soil classification diagnostic criteria that can be captured through digital morphometrics and incorporated into the classification system.

22.7 Conclusion

It is clear that the future for soil survey inventories, both spatial and point (pedon), is through digital means. The technology in digital soil mapping and digital morphometrics has advanced to the point where the techniques are common in the research and academic circles, but also in agencies, NGOs and private sector entities engaged in the collection and dissemination of soil survey information. Providing quantifiable data and measurements at small depth increments that will assist with deriving continuous depth functions of soil properties will increase use and application of soil information. It will help to better understand the soil heterogeneity and provide more detailed information to the user community for application and interpretation.

References

Brown LE (1970) Custer County Soil Conservation District Archives. Soil Conservation Service, Broken Bow, Nebraska

Hartemink AE, Minasny B (2014) Towards digital soil morphometrics. Geoderma 230–231:305–317

Kellogg CE (1936) Development and significance of the Great Groups of the United States. United States Department of Agriculture, Miscellaneous Publication No. 229, Washington, DC

Parker DE, Kurer DC, Steingraeber JA (1970) Soil Survey of Ozaukee County, Wisconsin. United States Department of Agriculture, Soil Conservation Service. US Government Printing Office, Washington, DC

Soil Survey Staff, Natural Resources Conservation Service, United States Department of Agriculture (2015a) Web Soil Survey, Ozaukee County, Wisconsin. Available online at http://websoilsurvey.nrcs.usda.gov/. Accessed May 2015

Soil Survey Staff, Natural Resources Conservation Service, United States Department of Agriculture (2015b) Web Soil Survey, Essex County, Vermont. Available online at http://websoilsurvey.nrcs.usda.gov/. Accessed July 2015

Soil Survey Staff, Natural Resources Conservation Service, United States Department of Agriculture (2015c) Official Series Description for Antigo silt loam. Available online at https://soilseries.sc.egov.usda.gov/OSD_Docs/A/ANTIGO.html, 15 May 2015

Chapter 23
Digital Soil Morphometrics Brings Revolution to Soil Classification

Judit Nagy, Adam Csorba, Vince Lang, Marta Fuchs and Erika Micheli

Abstract Soil classification systems are grouping soils with similar properties. The distinguishing properties are the ones that we are able to observe or measure. As the state of knowledge and the need of users are changing, the definitions should be tested and changes should be accommodated. The recent boom of observation technologies, data storage, and data processing achievements provided new opportunities to predict similarities and differences in soils. The tools of digital soil morphometrics are resulting in new parameters and properties and in deriving continuous depth functions. This chapter reviews the criteria of soil parameters and their novel methods for field observation and definition (horizon depth, texture, color, structure, organic matter, mottling, and carbonates). The internationally endorsed soil classification systems could potentially be supported with these new approaches. The review is based on the WRB and is supplemented with an example of predicting soil diagnostic horizons using digital soil morphometrics. The application of faster, efficient, and more objective measurements can bring revolution to the classification of soils.

Keywords Soil classification · Digital soil morphometrics · Diagnostics · World reference base

23.1 Introduction

One of the main aims of soil science is to understand the relationships between soil properties, processes, and functions, and recognize and predict soil changes in space and time. To be able to define differences and changes, accessible and reliable

J. Nagy (✉) · A. Csorba · V. Lang · M. Fuchs · E. Micheli
Department of Soil Science and Agricultural Chemistry, Szent István University, Gödöllő, Hungary
e-mail: nagy.judit@mkk.szie.hu

A.E. Hartemink and B. Minasny (eds.), *Digital Soil Morphometrics*,
Progress in Soil Science, DOI 10.1007/978-3-319-28295-4_23

soil information is essential. Most soil classification systems have definitions and criteria that are based on field observations supplemented by laboratory analyses. Field observations are often subjective, while laboratory analyses are often time and resource demanding and are performed on samples taken from certain portions of the profile. Digital soil morphometrics is defined as the application of tools and techniques for measuring, mapping, and quantifying soil profile attributes and deriving continuous depth functions (Hartemink and Minasny 2014).

In this chapter, we discuss the potential applications of digital soil morphometrics to predict the building blocks of the major differentiation criteria in soil classification systems. The review is based on selected soil attributes that are part of the definitions of diagnostic units of internationally endorsed soil classification systems. The selected properties are the major differentiation criteria in the definitions of the diagnostic units, hence the taxa of the World Reference Base for Soil Resources (IUSS WG WRB 2014). This chapter will review the potential application of digital morphometrics based on available literature. Some of the reviews will be discussed in the Results section.

23.2 Materials and Methods

The selected attributes as the major differentiation criteria in the definitions of the diagnostic units of internationally used soil classification systems are based on the World Reference Base for Soil Resources (IUSS WG WRB 2014). The review of the potential application of digital morphometrics is based on the available literature. Hence, some of the materials will be discussed in the Results section.

An example is based on reflectance spectroscopic measurements to predict diagnostic horizons. Thirteen soil profiles from different locations in Hungary were investigated by traditional and Vis–NIR laboratory spectroscopic methods. Using the field descriptions and the auxiliary laboratory data, the soils were classified to the reference soil group (RSG) level according to the WRB classification system. Samples collected from fixed depth intervals were investigated by laboratory Vis–NIR spectroscopic methods to infer the main soil horizons and derive parameters whose distribution along the soil profile can be related to certain key soil properties (organic carbon, $CaCO_3$, and clay content). For the spectral measurements, samples were collected at 5 cm depth intervals to 1.0 m depth and by 10 cm intervals between 1.0 and 1.5 m. The Vis–NIR reflectance spectra of the 325 air-dried, grounded, and sieved samples were acquired using the Analytical Spectral Devices (ASD) FieldSpec 3 MAX portable spectroradiometer with a contact probe attachment. The spectra were transformed to units of absorbance (log(1/reflectance)) and first derivatives were calculated using Savitzky–Golay method (Savitzky and Golay 1964). Principal component (PC) analysis was performed on the spectral dataset to reduce the high dimensionality. The PC scores were used as variables describing the spectral properties of the soils along the profile. To test the "profile description ability" of the spectral dataset, Fuzzy C-means clustering was performed on the

matrix of the PC factor scores using KNIME software (Berthold et al. 2007). The number of clusters determined prior the analysis was determined by Silhouette analysis using the R statistical software package (R Development Core Team 2008).

For reference laboratory analysis (organic carbon, $CaCO_3$, and clay content), samples from genetic horizons were collected from each soil profile. To estimate the reference soil parameters in the fixed depth intervals, mass-preserving spline functions were fitted on the reference soil properties using the SplineTool v2.0 software (ASRIS 2011). The spline estimated reference values and the Fuzzy-C membership values were plotted against the depth.

23.3 Results

23.3.1 Review of Some Key Soil Properties, Important for Diagnostic Soil Classification

Table 23.1 summarizes the diagnostic horizons, properties, and materials which play a key role in the differentiation of the RSGs in the WRB 2014. The table lists the soil parameters whose determination is necessary to define the reviewed diagnostic units. Based on the study of Hartemink and Minasny (2014), only the soil parameters which can be effectively determined by digital soil morphometric methods are indicated. The parameter list includes soil texture, soil texture variations along the profile, and clay content (combined indication of the three is ST); soil matrix color (MC); soil structure (SS); soil organic carbon content (OC); redoximorphic features and mottles (RF); and calcium carbonate content (CB).

ST plays key role in defining 15 horizons, 9 properties, and 1 material. MC plays key role in defining 15 horizons, 9 properties, and 3 materials. SS defines 15 horizons, 4 properties, and 1 material. OC defines 15 horizons, 1 property, and 3 materials. RF defines 8 horizons and 2 properties. Based on soil carbonate (CB), 6 horizons, 4 properties, and 2 materials are defined.

Hartemink and Minasny (2014) gave an overview of soil properties that have been successfully measured or predicted by the tools of digital soil morphometrics. The following chapter is summarizing how the new tools are supporting the establishment of criteria of the major elements of the WRB soil classification system.

Horizon Depth

Ever since Dokuchaev (1883) introduced the horizons as a basic feature in differentiation of soils, the concepts have been accepted by the soil science community (Bockheim et al. 2005). Horizon boundaries provide data about the conditions and processes that have formed the soil. There are great varieties in shape and depth of

Table 23.1 Summary of diagnostic horizons, properties, and materials whose presence or absence defines the reference soil groups (RSGs)

Diagnostics[a]	RSG[b]	ST[c]	MC[d]	SS[e]	OC[f]	RF[g]	CB[h]
Anthraquic hor.	**AT CM**		X	X		X	
Argic hor.	TC AN *FR GY CA* **RT AC LX AL LV**	X		X			
Calcic hor.	LP **CH KS CA**						X
Cambic hor.	**CM**	X	X	X	X	X	X
Chernic hor.	TC LP **CH**	X	X	X	X		X
Cryic hor.	**CR**						
Duric hor.	TC **DU**						
Ferralic hor.	TC AN **FR**	X					
Ferric hor.	TC					X	
Folic hor.					X		
Fragic hor.	TC **CM**	X	X	X	X		X
Fulvic hor.			X		X		
Gypsic hor.	LP **GY**	X					
Histic hor.					X		
Hortic hor.	**AT**		X		X		
Hydragric hor.	**AT** TC **CM**		X	X		X	
Irragric hor.	**AT CM**	X		X	X		
Melanic hor.			X		X		
Mollic hor.	**GL KS PH UM**	X	X	X	X		X
Natric hor.	TC **SN**	X		X			
Nitic hor.	TC **NT**	X		X			
Petrocalcic hor.	TC LP **CA**						X
Petroduric hor.	TC LP **DU**						
Petrogypsic hor.	TC LP **GY**						
Petroplinthic hor.	TC LP AN **PT** NT **CM**					X	
Pisoplinthic hor.	TC AN **PT** NT **CM**					X	
Plaggic hor.	**AT CM**	X	X		X		
Plinthic hor.	TC AN **PT** NT **CM**					X	
Pretic hor.	**AT CM**		X		X		
Protovertic hor.		X		X			
Salic hor.	**SC CM**						
Sombric hor.		X	X	X	X		
Spodic hor.	TC LP AN **PZ**	X	X	X	X		
Terric hor.	**AT CM**		X				
Thionic hor.	SC **CM**					X	
Umbric hor.	**GL UM**		X	X	X		
Vertic hor.	TC **VR** NT **CM**	X		X			
Abrupt text. diff.	**PL**	X					
Albeluvic glossae		X	X	X			
Andic prop.	**AN CM**						
Anthric prop.		X	X	X	X		X
Aridic prop.		X	X				
Continuous rock	**HS TC LP AN ST AC AL**						X
Geric prop.							
Gleyic prop.	**GL**		X			X	
Lithic discontinuity		X					
Protocalcic prop.				X			X

(continued)

Table 23.1 (continued)

Diagnostics[a]	RSG[b]	ST[c]	MC[d]	SS[e]	OC[f]	RF[g]	CB[h]
Reducing cond.	**GL PT PL ST**						
Retic prop.	**RT**	X	X	X			
Shrink-swell cracks	**VR**						
Sideralic prop.			X				
Stagnic prop.	**PT PL ST**	X	X			X	
Takyric prop.		X	X				
Vitric prop.	**AN CM**						
Yermic prop.		X	X				
Albic mat.			X				
Artifacts	**TC**						
Calcaric mat.							X
Colluvic mat.							
Dolomitic mat.							X
Fluvic mat.	**FL**	X	X	X	X		
Gypsiric mat.							
Hypersulfidic mat.							
Hyposulfidic mat.							
Limnic mat.							
Mineral mat.					X		
Organic mat.	**HS**				X		
Ornithogenic mat.							
Soil organic carbon							
Sulfidic mat.							
Technic hard mat.	**HS TC LP AN ST AC AL**						
Tephric mat.							

Soil attributes whose determination is necessary to define the diagnostic unit are marked by X. Based on Hartemink and Minasny (2014); the soil attributes that can be efficiently determined by digital soil morphometric tools are indicated

HS Histosols, *AT* Anthrosols, *TC* Technosols, *CR* Cryosols, *LP* Leptosols, *SN* Solonetz, *VR* Vertisols, *SC* Solonchaks, *GL* Gleysols, *AN* Andosols, *PZ* Podzols, *PT* Plinthosols, *NT* Nitisols, *FR* Ferralsols, *PL* Planosols, *ST* Stagnosols, *CH* Chernozems, *KS* Kastanozems, *PH* Phaeozems, *UM* Umbrisols, *DU* Durisols, *GY* Gypsisols, *CL* Calcisols, *RT* Retisols, *AC* Acrisols, *LX* Lixisols, *AL* Alisols, *LV* Luvisols, *CM* Cambisols, *AR* Arenosols, *FL* Fluvisols, *RG* Regosols

[a]Diagnostic horizons, properties, and materials

[b]Reference soil group—**Bold codes** represent RSGs where the presence of the diagnostic unit is a criterion

Normal codes represent RSGs where the absence of the diagnostic unit is a criterion

Italic codes represent RSGs where the absence of the diagnostic unit is a criterion unless it fulfills further requirements

[c]Soil texture, texture differences, clay content

[d]Matrix color

[e]Soil structure

[f]Organic matter, organic carbon

[g]Redoximorphic features, mottles

[h]Carbonates

horizon boundaries ranging from abrupt to diffuse and from smooth to broken. The depth and width of horizons are the criteria for almost all diagnostic units in many soil description or classification systems. Soil scientists spend significant time and often argue during the establishment of depth and width of the horizon depth based on key soil properties, it is expected that digital soil morphometrics may enhance soil horizon determination. Encouraging research results have been published by Doolittle and Collins (1995), Rooney and Lowery (2000), Legros (2006), Weindorf et al. (2012), Steffens and Buddenbaum (2013), and others on the application of the ground-penetrating radar (GPR), electrical resistivity (ER), hyperspectral imaging spectroscopy, and X-ray fluorescence (XRF) (all cited from Hartemink and Minasny 2014) (Table 23.2).

Soil Texture

Soil texture refers to the relative proportions of sand, silt, and clay within the fine earth fraction. Flowcharts are available presenting the way soil texture can be estimated (Rowell 1994; Thien 1979). A frequently used way to describe soil texture in the field is the "finger test" or determining by feel. Texture can be estimated by gently pushing the soil out between the thumb and the forefinger. The success greatly depends on the senses and the experience of the expert, performing the estimation, hence is subjective and final results can be concluded only after laboratory determination. The initial field decision on several diagnostic units and taxa has to be followed after the laboratory results are available. This often does not happen and causes inconsistences in data bases.

Texture plays a major role in the differentiation of albeluvic glossae, retic, vertic properties, fluvic material, lithic discontinuity, abrupt textural difference, further in the case of argic, cambic, fragic, irragric, natric, nitic, vertic horizons, and for the Vertisols reference soil group. Texture differences have significant importance as a criterion for argic horizon in the case of Acrisols, Alisols, Lixisols, and Luvisols, natric horizon in the case of Solonetz; further texture differences are a diagnostic criterion for fluvic material, abrupt textural difference, and retic properties.

Digital morphometrics provides tools to improve objectivity with regard to the determination of the soil texture in the field, making the establishment of many classification units.

Weindorf et al. (2012) tested portable XRF for the determination of soil texture in situ and on cores ex situ in the laboratory. Zhu et al. (2011) measured samples which covered a wide range of soils, and concluded that in situ determination of soil texture with pXRF yielded promising results for relatively dry soils as well as wet soils supplemented with portable moisture sensors. Ge et al. (2005) stated that soil moisture can affect the XRF signal but also offered an algorithm to mitigate similar problems. This issue is discussed further in Stockmann et al. (2015).

Diffuse reflectance spectroscopy was tested by Waiser et al. (2007) for in situ quantification of clay content of soils from a wide range of parent material types. A method based on in situ spectroscopic measurements coupled with chemometric

Table 23.2 Diagnostic horizons of the world reference base (WRB) with strong criteria related to horizon depth

WRB diagnostics	Criteria (simplified)
Anthraquic horizon	Thickness ≥15 cm
Argic horizon	Thickness of ≥7.5 or 15 cm
Calcic horizon	Thickness of ≥15 cm
Cambic horizon	Thickness of ≥15 cm
Chernic horizon	Thickness ≥25 cm
Cryic horizon	Thickness of ≥5 cm
Duric horizon	Thickness of ≥10 cm
Ferralic horizon	Thickness of ≥30 cm
Ferric horizon	Thickness of ≥15 cm
Folic horizon	Thickness of ≥10 cm
Fragic horizon	Thickness of ≥15 cm
Fulvic horizon	Combined thickness of ≥30 cm with ≤10 cm non-fulvic material in between
Gypsic horizon	Thickness of ≥15 cm
Histic horizon	Thickness of ≥10 cm
Hortic horizon	Thickness of ≥20 cm
Hydragric horizon	Thickness of ≥10 cm
Irragric horizon	Thickness of ≥20 cm
Melanic horizon	Combined thickness of ≥30 cm with ≤10 cm non-melanic material in between
Mollic horizon	Thickness of ≥10 cm or ≥20 cm
Natric horizon	Thickness of ≥7.5 or 15 cm
Nitic horizon	Thickness of ≥30 cm
Petrocalcic horizon	Thickness of ≥10 or 10 cm or ≥1 cm
Petrogypsic horizon	Thickness of ≥10 cm
Petroplinthic horizon	Thickness of ≥10 cm
Pisoplinthic horizon	Thickness of ≥15 cm
Plaggic horizon	Thickness of ≥20 cm
Plinthic horizon	Thickness of ≥15 cm
Pretic horizon	Combined thickness of ≥20 cm
Protovertic horizon	Thickness of ≥15 cm
Salic horizon	Thickness of ≥15 cm
Spodic horizon	Thickness of ≥25 cm
Terric horizon	Thickness of ≥20 cm
Thionic horizon	Thickness of ≥15 cm
Umbric horizon	Thickness of ≥10 cm if directly overlying continuous rock, technic hard material or a cryic, petroplinthic, or petroduric horizon, or ≥20 cm
Vertic horizon	Thickness of ≥25 cm

methods was successfully applied by Viscarra Rossel et al. (2009) to estimate soil color, mineral composition, and clay content of samples from multiple depths. Lagacherie et al. (2008) showed how reflectance spectrometry can be used in the laboratory to estimate clay and calcium carbonate content (Table 23.3).

Table 23.3 Diagnostic units (horizons, properties, materials) of the WRB with criteria related to soil texture

WRB diagnostics	Criteria (simplified)
Argic horizon	Defined texture classes (texture class of loamy sand or finer and ≥8 % clay)
Cambic horizon	Defined texture classes
Ferralic horizon	Defined texture class of sandy loam or finer
Fragic horizon	Defined texture classes (same as in Cambic horizon)
Chernic horizon	Defined texture classes if first color criterion is not fulfilled
Mollic horizon	Defined texture classes if first color criterion is not fulfilled
Natric horizon	Defined texture classes texture class of loamy sand or finer and ≥8 % clay
Nitic horizon	Defined clay content (≥30 %), and silt to clay ratio (<0.4)
Plaggic horizon	Defined texture classes
Protovertic horizon	≥30 % clay throughout
Vertic horizon	≥30 % clay throughout
Takyric properties	Texture class of clay loam, silty clay loam, or clay
Argic horizon	Defined textural differentiation to the overlying horizon
Cambic horizon	Defined clay increase compared to the directly underlying layer
Fragic horizon	Defined clay increase compared to the directly underlying layer
Irragric horizon	Higher clay content, particularly fine clay, than the underlying original soil; and defined differences in sand, silt, and clay contents between parts of the horizon
Natric	Defined textural differentiation to the overlying horizon
Nitic	<20 % difference (relative) in clay content over 15 cm to layers directly above and below
Abrupt textural difference	(within ≤5 cm) Doubling of the clay content or ≥20 % (absolute) increase in clay content (based on the clay content of the overlying layer)
Lithic discontinuity	Defined differences in particle-sized distribution between layers directly superimposed on the other
Albeluvic glossae	Clay content of the stronger colored parts is higher compared with the lighter colored parts, a specified for the argic horizon
Retic properties	Clay content of the stronger colored parts is higher compared with the lighter colored parts, as specified for the argic or natric horizon
Fluvic material	Stratification (may be) reflected in variation in texture

Soil Color

The result of soil color assessment in the field is affected by personal experience. The Munsell Color Theory has brought standardization to color communication as within the system each color has a logical and visual connection to the other colors. Color readings in the field depend on the moisture status of the current soil profile and the quality of light (Pendleton and Nickerson 1951; Post et al. 1993; Simonson 1993). The determination of color is difficult even for experts due to several factors affecting the readings including the quality and age of Munsell charts. Soil color is a diagnostic criterion in WRB for anthraquic horizon, cambic, chernic, fragic, fulvic, hortic, melanic, plaggic, pretic, sombric, umbric horizons, albeluvic glossae, gleyic, retic, sideralic, stagnic properties, and albic material (IUSS WG WRB 2006).

Table 23.4 Diagnostic units (horizons, properties, materials) of the WRB with criteria related to soil color

WRB diagnostics	Criteria (simplified)
Anthraquic horizon	A puddled layer with defined Munsell colors
Cambic horizon	Defined color change compared to the directly underlying layer
Chernic horizon	Defined Munsell colors
Fragic horizon	Defined color change compared to the directly underlying layer (same as in Cambic horizon)
Fulvic horizon	Defined Munsell colors
Hortic horizon	Defined Munsell color
Melanic horizon	Defined Munsell color
Mollic horizon	Defined Munsell color
Plaggic horizon	Defined Munsell color
Pretic horizon	Defined Munsell color
Sombric horizon	Lower Munsell color value or chroma than the overlying horizon
Spodic horizon	Defined Munsell color
Umbric horizon	Defined Munsell color
Albeluvic glossae	Defined Munsell color
Gleyic properties	Defined Munsell color
Retic properties	Defined Munsell color
Sideralic properties	Defined Munsell color chroma
Stagnic properties	Defined differences in Munsell colors to the surrounding materials
Albic materials	Defined Munsell colors

Soil color is the major differentiation criterion for the mollic and umbric horizons which defines Chernozems, Kastanozems, Phaeozems, and Umbrisols reference soil groups.

In the case of cambic and fragic horizons, MC has a basic significance. Fulfillment of the criteria depends on the defined color change compared to the directly underlying layer (WRB). The stagnic properties' criteria fulfillment also depends on the defined differences in Munsell colors to the surrounding material.

Viscarra Rossel (2009) used Vis–NIR to define soil color in the field and in the laboratory and their results were compared to Munsell color. They have found compatibility between spectroscopic measurements and Munsell readings (Table 23.4).

Soil Structure

Soil structure refers to the arrangement of the soil particles into soil units (ped, aggregates) resulting from several pedogenic processes (FAO 2006). Alternation of the dry and wet conditions, root activity, and fauna is important in the formation of SS (Materechera et al. 1992).

Structure is a differentiation criterion in the WRB in the case of mollic and umbric horizons; anthraquic, cambic, chernic, nitic, vertic, irragric, petrocalcic, calcic, further, in the case of Solonetz columnar or prismatic (or blocky) structure should present to fulfill the criteria.

Table 23.5 Diagnostic units (horizons, properties, materials) of the WRB with criteria related to soil structure

WRB diagnostics (horizons, properties, materials)	Criteria (simplified)
Anthraquic horizon	Platy or massive structure in ≥25 % of its volume
Cambic horizon	Soil aggregate structure in ≥50 % of the volume of the fine earth fraction
Chernic horizon	Granular or fine subangular blocky soil structure
Fragic horizon	Soil aggregate structure in ≥50 % of the volume of the fine earth fraction (same as in Cambic horizon)
Mollic horizon	Sufficiently strong structure
Natric horizon	Columnar or prismatic (or blocky) structure
Nitic horizon	Strong blocky structure breaking into polyhedral or flat-edged or nut-shaped elements
Protovertic horizon	Wedge-shaped soil aggregates or slickensides
Umbric horizon	Sufficiently strong structure
Vertic horizon	Wedge-shaped soil aggregates or slickensides
Takyric properties	Platy or massive structure
Anthraquic horizon	Platy or massive structure in ≥25 % of its volume
Cambic horizon	Soil aggregate structure in ≥50 % of the volume of the fine earth fraction
Chernic horizon	Granular or fine subangular blocky soil structure

The correct determination of SS is critical especially in the case of natric—columnar, prismatic (or blocky) structure required—because it determines the Solonetz reference soil group.

The notion of "strong structure" for mollic and umbric surface horizons is required because they are diagnostic for Umbrisols, Chernozems, Kastanozems, and Phaeozems reference soil groups. The definition of "strong" is too broad and the determination can be subjective even with expert knowledge. Either the clarification of phrasing of the definition "sufficiently strong structure" or the reformation of tools used for the structure determination is needed.

NIR and MIR spectroscopy have been applied to estimate soil organic carbon and clay content (Gomez et al. 2013) but no device is available that can measure the distinct aspects of the SS in the field (Hartemink and Minasny 2014). Hirmas and Hasiotis (2010) used laser imaging for measurement of structure (Table 23.5).

Organic Matter

Organic matter plays a crucial role in each existing classification system.

Organic matter content of surface horizons can determine Histosols, Chernozems, Kastanozems, and Phaeozems through mollic, chernic, and umbric surface horizons.

There are several measurement methods for determining organic matter and organic carbon in the laboratory but two results of two different measurement methods cannot be compared with each other.

Table 23.6 Diagnostic units (horizons, materials) of the world reference base (WRB) with criteria related to organic carbon (OC) content

WRB diagnostics	Criteria (simplified)
Cambic horizon	Does not form part of other horizons with OC criteria
Chernic horizon	Minimum organic carbon content (1 %) and thickness of the horizon (high base)
Folic horizon	Presence and minimum thickness of organic soil material (dry/aerated?) conditions)
Fragic horizon	<0.5 % soil organic carbon
Fulvic horizon	Specific organic matter nature[a] minimum organic carbon content (6 % weight average), and thickness of the horizon
Histic horizon	Presence and minimum thickness of organic soil material (wet conditions)
Hortic horizon	Minimum organic carbon content (1 %) and thickness of the horizon (anthropogenic influence, high phosphate content)
Irragric horizon	Minimum organic carbon content (0.5 % weight average) and thickness of the horizon (with anthropogenic influence)
Melanic horizon	Specific organic matter nature (higher[a] minimum organic carbon content (6 % weight average), and thickness of the horizon
Mollic horizon	Minimum organic carbon content (0.6 %) and thickness of the horizon (high base)
Plaggic horizon	Minimum organic carbon content (0.6 %) and thickness of the horizon (mollic like with anthropogenic influence and artifacts)
Pretic horizon	≥1 % organic carbon
Sombric horizon	Higher content of soil organic carbon respect to the directly overlying horizon or illuvial humus in some parts
Spodic horizon	Minimum organic carbon content (0.6 %) (subsurface accumulation)
Umbric horizon	Minimum organic carbon content (0.6 %) and thickness of the horizon (low base)
Anthric properties	Minimum organic carbon content (0.6 %) and thickness of the horizon (mollic like with anthropogenic influence)
Fluvic material	Irregular change in organic carbon content not relate to pedogenesis
Mineral material	Maximum organic carbon content (20 %)
Organic material	Minimum organic carbon content (20 %)

[a]Higher humic acid ratio compered to fulvic acids in the melanic horizon than in the fulvic horizon, determined by the melanic index (IUSS WG WRB 2006)

As the present definitions are hard to handle, clarification or simplification of limits are recommended (Michéli et al. 2014). Steffens et al. (2014) studied the soil organic matter content and composition applying imaging spectroscopy. They concluded that Vis–NIR imaging spectroscopy is an effective tool for mapping soil organic matter quality even if the layers are not distinguishable visually.

Viscarra Rossel and Hicks (2015) concluded that Vis–NIR spectroscopy is a useful, cheap technique to observe and monitor organic carbon composition. Other studies used Vis–NIR spectroscopy to estimate organic layers in forests (Chodak et al. 2002). Viscarra Rossel et al. (2008) applied a simple digital camera and found correlations for OC and Fe contents (Table 23.6).

Table 23.7 Diagnostic units (horizons, properties, materials) of the WRB with criteria related to redoximorphic features and mottles

WRB diagnostics	Criteria (simplified)
Anthraquic horizon	Iron manganese mottles or coatings
Ferric horizon	Defined presence of coarse mottles, concentrations, or nodules
Hydragric horizon	Fe or Mn coatings or concentrations, or redox depletions
Petroplinthic horizon	Yellowish, reddish, and/or blackish concentrations or nodules or concentrations
Pisoplinthic horizon	Yellowish, reddish, and/or blackish concentrations and/or nodules (strongly cemented to indurated)
Plinthic horizon	Discrete concentrations or nodules, or concentrations
Thionic horizon	Mottles or coatings (with accumulations of iron or aluminum sulfate or hydroxysulfate minerals)
Gleyic properties	>5 % (exposed area) mottles
Stagnic properties	Mottles and/or concentrations and/or nodules

Mottling

Mottles are differently colored spots in a soil matrix and are mostly the result of reduction and oxidation of Fe. Concreted mottles of oxides are diagnostic for the hydragric, ferric, plinthic, petroplinthic, and pisoplinthic horizons and for the stagnic color pattern. Fe or Mn coatings or concentrations or redox depletions are diagnostic criteria for hydragric horizon according to WRB. Mottles and redoximorphic features are key differentiation criteria for Stagnosols and Gleysols.

The presence of Fe^{II} ions can be determined in the field with a 0.2 % α, α dipyridyl solution in 10 % acetic acid solution, but these chemicals are slightly toxic. Steffens and Buddenbaum (2013) concluded that laboratory imaging spectroscopy facilitate the spatially correct soil classification including the quantification of soil mottling (Table 23.7).

Carbonates

Determination of calcium carbonate content in the field is established by adding a few drops of 10 HCl to the soil. The degree of effervescence refers to the presence and amount of calcium carbonate. The rate of reaction depends on soil texture and other materials such as plant tissues. Determination of the 15 % calcium carbonate content—which is the required amount for calcic horizon—has a decisive role in differentiation for Calcisols, Chernozems, Kastanozems, and Leptosols. Furthermore, determination of the origin of the carbonate in the field also requires field experience and could provide information about the processes under the current soil has been formed (FAO 2006).

In WRB, evidence of the leaching of carbonates from the cambic horizon is a diagnostic criterion for Cambisols. Differences in calcium carbonate content between parts of a horizon are part of the definition of the irragric horizon. Calcic

Table 23.8 Diagnostic units (horizons, properties, materials) of the WRB with criteria related to $CaCO_3$

WRB diagnostics	Criteria (simplified)
Calcic horizon	≥15 % $CaCO_3$, and ≥5 % (by volume) secondary carbonates, or ≥5 % $CaCO_3$ higher than an underlying layer and no lithic discontinuity, and does not form part of a petrocalcic horizon
Cambic horizon	≥5 % less carbonates
Chernic horizon	≥40 % (by mass) $CaCO_3$
Fragic horizon	Does not show effervescence after adding a 1 M HCL solution
Mollic horizon	If color is lighter than value of 3 moist and 5 dry and the chroma of 3 than ≥40 % $CaCO_3$ content
Petrocalcic horizon	Very strong effervescence after adding 1 M HCl solution, and shows induration or cementation at least partially by secondary carbonates
Continuous rock	Not part of a petrocalcic horizon
Protocalcic properties	Soft calcium carbonate accumulations in different forms
Dolomitic material	Strong effervescence with heated 1 M HCl solution

horizon or a layer with protocalcic properties is also a requirement for Calcisols, Chernozems, and Kastanozems (WRB) (Table 23.8).

23.3.2 Vis–NIR Spectroscopy for Distinguishing Soil Horizons

A previous study (Csorba et al. 2014) showed that Vis–NIR reflectance spectroscopy coupled with principal component variables (PC factor scores) can be effectively used as variables describing the spectral properties along the soil profile. This study focuses on the definition of diagnostic horizons.

The Silhouette analysis performed prior to the Fuzzy C-means clustering showed that the PC factor score values can be classified into three clusters (Clusters A, B, and C). Figure 23.1 shows the distribution of the samples along the first three principal components that explained 92 % of the total variance. The color coding and the symbols in Fig. 23.1a refer to the field-determined WRB diagnostic horizons, while Fig. 23.1b shows the classes obtained from the Fuzzy C-means clustering. Based on the visual inspection of the scatterplots, the clustering of samples is in good accordance with the determined diagnostic horizons. Major part of Cluster A samples were taken from a calcic, Cluster B from a mollic, and Cluster C from an argic horizon.

Three examples of the comparison of the Fuzzy-C membership values and the spline-resampled organic carbon, $CaCO_3$, and clay content values versus the depth are shown in Fig. 23.2. The cluster membership values of the Cluster A show similar pattern as the spline estimated $CaCO_3$ values. The membership values of the Cluster B show similar pattern as the spline estimated organic carbon values. The explanation of the distribution of the membership values of the Cluster C along the

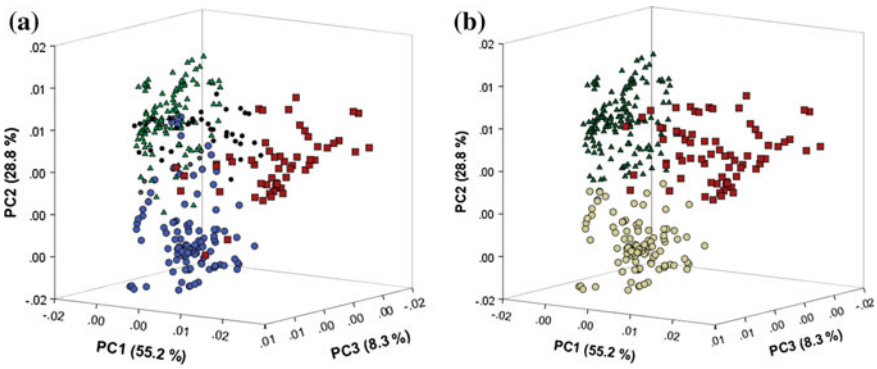

Fig. 23.1 The 3D scatterplots showing the distribution of samples along first three principal components. **a** The coloring and symbology refer to the WRB diagnostic horizon the samples belong to. Calcic *filled blue circle;* Argic *filled red square;* Mollic *filled green triangle;* Mollic—Calcic *open circle* Non-diagnostic horizon *black circle*. **b** The coloring and symbology refer the Fuzzy C-means clusters the samples belong to Cluster A *filled ash circle;* Cluster B *filled red square*; and Cluster C *filled green triangle*

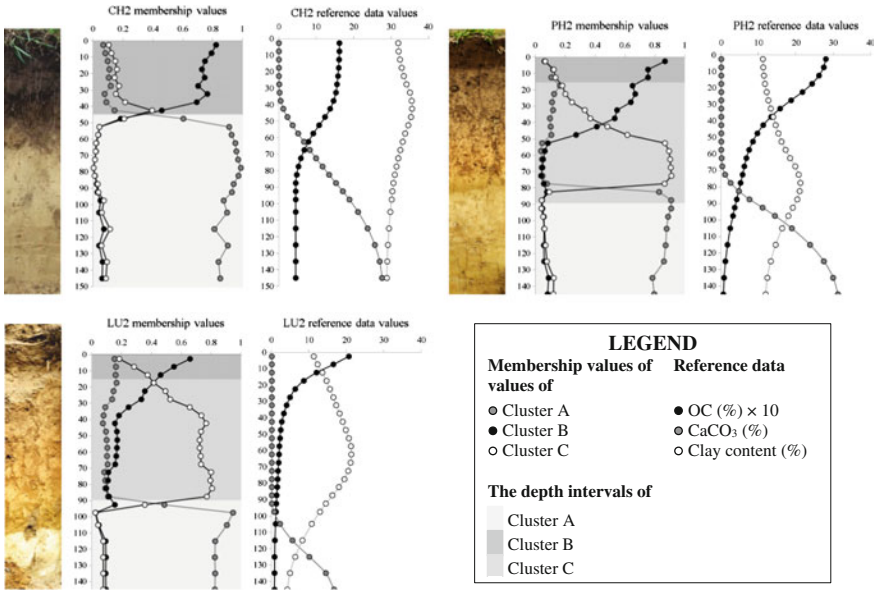

Fig. 23.2 Three examples of the distribution of the cluster membership values and the reference spline-resampled OC, $CaCO_3$, and clay content values (with *circles*). On the plot showing the membership values versus the depth, the depth intervals of the clusters are also indicated (with the *rectangles* of different shades of *gray*)

profile needs a different approach. Their distributions show similarity with the clay content only in the case of soil profiles where considerable clay illuviation has occurred.

23.4 Summary and Conclusions

During this study, the digital soil morphometric tools proved to be efficient in the determination of soil parameters playing key role in the definition of diagnostic units of the WRB were reviewed. Six soil parameters were investigated based on their role of defining the diagnostic criteria. The reviewed digital soil morphometrics tools and methods are supporting the prediction of properties that are part of the criteria of diagnostic units of WRB. Some of these attributes are determined or estimated in the field with subjective element and supported by laboratory analysis. The new tools can bring a revolution to soil classification and to soil science in general, as they provide cost effective and quick measurements and results to assist in the field decisions and the process of soil classification.

Effectiveness is not the only benefit of these methods; compared to the standard methods, these tools can provide a cleaner technology with minimizing or cease the environmental impacts of measurements.

The example study demonstrated the significance of Vis–NIR reflectance measurements in predicting diagnostic horizons. Because the technology supplies integrative measurements of soil, it can facilitate the collection of large amount of soil data and provide more information than the conventional—accurate but expensive—survey methods.

In summary, digital morphometrics provides the potential of less subjective, more time and cost efficient and environment friendly support or replacement of field and laboratory methods applied in soil classification.

Acknowledgement This work was supported by Research Centre of Excellence—9878-3/2015/FEKUT.

References

ASRIS (2011) ASRIS—Australian soil resource information system. http://www.asris.csiro.au. Accessed 21 Dec 2014

Berthold MR, Cebron N, Dill F, Gabriel TR, Kötter T, Meinl T, Ohl P, Sieb C, Thiel K, Wiswedel B (2007) KNIME—Konstanz information miner. Studies in classification, data analysis and knowlodge organization. Springer, pp 319–326

Chodak M, Ludvig B, Khanna P, Beese F (2002) Use of near infrared spectroscopy to determine biological and chemical characteristics of organic layers under spruce and beech stands. J Plant Nutr Soil Sci 165(1):27–33

Csorba A, Lang V, Fenyvesi L, Micheli E (2014) Identification of WRB soil classification units from vis-NIR spectral signatures. In: Kim PJ, Kang H-W et al (eds) 20th world congress of soil

science: in commemoration of the 90th anniversary of the IUSS. Jeju, South-Korea, 08.06.2014–13.06.2014. IUSS, Paper P4–539
Dokuchaev VV (1883) The Russian Chernozem Report to the Imperial Free Economic Society. St. Petersburg
Doolittle JA, Collins ME (1995) Use of soil information to determine application of ground penetrating radar. J Appl Geophys 33:101–108
Ge L, Lai W, Lin Y (2005) Influence of and correction for moisture in rocks, soils and sediments on in situ XRF analysis. X-Ray Spectrom 34:28–34
Gomez C, Le Bissonnais Y, Annabi M, Bahri H, Raclot P (2013) Laboratory Vis-NIR spectroscopy as an alternatibe method for estimating the soil aggregate stability indexes of Mediterranean soils. Geoderma 209–210, 86–97
Hartemink AE, Minasny B (2014) Towards digital soil morphometrics. Geoderma 230–231
Hirmas D, Hasiotis ST (2010) Field application of multistripe laser triangulation (MLT) scanning to enhance and quantify descriptions of soil and exogenic trace morphology. GSA Annual Meeting 31 Oct - 3 Nov 2010. Denver Colorado USA
IUSS Working Group WRB (2006) World Reference Base for Soil Resources 2006 World Soil Resources Report No. 103, FAO, Rome
IUSS WG WRB (2014) World reference base for soil resources 2014. International soil classification system for naming soils and creating legends for soil maps. World Soil Resources Reports No. 106. FAO, Rome
Materechera SA, Dexter AR, Alston AM (1992) Formation of aggregates by plant roots in homogenised soils. Plant Soil 142: 69–79
Michéli E, Owens PR, Láng V, Fuchs M, Hempel J (2014) Organic Carbon as a major differentiation criterion in soil classification systems. In: Hartemink AE, McSweeney K (eds) Soil carbon. Progress in soil science. Springer, pp 37–45
Lagacherie P, Baret F, Feret JB, Madeira Netto J, Robbez-Masson JM (2008) Estimation of soil clay and calcium carbonate using laboratory, field and airborne hyperspectral measurements. Remote Sens. Environ. 112, 825–835
Legros JP (2006). Mapping of the soil, Science Publishers, pp:1–35
Pendleton RL, Nickerson D (1951) Soil colors and special Munsell soil color charts. Soil Sci. 71, 35–43
Post DF, Bryant RB, Batchily AK, Huete, AR, Levine SJ, Mays MD, Esadafal R (1993) Correlations between field and laboratory measurements of soil color. In: Bigham, J. M., Ciolkosz, E. J. Soil Color Soil Sci Soc Am., Madison, WI. pp 35–49
R Development Core Team (2008) R: A language and environment for statistical computing. R Foundation for Statistical Computing, Vienna, Austria
Rooney DJ, Lowery B (2000) A profile cone penetrometer for mapping soil horizons. Soil Sci Soc Am J 64:2136–2139
Rowell DL (1994) Soil science: methods and applications. Longman, Harlow, England
Savitzky A, Golay MJE (1964) Smoothing and differentiation of data by simplified least squares procedures. Anal Chem 36:1627–1639
Simonson RW (1993) Soil color standards and terms for field use - history of their development. In: Bigham JM, Ciolkosz EJ Soil Sci Soc Am. Madison, WI. pp. 1–20
Steffens M, Buddenbaum H (2013) Laboratory imaging spectroscopy of a stagnic Luvisol profile-High resolution soil characterization, classification and mapping of elemental concentrations. Geoderma 195–196:122–132
Steffens M, Kohlpaintner M, Buddenbaum H (2014) Fine spatial resolution mapping of soil organic matter quality in a Histosol profile. Eur J Soil Sci 65(6):827–839
Stockmann U, Malone B, McBratney A, Minasny B (2015) Landscape scale exploratory radiometric mapping using proximal soil sensing. Geoderma 239:115–129
Thien SJ (1979) A flow diagram for teaching texture by feel analysis. J Agron Educ 8
Viscarra Rossel RA, Fouad Y, Walter C (2008) Using a digital camera to measure soil organic carbon and iron contents. Biosyst Eng 100(2): 149–159

Viscarra Rossel RA, Cattle SR, Ortega A, Fouad Y (2009) In situ measurements of soil colour, mineral composition and clay content by vis-NIR spectroscopy. Geoderma 150:253–266

Viscarra Rossel RA, Hicks W (2015) Estimates of soil organic carbon and its fractions with small uncertainty using visible–near infrared transfer functions. European Journal of Soil Science 66:438–450

Waiser TH, Morgan CLS, Brown DJ, Hallmark CT (2007) In Situ Characterization of Soil Clay Content with Visible Near-Infrared Diffuse Reflectance Spectroscopy. Soil Science Society of America Journal 71(2): 389–396

Weindorf DC, Zhu Y, Haggard B, Lofton J, Chakraborty S, Bakr N, Zhang W, Weindorf WC, Legoria M (2012) Enhanced pedon horizonation using portable X-ray fluorescence spectrometry. Soil Sci Soc Am J 76:522–531

Zhu Y, Weindorf DC, Zhang W (2011) Characterizing soils using a portable X-ray fluorescence spectrometer: 1 Soil texture. Geoderma 167–168:167–177

Chapter 24
From Profile Morphometrics to Digital Soil Mapping

José A.M. Demattê

Abstract Soil observation ranges from point observations to spatial evaluation. We can study the clay content at a point *or* evaluate its distribution across space. Digital morphometrics starts with a vision on the soil profile, to extract information from 'inside soils body' and make a diagnostic of its formation history and characters. On the other hand, soil develops as part of the landscape, which presents a continuous vision. Thus, the task is to extrapolate the pedon observation to space, taking us to a soil map, which is the basis for many applications in environmental and agricultural science. This chapter first demonstrates several practical information capture of soil profiles from its visible, near-, and mid-infrared reflectance. This instance tries to answer questions: How can spectroscopy differentiate soil profiles? How can it assist in soil classification? From this, we explore digital soil mapping with several examples. Strategies on soil mapping using pedotechnologies are discussed and exemplified with studies from a simple to complex geology. Finally, we discuss the perspectives of these techniques for getting a full description of soil distribution in the landscape.

Keywords Remote sensing · Pedotechnologies · Digital soil mapping · Spectroscopy

24.1 Introduction

Soil mapping is an important task which can provide beneficial information to address food, water, and soil security. Most parts of the world have a low-resolution (or large-scale) national soil maps and have limited high-resolution (fine-scale) maps in certain areas. Indeed, high-resolution maps, with a minimum of 1:20,000 cartographic scale, are of great importance because they have practical applications,

J.A.M. Demattê (✉)
Department of Soil Science, Luiz de Queiroz College of Agriculture, University of São Paulo, Pádua Dias Avenue 11, Piracicaba, SP 13418-900, Brazil
e-mail: jamdemat@usp.br

A.E. Hartemink and B. Minasny (eds.), *Digital Soil Morphometrics*,
Progress in Soil Science, DOI 10.1007/978-3-319-28295-4_24

such as soil and water conservation, soil productivity potential, soil monitoring, soil physical and chemical management, crop management, land use planning, price of land, government policies, and roads and urban planning. Thus, soil scientists have a great task on solving this problem: How to produce high-resolution soil maps more efficiently than the traditional method?

Conventional mapping is too costly and time-consuming; in addition, there is a lot of subjective information and requires highly skilled pedologists to obtain high-quality maps. Classical methods are still being used for profile observations, e.g., hammers, knifes, field pH kits, and color charts. New technologies for earth observations (i.e., remote sensing and digital soil mapping) have not been fully embraced by soil scientists. The point is as follows: Are these classical equipments sufficient to determine accurately information of the profile? Can we obtain new information more efficiently and accurately using technologies such as sensing tools? How accurate are the current maps? Can they be modernized to include estimates of uncertainty? Digital soil morphometrics has been proposed to acquire the most desirable and accurate information of the pedon that represent a soil unit.

The main purpose of this paper is to explore how soils can be observed with new pedotechnologies in order to reach the main goal, digital soil maps. We will go from the point information (the pedon) to the spatial domain (the map) using technologies showing advances, limitations, and issues.

24.2 Visualization of Soils

Soil can be visualized in several ways. A pedologist can go in a pit and observe the profile, or he/she can go outside and see the soil relative to its relief. The pedologists have a multiple vision of soils, and it can be suggested from 5 different perspectives:

Perspective 1: micro-perspective, the intrinsic soil characteristics, such as mineralogy, granulometry, porosity, and soil solution chemistry;
Perspective 2: longitudinal vision, related to the surface observation, but with a mental visualization of the undersurface, trying to understand what happens on surface that is related to the underground;
Perspective 3: soil profile or site perspective;
Perspective 4: related to the soil surface composed of the landscape elements, such as landforms, slopes, and drainage patterns;
Perspective 5: bird's eye vision and the distribution of the soil as observed remotely (i.e., from space).

All of these points of view will assist users to understand and visualize soils as a complete body. Indeed, the only way to understand what happens on spatial variation is to merge all these 'visions/perspectives' in one unique mental information and delineate them into soil classes. The importance of this concept is related to the new technologies for soil (pedotechnologies) such as digital soil mapping (DSM) or

digital soil morphometrics (DSMorph). DSM uses inferences to make soil maps (spatial vision), and the DSMoprh to study the soil unit or pedon (point vision).

24.3 Issues in Conventional Soil Mapping and Classification

In conventional soil mapping, surveyors created soil maps based on cartographic information of relief, boreholes, pit observations, and laboratory analysis. This method has been put in test since we now have technologies such as remote sensing. Campos and Demattê (2004) highlighted the importance of using a colorimeter to quantify soil color as a substitute to visual comparison using the Munsell soil color charts. They compared data from five pedologists that performed soil color assessment for the same samples using the Munsell color chart. They observed only 17.5 and 8.7 % agreement among pedologists for dried and moist samples, respectively. All pedologists overestimated the hue, which have consequences in soil classification. Given that field light conditions are highly variable, and the eye sensitivity which changes from individuals and with age, among other factors, we argue that automatic systems should be used for color determination. Bazaglia Filho et al. (2013) compared soil maps of the same area produced by four experienced pedologists and observed important differences and inconsistencies between the maps (Fig. 24.1). These findings prove the necessity to incorporate new technologies in soil mapping activity, not only to improve the accuracy of the information but also to minimize the subjectivity of pedologists' interpretation.

24.4 Advances in Soil Evaluation

McBratney et al. (2003) proposed the 'scorpan' model for digital soil mapping, where two factors were added to Jenny's equation, namely the *s* factor corresponding to soil data available at the beginning of the mapping process, including soil maps, data acquired by means of remote or proximal sensing, and expert pedological knowledge, and the *n* factor representing the geographic position of the soil. The collection of scorpan factors represent the underlying landscape characteristics that allowed the probable occurrence of a particular soil class to be mapped.

With the advances in earth observation technologies, new equipments have been developed such as spectral sensing. Spectral sensing applied to soils can be defined as follows: 'The science that studies the relationship between energy and matter (soils) without any contact between sensors and soil.' In this sense, the equipment can be positioned in any situation such as, in laboratory, in field, in a drone (unmanned aerial vehicle), in an airplane, or in a satellite.

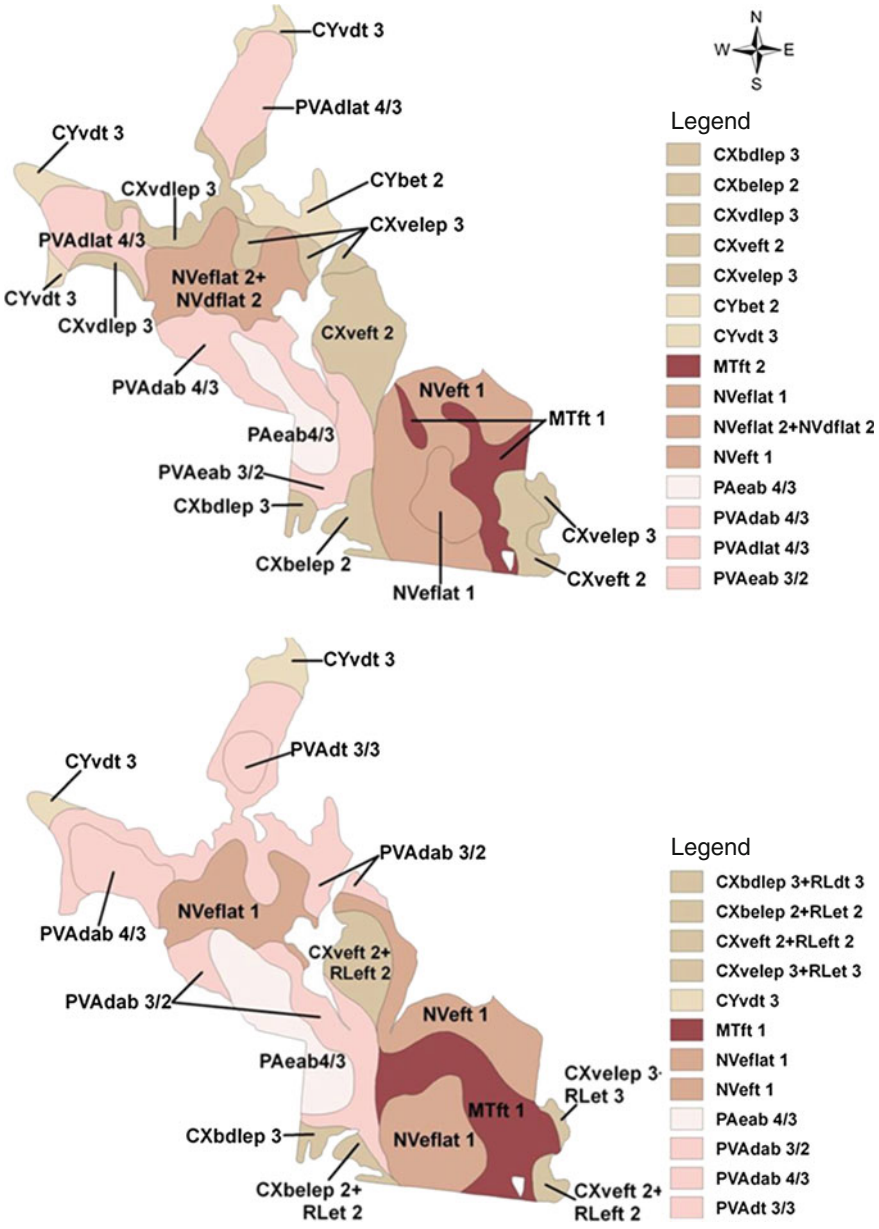

Fig. 24.1 Soil maps made by 2 different pedologists (*Source* Bazaglia Filho et al. 2013)

Much research has been done on laboratory sensing. Soil properties assessment using spectroscopic approaches in UV–Vis–NIR–SWIR–MIR ranges (from 100 to 25,000 nm) has gained importance in the last 20 years (Ben-Dor 2011).

Bellon-Maurel and McBratney (2011) reviewed the spectroscopic prediction of soil organic carbon and its use in carbon stock evaluation; they concluded that MIR had better results than Vis–NIR. This is also confirmed by Araújo et al. (2014). On the other hand, we should emphasize that MIR is most effective in laboratory conditions, while Vis–NIR is more useful in the field (Reeves III 2010). Particle size distribution was successfully predicted by Araújo et al. (2014) using Vis–NIR spectroscopy using a large calibration dataset from Brazil with an $R^2 = 0.88$ on clay content (Fig. 24.2).

When we go to aerial sensing, there will be limitations due to atmospheric conditions, spatial and spectral resolution, orthogonalization of images, and field conditions. Despite these, some good results with hyperspectral images have been

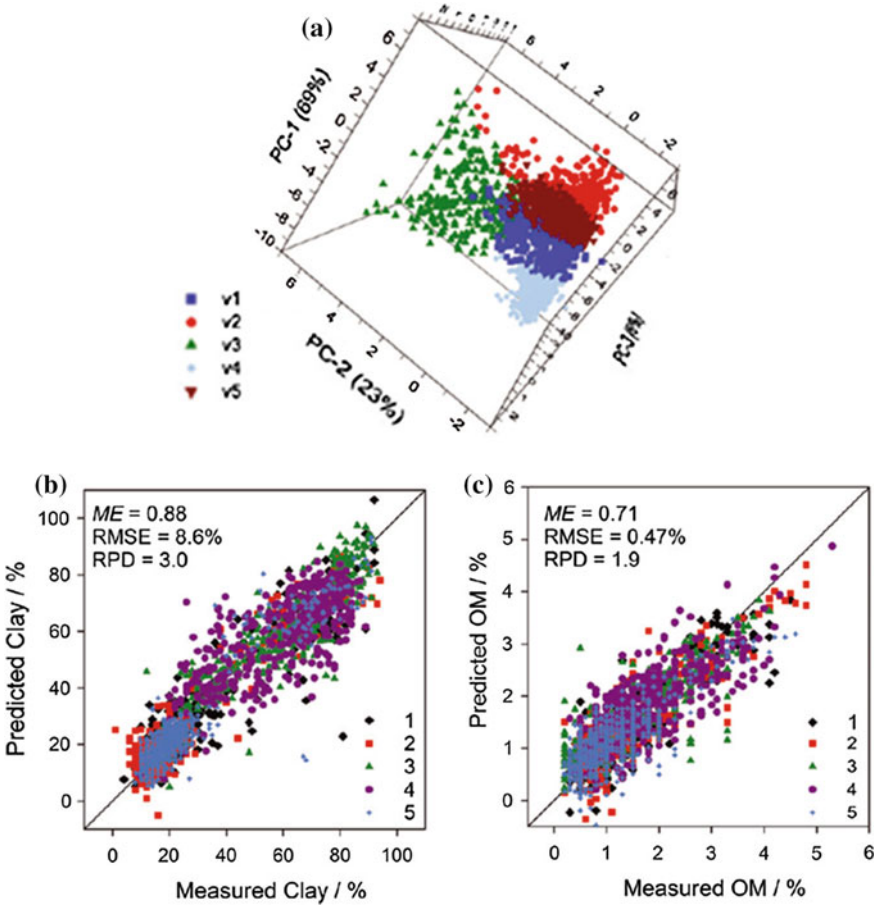

Fig. 24.2 **a** Scores of the three first principal components of PCA of the Vis–NIR spectra on the validation set; **b** validation scatter plot of predicted clay and organic matter (*Source* Araújo et al. 2014)

reported. Using Hyperion images, Lu et al. (2013) reported a cross-validation RMSE of 1.55 $cmol_c\ kg^{-1}$ for CEC quantification. Galvão et al. (2001) evaluated AVIRIS data to quantify TiO_2, Fe_2O_3, and Al_2O_3 contents and reported R^2 values of 0.74, 0.83, and 0.68, respectively. Franceschini et al. (2015) reached R^2 of 0.77 for clay quantification with an aerial hyperspectral sensor. Bartholomeus et al. (2007) observed correlation between spectral bands of ROSIS hyperspectral sensor and iron content determined by the dithionate–citrate method with R^2 value as high as 0.5 for reflectance measurements near 650 nm.

When we go to multispectral information, the accuracy is lower due to low spectral resolution. Using Landsat, Demattê et al. (2009) predicted clay, Al_2O_3, Fe_2O_3, and weathering indices, K, SiO_2, and TiO_2, with similar R^2 values of 0.61, 0.68, 0.67, 0.54, 0.65, and 0.72, respectively. Despite the reflectance information comes only from the surface soil, it can be a first reference of variations of the area.

Each of these techniques and levels of observation of soils have advantages and limitations which are shown in Table 24.1.

Recently, the importance and future of pedotechnologies have appeared such as several soil sensors that can assist in soil classification, including Vis–NIR–SWIR–MIR radiometers, ground penetrating radar, electrical resistivity meters, cone

Table 24.1 Advantages and limitations of each level of platform used for soil mapping and quantification

Level of platform	Advantages	Limitation
Laboratory	Controlled conditions, fast information acquisition; results can assist on soil classification and quantification; can optimize soil analysis with faster, nondestructive method; and can get data from various wavelengths ranges	Have to go to field to collect samples; it is not a direct in situ information; reading in laboratory can mask in situ condition; time-consuming in relation to field work
Field	Quick in situ information of soils; can assist in soil classification; gives the pedologist a quick mental view of what is happening on the relief; and can be done directly in a pit	Interference of moisture and other field conditions cannot be done all the time and depends on the weather; computers and instruments (i.e., specially sensors) are very sensitive to run in field, due to temperature and dust
Aerial	Provides aerial bird's eye view of the field, soils and relief; can 'see' greater area; and gives the spatial information which can be further integrated to the point information	Sees only the surface condition and cannot be used to classify soils, necessity of orthogonalization of images; corrections, and processing
Satellite	Provides a great overview of large areas; can indicate the first view of soil differentiation; and can indicate best areas to make boreholes and pits and soil surface colors, and soil attributes can be linked with relief	Need to have a very good atmospheric correction; depends on spatial and spectral resolution; gives information of the surface of soils and vegetation influence; and can only detect soils under bare condition

penetrometer, hyperspectral core scanner, portable X-ray fluorescence meter, gamma radiometer, and others.

On the other hand, to reach soil classification, we also need to understand the behavior and predictability of different soil attributes in different soils, such as soil texture class (Franceschini et al. 2013), clay activity (Demattê et al. 2007), weathering indices (Galvão et al. 2008), mineralogy suite (Madeira Netto 2001), and electrical conductivity (Ucha et al. 2002). Schuler et al. (2011) indicated that the gamma spectrometry is a promising tool to distinguish Reference Group WRB soil profile in the field and at the landscape scale, but it needs to be verified in other regions of the world. Radu et al. (2013) demonstrated the importance of portable XRF on soil monitoring. Ground penetrating radar (GPR) also can be used to indicate soil porosity (Causse and Sénéchal 2006) or compaction.

24.5 Applications

Soil classification is an interactive procedure which requires knowledge on soil and landscape relationships. Data derived from soil profile (control section) are the most important information for soil classification of a pedon (smallest, three-dimensional unit at the surface of the earth that is considered as an individual soil). Many classification systems require soil characterization from the laboratory as well as a complete morphological description of the soil horizons. The morphological evaluation of soil structure in the field, for example, requires determination of the type, shapes, and size of peds, while soil structure is determined by the activity of soil biota (macro- and microorganisms), clay content, mineralogy, organic matter, and aggregation. This requires opening soil pits of where the soil is described and classified based on a 2 m depth profile and 1.5-m lateral dimension, which is very time-consuming. Thus, the advantage of using spectral sensing on soil classification is to infer soil properties from sensors.

The method to classify soils using spectroscopy can be descriptive and/or in combination with quantitative analysis. The descriptive analysis was started by Stoner and Baumgardner (1981) and has recently been updated by Demattê et al. (2014)—Fig. 24.3a. The importance of descriptive analysis is that the users can mentally understand the role of spectra (intensities, absorptions, shapes) and compare it with their knowledge and the literature so they can be used in classification. Indeed, Bellinaso et al. (2010) reached an 80 % agreement between soils classified by their spectra and soils classified in the field following traditional soil survey protocols, as corroborated by Viscarra Rossel and Webster (2011).

Quantitative methods have been used to directly predict soil classes from soil spectra. For example, Vasques et al. (2014) introduced a system where the spectra of different soil layers (depth intervals) are evaluated and reached 90 % accuracy for some classes (Fig. 24.3c, d).

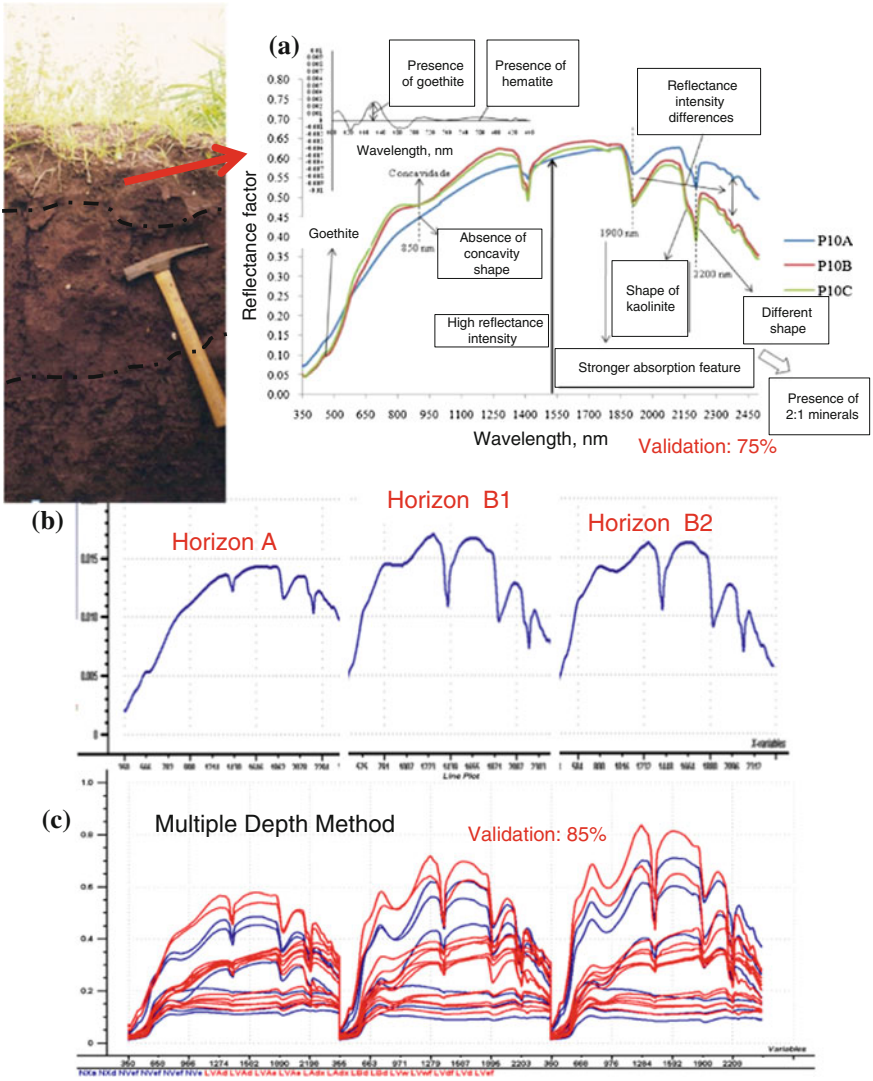

Fig. 24.3 Profile example of a Ferralsol. **a** Soil spectral analysis by descriptive method using MIRS, morphological interpretation of reflectance spectrum (Demattê et al. 2014); **b** spectra from each horizon inserted in the same dataset; **c** multidepth quantitative analysis, where we insert several profiles at the same time for discrimination and soil classification (Vasquez et al. 2014)

From a pedon, we can go to the longitudinal information. This type of vision is important to understand the dynamics of water and its relationship with the soil formed due to relief and transport processes. Beside this, in a toposequence, pedologists can detect the boundaries between soil classes and map them. This basic concept was evaluated by Demattê and Terra (2014) and shown in Fig. 24.4.

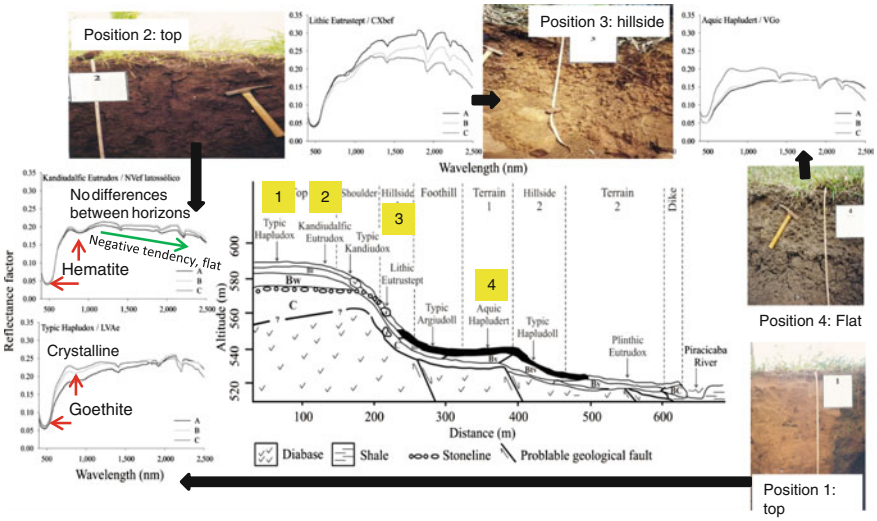

Fig. 24.4 Geomorphologic distribution of profiles along a toposequence and its respective spectral data from three horizons: *A*, *B*, *C* and horizons, *A*, *B*1, and *B*2, respectively. *Source* Adapted from Demattê and Terra (2014)

We can observe the variation from the soils on the top to the bottom of the hill. The differences are due to the changes in parent material and soil processes which were detected by spectra of the soil profile.

We can go from point information toward the hillslope as indicated in Fig. 24.5. It is observed that the soils were derived from two parent materials, sandstone and igneous rocks (basalt), resulting in Arenosols and Ferralsols. As shown in Fig. 24.5, the Vis–NIR spectra from horizons from a pit on the higher altitude have specific spectral features from horizon A to B. The spectrum has high reflectance with ascending tendency and higher reflectance in the SWIR. At another location with the same altitude, the spectrum was the same, thus indicating the same soil. These spectra are typical of the tropical Arenosols with less than 150 g kg^{-1} of clay throughout the profile. On the other hand, at the lower positions on landscape, where the soils derived from basalt, the spectra of the soils indicated low reflectance intensity with few spectral features. Despite this, the spectra also indicated no differences between horizons, and we classified it as Ferralsols, in agreement with literature.

Finally, we can go from the point information to the spatial domain of soil mapping. In this aspect, Vasquez et al. (2015) used spectral information of soil profiles associated with relief parameters to construct a soil map. Although this was done in a complex area, the results are promising reaching an accuracy up to 75 % in validation data (Fig. 24.6).

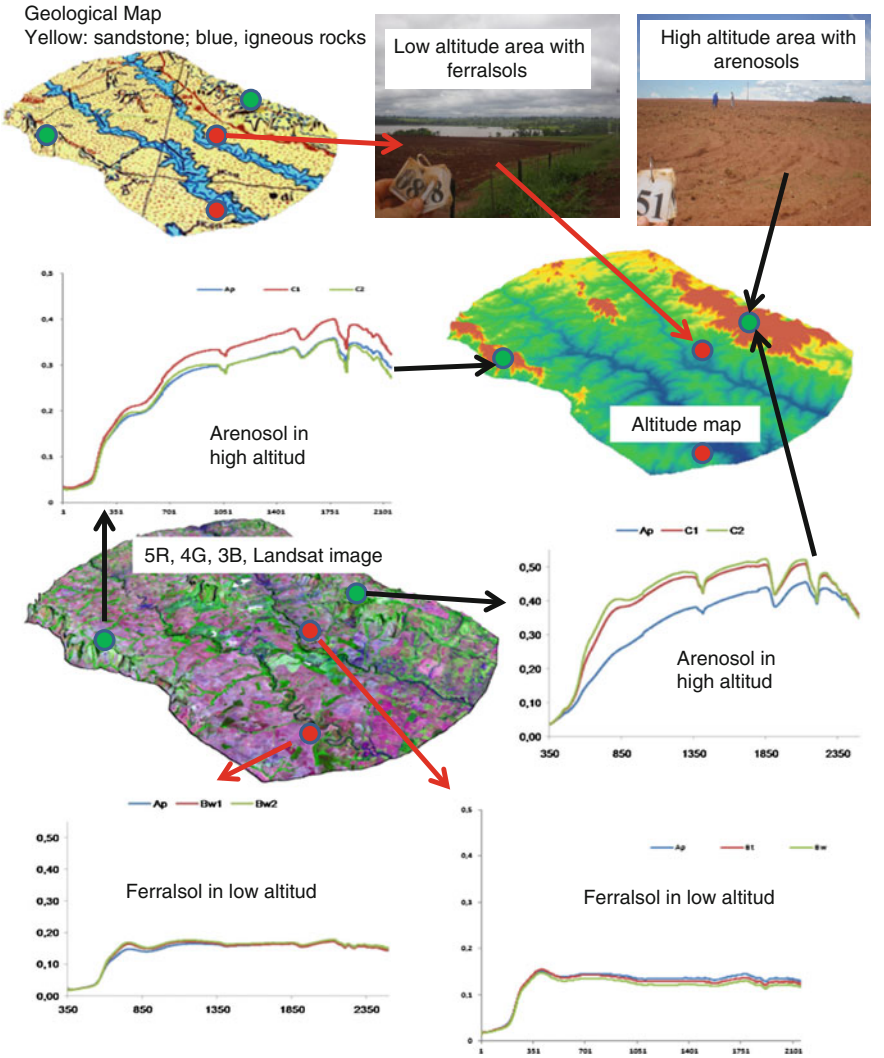

Fig. 24.5 The relationship between geological map, Landsat image, altitude, and Vis–NIR spectra from profiles. Spectra obtained from 400 to 2500 nm, from different depths in pits. *X* axis and *Y* axis are wavelengths in nm and reflectance factor, respectively

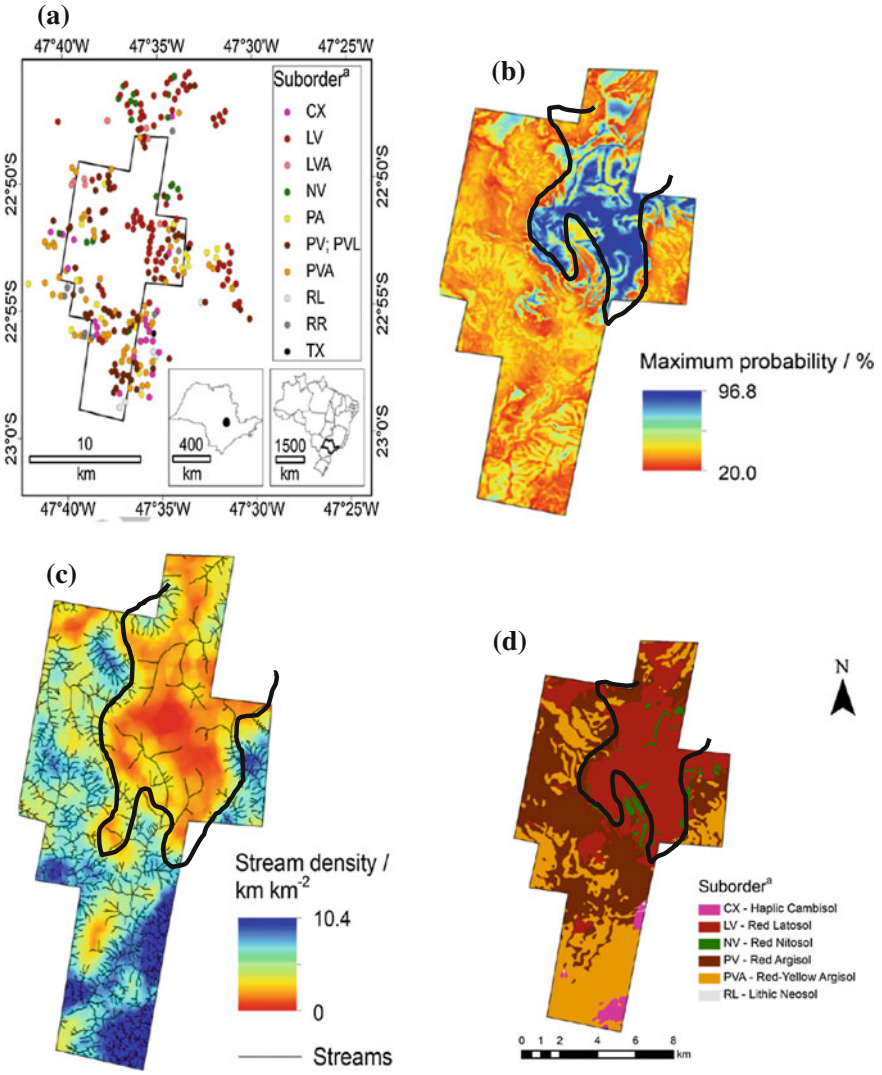

Fig. 24.6 **a** Study area with point information was obtained from profiles and boreholes; at each point, spectral reflectance from 400 to 2500 nm was collected; **b** maximum probability of predicted soil suborders determined from a multinomial logistic model, using geomorphic information and spectral variables; **c** stream density; **d** predicted soil map (*Source* Adapted from Vasquez et al. 2015)

24.6 Challenges

One of the main issues observed by researchers is the necessity to open a pit (Fig. 24.7a). It can be dug by manpower (usually two men can dig two pits per day depending on soil type and conditions). It can also be dug by a tractor, which can be expensive and requires transport of the tractor to the field. We can also make several

Fig. 24.7 **a** Classical methods to open profiles—manpower (Osmar Basagia and Gustavo Arruda; **b** machines; **c** auger for boreholes; **d** analyzing profiles by classical method (knife and hammer, J. A.M. Demattê); **e** inside a pit with sensors (Photograph by Budiman Minasny); **f** method to evaluate soil with depth by fiber optics (*Source* Ben Dor and Chudnovsky 2008); **g** method to evaluate soils by extracting cores (*Photograph* by Cristine L.S. Morgan)

boreholes with auger, but this does not give the structure information (Fig. 24.7c). With this challenge, we can try new strategies. The use of proximal sensors can also be a challenge as sensors, and computers can be sensitive for use in the field with dust, rough weather, and other issues. We can measure directly in the field using proximal sensors, or bring the soil samples to the laboratory. This will depend on the user's objectives. Traditional method requires collecting soil samples using a hammer or knife (Fig. 24.7d). Some new methods can circumvent this ancient procedure, for example, collecting spectral data in a pit with a spectrometer

Fig. 24.8 **a** Issues on determining soil structure by descriptive classical method (*Photograph by* J.A.M. Demattê); **b** the multistripe laser triangulation scanning (*Source* Plat et al. 2010; Eck et al. 2012; *Photograph* due to Daniel R. Hirmas)

(Fig. 24.7e), inserting an optic fiber in a borehole and evaluating the spectra at different depths or horizons (Ben-Dor et al. 2008), or collecting samples with an auger or hydraulic corer and analyzing them using spectrometer in the laboratory, as shown in Fig. 24.7g (Demattê et al. 2004; Morgan et al. 2009).

There are other issues looking toward soil evaluation and classification. The most important are moisture interference and quantitative determination of structure. Both are key properties in morphometrics. Structure is one of the most difficult to determine. Classical method requires careful interpretation of the shapes of the blocks in a pit. This is subject to pedologists' interpretation of sizes and shapes.

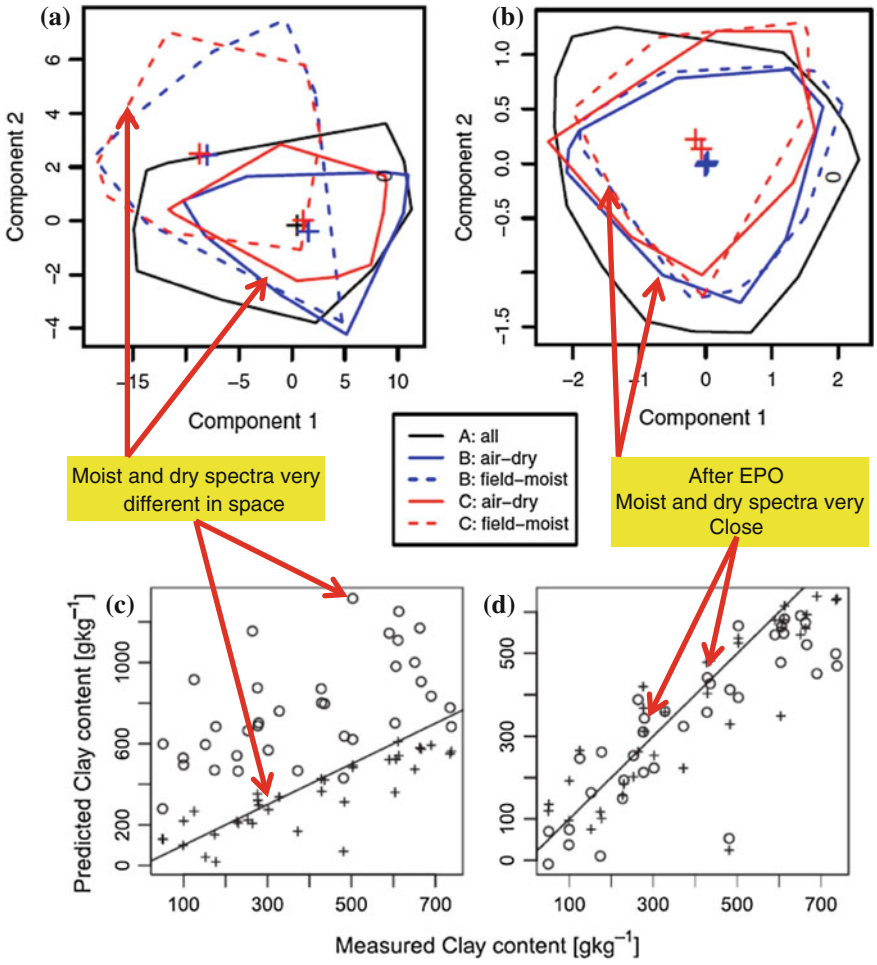

Fig. 24.9 **a**, **b** Spectra from each dataset (field and air-dried conditions) before and after EPO transform plotted in principal component space. *Lines* represent convex hulls plus signs represent centroids of each dataset. **c** PLS predicted clay content versus measured clay content before and **d** after EPO (*Source* Ackerson et al. 2015)

One interesting new idea is the use of the multistripe laser triangulation scanning (Plat et al. 2010; Eck et al. 2012), Fig. 24.8. This method can scan and obtain the shape and area parameters which can be correlated with patterns found in typical soils; thus, structure can be quantified objectively.

Moisture is another very important issue when using spectroscopy in field conditions. Moisture alters spectra by absorbing energy and decreasing reflectance intensity. With these interferences, we will have a nonlinear correlation between spectral sensing and soil properties. That is why in laboratory, we usually dry all samples, to take out this influence. A numerical technique called external parameter orthogonalization (EPO) has been developed to solve this issue as proposed by Minasny et al. (2011), validated in the field by Ge et al. (2014), and recently corroborated for tropical soils by Ackerson et al. (2015). Figure 24.9 illustrates the importance of this method.

24.7 Conclusions

In conclusion,

- Soils must be observed as a complete body, performed at the pedon and the landscape, and *related* to the dynamics of soil and transport processes. Thus, soils can be 'seen' from a point, longitudinal or spatial domain.
- The integration of the point observation on a profile by morphometrics (Hartemink and Minasny 2014) is an important component in the dynamics of pedological mapping using spectra strategies (Demattê et al. 2004) to achieve the *scorpan* mapping model. With these components (profile, landscape, and scorpan), we can reach the best soil map output.
- Sensing tools can rapidly quantify soil information in situ in real time. These are, for example, color, soil structure, clay content, iron content, organic matter content, mineralogy, and other attributes.
- It is imperative to integrate all types of sensors into single information for soil understanding. Since there are overlaps of quantitative information from one sensor to another, it is necessary to study the fundamentals of each instrument and its interaction with soil components.

Acknowledgements We acknowledge GeoSS Science Group (Geotechnologies on Soil Science Group: http://esalqgeocis.wix.com/english)

References

Ackerson JP, Demattê JAM, Morgan CLS (2015) Predicting clay content on field-moist intact tropical soils using a dried, ground Vis-NIR library with external parameter orthogonalization. Geoderma 259–260:196–204

Araújo SR, Wetterlind J, Demattê JAM, Stenberg B (2014) Improving the prediction performance of a large national Vis-NIR spectroscopic library by clustering into smaller subsets or the use of data mining calibration techniques. European Journal of Soil Science, in press

Bartholomeus H, Epema G, Schaepman M (2007) Determining iron content in mediterranean soils in partly vegetated areas, using spectral reflectance and imaging spectroscopy. Int J Appl Earth Obs Geoinf 9:194–203

Bazaglia Filho O, Rizzo R, Lepsch IF, do Prado H, Gomes FH, Mazza JA, Demattê JAM (2013) Comparison between detailed digital and conventional soil maps of an area with complex geology. Braz J Soil Sci 37:1136–1148

Bellinaso H, Demattê JAM, Araújo SR (2010) Spectral library and its use in soil classification. Braz J Soil Sci 34:861–870

Bellon-Maurel V, McBratney A (2011) Near-infrared (NIR) and mid-infrared (MIR) spectroscopic techniques for assessing the amount of carbon stock in soils—critical review and research perspectives. Soil Biol Biochem 43:1398–1410

Ben-Dor E, Heller D, Chudnovsky A (2008) A novel method of classifying soil profiles in the field using optical means. Soil Sci Soc Am J 72:1–13

Ben-Dor E (2011) Characterization of soil properties using reflectance spectroscopy. In: Thenkabail PS, Lyon JG, Huete A (eds) Hyperspectral remote sensing of vegetation. CRC press, Boca Raton, pp 513–557

Campos RC, Demattê JAM (2004) Cor do solo: uma abordagem da forma convensional de obtenção em oposição à automatização do método para fins de classificação de solos (Soil color: approach to a conventional assesment method in comparison to na authomatization process for soil classification). Braz J Soil Sci 28:853–863

Causse E, Sénéchal P (2006) Model-based automatic dense velocity analysis of GPR field data for the estimating of soil properties. J Geophys Eng 3:169–176

Demattê JAM, Campos RC, Alves MC, Fiorio PR, Nanni MR (2004) Visible-NIR reflectance: a new approach on soil evaluation. Geoderma 121:95–112

Demattê JAM, Nanni MR, Formaggio AR, Epiphanio JCN (2007) Spectral reflectance for the mineralogical evaluation of Brazilian low clay activity soils. Int J Remote Sens 28:4537–4559

Demattê JAM, Fiorio PR, Ben-Dor E (2009) Estimation of soil properties by orbital and laboratory reflectance means and its relation with soil classification. Open Remote Sens J 2:12–23

Demattê JAM, Terra FS (2014) Spectral pedology: a new perspective on evaluation of soils along pedogenetic alterations. Geoderma 217–218:190–200

Eck DV, Hirmas DR, Gimenez D (2012) Quantifying soil structure from field walls using multistripe laser triangulation scanning. Soil Sci Soc Am J 77:1319–1328

Franceschini MHD, Demattê JAM, Sato MV, Vicente LE, Grego CR (2013) Abordagens semiquantitativa e quantitativa na avaliação da textura do solo por espectroscopia de reflectância bidirecional no VIS-NIR-SWIR. Pesquisa Agropecuária Brasileira 48:1569–1582

Franseschini MHD, Dematte JAM, da Terra FS, Vicente LE, Bartholomeus H, de Souza Filha CR (2015) Imaging spectroscopy and accurate prediction of topsoil properties highly weathered soils: the influence of fractional vegetation cover. Int J Appl Earth Obs Geoinf 38:358–370

Galvão LS, Pizarro MA, Epiphanio JCN (2001) Variations in reflectance of tropical soils: spectral-chemical composition relationships from AVIRIS data. Remote Sens Environ 75: 245–255

Galvão LS, Formaggio AR, Couto EG, Roberts DA (2008) Relationships between the mineralogical and chemical composition of tropical soils and topography from hyperspectral remote sensing data. ISPRS J Photogrammetry Remote Sens 63:259–271

Ge Y, Morgan CLS, Ackerson JP (2014) VisNIR spectra of dried ground soils predict properties of soils scanned moist and intact. Geoderma 221:61–69

Hartemink AE, Minasny B (2014) Towards digital soil morphometrics. Geoderma 230–231: 305–317

Lu P, Wang L, Niu Z, Li L, Zhang W (2013) Prediction of soil properties using laboratory VIS-NIR spectroscopy and Hyperion imagery. J Geochem Explor 132:26–33

Madeira Netto J (2001) Comportamento espectral dos solos. In: Meneses PR, Madeira Netto JS (ed) Sensoriamento remoto: reflectância dos alvos naturais. UnB, Brasília. Embrapa Cerrados, Planaltina, cap. 4, pp 127–154

McBratney AB, Mendonça Santos ML, Minasny B (2003) On digital soil mapping. Geoderma 117:3–52

Minasny B, McBratney AB, Bellon-Maurel V, Roger JM, Gobrecht A, Ferrand L, Joalland S (2011) Removing the effect of soil moisture from NIR diffuse reflectance spectra for the prediction of soil organic carbon. Geoderma 167–68:118–124

Morgan CLS, Waiser T, Brown DJ, Hallmark CT (2009) Simulated in situ characterization of soil organic and inorganic carbon with visible near-infrared diffuse reflectance spectroscopy. Geoderma 151:249–256

Platt BE, Hasiotis ST, Hirmas DR (2010) Use of low-cost multistripe laser triangulation (MLT) scanning technology for three-dimensional, quantitative paleoichnological and neoichnological studies. J Sediment Res 80:590–610

Radu T, Gallagher S, Byrne B, Harris P, Coveney S, McCarron S, McCarthy T, Diamond D (2013) Portable X-Ray fluorescence as a rapid technique for surveying elemental distributions in soil. Spectrosc Lett 46:516–526

Reeves JB III (2010) Near-versus mid-infrared diffuse reflectance spectroscopy for soil analysis emphasizing carbon and laboratory versus on-site analysis: where are we and what needs to be done? Geoderma 158:3–14

Schuler U, Erbe P, Zarel M, Rangubpit W, Surinkum A, Stahr K (2011) A gamma-ray spectrometry approach to field separation of illuviation-type WRB reference soil groups in northern Thailand. J Plant Nutr Soil Sci 174:536–544

Stoner ER, Baumgardner MF (1981) Characteristic variations in reflectance of surface soils. Soil Sci Soc Am J 45:1161–1165 Madison

Ucha JM, Botelho M, Vilas Boas GS, Ribeiro LP, Santana PS (2002) Uso do radar penetrante no solo (GPR) na investigação dos solos dos Tabuleiros Costeiros do litoral norte do Estado da Bahia [Experimental use of groud-penetrating radar (GPR) to investigate tablelands in the Noethern Coast of Bahia, Brazil]. Braz J Soil Sci 26:373–480

Vasques GM, Demattê JAM, Viscarra Rossel R, Ramirez Lopez L, Terra FS (2014) Soil classification using visible/near-infrared diffuse reflectance spectra from multiple depths. Geoderma 223–225:73–78

Vasques GM, Demattê JAM, Viscarra-Rossel R, Ramirez-Lopez L, Terra FS, Rizzo R, Souza Filho B (2015) Integrating geospatial and multi-depth laboratory spectral data for mapping soil classes in a geologically complex area in southeastern Brazil. Eur J Soil Sci. doi:10.1111/ejss.12255

Viscarra Rossel RA, Webster R (2011) Discrimination of Australian soil horizons and classes from their visible-near infrared spectra. Eur J Soil Sci 62:637–647

Chapter 25
Cone Penetrometers as a Tool for Distinguishing Soil Profiles and Mapping Soil Erosion

Francisco J. Arriaga, Birl Lowery, Dalvan J. Reinert and Kevin McSweeney

Abstract Erosion of the productive surface soil from a landscape reduces crop production and alters chemical and physical properties of the soil, especially the thickness of the effective rooting depth and surface horizon thickness. Fast and reliable tools are needed to detect and map the thickness of soil horizons of eroded landscapes to allow for proper management of eroded soil for optimum agricultural production and environmental protection. A truck-mounted, constant-rate profile cone penetrometer was used to determine the horizon thickness and thus map the distribution of various erosion levels of an eroded Dubuque silt loam soil, in southwest Wisconsin, USA. The penetrometer was pushed into the ground with the hydraulic cylinder of a soil probe mounted on a 0.7 ton truck, to a depth of approximately 1.3 m. Data were collected continuously with a datalogger connected to a load cell and a string potentiometer depth gage. The 30° tip of the penetrometer was constructed following the American Society of Agricultural Engineers (ASAE) guidelines. Data collected with the penetrometer correlate well with previously constructed maps of soil erosion distribution for the study site constructed by soil borings using morphological observations, where depth to clay residuum (2Bt2 horizon) was used to determine erosion severity. Depth to clay residuum averaged 0.95, 0.74, and 0.45 m for the slight, moderate, and severe erosion levels, respectively. Of the total study area, approximately 44, 31, and 25 % consisted of slight, moderate, and severe erosion levels, respectively. Three-dimensional (3D)

F.J. Arriaga (✉) · B. Lowery
Department of Soil Science, University of Wisconsin-Madison, Madison, WI, USA
e-mail: francisco.arriaga@wisc.edu

D.J. Reinert
Department of Soil, University Federal de Santa Maria, Rio Grande do Sul, Brazil

K. McSweeney
Department of Natural Resources and Environmental Sciences,
University of Illinois, Urbana, IL, USA

A.E. Hartemink and B. Minasny (eds.), *Digital Soil Morphometrics*,
Progress in Soil Science, DOI 10.1007/978-3-319-28295-4_25

maps of the site were developed using data from the penetrometer. Development of limited invasive tools and methods for mapping eroded soil can aid in land management.

Keywords Erosion · Cone penetrometer · Three-dimensional soil map

25.1 Introduction

Our ability to understand the spatial distribution of soil properties is limited by the ability to accurately map soil at a sufficient scale to display spatial variability. There are many cases where detailed soil maps would be very valuable. For example, there is a need to understand how soil erosion changes soil properties with depth. Reclassification from one soil series to another can be triggered by erosion because of loss of topsoil depth. In general, soil erosion by water does not impact soil at the same level throughout the landscape, but erosion can occur with varying degrees of severity at the landscape scale. As such there is a need to understand soil spatial variability caused by erosion. Here, we propose the use of a static cone penetrometer (CP) to produce detailed maps of soil depth across eroded landscapes by using differences in cone index (CI) values.

Past use of cone penetrometers has mainly focused on soil compaction characterization in mechanized agriculture (Mirreh and Ketcheson 1972; Raper and Sharma 2004; Taylor and Gardner 1963). However, penetrometers have been extensively used by geotechnical and geophysical engineers as a less invasive and simpler tool to survey subsoil conditions such as relative density, shear strength, bearing capacity, and settlement. Improvements and integration with new technologies have been implemented into penetrometer designs such as incorporating global position systems (GPS) and improved data acquisition (Clark 1999; Raper et al. 1999). Raper et al. (1999) developed a tractor-mounted multiple-probe soil cone penetrometer, which allows for rapid data collection using five probes capable of obtaining a dense array of CI values. Figueirdo et al. (2013) noted that cone penetrometers have been used for the prediction of resilience modulus of subgrade pavement layers, as well as bearing capacity values from foundations of light structures. They also noted the use of the piezocone penetrometer to assess pore water pressure in an effort to obtain a detailed description of soil stratigraphy. Farooq et al. (2015) proposed the use of a dynamic CP to obtain strength of subgrade soil over the length of roads, including the strength of pavement base, subbase and subgrade materials, which amounts to developing a strength profile. Massarsch (2014) noted that CP has become a popular tool for investigation in geotechnical engineering in the past four decades, since they can provide a continuous and relatively fast measurement of the soil profile and that different sensors can be integrated in the same probe.

Soil scientists can take advantage of CP as a tool beyond soil compaction measurements for soil characterization applications. Such approach of using CP to

map soil horizons was proposed and demonstrated by Rooney and Lowery (2000). Grunwald et al. (2000) and Grunwald et al. (2001a, b) developed this concept by creating 3D soil maps. Nevertheless, this technique and resulting data have not been used to map eroded soils. Thus, the objective of this investigation was to develop a limited invasively tool and methods for mapping soil to assess erosion spatial patterns.

25.2 Materials and Methods

This study was conducted in southwestern Wisconsin, USA (Fig. 25.1), at the Lancaster Agricultural Research Station, University of Wisconsin-Madison (42° 52′ N, 90° 42′W). The area was not affected by glacial activity during the Quaternary period and is characterized by a rolling topography. Soil at the research site is classified as a Dubuque silt loam (fine-silty, mixed, mesic Typic Hapludalfs), consisting of loess underlain by a red clayey residuum (2Bt2 horizon) with a subangular blocky structure. The site was 90 by 45 m with a southwest aspect and a

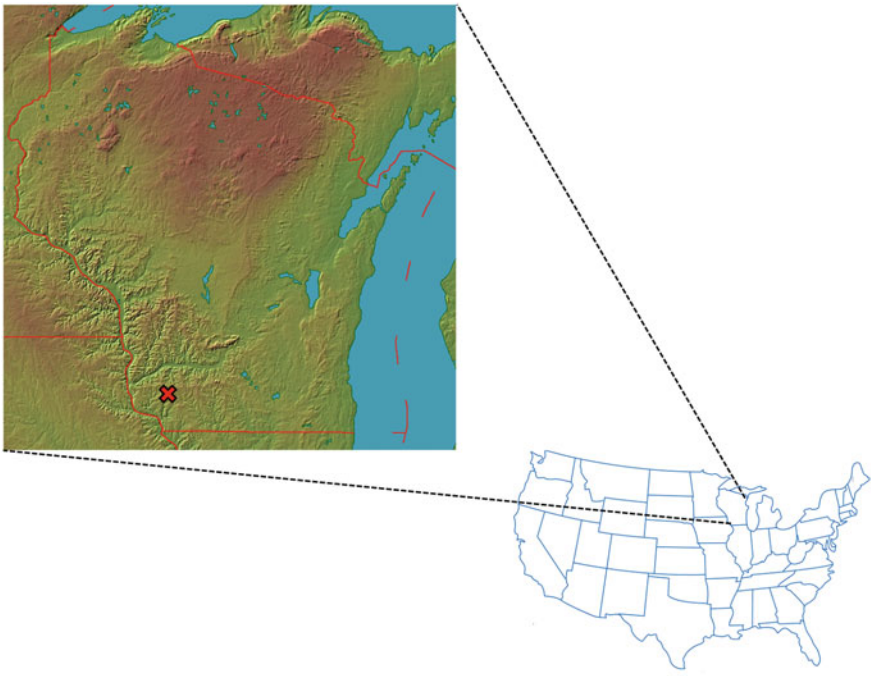

Fig. 25.1 Study site was located in the unglaciated region in southwestern Wisconsin, which is characterized by sloping terrain. Relief map created by Ray Sterner, John Hopkins University Applied Physics Laboratory (http://fermi.jhuapl.edu/states/states.html, copyright 1995)

Table 25.1 Horizon depth and textural classification for three erosion levels of a Dubuque silt loam in 1985 (adapted from Andraski and Lowery 1992)

Erosion level	Soil horizon	Average depth (cm)	Textural class	Sand content (%)	Clay content (%)
Slight	Ap	0–36	Silt loam	5	13
	Bt1	36–95	Silty clay loam	2	32
	2Bt2	95 to >113	Silty clay	5	54
Moderate	Ap	0–20	Silt loam	6	16
	Bt1	20–74	Silty clay loam	2	29
	2Bt2	74 to >99	Silty clay	3	45
Severe	Ap	0–17	Silt loam	5	17
	Bt1	17–45	Silty clay loam	3	33
	2Bt2	45–79	Silty clay	4	40

slope of 12 %. Previous soil mapping conducted in 1985 at this site (McSweeney, personal communication; Andraski and Lowery 1992) established three levels of historical erosion based on depth of soil above the clayey residuum. This mapping effort involved the use of a manual bucket auger (6.4 cm diam.) and a soil push probe (2.5 cm diam.) on a 15 × 15 m grid spacing to a depth of 1.2 m. Depth to the different horizons was recorded for each sampling location. Surface elevation information was acquired with a transit relative to a reference point in the field for all sampling locations. Three levels of past erosion (slight, moderate, and severe) were identified (Table 25.1; Andraski and Lowery 1992).

A CP (Arriaga and Lowery 2005; Rooney and Lowery 2000) was used to collect penetration resistance data of the soil profile on a 10 by 10 m grid in May 2000 for a total of 72 points. The CP followed specifications from the American Society of Agricultural Engineers standards (ASAE 1999) and consisted of a 30° cone with a 2.0-cm basal diameter threaded to a 1.25 cm in diameter by 1.5-m-long stainless steel rod. The CP rod was connected to a 1360-kg load cell (Omega Engineering, model LC-101-3K, Stamford CT) to measure penetration force, and a string potentiometer (UniMeasure Inc., model HX-PA-150, Corvallis OR) was used to measure depth. Output from the load cell and string potentiometer was measured every 0.05 s with an electronic data logger (Campbell Scientific, model CR21X, Logan UT). The CP was mounted to a hydraulic cylinder of a truck-mounted soil sampling probe (Giddings Machine Inc., model HDGSRPS, Windsor CO) to drive the CP into the ground at a rate of 5 cm s^{-1}. Surface elevation data were collected using the roving mode of a differentially corrected geographic positioning system (GPS) unit (Trimble Navigation Limited, model 4600LS, Sunnyvale CA) attached to an all-terrain vehicle. A GPS unit with beacon differential correction was utilized to georeference the CP measurement locations.

Penetration force data for a specific depth were transformed into CI (in kPa) using the following equation:

$$\mathrm{CI} = F_p / A_c$$

where F_p is the penetration force (in kN) and A_c is the basal area of the cone (in m^2). Each recorded depth had an associated CI value, thus creating a continuous measurement for the profile depth sampled for each CP location. Data were analyzed using a cluster analysis procedure (Minitab 13, State College PA) to identify three clusters, with the standardized variables option, and the Squared Pearson and Ward method for distance measure and linkage method, respectively. Clustering creates clusters, or groups, of observations that are similar within group and dissimilar between groups.

A contour map of the erosion levels within the field was created using Surfer© (Golden Software Inc., Golden CO) with the clustering classification information for each field CP sampling location. A 3D representation of the soil horizons' thickness was generated using the Environmental Visualization System software (C-Tech Development Corporation, Henderson NV).

Results from the 1985 study were compared to maps developed with the CP in this study. The manual mapping using soil augers and probes took about six days, and data were plotted on a surface chart. This compares to collecting CP data in less than a day with the described CP system.

25.3 Results and Discussion

Frequent erosion or severe erosion events had decreased the overall soil profile depth by approximately 20 cm. The depth of the Ap horizon decreased as erosion progresses to a severe phase, bringing root-restricting layers such as clayey or high-density layers and/or bedrock closer to the soil surface. Three levels of past erosion were observed in the field during the soil survey conducted in 1985. The main indicator of erosion level, or severity, was depth to the clay residuum (2Bt2 horizon) which ranged between 45 and 95 cm (Table 25.1). A surface plot of the 2Bt2 horizon was developed from the data obtained during the manual survey, and areas within the field were classified as slightly, moderately, or severely eroded (Fig. 25.2). Although this type of survey is time- and labor-consuming, the information obtained is valuable to land managers. A manager can target soil conservation, and other practices (e.g., application of manure to improve soil properties and crop productivity) to make better use of resources by having knowledge of how areas in a field are affected by erosion. The study area is characterized by a deposit of loess draped on steep long slopes, with high rainfall from spring to fall. There is

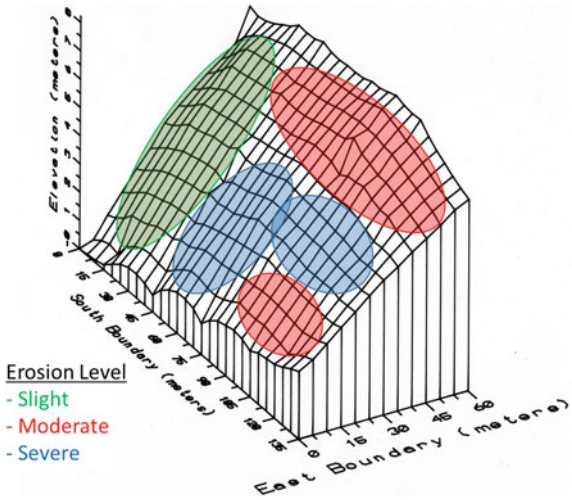

Fig. 25.2 Grid surface representation of the depth to the 2Bt2 soil horizon created with soil survey techniques on a 15 × 15 m grid with a hand auger. Areas depicted in different colors approximate the three different erosion levels present in this field

a root restrictive layer in most of the soil series mapped on this landscape, which can restrict vertical water movement (Andraski and Lowery 1992). This combination of climate, landscape, and soil characteristics can accelerate soil erosion. There has been considerable erosion causing extensive topographic changes. Existing soil maps do not provide sufficient detail on depth to restrictive soil layers. The manual process of mapping erosion at this scale is not feasible for large areas given the time and labor investment required. Therefore, the work presented here focused on using a CP to speed the mapping and make this information more readily available to land managers.

Collection of CP data took two persons' one day of field work (10 h) to collect, georeference the measurement location points, and survey the field with a GPS to develop a digital elevation map. In contrast, the manual survey was conducted over six days with the same number of people.

Since achieving consistent measurement depth for every single CP point was not possible due to restrictive features within the soil profile, the collected CP data were truncated to a constant depth of 0.90 m to minimize the introduction of unwanted artifacts during the clustering, that is minimize the chances that readings were placed in clusters based on depth. After clustering the CI data, the three erosion levels could be identified in the three CP clusters (Fig. 25.3). Two features on the CP data can be observed that help establishing clusters. The first is the maximum CI value, and the second is the variability in CI values. Maximum CI values and variability increased with increasing erosion severity; thus, clusters 1, 2 and 3 are identified with slight, moderate, and severe erosion levels, respectively. The clustering approach seems feasible since differences in soil texture and structure

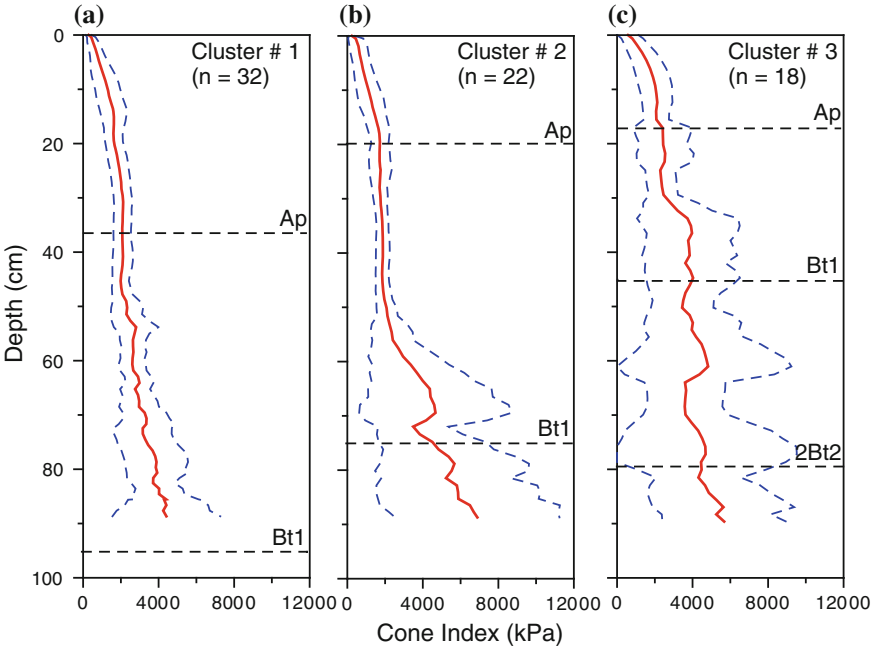

Fig. 25.3 Cone index as a function of depth for the three cluster groups associated with the different erosion levels. The *dashed blue lines* represent the standard deviation. Clusters 1, 2, and 3 are representative of the slight, moderate, and severe erosion levels, respectively

between soil horizons is marked, which affect CI values. Additionally, the presence of rocks, mainly chert, in deeper soil horizons created a characteristic CI profile. It should be noted that soil morphological information of the site was important in explaining the differences between clusters and assigning an erosion level to them.

Once the individual CP sampling points were allocated into a cluster, this information was integrated with the GPS data to determine the location of the different erosion levels on the landscape. These data were combined to create an elevation map including the erosion level classification for each CP sampling point (Fig. 25.4). This map appears to have good agreement to the map originally created (Fig. 25.2). Once these data were aggregated, a soil erosion severity contour map was developed by kriging the CP sampling point erosion classification (Fig. 25.5). This type of map can be more useful to a manager and could be imported into precision agriculture systems to assist with land management. The slight, moderate, and severe erosion levels occupied 25, 31, and 44 %, respectively, of the total field area. Further, combining the CP data with profile depth information and a 3D

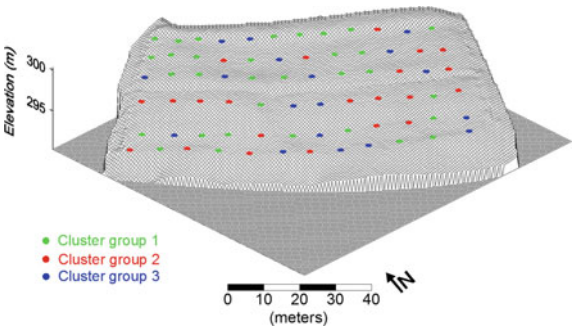

Fig. 25.4 Digital elevation map of the study site near Lancaster, Wisconsin, USA. Symbols in different colors show the location of penetrometer measurements, and the cluster group each measurement point was classified

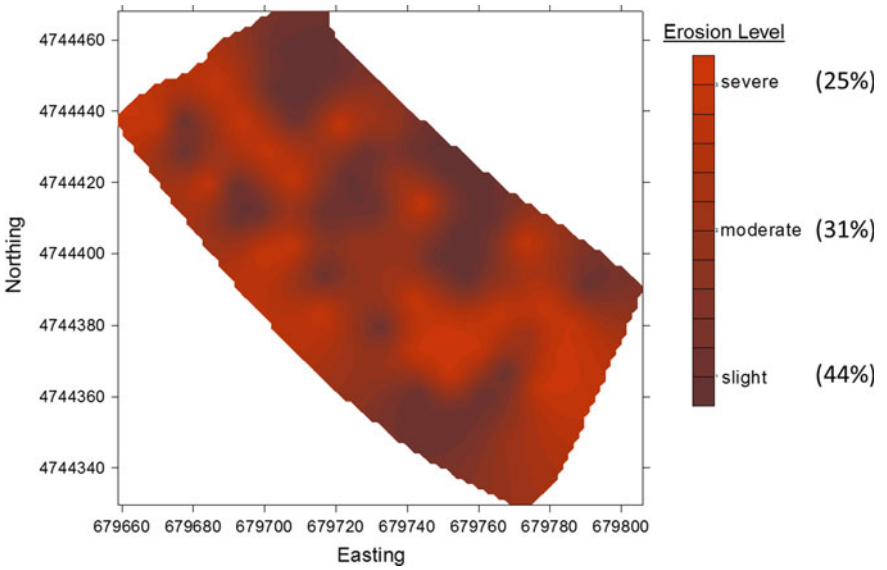

Fig. 25.5 Erosion contour map of a field near Lancaster, Wisconsin, USA. Percentage values in the legend near the erosion levels indicate the amount of the field in the respective erosion level. Adapted with permission from Arriaga and Lowery (2005)

kriging procedure, a 3D soil horizon representation was generated (Fig. 25.6). Using the volume information generated with the 3D soil horizon representation, it was estimated that the moderate and severe erosion levels have lost 484 and 900 m^3 more soil than the slight erosion level.

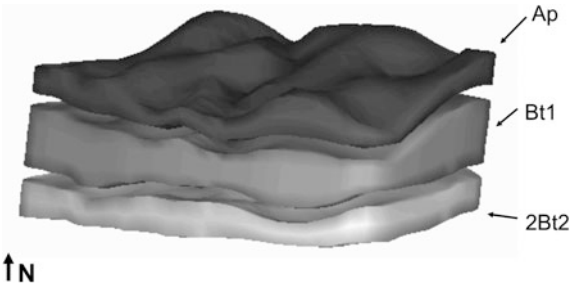

Fig. 25.6 Three-dimensional representation of the soil horizon thicknesses and surface elevation shows the areas where erosion has occurred. The scale on the vertical axis is exaggerated 10 times to accentuate depth differences. Adapted with permission from Arriaga and Lowery (2005)

25.4 Conclusions

Cone index data were collected with a CP on an eroded landscape and correlated to erosion severity in the unglaciated region of southwest Wisconsin, USA. The CP technique presented here for mapping eroded soil is suitable for displaying spatial variation of larger areas at considerable detail. Data were collected in only a fraction of the time and labor necessary compared to hand-augering methods. However, the CP technique requires some knowledge of the landscape been surveyed; therefore, some type of soil sampling remains needed for ground truthing. Soil maps developed with this procedure can be of benefit for land managers and can help target restorative efforts or conservation practices. Future enhancements to the CP technique should include the simultaneous measurement of other soil properties, such as water content and electrical conductivity, to improve the classification and profile description of individual sampling points (e.g., Sun et al. 2004). The advent of electronics miniaturization and reduction in costs will bring interesting possibilities to the future of soil morphometrics.

References

American Society of Agricultural Engineers (ASAE) Standards (1999) Soil cone penetrometer. In: Agricultural engineering yearbook. ASAE Standard: ASAE 313.3, American Society Agricultural Engineering, St. Joseph, MI, Feb 99, pp 832–833

Andraski BJ, Lowery B (1992) Erosion effects on soil water storage, plant water uptake and corn growth. Soil Sci Soc Am J 56:1911–1919

Arriaga FJ, Lowery B (2005) Spatial distribution of carbon over an eroded landscape in southwest Wisconsin. Soil Tillage Res 81(2):155–162

Clark RL (1999) Evaluation of the potential to develop soil strength maps using a cone penetrometer. In: ASAE Annual International Meeting, Paper, no. 99-3109, ASAE St. Joseph, MI, pp 49085–49659

Figueiredo F, Cunha RP, Conciani W (2013) An overview on existing dynamic cone penetration test research related to the Central Area of Brazil. In: Coutinho RQ, Mayne PW (eds) Geotechnical and geophysical site characterization. Taylor and Francis Group, London, pp 1669–1675. ISBN 978-0-415-62136-6

Farooq YE, Duggal AK, Farooq A (2015) Case study on correlation between California bearing ration (CBR) and dynamic cone penetration test (DCPT). Int J Civil Struct Eng Res 3:39–41

Grunwald S, Barak P, McSweeney K, Lowery B (2000) Soil landscape models at different scales portrayed in virtual reality modeling language (VRML). Soil Sci 165:598–615

Grunwald S, Rooney DJ, McSweeney K, Lowery B (2001a) Development of pedotransfer functions for a profile cone penetrometer. Geoderma 100:25–47

Grunwald S, Lowery B, Rooney DJ, McSweeney K (2001b) Profile cone penetrometer data used to distinguish between soil materials. Soil Tillage Res 62:27–40

Massarsch KR (2014) Cone penetration testing—a historic perspective. In: Robertson PK, Cabal KL (eds) Proceedings 3rd international symposium on cone penetration testing. Las Vegas, Nevada, USA, 13–14 May 2014, pp. 97–134

Mirreh HF, Ketcheson JW (1972) Influence of bulk density and matric pressure to soil resistance to penetration. Can J Soil Sci 52:477–483

Raper RL, Sharma AK (2004) Soil moisture effects on energy requirements and soil disruption of subsoiling a coastal plain soil. Trans ASAE 47(6):1899–1905

Raper RL, Washington BH, Jarrell JD (1999) A tractor-mounted multiple-probe soil cone penetrometer. Appl Eng Agric 15(4):287–290

Rooney D, Lowery B (2000) A profile cone penetrometer for mapping soil horizons. Soil Sci Soc Am J 64:2136–2139

Sun Y, Schulze Lammers P, Ma D (2004) Evaluation of a combined penetrometer for simultaneous measurement of penetration resistance and soil water content. J Plant Nutr Soil Sci 167(6):745–751

Taylor HM, Gardner HR (1963) Penetration of cotton seedling taproots as influenced by bulk density, moisture content, and strength of soil. Soil Sci 96:153–156

Chapter 26
Use of Ground-Penetrating Radar to Determine Depth to Compacted Layer in Soils Under Pasture

Edwin Muñiz, Richard K. Shaw, Daniel Gimenez, Carey A. Williams and Laura Kenny

Abstract New Jersey, like many states in the northeastern USA, has a high demand for grazing land for horses. Grazing lands are often intensively used because of the limited possibilities for crop rotation. A ground-penetrating radar (GPR) study was conducted in an area under different management with soils formed in old alluvium and fluviomarine sediments (Ultisols). In the grazing field, no significant signs of compaction were detected with GPR. In the feeding fields, compaction was significant within 24 cm soil from the soil surface. The GPR data were used to generate a contour map representing the depth to the compacted layer. It is concluded that soil compaction can be adequately mapped using GPR.

Keywords GPR · Soil compaction · Grazing land

26.1 Introduction

Ground-penetrating radar (GPR) is a noninvasive technology for the study of the subsurface soil features (De Benedetto et al. 2013). GPR has been effectively used in a range of investigations, including locating burials (Miller 1996), underground utilities (Cheng et al. 2013), and assessing soil properties (Doolittle and Butnor 2008). This technology complements traditional and more labor-intensive method of collecting field data and can provide a continuous image of the soil subsurface (Doolittle and Butnor 2008; Paterson and Laker 1996). Freeland et al. (1998)

E. Muñiz (✉) · R.K. Shaw
United States Department of Agriculture, Natural Resources Conservation Service, Somerset, NJ, USA
e-mail: Edwin.Muniz@nj.usda.gov

D. Gimenez · C.A. Williams · L. Kenny
Rutgers, The State University of New Jersey, New Brunswick, NJ, USA

A.E. Hartemink and B. Minasny (eds.), *Digital Soil Morphometrics*,
Progress in Soil Science, DOI 10.1007/978-3-319-28295-4_26

utilized the continuous profiling capabilities of GPR to determine soil horizons, depth to bedrock, preferential flow paths, and differentiate soil parent materials. Petersen et al. (2006) used GPR to identify variations in soil compaction and soil texture. They demonstrated the use of GPR to identify areas of loamy soils with high risk for soil compaction compared to areas of sandy soils where the risks for soil compaction are lower.

Soil compaction exerts a negative impact on soil productivity as it reduces pore spaces and decreases gas exchange, reduces water and root movement, and increases soil bulk density. New Jersey, like many states in the northeastern USA, has a high demand for grazing land. The equine industry ranks number 8 in sales value by agricultural commodity statewide and 26th in the USA (USDA NASS 2014). The equine industry generates substantial revenues, and the land is often intensively used, and in many instances, soils are compacted. Soil compaction poses a serious threat to pasture quality and nutritional value and a potential threat to surface water quality by runoff. GPR could be a quick and effective technology to assess soil compaction.

The objectives of this study were to (1) compare the effectiveness of a 400 MHz and 900 MHz GPR antenna to identify compacted soil layers and (2) generate a map showing depth to compacted layer that can be used for planning and implementation of best management practices.

26.2 Materials and Methods

26.2.1 The Study Site

The study was conducted at the Equine Research Farm located in the Rutgers Agricultural Research Farm (40°28′16″N, 74°25′42″W) in New Brunswick, New Jersey, USA. The study area is approximately 6.6 ha and consists mostly of grazing land, with a mix of good standing pasture, and areas used for feeding where the horses concentrate. The study area is located in a transition zone between two soils. The area is mapped as Nixon and Fallsington soil series with a Soil Taxonomic Classification of fine-loamy, mixed, semiactive, mesic Typic Hapludults and fine-loamy, mixed, active, mesic Typic Endoaquults, respectively (Soil Survey Staff 1999), or Haplic Acrisols and Stagnic Acrisols according to the World Reference Base (IUSS Working Group WRB 2014). Nixon is formed in old alluvium with a moderate permeability in the solum, very deep to bedrock (>150 cm), seasonal high water table exceeding 102 cm, and an extremely acid to strongly acid soil reaction. Fallsington is formed in fluviomarine sediments with a moderately high permeability in the solum, very deep to bedrock, seasonal high water table from the soil

surface to 30 cm, and an extremely acid to strongly acid soil reaction. The geology in the area is dominated by Lower Paleozoic to Precambrian sediments and igneous rocks that have been metamorphosed in the eastern part and crustal trough or basin in the central part from the Triassic period (USDA-NRCS 2006). The average annual precipitation in the area is 746–1645 mm (ONJSC 2014) with a maximum precipitation as high-intensity and convective thunderstorms in spring and early in summer.

26.2.2 GPR Readings

The effectiveness of a 400 and 900 MHz antennas to detect compacted layers were compared on two plots of 2.8 m^2 with different pasture quality (Fig. 26.1). Plot 1 was mostly grazing land with a mix of good standing pasture on Fallsington soil, and Plot 2 was an area used for feeding where the horses concentrate with pasture in

Fig. 26.1 Location of Plots 1 and 2 showing the grassland quality and position in the landscape

poor condition on the Nixon soil. Field data were collected in two small soil pits (30 cm soil depth) to compare with the GPR scans by matching the high dielectric signals from the GPR to the zones with root-restrictive layers identified by visual inspection.

The study was expanded across a 6.6 ha area that was divided into 16 plots of different shapes and sizes for prescribe grazing management. Data were collected with the GPR in a zigzag pattern with a north–south alignment and an average spacing of 8 m. In addition, field data were collected randomly throughout the area by digging small soil pits and describing depth to compacted layer. The data were used to validate the information obtained from GPR.

The GPR system used was the TerraSIRch Subsurface Interface Radar (SIR) System-3000 and the 400 and 900 MHz antennas manufactured by Geophysical Survey Systems, Inc. This GPR system was mounted on a standard survey cart with an integrated survey wheel encoder and georeferenced with the Garmin Global Positioning System Map 76 receiver. The 400 and 900 MHz antennas are shielded with a maximum depth in optimum soil conditions (dry, sandy, low electrical conductivity) from 4 to 1 m, respectively. The instrument was calibrated over a known buried metal object as recommended by Zobeck et al. (1985). Equations (26.1) and (26.2) were used to estimate the velocity of propagation in the soil (v) and the dielectric permittivity (Er) of the soil. These parameters were used to convert the two-way travel time of the propagated radar energy into a depth scale.

$$v = \frac{2 \times D}{t} \tag{26.1}$$

where v is the velocity of propagation in the soil (m/ns), D is the depth of penetration of the radar wave to a known object (m), t is the travel time (ns), and

$$Er = \left(\frac{c}{v}\right)^2 \tag{26.2}$$

where c is the speed of light or 0.2998 m/ns. Velocity of propagation and dielectric permittivity were used to convert the two-way travel time of the propagated radar energy into a depth scale.

The data were processed in RADAN 7 (GSSI 2012) by editing the initial positioning time zero, horizontal high, and low pass filtration, with background noise removal for the purpose of improving the resolution and interpretations of the compacted layers. The interpreted radar data (presence and depth to compacted layer) were used to generate a contour map in ArcMap (ESRI 2013). A polygon-type map was created by linear kriging and using the mean for duplicated positions in a simple type without data transformation and creating a contour map with depth to the compacted layer.

26.3 Results and Discussion

The 400 MHz antenna provided greater signal penetration than the 900 MHz antenna. However, signal scattering was severe with the 400 MHz antennas due to the presence of both a relatively high moisture content associated with the seasonal high water table (Fig. 26.2) and an argillic horizon with clay content ranging between 18 and 25 % (Fig. 26.3). Even though the signal penetration extended to a depth between 125 and 200 cm, soil features were not well defined and were masked by the signal noise.

The 900 MHz antenna provided slightly improved imagery of the subsurface (Figs. 26.4 and 26.5), even with a more noticeable amount of coarse fragments found in the Nixon soil (Fig. 26.6). In plot 1, with good standing pasture, no soil

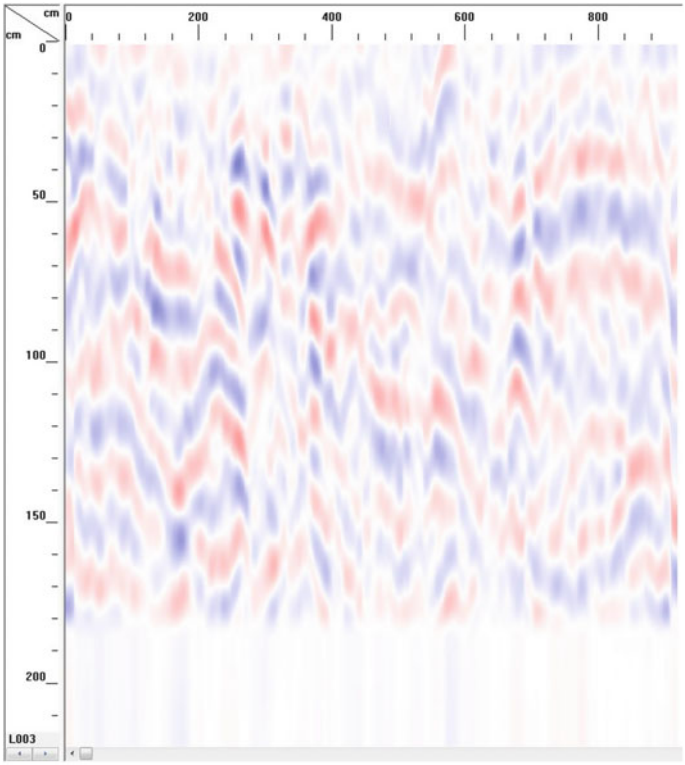

Fig. 26.2 Plot 1 400 MHz showing high reflectance as a result of a seasonal high water table. Horizontal and vertical scales are in cm

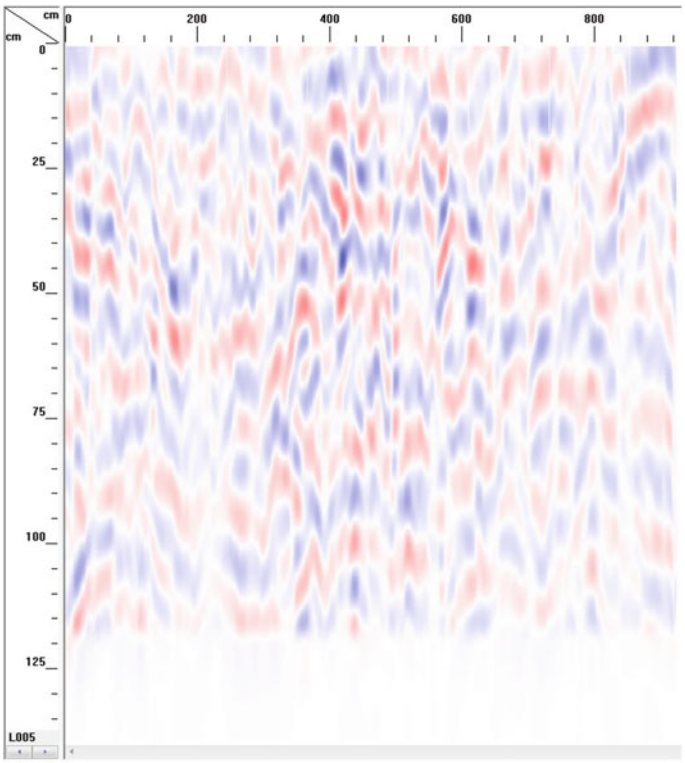

Fig. 26.3 Plot 2 400 MHz GPR readings showing high reflectance as a result of clay increase in the soil profile. Horizontal and vertical scales are in cm

compaction was detected with the exception of a very thin layer with platy soil structure that showed a higher dielectric near the surface. In addition, this soil had a higher moisture content compared to plot 2. Plot 1 was located in a lower position in the landscape and was likely less accessed by the horses due to its wetness. In plot 2, soil compaction was detected ranging in depth from 0 to 24 cm; this area included watering and feeding facilities in addition to the animal shelter. The compaction could also be associated with mechanical activities following reseeding of the pasture. Field observations detected a decrease in root abundance, distribution, and size between the Ap2 and Bt horizons (Fig. 26.6), thus supporting the interpretations from the GPR scan.

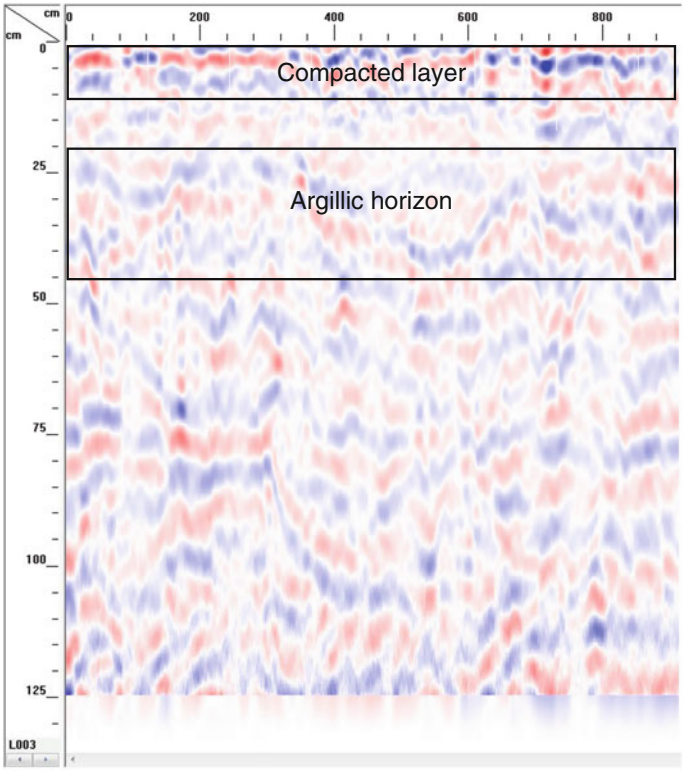

Fig. 26.4 Plot 1 900 MHz GPR reading showing a thin compacted layer and an argillic horizon. Horizontal and vertical scales are in cm

For the second part of the project, the data for the entire field showed an average depth of 8.7 cm to the top of a compacted layer (Table 26.1). A map was generated with the distribution of the depth to the compacted layer in 8-cm increments in relation to the topography (Fig. 26.7), which shows the general relationship between a higher dielectric and topography. With flat to slightly rolling topography, a discontinuous compacted layer at the soil surface was found over the argillic horizon, which began at about 24 cm in depth (Fig. 26.8). This topography is typical for an area that is wet for a prolonged time, with limited traffic, and also corresponds to the narrow corridor used to move the horses during the field rotation.

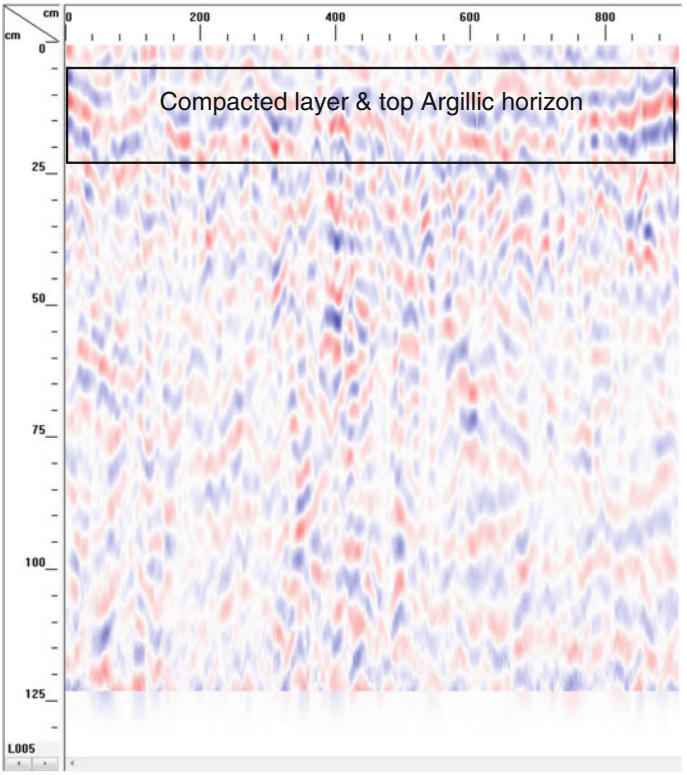

Fig. 26.5 Plot 2 900 MHz GPR reading showing compacted layer between 5 and 24 cm from the soil surface. Horizontal and vertical scales are in cm

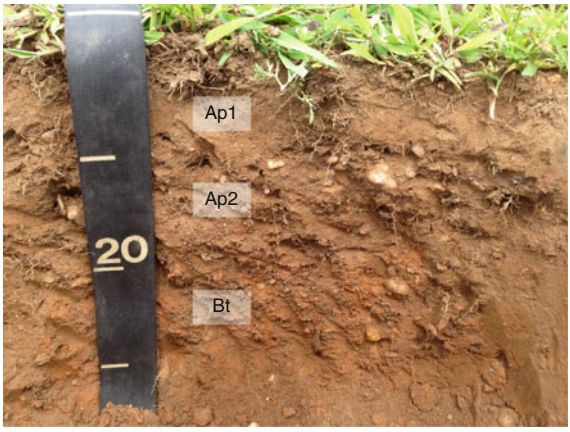

Fig. 26.6 Nixon soil profile for Plot 2 showing an increase in coarse fragments starting around 10 cm, an argillic horizon around 20 cm, and a decrease in root abundance, distribution, and size starting around 10 cm

Table 26.1 Descriptive statistics for the depth to compaction over the entire field detected with GPR

Depth (cm)	
Mean	8.7
Standard error	0.0128
Median	4.6
Mode	0
Standard deviation	10.6708
Sample variance	113.8666
Kurtosis	1.1645
Skewness	1.2933

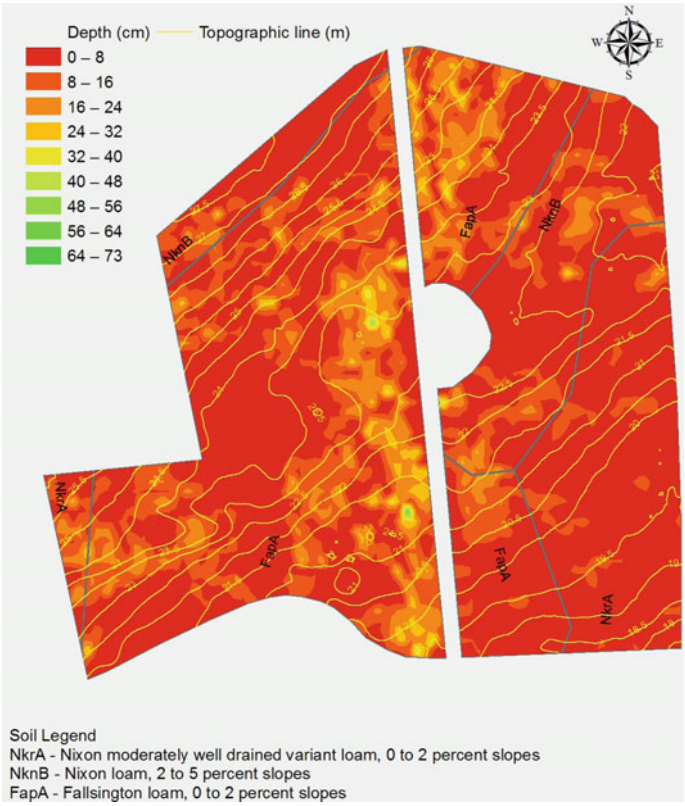

Fig. 26.7 Compacted zone distribution map generated using kriging. Showing depth to soil compaction in cm interpreted from the GPR

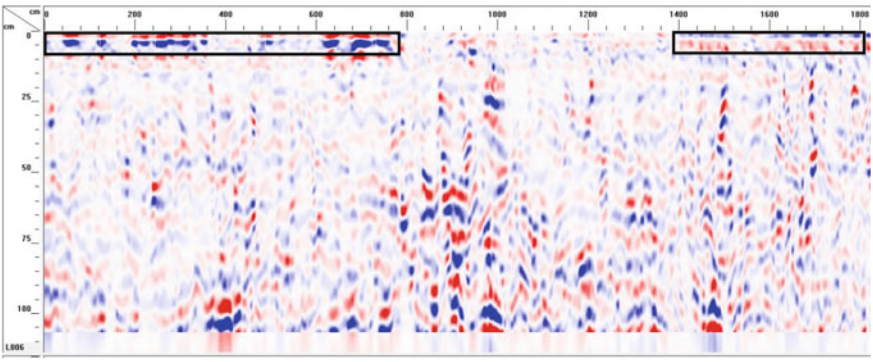

Fig. 26.8 Zone with discontinuous compacted layer with a high dielectric

26.4 Conclusions

In combination with field verification, ground-penetrating radar (GPR) is a valuable and diverse tool in the soil scientist's toolbox with the potential to be used in locating problematic areas and identifying the extent of soil compaction. In this investigation, results of the GPR correlated with the observations made in soil pits. Since GPR data do not provide information on the degree of soil compaction, calibration would be needed to use as a survey tool.

References

Cheng NF, Conrad Tang HW, Chan CT (2013) Identification and positioning of underground utilities using ground penetrating radar (GPR). Sustainable Environ Res 23(2):141–152

De Benedetto D, Castrignano A, Rinaldi M, Ruggieri S, Santoro F, Figorito B, Gualano S, Diacono M, Tamborrino R (2013) An approach for delineating homogeneous zones by using multi-sensor data. Geoderma 199:117–127

Doolittle JA, Butnor JR (2008) Chapter 6, soils, peatlands, and biomonitoring. 179–202 pp. In: Jol HM (ed) Ground penetrating radar: theory and applications. Elsevier, Amsterdam, The Netherlands

ESRI (2013) ArcGIS 10.2 for desktop: version 10.2.0.3348. Redlands, Environmental Systems Research Institute, CA

Freeland RS, Yoder RE, Ammons JT (1998) Mapping shallow underground features that influence site-specific agricultural production. J Appl Geophys 40:19–27

GSSI (2012) Radar data analyzer for windows: version 7.4.14.1113. Nashua, NH

IUSS Working Group WRB (2014) World reference base for soil resources 2014. International soil classification system for naming soils and creating legends for soil maps. World Soil Resources Reports No. 106. FAO, Rome

Miller PS (1996) Disturbances in the soil: finding buried bodies and other evidence using ground penetrating radar. J Forensic Sci 41(4):648–652

ONJSC (2014) New Jersey Agricultural Experiment Station. Northern New Jersey monthly precipitation. Available at: http://climate.rutgers.edu/stateclim/

Paterson DG, Laker MC (1996) Using ground penetrating radar to investigate spoil layers in rehabilitated minesoils. S Afr J Plant Soil 16(3):131–134

Petersen H, Fleige H, Rabbel W, Horn R (2006) Geophysical methods for imaging soil compaction and variability of soil texture on farm land. Adv Geol 38:261–272

Soil Survey Staff (1999) Soil taxonomy: a basic system of soil classification for making and interpreting soil surveys. 2nd edn. Natural resources conservation service. U.S. department of agriculture handbook 436

USDA NASS (2014) Census of agriculture. Available at: www.nass.usda.gov/

USDA-NRCS (2006). Land Resource regions and major land resource areas of the United States, the Caribbean, and the Pacific Basin. U.S. Department of Agriculture Handbook 296

Zobeck TM, Lyon JG, Mapes DR, Ritchie A Jr (1985) Calibrating ground penetrating radar data for soil applications. Soil Sci Soc Am J 49:1587–1590

Part V
Summary and Conclusions

Chapter 27
Developments in Digital Soil Morphometrics

Alfred E. Hartemink and Budiman Minasny

Abstract Digital soil morphometrics is defined as the application of instruments and techniques for measuring and mapping soil profile properties and deriving continuous depth functions. Here, we discuss some of the main results that were presented at the "Inaugural Global Workshop on Digital Soil Morphometrics" that was held in June 2015. We focus on instruments and techniques that have been used to measure soil properties in the field as well as in the laboratory, on modelling of soil depth functions, on the mapping of the soil profile (soil profile imaging) and on the use and applications of digital soil morphometrics. There have been considerable advancements in sampling and analysing soil profile properties in the field. Some instruments are restricted to dry soil, whereas others are affected by ambient light conditions. The mapping of the soil profile has yielded several methods to derive soil horizons and can deal with the variation within soil horizons. There are a certain number of soil depth functions that can be used for most soil properties and soil types. The use and application of digital soil morphometrics is mostly confined to enhanced pedological insight including soil classification, but with time, we envision that it can transform the way we observe, analyse and understand soils.

Keywords Pedology · Soil mapping · Morphology · Proximal soil sensing

A.E. Hartemink (✉)
Department of Soil Science, University of Wisconsin—Madison, FD Hole Soils Lab, 1525 Observatory Drive, Madison, WI 53706, USA
e-mail: alfred.hartemink@wisc.edu

B. Minasny
Department of Environmental Sciences, Faculty of Agriculture and Environment, The University of Sydney, Sydney, NSW 2006, Australia
e-mail: budiman.minasny@sydney.edu.au

A.E. Hartemink and B. Minasny (eds.), *Digital Soil Morphometrics*,
Progress in Soil Science, DOI 10.1007/978-3-319-28295-4_27

27.1 Introduction

The soil pit is at the core of many soil investigations. Although there are non-intrusive and less destructive ways of observing soils, the soil pit reveals a level of detail that is very hard to obtain by other methods. Soil profile descriptions have largely relied on morphometrics by which the soil properties are measured and visually observed and then combined with analytical data from samples taken to the laboratory into a full pedon description. Pedon descriptions were originally intended for soil mapping and soil classification purposes but now they are also being used in different soil studies including soil-landscape studies, site characterization and wider biophysical investigations (geomorphology, hydrology, etc.). Pedon descriptions are also an important input into the digital mapping of soils.

The horizon integrates many of the soil properties and processes. Delineation of soil horizons in the field is based on differences in soil texture, colour, coarse fragments, clay bridges, structural change, organic matter, mineralogy, concretions and accumulations, HCl effervescence or the effect of frosts. Some of these can be quantified with reasonable accuracy in the field and have been done so since the 1930s (Fig. 27.1). When samples have been taken of horizons and laboratory results obtained, the delineation becomes final. An accurate and objective description of the soil profile depends on the identification and exact delineation of soil horizons and an assessment of the within soil horizon variation. Pedon descriptions mostly occur at one side of the pit in a relatively narrow area (<20 cm). Commonly, one sample is taken of each horizon. All this has reduced our abilities to capture the horizontal (e.g. within horizons) as well the vertical variation in soil properties.

In 2014, we published a paper that brought together a range of new instruments and techniques by which the properties of soil profiles can be observed, measured and modelled. We coined the term "Digital soil morphometrics" which we defined as: the application of instruments and techniques for measuring and mapping soil profile properties and deriving continuous depth functions (Hartemink and Minasny 2014). Digital soil morphometrics is not restricted to in situ or in the soil pit measurements. It combines field observations and measurements with samples taken to the laboratory and also includes measurements on soil cores or soil monoliths (Fig. 27.2). Examples of such studies include Steffens and Buddenbaum (2013) and Roudier et al. (2016) who used NIR measurements and digital images to establish soil horizons and within profile variation. With a rapidly growing technology kit, in situ measurements of soil properties are on the increase but explorative and detailed data analysis remains a desk study.

In 2014, a working group was established of the *International Union of Soil Sciences* (IUSS) that held its inaugural global workshop in Madison, USA, in June 2015. In this chapter, we review the progress and developments in digital soil morphometrics largely based on what was presented at the workshop in 2015. We review the developments in the measurement of soil properties, mapping of the soil profile, the modelling of depth functions and the use and application of digital soil morphometrics.

Figure 1. Portable equipment for a rapid determination of soil texture by Cenco-Wilde method.

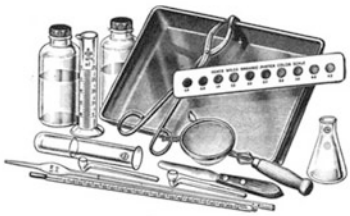

Figure 2. Equipment for the rapid colorimetric determination of soil organic matter.

Soil microscope with cross-slide stand attached to the wall of a soil pit; the leather box stores the battery for the oblique illuminator, from Kubiëna (1938)

Figure 13. Portable Beckman Model N potentiometer.

Figure 14. Hellige-Truog Soil Reaction Tester.

Fig. 27.1 Instruments used for assessing soil properties in the field: soil texture and SOM equipment, in situ soil micromorphology (Kubiëna 1938), portable N and pH metre. All instruments from before 1940

27.2 Measuring Soil Properties

The measurement of soil properties in the field has expanded largely through developments in proximal soil sensing. McBratney et al. (2011) defined proximal soil sensing through a variety of modalities: proximal or remote, in situ and ex situ (field and laboratory), non-invasive or intrusive and mobile or stationary. In digital soil morphometrics, proximal soil sensing is confined to in situ and ex situ stationary measurements of soil morphology and properties with depth. The portable XRF (pXRF) and vis-NIR have widely used in the measurement of elements and properties of soil profiles. Examples include Hseu et al. (2016) who used the pXRF to distinguish soils high in chromium and nickel, and Jones and McBratney (2016) who combined pXRF and vis-NIR to predict mineral composition and soil horizons. Stockmann et al. (2016) showed that Fe measured by pXRF depends on the moisture content of the soil and affected by the soil texture and mineralogy. A good correlation was found between field and laboratory measurements that potentially can be used for calibration of field measurements in different soils. Other instruments that have been used to measure field properties include a three-dimensional surface scanner that yields information on soil architecture, soil structure and porosity

Fig. 27.2 Some current instruments for assessing soil properties used in the field including digital photography, pXRF, 3D surface scanner (Hirmas et al. 2016) and vis-NIR

(Hirmas et al. 2016) and image analysis of topsoil properties by mobile phones that provides information on several soil fertility properties (Aitkenhead et al. 2016).

The range of soil properties that can be measured in the field is increasing and is affected by the technology as well as by the ambient conditions (light, soil moisture in particular) and the heterogeneity of the soil studied. The advantages of in situ soil property measurements are rapid assessment and interpretation of observations and no sampling and laboratory costs. Most digital soil morphometrics studies combine field measurements with data obtained in the laboratory and

detailed data analysis. The operational dimension of a pedon characterization needs to be developed; that includes the width and depth of the profile as well as measurements in the side wall.

27.3 Modelling Depth Functions

Every soil property has its own vertical distribution pattern and depth function that approximate the anisotropic character of soil properties (Jenny 1941). The traditional way of depicting depth function is by horizon; such data can then be used to fit a function and various functions have been used for different soil properties. These functions reflect a range of soil processes and the soil conditions that have resulted from these processes. Obvious examples include the accumulation of soil organic carbon in the topsoil yielding an exponential function or the accumulation of clay in the B horizon resulting in a peak function. Minasny et al. (2016) proposed six depth function typologies: uniform, gradational, duplex, exponential, wetting front, abrupt, peak and minima–maxima (Fig. 27.3). These depth functions can be related to most of the soil-forming processes (Bockheim and Gennadiyev 2000). Recent studies have used depth functions of electrical conductivity to delineate paleosols (Borchardt 2016) or to distinguish different groups of Ferralsols (Pinheiro et al. 2016). Soil profile data have also been used for probabilistic representation of soil horizons (Beaudette et al. 2016), and software has been developed to numerically and graphically summarize large pedon databases (Roecker et al. 2016). Given the importance of soil carbon research, several studies have compared different functions for the predicting of soil carbon (Bonfatti et al. 2016; Pereira et al. 2016).

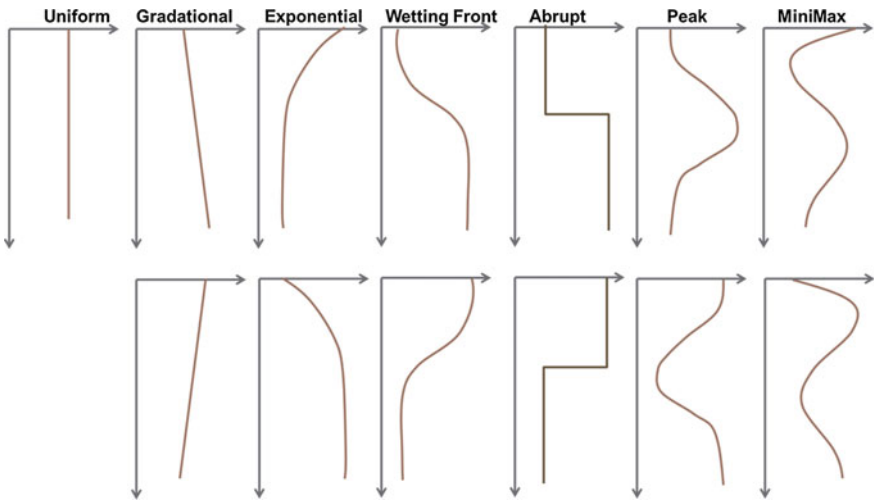

Fig. 27.3 General typologies of soil depth functions (Minasny et al. 2016)

Given the current trend, we envision that soil depth functions will continue to receive considerable research attention. Research will focus on rapid ways to determine a particular function for a particular soil property in a soil, and this will be greatly enhanced by new measurement instruments and techniques. Many of the new instruments and techniques allow for much finer sampling intervals by which the functions more realistically depict changes with depth, as well as assisting in the delineation of soil horizons and determination of major soil processes. The development of soil depth functions also plays an important role in the Universal Soil Classification System (Michéli et al. 2016).

27.4 Mapping the Soil Profile

The mapping of the soil profile, or soil profile imaging, has advanced through digital photogrammetry, fine scale sampling of the soil profile and laboratory analysis, and detailed analysis of monoliths take to the laboratory. The soil depth function can be considered a transect across the soil profile wall, whereas soil profile imaging is a map of the wall showing changes with depth as well variation across a specific depth. The mapping of the soil profile wall has been done for soil horizons as well as a range of soil properties. Roudier et al. (2016) combined digital images and NIR on three soil monoliths from New Zealand. The digital images were used to enhance the NIR readings and subsequent principal component analysis and image segmentation provided information about the soil horizons as well as the structure. Adhikari et al. (2016) and Grauer-Gray and Hartemink (2016) used 10 × 10 cm raster sampling of an Entisol and a Mollisol soil profile wall. The samples were scanned by pXRF, and the properties were kriged and clustered. The maps revealed horizon boundaries and showed considerable variation within each horizon for different properties. At a finer scale, Libohova et al. (2016) used image analysis of thin sections to estimate saturated hydraulic conductivity. Kim et al. (2016) used tabular pedon data to visualize soil structure and eventually soil profiles.

The mapping of the soil profile wall using hyperspectral images as well as fine scale sampled data from the profile wall provides insight in the changes with depth and variation within the soil horizon and treats the soil as a continuum in all directions. These studies showed that properties varied throughout the profile, and some questions were raised as to whether soil horizons are analogues to polygons in soil maps. Some of the theory and practice developed in digital soil mapping (spatial variation, clustering and regression kriging) is directly applicable. Direct image analysis is a rapidly evolving field that has not been fully explored in digital soil morphometrics.

27.5 Use and Applications

Digital soil morphometrics has been used to quantify soil properties and soil depth functions and to map variation across a soil profile wall. It brings insights into pedological processes and properties. The application and use is also emerging in several other fields including mapping (Dematte 2016). Examples include the mapping of eroded topsoils using a cone penetrometer (Arriaga et al. 2016), and the mapping of a compacted subsoil in pasture using GPR (Muniz et al. 2016). Digital soil morphometrics also has potential to be used in soil classification, and aspects are being used in the newly developing Universal Soil Classification System (Hempel et al. 2013; Michéli et al. 2016).

27.6 Conclusions

Many studies end with conclusions that essentially read as follows: (i) it depends, and (ii) we need more research. We are tempted to say something similar as the use of digital soil morphometrics is indeed site and soil dependent, and we do need more research to investigate its limitations and benefits. Some properties can be easily measured in the field and in certain soils, others are more cumbersome to measure but can be measured in any soil and under any condition (moisture, ambient light). A combination of instruments generally provides the most information, which may slow down the speed of the investigation but may yield the best results. With time, guidelines will be developed for measuring and sampling different properties and soils and under different conditions. Likewise, a suite of approaches for depth curves as well as decision trees for the mapping of soil properties over the entire soil wall will become available—just like we have in digital soil mapping. The within soil horizon variation and rapid ways to assess such variation may require substantial research and some of this can be conducted by using the existing pedon databases. Various studies have tackled this issue using soil monoliths or core samples. Other research questions include the sampling dimension of the soil profile wall, horizon assessment using NIR or XRF that aligns with the Universal Soil Classification System and improved methods for assessing soil structure. The use and application of digital soil morphometrics will exceed the pedology and soil classification purpose that it currently serves—it will be used in rapid soil assessment that is needed in a range of biophysical studies. In conclusion, we think that digital soil morphometrics has the potential to greatly enhance our understanding of soils and how we view them.

Acknowledgments We are grateful to all participants of the June 2015 Inaugural Global Workshop on Digital Soil Morphometrics for their sharing of ideas, results and the many fruitful discussions.

References

Adhikari K, Hartemink AE, Minasny B (2016) Mapping a Profile Wall of a Typic Udipsamments from the Central Sands in Wisconsin, USA. In: Hartemink AE, Minasny B (eds) Digital soil morphometrics. Springer, Dordrecht (this volume)

Aitkenhead MJ, Donnelly D, Coull M, Gwatkin R (2016) Estimating soil properties with a mobile phone. In: Hartemink AE, Minasny B (eds) Digital soil morphometrics. Springer, Dordrecht (this volume)

Arriaga FJ, Lowery B, Reinert D, McSweeney K (2016) Cone penetrometers as a tool for distinguishing soil profiles and mapping soil erosion. In: Hartemink AE, Minasny B (eds) Digital soil morphometrics. Springer, Dordrecht (this volume)

Beaudette DE, Roudier P, Skovlin J (2016) Probabilistic representation of genetic soil horizons. In: Hartemink AE, Minasny B (eds) Digital soil morphometrics. Springer, Dordrecht (this volume)

Bockheim JG, Gennadiyev AN (2000) The role of soil-forming processes in the definition of taxa in Soil Taxonomy and the World Soil Reference Base. Geoderma 95:53–72

Bonfatti BR, Hartemink AE, Giasson E (2016) Comparing soil C stocks from soil profile data using four different methods. In: Hartemink AE, Minasny B (eds) Digital soil morphometrics. Springer, Dordrecht (this volume)

Borchardt G (2016) Electrical conductivity depth functions for delineating paleosols. In: Hartemink AE, Minasny B (eds) Digital soil morphometrics. Springer, Dordrecht (this volume)

Dematte JAM (2016) From Profile morphometrics to digital soil mapping. In: Hartemink AE, Minasny B (eds) Digital soil morphometrics. Springer, Dordrecht (this volume)

Grauer-Gray J, Hartemink AE (2016) Variation of soil properties in a Mollisol profile wall. In: Hartemink AE, Minasny B (eds) Digital soil morphometrics. Springer, Dordrecht (this volume)

Hartemink AE, Minasny B (2014) Towards digital soil morphometrics. Geoderma 230–231:305–317

Hempel J, Micheli E, Owens P, McBratney A (2013) Universal soil classification system report from the International Union of Soil Sciences Working Group. Soil Horizons. doi:10.2136/sh12-12-0035

Hirmas DR, Gimenez D, Mome Filho EA, Drager K, Platt BF, Eck DV (2016) Quantifying soil structure and porosity using three-dimensional laser scanning In: Hartemink AE, Minasny B (eds) Digital soil morphometrics. Springer, Dordrecht (this volume)

Hseu Z-Y, Chen Z-S, Tsai C-C, Jien S-H (2016) Portable X-ray fluorescence (pXRF) for determining Cr and Ni contents of serpentine soils in the field. In: Hartemink AE, Minasny B (eds) Digital soil morphometrics. Springer, Dordrecht (this volume)

Jenny H (1941) Factors of soil formation. A system of quantitative pedology. McGraw-Hill, New York

Jones E, McBratney AB (2016) In situ analysis of soil mineral composition through conjoint use of visible, near-infrared and X-ray fluorescence spectroscopy. In: Hartemink AE, Minasny B (eds) Digital soil morphometrics. Springer, Dordrecht (this volume)

Kim H, Dorantes M, Schulze DL, Benes B (2016) Computer graphics procedural modeling of soil structure. In: Hartemink AE, Minasny B (eds) Digital soil morphometrics. Springer, Dordrecht (this volume)

Kubiëna WL (1938) Micropedology. Collegiate Press, Ames, Iowa

Libohova Z, Schoeneberger PJ, Owens P, Wills S, Wysocki DA, Williams C, Seybold C (2016) Comparative analysis of Saturated Hydraulic Conductivity (Ksat) derived from image analysis of soil thin sections, pedotransfer functions, and field-measured methods. In: Hartemink AE, Minasny B (eds) Digital soil morphometrics. Springer, Dordrecht (this volume)

McBratney A, Minasny B, Whelan B (2011) Defining proximal soil sensing. The second global workshop on proximal soil sensing—Montreal, 15–18 May 2011

Michéli E, Láng V, Owens PR, McBratney A, Hempel J (2016) Testing the pedometric evaluation of taxonomic units on soil taxonomy—A step in advancing towards a universal soil classification system. Geoderma

Minasny B, Stockmann U, Hartemink AE, McBratney A (2016) Measuring and modelling soil depth functions In: Hartemink AE, Minasny B (eds) Digital soil morphometrics. Springer, Dordrecht (this volume)

Muniz E, Shaw RK, Gimenez D, Williams C, Kenny L (2016) Use of ground penetrating radar to determine depth to compacted layer in soils under pasture In: Hartemink AE, Minasny B (eds) Digital soil morphometrics. Springer, Dordrecht (this volume)

Pereira OJR, Montes CR, Lucas Y, Melfi AJ (2016) Evaluation of pedotransfer equations to predict deep soil carbon stock in tropical podzols compared to other soils of the Brazilian Amazon forest. In: Hartemink AE, Minasny B (eds) Digital soil morphometrics. Springer, Dordrecht (this volume)

Pinheiro HSK, de Carvalho W, da Silva Chagas C, dos Anjos LHC, Owens PR (2016) Using soil depth functions to help separate Dystric from Xanthic Ferralsols in the landscape. In: Hartemink AE, Minasny B (eds) Digital soil morphometrics. Springer, Dordrecht (this volume)

Roecker S, Skovlin J, Beaudette DE, Wills S (2016) Digital summaries of pedon descriptions. In: Hartemink AE, Minasny B (eds) Digital soil morphometrics. Springer, Dordrecht (this volume)

Roudier P, Manderson A, Hedley C (2016) Advances towards quantitative assessments of soil profile properties. In: Hartemink AE, Minasny B (eds) Digital soil morphometrics. Springer, Dordrecht (this volume)

Steffens M, Buddenbaum H (2013) Laboratory imaging spectroscopy of a stagnic Luvisol profile—High resolution soil characterisation, classification and mapping of elemental concentrations. Geoderma 195:122–132

Stockmann U, Jun Jang H, Minasny B, McBratney AB (2016) The effect of soil moisture and texture on Fe concentration using portable X-ray fluorescence spectrometers. In: Hartemink AE, Minasny B (eds) Digital soil morphometrics. Springer, Dordrecht (this volume)

Index

A.E. Hartemink and B. Minasny (eds.), *Digital Soil Morphometrics*,
Progress in Soil Science, DOI 10.1007/978-3-319-28295-4